

NON-COVALENT INTERACTIONS  
IN QUANTUM CHEMISTRY AND PHYSICS:  
THEORY AND APPLICATIONS

---



# NON-COVALENT INTERACTIONS IN QUANTUM CHEMISTRY AND PHYSICS: THEORY AND APPLICATIONS

---

*Edited by*

ALBERTO OTERO DE LA ROZA  
GINO A. DiLABIO



Elsevier

Radarweg 29, PO Box 211, 1000 AE Amsterdam, Netherlands  
The Boulevard, Langford Lane, Kidlington, Oxford OX5 1GB, United Kingdom  
50 Hampshire Street, 5th Floor, Cambridge, MA 02139, United States

Copyright © 2017 Elsevier Inc. All rights reserved.

No part of this publication may be reproduced or transmitted in any form or by any means, electronic or mechanical, including photocopying, recording, or any information storage and retrieval system, without permission in writing from the publisher. Details on how to seek permission, further information about the Publisher's permissions policies and our arrangements with organizations such as the Copyright Clearance Center and the Copyright Licensing Agency, can be found at our website: [www.elsevier.com/permissions](http://www.elsevier.com/permissions).

This book and the individual contributions contained in it are protected under copyright by the Publisher (other than as may be noted herein).

#### Notices

Knowledge and best practice in this field are constantly changing. As new research and experience broaden our understanding, changes in research methods, professional practices, or medical treatment may become necessary.

Practitioners and researchers must always rely on their own experience and knowledge in evaluating and using any information, methods, compounds, or experiments described herein. In using such information or methods they should be mindful of their own safety and the safety of others, including parties for whom they have a professional responsibility.

To the fullest extent of the law, neither the Publisher nor the authors, contributors, or editors, assume any liability for any injury and/or damage to persons or property as a matter of products liability, negligence or otherwise, or from any use or operation of any methods, products, instructions, or ideas contained in the material herein.

#### Library of Congress Cataloging-in-Publication Data

A catalog record for this book is available from the Library of Congress

#### British Library Cataloguing-in-Publication Data

A catalogue record for this book is available from the British Library

ISBN: 978-0-12-809835-6

For information on all Elsevier publications visit our website at  
<https://www.elsevier.com/books-and-journals>



*Publisher:* John Fedor  
*Acquisition Editor:* John Fedor  
*Editorial Project Manager:* Sarah Watson  
*Production Project Manager:* Maria Bernard  
*Designer:* Victoria Pearson

Typeset by VTeX

*To our colleagues*

# Contributors

---

- Gregory J.O. Beran** Department of Chemistry, University of California Riverside, Riverside, CA, USA
- Kristian Berland** Centre for Materials Science and Nanotechnology, SMN, University of Oslo, Oslo, Norway
- Jan Gerit Brandenburg** Department of Chemistry, University College London, London, UK
- Jean-Luc Brédas** Laboratory for Computational and Theoretical Chemistry of Advanced Materials, Division of Physical Science and Engineering, King Abdullah University of Science and Technology, Thuwal, Saudi Arabia
- Valentino R. Cooper** Materials Science and Technology Division, Oak Ridge National Laboratory, Oak Ridge, TN, USA
- Gino A. DiLabio** Department of Chemistry, The University of British Columbia, Kelowna, BC, Canada
- Michael J. Ford** School of Mathematical and Physical Sciences, University of Technology Sydney, Sydney, Australia
- E. Francisco** Departamento de Química Física y Analítica, Facultad de Química, Universidad de Oviedo, Oviedo, Spain
- Lars Goerigk** School of Chemistry, The University of Melbourne, Melbourne, Australia
- Tim Gould** Queensland Micro- and Nanotechnology Centre, Griffith University, Nathan, Australia
- Joshua D. Hartman** Department of Chemistry, University of California Riverside, Riverside, CA, USA
- Yonaton N. Heit** Department of Chemistry, University of California Riverside, Riverside, CA, USA
- Andreas Heßelmann** Lehrstuhl für Theoretische Chemie, Universität Erlangen-Nürnberg, Erlangen, Germany
- Per Hyldgaard** Microtechnology and Nanoscience, MC2, Chalmers University of Technology, Göteborg, Sweden
- Erin R. Johnson** Department of Chemistry, Dalhousie University, Halifax, NS, Canada
- Christopher N. Lam** Center for Nanophase Materials Science, Oak Ridge National Laboratory, Oak Ridge, TN, USA
- Musen Li** International Centre for Quantum and Molecular Structure, College of Sciences, Shanghai University, Shanghai, China
- Bengt I. Lundqvist** Department of Physics, Chalmers University of Technology, Göteborg, Sweden
- A. Martín Pendás** Departamento de Química Física y Analítica, Facultad de Química, Universidad de Oviedo, Oviedo, Spain
- Benedetta Mennucci** Department of Chemistry, University of Pisa, Pisa, Italy
- Sarah L. Price** Department of Chemistry, University College London, London, UK
- Mahesh Kumar Ravva** Laboratory for Computational and Theoretical Chemistry of Advanced Materials, Division of Physical Science and Engineering, King Abdullah University of Science and Technology, Thuwal, Saudi Arabia
- Jeffrey R. Reimers** International Centre for Quantum and Molecular Structure, College of Sciences, Shanghai University, Shanghai, China; School of Mathematical and Physical Sciences, University of Technology Sydney, Sydney, Australia
- Chad Risko** Department of Chemistry and Center for Applied Energy Research, University of Kentucky, Lexington, KY, USA
- Elsebeth Schröder** Microtechnology and Nanoscience, MC2, Chalmers University of Technology, Göteborg, Sweden

**C. David Sherrill** Center for Computational Molecular Science and Technology, School of Chemistry and Biochemistry, and School of Computational Science and Engineering, Georgia Institute of Technology, Atlanta, GA, USA

**Anthony J. Stone** University Chemical Laboratory, University of Cambridge, Cambridge, UK

**Bobby G. Sumpter** Center for Nanophase Materials Science, Oak Ridge National Laboratory, Oak Ridge, TN, USA

**Timo Thonhauser** Department of Physics, Wake Forest University, Winston-Salem, NC, USA;  
Department of Chemistry, Massachusetts Institute of Technology, Cambridge, MA, USA

**Dongya Wan** International Centre for Quantum and Molecular Structure, College of Sciences, Shanghai University, Shanghai, China

**Yangyang Wang** Center for Nanophase Materials Science, Oak Ridge National Laboratory, Oak Ridge, TN, USA

# Foreword

---

In 2004, I attended a seminar by Mark Ratner in which he delivered this memorable introduction: “Chemistry of the 20th century was about intramolecular interactions; chemistry of the 21st century will be about intermolecular interactions.” The present volume is an inspiring look at the promise of computational chemistry in the 21st century. It deals with molecular crystals, surfaces, biological complexes, etc., all dominated by noncovalent van der Waals (vdW) or dispersion interactions, the weakest and computationally most challenging interactions in nature. Each of the various chapters is a comprehensive review of its subject area. There are chapters on fundamental physical principles, computational approaches rooted both in wavefunction theory (WFT) and density-functional theory (DFT), visualization tools, and applications.

The applications range from crystal polymorph prediction, to the structures of organic electronic materials, to adsorption of molecules on metal surfaces. The scale of these applications was unimaginable for computational scientists even 10 or 15 years ago. Circa 2000, model force fields were the only viable approach to large-scale computations involving noncovalent interactions. The deficiencies were severe. How should the numerous required parameters be obtained? Even after obtaining them, how can changes in the chemical environment of each atom be conveyed?

The first nonempirical DFT-based strategy for computing intermolecular interactions appeared circa 2004 (“vdW-DF”). This

is a beautifully seamless density-functional method with electron gas theory at its heart. In 2005, the first nonempirical DFT method for computing pairwise interatomic dispersion coefficients for atoms in molecules (“XDM”) was introduced. XDM uses the position-dependent dipole moment of each electron and its exchange hole to generate the dispersion interactions. Other nonempirical DFT approaches with the power to sense chemical environments rapidly followed.

These developments were dramatic and timely. Density-functional theory was our prime hope for computations on very large systems in chemistry, biology, materials and surface science. Since the mid 1980s, progress in density functionals for intramolecular bonding and molecular structure had revolutionized quantum chemistry. Without the inherent ability to describe noncovalent interactions, however, DFT was doomed. The decade from 2000 to 2010 marked a welcome DFT resurgence.

The interplay between WFT and DFT was, at the time, critical, and continues to be. It is WFT that provides the necessary reference data on which to assess developments in DFT. The early “S22” and “S66” intermolecular WFT data sets were invaluable. The number and diversity of reference data sets continues to grow, and now includes molecular crystal data extracted from experimental sublimation enthalpies.

The chapters in this volume address all of the above and more. It has been an exhilarat-



ing 15 years (or so) as the computational science of noncovalent interactions has adapted

itself to the 21st-century future. You will find an excellent overview here.

Axel D. Becke  
Dalhousie University, Halifax, Canada  
October 2016

# Physical Basis of Intermolecular Interactions

---

*Anthony J. Stone*

University Chemical Laboratory, University of Cambridge, Cambridge, UK

## 1.1 INTRODUCTION

---

Noncovalent interactions occur everywhere: in interactions between molecules in gases, liquids and solid materials of all kinds, but also between parts of large molecules such as proteins. Understanding and predicting the behavior of such systems calls for a detailed physical understanding of the nature of these interactions, and their behavior as functions of the separation and relative orientation of the molecules.

While methods are available to calculate interaction energies between molecules to high accuracy, such methods are usually impracticable for applications such as simulations of large molecules or large numbers of small molecules. In many applications there is a conflict between accuracy and computational efficiency, so it is important to find an appropriate compromise. In such cases accurate calculations are needed as a basis for deriving simplified models. It was usual in the past to fit model parameters to empirical data, but it is difficult to obtain enough satisfactory data in this way, and it is generally better to derive the models from *ab initio* calculations and to test them, and perhaps refine them, by reference to the empirical data. An understanding of the theoretical basis for the interaction is also helpful in finding the best form for the model potential function.

This chapter provides an overview of the general ideas underlying the calculation of intermolecular interactions. For more details the reader is referred to Ref. [1]. We deal here only with the most common case, of closed-shell molecules in nondegenerate ground states, and we develop the concepts from a perturbation-theory viewpoint. An alternative approach is energy decomposition analysis, which will be treated in Chapter 2.

### 1.1.1 Pairwise Additivity

When dealing with an assembly of several molecules, it is usually impractical to treat the system as a whole. Instead we usually start by assuming *pairwise additivity*: that is, the total

energy of the system is calculated as a sum of interaction energies between pairs of molecules:

$$W = \sum_i W_i + \sum_{i>j} E_{ij}. \quad (1.1)$$

Here  $W_i$  is the energy of the isolated molecule  $i$ , and  $E_{ij}$  is the interaction energy between the pair  $i$  and  $j$  taken in the absence of other molecules but in the geometry that they have in the whole system. The notation for the second sum indicates that we sum over both  $i$  and  $j$ , but include only terms with  $i > j$  so as to avoid double-counting.

Eq. (1.1) is often a good approximation, and sometimes exact. If so, we say that the interaction is *pairwise additive*. Often, however, it is not good enough, especially if we need high accuracy, and then we have to add correction terms:

$$W = \sum_i W_i + \sum_{i>j} E_{ij} + \sum_{i>j>k} E_{ijk} + \sum_{i>j>k>l} E_{ijkl} + \dots \quad (1.2)$$

$E_{ijk}$  is the three-body correction needed to the pairwise sum  $E_{ij} + E_{jk} + E_{ik}$  to get the energy correct for the set of three molecules  $\{i, j, k\}$  in the absence of the other molecules but in the geometry that they have in the whole system.  $E_{ijkl}$  is a four-body correction, and so on. This formulation is only useful if the series converges very quickly, as the number of correction terms in each sum increases very rapidly. Fortunately, it often converges quickly enough to be useful, though there are cases, especially when polar polarizable molecules are involved, as, for example, in hydrogen bonding, where the higher many-body corrections cannot be ignored.

### 1.1.2 Perturbation Theory

Covalent binding energies are typically of the order of a few eV (a few hundred kJ/mol), as are the excitation energies of typical closed-shell molecules, but noncovalent interaction energies are of the order of a few tens of kJ/mol or less. Consequently perturbation theory is a useful tool in the study of noncovalent interactions, and indeed has been used for this purpose since London's pioneering work in the 1930s [2,3]. It works well and generally gives good results at second order, though some effects need higher-order terms.

When a pair of interacting molecules  $A$  and  $B$  are far enough apart that overlap between their wavefunctions can be ignored, we can write the unperturbed wavefunctions  $\Psi_{ij}^{AB}$  for the combined system as simple products of the wavefunctions for the individual molecules:

$$\Psi_{ij}^{AB} = \Psi_i^A(\mathbf{q}_A) \times \Psi_j^B(\mathbf{q}_B), \quad (1.3)$$

where  $\mathbf{q}_A$  represents the set of coordinates for the particles (electrons and nuclei) of molecule  $A$ , and likewise for molecule  $B$ . (See below for the justification of this.)  $\Psi_i^A(\mathbf{q}_A)$  is one of the wavefunctions for molecule  $A$ , and satisfies  $\mathcal{H}^A \Psi_i^A = E_i^A \Psi_i^A$ , where the Hamiltonian  $\mathcal{H}^A$  depends on the coordinates  $\mathbf{q}_A$  and their conjugate momenta. All of this applies similarly to molecule  $B$ .

The unperturbed Hamiltonian is then just the sum of the individual Hamiltonians:

$$\mathcal{H}_0 = \mathcal{H}^A(\mathbf{q}_A) + \mathcal{H}^B(\mathbf{q}_B), \quad (1.4)$$

each individual Hamiltonian depending only on the coordinates of its own nuclei and electrons, and their associated momenta. The perturbation comprises the electrostatic interactions between the particles of  $A$  and those of  $B$ :

$$\mathcal{H}' = \sum_{a \in A} \sum_{b \in B} \frac{e_a e_b}{4\pi \epsilon_0 r_{ab}}, \quad (1.5)$$

where  $e_a$  and  $e_b$  are the charges on particles  $a$  and  $b$  and  $r_{ab}$  is the distance between them.

The ground-state energy of the system at zeroth order is the sum of the energies of the isolated molecules. The first-order energy is  $\langle \Psi_{00}^{AB} | \mathcal{H}' | \Psi_{00}^{AB} \rangle$ , and is just the classical electrostatic interaction energy between the molecular charge distributions. For the second-order energy, still at large separations, we apply the usual formula from perturbation theory:

$$E^{(2)} = - \sum'_{ij} \frac{\langle 00 | \mathcal{H}' | ij \rangle \langle ij | \mathcal{H}' | 00 \rangle}{E_{ij} - E_{00}}, \quad (1.6)$$

where  $|ij\rangle \equiv |\Psi_{ij}^{AB}\rangle$ , and the prime on the sum conventionally indicates that the sum is over all states except the ground state  $ij = 00$ . It is customary to separate this into three terms, one where  $j = 0$  (that is, molecule  $B$  is in its ground state), one where  $i = 0$  and the third where neither is zero:

$$E_{\text{ind}}^A = - \sum_{i \neq 0} \frac{\langle 00 | \mathcal{H}' | i0 \rangle \langle i0 | \mathcal{H}' | 00 \rangle}{E_{i0} - E_{00}}, \quad (1.7)$$

$$E_{\text{ind}}^B = - \sum_{j \neq 0} \frac{\langle 00 | \mathcal{H}' | 0j \rangle \langle 0j | \mathcal{H}' | 00 \rangle}{E_{0j} - E_{00}}, \quad (1.8)$$

$$E_{\text{disp}} = - \sum_{i \neq 0, j \neq 0} \frac{\langle 00 | \mathcal{H}' | ij \rangle \langle ij | \mathcal{H}' | 00 \rangle}{E_{ij} - E_{00}}. \quad (1.9)$$

These are respectively the second-order induction energy of  $A$  in the field of  $B$ , the second-order induction energy of  $B$  in the field of  $A$ , and the second-order dispersion energy.

This formulation does not yet take account of the fact that electrons are indistinguishable. The full Hamiltonian  $\mathcal{H} = \mathcal{H}_0 + \mathcal{H}'$  is symmetric with respect to exchange of electrons between the molecules, but the wavefunction  $\Psi = \Psi_0^A \Psi_0^B$  does not take account of this symmetry: it should be antisymmetric with respect to all electron permutations, according to the Pauli principle, but it is not. The individual  $\Psi_0^A$  and  $\Psi_0^B$  are antisymmetric with respect to permutations of their own electrons, but the product is not antisymmetric with respect to permutations that exchange electrons between the molecules. We should use the antisymmetrized wavefunction  $\mathcal{A}\Psi$ , where the antisymmetrizer  $\mathcal{A} = (N!)^{-1} \sum_P (-1)^P P$  is a sum over all the  $N!$  permutations of the  $N$  electrons, with a sign change for odd permutations.

The energy expression  $\langle \Psi | \mathcal{H} | \Psi \rangle / \langle \Psi | \Psi \rangle$  has to be replaced by  $\langle \Psi | \mathcal{A} \mathcal{H} \mathcal{A} | \Psi \rangle / \langle \Psi | \mathcal{A} \mathcal{A} | \Psi \rangle$ . Since  $\mathcal{A}$  commutes with  $\mathcal{H}$  and  $\mathcal{A}^2 = \mathcal{A}$ , this reduces to  $\langle \Psi | \mathcal{H} \mathcal{A} | \Psi \rangle / \langle \Psi | \mathcal{A} | \Psi \rangle$ .

However, if the molecules are far enough apart this does not change the energy, because the extra terms contribute nothing. To see why, consider two helium atoms, initially well separated, with electrons 1 and 2 on atom  $A$  and electrons 3 and 4 on atom  $B$ . We write the ground state as  $|12; 34\rangle$ . This is antisymmetric with respect to interchange of electron 1 with 2, or 3 with 4, but not with respect to all electron permutations that exchange electrons between the atoms. Antisymmetrization introduces terms like  $\langle 12; 34 | \mathcal{H} | 13; 24 \rangle$ , in which electrons 2 and 3 are exchanged in the right-hand factor, so that electron 2 is on atom  $A$  in the left-hand factor and on atom  $B$  in the right-hand factor. At long range the overlap between these is entirely negligible and the integral over electron 2 vanishes. The same applies to electron 3. Consequently the contribution to the whole integral is zero. The only term that survives is  $\langle 12; 34 | \mathcal{H} | 12; 34 \rangle$ , with the same electron assignments on both sides, so the result is the same for the fully antisymmetrized wavefunction as for  $|12; 34\rangle$  alone, with no exchanges.

When the atoms approach more closely, however, the “exchange” terms such as  $\langle 12; 34 | \mathcal{H} | 13; 24 \rangle$  are no longer negligible. If the overlap between the wavefunctions of the two atoms is of order  $S$ , then the overall matrix element involves a factor of the order of  $S$  for each electron involved in an exchange. Here 2 and 3 are exchanged, so there is a factor  $S^2$  in the integral. Since  $S$  decays exponentially with increasing distance, these additional terms also decay exponentially.

Many methods have been proposed for dealing with the effects of exchange in intermolecular interactions. The following chapter gives a full discussion. The currently favored method is symmetry-adapted perturbation theory (SAPT) [4–6] or the variants SAPT(DFT) [7–9] and DFT-SAPT [10–12] based on density functional theory (equivalent but derived independently).

In this approach, the perturbation expansion is carried out without exchange, each molecule retaining its own electrons, but each term in the resulting wavefunction is antisymmetrized with respect to the electrons before the energy is evaluated. The consequence is that there is still an analogue of each long-range term, arising from those permutations of the electrons that leave each electron on its original molecule, and an exchange correction, which is the rest of the energy of the antisymmetrized term. At first order, the exchange correction is the familiar Pauli closed-shell repulsion. At second order, there are exchange-dispersion and exchange-induction terms.

In the original SAPT method, the wavefunctions for the individual molecules are obtained from Hartree–Fock calculations, using perturbation theory to describe the intramolecular electron correlation for each molecule as well as the intermolecular interaction, so that the whole method becomes a triple perturbation theory. In the DFT variants, intramolecular correlation is described by the exchange-correlation functional, so the treatment becomes much simpler, and it also turns out to be as accurate and sometimes better.

Symmetry-adapted perturbation theory is discussed in more detail in the next chapter, but before moving on let us note that the basis set for each molecule may comprise atomic basis functions on its own atoms only (a “monomer-centered” or MC basis), or on the atoms of both molecules (a “dimer-centered” or DC basis) and in either case may include additional “mid-bond” basis functions in the region between the molecules. In every case, the same

basis set is used for the individual molecules and the dimer, so the possibility of basis-set superposition error (BSSE) does not arise [1].

### 1.1.3 Classification of Interactions

The long-range effects are of three kinds: *electrostatic*, *induction*, and *dispersion*. The electrostatic effect is the simplest to understand in general terms: it is the first-order energy in perturbation theory and describes the straightforward classical interaction between the static charge distributions of the two molecules. It is strictly pairwise additive and may be either attractive or repulsive. Induction effects arise from the distortion of a particular molecule in response to the electric field of all its neighbors, and are always attractive. Because the fields of several neighboring molecules may reinforce each other or cancel out, induction is strongly nonadditive. Dispersion is an effect that cannot easily be understood in classical terms, but it arises because the charge distributions of the molecules are constantly fluctuating as the electrons move. The motions of the electrons in the two molecules become correlated, in such a way that lower-energy configurations are favored and higher-energy ones disfavored. The average effect is a lowering of the energy, and since the correlation effect becomes stronger as the molecules approach each other, the result is an attraction.

All of these effects derive ultimately from the electrostatic interaction (Eq. (1.5)), which at long range can be expanded as a power series in  $1/R$ , where  $R$  is the distance between the molecules. Consequently the long-range energies can also be expressed as power series in  $1/R$ .

Two other effects that can arise at long range are resonance and magnetic effects. Resonance interactions occur either when at least one of the molecules is in a degenerate state—usually an excited state—or when the molecules are identical and one is in an excited state. Consequently they do not occur between ordinary closed-shell molecules in their ground states, and they will not be discussed further here. Magnetic interactions involving the electrons can occur only when both molecules have unpaired spins, but in any case are small. Magnetic interactions involving nuclei can occur whenever there are nuclei with nonzero spin, which is quite common, but the energies are several orders of magnitude smaller still, and are never of any significance in the context of intermolecular forces.

At short range the extra “exchange” terms have to be included. The most important is described as exchange-repulsion or just exchange. It is a correction to the first-order energy of long-range perturbation theory, and can be thought of in physical terms as comprising two effects: an attractive part, arising because the electrons become free to move over both molecules rather than just one, increasing the uncertainty in their positions and so allowing the momentum and energy to decrease; and a repulsive part, arising because the wavefunction has to adapt to maintain the Pauli antisymmetry requirement that electrons of the same spin may not be in the same place, and this costs energy. The latter dominates, leading to a repulsive effect overall. It is usual to take these effects together. The second-order exchange terms, exchange-induction and exchange-dispersion, are generally somewhat smaller than the exchange-repulsion, but they are far from negligible, especially as the total interaction energy is the result of cancellation between positive and negative terms and is often smaller than many of the individual terms. Another short-range term is the charge-transfer energy, but in SAPT it arises as part of the induction energy. All the exchange terms depend on the

overlap between the molecular wavefunctions, so they decay exponentially with increasing separation.

The behavior of the long-range terms is further modified at short range by penetration effects, arising from the overlap of the molecular charge distributions. This is discussed further below.

## 1.2 ELECTROSTATIC INTERACTIONS

The electrostatic interaction between molecules  $A$  and  $B$  is the expectation value of the operator  $\mathcal{H}'$  given in Eq. (1.5) above, and is just the classical interaction between the unperturbed molecular charge distributions  $\rho_A$  and  $\rho_B$ , which can be written in several ways:

$$E_{\text{es}}^{AB} = \int \frac{\rho_A(\mathbf{r})\rho_B(\mathbf{r}')}{4\pi\epsilon_0|\mathbf{r}-\mathbf{r}'|} d^3\mathbf{r} d^3\mathbf{r}' = \int \rho_A(\mathbf{r})V_B(\mathbf{r}) d^3\mathbf{r} = \int \rho_B(\mathbf{r}')V_A(\mathbf{r}') d^3\mathbf{r}'. \quad (1.10)$$

That is, it can also be viewed as the energy of  $A$  in the electrostatic potential  $V_B$  due to  $B$ :

$$V_B(\mathbf{r}) = \int \frac{\rho_B(\mathbf{r}')}{4\pi\epsilon_0|\mathbf{r}-\mathbf{r}'|} d^3\mathbf{r}', \quad (1.11)$$

or as the energy of  $B$  in the electrostatic potential due to  $A$ . This energy is well defined at any distance, and is easily computed exactly from the wavefunctions for the interacting molecules  $A$  and  $B$ . It is important, however, that the wavefunctions are calculated as accurately as possible, and in particular it is important, if density functional theory is used, to apply an asymptotic correction [13,14] to the exchange-correlation potential. If this is not done, the long-range limit of the exchange-correlation potential will usually be incorrect, and the charge densities too diffuse. Many ab initio programs do not apply any asymptotic correction by default, and some do not offer it at all.

In any case the direct evaluation of Eq. (1.10) is not practical in many applications, such as simulations of liquids. Instead we describe the charge distribution and the resulting electrostatic potential in terms of its *multipole moments*. The charge  $q$  is just the total charge:

$$q = \int \rho(\mathbf{r}) d^3\mathbf{r}, \quad (1.12)$$

while the electric dipole moment vector  $\mu_\alpha$  is

$$\mu_\alpha = \int r_\alpha \rho(\mathbf{r}) d^3\mathbf{r}, \quad (1.13)$$

where  $\alpha = x, y$  or  $z$  and  $r_\alpha$  is a component of the position vector  $\mathbf{r}$ . This is a classical viewpoint; from a quantum mechanical viewpoint we regard the dipole moment as an operator  $\hat{\mu}_\alpha = e r_\alpha$  and write Eq. (1.13) as  $\mu_\alpha = \langle \Psi | \hat{\mu}_\alpha | \Psi \rangle$ . Molecular dipoles arise from the movement of electron density from less electronegative to more electronegative atoms when bonds are formed, but also from asymmetry of the electron distribution around individual atoms.

The quadrupole moment  $\Theta_{\alpha\beta}$  is a little more complicated. If we write

$$M_{\alpha\beta} = \int r_{\alpha} r_{\beta} \rho(\mathbf{r}) d^3\mathbf{r} \quad (1.14)$$

then  $\Theta_{\alpha\beta} = \frac{3}{2}M_{\alpha\beta} - \frac{1}{2}M_{\gamma\gamma}\delta_{\alpha\beta}$ . We are using Einstein's repeated-suffix summation convention, where a repeated suffix is automatically summed over, so that  $M_{\gamma\gamma} \equiv \sum_{\gamma} M_{\gamma\gamma} = M_{xx} + M_{yy} + M_{zz}$ .  $\Theta_{\alpha\beta}$  is defined in this "traceless" form (that is, so that  $\Theta_{\alpha\alpha} = 0$ ) because the trace  $M_{\gamma\gamma}$  does not occur in the multipole expression for the electrostatic energy.

Quadrupole moments arise where positive and negative charge density occur in alternate quadrants of space. For a water molecule aligned with its symmetry axis along the  $z$  direction and the H atoms in the  $xz$  plane, for example, there is a surplus of positive charge around the H atoms and a surplus of negative charge in the lone pairs, which are near the  $yz$  plane, so the water molecule has a substantial  $\Theta_{xx} - \Theta_{yy}$  quadrupole moment. Another example is  $\text{CO}_2$ , where the O atoms are negatively charged and relatively far from the origin, while the positively charged C atom is at the origin. Consequently if  $\text{CO}_2$  is aligned along the  $z$  axis,  $\Theta_{zz}$  is large and negative.

An important source of quadrupole moment comes from  $\pi$  electrons. A single occupied  $\pi_z$  orbital has its electron density close to the local  $z$  axis, so like  $\text{CO}_2$  it has a significant negative  $\Theta_{zz}$ . Singly-bonded halogen atoms have the  $p_{\sigma}$  orbital only partly occupied, while the  $p_{\pi}$  orbitals are fully occupied, so (if we take the  $z$  axis along the bond) there is a positive  $\Theta_{zz}$  quadrupole moment associated with such atoms, and this is the main feature leading to halogen bonding.

Higher moments—octopole, hexadecapole, and so on—are defined similarly. The general rank  $n$  multipole moment of charge density  $\rho(\mathbf{r})$  with respect to the origin of coordinates is

$$\xi_{\alpha\beta\dots\nu}^{(n)} = \frac{(-1)^n}{n!} \int \rho(\mathbf{r}) r^{2n+1} \nabla_{\alpha} \nabla_{\beta} \dots \nabla_{\nu} \left( \frac{1}{r} \right) d^3\mathbf{r}. \quad (1.15)$$

This rank- $n$  tensor has  $3^n$  components, but they can all be expressed in terms of a few independent parameters. The  $\nabla$  operators commute, so the moment  $\xi_{\alpha\beta\dots\nu}^{(n)}$  is invariant under permutation of its suffixes; and  $\xi^{(n)}$  is traceless with respect to any pair of suffixes because  $\nabla^2(1/r) = 0$  by Laplace's equation. That is, we can reorder the  $\nabla$  operators, so that, for example, the product  $\nabla_{\alpha}\nabla_{\beta}$  is next to the  $(1/r)$ , and if we then set  $\alpha = \beta = x, y,$  and  $z$  in turn and sum the results, we get  $\nabla^2(1/r)$ , which is zero. These two properties together imply that  $\xi^{(n)}$  has only  $2n + 1$  independent components. In fact, these  $2n + 1$  components behave under rotation like components of a rank  $n$  spherical harmonic, and for many purposes it is more convenient to define them in terms of spherical harmonics and to use spherical tensor algebra to manipulate them. However, we shall not pursue that here; for full details of that approach see Ref. [1].

The multipole moments depend on the choice of origin. The total charge  $q$  is independent of origin; the dipole moment  $\mu_{\alpha}$  is independent of origin only if the charge is zero; the quadrupole moment  $\Theta_{\alpha\beta}$  is independent of origin only if the charge and dipole are zero; and in general the moment of rank  $n$  is independent of origin only if all moments of lower rank



are zero. Consequently it is important to specify the origin of coordinates when giving numerical values of dipole moments of charged molecules, or (more commonly) quadrupole moments of polar molecules.

The interaction energy between multipoles on sites at  $\mathbf{R}_a$  and  $\mathbf{R}_b$  can be expressed using the interaction tensors  $T_{\alpha\beta\dots\nu}^{(n)}$ , defined by

$$T_{\alpha\beta\dots\nu}^{(n)} = \frac{1}{4\pi\epsilon_0} \nabla_\alpha \nabla_\beta \dots \nabla_\nu \frac{1}{R} \quad (1.16)$$

where  $R$  is the length of the vector  $\mathbf{R} = \mathbf{R}_b - \mathbf{R}_a$ , and  $\nabla_\alpha = \partial/\partial R_\alpha$ . Thus

$$4\pi\epsilon_0 T = \frac{1}{R}, \quad (1.17)$$

$$4\pi\epsilon_0 T_\alpha = \nabla_\alpha \frac{1}{R} = -\frac{R_\alpha}{R^3}, \quad (1.18)$$

$$4\pi\epsilon_0 T_{\alpha\beta} = \nabla_\alpha \nabla_\beta \frac{1}{R} = \frac{3R_\alpha R_\beta - R^2 \delta_{\alpha\beta}}{R^5}, \quad (1.19)$$

and so on.

In terms of these quantities the electrostatic interaction between charge distributions  $\rho^a$  and  $\rho^b$  is described by the multipole expansion

$$E_{\text{es}}^{ab} = T q^a q^b + T_\alpha (q^a \mu_\alpha^b - \mu_\alpha^a q^b) + T_{\alpha\beta} (\frac{1}{3} q^a \Theta_{\alpha\beta}^b - \mu_\alpha^a \mu_\beta^b + \frac{1}{3} \Theta_{\alpha\beta}^a q^b) + \dots, \quad (1.20)$$

or for the common case of neutral molecules,

$$E_{\text{es}}^{ab} = -T_{\alpha\beta} \mu_\alpha^a \mu_\beta^b - \frac{1}{3} T_{\alpha\beta\gamma} (\mu_\alpha^a \Theta_{\beta\gamma}^b - \Theta_{\alpha\beta}^a \mu_\gamma^b) - T_{\alpha\beta\gamma\delta} (\frac{1}{15} \mu_\alpha^a \Omega_{\beta\gamma\delta}^b - \frac{1}{9} \Theta_{\alpha\beta}^a \Theta_{\gamma\delta}^b + \frac{1}{15} \Omega_{\alpha\beta\gamma}^a \mu_\delta^b) + \dots, \quad (1.21)$$

where  $\Omega_{\alpha\beta\gamma}$  is the octopole moment.

The exact electrostatic energy  $E_{\text{es}}$  remains finite unless nuclei come into contact, when there is a  $Z_a Z_b / (4\pi\epsilon_0 R)$  singularity. However, Eq. (1.20) is a series in powers of  $1/R$ , and this series will in general diverge for small but nonzero  $R$ . Strictly speaking, the series only converges at distances such that spheres enclosing the two charge densities do not intersect, but in practice the error is small if the spheres enclose almost all of the charge. This means that for best convergence we should choose the origin of each molecule at the center of the smallest sphere that contains all its charge, but even so there may be regions outside the charge density but inside the sphere, so there may be configurations where the molecules themselves do not overlap but the spheres enclosing them do, and in that case the series may not converge.

There are cases where the multipole series for the electrostatic energy converges. All closed-shell atomic ions, such as  $\text{Cl}^-$ , are spherical, and have nonzero charge but zero higher moments, so that, for example, the series for  $\text{Na}^+ \dots \text{Cl}^-$  terminates at the first term and is trivially convergent. Even when the series converges, however, it will still be in error if the charge densities overlap, because the series treats the charge density as if it were concentrated

at a point, rather than extended in space. This error is called the “penetration error.” Furthermore, it is usually necessary in practice to truncate the series at a finite number of terms, leading to a “truncation error.”

These features mean that the multipole expansion cannot usually be used in practice to describe interactions between *molecular* multipoles. Consequently electrostatic interactions are better described in terms of “distributed multipoles.” Here the charge density is divided into small regions, usually atoms, and the density around each is described by multipole moments. A long-standing and widely used procedure for evaluating these moments is distributed multipole analysis [15,16], but the recently-developed iterated stockholder analysis (ISA) [17,18] appears to be the most satisfactory. In the stockholder procedure, originally due to Hirshfeld [19], each atom  $a$  in the molecule is assigned a weight function  $w_a(r_a)$ , which is a function only of the distance  $r_a = |\mathbf{r} - \mathbf{r}_a|$  from atom  $a$ . The density assigned to atom  $a$  is then taken as

$$\rho_a(\mathbf{r}) = \rho(\mathbf{r}) \frac{w_a(r_a)}{\sum_{a'} w_{a'}(r_a)}. \quad (1.22)$$

As originally proposed by Hirshfeld, the weight functions were the spherically-averaged densities of the isolated neutral atoms, but this is not satisfactory when the atoms are not neutral in the molecule. In the iterative version they are defined [17] as the spherical averages of the atom densities from Eq. (1.22):

$$w_a(\mathbf{r}) = \langle \rho_a(\mathbf{r}) \rangle_{\text{sph}}. \quad (1.23)$$

Eqs. (1.22) and (1.23) are solved iteratively, starting with an arbitrary choice of weight functions. Lillestolen and Wheatley [17] showed that the iteration always converges provided that the weight functions all remain positive everywhere. Their original method, in which the weight functions were defined on a grid, converged very slowly, but a revised method using a basis-function expansion gives better convergence [18].

This procedure leads to atomic densities that are as nearly spherical as possible. It turns out that the multipole moments derived from these densities usually give a good account at low rank of the electrostatic interaction between molecules [18]. For some applications, charges alone may suffice, but for accurate work, atomic dipoles and quadrupoles are usually needed. This is readily understandable in terms of simple valency theory: bonding involves  $s$  and  $p$  orbitals, and an  $sp^n$  hybrid orbital has a density concentrated in the direction of the  $p$  orbital, leading to a separation of electron and nuclear charge and hence a dipole moment. Occupancy of a  $p_z$  orbital (say) in a  $\pi$  bond leads to electron density concentrated in the  $+z$  and  $-z$  directions and hence a quadrupole moment. Higher moments—octopole, hexadecapole and so on—are usually much less important.

Fig. 1.1 shows the results of the ISA procedure for pyridine [20]. The  $10^{-3}$  a.u. isodensity surface for each atom is colored according to the anisotropic part of the electrostatic potential due to that atom’s charge density—that is, the potential arising from the atomic dipole, quadrupole, etc., omitting the potential due to the atomic charge. If the potential due to any atom could be represented accurately by a point charge at the nucleus, the isodensity surface for that atom would be all white. Clearly, that is not the case for any of the atoms in pyridine, so higher atomic moments are needed.

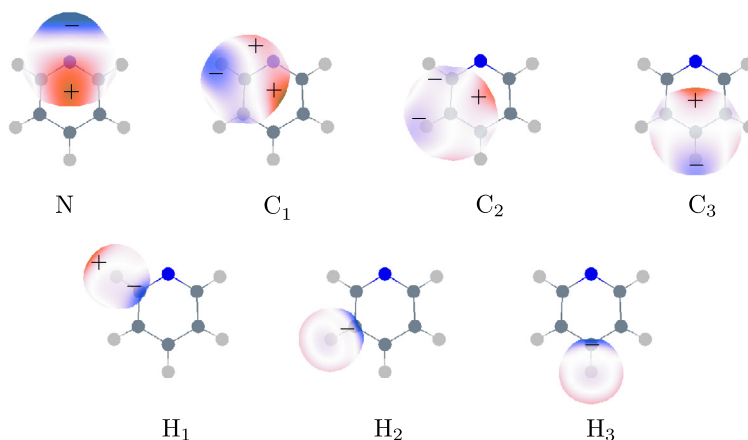


**FIGURE 1.1** The  $10^{-3}$  a.u. isodensity surfaces of the ISA-based “atoms” in pyridine. The pyridine density was computed using the CAMCASP program with a d-aug-cc-pVTZ basis, and the ISA calculations were performed using the aug-cc-pVQZ/ISA-set2 auxiliary basis set. The color coding indicates the anisotropic part of the electrostatic potential on the surface arising from atomic multipoles located on the nuclei; that is, the atomic charge contributions are not included. The scale runs from gray (red) through white to gray (blue), with the sign indicated by + or -. Reprinted with permission from *J. Chem. Theory Comput.* 12 (2016) 4184–4208. Copyright 2016 American Chemical Society.

The use of distributed multipoles deals with most of the difficulties in the use of the multipole expansion, but at short distances even the distributed-multipole treatment is in error. Molecular charge densities are not concentrated at one point, or even at the several atom positions, but extend over a few bohr around each atom. When atoms in molecules approach, their charge densities penetrate each other, and their nuclear charges are not fully screened by the surrounding electron density. There is then an attraction between the penetrating electrons of each atom and the nucleus of the other, an effect which is not described by the multipole expansion. This is the penetration energy. It depends on overlap of the charge densities, so it varies with separation in approximately the same way as the exchange repulsion, which we discuss in the next section, and can usually be modeled in the same way.

### 1.3 EXCHANGE REPULSION

At long range, the first-order energy in perturbation theory is just the electrostatic interaction. At shorter range, however, exchange effects arise. Antisymmetrization between the molecules imposes the Pauli exclusion principle, preventing electrons of the same spin from ever being in the same place, and this restriction increases the energy, adding an exchange (or “exchange-repulsion”) term to the first-order energy.

The exchange-repulsion energy increases steeply as the distance between atoms decreases. It describes the shape of the molecule and accounts for effects such as steric repulsion. Its calculation is straightforward, like the electrostatic energy, but again it is too time-consuming for use in applications such as simulations, and we need to represent it by a simpler model.

As atoms are approximately spherical, even within a molecule, it is natural to use an atom–atom form of model, and for many years the most common has been the Lennard-Jones  $R^{-12}$  atom–atom repulsion, though the Born–Mayer  $A \exp(-BR)$  form has also been widely used.

It has been found [21] that the exchange-repulsion energy between atoms is very nearly proportional to the overlap between the atom densities:

$$E_{\text{er}} \approx K S_{\rho}^{\gamma}, \quad (1.24)$$

where

$$S_{\rho} = \int \rho^a(\mathbf{r}) \rho^b(\mathbf{r}) d^3\mathbf{r}, \quad (1.25)$$

and  $\gamma$  is close to but slightly smaller than unity. Note that we are dealing here with the overlap between *densities*, not the more familiar overlap between wavefunctions. It has been shown [20] that if the asymptotic correction is applied in DFT calculation of the densities, the exponent  $\gamma$  is equal to 1, and this has important consequences in the application of Eq. (1.24), because we can now write the molecular density as a sum of atom densities, to obtain  $S_{\rho}$  and hence  $E_{\text{er}}$  as a sum of atom–atom terms:

$$E_{\text{er}} = K S_{\rho} = K \sum_{a \in A} \sum_{b \in B} \int \rho^a(\mathbf{r}) \rho^b(\mathbf{r}) d^3\mathbf{r}. \quad (1.26)$$

This approach has been used to describe the exchange-repulsion interaction between polyatomic molecules [22,23].

The atom–atom density overlap decreases exponentially with increasing separation between the atoms, which favors the Born–Mayer form of repulsion model, and indeed the Lennard-Jones  $R^{-12}$  repulsion has long been recognized as inadequate, and is still in use only because of its computational convenience. (The  $R^{-12}$  repulsive term in the Lennard-Jones form is guaranteed to dominate the attractive  $R^{-6}$  term at short range, but the repulsive term  $A e^{-BR}$  in the Born–Mayer form remains finite as  $R \rightarrow 0$ , while the attractive  $-C_6 R^{-6}$  term representing the dispersion energy goes to  $-\infty$ , which leads to difficulties in Monte Carlo simulations because a simulation step can jump into the spurious negative-energy region at small  $R$ .)

In order to use Eq. (1.26), we need to partition the total electron density into atomic contributions. The ISA procedure provides a very effective way to do this, yielding atomic densities that are as nearly as possible spherical but which sum exactly to the total electron density. Fig. 1.1 illustrates this. The  $10^{-3}$  a.u. isodensity surface corresponds quite closely to the usual van der Waals atom surface, but it is clear from Fig. 1.1 that these surfaces are not quite spherical. The N atom surface in particular is somewhat extended away from the center of the molecule, while the H atom surfaces are not quite centered on the H nucleus but are slightly displaced toward the neighboring carbon atom. These features can be described by a modification of the Born–Mayer repulsion expression:

$$E_{\text{er}}^{ab} = K \exp[-\alpha^{ab}(R_{ab} - \rho^{ab}(\Omega_{ab}))]. \quad (1.27)$$

In this expression,  $K$  is a constant energy factor, usually taken to be 1 millihartree,  $R_{ab}$  is the distance between nuclei  $a$  and  $b$ , and  $\rho^{ab}(\Omega_{ab})$  describes the atom shapes as a function of the

relative orientation of atoms  $a$  and  $b$ . In fact, we can see from Eq. (1.27) that  $\rho^{ab}(\Omega_{ab})$  is the separation  $R$  for which the repulsion energy takes the value  $K$ , when the relative orientation is  $\Omega_{ab}$ . To a reasonably good approximation we can view the atomic van der Waals radius as a function of direction, and then  $\rho^{ab}(\Omega_{ab})$  is approximately the sum of the van der Waals radii of each atom in the direction of the other.

This formulation of the exchange repulsion has been used empirically for a long time [24]. It is only recently that it has been possible to justify it theoretically [20], but the nonspherical nature of atoms in molecules has been well documented for many years. Nyburg and Faerman [25] showed by a study of atom–atom distances in molecular crystal structures listed in the Cambridge Crystal Structure Database (CCSD [26]) that halogen atoms in molecules have a significantly reduced van der Waals radius on the side away from the bond, and it was only when this feature was taken into account that it was possible to construct a simple potential model that described correctly the structure of crystalline  $\text{Cl}_2$  [27] and the liquid structure of  $\text{Cl}_2$ ,  $\text{Br}_2$ , and  $\text{I}_2$  [28–30]. More recently, the structures of halogen-bonded complexes can be described very largely in terms of electrostatic interactions involving the halogen atom quadrupole moment, but it is also necessary to take into account the anisotropy of the halogen repulsion [31].

## 1.4 INDUCTION

The induction interaction can be regarded at long range as a classical effect: the polarization response of each molecule to the electrostatic field of the other. The perturbation operator describing the interaction between a uniform external electric field  $\mathbf{F}$  and a molecule is  $\hat{V} = \mathbf{F} \cdot \hat{\boldsymbol{\mu}} = F_\alpha \hat{\mu}_\alpha$ , where  $\hat{\boldsymbol{\mu}}$  is the dipole moment operator for the molecule, and we are again using the Einstein repeated-suffix convention. Ordinary second-order perturbation theory now gives the energy change as  $E_{\text{ind}} = -\frac{1}{2}\alpha_{\alpha\beta} F_\alpha F_\beta$ , where the polarizability tensor  $\alpha_{\alpha\beta}$  is

$$\alpha_{\alpha\beta} = \sum_n' \frac{\langle 0 | \hat{\mu}_\alpha | n \rangle \langle n | \hat{\mu}_\beta | 0 \rangle + \langle 0 | \hat{\mu}_\beta | n \rangle \langle n | \hat{\mu}_\alpha | 0 \rangle}{E_n - E_0}, \quad (1.28)$$

and the  $|n\rangle$  are the states of the molecule, with energies  $E_n$ , and the sum is taken over all states of the molecule except the ground state  $|0\rangle$ .

The electric field here is the field due to all sources—all neighboring molecules, as well as any external field—and consequently the induction energy is *nonadditive*. To see how this happens, consider the examples illustrated in Fig. 1.2. The electric field at a distance  $R$  from a dipole moment  $\mu$  in the direction of the dipole is  $F = 2\mu/(4\pi\epsilon_0 R^3)$ , so the induction energy of an atom with polarizability  $\alpha$  at that position, as shown in Fig. 1.2A, is  $-\frac{1}{2}\alpha F^2 = -2\alpha\mu^2/(4\pi\epsilon_0 R^3)^2$ .

If there are two dipoles on opposite sides of the atom, both pointing in the same direction, as in Fig. 1.2B, the electric field is twice as large, but the induction energy, which depends on the square of the electric field, is four times as large. If the two dipoles point in opposite directions, on the other hand, as in Fig. 1.2C, their electric fields cancel out, so the induction energy is zero.

$$\begin{array}{ll}
 \text{(A)} & \begin{array}{c} \xrightarrow{\mu} \textcircled{\alpha} \\ \xleftarrow{R} \end{array} & -2\alpha\mu^2/(4\pi\epsilon_0)^2 R^6 \\
 \text{(B)} & \begin{array}{c} \xrightarrow{\mu} \textcircled{\alpha} \xrightarrow{\mu} \\ \xleftarrow{R} \quad \xleftarrow{R} \end{array} & -8\alpha\mu^2/(4\pi\epsilon_0)^2 R^6 \\
 \text{(C)} & \begin{array}{c} \xrightarrow{\mu} \textcircled{\alpha} \xleftarrow{\mu} \\ \xleftarrow{R} \quad \xleftarrow{R} \end{array} & 0
 \end{array}$$

FIGURE 1.2 Nonadditivity of the induction energy. (A) Polarizable atom in the field of a single dipole; (B) atom in the field of two parallel dipoles; (C) atom in the field of two opposing dipoles.

Enhancements and cancellations like these are common. The ion sites in an ionic crystal may have a local symmetry in which vectors such as the electric field are zero by symmetry, so there is no dipole–dipole induction energy. On the other hand, a water molecule in the cyclic water trimer or tetramer has a proton donor on one side and a proton acceptor on the other, and the electric fields due to these add vectorially, giving an increased induction energy.

Further complications arise because the induced dipole moment itself has an electric field, which polarizes its neighbors in turn. Suppose that two neighboring nonpolar atoms are subject to an external electric field along the line between them. The induced dipole moment of each atom produces an additional electric field that must be added to the applied field, so we have

$$\begin{aligned}
 \mu^A &= \alpha^A (F + 2\mu^B / (4\pi\epsilon_0 R^3)), \\
 \mu^B &= \alpha^B (F + 2\mu^A / (4\pi\epsilon_0 R^3)),
 \end{aligned} \tag{1.29}$$

where the dipole moments now include the extra induced dipole. Solution of these equations gives

$$\mu^A = \alpha^A F \frac{1 + 2\alpha^B / (4\pi\epsilon_0 R^3)}{1 - 4\alpha^A \alpha^B / (4\pi\epsilon_0)^2 R^6}, \tag{1.30}$$

and similarly for  $\mu^B$ . The effect is to enhance the field at each molecule and the resulting induced moment.

This is a real effect, whether the electric field is external or due to other molecules, and has to be taken into account in the evaluation of the induction energy of an assembly of molecules. Usually equations analogous to Eq. (1.29), but including any static dipole moments, are set up for the whole system and solved iteratively.

The second-order energy in perturbation theory doesn't describe this cooperative effect; for that we would need to take the perturbation theory to higher, even infinite, order. Since that is impracticable, it is common to handle it by evaluating the so-called  $\delta^{\text{HF}}$  correction. The procedure for doing this is first to carry out a Hartree–Fock supermolecule calculation to obtain the energy difference  $\Delta E = E(AB) - E(A) - E(B)$ , using the dimer basis for each molecule as well as for the dimer itself to avoid basis set superposition error [32]. From  $\Delta E$  we subtract the first-order electrostatic and exchange and second-order induction and exchange-induction energies obtained from a SAPT (not SAPT-DFT) calculation with the

Hartree–Fock wavefunctions for  $A$  and  $B$ . The result contains the higher-order induction terms.

A difficulty arises in Eq. (1.30) when  $R = [4\alpha^A\alpha^B/(4\pi\epsilon_0)^2]^{1/6}$ . In this case, Eq. (1.30) becomes singular. This is the “polarization catastrophe.” It is not a real effect; it arises because the polarizability is being treated as a point property, whereas the polarizable charge density extends over a finite region of space. Nevertheless, it can cause difficulties in practical calculations of the induction energy, especially in Monte Carlo simulations where a step may take a pair of molecules close to the singularity or beyond it.

The dipole–dipole polarization is just the first term in a series expansion of the induction energy. The response of a molecule to external fields, like the unperturbed charge distribution, can be expressed as a multipole series, where the induced dipole is the first term. There may also be induced quadrupoles, octopoles, and so forth. Furthermore, the electric field need not be uniform; indeed the electric fields around molecules are frequently far from uniform.

If the electrostatic potential at position  $\mathbf{r}$  is  $V(\mathbf{r})$ , the electric field is

$$F_\alpha = -\frac{\partial V}{\partial r_\alpha}, \quad (1.31)$$

the *field gradient* is

$$F_{\alpha\beta} = \frac{\partial F_\alpha}{\partial r_\beta} = -\frac{\partial^2 V}{\partial r_\alpha \partial r_\beta}, \quad (1.32)$$

and so on. In addition to the dipole–dipole polarizability (the dipole induced by a uniform field), a molecule may also have a dipole–quadrupole polarizability  $A_{\alpha,\beta\gamma}$ , which describes the dipole induced by a field gradient:

$$\Delta\mu_\alpha = \alpha_{\alpha\beta}F_\beta + \frac{1}{3}A_{\alpha,\beta\gamma}F_{\beta\gamma} + \dots \quad (1.33)$$

The dipole–quadrupole polarizability also describes the quadrupole moment induced by an electric field, while the quadrupole–quadrupole polarizability  $C_{\alpha\beta,\gamma\delta}$  describes the quadrupole moment induced by a field gradient:

$$\Delta\Theta_{\beta\gamma} = A_{\alpha,\beta\gamma}F_\alpha + C_{\alpha\beta,\gamma\delta}F_{\gamma\delta} + \dots \quad (1.34)$$

Only for the smallest molecules can we use molecular polarizabilities to calculate induction interactions. The responses of molecules to external fields, and the fields themselves, generally vary in too complicated a way for this. Instead we need to treat atoms or groups of atoms individually by using *distributed polarizabilities* [33]. An external field at a particular atom in a molecule modifies the charge distribution of that atom and its near neighbors, and that response can be described in various ways. We can view the external field at atom  $a$  as polarizing only atom  $a$  directly, but recognize that the induced moments on atom  $a$  produce secondary fields that modify the polarization of neighboring atoms. The difficulty with this is that the neighboring atoms are close enough for polarization catastrophes to arise, and the secondary fields have to be damped in some way to prevent that. Thole [34]

proposed doing this by modifying the usual  $r^{-1}$  interaction between charges to a nonsingular form, in effect recognizing that the atomic charge is not concentrated at a point but spread out, and this approach is quite widely used, but it is ad hoc and empirical. A better method is to calculate distributed polarizabilities ab initio. The CAMCASP program of Misquitta and Stone [20] calculates explicitly nonlocal polarizabilities that give, for example, the multipole moments induced at atom  $b$  by an electric field at atom  $a$ , without using the multipole expansion. A simpler description uses local polarizabilities, where the secondary induced moments of the neighbors of atom  $a$  are described by a multipole expansion on atom  $a$  itself, and hence by local polarizabilities on atom  $a$ . The local polarizabilities are obtained from the nonlocal distributed polarizabilities by methods due to Le Sueur and Stone [35] and Lillestolen and Wheatley [36]. The polarizabilities may be further refined by the method of Williams and Stone [37], in which any local or nonlocal polarizability model can be fitted to an array of point-to-point polarization responses, each being the change in potential at one point outside the molecule arising from the polarization due to a unit charge at another point.

Where a simpler model of induction is needed, the Drude model may be useful [38,39]. In this approach, each atom carries a floating negative charge attached to a balancing positive charge on the nucleus by a harmonic spring. The floating charge is displaced by an applied field, leading to an induced dipole moment, so it describes an atomic polarizability. The separated charges interact with the charges on other atoms by ordinary coulomb interactions, accounting to some extent for secondary polarization. The charge  $q$  and spring constant  $k$  can be fitted to ab initio or experimental data; for a single atom the polarizability of the model is  $q^2/k$ . It is usual to apply some form of damping to the interactions between the Drude oscillators.

### 1.4.1 Charge Transfer Energy

The charge-transfer contribution to the energy has been a highly contentious issue for many years. The charge-transfer concept was first introduced by Mulliken [40] to account for the very strong spectroscopic transitions that can occur in a complex between an electron donor  $D$  with low ionization energy and an acceptor  $A$  with high electron affinity, but that do not occur in either component alone. In this case the ionic state  $D^+ \cdots A^-$  is not far in energy above the ground state, and is further stabilized by the electrostatic attraction between the ions. The two states mix, and it turns out that as a result the transition dipole between the ground state and the ionic “charge-transfer” state is very large, accounting for the high intensity. The mixing also leads to an energy stabilization, which is the charge-transfer contribution to the interaction energy. From the beginning there has been controversy over the importance of this contribution, and it still continues [41,42].

From another point of view, the charge-transfer energy can be seen as part of the induction energy, which arises from the distortion of the charge distribution of each molecule in response to the electric field of its neighbors. If the distortion is confined within each molecule, for example by restricting the molecular basis sets, there is no charge transfer, while larger and more extensive basis sets with basis functions on the neighboring molecule sites can allow charge transfer. Consequently the difference in induction energy between these two



calculations gives an estimate of the charge-transfer energy. Such calculations have been proposed by Khaliullin et al. [43] and Stone and Misquitta [44]. Another method of suppressing the charge-transfer part of the induction energy has been proposed by Misquitta [45]; it involves suppressing tunneling into the deep potential wells around each nucleus in the partner molecule.

Evidently the charge-transfer energy depends on overlap between the molecular electron densities, so it decreases exponentially with increasing separation. It will be apparent, however, that it is rather ill-defined, and these and other methods of calculating it give variable results, though usually within a factor of 2 of each other [46]. A method of calculation that gives energies described as “charge-transfer” with magnitudes far outside this range—usually a factor of 10 or so larger—is the Natural Bond Orbital (NBO) procedure of Weinhold and others [47]. However this procedure uses a reference state that is constructed from “natural bond orbitals” and is substantially higher in energy than the noninteracting molecules; moreover, the energies of the isolated molecules are not considered. The resulting “charge-transfer” energy is an artefact of this inflated reference energy and is heavily contaminated with basis-set superposition error [48]. Moreover, the NBO procedure does not attempt to provide a complete and coherent account of the intermolecular interaction, and the use of the NBO “charge-transfer” term in isolation or in combination with SAPT energy terms is highly misleading in the context of noncovalent interactions.

## 1.5 DISPERSION

---

The remaining important contribution to the interaction energy between molecules is the dispersion energy. The picture originally given by London [2,3] is still instructive. Here each atom is represented by a Drude model: a one-dimensional harmonic oscillator in which the electron cloud, mass  $m$ , is bound to the nucleus by a harmonic potential with force constant  $k$ . The Hamiltonian for each atom takes the form  $p^2/2m + \frac{1}{2}kx^2$ . There is an atomic dipole proportional to the displacement  $x$  of the electrons from the nucleus, and for two adjacent atoms the interaction energy of these dipoles is proportional to the product of the dipole moments. Accordingly the Hamiltonian for the complete system takes the form

$$\mathcal{H} = \frac{1}{2m}(p_A^2 + p_B^2) + \frac{1}{2}k(x_A^2 + x_B^2 + 2cx_Ax_B), \quad (1.35)$$

where  $c$  is some coupling constant. This can be separated into two uncoupled oscillators corresponding to the normal modes  $(x_A \pm x_B)/\sqrt{2}$ :

$$\begin{aligned} \mathcal{H} &= \frac{1}{4m}(p_A + p_B)^2 + \frac{1}{4}k(1+c)(x_A + x_B)^2 \\ &+ \frac{1}{4m}(p_A - p_B)^2 + \frac{1}{4}k(1-c)(x_A - x_B)^2. \end{aligned} \quad (1.36)$$

The normal mode frequencies are  $\omega_{\pm} = \omega_0\sqrt{1 \pm c}$ , where  $\omega_0 = \sqrt{k/m}$  is the frequency of an isolated oscillator.

Now a classical system would have a minimum energy of zero, whether coupled or not. The quantum system however has zero-point energy, and the energy of the coupled system in its lowest state is

$$\frac{1}{2}\hbar(\omega_+ + \omega_-) = \frac{1}{2}\hbar\omega_0(\sqrt{1+c} + \sqrt{1-c}) = \frac{1}{2}\hbar\omega_0\left[2 - \frac{1}{4}c^2 - \frac{5}{64}c^4 - \dots\right], \quad (1.37)$$

so that there is an energy lowering, compared with the zero-point energy  $\hbar\omega_0$  of two uncoupled oscillators, of

$$E_{\text{disp}} = -\hbar\omega_0\left(\frac{1}{8}c^2 + \frac{5}{128}c^4 + \dots\right). \quad (1.38)$$

The interaction between the atoms leads to a correlation between the motion of their electrons, and this is manifested in a lowering of the energy. Notice that the energy depends on the square of the coupling constant  $c$  and is always negative, so regardless of the sign of the coupling, the correlation between the motion of the electrons leads to a lowering of the energy. For interacting Drude oscillators, the coupling  $c$  is proportional to  $R^{-3}$ , so the leading term in the dispersion energy is proportional to  $R^{-6}$ .

This simple model contains the essential physics, and indeed the Drude model has been used with some success to describe the dispersion interaction between molecules [39], but for accurate calculations we need to apply perturbation theory.

First we generalize Eq. (1.28) to describe the response to an oscillating electric field with angular frequency  $\omega$ :

$$\alpha_{\alpha\beta}(\omega) = \sum_n' \frac{\omega_{n0}(\langle 0|\hat{\mu}_\alpha|n\rangle\langle n|\hat{\mu}_\beta|0\rangle + \langle 0|\hat{\mu}_\beta|n\rangle\langle n|\hat{\mu}_\alpha|0\rangle)}{\hbar(\omega_{n0}^2 - \omega^2)}. \quad (1.39)$$

Here  $\hbar\omega_{n0}$  is the energy difference  $E_n - E_0$ , expressed in terms of an angular frequency  $\omega_{n0}$ . In this form there are evidently singularities when  $\omega$  is equal to any of the transition frequencies  $\omega_{n0}$ , but they go away if we take account of the finite lifetimes  $\Gamma_n$  of the excited states by replacing  $\omega_{n0}$  in Eq. (1.39) by  $\omega + \frac{1}{2}i\Gamma_n$ , because the denominator is then nonzero for all real  $\omega$ . For our purposes, however, this is unimportant, and we need the polarizability at imaginary frequency  $i\omega$ . This doesn't have much physical meaning, but mathematically it just has the minus sign in the denominator of Eq. (1.39) replaced by a plus sign, removing the singularities and also making  $\alpha(i\omega)$  a monotonically decreasing function of  $\omega$ . Not only is it mathematically well-behaved, it is also quite straightforward to calculate. Note also that if we set  $i\omega = 0$  we recover the static polarizability, Eq. (1.28).

In terms of this quantity the dipole-dipole dispersion energy takes the form

$$E_{\text{disp}}^{AB} = -\frac{\hbar}{2\pi} T_{\alpha\gamma} T_{\beta\delta} \int_0^\infty \alpha_{\alpha\beta}^A(i\omega) \alpha_{\gamma\delta}^B(i\omega) d\omega, \quad (1.40)$$

where the  $T_{\alpha\gamma}$  tensor is as defined in Eq. (1.19). Because of the well-behaved nature of  $\alpha(i\omega)$  the integral can be accurately evaluated by numerical quadrature using only a dozen or so  $\omega$  values.

This is the leading term in the expansion of the dispersion energy as a power series, and it has  $R^{-6}$  distance dependence, since  $T_{\alpha\gamma}$  and  $T_{\beta\delta}$  have an  $R^{-3}$  distance factor (see Eq. (1.19)). The next term involves the dipole–dipole polarizability on one molecule and the dipole–quadrupole polarizability on the other, and has  $R^{-7}$  distance dependence. The  $R^{-8}$  term involves a dipole–dipole polarizability on one molecule and dipole–octopole or quadrupole–quadrupole on the other, or dipole–quadrupole polarizabilities on both. All of these, and higher terms, can be calculated using the CAMCASP program [20].

This then leads to the long-range description of the dispersion interaction, conventionally expressed in the form

$$E_{\text{disp}} = -\frac{C_6}{R^6} - \frac{C_7}{R^7} - \dots - \frac{C_n}{R^n} - \dots, \quad (1.41)$$

where the dispersion coefficients  $C_n$  may depend on the relative orientation of the molecules.

This series evidently diverges at short range, for the usual reason that the expansion treats the interacting systems as assemblies of point polarizabilities. In reality the charge is distributed in space, so the dispersion energy remains finite at short range. Also, as in the case of the induction energy, there is a substantial positive exchange contribution to the dispersion energy when the molecules overlap. Dealing with this short-range behavior is troublesome, as it is for the other terms. Again, much of the trouble is avoided by using a distributed model, with dispersion sites at each atom:

$$E_{\text{disp}} = - \sum_{a \in A, b \in B} \left( \frac{C_6^{ab}}{R_{ab}^6} + \frac{C_7^{ab}}{R_{ab}^7} + \dots + \frac{C_n^{ab}}{R_{ab}^n} + \dots \right). \quad (1.42)$$

The long-range site–site dispersion coefficients are evaluated using local polarizabilities at imaginary frequency, which may be calculated using the CAMCASP program. In the case of large flexible molecules, it is usually necessary to take account of the dispersion interaction between different parts of the same molecule, in which case the distributed-dispersion form (Eq. (1.42)) can be used, with sites  $a$  and  $b$  on the same molecule. This is satisfactory when the density fluctuations responsible for the dispersion energy are confined to the locality of each atom, but for extended conjugated systems there are long-range fluctuations and the simple distributed picture breaks down [49].

It is still necessary to deal with the divergence of the atom–atom dispersion energy series at short range, usually by using the damping procedure proposed by Tang and Toennies [50], where the  $R^{-n}$  term is multiplied by a damping function  $f_n(R)$  which is the incomplete gamma function of order  $n + 1$ :

$$f_n(R) = P(n + 1, bR) = 1 - \exp(-bR) \sum_{k=0}^n \frac{(bR)^k}{k!}. \quad (1.43)$$

The parameter  $b$  is a scaling factor, usually taken to be equal to the parameter  $B$  in the Born–Mayer repulsion, as recommended by Tang and Toennies [50], but often treated as an adjustable parameter.

**TABLE 1.1** SAPT(DFT) energies in kJ/mol for a few small-molecule dimers. The final column shows comparison energies. See text for details and discussion

	Elst.	Exch.	Ind.	Disp.	Total	
Ar...Ar	-0.583	1.966	-0.076	-2.455	-1.147	-1.19 <sup>a</sup>
HF...HF	-28.270	27.787	-11.368	-7.840	-19.690	-19.08 ± 1.2 <sup>b</sup>
HF...ClF	-16.643	20.510	-5.579	-9.001	-10.712	-8.94 <sup>c</sup>
C <sub>6</sub> H <sub>6</sub> ...C <sub>6</sub> H <sub>6</sub>						
Disp.-parallel	-5.993	22.127	-2.803	-24.687	-11.355	-11.47 <sup>d</sup> , -11.29 <sup>e</sup>
T	-6.839	14.271	-2.400	-16.033	-11.002	-11.14 <sup>d</sup> , -11.23 <sup>e</sup>
Tilted T	-6.751	14.434	-2.283	-16.794	-11.394	-11.59 <sup>d</sup> , -11.69 <sup>e</sup>

<sup>a</sup> Aziz and Chen [51].<sup>b</sup> Pine and Howard [52].<sup>c</sup> Pliego et al. [53].<sup>d</sup> Podeszwa et al. SAPT(DFT) [54].<sup>e</sup> Podeszwa et al. CCSD(T) [54].

### 1.5.1 Many-Body Dispersion

The dispersion energy is approximately additive, but there are small many-body contributions. The leading term in the multipole expansion of the three-body dispersion is the triple-dipole analogue of Eq. (1.40):

$$E_{\text{disp}}^{ABC} = -\frac{\hbar}{\pi} T_{\beta\gamma}^{AB} T_{\delta\epsilon}^{BC} T_{\phi\alpha}^{CA} \int_0^\infty \alpha_{\alpha\beta}^A(i\omega) \alpha_{\gamma\delta}^B(i\omega) \alpha_{\epsilon\phi}^C(i\omega) d\omega. \quad (1.44)$$

For spherical atoms this reduces to

$$E_{\text{triple-dipole}} = C_9 \frac{1 + 3 \cos \hat{A} \cos \hat{B} \cos \hat{C}}{R_{AB}^3 R_{BC}^3 R_{CA}^3}, \quad (1.45)$$

where  $R_{AB}$ , etc., are the lengths of the sides of the triangle formed by the three atoms, and  $\hat{A}$ ,  $\hat{B}$  and  $\hat{C}$  are the angles of the triangle.  $C_9$  is positive, so the triple-dipole energy is positive for three atoms in an equilateral triangle, as in a close-packed solid, and it reduces the binding energy in solid argon by about 7%.

## 1.6 EXAMPLES

Many examples of the application of SAPT(DFT) are discussed in Chapter 2, but some aspects of the method are illustrated here by Tables 1.1 and 1.2, which show the SAPT(DFT) energy terms for a few cases. These were obtained with the CAMCASP program [20], using the aug-cc-pVTZ basis [55] in all cases except the benzene dimer, where the Sadlej basis [56] was used. Table 1.1 shows the induction and dispersion energies as totals, “ind” comprising induction, exchange-induction and the  $\delta^{\text{HF}}$  estimate of the higher-order induction, and “disp” comprising dispersion and exchange-dispersion. These are separated into their components

**TABLE 1.2** Details of SAPT(DFT) dispersion and induction energies in kJ/mol. See text for details and discussion

	Ind.	ExInd.	$\delta^{\text{HF}}$	CT.	Disp.	ExDisp.
Ar...Ar	-0.782	0.769	-0.063	-0.003	-2.637	0.183
HF...HF	-14.701	7.997	-4.663	-1.550	-9.382	1.543
HF...ClF	-12.637	10.169	-3.111	-1.055	-10.339	1.339

in [Table 1.2](#), which also shows an estimate of the part of the total induction energy that can be attributed to charge transfer.

### 1.6.1 Inert Gas Dimers

The argon dimer is bound by the dispersion energy, mainly balanced by the exchange-repulsion at the equilibrium distance. However, [Table 1.1](#) shows that there is a significant electrostatic attraction at this distance. This arises from the penetration of the electron density of each atom into the other, so that the electrons of each atom are not completely screened from the nucleus of the other atom by its electrons. The induction energy is very small, but not zero, again because of the interpenetration of the electron densities.

### 1.6.2 Hydrogen Bonds

The hydrogen bond is an important feature in many intermolecular interactions, especially in biological systems. The IUPAC definition of the hydrogen bond is very broad [\[57,58\]](#), but in the most common cases it takes the form  $X\text{-H}\cdots Y\text{-Z}$ , where  $X$  is more electronegative than  $H$  and  $Y$  has an electron-rich region such as a lone pair or a  $\pi$  bond. All of the main contributions to the intermolecular interaction energy are present.  $X$  and  $Y$  tend to carry negative charges, so the  $H$  is attracted to the electron-rich region of  $Y$  while  $X$  is repelled by it, leading to a nearly linear  $X\text{-H}\cdots Y$ . All multipole-multipole interactions except charge-charge average to zero over orientations, so they vary between large positive values in some orientations to large negative values in others. Consequently the electrostatic term is important in determining the geometry. A model that uses an accurate description of the electrostatics with a hard-sphere repulsion, but ignores induction and dispersion, is very successful in predicting geometries [\[59,60\]](#). [Table 1.2](#) shows that for HF dimer the largest contributions are the electrostatic and exchange-repulsion terms. The assumption of hard-sphere repulsion is not always sufficient, as some atoms, especially halogens, are not quite spherical, and most failures of the model can be attributed to this. In contrast, the induction and dispersion terms are always negative and vary less with orientation, so they make an important contribution to the binding without a strong effect on geometry. The nonadditive nature of induction is responsible for another important and characteristic feature of hydrogen bonding, namely its cooperative nature in structures such as the water trimer and tetramer and many other examples [\[61\]](#).

The question of the charge-transfer contribution to hydrogen bonding has been highly controversial ever since Mulliken's original paper [\[40\]](#). SAPT calculations show a significant but relatively small charge-transfer contribution. As mentioned above, the very large values

described as charge-transfer in the Natural Bond Orbital approach are misleading, as they are very heavily contaminated by basis-set superposition error [48]. The charge-transfer energy does not arise naturally as a separate contribution in SAPT(DFT), and the several methods proposed for estimating it give somewhat different results. The values given in Table 1.2 were obtained using the method of Misquitta [45].

### 1.6.3 Halogen Bonds

The halogen bond has emerged as a new entity, or rather a newly-recognized one, in the last couple of decades [62,63]. It can be represented as  $W-X \cdots Y$ , where  $X$  is a halogen (but not usually fluorine) and  $Y$  has an electron-rich region as in the hydrogen-bond case. The electrostatic interaction is the dominant feature here, somewhat unexpectedly in view of the electronegativity of the halogens. It arises from the substantial quadrupole moment of the halogen atom, which in turn is due to the full occupancy of the  $p-\pi$  orbitals but only partial occupancy of the  $p-\sigma$ —the so-called “ $\sigma$ -hole”. The consequence is a positive electrostatic potential along the extension of the  $W-X$  bond beyond the  $X$  atom, and this interacts favorably with the electron-rich region of the  $Y$  atom. The example of  $\text{HF} \cdots \text{ClF}$  in Table 1.1 shows that the electrostatic interaction is the dominant attractive term, though the induction and dispersion are also important.

This leads to an expectation that the  $W-X \cdots Y$  geometry should be linear, and in fact halogen bonds tend to be more nearly linear than hydrogen bonds. This is due not only to the electrostatics but to the flattened shape of bonded halogen atoms, because the  $X \cdots Y$  distance can be shorter when the  $W-X \cdots Y$  is linear than when it is bent [31]. The crystal structure of  $\text{Cl}_2$  can be explained using model intermolecular potentials only if the shape of the Cl atoms is described correctly [27], and the same is true for the structures of the  $\text{Cl}_2$ ,  $\text{Br}_2$ , and  $\text{I}_2$  liquids [28–30].

The basic feature of the halogen bond, the  $\sigma$ -hole, is not in fact unique to halogens, and has been identified in compounds of other atoms, including sulfur, selenium, phosphorus, and germanium [64]. The idea that it is a region of positive electrostatic potential on the extension of a  $\sigma$  bond has been extended by some to include virtually any region of positive electrostatic potential on the molecular surface, leading to concepts such as the “ $\pi$ -hole” [65,66].

### 1.6.4 Energy Landscapes

Sometimes the lowest-energy configuration of a molecular complex is a well-defined minimum of the energy as a function of relative geometry. In such cases the structure is easily found. In other cases there are several minima with similar energies, and it is necessary to explore the “energy landscape” in more detail [67]. A well-known example is the benzene dimer, where the determination of the preferred structure has proved a difficult problem for theory. Benzene has a significant negative quadrupole moment, arising partly from the negative  $\pi$ -electron density above and below the molecular plane, and partly from the small charge difference between the C and H atoms. For quadrupolar molecules with a three-fold or higher axis of symmetry, where the only nonzero quadrupole moment is  $Q_{20}$ , there are two favorable geometries. These are the “T” and the “displaced-parallel” structures, the former

having the symmetry axis of one molecule along the line of centers and the other perpendicular to it, and the latter having both symmetry axes tilted away from the line of centers by about  $60^\circ$ . Since the quadrupole–quadrupole interaction has an  $R^{-5}$  distance dependence, the electrostatically-favored geometry depends on the relative distances in these two orientations. Janda et al. [68] showed by molecular beam methods that benzene dimer has a nonzero dipole moment, suggesting that the T structure was likely, as the displaced parallel structure would be nonpolar.

The theoretical picture is complicated by the other energy components. Table 1.1 gives the energy components and total energies calculated by SAPT(DFT) using the Sadlej basis [56], together with the more accurate calculations of Podeszwa et al. [54], using the somewhat larger aug-cc-pVTZ basis [55] with additional mid-bond functions. The displaced-parallel, T and tilted-T geometries are respectively the M1, S3, and M2 configurations found by Podeszwa et al. [54].

It is clear that the differences in total energy are very small—of the order of a few tenths of a kJ/mol. The results from the Sadlej basis are in reasonable agreement with those from the better basis, so we can use them to explore the behavior of the individual components. Comparing the T and displaced-parallel structures, we can see that the T has a somewhat stronger electrostatic attraction and a substantially weaker repulsion, but the displaced-parallel structure has a much stronger dispersion term. The overall energy difference of about 0.3 kJ/mol is the net result of much larger differences in the individual energy terms.

However the global minimum is not the T structure but a tilted T, in which the benzene forming the stem of the T is rotated by about  $10^\circ$  about its  $C_6$  axis, while the one forming the head of the T is rotated about a parallel axis by a similar amount in the opposite direction. The SAPT-DFT calculation shows that this reduces the electrostatic attraction and the induction energy, each by about 0.1 kJ/mol, and increases the repulsion by about 0.16 kJ/mol, but improves the dispersion energy by about 0.75 kJ/mol, giving an overall stabilization of about 0.4 kJ/mol. The smallness of these numbers accounts for the difficulty in determining the preferred equilibrium structure.

The picture is further complicated by the fact that there are multiple versions of these minima, because of the  $D_{6h}$  symmetry of the benzene molecule, and low barriers between them. Recent experimental spectroscopy and theoretical analysis by Schnell et al. [69] has shown that the tunneling splittings in the microwave spectrum of the benzene dimer are well explained in terms of this picture of the energy landscape.

---

## 1.7 SUMMARY

---

After many years of unsuccessful attempts to find a satisfactory approach to the calculation of intermolecular interactions, symmetry-adapted perturbation theory, especially in its density-functional-based form, has become a well established approach, giving reliable interaction energies and an informative analysis of their component contributions. As implemented in the CAMCASP program [20] it provides a practical procedure for developing accurate analytic intermolecular potential energy functions for use in applications such as condensed-phase simulations and crystal structure predictions.

## References

- [1] A.J. Stone, *The Theory of Intermolecular Forces*, 2nd ed., Oxford University Press, Oxford, 2013.
- [2] F. London, *Z. Phys. Chem. B* 11 (1930) 222–251.
- [3] F. London, *Trans. Faraday Soc.* 33 (1937) 8–26.
- [4] B. Jeziorski, R. Moszynski, A. Ratkiewicz, S. Rybak, K. Szalewicz, H.L. Williams, in: E. Clementi (Ed.), *Methods and Techniques in Computational Chemistry: METECC94*, vol. B, STEF, Cagliari, 1993, p. 79.
- [5] B. Jeziorski, R. Moszynski, K. Szalewicz, *Chem. Rev.* 94 (1994) 1887–1930.
- [6] K. Szalewicz, *WIREs Comput. Mol. Sci.* 2 (2012) 254–272.
- [7] A.J. Misquitta, K. Szalewicz, *Chem. Phys. Lett.* 357 (2002) 301–306.
- [8] A.J. Misquitta, B. Jeziorski, K. Szalewicz, *Phys. Rev. Lett.* 91 (2003) 033201.
- [9] A.J. Misquitta, K. Szalewicz, *J. Chem. Phys.* 122 (2005) 214109.
- [10] A. Hesselmann, G. Jansen, *Chem. Phys. Lett.* 357 (2002) 464–470.
- [11] A. Hesselmann, G. Jansen, *Chem. Phys. Lett.* 362 (2002) 319–325.
- [12] A. Hesselmann, G. Jansen, *Chem. Phys. Lett.* 367 (2003) 778–784.
- [13] D.J. Tozer, N.C. Handy, *J. Chem. Phys.* 109 (1998) 10180–10189.
- [14] M. Grüning, O.V. Gritsenko, S.J.A. van Gisbergen, E.J. Baerends, *J. Chem. Phys.* 114 (2001) 652–660.
- [15] A.J. Stone, *Chem. Phys. Lett.* 83 (1981) 233–239.
- [16] A.J. Stone, M. Alderton, *Mol. Phys.* 56 (1985) 1047–1064.
- [17] T.C. Lillestolen, R. Wheatley, *J. Chem. Phys.* 131 (2009) 144101.
- [18] A.J. Misquitta, A.J. Stone, F. Fazeli, *J. Chem. Theory Comput.* 10 (2014) 5405–5418.
- [19] F.L. Hirshfeld, *Theor. Chim. Acta* 44 (1977) 129–138.
- [20] A.J. Misquitta, A.J. Stone, *J. Chem. Theory Comput.* 12 (2016) 4184–4208.
- [21] Y.S. Kim, S.K. Kim, W.D. Lee, *Chem. Phys. Lett.* 80 (1981) 574–575.
- [22] J.B.O. Mitchell, S.L. Price, *J. Phys. Chem. A* 104 (2000) 10958–10971.
- [23] P. Söderhjelm, G. Karlström, U. Ryde, *J. Chem. Phys.* 124 (2006) 244101.
- [24] S.L. Price, A.J. Stone, *Mol. Phys.* 40 (1980) 805–822.
- [25] S.C. Nyburg, C.H. Faerman, *Acta Crystallogr., Sect. B Struct. Sci.* B41 (1985) 274–279.
- [26] F.H. Allen, *Acta Crystallogr., Sect. B* 58 (2002) 380–388.
- [27] S.L. Price, A.J. Stone, *Mol. Phys.* 47 (1982) 1457–1470.
- [28] P.M. Rodger, A.J. Stone, D.J. Tildesley, *J. Chem. Soc. Faraday Trans. II* 83 (1987) 1689–1702.
- [29] P.M. Rodger, A.J. Stone, D.J. Tildesley, *Mol. Phys.* 63 (1988) 173–188.
- [30] P.M. Rodger, A.J. Stone, D.J. Tildesley, *Chem. Phys. Lett.* 145 (1988) 365–370.
- [31] A.J. Stone, *J. Am. Chem. Soc.* 135 (2013) 7005–7009.
- [32] S.F. Boys, F. Bernardi, *Mol. Phys.* 19 (1970) 553–566.
- [33] A.J. Stone, *Mol. Phys.* 56 (1985) 1065–1082.
- [34] B.T. Thole, *J. Phys. Chem. Lett.* 59 (1981) 341–350.
- [35] C.R. Le Sueur, A.J. Stone, *Mol. Phys.* 83 (1994) 293–308.
- [36] T.C. Lillestolen, R.J. Wheatley, *J. Phys. Chem. A* 111 (2007) 11141–11146.
- [37] G.J. Williams, A.J. Stone, *J. Chem. Phys.* 119 (2003) 4620–4628.
- [38] P. Drude, *Ann. Phys.* 306 (1900) 566.
- [39] M.W. Cole, D. Velegol, H.-Y. Kim, A.A. Lucas, *Mol. Simul.* 35 (2009) 849–866.
- [40] R.S. Mulliken, *J. Am. Chem. Soc.* 74 (1952) 811–824.
- [41] M.J.S. Dewar, C.C. Thompson, *Tetrahedron* 22 (S7) (1966) 97–114.
- [42] T.K. Ghanty, V.N. Staroverov, P.R. Koren, E.R. Davidson, *J. Am. Chem. Soc.* 122 (2000) 1210–1214.
- [43] R.Z. Khaliullin, A.T. Bell, M. Head-Gordon, *J. Chem. Phys.* 128 (2008) 184112.
- [44] A.J. Stone, A.J. Misquitta, *Chem. Phys. Lett.* 473 (2009) 201–205.
- [45] A.J. Misquitta, *J. Chem. Theory Comput.* 9 (2013) 5313–5326.
- [46] E. Ronca, L. Belpassi, F. Tarantelli, *Comput. Phys. Commun.* 15 (2014) 2682–2687.
- [47] F. Weinhold, C.R. Landis, *Valency and Bonding: A Natural Bond Orbital Donor–Acceptor Perspective*, Cambridge University Press, Cambridge, 2005.
- [48] A.J. Stone, *J. Phys. Chem. A* 121 (2017) 1531–1534.
- [49] A.J. Misquitta, J. Spencer, A.J. Stone, A. Alavi, *Phys. Rev. B* 82 (2010) 075312.
- [50] K.T. Tang, J.P. Toennies, *J. Chem. Phys.* 80 (1984) 3726–3741.



- [51] R.A. Aziz, H.H. Chen, *J. Chem. Phys.* 67 (1977) 5719–5726.
- [52] A.S. Pine, B.J. Howard, *J. Chem. Phys.* 84 (1986) 590–596.
- [53] J. Plięgo, R. Josefredo, S.M. Resende, W.B. De Almeida, *Theor. Chim. Acta* 93 (1996) 333–342.
- [54] R. Podeszwa, R. Bukowski, K. Szalewicz, *J. Phys. Chem. A* 110 (2006) 10345–10354.
- [55] R.A. Kendall, J. Dunning, H. Thom, R.J. Harrison, *J. Chem. Phys.* 96 (1992) 6796–6806.
- [56] A.J. Sadlej, *Theor. Chim. Acta* 79 (1991) 123–140.
- [57] E. Arunan, G.R. Desiraju, R.A. Klein, J. Sadlej, S. Scheiner, I. Alkorta, D.C. Clary, R.H. Crabtree, J.J. Dannenberg, P. Hobza, H.G. Kjaergaard, A.C. Legon, B. Mennucci, D.J. Nesbitt, *Pure Appl. Chem.* 83 (2011) 1637–1641.
- [58] E. Arunan, G.R. Desiraju, R.A. Klein, J. Sadlej, S. Scheiner, I. Alkorta, D.C. Clary, R.H. Crabtree, J.J. Dannenberg, P. Hobza, H.G. Kjaergaard, A.C. Legon, B. Mennucci, D.J. Nesbitt, *Pure Appl. Chem.* 83 (2011) 1619–1636.
- [59] A.D. Buckingham, P.W. Fowler, *Can. J. Chem.* 63 (1985) 2018–2025.
- [60] A.D. Buckingham, P.W. Fowler, A.J. Stone, *Int. Rev. Phys. Chem.* 5 (1986) 107–114.
- [61] M.P. Hodges, A.J. Stone, S.S. Xantheas, *J. Phys. Chem. A* 101 (1997) 9163–9168.
- [62] A.C. Legon, *Phys. Chem. Chem. Phys.* 12 (2010) 7736–7747.
- [63] P. Politzer, J.S. Murray, T. Clark, *Phys. Chem. Chem. Phys.* 12 (2010) 7748–7757.
- [64] P. Politzer, J.S. Murray, T. Clark, *Phys. Chem. Chem. Phys.* 15 (2013) 11178–11189.
- [65] X. Pang, H. Wang, X.R. Zhao, W.J. Jin, *CrystEngComm* 15 (2013) 2722.
- [66] A. Bauzá, R. Ramis, A. Frontera, *J. Phys. Chem. A* 118 (2014) 2827–2834.
- [67] D.J. Wales, *Energy Landscapes*, Cambridge University Press, Cambridge, 2003.
- [68] K.C. Janda, J.C. Hemminger, J.S. Winn, S.E. Novick, S.J. Harris, W. Klemperer, *J. Chem. Phys.* 63 (1975) 1419–1421.
- [69] M. Schnell, U. Erlekam, P.R. Bunker, G. von Helden, J.-U. Grabow, G. Meijer, A. van der Avoird, *Phys. Chem. Chem. Phys.* 15 (2013) 10207–10223.

# Energy Partition Analyses: Symmetry-Adapted Perturbation Theory and Other Techniques

---

*E. Francisco, A. Martín Pendás*

Departamento de Química Física y Analítica, Facultad de Química, Universidad de Oviedo,  
Oviedo, Spain

## 2.1 INTRODUCTION

---

We are about 10 years away from the 100th anniversary of the first applications of quantum mechanics to chemistry. Today, most educated people are aware of the importance of this pillar of human knowledge, and many of them have heard about Schrödinger's equation. With the advent of high performance computing facilities, the accuracy of our simulations has increased in a way hardly imaginable a few decades ago. The dissemination and popularization of the most remarkable discoveries of quantum chemistry among nonspecialists has led to the belief that we have reached an almost complete knowledge of those seemingly simple problems that were investigated, for instance, by Walter Heitler and Fritz London [1]. Partly because of this, many researchers have taken for granted (or fully established) basic models and protocols that are blindly used in large scale simulations. One may think, for instance, that the nature, type, and strength of the forces and interactions existing between the atoms of an individual molecule have ceased to arouse the interest of quantum chemists for being already very well known. As, within this line of reasoning, strong covalent interactions have been basically tamed, it is time to turn our attention toward weak or noncovalent interactions, where knowledge is still being generated and the old paradigms may not work so well. This has led to a dichotomic situation, in which, for example, new intermolecular components in force fields are being actively developed while intramolecular terms are fixed. We think that there is still plenty of room for discussion regarding the nature of covalent intramolecular and noncovalent intermolecular interactions and that future developments may learn from a renewed joint treatment of both. This is the main goal of this chapter.

From the very beginning of quantum chemistry it has been clear that completely isolated molecules do not exist. Even in a very rarefied gas, where the approximation that molecules

do not see each other may be excellent, intermolecular interactions are indeed very strong in the case of their (unusual) collisions. There are circumstances, however, when a single molecule can be safely investigated ignoring the rest. This occurs when all the terms in the Hamiltonian of the complete system ( $\mathcal{H}$ ) that mix coordinates of two different molecules or fragments can be ignored. In turn, this is possible provided that they are far apart, for then all the interaction terms in  $\mathcal{H}$  cancel. In these situations,  $\mathcal{H}$  and the total energy  $E$  are given in very good approximation by the sum of the individual Hamiltonians and molecular energies, respectively. However, when this ideal situation does not occur, quantum-mechanical molecular Hamiltonians and energies are intrinsically nonseparable, and the task we face is much more complicated. Naively, we might think that what we should do is to follow the simple recipe offered by quantum chemistry, namely solving Schrödinger's equation for the interacting system. Of course, as this is possible neither now nor in the foreseeable future, except for systems formed by a small number of molecules, we are required to design and/or invent methods, necessarily approximate, that allow us to know either how two (or many) atoms in a molecule or two (or many) different molecules in a system interact with each other.

The set of techniques developed to calculate the interaction between two molecules (or two atoms in a molecule), to ascertain the nature and type of these interactions, and to discover why these interactions are stabilizing in some cases while destabilizing in others, are collectively referred to as Energy Decomposition Analyses (EDAs). Many EDAs, each of them with possibly several variants, have emerged over the years. Only a small number of them will be briefly explained and reviewed in this chapter.

Regardless how an energetic partition is defined, it should meet several conditions according to Hayes and Stone [2]. For instance, the total interaction energy should be composed of energy contributions endowed with a physically rooted meaning and stable with respect to changes such as computational parameters. Furthermore, this interaction energy should be very similar to that obtained from a high-quality supermolecular calculation, where the interaction energy is calculated as the difference between the energy of the composite system A+B and the energies of the isolated, i.e., noninteracting, molecules A and B at the supermolecular geometry. It is also highly desirable that any EDA be valid in the broadest possible spectrum of intermolecular distances and that it can be applied to completely arbitrary interacting fragments. Finally, an EDA should allow for an easy computational implementation, being free of convergence problems and, at the same time, not too computationally expensive. As we will show in this chapter, most methods developed so far fail to satisfy one or more of the above criteria.

The most difficult requirement to meet is to find an EDA in which the interaction energy can be calculated with the same accuracy and the interpretation of its components is the same regardless of the distance between the fragments. We will see, for instance, that as the two fragments approach, and their electron densities start to overlap to an appreciable extent, several conflicting interpretations of the different energetic terms arise. In many cases, a given term has different names in two EDAs when it refers to the same physical interaction. Other times, the opposite happens and two physically different interactions are termed the same way in two or more EDAs. Our efforts in the present contribution will point toward clarifying the language used in different energy partition methods, the relation between them, and the problems interpreting equally named, sometimes vaguely related quantities. We will dedicate

extra effort to comment and discuss the so-called real-space EDAs, which in our opinion, satisfy Hayes and Stone's requirements [2] in a mostly consistent way.

We have divided the chapter as follows. In the following section, perturbation theory (PT) methods for intermolecular interactions in the long-range limit are reviewed. Different flavors of symmetry adapted PTs for overlapping fragments are discussed in Section 2.3. Other approaches to intermolecular interactions known as supermolecular EDAs are considered in Section 2.4. Both orbital-based and real-space supermolecular EDAs are described, focussing our attention on the latter case in the Interacting Quantum Atoms (IQA) approach [3–5]. In Section 2.5, a comparison of the different energetic terms as obtained in all discussed EDAs will be carried out. To end the chapter, a final overview and some conclusions will be given in Section 2.6.

## 2.2 THE LONG-RANGE LIMIT AND PERTURBATION THEORY

In this section, we will firstly discuss very briefly the main equations of perturbation theory (PT) and its most popular variant, known as Rayleigh–Schrödinger (RS) PT. Then, RS PT will be applied to intermolecular interactions in the long-range limit, i.e., when the electron densities of the two molecules involved in the interaction do not overlap significantly. When this limit is reached and the effects of Pauli's principle on the intermolecular interaction vanishes, PT receives the name of the polarization approximation (PA).

### 2.2.1 Rayleigh–Schrödinger Perturbation Theory

To discuss symmetry adapted perturbation theories (SAPT) it is appropriate to introduce the main equations of PT first. Let us consider a system with a Hamiltonian  $\mathcal{H}^0$  for which the Schrödinger equation has been solved, so the exact energies and wavefunctions are already known:

$$\mathcal{H}^0|n^0\rangle = E_n^0|n^0\rangle, \quad (2.1)$$

where the index  $n$  represents the ground state ( $n = 0$ ) and excited states ( $n = 1, 2, \dots$ ) of the unperturbed system. Schrödinger's equation for a perturbed system with a Hamiltonian  $\mathcal{H} = \mathcal{H}^0 + \mathcal{H}'$  is

$$\mathcal{H}|n\rangle = E_n|n\rangle. \quad (2.2)$$

For the ground state  $|0\rangle$ , Eq. (2.2) can also be written as

$$\mathcal{H}'|0\rangle = (\mathcal{H} - \mathcal{H}^0)|0\rangle, \quad (2.3)$$

$$\mathcal{H}'|0\rangle = (E_0 - \mathcal{H}^0)|0\rangle. \quad (2.4)$$

Left-multiplying the last equation by  $\langle 0^0|$ , integrating and using the intermediate normalization (IN)  $\langle 0|0^0\rangle = \langle 0^0|0\rangle = 1$ , which means that  $|0\rangle$  is not normalized, we have

$$\langle 0^0|\mathcal{H}'|0\rangle = \langle 0^0|(E_0 - \mathcal{H}^0)|0\rangle = E_0 - E_0^0 = \Delta E_0. \quad (2.5)$$

We now introduce  $R_0$ , the reduced resolvent of the ground state

$$R_0 = \sum_{n=1}^{\infty} \frac{|n^0\rangle\langle n^0|}{E_0^0 - E_n^0}. \quad (2.6)$$

When  $R_0$  acts on any function  $|\phi\rangle$ , orthogonal to  $|0^0\rangle$  (for instance,  $|n^0\rangle$  with  $n \neq 0$ ), it behaves as  $(E_0^0 - \mathcal{H}^0)^{-1}$ , i.e.,

$$R_0(E_0^0 - \mathcal{H}^0)|\phi\rangle = (E_0^0 - \mathcal{H}^0)R_0|\phi\rangle = |\phi\rangle. \quad (2.7)$$

However,  $R_0$  is not the inverse of  $(E_0^0 - \mathcal{H}^0)$  since  $R_0(E_0^0 - \mathcal{H}^0)|0^0\rangle = 0 \neq |0^0\rangle$ , and, similarly,

$$R_0|0^0\rangle = \sum_{n=1}^{\infty} \frac{|n^0\rangle\langle n^0|0^0\rangle}{E_0^0 - E_n^0} = 0 \Rightarrow (E_0^0 - \mathcal{H}^0)R_0|0^0\rangle = 0. \quad (2.8)$$

Adding  $(E_0^0 - E_0)|0\rangle$  to both sides of Eq. (2.4) and operating on both sides of the resulting equation with the reduced resolvent  $R_0$  yields

$$R_0(E_0^0 - \mathcal{H}^0)|0\rangle = R_0(E_0^0 - E_0 + \mathcal{H}')|0\rangle. \quad (2.9)$$

From the definition of  $R_0$  (Eq. (2.6)) and the IN, it can be shown that

$$R_0(E_0^0 - \mathcal{H}^0)|0\rangle = |0\rangle - |0^0\rangle. \quad (2.10)$$

Finally, from Eqs. (2.5), (2.9), and (2.10), we obtain

$$|0\rangle = |0^0\rangle + R_0(E_0^0 - E_0 + \mathcal{H}')|0\rangle, \quad (2.11)$$

$$E_0 = E_0^0 + \langle 0^0|\mathcal{H}'|0\rangle. \quad (2.12)$$

These are the basic equations in PT. The ground-state energy,  $E_0$ , and wavefunction of the perturbed system,  $|0\rangle$ , are given in terms of the unperturbed energy and wavefunction,  $E_0^0$  and  $|0^0\rangle$ , plus some corrections that, unfortunately, depend on the unknown wavefunction and energy. Several strategies can be used to solve Eqs. (2.11) and (2.12). For instance, in the Brillouin–Wigner [6] iterative scheme one uses  $|0^0\rangle$  as an approximate wavefunction  $|0\rangle$  in the right-hand side of Eq. (2.11),  $|0\rangle \simeq |0^0\rangle + R_0(E_0^0 - E_0 + \mathcal{H}')|0^0\rangle$ , this approximate  $|0\rangle$  is used again in the right-hand side of Eq. (2.11), and so on a prefixed number of times  $M$ , resulting in

$$|0\rangle \simeq \sum_{m=0}^M \left[ R_0(E_0^0 - E_0 + \mathcal{H}') \right]^m |0^0\rangle. \quad (2.13)$$

Using Eq. (2.13) in Eq. (2.12) gives

$$E_0 = E_0^0 + \sum_{m=0}^M \langle 0^0|\mathcal{H}' \left[ R_0(E_0^0 - E_0 + \mathcal{H}') \right]^m |0^0\rangle. \quad (2.14)$$

$E_0$  in this equation is now treated as a parameter that can be manipulated such that the equation is satisfied. Regrettably, the Brillouin–Wigner perturbation theory is not size-consistent, failing to predict that  $E_{R \rightarrow \infty}(A + B)$ , the total energy of the supermolecule A+B when A and B are separated by a sufficiently large distance, must be equal to  $E(A) + E(B)$ . Another unpleasant feature is that one must decide in advance at what  $m = M$  value we terminate the series in Eq. (2.14), because  $E_0$  enters the definition of the operator in square brackets.

As an alternative, in the size-consistent Rayleigh–Schrödinger (RS) PT the total energy is computed step by step. Expanding  $E_0$  as  $E_0 = \sum_{k=0}^{\infty} E_0^k$  and using this expansion in both members of Eq. (2.14), we identify the successive corrections  $E_0^1, E_0^2, \dots, E_0^k, \dots$  as the terms of the order of  $\mathcal{H}', (\mathcal{H}')^2, \dots, (\mathcal{H}')^k, \dots$ . We get for  $m = 0$

$$E_0^1 = \langle 0^0 | \mathcal{H}' | 0^0 \rangle. \quad (2.15)$$

For  $m = 1$ , we have  $E_0^2 = \langle 0^0 | \mathcal{H}' R_0 (E_0^0 - E_0 + \mathcal{H}') | 0^0 \rangle$ , and remembering that  $R_0 | 0^0 \rangle = 0$  (Eq. (2.8)), we have

$$E_0^2 = \langle 0^0 | \mathcal{H}' R_0 \mathcal{H}' | 0^0 \rangle. \quad (2.16)$$

For  $m = 2$ ,  $E_0^3$  will be given by the third-order terms of the expression

$$\langle 0^0 | \mathcal{H}' \left[ R_0 (E_0^0 - E_0^0 - E_0^1 - E_0^2 - \dots + \mathcal{H}') \right]^2 | 0^0 \rangle, \quad (2.17)$$

namely,

$$E_0^3 = \langle 0^0 | \mathcal{H}' R_0 \mathcal{H}' R_0 \mathcal{H}' | 0^0 \rangle - E_0^1 \langle 0^0 | \mathcal{H}' R_0^2 \mathcal{H}' | 0^0 \rangle. \quad (2.18)$$

Although it is not possible to give a general expression for the  $k$ th correction, it is worth remarking that the corrections of successive orders within RS PT are independent of the maximum order chosen.

### 2.2.2 The Polarization Approximation

We consider now two molecules or fragments A and B with Hamiltonians  $\mathcal{H}^A$  and  $\mathcal{H}^B$  and Schrödinger equations  $\mathcal{H}^A |i^A\rangle = E_i^A |i^A\rangle$  and  $\mathcal{H}^B |j^B\rangle = E_j^B |j^B\rangle$ , with  $i, j = 0, 1, 2, \dots$ . The sum  $\mathcal{H}^0 = \mathcal{H}^A + \mathcal{H}^B$  and the simple products  $|i^A j^B\rangle = |i^A\rangle |j^B\rangle$  are the Hamiltonian and eigenstates of the unperturbed A+B supermolecule:

$$\mathcal{H}^0 |i^A j^B\rangle = (E_i^A + E_j^B) |i^A j^B\rangle = E_{ij}^0 |i^A j^B\rangle. \quad (2.19)$$

If A and B interact with each other but the interaction energy  $E_{\text{int}}$  is much smaller than  $E_i^A$  and  $E_j^B$ , one can try using PT to determine  $E_{\text{int}}$ , by defining the perturbation or interaction Hamiltonian  $\mathcal{H}'$  as the (standard) electrostatic expression (in atomic units)

$$\mathcal{H}' = - \sum_{i \in A} \sum_{\beta \in B} Z_{\beta} r_{i\beta}^{-1} - \sum_{j \in B} \sum_{\alpha \in A} Z_{\alpha} r_{j\alpha}^{-1} + \sum_{i \in A} \sum_{j \in B} r_{ij}^{-1}, \quad (2.20)$$

where  $\alpha, \beta, \dots$  label nuclei and  $i, j, \dots$  are electrons. Within RS PT the first- and second-order energy corrections, given by Eqs. (2.15) and (2.16), take now the forms

$$\mathcal{U}^{(1)} = \langle 0^A 0^B | \mathcal{H}' | 0^A 0^B \rangle, \quad (2.21)$$

$$\mathcal{U}^{(2)} = \langle 0^A 0^B | \mathcal{H}' R_0 \mathcal{H}' | 0^A 0^B \rangle. \quad (2.22)$$

$\mathcal{U}^{(1)}$  is the electrostatic interaction between the unperturbed fragments A and B ( $E_{\text{elstat}}$ )

$$\mathcal{U}^{(1)} = E_{\text{elstat}} = \iint d\mathbf{r}_1 d\mathbf{r}_2 r_{12}^{-1} \rho_i^A(\mathbf{r}_1) \rho_i^B(\mathbf{r}_2), \quad (2.23)$$

where  $\rho_i^A(\mathbf{r}_1)$  is the total charge density of A, including the nuclear contributions, with a similar definition for  $\rho_i^B(\mathbf{r}_2)$ . On the other hand,  $R_0$  can be written in the form

$$R_0 = R_{0,\text{ind}}^{A \rightarrow B} + R_{0,\text{ind}}^{B \rightarrow A} + R_{0,\text{disp}} = R_{0,\text{ind}} + R_{0,\text{disp}}, \quad (2.24)$$

where

$$R_{0,\text{ind}}^{A \rightarrow B} = \sum_{i \neq 0} \frac{|i^A 0^B\rangle \langle i^A 0^B|}{E_{00}^0 - E_{i0}^0}, \quad (2.25)$$

$$R_{0,\text{ind}}^{B \rightarrow A} = \sum_{j \neq 0} \frac{|0^A j^B\rangle \langle 0^A j^B|}{E_{00}^0 - E_{0j}^0}, \quad \text{and} \quad (2.26)$$

$$R_{0,\text{disp}} = \sum_{i,j \neq 0} \frac{|i^A j^B\rangle \langle i^A j^B|}{E_{00}^0 - E_{ij}^0}. \quad (2.27)$$

$R_{0,\text{ind}}^{A \rightarrow B}$  includes only the terms in Eq. (2.6) with B in the ground state ( $0^B$ ) and A in excited states ( $i^A \neq 0^A$ ),  $R_{0,\text{ind}}^{B \rightarrow A}$  the terms with A in the ground state ( $0^A$ ) and B in excited states ( $j^B \neq 0^B$ ), and the third one,  $R_{0,\text{disp}}$ , the terms with both A and B in excited states ( $i^A \neq 0^A$ ,  $j^B \neq 0^B$ ).

Using Eq. (2.24) in Eq. (2.22),  $\mathcal{U}^{(2)}$  becomes

$$\mathcal{U}^{(2)} = \mathcal{U}_{\text{ind}}^A + \mathcal{U}_{\text{ind}}^B + \mathcal{U}_{\text{disp}} = \mathcal{U}_{\text{ind}} + \mathcal{U}_{\text{disp}}, \quad (2.28)$$

where  $\mathcal{U}_{\text{ind}}^A$  and  $\mathcal{U}_{\text{ind}}^B$  represent the induction energy of molecule A in the field of B and of molecule B in the field of A, respectively, and  $\mathcal{U}_{\text{disp}}$  is the second-order dispersion energy. All these terms, together with  $E_{\text{elstat}}$ , are at the root of a large part of the contemporary language on intermolecular interactions. All of them have been considered to some extent in Chapter 1, so here we will treat only those aspects not covered there.

The intermolecular PT considered so far is only valid in the nonoverlapping or long-range limit, i.e., when there are no points in space where the wavefunctions of both fragments are simultaneously different from zero. Equivalently, there must be two nonoverlapping regions  $\Omega_A$  and  $\Omega_B$  such that  $|i^A\rangle \neq 0$  only when all the electrons of A reside in  $\Omega_A$  and  $|j^B\rangle \neq 0$  only when all the electrons of B reside in  $\Omega_B$ . However, even in this long-range limit, the correct

zeroth-order wavefunction for the A+B supermolecule must be of the form  $\mathcal{A}|i^A\rangle|j^B\rangle$ , where  $\mathcal{A}$  is an antisymmetrizer operator that exchanges the electrons of A and B in all possible ways (see below). Otherwise, even though  $|i^A\rangle|j^B\rangle$  remains the same or changes its sign when an arbitrary permutation of the electrons of A or B is performed ( $|i^A\rangle$  and  $|j^B\rangle$  are individually antisymmetric), the simple product is neither symmetric nor antisymmetric with respect to the exchange of electrons between both fragments, and does not satisfy the Pauli antisymmetry principle. Nevertheless, it can be shown that this lack of symmetry of  $|i^A\rangle|j^B\rangle$  has no energetic consequences, so that Eqs. (2.21) and (2.22) are exactly valid when A and B do not overlap. In this regime, one can assign a fixed number of electrons  $N_A$  to fragment A and another number  $N_B$  to fragment B. The charge-transfer phenomenon is therefore excluded by hypothesis when the fragments do not overlap. Out of the long-range regime but when the overlap is still small, the identity  $E_{\text{int}} \simeq \mathcal{U}^{(1)} + \mathcal{U}^{(2)}$  remains approximately valid, at least up to second order in PT. All the methods that ignore the Pauli principle are normally gathered collectively to be within the polarization approximation (PA).

## 2.3 SYMMETRY ADAPTED PTS: BASIC FORMALISM AND FLAVORS

As fragments A and B approach each other and the overlap between them becomes significant, the polarization approximation just discussed starts to fail. This failure is not due to the breakdown of the multipolar approach (MA), frequently used to compute the electrostatic interaction  $E_{\text{elstat}}$  (see Chapter 1, Ref. [7], and Section 2.5.2 below) since the MA can be fully avoided and the failure persists. The reasons for abandoning simple PT due to its deficiencies when one leaves the long-range regime are conceptually much more profound. When fragments A and B overlap, we cannot ignore the role of  $\mathcal{A}$  acting on  $|i^A\rangle|j^B\rangle$ , i.e., the exchange of electrons between both molecules. One can even go further. While it is true that obviating the operator  $\mathcal{A}$  in the long-range limit (i.e., taking  $\mathcal{A}|i^A\rangle|j^B\rangle \equiv |i^A\rangle|j^B\rangle$  or use  $\mathcal{A} = \hat{1}$ , the unit operator) has no energetic consequences, it brings very relevant conceptual issues: Even when carrying out RS PT up to infinite order with standard bases, it is not possible to obtain the correct wavefunction without a proper antisymmetrization of  $|i^A\rangle|j^B\rangle$ . For instance, in the  $R_{\text{H-H}'} \rightarrow \infty$  limit of the  $\text{H}_2$  molecule, the overlap between the true wavefunction and the simple product  $a(1)b(2)$  is  $\sim 2^{-1/2}$ , a number at all close to 1.0.

Electron exchange is the main cause of repulsion between molecules at short distances, preventing them from interpenetrating. However, the antisymmetrization of each  $|i^A\rangle|j^B\rangle$  brings another problem. The set  $\{|i^A\rangle|j^B\rangle\}$  is orthonormal, with each of its elements being an eigenstate of the unperturbed Hamiltonian  $\mathcal{H}^0$ . From this point of view, this orthonormal set is the one that should be used within PT. On the other hand, the antisymmetrized set  $\{\mathcal{A}|i^A\rangle|j^B\rangle\}$  is not orthonormal so that their elements are not eigenstates of any Hermitian operator and cannot be used in standard RS PT. Different methods have been tried to solve these deficiencies (see Ref. [7] and references therein). One of these methods is the Symmetry Adapted Perturbation Theory (SAPT) [8–12], which has many different flavors. SAPT avoids the orthonormality problems of the set  $\{\mathcal{A}|i^A\rangle|j^B\rangle\}$  by working with the simple products  $\{|i^A\rangle|j^B\rangle\}$ , and avoids the noncompliance with the Pauli principle by working with  $\{\mathcal{A}|i^A\rangle|j^B\rangle\}$  as well. Hence, both sets are necessary in SAPT.



In one of the first formulations of SAPT, proposed by Jeziorski and Kołos [13], the Schrödinger equation is solved iteratively, forcing at each step the correct symmetry of the intermediate solutions. To see how this particular SAPT scheme arises, let us firstly see what happens when the appropriate symmetry of the intermediate solutions is obviated. The starting point are Eqs. (2.11) and (2.12) that are now written as

$$\psi_0(n) = \phi^0 + R_0[-\mathcal{E}_0(n) + \mathcal{H}']\psi_0(n-1), \quad (2.29)$$

$$\mathcal{E}_0(n) = \langle \phi^0 | \mathcal{H}' | \psi_0(n-1) \rangle, \quad (2.30)$$

where  $n = 1, 2, 3, \dots$  is the iteration number,  $\psi_0$  is the exact ground-state solution of the Schrödinger equation for the perturbed/interacting system ( $\mathcal{H}\psi_0 = E_0\psi_0$ ),  $\phi^0 \equiv |0^A 0^B\rangle$  is the ground-state eigenstate of the unperturbed Hamiltonian  $\mathcal{H}^0$  (see Eq. (2.19)), and  $\mathcal{E}_0 = E_0 - E_0^0$ , where  $E_0^0 \equiv E_{00}^0$  is the ground-state eigenvalue of  $\mathcal{H}^0$ . The iterative process is started ( $n = 1$ ) with  $\psi_0(0) = \phi^0$ . Using this wavefunction in Eq. (2.30) we obtain

$$\mathcal{E}_0(1) = \langle \phi^0 | \mathcal{H}' | \phi^0 \rangle = E_{\text{elstat}} \equiv E_{\text{pol}}^{(1)}, \quad (2.31)$$

which is the electrostatic interaction energy between the unperturbed fragments ( $E_{\text{elstat}}$ ) or first-order energy in the PA ( $E_{\text{pol}}^{(1)}$ ). Inserting the above result and  $\psi_0(0) = \phi^0$  in Eq. (2.29),  $\psi_0(1)$  turns out to be  $\psi_0(1) = \phi^0 + R_0\mathcal{H}'\phi^0$ , where we have taken into account that  $R_0\phi^0 = 0$ . This  $\psi_0(1)$  coincides with the first-order wavefunction of standard RS PT. Using now  $\psi_0(1)$  in Eq. (2.30) leads to

$$\mathcal{E}_0(2) = \langle \phi^0 | \mathcal{H}' (1 + R_0\mathcal{H}') | \phi^0 \rangle = E_{\text{pol}}^{(1)} + \langle \phi^0 | \mathcal{H}' R_0\mathcal{H}' | \phi^0 \rangle = E_{\text{pol}}^{(1)} + E_{\text{pol}}^{(2)}, \quad (2.32)$$

where  $E_{\text{pol}}^{(2)} \equiv \mathcal{U}^{(2)}$  is the second-order energy in the PA. Repeating the iterations for higher  $n$  and collecting the terms with the same power of the perturbation  $\mathcal{H}'$ , the exact expression of RS PT (plus some higher-order terms) is obtained. The rate at which this iterative process converges depends crucially on the starting  $\psi_0(0)$ . The choice  $\psi_0(0) = \phi^0$  is particularly inappropriate, even at large intermolecular distances. Indeed, in the long-range limit,  $\mathcal{E}_0(n)$  becomes an arbitrarily good approximation of the interaction energy for large values of  $n$ . However, due the lack of symmetry of  $\phi^0 = |0^A 0^B\rangle$ , the interaction energy due to the exchange of electrons between the two molecules, or exchange interaction energy, is not reproduced at any finite order.

A much more interesting  $\psi_0(0)$  to start iterations in Eq. (2.30) is  $\psi_0(0) = \mathcal{N}\mathcal{A}\phi^0 = \mathcal{B}\phi^0$ , where  $\mathcal{N} = \langle \phi^0 | \mathcal{A} | \phi^0 \rangle^{-1}$  and  $\mathcal{A}$  is a partial antisymmetrizer that runs over the  $N!/(N_A!N_B!)$  intersystem permutations of the electrons [14], exchanging coordinates of electrons associated to A with coordinates of electrons associated to B, and  $\mathcal{N}$  ensures compliance with the intermediate normalization condition  $\langle \phi^0 | \psi_0 \rangle = 1$ . The first iteration in Eq. (2.30) gives the first-order correction to the energy

$$\mathcal{E}_0(1) = \frac{\langle \phi^0 | \mathcal{H}' \mathcal{A} | \phi^0 \rangle}{\langle \phi^0 | \mathcal{A} | \phi^0 \rangle} \quad (2.33)$$

that may be split into the polarization part,  $E_{\text{pol}}^{(1)}$  (see Eq. (2.31)), and the rest,

$$\mathcal{E}_0(1) = E_{\text{pol}}^{(1)} + E_{\text{exch}}^{(1)}. \quad (2.34)$$

The last two equations define the exchange interaction energy.

The first iteration wavefunction  $\psi_0(1)$  can be derived using the commutation property  $[\mathcal{A}, \mathcal{H}] = 0$ , the fact that  $\phi^0$  is an eigenstate of  $\mathcal{H}^0$  with eigenvalue  $E_0^0$ , and the properties of the reduced resolvent  $R_0$ . After a lengthy manipulation the result is [15]

$$\psi_0(1) = \psi_0(0) - \mathcal{N} R_0 \mathcal{A} (\mathcal{E}_0(1) - \mathcal{H}') \phi^0. \quad (2.35)$$

When this  $\psi_0(1)$  is used in Eq. (2.30) we obtain

$$\mathcal{E}_0(2) = \mathcal{E}_0(1) - \mathcal{N} \langle \phi^0 | \mathcal{H}' R_0 \mathcal{A} (\mathcal{E}_0(1) - \mathcal{H}') | \phi^0 \rangle. \quad (2.36)$$

The above equations correspond to the PT derived by Murrel and Shaw [16] and Musher and Amos (MS-MA) [17]. They are actually a special case of a more general iterative scheme proposed by Jeziorski and Kołos, whose basic equations are modifications of Eqs. (2.29) and (2.30) [13]. The difference lies in the fact that  $\psi_0(n-1)$  in Eqs. (2.29) and (2.30) is replaced by  $\mathcal{F}\psi_0(n-1)$  and  $\mathcal{G}\psi_0(n-1)$ , respectively, where  $\mathcal{F}$  and  $\mathcal{G}$  are operators that must fulfill  $\mathcal{F}\psi_0 = \psi_0$  and  $\mathcal{G}\psi_0 = \psi_0$  after convergence. The MS-MA scheme corresponds to  $\mathcal{F} = \mathcal{G} = 1$  and  $\psi_0(0) = \mathcal{B}\phi^0 = \langle \phi^0 | \mathcal{A} | \phi^0 \rangle^{-1} \mathcal{A}\phi^0$ . The PA fits also in the above scheme choosing  $\mathcal{F} = \mathcal{G} = 1$  and  $\psi_0(0) = \phi^0$ . In the so-called symmetrized polarization scheme  $\mathcal{F} = 1$ ,  $\mathcal{G} = \mathcal{B}$ , and  $\psi_0(0) = \phi^0$ . Eisenschitz and London [18], Hirschfelder [19], and van der Avoird [20] employed  $\mathcal{F} = \mathcal{A}$ ,  $\mathcal{G} = \mathcal{B}$ , and  $\psi_0(0) = \mathcal{B}\phi^0$ . Finally, Jeziorski and Kołos [13] in their variant of SAPT choose  $\mathcal{F} = \mathcal{A}$ ,  $\mathcal{G} = 1$ , and  $\psi_0(0) = \mathcal{B}\phi^0$ .

A detailed comparison between the different energetic terms obtained in the different flavors of SAPT with those coming from the PA requires a careful study of the antisymmetrizer  $\mathcal{A}$ . This operator can be written in the form

$$\mathcal{A} = C(1 - p^{(1)} + p^{(2)} - \dots) = C(1 + \mathcal{P}), \quad (2.37)$$

where  $C$  is a constant and  $p^{(1)}$  denotes the operator that exchanges one of the electrons of A with one of the electrons of B,  $p^{(2)}$  the operator that exchanges two of the electrons of A with two of the electrons of B, and so on. In particular,

$$p^{(1)} = \sum_{i \in A} \sum_{j \in B} p_{ij}^{(1)}, \quad (2.38)$$

where  $p_{ij}^{(1)}$  exchanges the coordinates of electron  $i$  in fragment A and electron  $j$  in fragment B. It can be shown that  $\langle 0^A 0^B | p_{ij}^{(1)} | 0^A 0^B \rangle \sim s^2$ , where  $s$  is a measure of a typical overlap between orbitals of A and B. Considering this and neglecting terms of order  $s^4$  and higher, Eq. (2.33) for  $\mathcal{E}_0(1)$  results in

$$\mathcal{E}_0(1) \simeq \frac{\langle 0|\mathcal{H}'(1-p^{(1)}+\dots)|0\rangle}{\langle 0|(1-p^{(1)}+\dots)|0\rangle} \quad (2.39)$$

$$\simeq \left[ \langle 0|\mathcal{H}'|0\rangle - \langle 0|\mathcal{H}'p^{(1)}|0\rangle \right] \left[ 1 + \langle 0|p^{(1)}|0\rangle \right] + \mathcal{O}(s^4) \quad (2.40)$$

$$\simeq E_{\text{pol}}^{(1)} - \langle 0|\mathcal{H}'p^{(1)}|0\rangle + E_{\text{pol}}^{(1)}\langle 0|p^{(1)}|0\rangle + \mathcal{O}(s^4), \quad (2.41)$$

where  $1/(1-x) \simeq 1+x$  has been used to expand the denominator of Eq. (2.39),  $|0^A 0^B\rangle \equiv \phi^0$  has been abbreviated as  $|0\rangle$ , and we have used  $E_{\text{elstat}} = E_{\text{pol}}^{(1)} = \langle 0|\mathcal{H}'|0\rangle$ . Comparing the last equation with Eq. (2.34),  $E_{\text{exch}}^{(1)}$  turns out to be

$$E_{\text{exch}}^{(1)} = -\langle 0|\mathcal{H}'p^{(1)}|0\rangle + E_{\text{pol}}^{(1)}\langle 0|p^{(1)}|0\rangle + \mathcal{O}(s^4). \quad (2.42)$$

From Eqs. (2.33), (2.34), and (2.37),  $E_{\text{exch}}^{(1)}$  before expanding  $\mathcal{A}$  as in Eq. (2.37), is given by

$$E_{\text{exch}}^{(1)} = \frac{\langle \phi_0 | (\mathcal{H}' - E_{\text{pol}}^{(1)}) \mathcal{P} | \phi^0 \rangle}{1 + \langle \phi^0 | \mathcal{P} | \phi^0 \rangle}. \quad (2.43)$$

An accurate computation of the above expression is difficult because of the multiple electron exchanges that define  $\mathcal{P}$ , though a matrix formalism has been developed that allows this evaluation. Nonetheless, Eq. (2.42) represents a very good approximation at intermolecular distances corresponding to typical van der Waals minima since its error is of the fourth order in the intermolecular overlap integrals.

It can be shown that the first-order SAPT correction to the energy  $\mathcal{E}_0(1)$  (Eq. (2.33)) is identical to the so-called Heitler–London (HL) energy defined as [15]

$$E_{\text{HL}} = \frac{\langle \mathcal{A}\phi^0 | \mathcal{H} | \mathcal{A}\phi^0 \rangle}{\langle \mathcal{A}\phi^0 | \mathcal{A}\phi^0 \rangle} - E_0^A - E_0^B. \quad (2.44)$$

Besides this,  $\mathcal{E}_0(1)$  coincides with the first-order energy of the intermolecular perturbation theory (IMPT) of Stone and Hayes [2,21]. To see this, we must realize that the zeroth- plus first-order energy in IMPT can be obtained as the energy of the nonorthogonal Slater determinant formed by all the occupied molecular orbitals ( $\phi$ ) of the fragments in their ground states and, since orbitals of fragment A (B) are orthonormal among themselves but orbitals of fragment A are not orthogonal to orbitals of fragment B, this energy is given by

$$(E_0 + E_1)^{\text{IMPT}} = \sum_{i,j} h_{ij} S_{ji}^{-1} + \frac{1}{2} \sum_{i,k,j,m} \langle ik | jm \rangle (S_{ji}^{-1} S_{mk}^{-1} - S_{mi}^{-1} S_{jk}^{-1}), \quad (2.45)$$

where  $h_{ij} = \langle \phi_i | \hat{h} | \phi_j \rangle$  and  $\hat{h}$  is the mono-electronic Hamiltonian that includes the kinetic energy term ( $\hat{t}$ ), the attraction to the nuclei of molecule A ( $-\sum_{\alpha \in A} Z_\alpha / r$ ), and the attraction to the nuclei of molecule B ( $-\sum_{\beta \in B} Z_\beta / r$ ).  $\langle ik | jm \rangle$  is the two-electron repulsion integral  $\langle \phi_i(1)\phi_k(2) | r_{12}^{-1} | \phi_j(1)\phi_m(2) \rangle$  and  $S_{ij} = \langle \phi_i | \phi_j \rangle$ , with  $S_{ij} \neq \delta_{ij}$  if  $\phi_i \in A$  and  $\phi_j \in B$ . However,

the above expression coincides with the first term in Eq. (2.44) when the  $N!/(N_A!N_B!)$  inter-system permutations are included in  $\mathcal{A}$ . Separating the energy of the isolated fragments from Eq. (2.45) one has  $E_0^{\text{IMPT}} = E_0^A + E_0^B$ , while  $E_1^{\text{IMPT}}$  can be written as

$$E_1^{\text{IMPT}} = E_{\text{elstat}} + E_X + E_{\text{rep}}, \quad (2.46)$$

where  $E_{\text{elstat}} = E_{\text{pol}}^{(1)}$  is the electrostatic interaction energy previously seen,

$$E_X = - \sum_{i \in A, j \in B} \langle \phi_i \phi_j | \phi_j \phi_i \rangle \quad (2.47)$$

is the exchange interaction between the orbitals of fragment A and the orbitals of fragment B, and the repulsion energy,  $E_{\text{rep}}$ , is a combination of one and two electron corrections to the orthogonal energy as given by Eq. (2.45) if  $S_{ij} = \delta_{ij}$ ,

$$\begin{aligned} E_{\text{rep}} = & \sum_{i,j} h_{ij} (S_{ji}^{-1} - \delta_{ji}) \\ & + \frac{1}{2} \sum_{i,k,j,m} \langle ik | jm \rangle (S_{ji}^{-1} S_{mk}^{-1} - S_{mi}^{-1} S_{jk}^{-1} - \delta_{ji} \delta_{mk} + \delta_{mi} \delta_{jk}). \end{aligned} \quad (2.48)$$

It is a common practice to join  $E_X + E_{\text{rep}} = E_{\text{xr}}$  and call it exchange-repulsion, although it is important to maintain their individuality for further discussions. It is possible to demonstrate in detail in simple cases (for instance, in the triplet state of  $\text{H}_2$  molecule) that  $E_{\text{xr}}$  exactly coincides with the first-order exchange of SAPT theories, i.e.,  $E_{\text{xr}} \equiv E_{\text{exch}}^{(1)}$ , so that Eqs. (2.34) and (2.46) are actually equivalent, albeit it is not usual to separate the true exchange,  $E_X$ , from repulsion,  $E_{\text{rep}}$ , in SAPT. Looking at Eq. (2.48) it becomes evident that  $E_{\text{rep}}$  includes antisymmetrization corrections to all the energetic terms (kinetic energy, nuclear attractions, Coulomb, and exchange contributions) in the Hamiltonian, both at intra- and interfragment levels. Due to this, the notation  $E_{\text{exch}}^{(1)}$  used in SAPT slightly confusing.

To compute  $\mathcal{E}_0(2)$  in SAPT we start from Eq. (2.36), in which  $\mathcal{E}_0(1)$  is already separated from the second-order corrections:

$$\mathcal{E}_0(2) - \mathcal{E}_0(1) = - \frac{\langle 0 | \mathcal{H}' R_0 \mathcal{A} (\mathcal{E}_0(1) - \mathcal{H}') | 0 \rangle}{\langle 0 | \mathcal{A} | 0 \rangle}. \quad (2.49)$$

Using the properties of  $R_0$ , it can be shown that  $\langle 0 | \mathcal{H}' R_0 \mathcal{A} \mathcal{E}_0(1) | 0 \rangle = 0$ , so that

$$\mathcal{E}_0(2) - \mathcal{E}_0(1) = \frac{\langle 0 | \mathcal{H}' R_0 \mathcal{A} \mathcal{H}' | 0 \rangle}{\langle 0 | \mathcal{A} | 0 \rangle}. \quad (2.50)$$

If Eq. (2.37) for  $\mathcal{A}$  is inserted in Eq. (2.50), we can employ the same strategy applied to derive Eq. (2.40), obtaining in this case

$$\mathcal{E}_0(2) - \mathcal{E}_0(1) = \mathcal{U}_{\text{ind}} + \mathcal{U}_{\text{disp}} + E_{\text{exch}}^{(2)}, \quad (2.51)$$

where  $\mathcal{U}_{\text{ind}}$  and  $\mathcal{U}_{\text{disp}}$  are the induction and dispersion interaction energies of the PA (Eq. (2.28)), and  $E_{\text{exch}}^{(2)}$  represents the exchange correction arising from properly take into account the antisymmetry of the wavefunction. If the second identity in Eq. (2.24) is used,  $E_{\text{exch}}^{(2)}$  can be split into its induction and dispersion contributions

$$E_{\text{exch}}^{(2)} = E_{\text{exch-ind}}^{(2)} + E_{\text{exch-disp}}^{(2)}, \quad (2.52)$$

with

$$E_{\text{exch-ind}}^{(2)} = -\langle 0 | \mathcal{H}' R_{0,\text{ind}} p^{(1)} \mathcal{H}' | 0 \rangle + \langle 0 | \mathcal{H}' R_{0,\text{ind}} \mathcal{H}' | 0 \rangle \langle 0 | p^{(1)} | 0 \rangle + \mathcal{O}(s^4), \quad (2.53)$$

$$E_{\text{exch-disp}}^{(2)} = -\langle 0 | \mathcal{H}' R_{0,\text{disp}} p^{(1)} \mathcal{H}' | 0 \rangle + \langle 0 | \mathcal{H}' R_{0,\text{disp}} \mathcal{H}' | 0 \rangle \langle 0 | p^{(1)} | 0 \rangle + \mathcal{O}(s^4). \quad (2.54)$$

In summary, within SAPT we obtain the same energy corrections known from the PA, which neglects the overlap between the molecular orbitals of both fragments and the antisymmetry of the wavefunction, plus their counterparts of exchange, that take into account these two effects:

$$E_{\text{int}} = E_{\text{pol}}^{(1)} + E_{\text{exch}}^{(1)} + E_{\text{pol}}^{(2)} + E_{\text{exch}}^{(2)} + \dots = \sum_n \left[ E_{\text{pol}}^{(n)} + E_{\text{exch}}^{(n)} \right]. \quad (2.55)$$

The polarization corrections in SAPT,  $E_{\text{pol}}^{(n)}$ , are the coefficients in the Taylor expansion of the ground-state eigenvalue  $E_0(\lambda)$  of the Hamiltonian  $\mathcal{H} = \mathcal{H}^0 + \lambda \mathcal{H}'$ , and are identical to their RS PT analogues. The name *pol*, also used to refer to these terms, comes from Hirschfelder [22], and is due to the fact that they completely ignore the exchange of electrons between fragments A and B. Contrarily to  $E_{\text{pol}}^{(n)}$  and  $E_{\text{exch}}^{(1)}$ , the exchange terms with  $i > 1$ , and consequently the convergence rates of the expansion in Eq. (2.55), differ in different formulations of SAPT. In many relevant cases (for instance, for describing van der Waals interactions between not-too-polar fragments), this is not a serious problem because the first four terms in Eq. (2.55) dominate the interaction and  $E_{\text{exch}}^{(2)}$  does not differ much in different formulations of SAPT.

Up to this point, we have been assuming that the Schrödinger equation for the isolated (i.e., noninteracting) fragments has been exactly solved and, consequently, that the eigenvalues and eigenstates of the Hamiltonian  $\mathcal{H}^0$  are known. This is, of course, not true in general. For molecules with more than a single electron, it is only possible to know approximate energies and wavefunctions of both fragments. This complicates the different SAPT schemes considerably. The usual way to proceed is by starting with approximate wavefunctions describing the fragments, as for instance Slater determinants obtained by solving their Hartree–Fock (HF) self-consistent-field (SCF) equations. Then, both fragments are made to interact, and a three-parameter perturbation theory is applied, which is able to determine the interaction energy between the fragments, as well as approximate the correlation energy within each fragment. The unperturbed Hamiltonian  $\mathcal{H}^0$  is taken as the sum of the Fock operators of both fragments,  $\mathcal{H}^0 = F^A + F^B = F$ , and the perturbation ( $\mathcal{H}'$ ) includes the electrostatic interaction between the particles (electrons+nuclei) of A and the particles of B, given by Eq. (2.20) (usually named  $V$  in the present context), and the difference between the true Hamiltonian and the Fock operator of each molecule,  $W^X = \mathcal{H}^X - F^X$  ( $X = A, B$ ). Denoting as  $\zeta$ ,  $\lambda_A$ , and  $\lambda_B$  the formal

expansion parameters of the theory,  $\mathcal{H}$  will thus be written as [9]

$$\mathcal{H} = F + [\zeta V + \lambda_A W^A + \lambda_B W^B] = F + \mathcal{H}'. \quad (2.56)$$

By applying the triple PT one can derive the expansion

$$E = \sum_{n=0}^{\infty} \sum_{i=0}^{\infty} \sum_{j=0}^{\infty} [E_{\text{pol}}^{(nij)} + E_{\text{exch}}^{(nij)}] = \sum_{n=0}^{\infty} [E_{\text{pol}}^{(n)} + E_{\text{exch}}^{(n)}], \quad (2.57)$$

where  $E_{\text{pol}}^{(nij)}$  and  $E_{\text{exch}}^{(nij)}$  are of  $n$ th order in  $V$ , and of orders  $i$  and  $j$  in  $W^A$  and  $W^B$ , respectively. Terms with  $n = 0$  lack the exchange contributions and correspond to switching off the interfragment perturbation  $V$  or making  $\zeta = 0$ . If we set  $n = i = j = 0$ , the term  $E_{\text{pol}}^{000}$  corresponds to the sum of the HF SCF orbital energies of both fragments. This is equivalent to the sum of the zeroth-order total energies of fragments A and B within the many-body Møller–Plesset (MP) perturbation theory. If the term  $E_{\text{pol}}^{011}$  is added to  $E_{\text{pol}}^{000}$  the result is the sum of the total HF energies of both molecules. Finally, if terms  $E_{\text{pol}}^{0ij}$  up to certain maxima values of  $i$  and  $j$  are added,  $E$  corresponds to the sum of the total energy of fragment A described at the MP $i$  level and the total energy of fragment B described at the MP $j$  level.

Corrections with  $n > 0$  in Eq. (2.57) describe different types of interaction between the two fragments. Among these, the terms with  $i = j = 0$  are the most important ones:  $E_{\text{pol}}^{(n00)}$  and  $E_{\text{exch}}^{(n00)}$  correspond to the polarization and exchange interactions between the fragments A and B described at the HF level. As previously seen,  $E_{\text{pol}}^{(100)} \equiv E_{\text{elstat}}$  is the classical electrostatic interaction between the HF densities of the fragments, while  $E_{\text{exch}}^{(100)}$  is the main component of the Pauli or exchange repulsion. In the same way,  $E_{\text{pol}}^{(200)}$  and  $E_{\text{exch}}^{(200)}$  gather the induction plus dispersion direct and exchange interactions, respectively.  $E_{\text{pol}}^{(nij)}$  and  $E_{\text{exch}}^{(nij)}$  with  $i$  and/or  $j$  greater than 0 collect all the effects of intrafragment correlation (IC) over the HF *uncorrelated* interactions. For instance,  $E_{\text{pol}}^{(1ij)}$  and  $E_{\text{exch}}^{(1ij)}$  take into account the effects of IC on the electrostatic and exchange repulsion interaction energies, respectively, and  $E_{\text{pol}}^{(2ij)}$  and  $E_{\text{exch}}^{(2ij)}$  the effect of IC on the induction + dispersion direct and exchange interactions.

It is customary to add the intrafragment indices and use  $E^{(nk)}$  to identify  $n$ th order in  $V$  and  $k$ th order in  $W^A + W^B$ . The terms due to intrafragment correlation ( $k > 0$ ) are obviously much more difficult to evaluate than the leading term ( $k = 0$ ), corresponding to an HF description of the monomers. The difficulty increases with  $k$  and is greater for the exchange than for the direct terms since the former requires the calculation of multiple overlap integrals between nonorthogonal orbitals. In most cases, among all the intrafragment correlation exchange contributions to the exchange energy only the corrections that are first order in  $V$  ( $n = 1$ ) give a nonnegligible contribution to  $E_{\text{int}}$ .

From its inception until the late 1990s, the correlation energy corrections in SAPT have been taken into account by means of wavefunction electronic structure methods (for instance, the Coupled Cluster (CC) theory). The most recent version [23] truncates the expansion in  $V$

at the third-order and the expansions in  $W^A$  and  $W^B$  at different orders depending on the particular component (the most important components are selectively summed to infinity). However, in the early 2000s, the SAPT methodology including only the lowest orders expressions, less demanding computationally, was formulated replacing the SCF HF orbitals and orbital energies by their counterparts from the Density Functional Theory (DFT) [24] and using the Hamiltonian  $\mathcal{H} = \mathcal{K} + \mathcal{W}^{\text{KS}} + V$ , where  $\mathcal{K} = \mathcal{K}^A + \mathcal{K}^B$  is the sum of the Kohn–Sham (KS) operators of the two fragments, and  $\mathcal{W}^{\text{KS}} = \mathcal{H}^A + \mathcal{H}^B - \mathcal{K}$  [25]. The energy corrections included were

$$E_{\text{int}} = E_{\text{pol}}^{(10)} + E_{\text{exch}}^{(10)} + E_{\text{ind}}^{(20)} + E_{\text{disp}}^{(20)} + E_{\text{exch-ind}}^{(20)} + E_{\text{exch-disp}}^{(20)}. \quad (2.58)$$

The SAPT(DFT) approach is much less demanding computationally than evaluating the regular (non-DFT) SAPT expressions with high-order treatment of electron correlation. Although the first SAPT(DFT) results were disappointing, even for the  $E_{\text{pol}}^{(10)}$  component, it was later revealed that some of the shortcomings were due to the incorrect asymptotic behavior of the exchange-correlation (xc) potentials [23]. After correcting this, the revised approach recovered accurately the first three terms of Eq. (2.58), though the dispersion energies remained inaccurate. However, after the dispersion energies were computed using a method based on the use of coupled KS polarizabilities, the corrected SAPT(DFT) scheme became extremely accurate [23].

An SAPT version has been also developed that allows determining the nonadditive energy components of a trimer A–B–C of closed-shell fragments.

## 2.4 SUPERMOLECULAR EDAS

---

The usual way to proceed in a PT-based calculation of intermolecular interactions, and specifically in SAPT, is to perform quantum-mechanical calculations in the fragments (probably incorporating correlation effects) and subsequently bring the theory up to a given order in the perturbation. Quantum-mechanical calculations in the supermolecule AB are, in principle, not performed in PT calculations. Regardless of whether the antisymmetry of the wavefunction of the whole system is properly taken into account or not, each fragment A and B in PT has a definite number of electrons, so that charge-transfer energy terms are not allowed. The antisymmetrizer operator  $\mathcal{A}$  in SAPT allows for intersystem permutations of electrons, but none of its components ( $p^{(1)}, p^{(2)}, \dots$ ) modify the total number of electrons in each fragment.

A rather different approach to intermolecular interactions and EDAs is based on computing the interaction energy as the total energy of the supermolecule,  $E^{AB}$ , minus the total energy of the fragments,  $E^A$  and  $E^B$ ,

$$E_{\text{int}} = E^{AB} - E^A - E^B, \quad (2.59)$$

obtaining the three total energies from independent quantum-chemical calculations performed in the fragments and in the supermolecule. This strategy is commonly known as the

supermolecular procedure.  $E_{\text{int}}$  is much smaller than any of the three total energies, which, turn, have errors in their computation equal to  $\Delta E^{AB}$ ,  $\Delta E^A$ , and  $\Delta E^B$ . Hence, an accurate determination on  $E_{\text{int}}$  in the supermolecular approach would require  $\Delta E^{AB} \simeq \Delta E^A + \Delta E^B$ . This is a difficult condition to meet. The main factor affecting the inaccuracy of the  $E_{\text{int}}$  values, besides the size-consistent character of the quantum-mechanical method used in the calculations, rests in the so-called basis set superposition error (BSSE) [26]. BSSE has its origin in the lower variational flexibility of the atomic basis sets used to obtain  $E^A$  and  $E^B$  ( $b_A$  and  $b_B$ ) as compared to the basis  $b_{A+B}$  used to obtain  $E^{AB}$ . As a consequence  $\Delta E^{AB} < \Delta E^A + \Delta E^B$  and  $E_{\text{int}}$  is too attractive [27]. A huge amount of work has been done to minimize the BSSE, and, after much debate, the counterpoise (CP) method of Boys and Bernardi [28], that consists in using the supermolecule basis  $b_{A+B}$  to obtain  $E^A$  and  $E^B$ , as well as  $E^{AB}$ , is the established method in supermolecular EDAs (see Chapter 4).

The second factor affecting the accuracy of the  $E_{\text{int}}$  values is the size-consistency of the quantum-mechanical method. A method is size-consistent if it correctly predicts that  $E^{AB} \rightarrow E^A + E^B$  as the inter-fragment distance  $R$  increases to infinity. This characteristic obviously depends on the method itself: HF for closed shell fragments, full configuration interaction (CI), and PT schemes based on appropriate size-consistent references (like MP $n$  or CC expansions) are size-consistent, whereas truncated CIs are not. Standard xc functionals are built to ensure size-consistency, so this is usually not an issue in DFT.

A final problem with the supermolecular approach is related to the (in)ability of methods to adequately capture some parts of the intermolecular  $E_{\text{int}}$ . In the same way as HF does not include correlation and cannot describe dispersion, most DFT functionals are not asymptotically correct and have the same problem. Several solutions have been proposed [29], and reasonable functionals suitable for dealing with dispersion exist nowadays (see Chapters 3 and 8, respectively).

It is sometimes argued that the supermolecular approach offers little insight into the physical meaning of the different contributions to  $E_{\text{int}}$ . However,  $E_{\text{int}}$  is just the *final result* of a supermolecule calculation. The analysis of the type, nature, magnitude, and properties of the different energy contributions to  $E^{AB}$  is the essential task of all EDAs. In supermolecular EDAs, in contrast to PT-based methods, one does not calculate all these energy components independently of each other, adding them all at the end to give  $E_{\text{int}}^{AB}$ . Usually, what is done is just the opposite. Starting from the wavefunction of the supermolecule, possibly using fictitious intermediate states or wavefunctions (at least in some EDAs), one tries to separate intrafragment contributions from those ascribed to their mutual interaction. Broadly speaking, to carry out this general objective, two different classes of methods, both of them with multiple variants and sometimes closely related, are typically employed. In orbital-based EDAs, the energy partition is performed in the orbital or Fock space, while in real-space EDAs partitioning is performed in the three dimensional (3D) space.

In orbital-based EDAs the electrons occupy a given set of molecular orbitals each of which is unequivocally ascribed to fragment A or fragment B. As a consequence, each fragment has, for instance, its own electron density and the electrostatic interaction between A and B takes place, as in PT, between two distinguishable (in general interpenetrating) charge clouds. For the same reason, a number of electrons is assigned to each fragment:  $N_A$  to A,  $N_B$  to B. This, however, does not preclude energy contributions such as the charge-transfer terms from being taken into account since the assignment of a given number of electron to A and B is not



unique. This picture differs from that of real-space EDAs. In these, electrons occupy molecular orbitals that do not belong to a specific fragment, and the problem of determining which electron belongs to A or B is replaced by that of partitioning the 3D space into physically meaningful regions. Nevertheless, the most fundamental difference between orbital-based EDAs and real-space EDAs is that, in the latter, all energetic contributions are invariant with respect to orbital transformations.

In the following two sections some of the most popular orbital and real-space partitions are briefly reviewed. In the case of real-space EDAs, we will mainly focus on the Interacting Quantum Atoms (IQA) method [3–5], an orbital invariant real-space EDA based on the partition of the physical space defined by the Quantum Theory of Atoms in Molecules (QTAIM) developed by Bader and coworkers.

### 2.4.1 Orbital Based Partitions

#### **Kitaura–Morokuma EDA**

One of the best known orbital-based EDAs that has inspired subsequent partitions is the Morokuma EDA [30,31], later modified by Kitaura and Morokuma (KM) [32]. The supermolecule and fragment wavefunctions in this partition are given by Slater determinants. As in many other orbital-based EDAs,  $E_{\text{int}}$  is computed in a series of calculations. In a first step, the energetic cost to modify the geometry of the isolated fragments to those they have in the supermolecule ( $E_{\text{prep}}$ ) is computed. After this, the electrostatic interaction  $E_{\text{elstat}}$  is obtained using Eq. (2.23) with the unperturbed fragment densities. An undistorted antisymmetric wavefunction for the supermolecule is then formed by considering together the original orbitals of both fragments and the subsequent antisymmetrization. This adds the exchange energy  $E_{\text{X}}$  and the repulsion energy  $E_{\text{rep}}$  to the KM interaction. Their sum defines the exchange-repulsion energy,  $E_{\text{xr}} \equiv E_{\text{exch}} = E_{\text{X}} + E_{\text{rep}}$ . In this way, leaving aside  $E_{\text{prep}}$ ,  $E_{\text{xr}}$  is equal to  $E_{\text{exch}}^{(1)}$ , the first-order exchange of SAPT theories, and the sum  $E_{\text{elstat}} + E_{\text{xr}}$  is equivalent to the first-order interaction energy of the IMPT of Stone and Hayes (Eq. (2.46)).

A restricted optimization of the fragment orbitals of each fragment in the electric field of the other, avoiding the mixing of A and B primitives, adds the induction or polarization energy  $E_{\text{pol}}$  to  $E_{\text{int}}$ . Denoting *occ A*, *vir A*, *occ B*, and *vir B* the occupied and virtual orbitals of A and B, respectively,  $E_{\text{pol}}^A$  is attributed to the interaction of blocks *occ A* and *vir A*, while  $E_{\text{pol}}^B$  is due to the interaction of blocks *occ B* and *vir B*. An energy term due to electron charge transfer (CT) from A to B and *vice versa* is also included in the KM EDA as follows. Two SCF calculations are performed. In the first, only the diagonal blocks of the Fock matrix ( $F$ ) and overlap ( $S$ ) matrices (i.e., *occ A* – *occ A*, *occ B* – *occ B*, *vir A* – *vir A*, and *vir B* – *vir B*) are considered in the SCF convergence cycles, setting to zero the rest of blocks. This gives a total energy  $E_1$ . In the second SCF calculation, the blocks *vir A* – *occ B* and *vir B* – *occ A* are also connected. This gives another energy  $E_2$ . The CT energy is then defined as  $E_{\text{CT}} = E_2 - E_1$ . Finally, a remainder residual (mix) energetic term  $E_{\text{mix}}$  collects the rest of energetic contributions to the interaction energy not ascribable to other components. Overall

$$E_{\text{int}}^{\text{KM}} = E_{\text{prep}} + E_{\text{elstat}} + E_{\text{xr}} + E_{\text{pol}} + E_{\text{CT}} + E_{\text{mix}}. \quad (2.60)$$

The KM approach suffers from BSSE, a common problem of orbital-based EDAs, and several methods have been proposed to correct it. In some implementations [33], only the terms  $E_{\text{xr}}$  and  $E_{\text{CT}}$  are corrected for BSSE, while the others remain as in the original KM EDA scheme. Another problem of KM and other orbital-based EDA partitions has to do with using nonstationary states, as for instance the antisymmetric product of undistorted fragment orbitals, or fictitious states (obtained by switching off or switching on different blocks of the Fock matrix to compute some specific energy contributions [34]) in their formulation. Besides this, it is difficult to generalize to correlated (i.e., multideterminant) descriptions of the fragments and the supermolecule. Nevertheless, the KM approach retains its historical importance.

### Ziegler–Rauk EDA

Another equally important orbital-based EDA developed around the same time as KM, and with which it shares several similarities, is the Ziegler and Rauk (ZR) decomposition (ZREDA) [35–37]. This scheme has been revitalized in recent years [38] thanks to its easy adaptation to DFT frameworks. As KM, ZREDA includes also the terms  $E_{\text{prep}}$ , the energy cost associated to distort the fragments equilibrium geometries to their final geometries in the supermolecule,  $E_{\text{elstat}}$ , computed from the fragment charge densities obtained with the HF or (more often) KS orbitals of the isolated fragments, and  $E_{\text{xr}}$ , commonly referred to as  $\Delta E_{\text{Pauli}}$  in this partition. The latter is computed from an antisymmetric HF or KS determinant formed from those of the fragments,  $\Phi^0 = \mathcal{A}\Phi^A\Phi^B$ . This term is a catch-all that may be assimilated to the  $E_{\text{exch}}$  contribution in perturbation approaches. It contains pure exchange contributions ( $E_{\text{X}}$ ), but also (as in IMPT) all the other energy terms due to the nonorthogonality of orbitals ascribed to different fragments (see Eq. (2.48)). Note that, if ZR is used in a DFT context, as it is usual, the identification of  $\Delta E_{\text{Pauli}}$  with the exchange-repulsion term ( $E_{\text{xr}}$ ) of other partitions is not exact since the ZR exchange and kinetic terms correspond to a noninteracting KS system, usually very different from the real interacting-electrons system. The final step in ZREDA is relaxing  $\Phi^0$  to the final stationary supermolecular state. The decrease in energy is known as the orbital interaction term,  $\Delta E_{\text{orb}}$ , and includes within it the terms  $E_{\text{pol}}$ ,  $E_{\text{CT}}$ , and  $E_{\text{mix}}$  of KM. Overall, in the ZR partition

$$E_{\text{int}} = E_{\text{prep}} + E_{\text{elstat}} + \Delta E_{\text{Pauli}} + \Delta E_{\text{orb}}. \quad (2.61)$$

### Localized Molecular Orbital EDA

The localized molecular orbital EDA (LMOEDA) method [39,40] is a hybrid between the KM and IMPT schemes. As the name suggests, it is normally formulated using localized molecular orbitals (LMO)—although this is not strictly necessary—in both the HF and the DFT contexts. For an HF description, the  $E_{\text{elstat}}$ ,  $E_{\text{X}}$ , and  $E_{\text{rep}}$  components in LMOEDA are equivalent to KM. The polarization contribution,  $E_{\text{pol}}$ , is obtained as  $E(\Phi) - E(\Phi^0)$ , where  $E(\Phi)$  is the total energy of the final relaxed wavefunction of the supermolecule ( $\Phi$ ) and  $E(\Phi^0)$  is the total energy of the antisymmetric HF determinant formed as in ZREDA, i.e.,  $\Phi^0 = \mathcal{A}\Phi^A\Phi^B$ . At the HF level,  $E_{\text{pol}}$  in LMOEDA is thus equal to  $\Delta E_{\text{orb}}$  in ZREDA, and gathers the polarization ( $E_{\text{pol}}$ ), charge transfer ( $E_{\text{CT}}$ ), and residual ( $E_{\text{mix}}$ ) terms of the KM approach. The last contribution to  $E_{\text{int}}$  in LMOEDA is the dispersion energy,  $E_{\text{disp}}$ . At the HF level, this term contains simply correlation energy because it is defined as the difference between the energy of a correlated description of the supermolecule (CCSD(T) or MP2, for instance) and

the energy of the relaxed HF wavefunction  $\Phi$ . The formulation of LMOEDA in a DFT context only requires minor adaptations related to handling an electron density that has to be built with the nonorthogonal orbitals that appear in the antisymmetric KS determinant  $\mathcal{A}\Phi^A\Phi^B$ . The total interaction energy in LMOEDA is thus given by the expression

$$E_{\text{int}} = E_{\text{elstat}} + E_{\chi} + E_{\text{rep}} + E_{\text{pol}} + E_{\text{disp}}. \quad (2.62)$$

BSSE can be corrected using the same methods used in the KM scheme.

### Natural EDA

The Natural Energy Decomposition Analysis (NEDA) of Glendening and Streitwieser [41–44] resembles in many respects the KM scheme, but has some other quite different elements. The first step in NEDA is to construct deformed fragment wavefunctions  $\Phi_{\text{def}}^A$  and  $\Phi_{\text{def}}^B$  from the final relaxed wavefunction  $\Phi$  as follows. First, the HF or DFT supermolecular wavefunction  $\Phi$  is taken. Then, the set of matrix transformations ultimately leading to the so-called natural bond orbitals (NBO) of Weinhold and coworkers [45–49] is carried out. Secondly, the Fock matrix in the NBO basis, discarding all the off-diagonal elements that connect NBOs that couple any two orbitals localized on different fragments (these elements are associated to charge transfer), is formed. Finally, this CT-free Fock matrix is diagonalized, leading to a new set of orthogonal orbitals, from which  $\Phi_{\text{def}}^A$  and  $\Phi_{\text{def}}^B$  are constructed.

The energy required to deform the fragments,  $E_{\text{def}}^X = E(\Phi_{\text{def}}^X) - E(\Phi^X)$  ( $X = A, B$ ) is the first contribution to the interaction energy in NEDA. Since  $\Phi_{\text{def}}^A$  and  $\Phi_{\text{def}}^B$  are not variational states of the fragments,  $E_{\text{def}}^A$  and  $E_{\text{def}}^B$  are destabilizing contributions. From  $\Phi_{\text{def}}^A$  and  $\Phi_{\text{def}}^B$  a single-determinant supermolecular wavefunction, called the localized state  $\Phi_{\text{loc}} = \mathcal{A}\Phi_{\text{def}}^A\Phi_{\text{def}}^B$  is built. The CT interaction energy is then defined as  $E_{\text{CT}} = E(\Phi) - E(\Phi_{\text{loc}})$ . Finally, the joint electrostatic, polarization, and exchange is obtained as  $E_{\text{elstat}} + E_{\text{pol}} + E_{\chi} = E(\Phi_{\text{loc}}) - E(\Phi_{\text{def}}^A) - E(\Phi_{\text{def}}^B)$ . Actually, this difference may be partitioned into the three contributions.  $E_{\text{elstat}}$  can be obtained from Eq. (2.23) with the fragment densities associated to  $\Phi_{\text{def}}^{A,\infty}$  and  $\Phi_{\text{def}}^{B,\infty}$ , where “ $\infty$ ” here means that  $\Phi_{\text{def}}^A$  and  $\Phi_{\text{def}}^B$  were obtained as indicated in the three steps above when the fragments are infinitely separated (this  $E_{\text{elstat}}$  is thus equal to the CP-corrected KM value).  $E_{\text{pol}}$  is obtained as the difference between the electrostatic interaction computed with the localized orbitals of  $\Phi_{\text{loc}}$  and the  $E_{\text{elstat}}$  obtained with  $\Phi_{\text{def}}^{A,\infty}$  and  $\Phi_{\text{def}}^{B,\infty}$ , and  $E_{\chi}$  is obtained from Eq. (2.47) with the localized orbitals of  $\Phi_{\text{def}}^A$  and  $\Phi_{\text{def}}^B$ . At variance with IMPT, SAPT, or ZREDA,  $E_{\chi}$  in NEDA is not obtained from noninteracting densities, but from antisymmetric ones. Overall, the NEDA interaction energy is

$$E_{\text{int}} = E_{\text{def}}^A + E_{\text{def}}^B + E_{\text{CT}} + E_{\text{elstat}} + E_{\text{pol}} + E_{\chi}. \quad (2.63)$$

### Other Orbital-Based EDAs

There are many other orbital-based EDAs that we will not present in this chapter. In general, they are formulated in terms of localized molecular orbital descriptions. Among the most well known of these we mention the pair interaction EDA (PIEDA) of Fedorov and Kitaura [50], formulated within the Fragment Molecular Orbital (FMO) theory [51–54], the

absolutely localized molecular orbital (ALMO) partition of Khaliullin et al. [55–57], and the fairly similar Block-Localized-Wavefunction (BLW) EDA of Mo et al. [58,59] A detailed discussion of these methods can be found in Ref. [34].

### 2.4.2 Real-Space Partitions

There are two features common to all the orbital EDAs just described: (i) the association of specific molecular orbitals to each of the two fragments and (ii) the use of intermediate wavefunctions to extract different interaction energy components. There is a degree of arbitrariness regarding the first point since, after a determinant has been built from a set of orthogonal or nonorthogonal orbitals, strictly speaking, a rigorous ascription of these orbitals to fragments is no longer possible. The reason for this is that each orbital is usually ascribed to the fragment in which it is more localized, but different orbital transformations that leave the multielectron wavefunction invariant can be found that give differently localized orbital sets. Regarding the second point, the physical meaning of each energetic term of the interaction energy may be different in different EDAs depending on the intermediate function from which it was obtained.

A different type of approach to energy partitions that tries to avoid the shortcomings of orbital EDAs follows from real-space analyses. Real-space EDAs use molecular orbitals, but only in a nonessential way, as a practical means of realizing the partition effectively. The basic tenet in these techniques is that all energetic quantities should be invariant under orbital transformations, i.e., in real-space EDAs, no energetic component should change when a given multielectron wavefunction is expressed in terms of a different set of orbitals. This is so because all the energy components are built from reduced density matrices (RDMs). Once this essential fact has been established, avoiding from the outset the possible ambiguity of associating an orbital to one fragment or another, the only problem left is partitioning the physical space into physically meaningful domains associated to the interacting molecules. Many possibilities to carry out this partition exist, both in terms of fuzzy regions or by using nonoverlapping domains that divide the space exhaustively. In this chapter, we will only comment on the partition provided by the Quantum Theory of Atoms in Molecules (QTAIM) of Bader and coworkers [60], that belongs to this second category. Deeply rooted in quantum mechanics, the QTAIM divides the space into atomic basins or domains  $\Omega_A$ , the interatomic surfaces being zero-flux surfaces of the gradient of the electron density. The union of all these  $\Omega_A$  domains fills the space completely:  $\bigcup_A \Omega_A = R^3$ , and any union of  $\Omega_A$ 's, e.g., those forming a molecule, is also a QTAIM region.

The most obvious real-space EDA based on the QTAIM partition of  $R^3$  is the Interacting Quantum Atoms (IQA) approach [3–5]. The starting point of IQA is the expression of the total energy of a molecular system,  $E$ , in terms of the first- ( $\rho_1$ ) and second-order ( $\rho_2$ ) RDMs. Using the standard Coulomb Hamiltonian,  $E$  is given as

$$\begin{aligned}
 E &= h + V_{ee} + V_{nn} \\
 &= \int_{\infty}^{\infty} \hat{h} \rho_1(\mathbf{r}_1; \mathbf{r}'_1) |_{\mathbf{r}'_1 \rightarrow \mathbf{r}_1} d\mathbf{r}_1 + \frac{1}{2} \int_{\infty}^{\infty} \int_{\infty}^{\infty} \rho_2(\mathbf{r}_1, \mathbf{r}_2) r_{12}^{-1} d\mathbf{r}_1 d\mathbf{r}_2 + V_{nn}, \quad (2.64)
 \end{aligned}$$

where  $V_{nn} = \sum_{A>B} V_{nn}^{AB}$ , with  $V_{nn}^{AB} = Z^A Z^B R_{AB}^{-1}$ , is the nuclear repulsion energy,  $\hat{h}$  is the one-electron Hamiltonian,  $\hat{h} = \hat{t} - \sum_B Z^B / r_B$ , with kinetic ( $\hat{t}$ ) and electron–nucleus terms,  $\rho_1(\mathbf{r}_1; \mathbf{r}'_1)$  is the nondiagonal first-order RDM,  $\rho_2(\mathbf{r}_1, \mathbf{r}_2)$  is the diagonal second-order RDM or pair density, and the subscript “ $\infty$ ” means that the integration is extended to  $R^3$ . The diagonal part of  $\rho_1(\mathbf{r}; \mathbf{r}')$ , that is  $\rho_1(\mathbf{r}; \mathbf{r})$ , is the electron density  $\rho(\mathbf{r})$ .

After the space is partitioned into QTAIM basins, the IQA method simply proceeds by partitioning all the mono- and bi-electronic integrals into one- and two-basin contributions, respectively,

$$E = \sum_A T_A + \sum_{A,B} V_{en}^{AB} + \sum_{A \geq B} V_{ee}^{AB} + \sum_{A > B} V_{nn}^{AB}, \quad (2.65)$$

where  $T_A$  is the kinetic energy of the electrons in basin  $\Omega_A$ ,  $V_{en}^{AB}$  the nuclear attraction of the electron in  $\Omega_A$  to the nucleus  $B$ ,  $V_{ee}^{AA}$  the electron repulsion energy of the electrons in  $\Omega_A$  among themselves, and  $V_{ee}^{AB}$  (with  $A \neq B$ ) the repulsion energy of the electrons in  $\Omega_A$  with those in  $\Omega_B$ . All intra-atomic components are gathered together to form the atomic self-energy,  $E_{\text{self}}^A$ ,

$$E_{\text{self}}^A = T^A + V_{en}^{AA} + V_{ee}^{AA}, \quad (2.66)$$

while all the inter-basin ones form the inter-basin interaction energy,  $E_{\text{int}}^{AB}$ ,

$$E_{\text{int}}^{AB} = V_{en}^{AB} + V_{en}^{BA} + V_{ee}^{AB} + V_{ee}^{BA}. \quad (2.67)$$

The total energy acquires then a familiar form in atomistic simulations

$$E = \sum_A E_{\text{self}}^A + \sum_{A > B} E_{\text{int}}^{AB}. \quad (2.68)$$

Eqs. (2.66) to (2.68) may be generalized when the molecular system is partitioned into a set of groups  $\mathcal{G}, \mathcal{H}, \dots$  each containing an arbitrary number of atoms. It is only necessary to define the self-energy of a group  $\mathcal{G}$  as

$$E_{\text{self}}^{\mathcal{G}} = \sum_{A \in \mathcal{G}} E_{\text{self}}^A + \sum_{(A \in \mathcal{G}) > (B \in \mathcal{G})} E_{\text{int}}^{AB}, \quad (2.69)$$

where the second sum runs over all pairs of atoms in  $\mathcal{G}$  and the interaction energy between the groups  $\mathcal{A}$  and  $\mathcal{B}$  is

$$E_{\text{int}}^{\mathcal{GH}} = \sum_{A \in \mathcal{G}} \sum_{B \in \mathcal{H}} E_{\text{int}}^{AB}. \quad (2.70)$$

The atomic or group self-energies measure the proper energy of a component of the system in the molecule. These energies differ from their values in a given *in vacuo* reference state. Once such reference states are defined, an atomic deformation energy (or, in general, group deformation energy) may immediately be defined as the difference

$$E_{\text{def}}^A = E_{\text{self}}^A - E_{\text{vac}}^A. \quad (2.71)$$

With this

$$E_{\text{int}} = E - \sum_A E_{\text{vac}}^A = \sum_A E_{\text{def}}^A + \sum_{A>B} E_{\text{int}}^{AB}. \quad (2.72)$$

We should note at this point that the introduction of *in vacuo* reference states is not really necessary in IQA. This real-space EDA is a reference-free energy partition, this virtue being shared by a very limited number of other methods. Another interesting feature that characterizes the IQA partition is that BSSE errors are immediately CP corrected. These errors only affect the  $E_{\text{def}}^A$ 's (and hence the final  $E_{\text{int}}$  value) but never the interaction terms.

Albeit not very frequently in the IQA method, it is possible in principle to separate each deformation energy in two contributions,  $E_{\text{def}}^A = E_{\text{CT}}^A + E_{\text{shape-def}}^A$ , the first one due to the charge transfer (CT) to (from) atom A from (to) the rest of atoms in the molecule, and the second to a shape deformation of the atom in passing from the *in vacuo* state (spherical shape) to the molecule (QTAIM  $\Omega_A$  basin). Secondly, the electronic repulsion terms  $V_{ee}^{AB}$  contain Coulombic, exchange, and correlation energy contributions, so that a finer partition of  $E_{\text{int}}^{AB}$  than that given in Eq. (2.67) is possible. This can be done by separating in  $\rho_2$  the Coulombic part,  $\rho_2(\mathbf{r}_1, \mathbf{r}_2) = \rho(\mathbf{r}_1)\rho(\mathbf{r}_2) + \rho_{xc}(\mathbf{r}_1, \mathbf{r}_2)$ , where  $\rho_{xc}$  is the  $xc$  density. Exchange itself is not well-defined in general correlated cases, but can be obtained in an invariant manner from the Fock–Dirac expression,  $\rho_X(\mathbf{r}_1, \mathbf{r}_2) = \rho_1(\mathbf{r}_1; \mathbf{r}_2)\rho_1(\mathbf{r}_2; \mathbf{r}_1)$ , so that  $\rho_{xc}(\mathbf{r}_1, \mathbf{r}_2) = \rho_X(\mathbf{r}_1, \mathbf{r}_2) + \rho_{\text{corr}}(\mathbf{r}_1, \mathbf{r}_2)$ . This partition allows us to write

$$V_{ee}^{AB} = V_C^{AB} + V_X^{AB} + V_{\text{corr}}^{AB}. \quad (2.73)$$

Adding up all the classical interactions, we can define a global classical interaction,

$$V_{\text{cl}}^{AB} = V_{nn}^{AB} + V_{ne}^{AB} + V_{en}^{AB} + V_C^{AB}. \quad (2.74)$$

Then

$$E_{\text{int}}^{AB} = V_{\text{cl}}^{AB} + V_X^{AB} + V_{\text{corr}}^{AB}. \quad (2.75)$$

In terms of all these quantities,  $E_{\text{int}}$  for a supermolecule formed by two fragments  $\mathcal{G}$  and  $\mathcal{H}$  will be given by

$$E_{\text{int}} = E_{\text{def}}^{\mathcal{G}} + E_{\text{def}}^{\mathcal{H}} + V_{\text{cl}}^{\mathcal{GH}} + V_X^{\mathcal{GH}} + V_{\text{corr}}^{\mathcal{GH}}, \quad (2.76)$$

where the last term is zero in the absence of correlation. From  $\rho_2(\mathbf{r}_1, \mathbf{r}_2) = \rho(\mathbf{r}_1)\rho(\mathbf{r}_2) + \rho_X(\mathbf{r}_1, \mathbf{r}_2) + \rho_{\text{corr}}(\mathbf{r}_1, \mathbf{r}_2)$  and Eq. (2.66) it is clear that the separate influence of Coulombic repulsion, exchange, and correlation on the self-energy of each atom may also be elucidated within the IQA partition.

All the IQA energy terms are expectation values within the physically well-founded QTAIM domains. Hence, all of these contributions have a clear, unique, and unambiguous interpretation. At difference with most orbital EDAs, no fictitious states with artificially constructed wavefunctions appear at any step. Actually, in IQA there is only one step, as all the energy components are obtained from the analysis of a single supermolecular wavefunction. Only if binding energies are necessary the energies of the isolated fragments are also required. There are problems neither with the fulfillment of the Pauli Principle nor the antisymmetry

requirement of the wavefunction. Electrons in IQA are fully indistinguishable, so no fragment labels may be attached to them. Each electron belongs to a fragment when it is located within the basin of that fragment. IQA does not require that each fragment has an integer number of electrons, either. In fact, this number may change as the distance between the two fragments is modified. That is, charge transfer is intrinsically built-in, and affects all the energies. As a consequence, IQA may be applied at any point along dissociation curves, from the long-range to the covalent regimes. For instance, in a CT complex with full electron transfer, the self-energy of the fragments will tend to those of a cation and an anion. No perturbative method is able to describe this type of situation.

Another property of the IQA partition emanates from Eqs. (2.69), (2.70), (2.73), and (2.76). From them, it is obvious that IQA is able to dissect every intra- and interfragment energetic component into intra-atomic and inter-atomic specific interactions, i.e., the role played by each pair of atoms can be individually examined, and the relative importance of Coulombic, exchange, and correlation terms be evaluated. In other words, the IQA scheme in particular and all real-space EDAs in general, thanks to their extremely detailed decomposition of the energy of a system, may reveal intermolecular interactions without paying any additional computational price.

Finally, we note that IQA may deal with partitions of the supermolecule into more than two fragments as easily as in the simplest case of having only two fragments. No extra computations are needed in those cases. Moreover, supermolecular wavefunctions (or more specifically, first- and second-order RDMs) used in the IQA partition may be of any kind. Until now, IQA has been applied with Hartree–Fock, complete active space (CAS) SCF, full-CI, and coupled-cluster singles and double (CCSD) RDMs. Very recently, a Kohn–Sham Density Functional Theory (KS-DFT) description of the supermolecule has also been included in the IQA scheme [61].

## 2.5 PHYSICAL AND CHEMICAL INSIGHT: COMPARISON OF ENERGETIC TERMS

---

After presenting different perturbation and supermolecular EDAS, including the real-space IQA partition, we will compare now the different energy components obtained in these methods. To achieve an even better understanding of the different schemes, besides actual calculations in a set of relatively simple dimers, we will take the triplet state of the  $H_2$  molecule. This is possibly the simplest interacting system with Pauli repulsion and has been repeatedly used as a test [7,62].

### 2.5.1 A Toy Example: The Dissociative Heitler–London Triplet of $H_2$ Molecule

Let us call  $H_a$  and  $H_b$  the two interacting H atoms. Their isolated wavefunctions are pure  $1s$  orbitals,  $a(r_1) = \pi^{-1/2}e^{-r_1}$ ,  $b(r_2) = \pi^{-1/2}e^{-r_2}$ , the spatial part of the HL two-electron nor-

malized wavefunction is [7,62]

$$\Phi = \frac{[a(r_1)b(r_2) - b(r_1)a(r_2)]}{\sqrt{2(1 - S^2)}}, \quad (2.77)$$

where  $S$  is the  $\langle a|b \rangle$  orbital overlap, and the Hamiltonian can be written as  $\mathcal{H} = \hat{h}_1 + \hat{h}_2 + r_{12}^{-1} + R_{ab}^{-1}$ , with  $\hat{h} = \hat{t} - 1/r_a - 1/r_b$ . Notice that  $a(r)$  and  $b(r)$  are eigenfunctions of  $\hat{h}_a = \hat{t} - 1/r_a$  and  $\hat{h}_b = \hat{t} - 1/r_b$ , respectively, with eigenvalues  $E_0^A = E_0^B = -1/2$  a.u. The energy of this state,  $\langle \Phi | \mathcal{H} | \Phi \rangle$ , equals

$$E = \frac{1}{1 - S^2} (h_{aa} + h_{bb} - 2h_{ab}S + J_{ab} - K_{ab}) + R_{ab}^{-1}, \quad (2.78)$$

where  $h_{aa} = E_0^A + \langle a^2 | r_b^{-1} \rangle$ ,  $h_{bb} = E_0^B + \langle b^2 | r_a^{-1} \rangle$ ,  $h_{ab} = h_{ba} = E_0^A S + \langle ab | r_b^{-1} \rangle$ , and  $J_{ab}$  and  $K_{ab}$  are the standard Coulomb and Exchange two-electron integrals,

$$\begin{aligned} J_{ab} &= \langle a(r_1)b(r_2) | r_{12}^{-1} | a(r_1)b(r_2) \rangle \equiv (aa|bb), \\ K_{ab} &= \langle a(r_1)b(r_2) | r_{12}^{-1} | b(r_1)a(r_2) \rangle \equiv (ab|ab). \end{aligned} \quad (2.79)$$

Using the aforementioned eigenvector character of  $a(r)$  and  $b(r)$ , we may extract the energy of the isolated H atoms from Eq. (2.78) recovering the well-known textbook expression [7,62]

$$E = E_0^A + E_0^B + \frac{J - K}{1 - S^2} + R_{ab}^{-1}, \quad (2.80)$$

where  $J$  and  $K$  are the HL direct (or Coulomb) and exchange energies,

$$\begin{aligned} J &= J_{ab} - \langle a^2 | r_b^{-1} \rangle - \langle b^2 | r_a^{-1} \rangle, \\ K &= K_{ab} - S \langle ab | r_b^{-1} \rangle + \langle ab | r_a^{-1} \rangle. \end{aligned} \quad (2.81)$$

These quantities should not be confused with  $J_{ab}$  and  $K_{ab}$ . It is important to note that the HL state  $\Phi$  coincides with the correctly normalized Slater determinant formed with the nonorthogonal  $a$  and  $b$  orbitals:

$$\Phi = \frac{|ab\rangle}{\sqrt{2 \det(\mathcal{S})}}, \quad (2.82)$$

where  $\mathcal{S}$  is the orbital overlap matrix, so that the energy expression in Eq. (2.45) coincides with Eq. (2.80). Since  $J + R_{ab}^{-1}$  is immediately identified as  $E_{\text{elstat}}$ , we have

$$E_{\text{elstat}} = J + R_{ab}^{-1}, \quad (2.83)$$

$$E_{\text{X}} = -K_{ab}, \quad (2.84)$$

$$E_{\text{rep}} = \frac{S^2 J - K}{1 - S^2} + K_{ab}, \quad \text{and} \quad (2.85)$$

$$E_{\text{exch}}^{(10)} = E_{\text{X}} + E_{\text{rep}} \equiv E_{\text{Xr}}, \quad (2.86)$$



where  $E_X$ ,  $E_{\text{rep}}$ , and  $E_{\text{xr}}$  are the exchange, repulsion, exchange-repulsion energies of Stone’s IMPT, and  $E_{\text{exch}}^{(10)}$  is the first-order exchange in SAPT.

In the above simple approximation, the monomers’ functions are not relaxed, so that the total energy  $E$  is equal to the zeroth-order energy ( $E_0 = E_0^A + E_0^B$ ) plus the first-order perturbation energy. No second-order terms (polarization and dispersion) appear.

Looking at Eq. (2.78) we see that upon building  $\Phi$  (Eq. (2.77)) from the isolated H wavefunctions  $a$  and  $b$  (i.e., upon antisymmetrizing) all the molecular energy components change. Separating all of them into fragment contributions is the main goal of a supermolecular EDA. It is relatively simple to show that, to first order in  $S$ , the modification of the electron density at any point  $r$  induced by the antisymmetrizing process is given by  $\Delta\rho(r) = -2Sa(r)b(r)$ , so a charge transfer from the internuclear region toward the rear parts of the internuclear axis takes place, as different textbooks explain (see, for instance, Ref. [62]) and relate to Pauli exclusion. Once this is known, the nature of the energy changes taking place upon bond formation may be easily rationalized. For instance, the contraction of the density and the appearance of a spatial node just in the middle of the internuclear axis increases the kinetic energy, and forces a considerably more negative electron–own-nucleus interaction and a much less attractive electron–other-nucleus contribution. Nonetheless, the increased kinetic energy exactly compensates the extra electron–own-nucleus. This cancellation leads to small energy variations. It can be safely said that this behavior is generally valid, lying behind much of the magic of the small energy differences of chemistry. The antisymmetrizing process also greatly affects the electron–electron repulsion: From Eq. (2.78), its value scales from  $J_{ab} - K_{ab}$  to  $(J_{ab} - K_{ab})/(1 - S^2)$ , which is a large effect at not too long interfragment distances.

In ZREDA,  $E_{\text{elstat}}$  is given also by Eq. (2.83),  $\Delta E_{\text{orb}}$  is zero, since orbitals have not been relaxed, and  $\Delta E_{\text{Pauli}}$  matches  $E_{\text{exch}}^{(10)}$  exactly. The HF SCF solution would end up with a set of modified orbitals that we could localize to make them resemble the atomic ones, but Eq. (2.78) would survive unchanged.  $\Delta E_{\text{orb}}$  is thus a complex combination of kinetic and potential terms, much as  $\Delta E_{\text{Pauli}}$  is. KM, LMOEDA, and NEDA partitions lead to identical results, since no orbital mixing beyond that forced by symmetry is included.

Within the real-space IQA partition,  $\Phi$  is analyzed *per se*. Due to symmetry, the  $\Omega_A$  and  $\Omega_B$  domains in homodiatom molecules coincide, respectively, with the left and right semispaces separated by the plane that intersects orthogonally the internuclear axis at its middle point. Each integral in Eq. (2.78) may be separated into atomic domains. Each one-electron integral will be the sum of two domain contributions, e.g.,

$$h_{aa} = \int_{\Omega_A} a(r)\hat{h}a(r) dr + \int_{\Omega_B} a(r)\hat{h}a(r) dr = h_{aa}^A + h_{aa}^B, \quad (2.87)$$

and two-electron terms, like  $J_{ab}$ , will be split as  $J_{ab} = J_{ab}^{AA} + J_{ab}^{AB} + J_{ab}^{BA} + J_{ab}^{BB}$ , where the four contributions correspond to the four possible distributions of the two electrons in  $\Omega_A$  and  $\Omega_B$ , i.e.,  $(\mathbf{r}_1, \mathbf{r}_2 \in \Omega_A)$ ,  $(\mathbf{r}_1 \in \Omega_A, \mathbf{r}_2 \in \Omega_B)$ ,  $(\mathbf{r}_1 \in \Omega_B, \mathbf{r}_2 \in \Omega_A)$ , and  $(\mathbf{r}_1, \mathbf{r}_2 \in \Omega_B)$ , respectively. By symmetry, each atomic kinetic energy is half the total kinetic energy,  $T^a = T^b = T/2$ . In the long-range limit ( $R_{ab} \rightarrow \infty$ ), it is clear that  $E_{\text{self}}^A$  and  $E_{\text{int}}^{AB}$  will tend to  $E_0^A$  and zero, respectively. As  $R_{ab}$  decreases or  $S$  increases,  $T^a$  and  $V_{ne}^{aa}$  (as we have seen) will become more positive and more negative, respectively, although both quantities do not exactly balance each other.

In real-space partitions there is a nonzero probability that any number  $n \leq N$  of electrons ( $N$  being the total number of electrons of the system) are found in a given basin. In the present case, both electrons may be in  $\Omega_A$  or in  $\Omega_B$ . This implies that there will be an intra-basin electron repulsion, even though the average electron population of each basin is 1.0,  $\langle n \rangle_{\Omega_A} = \langle n \rangle_{\Omega_B} = 1.0$ . In other words,  $J_{ab}$  (and, similarly,  $K_{ab}$ ) accounts for both intra-basin ( $J_{ab}^{AA}$  and  $J_{ab}^{BB}$ ) and inter-basin ( $J_{ab}^{AB} + J_{ab}^{BA}$ ) contributions.

Finally, when electron repulsion is split into Coulomb and  $xc$  terms, strictly speaking, it is only permissible to use  $\rho$  and  $\rho_{xc}$ , respectively. In consequence,  $\rho$  at any point contains contributions of both electrons. Then, the electrostatic electron–electron interaction,  $\int d\mathbf{r}_1 d\mathbf{r}_2 r_{12}^{-1} \rho(\mathbf{r}_1) \rho(\mathbf{r}_2)$ , will include self-interaction terms, and the same applies to the  $xc$  term. If we add all classical interaction terms to build the IQA  $V_{\text{cl}}^{AB}$  (Eq. (2.74)), the noninterpenetrating character of the atomic densities makes this term positive, i.e., destabilizing (see next section). This is at variance with the standard  $E_{\text{elstat}}$ , and may be shown to be always the case in symmetric interactions. The magnitudes of both self-interaction and intra-atomic electron repulsion components depend on the probability of finding the two electrons in a region, i.e., on the delocalization of the electrons (which is controlled by  $S$ ). As this probability tends to 0 in the long-range limit, both components decay exponentially with  $R_{ab}$ , converging on their perturbative or orbital-EDA counterparts. There is a difference, however. Real-space techniques like IQA do not need any external reference to obtain interactions. They are obtained directly from the wavefunction.

After this general discussion of the first excited triplet state of  $\text{H}_2$ , we will compare different energy terms using different methods in a set of very simple dimers that cover different types of interactions, from fully covalent bonds to weak intermolecular interactions. The SAPT calculations were performed using the `sapt12` code [23], KM and LMOEDA numbers come from the `gamess` package [63], ZREDA decompositions with Gaussian basis sets were obtained with our `imolint` program [64], NEDA partitions were carried out with the NBO5 code [65], and the IQA/QTAIM real-space calculations with our `promolden` [66] program. In all the cases, the geometry has been optimized with common aug-cc-pVnZ ( $n = \text{D, T}$ ) basis sets, selectively applying CP corrections. To obtain these, the energy of each fragment was computed with both its own basis set and the basis set of the supermolecule A+B. The most relevant energy contributions with the different EDAs and levels of calculation are collected in Tables 2.1 (LMOEDA), 2.2 (IQA RHF), 2.3 (IQA RHF H–H EDA like), 2.4 (NEDA), 2.5 (ZREDA), 2.6 (SAPT0), 2.7 (IQA full-CI), and 2.8 (IQA CAS).

## 2.5.2 The Coulombic or Electrostatic Interaction

We will start with the electrostatic interaction energy between the fragments,  $E_{\text{elstat}}$ , which is present in all of the partition schemes discussed so far. In the PA, SAPT, and all orbital EDAs,  $E_{\text{elstat}}$  is given by Eq. (2.23), where  $\rho_i^A(\mathbf{r})$  and  $\rho_i^B(\mathbf{r})$  are the total densities of fragments A and B, respectively. In all these partitions, except in NEDA, these densities are obtained from the molecular orbitals of the isolated fragments (with the geometry they have in the supermolecule). In other words,  $\rho_i^A(\mathbf{r})$  ( $\rho_i^B(\mathbf{r})$ ) is determined as if fragment B (A) did not

exist. The counterpart of  $E_{\text{elstat}}$  in IQA is given by Eq. (2.74), that can be recast in the form

$$V_{\text{cl}}^{AB} \equiv E_{\text{elstat}}^{\text{IQA}} = \int_{\Omega_A} d\mathbf{r}_1 \int_{\Omega_B} d\mathbf{r}_2 r_{12}^{-1} \rho_t(\mathbf{r}_1) \rho_t(\mathbf{r}_2), \quad (2.88)$$

where  $\rho_t(\mathbf{r}) = \sum_B Z^B \delta(\mathbf{r} - \mathbf{R}_B) - \rho(\mathbf{r})$ . Purely from a formal point of view, this expression is entirely analogous to Eq. (2.23) if we define

$$\rho_t^A(\mathbf{r}) = \begin{cases} \rho_t(\mathbf{r}) & : \mathbf{r} \in \Omega_A, \\ 0 & : \mathbf{r} \notin \Omega_A, \end{cases} \quad (2.89)$$

and the integrations over  $\mathbf{r}_1$  and  $\mathbf{r}_2$  are extended to all space. However, the resemblance ends here. Eq. (2.23) assumes that electrons in different fragments are distinguishable, whereas in IQA and other orbital-free techniques only the full density  $\rho_t(\mathbf{r})$  is available, so that superscripts A and B for  $\rho_t(\mathbf{r})$  in Eq. (2.88), are unnecessary and also wrong from a purely conceptual viewpoint. This does not mean that there are no circumstances in which  $E_{\text{elstat}}^{\text{IQA}}$  would equal the  $E_{\text{elstat}}$  value computed with a method that assumes that electrons in fragments A and B as distinguishable. For instance, in the long-range limit, every orbital that appears in the density  $\rho_t^A(\mathbf{r})$  of an orbital-based partition has a negligible overlap with all the orbitals that define  $\rho_t^B(\mathbf{r})$ . In this limit, the basins  $\Omega_A$  and  $\Omega_B$  have an integer number of electrons and  $E_{\text{elstat}}^{\text{IQA}}$  and  $E_{\text{elstat}}$  will be equal.

There is also another important issue that differentiates in an essential way the IQA scheme from the orbital-based and SAPT partitions. In terms of the orbitals that define  $\rho_t^A(\mathbf{r})$  and  $\rho_t^B(\mathbf{r})$  in the latter partitions,  $E_{\text{elstat}}$  can be written as (assuming, for simplicity, that each fragment is formed by a single atom):

$$E_{\text{elstat}} = - \sum_{i \in A} \left\langle i \left| \frac{Z^B}{r_{iB}} \right| i \right\rangle - \sum_{j \in B} \left\langle j \left| \frac{Z^A}{r_{jA}} \right| j \right\rangle + \sum_{i \in A, j \in B} \langle ij | ij \rangle + \frac{Z^A Z^B}{R_{AB}}, \quad (2.90)$$

and  $E_X$  is given (in SAPT) by Eq. (2.47). From Eqs. (2.90) and (2.47) it is clear that in SAPT an electron in orbital  $i \in A$  or in orbital  $j \in B$  never interacts with itself, i.e., self-interaction is absent from orbital and SAPT partitions. Contrarily, electron repulsion in any method that uses invariant RDMs faces the problem of electrostatic self-interaction. This means that a given electron at  $\mathbf{r}_1$  will interact with itself when at  $\mathbf{r}_2$ . In orbital parlance,  $i = j$  terms are included in the third sum of Eq. (2.90). This Coulombic self-interaction is corrected by the invariant definition of exchange, which is thus also affected by self-interaction (again,  $i = j$  terms in Eq. (2.47)). In fact, a large part of the Fermi hole that builds around an electron is due to the self-interaction correction [67], or proper electron counting. There is no way out: using invariant densities implies self-interaction. As an example,  $V_X^{AB}$  will be nonzero even in the  $\text{H}_2$  molecule, where an equal spin pair does not exist but a self-interaction one does. In strong bonding interactions,  $V_{xc}^{AB}$ , being the nonclassical interaction energy, measures covalency, while  $V_{\text{cl}}$  describes ionicity.

Leaving aside the essential differences between  $E_{\text{elstat}}$  and  $E_{\text{elstat}}^{\text{IQA}}$ , it is worth pausing a bit in the description of how they can be evaluated in practical terms. This evaluation may

be direct, i.e., from 3D one-electron and 6D two-electron integrals between orbitals, or may be Laplace-expanded (see Chapter 1) to give rise to the multipolar series. In principle, both approaches can be used with  $E_{\text{elstat}}$  and  $E_{\text{elstat}}^{\text{IQA}}$ . Locating two parallel reference frames centered on fragments A and B and separated by the vector  $\mathbf{R} = R\hat{\mathbf{R}}$ , the multipolar electrostatic interaction is

$$E_{\text{elstat}}^m = \sum_{l_1 m_1} \sum_{l_2 m_2} C_{l_1 m_1, l_2 m_2}(\hat{\mathbf{R}}) \frac{Q_{l_1 m_1}^A Q_{l_2 m_2}^B}{R^{l_1 + l_2 + 1}}, \quad (2.91)$$

where the  $C$  coefficient is a tensor-coupling term dependent on the orientation of both frames only and the  $Q$ 's are the fragments' multipole moments,

$$Q_{lm}^A = \sqrt{\frac{4\pi}{2l+1}} \int d\mathbf{r} \rho_t^A(\mathbf{r}) r^l S_{lm}(\hat{\mathbf{r}}), \quad (2.92)$$

with  $S_{lm}$  denoting a real spherical harmonic [68].

If the expansion converges,  $E_{\text{elstat}}$  may be obtained very quickly at different  $\mathbf{R}$ 's, and the  $R$  and  $\hat{\mathbf{R}}$  dependence written easily in terms of the  $Q_{lm}^A$  moments. Unfortunately, the multipolar expansion is only asymptotically convergent (see Chapter 1 and Ref. [7]) and, even when strictly convergent,  $E_{\text{elstat}}^m$  is in error with respect to its exact value. The difference is called the penetration energy,  $E_{\text{pen}} = E_{\text{elstat}} - E_{\text{elstat}}^m$ . For instance, in the trivial case of the  $\text{H}_2$  molecule, each isolated atom density in orbital EDAs and SAPT has spherical symmetry, so that the only nonzero multipole moment at any  $R$  is  $Q_{00} = N - Z = 0$ . Hence,  $E_{\text{elstat}}^m = 0$  at any distance, and the full  $E_{\text{elstat}}$  value is due to penetration. It is thus clear that the degree of validity of the multipolar approach depends on the magnitude  $E_{\text{pen}}$ . At the singlet aug-cc-pVTZ//FCI geometry of  $\text{H}_2$  molecule, this is equal to  $-2.58$  kcal/mol ( $-2.63$  if CP corrected) for both the bonding ground-state singlet (S) and the dissociative first-excited triplet (T) (see Table 2.1). Here we find a first interpretation problem with  $E_{\text{elstat}}$ : it does not depend on the molecular electronic state under study. This behavior, perfectly admissible in the long-range regime, is, at best, quite disturbing in the general case.

When Eq. (2.91) is applied within the IQA partition, the  $Q_{lm}^A$  multipoles are known as QTAIM atomic multipoles. Due to the irregular shapes of QTAIM basins, their numerical evaluation by means of Eq. (2.92) is computationally more expensive than in the case of orbital EDAs. Actually, the  $Q_{lm}^\Omega$ 's do not necessarily tend to vanish when  $l$  increases, though the power  $l_1 + l_2 + 1$  in the denominator of Eq. (2.91) makes this expression convergent in many cases. This approach has been pursued successfully by Paul Popelier, among others [69]. Needless to say, QTAIM atomic multipoles contain self-interaction and reflect the changes suffered by the fragments' electronic distribution upon interaction.

All the convergence issues of Eq. (2.91), both in orbital and real-space partitions, disappear if, instead of the Laplace formula for  $r_{12}^{-1}$ , we use its bipolar expansion [70,71]. By doing this, we arrive at the following absolutely convergent and exact expression for  $E_{\text{elstat}}$  [70]:

$$E_{\text{elstat}} = \sum_{l_1 m_1} \sum_{l_2 m_2} \sum_{l_3 = |l_1 - l_2|}^{l_1 + l_2} \sum_{m_3} S_{l_3 m_3}(\hat{R}) D_{l_1 m_1 l_2 m_2}^{l_3 m_3} \times \left[ \int_0^\infty r_1^2 dr_1 \int_0^\infty r_2^2 dr_2 \rho_{l_1 m_1}^A(r_1) V_{l_1 l_2 l_3}(r_1, r_2, R) \rho_{l_2 m_2}^B(r_2) \right], \quad (2.93)$$

where  $S_{lm}$  are real spherical harmonics [7],  $\rho_{lm}^A(r) = \int \sin(\theta) d\theta d\phi \rho_l^A(\mathbf{r}) S_{lm}(\hat{r})$ ,  $D$  coefficients are Gaunt coupling terms, defined as

$$D_{l_1 m_1 l_2 m_2}^{l_3 m_3} = \langle S_{l_3 m_3} | S_{l_1 m_1} | S_{l_2 m_2} \rangle, \quad (2.94)$$

and  $V_{l_1 l_2 l_3}(r_1, r_2, R)$  are functions which depend on the relative values of  $r_1, r_2$ , and  $R$ . They divide the  $r_1, r_2, R$  space into four different regions. If  $r_1 + r_2 < R$  always, i.e., when the densities do not overlap spherically, it can be shown that  $V$  contains a  $\delta_{l_3, l_1 + l_2}$  term, and that the above expression coincides with the standard multipole expansion (Eq. (2.91)). The nonoverlapping condition may be fulfilled with QTAIM's densities whenever  $R$  is large enough but, strictly speaking, it will never be attained with overlapping fragments. Another point is that the comparison between Eqs. (2.91) and (2.93) provides an explicit expression for  $E_{\text{pen}}$ .

An HF (full-CI) IQA analysis of the  $\text{H}_2$  triplet gives  $E_{\text{elstat}}^{\text{IQA}} = 60.01$  kcal/mol (60.06 kcal/mol), a large value compared to that of an orbital EDA (for instance,  $E_{\text{elstat}}^{\text{IQA}} = -2.63$  kcal/mol in LMOEDA, Table 2.1). This is basically due to the self-interaction caused by the nonnegligible probability of finding the two electrons in one of the atomic domains ( $\approx 0.13$ ), a fact that shows that despite the usual belief that a triplet is a system that excludes heavily the two electrons, there is still considerable delocalization in real space. In other words, if electrons and nuclei were completely localized in their atomic regions and described by the molecular density  $\rho$ , the classical interaction would still be about +60 kcal/mol. This is an orbital-invariant result.

Let us consider the LiH molecule now. Here, the relevant question of how to choose the states of the isolated atoms arises since any reference-dependent EDA partition will provide very different answers if one chooses an atomic or an ionic reference. In the former case, the LMOEDA HF  $E_{\text{elstat}}$  at the CCSD geometry is  $-7.22$  kcal/mol, that changes to  $-175.04$  if the ionic reference is chosen. This is the same value obtained in SAPT, for instance. The rest of the energy components will change accordingly. In IQA, the HF  $V_{\text{cl}}^{AB} \equiv E_{\text{elstat}}^{\text{IQA}}$  value is  $-134.77$  kcal/mol, that changes to  $-141.23$  and  $-145.75$  at the CAS and full-CI levels, respectively. These are reference-independent values. The IQA HF and full-CI net charges ( $Q_{00}$ ) of the Li atom are  $+0.857 |e|$  and  $+0.899 |e|$ , respectively. A simple scaling of  $E_{\text{elstat}}^{\text{IQA}}$  to complete ionization leads to about  $-183$  kcal/mol (HF) and  $-187$  kcal/mol (full-CI), fairly similar to the SAPT or LMOEDA  $E_{\text{elstat}}$  values. Moreover,  $E_{\text{elstat}}^{\text{IQA}}$  in IQA changes automatically from a typical atomic value in the long-range limit to the ionic value found at distances close to equilibrium. A similar scenario can only be found in NEDA, where deformed fragments are also used: the NEDA net charges of the Li atom in LiH and LiF are  $0.8446 |e|$  and  $0.9778 |e|$ , respectively, very close to the IQA results and also reference-independent. We should note, however, that all the other energy components in NEDA become affected by the reference.

**TABLE 2.1** LMOEDA energy decomposition results. All units in kcal/mol. All data are CP corrected and “ion” means an ionic reference.  $E_{\text{int}}^{\text{CCSD}}$  may be obtained as  $E_{\text{int}}^{\text{HF}} + E_{\text{disp}}^{\text{CCSD}}$

	$E_{\text{elstat}}$	$E_{\text{pol}}$	$E_{\chi}$	$E_{\text{rep}}$	$E_{\text{disp}}^{\text{CCSD}}$	$E_{\text{int}}^{\text{HF}}$
H <sub>2</sub> (S)	-2.63	-80.96	0.00	0.00	-24.93	-83.58
H <sub>2</sub> (T)	-2.63	-89.99	-199.43	427.82		135.78
HF	-115.39	-343.53	-229.74	588.73	-35.91	-99.92
HCl	-66.56	-146.74	-105.33	238.63	-22.41	-80.00
LiH	-7.22	-37.21	-5.27	15.62	-22.91	-34.08
LiF	-38.93	-130.79	-58.76	135.68	-39.21	-92.81
HF (ion)	-233.57	-149.55	0.00	0.00	6.63	-383.12
HCl (ion)	-151.31	-183.85	0.00	0.00	-1.19	-335.16
LiH (ion)	-175.04	-28.23	-17.85	56.26	1.37	-164.86
LiF (ion)	-207.49	-21.67	-22.70	66.31	2.78	-185.55
F <sub>2</sub>	-153.54	-295.83	-310.05	786.88	-52.98	27.46
Cl <sub>2</sub>	-53.00	-123.08	-129.95	281.24	-23.37	-24.79
HF-HF	-5.41	-1.42	-3.64	6.83	-0.32	-3.64
HF-ClF	-2.67	-0.53	-2.11	3.69	-0.25	-1.61
BH <sub>3</sub> -NH <sub>3</sub>	-77.90	-62.44	-115.90	222.86	-5.36	-33.38
H <sub>2</sub> O-H <sub>2</sub> O	-6.43	-1.40	-5.29	9.40	-0.45	-3.72

Summarizing, orbital EDAs obtain  $E_{\text{elstat}}$  as the Coulomb interaction between the interpenetrating and distinguishable densities of the interacting fragments. Except in NEDA, the densities are assumed to be those of the isolated fragments. Although reasonable and logical in the long-range limit, this assumption, clearly inherited from perturbation theory, is not tenable at short inter-fragment distances, where considerable charge transfer may take place. Moreover,  $E_{\text{elstat}}$  in orbital EDAs does not incorporate self-interaction corrections. On the contrary, the IQA approach and other real-space techniques compute the electrostatic interaction from densities in the molecule, without any recourse to references. If fragments are charged, this interaction in IQA will be dominated by the charge-charge interaction. Otherwise, the dominant contribution will come from the dipoles or the higher-order multipoles. A comparison of LMOEDA (Table 2.1) and IQA values (Table 2.2) is illustrative of the differences between a typical real-space partition and an orbital-based EDA.  $E_{\text{elstat}}^{\text{IQA}}$  is highly destabilizing for covalently bonded dimers, negative and large for strongly charged fragments, and small and stabilizing for hydrogen-bonded dimers like water dimer, all in agreement with what one might expect. Two examples of the former are the H<sub>2</sub> (singlet) and F<sub>2</sub> molecules, for which  $E_{\text{elstat}}^{\text{IQA}}$  is destabilizing (25.2 and 48.2 kcal/mol at the CAS level, respectively), while the LMOEDA  $E_{\text{elstat}}$  values are -108.5 and -153.54 kcal/mol if CP corrected. The stabilizing value in F<sub>2</sub> is striking considering that this molecule is unbound at the HF level, but it is simply a consequence of the strong overlap between the densities of both fluorine atoms.

The case of HCl molecule also deserves comment. The LMOEDA  $E_{\text{elstat}}$  value is -66.56 when the neutral atoms are taken as reference, and -151.31 kcal/mol when the ionic reference is employed. However, in IQA,  $E_{\text{elstat}}^{\text{IQA}}$  is destabilizing (21.77 kcal/mol at the CAS level), which is compatible with the highly covalent character of this molecule, and contrasts with

**TABLE 2.2** IQA RHF energy decomposition results. All units in kcal/mol. All data are CP corrected and “ion” means an ionic reference

	$E_{\text{def}}^A$	$E_{\text{def}}^B$	$E_{\text{elstat}}^{\text{IQA}}$	$V_{\text{xc}}^{AB}$	$E_{\text{int}}^{AB}$	$E_{\text{int}}$
H <sub>2</sub> (S)	27.42	27.42	25.22	-163.63	-138.41	-83.56
H <sub>2</sub> (T)	73.36	73.36	60.01	-70.97	-10.96	135.76
H-F	194.71	21.86	-235.01	-81.50	-316.51	-99.94
H-Cl	77.52	-13.48	19.70	-163.68	-143.98	-79.93
Li-H	120.02	11.53	-134.77	-30.87	-165.64	-34.09
Li-F	141.15	-38.10	-165.91	-29.64	-195.54	-92.49
H-F (ion)	-118.95	52.32	-235.01	-81.50	-316.51	-383.14
H-Cl (ion)	-236.13	45.02	19.70	-163.68	-143.98	-335.09
Li-H (ion)	-3.17	3.93	-134.77	-30.87	-165.64	-164.87
Li-F (ion)	17.97	-7.66	-165.91	-29.64	-195.54	-185.23
F <sub>2</sub>	110.32	110.32	45.20	-238.34	-193.14	27.50
Cl <sub>2</sub>	69.62	69.62	29.93	-195.38	-145.76	-26.21
HF-HF	3.59	6.21	-4.96	-8.44	-13.40	-3.60
HF-ClF	5.34	2.07	-2.81	-6.44	-9.24	-1.84
BH <sub>3</sub> -NH <sub>3</sub>	46.65	89.80	-72.24	-98.46	-170.70	-34.25
H <sub>2</sub> O-H <sub>2</sub> O	4.71	6.25	-5.72	-9.49	-15.22	-4.26

$E_{\text{elstat}}^{\text{IQA}} = -224.66$  kcal/mol in the lithium fluoride molecule. Finally, it is important to note that, despite everything we have said above, orbital and real-space electrostatic energies tend to be increasingly similar as charge transfer is not dominant and we shift from the short- to the long-range regime. For instance,  $E_{\text{elstat}}$  at the HF level for the BH<sub>3</sub>-NH<sub>3</sub> and (H<sub>2</sub>O)<sub>2</sub> complexes are -77.90 and -6.43 kcal/mol, relatively similar to their IQA analogues (-72.24 and -5.72 kcal/mol).

### 2.5.3 Exchange and Antisymmetry

As we have seen, taking into account electron indistinguishability and the correct antisymmetry of the zeroth-order wavefunction makes the formulation of SAPT and other perturbation methods considerably difficult. However, it is also true that, besides the electrostatic interaction, most of these methods agree on the first-order energy correction or exchange-repulsion energy. If the exchange interaction energy  $E_{\chi}$  is further separated assuming that the orbitals of both fragments are orthogonal, the remaining energy component is  $E_{\text{rep}}$ . The energy rise due to this term may be loosely ascribed to Pauli repulsion, and a detailed analysis of it unveils that all the energy components, and not exclusively the increase in kinetic energy as it is some times stated [38], are the responsible for this positive value of  $E_{\text{rep}}$ .

Taking again the very simple but representative case of the HL H<sub>2</sub> triplet as a bench test, we illustrate in Fig. 2.1 how the different energetic terms in this system behave as a function of distance. From  $R_{\text{HH}}$  down to about 1.0 bohr, the electrostatic component  $E_{\text{elstat}}$  is much smaller than  $E_{\chi}$  and  $E_{\text{rep}}$ , so that the full interaction ( $E$ ) is determined by the latter two interactions.  $E_{\text{rep}}$  dominates over  $E_{\chi}$ , which leads to the well known repulsive wall of this system as  $R_{\text{HH}}$  decreases.

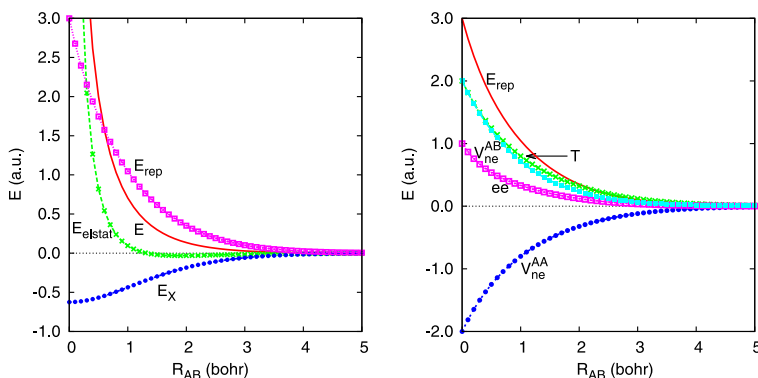


**FIGURE 2.1** Contributions to the repulsive wall in the Heitler-London  $H_2$  triplet. (Left) Total binding energy ( $E$ , solid line) separated into its  $E_{\text{elstat}}$  (crosses),  $E_X$  (solid circles), and  $E_{\text{rep}}$  (empty squares) components. (Right) Decomposition of  $E_{\text{rep}}$  (solid line) into one- and two-electron contributions: kinetic ( $T$ , crosses), electron-own-nucleus ( $V_{ne}^{AB}$ , solid circles), electron-other-nucleus ( $V_{ne}^{AA}$ , solid squares), and two-electron terms (ee, empty squares).

**TABLE 2.3** IQA HF energy decomposition results in the triplet state of  $H_2$ . All units in kcal/mol, except kinetic energies in Hartree. All data are CP corrected. Results obtained at the equilibrium geometry of the singlet

	$E_{\text{def}}^A$	$E_{\text{kin}}^A$	$E_{\text{elstat}}^{\text{IQA}}$	$V_X^{AB}$	$E_{\text{int}}^{AB}$	$E_{\text{int}}$
$\Phi_A \Phi_B$ (T)	-35.79	0.50	47.79	-178.15	-130.36	-201.94
$\mathcal{A}(\Phi_A \Phi_B)$ (T)	101.22	0.77	56.05	-32.54	23.51	225.95
$\Phi$ (T)	73.37	0.58	60.00	-71.00	-11.00	135.74

$E_{\text{rep}}$  is always repulsive, but does not diverge at  $R_{\text{HH}} = 0$ , where it takes a value equal to 3.0 a.u. The rise in  $E_{\text{rep}}$  due to kinetic energy corrections is about twice that value due to the two-electron terms. However, since kinetic and electron-own-nucleus corrections cancel, the repulsion ends up being dominated by the destabilizing electron-other-nucleus corrections. The other way around, one may almost cancel out the electron-nucleus corrections, and consider the kinetic and two-electron contributions as creators of the repulsion, this time with the kinetic correction dominating the change.

The effects of antisymmetry on the IQA results of HL  $H_2$  triplet are collected in Table 2.3. After the simple Hartree product  $\Phi_A \Phi_B$  is antisymmetrized,  $V_X^{AB}$  is reduced from -178.15 to -32.54 kcal/mol. This effect is also observed in NEDA, where  $E_X = -9.96$  kcal/mol. Antisymmetrizing increases the atomic kinetic energy that goes from 0.50 a.u. in  $\Phi_A \Phi_B$  to 0.77 a.u. in the antisymmetrized state, and changes the deformation energy  $E_{\text{def}}^A$  from negative in the Hartree product (-35.79 kcal/mol) to highly positive in  $\mathcal{A}(\Phi_A \Phi_B)$  (101.22 kcal/mol).  $E_{\text{int}}^{AB}$  is equal to 23.51 kcal/mol in  $\mathcal{A}(\Phi_A \Phi_B)$ , which together with the large  $E_{\text{def}}^A$  value agrees with the traditional Pauli image. Orbital relaxation reduces  $E_{\text{def}}^A$  down to 73.36 kcal/mol, enhances a little  $V_X^{AB}$ , which is now equal to -71.00 kcal/mol, and makes  $E_{\text{int}}^{AB} = -11.00$  kcal/mol. However, this stabilizing value is not able to overpass the large deformation, yielding a final value of  $E_{\text{int}}$  equal to 135.74 a.u.









so that none of the remaining energy contributions include correlation. For instance,  $E_{\text{elstat}}$  in LMOEDA is computed from Hartree–Fock densities. This causes that LMOEDA’s  $E_{\text{disp}}$  are smaller than SAPT’s  $E_{\text{disp}}$  (see [Tables 2.1 and 2.6](#)).

## 2.6 OVERVIEW AND CONCLUSIONS

In this last section, we give a final overview and discuss the overall performance of the different EDAs we have discussed in the chapter, taking the HF–HF and H<sub>2</sub>O–H<sub>2</sub>O dimers, and the BH<sub>3</sub>–NH<sub>3</sub> and HF–ClF complexes as examples. CCSD LMOEDA interaction energies can be obtained by adding the last two columns of [Table 2.1](#). SAPT0 numbers in [Table 2.6](#) show that, except in BH<sub>3</sub>–NH<sub>3</sub>, the induction and dispersion terms in the remaining three systems are about  $-1$  kcal/mol. In the HF and water dimers, exchange-repulsion is about 60% of the electrostatic interaction. The latter is in turn a rough estimate of the total interaction energy so, broadly speaking, exchange-repulsion almost cancels the joint induction plus dispersion terms. In the BH<sub>3</sub>–NH<sub>3</sub> complex, however, this repulsion is considerably larger than its  $E_{\text{elstat}}$  value. Polarization and dispersion in this complex ( $-44.4$  and  $-15.4$  kcal/mol, respectively) are not negligible.

The SAPT0 exchange-repulsion energy may be split into the exchange and repulsion components in orbital EDAs. In LMOEDA,  $E_{\chi}$  is an important quantity that cannot be overlooked. In the BH<sub>3</sub>–NH<sub>3</sub> complex,  $E_{\chi}$  is considerably larger than  $E_{\text{elstat}}$ . In the other three systems these two energies are comparable. In weak complexes, LMOEDA  $E_{\chi}$  turns out to be a good estimate of the total interaction energy. Regarding ZREDA, we observe in [Table 2.5](#) that  $\Delta T_{\text{Pauli}}$  is marginally greater (in absolute value) than  $\Delta V_{\text{Pauli}}$  in the HF and water dimers, and also in HF–ClF. In BH<sub>3</sub>–NH<sub>3</sub>,  $\Delta T_{\text{Pauli}}$  (351.32 kcal/mol) is more than 100 kcal/mol greater than  $\Delta V_{\text{Pauli}}$  ( $-244.36$  kcal/mol). So, as we indicated above,  $\Delta T_{\text{Pauli}}$  is by no means the only contribution to  $\Delta E_{\text{Pauli}}$ . With respect to orbital relaxation, the kinetic energy in the HF dimer decreases by 20.32 kcal/mol, at the expense of increasing the Coulomb repulsion in 18.90 kcal/mol. In the HF–ClF complex and water dimer,  $\Delta E_{\text{orb}}^{\text{kin}}$  is also negative ( $-14.37$  and  $-27.21$  kcal/mol, respectively), but the Coulomb repulsion is much smaller (6.41 and 2.22 kcal/mol). The BH<sub>3</sub>–NH<sub>3</sub> has a completely different behavior as both  $\Delta E_{\text{orb}}^{\text{kin}}$  and  $\Delta E_{\text{orb}}^{\text{Coul}}$  are negative and large ( $-260.13$  and  $-137.16$  kcal/mol, respectively) and  $\Delta E_{\text{orb}}^{\text{xc}}$  is much larger (29.76 kcal/mol) than in the other three complexes.

Among all orbital partitions, NEDA is the one showing more similarities with the IQA scheme. However,  $E_{\text{elstat}}$  in NEDA is computed from noninteracting orbitals, whereas  $E_{\text{elstat}}^{\text{IQA}}$  is obtained from the final electron density. In the same way, localized orbitals are used to compute  $E_{\chi}$  in NEDA, while the analogous quantity in IQA ( $V_X^{AB}$ ) is derived from the supermolecular xc density. These two facts make the comparison between both approaches difficult. NEDA CT energies hide all relaxation effects from the localized state, including density distortions with their associated Coulomb effects, plus exchange and kinetic energy modification. Hence,  $E_{\text{pol}} + E_{\text{elstat}}$  in NEDA contain a large part of  $E_{\text{elstat}}^{\text{IQA}}$ . Due to self-interaction in IQA, NEDA  $E_{\chi}$  is much smaller than  $V_X^{AB}$ . The kinetic energy relaxation (large and negative, as seen in ZREDA) included in the NEDA  $E_{\text{CT}}$  term makes the deformation energies of this

partition usually larger than those in IQA. Notice that CT in NEDA and orbital relaxation in ZREDA are equivalent. However, the use of NBOs to construct the CT term in NEDA makes the comparison rather useless. In fact,  $E_{CT}$  turns out to be considerably larger in NEDA. In other words, NEDA's antisymmetric state usually lies considerably above the standard  $\Phi^0$  constructed from noninteracting orbitals.

This last point illustrates the interpretative difficulties associated to using artificial intermediate states in EDAs. Different prescriptions may lead to different final energetic contributions, even though they have the same formal definition. Spurious states and references are absent from real-space partitions, endowing them with considerable simplicity. As an example, the IQA approach only uses terms with a clear physical meaning. Of course, spurious states can also be used in IQA (this allows us to compare IQA results with other prescriptions, as we have tried to show) but are not an essential ingredient of the method. Moreover, real-space methods can be applied equally well to strong covalent interactions where PT fails and most orbital EDAs have interpretative problems. Nevertheless, a final point should be added. While we defend clearly the IQA method over all others, the energy partition of intermolecular interactions is a far from settled problem. Except in the (very) long-range limit, where most methods converge and the different contributions become well defined, we face a zoo of terms. Energetic contributions with the same physical meaning are often named differently in two or more EDAs. Other times it is just the reverse and the same name is unfortunately used in different EDAs to refer to quite different physical interactions. Two pieces of advice for nonexperts are: (i) use whatever method you feel most comfortable with but clearly state what you are doing, always bearing in mind the meaning of any contribution you will be using, and (ii) be very careful when criticizing the results of others as they could be referring to quantities with a very different meaning. In passing, energy partitions that use real-space quantities, with well-defined energetic contributions at the strong and weak interacting limits, may turn out to be useful alternatives to standard approaches in the long run.

## Acknowledgments

The authors thank the Spanish MINECO, grants CTQ2012-31174, CTQ2015-65790-P and the FICYT, grant FC-GRUPIN14-049 for financial support.

## References

- [1] W. Heitler, F. London, *Z. Phys.* 44 (1927) 455.
- [2] I.C. Hayes, A.J. Stone, *Mol. Phys.* 53 (1984) 83–105.
- [3] M.A. Blanco, A. Martín Pendás, E. Francisco, *J. Chem. Theory Comput.* 1 (2005) 1096–1109.
- [4] E. Francisco, A. Martín Pendás, M.A. Blanco, *J. Chem. Theory Comput.* 2 (2006) 90–102.
- [5] A. Martín Pendás, M.A. Blanco, E. Francisco, *J. Comput. Chem.* 28 (2007) 161–184.
- [6] S. Wilson, I. Hubac, *Brillouin–Wigner Methods for Many-Body Systems*, 1st ed., Springer, Dordrecht, 2010.
- [7] A.J. Stone, *The Theory of Intermolecular Forces*, Oxford University Press, 2013.
- [8] B. Jeziorski, R. Moszynski, K. Szalewicz, *Chem. Rev.* 94 (1994) 1887–1930.
- [9] B. Jeziorski, R. Moszynski, A. Ratkiewicz, S. Rybak, K. Szalewicz, H.L. Williams, in: E. Clementi (Ed.), *Methods and Techniques in Computational Chemistry: METECC-94*, vol. B, 1993, p. 79.
- [10] K. Szalewicz, *Comput. Mol. Sci.* 254 (2012) 2.
- [11] E.G. Hohenstein, C.D. Sherrill, *Comput. Mol. Sci.* 304 (2012) 2.
- [12] K. Szalewicz, K. Patkowski, B. Jeziorski, *Struct. Bond.* 116 (2005) 43–117.



- [63] M.W. Schmidt, K.K. Baldridge, J.A. Boatz, S.T. Elbert, M.S. Gordon, J.H. Jensen, S. Koseki, N. Matsunaga, K.A. Nguyen, S.J. Su, T.L. Windus, M. Dupuis, J.A. Montgomery, *J. Comput. Chem.* 14 (1993) 1347.
- [64] E. Francisco, A. Martín Pendás, IMOLINT (Unpublished).
- [65] E.D. Glendening, J.K. Badenhoop, A.E. Reed, J.E. Carpenter, J.A. Bohmann, C.M. Morales, F. Weinhold, NBO 5.0, Theoretical Chemistry Institute, University of Wisconsin, Madison, 2001.
- [66] A. Martín Pendás, E. Francisco, PROMOLDEN: a QTAIM/IQA code (Unpublished).
- [67] E. Francisco, A. Martín Pendás, A. Costales, *Phys. Chem. Chem. Phys.* 16 (2014) 4586–4597.
- [68] T. Helgaker, J. Olsen, P. Jorgensen, *Molecular Electronic-Structure Theory*, John Wiley & Sons, Ltd., New York, 2000, Chapter 6.
- [69] P.L.A. Popelier, D.S. Kosov, *J. Chem. Phys.* 114 (2001) 6539.
- [70] A. Martín Pendás, M.A. Blanco, E. Francisco, *J. Chem. Phys.* 120 (2004) 4581.
- [71] K.G. Kay, H.D. Todd, H.J. Silverstone, *J. Chem. Phys.* 51 (1969) 2363–2367.
- [72] E. Francisco, A. Martín Pendás, M.A. Blanco, *J. Chem. Phys.* 126 (2007) 094102.
- [73] A. Martín Pendás, E. Francisco, M.A. Blanco, *Faraday Discuss.* 135 (2007) 423.
- [74] A. Martín Pendás, E. Francisco, M.A. Blanco, *J. Phys. Chem. A* 111 (2007) 1084.
- [75] E. Francisco, A. Martín Pendás, *Mol. Phys.* 114 (2015) 1334.

# Intermolecular Interaction Energies from Kohn–Sham Random Phase Approximation Correlation Methods

---

*Andreas Heßelmann*

Lehrstuhl für Theoretische Chemie, Universität Erlangen-Nürnberg, Erlangen, Germany

*In memory of Janos Angyan*

## 3.1 INTERMOLECULAR INTERACTIONS AND THE ELECTRON CORRELATION PROBLEM

---

The description of the correlated movement of many particles remains an unsolved problem. For all but the simplest systems involving interactions of two or three particles, an exact analytic solution may never be derived. Precise numerical solutions to few-body systems are computationally highly demanding and in case of larger systems (including, e.g., more than 10 interacting particles) the problem becomes intractable.

While the foregoing description holds true for basically any type of many-body system, a number of approaches have been derived for quantum many-body systems since the basic equations that describe their behavior became known [1,2]. The simplest approach to describe a many-body system is to completely neglect any correlation between particles. When these particles are electrons, two different types of interactions, shown as paths in Fig. 3.1, may occur [3]. In the first case (upper path in the figure), an extra electron enters a many-electron system and is scattered by a system electron—the two electrons will exchange a virtual photon, indicated by the wiggly line in the figure. The system electron is lifted out from its current state, as marked by the unfilled circle in panel 2a. However, it *instantaneously* drops back into its original state. For the extra electron this means that its movement through the many-electron system would never be correlated with the movements of the system electrons. In fact, from the point of view of the extra electron, it would not make any difference if the system electrons are located at fixed positions or whether they move within the system. So, on average, the only “disturbance” the extra electron feels is the mean field produced



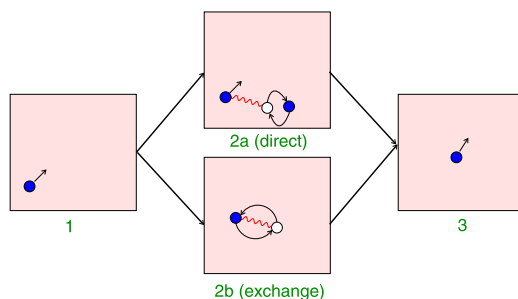


**FIGURE 3.1** Possible first order interactions between two electrons described by the Hartree–Fock method. (1) An extra electron enters the system; (2a) direct (Coulomb) interaction—the extra particle lifts an electron out of its place and creates a particle–hole pair that is destroyed instantaneously; (2b) exchange interaction—same as in (2a), but the extra electron exchanges with the system electron; (3) the extra electron leaves the system.

by the sum of charges of the electrons from the system. The underlying quantum chemistry method describing interactions of the type described in path 1–2a–3 of Fig. 3.1 is the Hartree method [4].

The Hartree self-consistent field method can be performed by approximating the (generally) complicated many-electron wavefunction by the product of one-electron wavefunctions (spin orbitals) that is varied in a self-consistent way so that the total energy of the system is minimized [5]. It was pointed out by Fock and Slater [6–9] that the Hartree wavefunction ansatz violates the Pauli principle (or antisymmetry condition) that allows no more than one electron per spin-orbital. Fock and Slater used antisymmetrized sums of products of spin-orbitals as the wavefunction ansatz to fulfill this fundamental postulate of quantum mechanics. The resulting Hartree–Fock self-consistent field method [10] developed by Fock and Slater still constitutes the basis of quantum chemistry wavefunction methods to the present day.

In Fig. 3.1, the antisymmetry condition on the wavefunction leads to two possible first-order scattering processes: the “direct” interaction path 1–2a–3, which is also described by the Hartree method, and the additional path 1–2b–3 in which the extra electron exchanges with one electron of the system. For an external observer there appears to be little difference whether the electron takes the path 1–2a–3 or 1–2b–3 since the electrons are indistinguishable particles. Yet, the second interaction process is clearly different from the first as it is a pure quantum mechanical effect that would not appear in a classical many-body system. It can even be regarded as a correlation interaction (between electrons with parallel spin only, however) because exchange interactions lead to a repulsion of the electrons (due to the appearance of the so called Fermi hole [11]) that can affect their movements to first-order. The inclusion of first-order exchange interactions also corrects the unphysical self-interaction error of the Hartree method which originates from a double counting of Coulombic interactions [12].

But is the Hartree–Fock method accurate enough to describe intermolecular interactions between two electronic systems? Fig. 3.2 shows the interaction energy potential of the helium dimer calculated with various quantum chemical methods. The interaction energies were

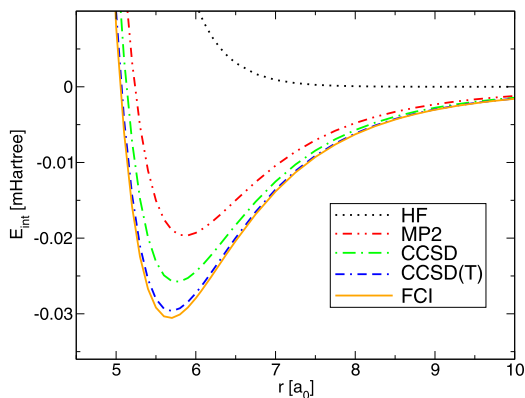


FIGURE 3.2 Helium dimer interaction potential calculated with HF (Hartree–Fock), MP2 (second-order Møller–Plesset perturbation theory), CCSD (coupled-cluster singles doubles), CCSD(T) (CCSD with perturbative triples) and FCI (full configuration interaction). The aug-cc-pVQZ basis set was used in the calculations.

calculated with the supermolecular method using the equation:

$$E_{\text{int}}(\text{AB}) = E(\text{AB}) - E(\text{A}) - E(\text{B}), \quad (3.1)$$

where AB denotes the dimer system composed of two monomers A and B. While rare gas dimers are special in the sense that the attraction is almost completely due to the so-called dispersion interaction [13], Fig. 3.2 shows that the Hartree–Fock method is unable to even qualitatively describe the attractive interaction between the two helium atoms. Fig. 3.2 also presents a series of electron correlation methods which range from a second-order treatment of electron correlation effects (MP2) to those which treat electron–electron interactions through infinite orders (CCSD, CCSD(T), and FCI). Different types of interactions which can occur in second- and higher-orders are sketched in Fig. 3.3. While, unlike HF, all electron correlation methods are able to describe an attractive bonding between the two helium atoms, it is noticeable that there are significant differences between the interaction energy curves.

The MP2 method, as the least “complete” method regarding a perturbation theory expansion of the correlation energy, significantly underestimates the interaction energy at the equilibrium, see Fig. 3.2, as compared to the FCI interaction potential. The FCI method takes into account “all” electronic excitations from the reference determinant [10] to describe the many-electron wavefunction and thus can be regarded as an exact nonrelativistic solution method to the Schrödinger equation, subject to the basis set incompleteness error (see below). One can clearly see in the diagram in Fig. 3.2 that the interaction energy potential gets closer and closer to the exact FCI curve the better the approximation to the wavefunction is. The CCSD method, as noted above, describes electron correlation effects to infinite order in contrast to the MP2 method. Compared to, for example, the CI singles doubles (CISD) method, the CCSD wavefunction contains higher than double excitations through a coupling of connected singles and doubles excitation operators. It turns out that this property is crucial for the method to be size-extensive, that is, that the energy properly scales with the number of electrons [14]. Basically all coupled-cluster methods and their derivatives, such as RPA

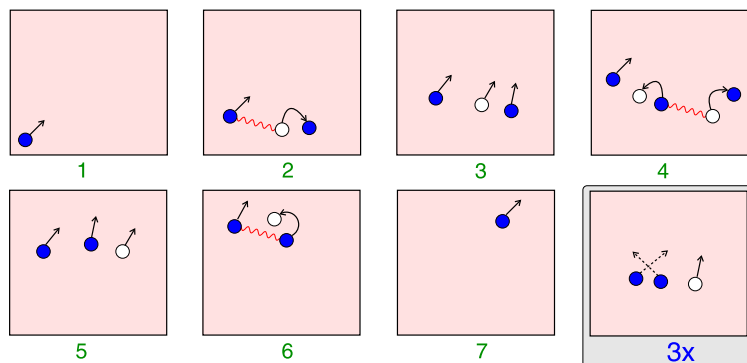


**FIGURE 3.3** Possible second- and higher-order interactions between two electrons described, e.g., by second-order Møller–Plesset perturbation theory (MP2) and the direct random-phase approximation (RPA), respectively. (1) An extra electron enters the system; (2) the extra electron interacts with an electron of the system and lifts it out of its place, thus creating a hole; (3) the extra electron plus the “hole” and the “lifted-out” electron (particle–hole pair) travel through the system; (3x) as an alternative to (3), the extra electron and the “lifted-out” electron exchange places; (4) the lifted-out electron creates another particle–hole pair and drops back in its hole; (5) same as (3); (6) the extra electron again interacts with the “lifted-out” electron knocking it back into the hole, thus destroying the particle–hole pair; (7) The path 1–2–3–4–5 corresponds to a direct (Coulomb) correlation process while the path 1–2–3x–4–5 corresponds to an exchange correlation process in second order. MP2 theory accounts for the sum of the processes 1–2–3–4–5 and 1–2–3x–4–5 while RPA describes the sum of all repeated particle–hole interactions, i.e.,  $\sum_{n=0}^{\infty} 1-2-3-(4-5)_n-6-7$ .

methods, fulfill this requirement since the exponential ansatz of the wavefunction ensures that no unlinked diagrams can occur in any order of a perturbation theory expansion of the correlation energy [14,15]. It goes without saying that the properties of size extensivity and size consistency are crucial in the description of intermolecular interactions. However, size consistency is a less stringent requirement as it only postulates a correct scaling of the energy with the system size for noninteracting systems. For instance, for a supersystem containing  $N$  noninteracting identical molecules  $A$  (for example, a system where the distance between all  $N$  molecules is large), size-consistency postulates that

$$E(N \cdot A) \underset{R_{AA} \rightarrow \infty}{=} N \cdot E(A) \quad (3.2)$$

for the total energy of the system. Compared to this, the property of size-extensivity postulates the correct scaling of a method with the number of electrons at any geometry and not only in the limiting case of well-separated subsystems.

If the CCSD wave function is further augmented with perturbative triple excitations, as is done in the CCSD(T) method, the interaction energy potential for  $\text{He}_2$  finally comes very close to the exact FCI curve, see Fig. 3.2. This shows that a systematic improvement of the wavefunction through the steps  $\text{MP2} \rightarrow \text{CCSD} \rightarrow \text{CCSD(T)}$  also leads to a higher accuracy of the interaction energy potential for the helium dimer. This is a very useful property of correlated wavefunction methods since it allows one to assess the exact (nonrelativistic) limit for a given property for larger systems for which exact (FCI) calculations are not feasible. To give an example, if the differences between the MP2 results and CCSD results are small compared

to the magnitude of the second-order correlation energy, then this indicates that higher than second-order correlation effects are negligible, and it will be unlikely that a further improvement of the wavefunction by including triples excitations will yield a significant change in the result. In contrast, if the difference of the results yielded by the MP2 and CCSD method are large, as is the case with the He<sub>2</sub> interaction potentials (see Fig. 3.2), then one can also assume that a further augmentation of the wavefunction is necessary to come close to the exact result. Fortunately, it turns out that for intermolecular interactions between two molecules which do not possess a multi-reference character (i.e., for which a single determinant suffices to describe the electronic structure) the CCSD(T) method can be regarded as almost exact (as for the helium dimer example considered here). Because of this, the CCSD(T) method is often used as a reference to other quantum chemistry methods (see Sections 3.5, 3.6, and 3.7, and also Chapter 4).

However, while the accuracy can significantly be improved by progressing along the series MP2→CCSD→CCSD(T), the computational expense increases severely due to the increasing computational cost scaling of  $\mathcal{N}^5$  for MP2,  $\mathcal{N}^6$  for CCSD, and  $\mathcal{N}^7$  for CCSD(T) with the system size  $\mathcal{N}$ . In the case of CCSD(T), this means that the computational cost increases formally by a factor of 128 when the size doubles. Due to this unfortunate property, CCSD(T) cannot be used for large electronic systems, at least not unless some approximations in the computational algorithm are made.

One possible approach to reduce the computational cost of quantum chemical methods is to use small basis sets. For example, both the CCSD and CCSD(T) methods scale as  $M^4$  with the basis set size  $M$  so that a truncation of a given basis set to only half the size of the original basis set would reduce the computational cost by a factor of 16. Fig. 3.4 shows the dependency of the helium dimer interaction energy potential on the basis set size for the four correlation methods MP2, CCSD, CCSD(T) and FCI. The basis sets used in Fig. 3.4 are the correlation-consistent valence double (10 basis functions) to hextuple (182 basis functions) zeta basis sets including polarization functions by Dunning et al. [17–20]. For comparison the complete basis set estimate for the FCI interaction potential by Mourik et al. [16] has been included in all diagrams in the figure. It can be observed that all methods considered in Fig. 3.4 exhibit a strong dependence on the basis set size. For example, all methods describe little attraction between the helium atoms when the cc-pVDZ or cc-pVTZ basis sets are used. A slow convergence to the basis set limit with increasing basis set size is seen, as indicated by the large differences between the interaction potentials for the cc-pV5Z and cc-pV6Z basis sets. In the case of the FCI method, the interaction energy at the minimum of the curve obtained using the cc-pV6Z basis set is still about +0.013 millihartree off from the CBS estimate, which amounts to a relative error of almost 40% of the total interaction energy at the equilibrium geometry.

This slow convergence problem can essentially be attributed to the neglect of diffuse functions in the basis set. To highlight this, Fig. 3.5 shows the same results as in Fig. 3.4, but using the cc-pVXZ basis sets by Dunning et al. [17–20] augmented by diffuse functions (i.e., aug-cc-pVXZ). A much faster convergence to the respective basis set limits is achieved with the aug-cc-pVXZ basis sets. Perhaps the most striking aspect of the comparison between both figures is the fact that the smallest diffuse basis set aug-cc-pVDZ yields interaction energy potentials which are equal in quality to the potentials obtained by using the unaugmented cc-pV5Z basis set. In summary one can thus conclude:

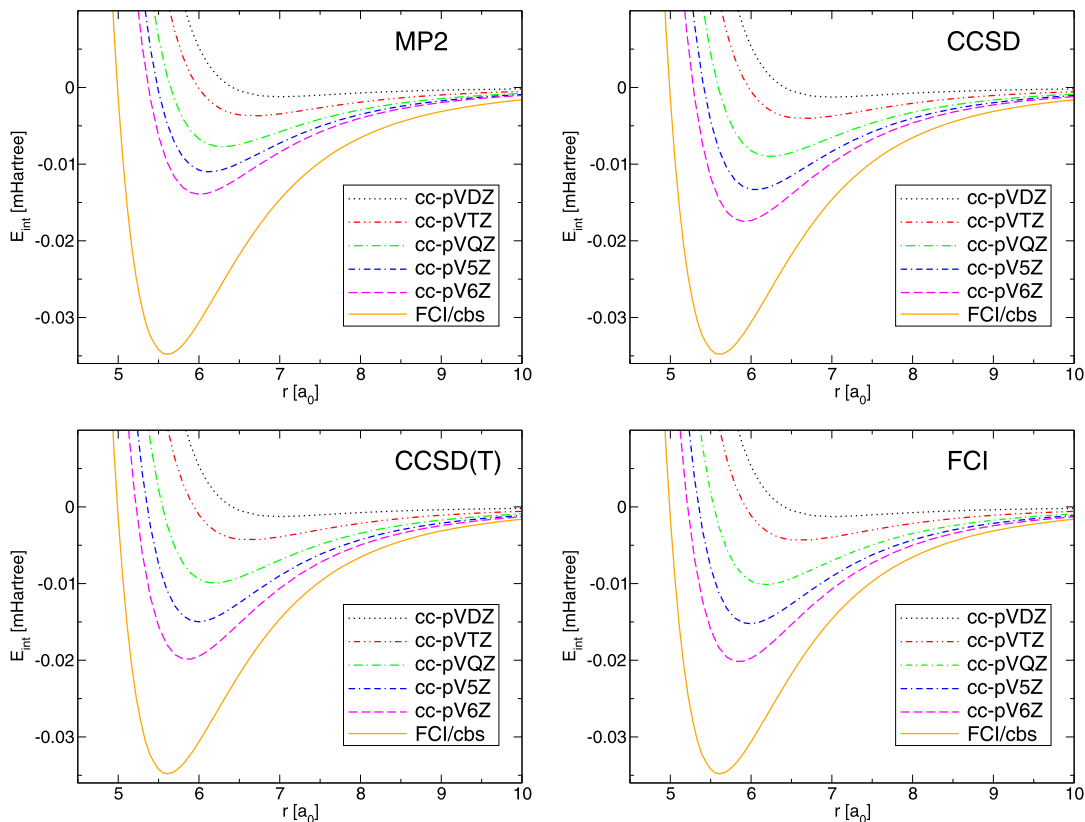


**FIGURE 3.4** Helium dimer interaction potential calculated with four different correlation methods using the cc-pVXZ basis sets with  $X = 2, \dots, 6$ . The complete basis set (CBS) estimate for the FCI interaction energy curve from Ref. [16] is also shown for comparison.

- Basis sets for determining interaction energy potentials by correlated wavefunction approaches require high angular momentum functions. These are necessary to adequately approximate the interelectronic cusp describing the *intramolecular* correlation contributions to the total interaction energy [21,22].
- The basis sets should also be augmented with diffuse functions. This is crucial in order to properly describe the *intermolecular* correlation effects (sometimes referred to as dispersion or van der Waals interactions).

Therefore, a number of problems associated with the accurate determination of intermolecular interaction potentials are apparent. From Fig. 3.2 it can be seen that wavefunction methods employing, at least, triple excitations are required in order to approach the exact potential. Figs. 3.4 and 3.5 demonstrate, however, that the calculations must also employ large basis sets including diffuse functions. Unfortunately, the computational cost of these approaches increases rapidly both with the system size and the basis set size.

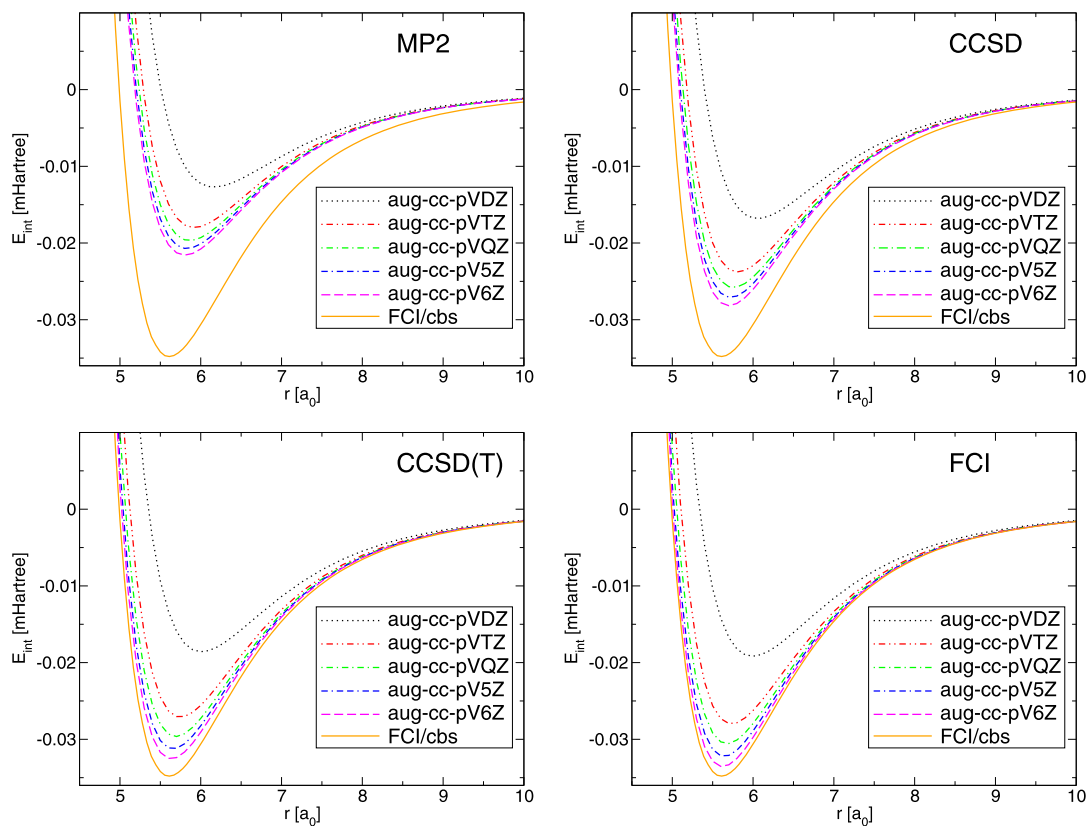


**FIGURE 3.5** Helium dimer interaction potential calculated with four different correlation methods using the aug-cc-pVXZ basis sets with  $X = 2, \dots, 6$ . The complete basis set (CBS) estimate for the FCI interaction energy curve from Ref. [16] is also shown for comparison.

Nowadays a number of approaches exist which can be applied to reduce the computational cost of electron correlation methods. For example, local correlation methods can be used to reduce the steep scaling behavior of the underlying electron correlation method even down to linear scaling [23]. Furthermore, explicitly correlated methods can be used to reduce the strong basis set dependence by introducing basis functions which depend on the electronic distances explicitly [24] (see Chapter 4). However, in the case of local correlation methods, there is still the problem that all intermolecular electron pairs would have to be treated to adequately describe the long-range correlation energy within the system. Special care must be exercised in the determination of potential energy surfaces due to the fact that the screening over electron pairs, i.e., omitting distant pairs, may lead to discontinuities in the potential. In the case of explicitly correlated methods, the computational expense is reduced as compared to the use of large quintuple- or hextuple-basis sets, but such methods are generally more costly than standard (i.e., nonexplicitly correlated) approaches that are performed using small

to intermediate size basis sets. Furthermore, explicitly correlated methods also demand more computer resources like hard disk space and main memory than standard approaches.

Considering the difficulties associated with the use of correlated wavefunction methods, it is not surprising that density functional theory methods (DFT) based on the generalized gradient approximation (GGA) [25] and including empirical dispersion corrections (for example, DFT-D3 methods) have evolved as a state-of-the-art for describing intermolecular interactions of extended molecular systems [26,27] (see also Chapters 5 and 6). This type of method offers a practical approach to resolving the issues noted above on the demands on the basis set, since standard DFT methods do not directly model the interelectronic cusp and since the dispersion correction has a low or completely absent dependence on the size of the basis sets employed. Total intermolecular interaction energies from standard DFT plus dispersion approaches are therefore well converged already with basis sets of triple-zeta quality. However, DFT-based methods do not possess one of the valuable properties of wavefunction approaches, namely the possibility of a systematic improvement, as exemplified in Fig. 3.2.

From this point of view, there is great value in the development of alternative approaches to the commonly used empirical DFT methods that possess the property of a systematic improvability of the underlying functional and that can describe electron correlation effects with a reduced computational expense as compared to common coupled cluster methods. Such approaches have been derived in the recent years. They are all based on the random-phase approximation (RPA).

### 3.2 THE REVIVAL OF THE RPA AS A GROUND-STATE ELECTRON CORRELATION METHOD

---

In the early 1950s, Bohm and Pines investigated the collective description of electron interactions in a dense electron gas in a series of seminal works [28–30]. Until then it was common to use the Hartree–Fock (HF) method to describe the ground-state energy and the quasiparticle properties of the homogeneous electron gas. The HF method, however, turned out to be unsuitable for describing long-range electron correlations [31]. In the high density limit of the homogeneous electron gas a phenomenon arises that cannot be described by a mean-field approach, namely the so-called plasmon oscillations [32]. When an electron moves through the dense electron gas its movement will be correlated with all other electrons in the system, giving rise to the collective motion of all electrons, see Fig. 3.6. Experimental evidence for the plasma waves in metallic systems was found when a thin metal foil is bombarded with high energy electrons [33]. Bohm and Pines were able to accurately describe the plasma loss measured in such experiments by separating the density fluctuations into two distinct terms: a term that arises from the random thermal motions of the electrons, which is also present in a noninteracting system, and a second term which describes the collective motions of the electrons caused by their interactions with each other [29]. The second contribution can be accurately approximated by neglecting the coupling of oscillations in different plasmon modes [29]. The justification for this approach was that the coupling term depends explicitly on the particle coordinates which are distributed nearly in random positions. Accordingly, it can be assumed that their average contribution tends to zero in the high density limit [29].

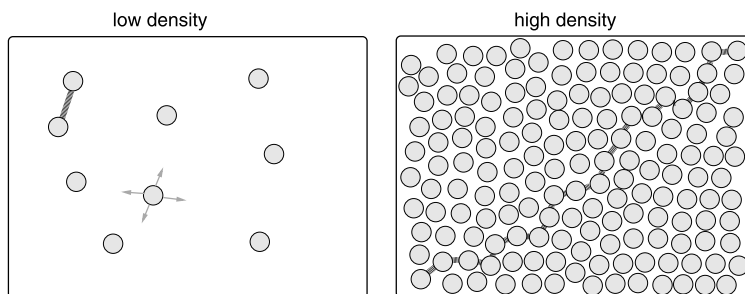


**FIGURE 3.6** Sketch of the homogeneous electron gas at low density (left) and high density (right). In the low-density case, close electrons can interact with each other but electrons that are far apart are almost uncorrelated (left box). In the high density case, all electrons mutually interact with each other and the movement of an electron in the left bottom corner can directly induce a correlated movement of an electron in the upper right corner due to a correlation of all other electrons within the system (sketched by the possible interactions as marked by the dashed lines in the right box).

It turns out that the approach by Bohm and Pines, which was termed as random phase approximation (RPA), is exact in this case [32,34]. The predictions for the correlation energy of homogeneous gases with metallic densities as yielded by the RPA method were also in a fairly good agreement (to within 4 mRy for  $r_s$  (Seitz radius) spanning values of 2 to 5) with Wigner's perturbation theory results [31,35]. However, it was soon realized that the RPA is not very accurate in this regime because it does not make a distinction between the correlation effect of same-spin electron pairs and antispin electron pairs [36–38].

Later, it was shown by Ehrenreich and Cohen that the dielectric constant predicted by the RPA [38,39] is conform to a time-dependent self-consistent field approach to the many electron problem [40]. In a series of works, McLachlan and Ball showed that this time-dependent extension to the Hartree(–Fock) method (TDHF) may be used to calculate the ground-state correlation energy of molecules [41,42], the stability conditions of a Hartree–Fock wavefunction [41,42], the excitation energies of a molecule (which are associated with the free oscillations of the coupled oscillator description of the many electron system [42]), the polarizability [42], and the dispersion interaction energy between atoms as the change of the zero-point energy of the oscillators when the atoms approach each other [43]. In a latter work, McLachlan and Ball also showed that the dispersion energy obtained at the TDHF level can take into account the nonadditive three-body forces in contrast to, for example, dispersion energies from second order perturbation theory methods [43]. A crucial difference between the original RPA by Bohm and Pines and the TDHF approach by McLachlan and Ball is that the latter takes into account electron exchange effects in the equations of motion for the electronic states [41]. It was found, however, that the correlation energy of ethylene diverges in the strong coupling limit (i.e., if the electron–electron interaction is fully switched on in the adiabatic connection approach, see Fig. 3.7) which has been attributed to the violation of the spin conservation and the exclusion principle of the pair-correlation function in this case [41]. (The pair-correlation function defines the correlation contribution to the pair function which describes the probability of simultaneously finding two electrons at two spatial coordinates.)



It may have been due to these unsatisfactory results that the RPA was not further considered as a possible ground-state electron correlation method for molecules. However, later works by Szabo and Ostlund [44,45] and Oddershede [46] revived interest in the RPA. The new RPA functional introduced by Szabo and Ostlund was designed such that, unlike the functional by McLachlan and Ball [41], it describes the long-range correlation energy between two closed-shell systems at the coupled Hartree–Fock level [44,45], which is consistent with the RPA result that is obtained from a corresponding response approach. The RPA functional proposed by Oddershede, which was also given by Szabo and Ostlund [44], has the advantage that it can be formulated solely by the amplitude solutions to the singlet excitation spectrum and thus is free from triplet instabilities of the RPA [46]. Such triplet instabilities of the RPA method often occur in  $\pi$ -electronic systems [47,48] and originate from the fact that the excitation and deexcitation operators used in the RPA method do not conform with the RPA ground-state wavefunction which is the HF wavefunction in normal (i.e., non-self-consistent [44]) RPA methods. However, the RPA methods by Szabo and Ostlund and by Oddershede have not been used further for describing the correlation energies of molecular systems since their introduction. Apart from the principal problems noted above, one reason for their lack of use might be that coupled cluster methods, which are more accurate and not much more computationally demanding, were developed at the same time—the first formulation and implementation of the full CCSD method was published by Purvis and Bartlett in 1982 [14,49,50]. In the years that followed, coupled-cluster methods have been established as the state-of-the-art for accurately describing electron correlation effects in molecular systems (see Chapter 4).

In the late 1990s, there was a revival of interest in the RPA as a method to improve the description of electron correlation energies as yielded by standard GGA-type density functional theory methods [51–53]. Yan et al. developed a GGA-type correlation density-functional that can be used to improve the RPA correlation energy for short-range electron correlation effects [54]. The combined RPA-DFT method was shown to largely improve total energies as compared to the RPA, but yielded only small corrections to atomization energies [54]. In 2001, Furche published a work that demonstrated a practical implementation of the RPA method in terms of molecular orbitals using a numerical integration technique over the coupling strength integrand formulated in terms of the RPA pair correlation function [55]. The total energy within this RPA method has been calculated by using Kohn–Sham (KS) instead of Hartree–Fock orbitals as input, and so the method can also be regarded as a post-KS approach. While it was found that the atomization energies for a number of small molecules do not considerably improve compared to results as yielded by the standard PBE exchange–correlation (xc) functional [56], a remarkable result of the KS-RPA method was that the dissociation of the triple-bonded nitrogen molecule is qualitatively correct [55]. Unlike corresponding coupled cluster methods limited to double excitations, for instance, this showed that the KS-RPA method is capable of describing strong static correlation effects. A later analysis by Fuchs et al. showed that the coupling strength integrand correctly switches to a constant dependence on the coupling strength in the dissociation limit if KS orbitals are used to describe the reference determinant [57]. In the case of HF-based RPA approaches, the coupling strength integrand lacks this behavior and the method then is unable to describe static electron correlation effects [58].

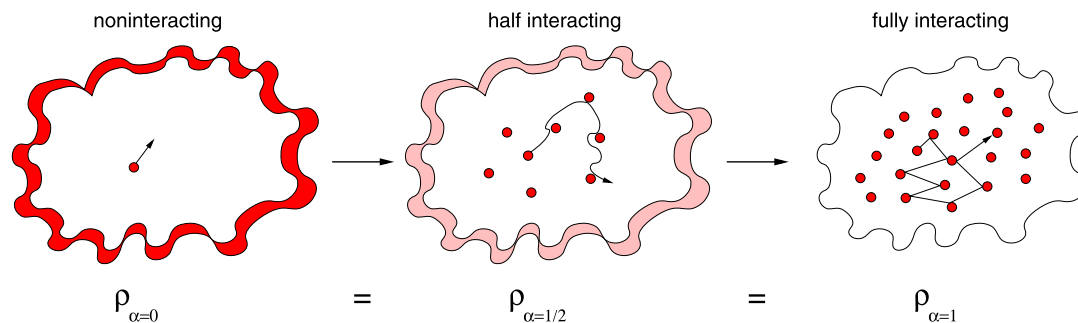


**FIGURE 3.7** Illustration of the adiabatic connection. The interactions within the many-body system are gradually switched on by varying the coupling strength parameter  $\alpha$  from 0 (noninteracting case) to 1 (fully interacting case). In the noninteracting case (left-hand side) a reference electron moves freely within the system ( $\alpha = 0$ ). When the interaction is switched on to one half of the full strength the movement of the electron is slightly perturbed by the other electrons ( $\alpha = 1/2$ ). In the fully interacting case the movement of the electron through the system is strongly influenced by all other electrons ( $\alpha = 1$ ). All along the path, the density of the system, as sketched by the border in the figures, is unchanged and is identical to the density of the fully interacting system, i.e.,  $\rho^{\text{system}} = \rho_\alpha$  for all  $\alpha \in [0, 1]$ . In the noninteracting and half-interacting cases, this is achieved by an additional external potential contribution as marked by the shaded area around the system.

This work clearly showed that the reference determinant used in conjunction with the RPA method can have a strong impact on the description of the electron correlation effects. Obviously, due to the results by Furche [55] and Fuchs et al. [57], a KS reference determinant is more beneficial than an HF one for the description of electron correlation effects within the RPA approach. A reason for this finding can be devised if the RPA correlation energy is viewed as an approximation to the exact correlation energy within the adiabatic connection fluctuation-dissipation theorem (AC-FDT) [59,60]: in the AC a noninteracting many-electron system is seamlessly connected with an interacting many-electron system by varying the coupling strength from 0 (no interactions) to 1 (full interactions) with the additional constraint that the density of the system (and therefore all properties) is identical to the density of the fully interacting system along the whole path, see Fig. 3.7. Clearly, the KS pseudo particle system obeys this condition by construction while the density yielded by the HF determinant is not exact due to the missing electron correlation contributions. Accordingly, “approximate” KS determinants from “approximate” density-functionals are better suited for use in AC-FDT methods than are HF determinants. (Another loosely related reason for the preference of KS-RPA over HF-RPA methods from a wavefunction perspective is given in Ref. [61], and in Section 3.4.2.)

Despite the promising results of the KS-RPA method presented in Ref. [55], its use as a standard quantum chemistry approach has been challenged by Furche due to the fact that the computational cost of the algorithm used in his work is comparable to the cost of the much more accurate CCSD method. Similar to the earlier works by Szabo and Ostlund [44,45], the new KS based RPA approach therefore might not have attracted much attention because of its moderate accuracy relative to its computational cost. However, in years that followed, Furche [62,63] and other groups [64–66] developed efficient algorithms which drastically reduced the computational cost of the RPA correlation energy calculation. One approach by

Eshuis, Yarkony and Furche [63], which exploits density fitting techniques to approximate two-electron integrals, reduces the computational expense of the RPA method to a scaling of  $\mathcal{N}^4$  for large-gap systems. This is lower than the scaling of the second-order Møller–Plesset perturbation theory method (MP2), which scales formally as  $\mathcal{N}^5$ . With this new algorithm, the calculation of the RPA correlation energy of the tetracene molecule required only about 10 h on a single CPU of a 2.80 GHz workstation [63]. The very recent RPA method by Kallay even further reduces the computational cost down to linear scaling with the aid of a transformation of the canonical orbitals to local orbitals [66]. With this approach, the calculation of an Amylose helix with over 1300 atoms and 13000 basis functions required only 2 days on a 6-core 3.50 GHz computer [66]. Fast algorithms for calculating the RPA correlation energy have also been developed for periodic systems within a pseudopotential plane-wave framework [67–69].

The increased use of the KS-RPA method for studying the electronic structure of molecules and solids in recent years can certainly be attributed, in part, to advances in the computational efficiency of the approach. If regarded as an implicit density functional, one of the most crucial advantages of the KS-RPA method over standard (hybrid/meta-)GGA DFT functionals is that it is capable of describing long-range correlation (dispersion) interactions. This has been demonstrated for molecular systems [65,70–72] (see also this work) as well as for bulk systems [73–80]. However, in the case of molecules it has been observed that interaction energies in dispersion-dominated systems are underestimated by the RPA as compared to high-level coupled cluster interaction energies [65,70]. For the equilibrium cohesive energies and lattice constants of the Ar and Kr noble gases, the KS-RPA method yields a clear improvement over standard DFT functionals while for neon only a moderate improvement is found [73]. It has been conjectured that the shortcomings of the RPA in the description of electron correlation effects can be ascribed to the inherent self-correlation error of the RPA, and this error manifests itself in a strong overestimation of the correlation energy [77].

A number of methods have been developed in the recent years that directly [58,64,81–87] or indirectly [82,88–102] tackle the self-correlation error of the RPA. These methods will be reviewed in Section 3.4 of this chapter.

The aim of this work is to give an overview of the different Kohn–Sham RPA methods which have been developed in the recent years and to demonstrate their successes and possible deficiencies in the description of intermolecular interaction energies. The various methods will be outlined in Sections 3.3 and 3.4. Section 3.4 is broken down into six subsections describing RPA methods including exchange interactions (Section 3.4.1), additional many-body corrections to the RPA correlation energy (Section 3.4.2), range-separated RPA methods (Section 3.4.3), generalized ACFDT methods (Section 3.4.4), particle–particle RPA methods (Section 3.4.5), and orbital-optimized RPA approaches (Section 3.4.6). It should be noted that the descriptions of the individual methods in Sections 3.3 and 3.4 are limited to a summary of the main ideas behind the different approaches. For a more detailed description of the various methods, the reader should consult the original works cited. In addition, a number of reviews about the RPA method may help to follow the basic theoretical and computational concepts of the KS-RPA methods [68,84,103] (see also the very informative work by Angyan et al. [97] for a summary of some of the recently developed extensions to the RPA method).

The performance of some of the RPA approaches for describing intermolecular interaction energies will then be presented in Sections 3.5 to 3.8. Section 3.5 discusses the performance

of the KS-RPA method for a number of intermolecular interaction benchmark sets, namely the S22 and S66 $\times$ 8 benchmark sets by Hobza et al. [104,105] and the IDISP benchmark set by Grimme et al. [106]. In Section 3.6 the RPA will be used within the framework of intermolecular perturbation theory methods. Section 3.6.1 highlights how accurately the RPA method can describe first- and second-order molecular properties. In Section 3.6.2, the orbital-optimized RPA method will be used and tested in conjunction with the symmetry-adapted intermolecular perturbation theory for directly calculating the intermolecular interaction energy in a perturbative way. In Section 3.7, the role of  $\sigma$ - versus  $\pi$ -stacking interactions will be analyzed by various RPA methods. Finally, the performance of the RPA method and two of its exchange extensions will be investigated for extended organic complexes with up to 808 electrons in Section 3.8. Section 3.9 summarizes some of the results of this work.

### 3.3 DERIVATION OF THE RPA

Until recently, the RPA method has not been regarded by chemists as a method to compute ground-state correlation energies, but it has been used to calculate molecular excitation energies [48]. The RPA equations determining the excitation energies  $\omega_n$  and the amplitudes  $X_n$  and  $Y_n$  are given by [44,107–109]:

$$\begin{pmatrix} \mathbf{A} & \mathbf{B} \\ -\mathbf{B} & -\mathbf{A} \end{pmatrix} \begin{pmatrix} \mathbf{X} \\ \mathbf{Y} \end{pmatrix} = \omega \begin{pmatrix} \mathbf{S} & \mathbf{0} \\ \mathbf{0} & \mathbf{S} \end{pmatrix} \begin{pmatrix} \mathbf{X} \\ \mathbf{Y} \end{pmatrix}, \quad (3.3)$$

where the matrices  $\mathbf{A}$ ,  $\mathbf{B}$ ,  $\mathbf{X}$  and  $\mathbf{Y}$  have dimensions  $N_{\text{occ}} \times N_{\text{virt}}$  with  $N_{\text{occ}}$  and  $N_{\text{virt}}$  being the number of occupied and unoccupied spin orbitals, respectively. Note that Eq. (3.3) has the complementary solution vectors  $\begin{pmatrix} \mathbf{Y} \\ \mathbf{X} \end{pmatrix}_n$  corresponding to an eigenvalue  $-\omega_n$ . The Hessian and overlap matrices occurring in Eq. (3.3) are defined as:

$$A_{ia,jb} = \langle \Psi_i^a | \hat{H} - E_0 | \Psi_j^b \rangle, \quad (3.4)$$

$$B_{ia,jb} = \langle \Psi_{ij}^{ab} | \hat{H} - E_0 | \Psi \rangle = \langle \Psi | \hat{H} - E_0 | \Psi_{ij}^{ab} \rangle, \quad (3.5)$$

$$S_{ia,jb} = \langle \Psi_i^a | \Psi_j^b \rangle. \quad (3.6)$$

$\hat{H}$  is the electronic Hamiltonian,  $E_0$  and  $\Psi_0$  the ground-state energy and wavefunction and  $\Psi_i^a$ ,  $\Psi_{ij}^{ab}$  are singly and doubly excited wavefunctions, respectively. Indices  $i, j, k, \dots$  label occupied and  $a, b, c, \dots$  label unoccupied orbitals. If the wavefunction  $\Psi$  in Eqs. (3.4) to (3.6) is approximated by the Hartree–Fock wavefunction, then the “normal” RPA (NRPA) approach [44,110] is obtained and the Hessian and overlap matrices are given by:

$$A_{ia,jb} = (\varepsilon_i - \varepsilon_a) \delta_{ij} \delta_{ab} + [ia|jb] - [ij|ab], \quad (3.7)$$

$$B_{ia,jb} = [ia|jb] - [ib|ja], \quad (3.8)$$

$$S_{ia,jb} = \delta_{ij} \delta_{ab}, \quad (3.9)$$

with  $\varepsilon_i$  and  $\varepsilon_a$  being occupied and virtual orbital energies and  $[rs|tu]$  defines a two-electron Coulomb repulsion integral in chemist's notation.

In the direct RPA method the exchange integral contributions to Eqs. (3.7) and (3.8) are neglected leading to:

$$A_{ia,jb}^{\text{direct}} = (\varepsilon + C)_{ia,jb} = (\varepsilon_i - \varepsilon_a)\delta_{ij}\delta_{ab} + [ia|jb], \quad (3.10)$$

$$B_{ia,jb}^{\text{direct}} = C_{ia,jb} = [ia|jb]. \quad (3.11)$$

With this, the RPA equations (Eq. (3.3)) can be transformed into an alternative eigenvalue equation which is only half the size [111]:

$$(\boldsymbol{\varepsilon}^2 + 2\boldsymbol{\varepsilon}^{1/2}\mathbf{C}\boldsymbol{\varepsilon}^{1/2})\mathbf{U} = \mathbf{U}\boldsymbol{\omega}^2. \quad (3.12)$$

(A corresponding transformation can also be done if exchange integrals are included, but this would require taking the square root of the then nondiagonal matrix  $\mathbf{A} - \mathbf{B}$  [107,112].) The solution vectors  $\mathbf{U}$  of Eq. (3.12) are related to the amplitudes  $\mathbf{X}$  and  $\mathbf{Y}$  through  $\mathbf{U} = \boldsymbol{\varepsilon}^{1/2}(\mathbf{X} + \mathbf{Y})$  for the positive roots of  $\boldsymbol{\omega}^2$  and  $\mathbf{U} = \boldsymbol{\varepsilon}^{1/2}(\mathbf{X} - \mathbf{Y})$  for the negative ones.

An interesting point is that, starting from Eq. (3.3), one can derive a number of different, yet equivalent, formulas for the ground-state correlation energy. The first one is closely connected to the zero-point energy of the set of harmonic oscillators which have the same oscillation frequencies as the electrons [42]. Noting that the RPA contains both excitation and de-excitation operators, a simpler approach for calculating the excitation energies is to decouple the two parts in Eq. (3.3) using  $\mathbf{B} = \mathbf{0}$ . This leads to the Tamm-Dancoff approximation (TDA) [113,114], also known as configuration interaction singles (CIS):

$$\mathbf{AZ} = \mathbf{Z}v. \quad (3.13)$$

Compared to the RPA, in the TDA no de-excitation operators are involved and thus the ground state within the TDA is uncorrelated. The ground state correlation energy can then be calculated by summing the differences of the zero point energies of the correlated RPA harmonic oscillators and the uncorrelated TDA harmonic oscillators [41,42,46]:

$$E_c^{\text{RPA}[\text{osc}]} = \frac{1}{2} \sum_i' (\omega_i - v_i), \quad (3.14)$$

where the prime indicates that only the positive roots of Eq. (3.3) are summed.

Alternatively, the correlation energy can be calculated using the adiabatic connection method [32,46,59,60,84]. In this method the electron-electron interaction is switched on by multiplying the interaction contributions in Eq. (3.3) with a coupling-strength parameter  $\alpha$  which varies between 0 (interaction turned off) and 1 (interaction turned on). The ground state correlation energy can then be obtained by an integral over the coupling strength [32,46,84]:

$$\begin{aligned}
E_c^{\text{RPA[AC]}} &= \frac{1}{2} \int_0^1 d\alpha \operatorname{Tr} \left( \mathbf{C} \left[ (\mathbf{X}_\alpha + \mathbf{Y}_\alpha)(\mathbf{X}_\alpha + \mathbf{Y}_\alpha)^T - \mathbf{1} \right] \right) \\
&= \frac{1}{2} \int_0^1 d\alpha \operatorname{Tr}(\mathbf{C}\mathbf{P}_\alpha^c),
\end{aligned} \tag{3.15}$$

where  $P_\alpha^c$  denotes the correlation part of the pair density of the many-electron system. The amplitudes  $\mathbf{X}_\alpha$  and  $\mathbf{Y}_\alpha$  are the solutions of the RPA eigenvalue equations (Eq. (3.3)) in which the two-electron repulsion integrals (Eqs. (3.10) and (3.11)) are scaled by the coupling strength  $\alpha$ . Alternatively, the correlation energy within the adiabatic connection approach can also be calculated without solving the eigenvalue equation (Eq. (3.3) or Eq. (3.12)). Defining

$$\lambda_{ia,jb} = \delta_{ia,jb} \frac{2\varepsilon_{ia}}{\varepsilon_{ia}^2 + \omega^2}, \tag{3.16}$$

$$\chi_\alpha = -(\mathbf{1} + \alpha\lambda\mathbf{C})^{-1}\lambda \tag{3.17}$$

with  $\varepsilon_{ia} = \varepsilon_a - \varepsilon_i$ , the RPA correlation energy within the adiabatic connection is given by [83]

$$E_c^{\text{RPA[AC]}} = -\frac{1}{2\pi} \int_0^1 d\alpha \int_0^\infty d\omega \operatorname{Tr}(\mathbf{C}[\chi_\alpha + \lambda]), \tag{3.18}$$

where  $\chi_\alpha$  is the response matrix of the system at coupling strength  $\alpha$ . While usually both the integration over the coupling strength  $\alpha$  and the frequency  $\omega$  in Eq. (3.18) can be performed numerically, an expansion of Eq. (3.17) in a Taylor series shows that

$$\int_0^1 d\alpha \chi_\alpha = -\lambda + \frac{1}{2}\lambda\mathbf{C}\lambda - \frac{1}{3}\lambda\mathbf{C}\lambda\mathbf{C}\lambda + \frac{1}{4}\lambda\mathbf{C}\lambda\mathbf{C}\lambda\mathbf{C}\lambda - \dots, \tag{3.19}$$

which represents [83] a power series expansion of the logarithm function  $-\ln(1+x)$ . The RPA energy within the adiabatic connection can therefore also be calculated by calculating the logarithm of a matrix instead of performing the coupling strength integration numerically [63, 83].

Finally, the RPA correlation energy can also be derived as a multideterminant wavefunction method by starting from the coupled-cluster doubles (CCD) method. The CCD amplitude equations are given by [14]

$$\langle \Psi_{ij}^{ab} | \hat{H} | (1 + \hat{T}_2 + \frac{1}{2}\hat{T}_2^2) | \Psi_0 \rangle = t_{ij}^{ab} E, \tag{3.20}$$

where  $E$  corresponds to the total energy and the quantities  $\hat{T}_2$  and  $t_{ij}^{ab}$  denote the operator- and tensor-form of the doubles excitation amplitudes, respectively. If the quadratic terms in  $\hat{T}_2$  are omitted, then the linearized coupled-cluster doubles method (LCCD) is obtained [10]. The LCCD method can be further simplified by removing intermediate (particle-particle and hole-hole) doubles contributions (sometimes referred to as ladder contributions, see also Section 3.4.5) in a many-body expansion of the correlation energy. With this step, leading to

the so-called ring-CCD (rCCD) method, the method is no longer exact through third order and only contains particle-hole interactions. It can thus be viewed as an RPA method which contains exchange interactions [44,46] (see also Section 3.4.1). The rCCD (Riccatti-type) amplitudes equations read [115]:

$$\mathbf{B} + \mathbf{AT} + \mathbf{TA} + \mathbf{TBT} = \mathbf{0}, \quad (3.21)$$

with  $\mathbf{A}$  and  $\mathbf{B}$  defined in Eqs. (3.7) and (3.8) and  $\mathbf{T}$  denoting the doubles amplitudes tensor. Finally, the omission of the exchange contributions leads to the direct-rCCD (drCCD) method which is equivalent to the (direct) RPA method [115]. Instead of solving the RPA eigenvalue equation (Eq. (3.3) or (3.12)), the RPA correlation energy can then alternatively be calculated by solving the Riccatti-type amplitude equation

$$\mathbf{C} + \boldsymbol{\varepsilon}\mathbf{T} + \mathbf{T}\boldsymbol{\varepsilon} + \mathbf{CT} + \mathbf{TC} + \mathbf{TCT} = \mathbf{0}. \quad (3.22)$$

The RPA correlation energy is then given as [115]

$$E_c^{\text{RPA}[\text{drCCD}]} = \frac{1}{2}\text{Tr}(\mathbf{CT}). \quad (3.23)$$

The equivalence between Eq. (3.23) and Eq. (3.14) has been shown by Scuseria et al. [115], thus demonstrating a direct connection between the adiabatic connection and the wavefunction approach. A comparison between Eqs. (3.23) and (3.15) seems to imply that the amplitudes can be obtained from a coupling-strength integration over the correlated pair density, i.e.,  $\mathbf{T} = \int_0^1 d\alpha \mathbf{P}_\alpha^c$ . However, it has been shown by Jansen et al. [116] that while  $E_c^{\text{RPA}[\text{AC}]} = E_c^{\text{RPA}[\text{drCCD}]}$  holds true, the coupling-strength integrated pair density generally differs from the amplitudes, i.e., the solutions of Eq. (3.22).

This brief overview shows that the RPA can be derived in a number of different ways, leading to various possible choices for an efficient computational implementation of the method. In the following section it will be shown that a number of extensions to the RPA can be derived on the grounds the approaches described in this section.

## 3.4 BEYOND DIRECT RPA

---

### 3.4.1 RPA Methods Including Exchange Interactions

In a many-body perturbation theory expansion of the direct RPA correlation energy introduced in Section 3.3, so-called exclusion principle violation diagrams (EPV) [12,14] occur in each order which are not canceled (an EPV diagram is a contribution with two identical particle or hole indices [12,14,61]). Consequently, the RPA usually strongly overestimates electron correlation energies even for small electronic systems. The most striking example of this is the fact that the RPA yields nonzero correlation energies for one-electron systems like the hydrogen atom. This nonzero self-correlation error basically has the same origin as the Coulomb self-interaction error of the Hartree method, namely the missing exchange

contributions which cancel the EPV diagrams in each order. In first-order perturbation theory, the correction is straightforward and unique, leading to the Hartree–Fock method. In second-order perturbation theory, again only one exchange diagram exists and this cancels the self-interaction of the direct Coulomb-correlation energy:

$$E_c^{(2)} = \frac{1}{2} \sum_{ijab} \frac{[ia|jb][ia|jb]}{\varepsilon_i + \varepsilon_j - \varepsilon_a - \varepsilon_b} - \frac{[ia|jb][ib|ja]}{\varepsilon_i + \varepsilon_j - \varepsilon_a - \varepsilon_b}. \quad (3.24)$$

Only the first contribution in this equation, the direct Coulomb-correlation contribution, is contained in the RPA energy, while the second exchange contribution is missing. As a result, the RPA method is not exact through second order of perturbation theory. Only by inclusion of the second term of Eq. (3.24) the second-order energy is free from a self-correlation error.

In third-order perturbation theory, however, the cancellation of EPV diagrams of the direct RPA method is not unique. Consequently, a number of different RPA methods including exchange interactions in various ways can be derived.

The simplest approach to account for the self-correlation error in RPA is the SOSEX (second-order screened exchange) method by Grüneis et al. [81] In this method the amplitudes from a conventional (direct) RPA calculation are contracted with antisymmetrized integrals to obtain the correlation energy,

$$E_c^{\text{SOSEX}} = \frac{1}{2} \text{Tr}(\mathbf{B}\mathbf{T}^{\text{dRPA}}), \quad (3.25)$$

where  $\mathbf{T}^{\text{dRPA}}$  indicates that the amplitudes are obtained from the solution of Eq. (3.22). The SOSEX correlation energy can also be formulated within the adiabatic connection via Eq. (3.15) by replacing the direct integrals  $\mathbf{C}$  with the antisymmetric integrals  $\mathbf{B}$ . It should be noted, however, that in contrast to the direct RPA method the SOSEX correlation energy is not exactly identical in the two different formulations [100]. It can easily be verified that the SOSEX correlation energy is exact in second-order perturbation theory (if single excitations are omitted, see below) while in third order it accounts for one additional exchange contribution which cancels the self-correlation energy of the direct Coulomb interaction term [61, 125].

A more complete exchange-RPA method that accounts for all particle–hole diagrams in third-order perturbation theory is the RPAX2 method [61,64]. The RPAX2 correlation energy is obtained by iteratively solving the amplitude equation [61]

$$\mathbf{T}^{(n+1)} = -\Sigma \circ \left[ (\mathbf{1} + \mathbf{T}^{(n)})\mathbf{C}(\mathbf{1} + \mathbf{T}^{(n)}) - \hat{P}(\mathbf{1} + \mathbf{T}^{(n)})\mathbf{C}(\mathbf{1} + \mathbf{T}^{(n)}) \right], \quad (3.26)$$

where  $\mathbf{T}^{(n)}$  denotes the amplitudes of the  $n$ th iteration. In Eq. (3.26),  $\Sigma_{ia,jb} = 1/(\varepsilon_a + \varepsilon_b - \varepsilon_i - \varepsilon_j)$  and the  $\circ$  operator denotes a Hadamard (element-by-element) matrix product. The operator  $\hat{P}$  in the second term on the right-hand side of Eq. (3.26) is a permutation operator that permutes two occupied or virtual indices. An omission of this second term leads to an amplitude update equation for the direct RPA method, i.e., an update equation for solving Eq. (3.22). Denoting the solution to Eq. (3.26) as  $\mathbf{T}^{\text{RPAX2}}$ , the RPAX2 correlation energy is



given by

$$E_c^{\text{RPAX2}} = \frac{1}{2} \text{Tr}(\mathbf{C}\mathbf{T}^{\text{RPAX2}}). \quad (3.27)$$

The RPAX2 method neglects mixed ph–pp and ph–hh (p, particle; h, hole) contributions as well as all pp and hh terms in a third-order expansion of the correlation energy. The mixed terms are captured by a number of historic exchange-RPA methods [44–46] and the more recent EXX-RPA (exact-exchange RPA) method [58,83,84] that is based on the adiabatic connection. In the EXX-RPA method the coupled response matrix is calculated by including both direct Coulomb and (exact) exchange interactions in the coupling matrix  $K$  using

$$\int_0^1 d\alpha \chi_\alpha^{\text{EXX}} = -\lambda + \frac{1}{2} \lambda \mathbf{K} \lambda - \frac{1}{3} \lambda \mathbf{K} \lambda \mathbf{K} \lambda + \frac{1}{4} \lambda \mathbf{K} \lambda \mathbf{K} \lambda \mathbf{K} \lambda - \dots, \quad (3.28)$$

with

$$K_{ia,jb}^{\text{EXX}} = \left[ ia \left| \frac{1}{r_{12}} + f_x(\mathbf{r}_1, \mathbf{r}_2, i\omega) \right| jb \right], \quad (3.29)$$

where the exchange kernel  $f_x$  is defined as the second functional derivative of the exchange energy with respect to the density [117]. The EXX-RPA correlation energy can then be calculated by [83]

$$E_c^{\text{EXX-RPA}} = -\frac{1}{2\pi} \int_0^1 d\alpha \int_0^\infty d\omega \text{Tr}(\mathbf{C} [\chi_\alpha^{\text{EXX}} + \lambda]). \quad (3.30)$$

Note that the EXX-RPA correlation energy is identical to the RPAX2 correlation energy for two-electron systems [58,64].

An alternative approach, based on a Bethe–Salpeter expansion instead of time-dependent DFT (TDDFT), to the inclusion of exchange interactions in the calculation of the coupled response matrix is to use the static approximate exchange kernel (AXK) [86]

$$K_{ia,jb}^{\text{AXK}} = -[ib|ja] \quad (3.31)$$

instead of the frequency-dependent exchange kernel in Eq. (3.29). The AXK-RPA method, as all exchange-RPA variants described in this section, is exact in second-order perturbation theory and is more complete in a perturbation theory expansion than SOSEX [86].

### 3.4.2 RPA Methods Including Additional Many-Body Contributions

The direct RPA method and all exchange-RPA methods described in Section 3.4.1 lack an explicit description of single excitations from the ground-state determinant. If the Hartree–Fock determinant is chosen as the reference state, then single excitation contributions to the correlation energy first appear in fourth-order perturbation theory. One may therefore argue that in this case the single excitations give only a minor contribution to the total correlation energy and can therefore be neglected. However, it has been found in a comparison of coupled cluster singles doubles (CCSD) and CCD methods (using an HF reference state) that

while the energies are very close, corresponding energy derivatives like first- and second-order electric molecular properties are not [50]. This situation arises because, while the CCD correlation energy is exact through third-order, the corresponding CCD one-particle density matrix, and thus all properties, is incorrect already in second-order. Because of this, the addition of singles excitations, even in HF-based RPA methods, is desirable.

In the case of Kohn–Sham-based RPA methods, singles excitation contributions already contribute to the second-order correlation energy, as described by the term

$$E_c^{(2)}[\text{singles}] = \sum_{ia} \frac{|f_{ia}|^2}{\varepsilon_i - \varepsilon_a}, \quad (3.32)$$

where  $f_{ia}$  denotes an occupied-virtual matrix element of the Fock matrix. This second-order singles term is always negative definite and can be quite large [118,119]. An RPA method which includes the second-order singles term has been developed by Ren et al. [68] Compared to the bare RPA method, this method yields an improvement for vdW-bonded complexes and atomization energies [68]. Noticing that the second-order singles term diverges for low-gap systems, these authors have also developed a renormalized singles method in which a certain class of singles contributions are summed up to infinity [68,100]. The addition of renormalized single excitation contributions (rSE) to RPA or SOSEX correlation energies improve the bare RPA and SOSEX methods for a number of properties [68,100].

In spite of the general improvements of the RPA+SE or RPA+rSE over the bare RPA method used in conjunction with Kohn–Sham (KS) reference states, it has to be noted that KS orbitals themselves to some extent account for single excitations. Evidence for this is provided by a comparison of (exact) KS correlation potentials with the Brueckner OEP (optimized effective potential) correlation potentials [120,121] and correlation potentials from an orbital optimized RPA method [61,65]. Moreover, according to the determinant overlaps, even KS determinants from approximate xc functionals are closer to the Brueckner CCD determinant than the HF determinant, as was found for a number of small molecules [61]. The Brueckner determinant  $\Phi^B$  is generally defined as the determinant that has maximum overlap with the exact wavefunction  $\Psi^{\text{exact}}$  [14],

$$\langle \Psi^{\text{exact}} | \Phi^B \rangle = \text{maximum}. \quad (3.33)$$

The maximum overlap criterion of Eq. (3.33) is conform to the requirement that single-excitation contributions to the exact wavefunction vanish, i.e.,

$$\langle \Psi^{\text{exact}} | (\Phi^B)_i^a \rangle = 0, \quad (3.34)$$

with  $(\Phi^B)_i^a$  denoting a singly-excited determinant with occupied orbital  $i$  replaced by an unoccupied orbital  $a$ . Accordingly, in Brueckner wavefunction methods single excitations are not described explicitly but they are absorbed into the reference state. Numerical results for CCSD and BCCD correlation energies in fact prove that there is little difference between an explicit description of singles (as in CCSD) and an implicit description of singles (as in BCCD) [122,123]. The Brueckner condition of Eq. (3.34) has also been used to account for singles excitations within RPA and SOSEX methods, see the work by Moussa [124]. The small

differences between the KS and Brueckner determinant [61] in fact demonstrate why KS-RPA methods are generally more accurate than HF-based RPA methods.

Another perturbative correction to RPA methods has been presented in Ref. [125]. In this work, a number of different exchange RPA methods are considered and have been explicitly corrected to reproduce the exact third-order correlation energy using

$$E_c^{\text{total}}(M) = E_c^{\text{total}}(M) - E_c^{(3)}(M) + E_c^{(3)}(\text{exact}), \quad (3.35)$$

where  $M$  denotes the respective (exchange-)RPA method and  $E_c^{(3)}(\text{exact})$  is the exact 3rd-order correlation energy (excluding singles terms) described by, e.g., 3rd-order Møller–Plesset perturbation theory (MP3). In particular, lacking in all exchange-RPA methods in the term  $E_c^{(3)}(M)$  are particle–particle and hole–hole correlation contributions [10] (see also Section 3.4.5):

$$E_c^{(3)}[pp] = \frac{1}{2} \sum_{ijklcd} \frac{[ia|jd][ac|db][ci|bj]}{(\varepsilon_i + \varepsilon_j - \varepsilon_a - \varepsilon_d)(\varepsilon_i + \varepsilon_j - \varepsilon_c - \varepsilon_b)}, \quad (3.36)$$

$$E_c^{(3)}[hh] = \frac{1}{2} \sum_{ijklab} \frac{[ia|lb][ki|jl][ak|bj]}{(\varepsilon_i + \varepsilon_l - \varepsilon_a - \varepsilon_b)(\varepsilon_k + \varepsilon_j - \varepsilon_a - \varepsilon_b)}. \quad (3.37)$$

With the exception of the SOSEX method, the 3rd-order correction of Eq. (3.35) leads to a significant improvement over the standard RPA methods both for reaction energies and intermolecular interactions if combined with a range of exchange-RPA methods [125]. This method has, however, only been tested by using a Hartree–Fock reference determinant [125].

### 3.4.3 Range-Separated RPA Methods

RPA correlation methods, like all correlation methods in which the electron–electron interaction is described explicitly, are plagued by a strong dependence on the size of the atomic orbital basis set (see Section 3.1). This dependence originates from the slow convergence of the shape of the interelectronic cusp when increasing the cardinal number of the basis set [21, 22]. Therefore, for small basis sets, RPA correlation energies will be affected by a basis set error that has to be accounted for. To give an example, in the water dimer, in the equilibrium structure, the RPAX2 interaction energy calculated using the aug-cc-pVDZ basis set [18,19] deviates by as much as 16% from the result obtained at the CBS limit. In the case of the stacked parallel displaced benzene dimer, the deviation is 38%. This shows, as expected, that the basis set error becomes larger when the correlation contribution to the interaction energy increases. It is therefore crucial to correct this basis set error in order to obtain accurate results. A standard approach for reducing this error in electron correlation methods is to make use of the fact that for sufficiently large cardinal numbers  $X$  the correlation energy will behave as [22,55,71]

$$E_c^{\text{RPA}}(X) = E_c^{\text{RPA}}(\infty) + \frac{A}{X^3}, \quad (3.38)$$

where  $A$  is some constant and  $E_c^{\text{RPA}}(\infty)$  denotes the RPA correlation energy at the extrapolated basis set limit. While the dependence of  $E_c^{\text{RPA}}$  on the basis set size as given by Eq. (3.38)

does not strictly hold for smaller basis set sizes, e.g., of triple-zeta quality, it nevertheless is possible to derive empirical extrapolation schemes to obtain results that are fairly close to the CBS limit even if only small basis set results are available. In this work, unless otherwise stated, the two-point extrapolation formula by Bak et al. will be used [126], namely

$$E_c(\infty) \approx \frac{X^3 E_c(X) - (X-1)^3 E_c(X-1)}{X^3 - (X-1)^3}. \quad (3.39)$$

This equation can be used to estimate the basis set limit if results for two consecutive cardinal numbers  $X$  and  $X-1$  are available. Other basis set extrapolation techniques which were explicitly designed for RPA methods have been developed by Eshuis et al. [71] and Della Sala et al. [127].

An alternative approach for overcoming the strong basis set dependence of RPA methods is to apply a range-separation (RS) of the electron–electron interaction operator by using, for instance [94,128],

$$\frac{1}{r_{12}} = \frac{\operatorname{erfc}(\mu r_{12})}{r_{12}} + \frac{\operatorname{erf}(\mu r_{12})}{r_{12}}. \quad (3.40)$$

The first term on the right hand-side is a short-ranged potential while the second term is long-ranged and converges to a finite value for small values of the electron–electron distance  $r_{12}$ . The parameter  $\mu$  controls the splitting between the two terms of the equations. For smaller values of  $\mu$  the contribution of the short-range potential increases and for larger values of  $\mu$  the long-range potential dominates. The idea of range-separated DFT methods [128] is to treat electron–electron interactions explicitly only for the long-range potential part  $\operatorname{erf}(\mu r_{12})/r_{12}$  while the short-range electron–electron interaction is described only implicitly via standard (hybrid-)GGA density functionals. With this the correlation energy is split up into

$$E_c^{\text{RS-DFT}} = E_c^{\text{DFT}}(\text{sr}) + E_c^{\text{WF}}(\text{lr}), \quad (3.41)$$

where  $E_c^{\text{DFT}}(\text{sr})$  is the correlation energy from a standard DFT calculation using a short-range correlation functional and  $E_c^{\text{WF}}(\text{lr})$  is the correlation energy calculated by a standard wavefunction approach (such as RPA) using the long-range interaction potential. It has been found that for several variants of Eq. (3.41) (using different wavefunction approaches) the basis set dependence of RS-DFT methods is significantly reduced as compared to full-range WF methods [89].

If used in conjunction with direct RPA, another benefit of RS-DFT methods is that they may lead to improvements over bare RPA because it is known that RPA is inaccurate for short-range electron correlation effects [54,129,130]. Indeed, it has been observed that RS-RPA and RS methods combined with other RPA methods like SOSEX often improve upon the RPA method for a number of properties, like atomization energies [82], dissociation energies, reaction energies and reaction barrier heights [82], and intermolecular interactions [82,90,94,96].

Perhaps one of the most striking examples of the benefits of range separation methods compared to standard wavefunction methods is demonstrated for the beryllium dimer; see Ref. [89]. In this work, a short-range PBE (srPBE) functional [133] is combined with the

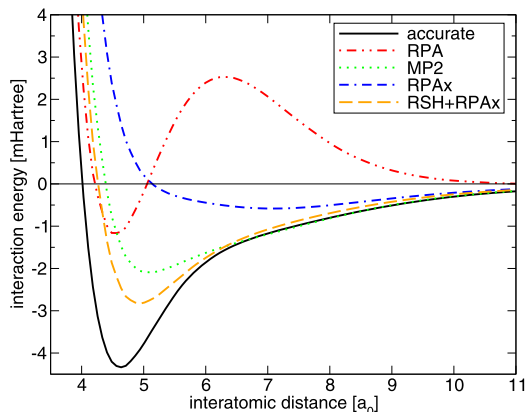


FIGURE 3.8  $\text{Be}_2$  interaction energy curve calculated using various methods with the cc-pV5Z basis set. The RPA, MP2, RPAX, and RSH+RPAX values are taken from Ref. [89] and the accurate reference curve is taken from Refs. [131, 132].

RPAX method for the long-range part. The RPAX correlation energy is based on the adiabatic connection formula (Eq. (3.15)) but the amplitudes  $\mathbf{X}_\alpha$  and  $\mathbf{Y}_\alpha$  are calculated using the antisymmetrized integrals in the Hessian (Eqs. (3.4) and (3.5)), i.e., the RPAX method takes into account exchange interactions. Fig. 3.8 shows the  $\text{Be}_2$  interaction energy curve of the RSH+RPAX method in comparison to bare RPA, RPAX, and second-order Møller–Plesset perturbation theory (MP2). As can be seen, neither the RPA curve nor the RPAX curve are able to qualitatively reproduce the accurate potential [131,132]. The RPA method yields an unphysical bump in the intermediate range and the RPAX potential is repulsive in the region around the true minimum of  $\text{Be}_2$ . Conversely, the RSH+RPAX not only yields a physically correct interaction potential but even outperforms standard MP2. It should be noted that even higher level wavefunction methods like CCD and CCSD fail to show a minimum for  $\text{Be}_2$  [134]. The reason for this can be attributed to complicated correlation effects that arise due to the near degeneracy of the  $2s$  and  $2p$  orbitals in the Be atom [134].

In Ref. [96] the range-separated DFT method was used in conjunction with two exchange RPA methods which are briefly mentioned herein. The first one corresponds to the ring coupled-cluster doubles method (rCCD) in which the correlation energy, if written in the spatial orbital basis [84], is defined as

$$E_c^{\text{RPA}[\text{SO1}]} = \frac{1}{2} \text{Tr} \left[ {}^1\mathbf{B}({}^1\mathbf{T} - {}^3\mathbf{T}) \right], \quad (3.42)$$

where the superscripts denote the solutions to the singlet and triplet part of the RPA equations, respectively. The correlation energy in Eq. (3.42) is denoted as RPAX-SO1 method in Ref. [96] because it is the first RPA scheme proposed by Szabo and Ostlund in Ref. [44]. Szabo and Ostlund have also proposed a second variant, hereafter referred to as RPAX-SO2 method,

which includes only singlet amplitude contributions

$$E_c^{\text{RPA[SO2]}} = \frac{1}{2} \text{Tr} \left[ {}^1\mathbf{C}^1\mathbf{T} \right]. \quad (3.43)$$

The advantage of the RPAX-SO2 functional, in contrast to the RPAX-SO1 method, is that it cannot be affected by triplet instabilities. However, Szabo and Ostlund did show that the RPAX-SO1 functional can describe long-range correlation energies at the coupled Hartree–Fock level and it may therefore be more suitable for the description of intermolecular interaction energies. The performance of range-separated hybrid variants of the functionals of Eqs. (3.42) and (3.43) will be analyzed in Section 3.5.

While RS-DFT methods reduce the strong dependence of full-range wavefunction electron correlation methods on the basis set size, the steep scaling behavior of the explicit long-range correlation contribution with respect to the molecular size still remains. Chermak and coworkers developed an RS hybrid RPA-DFT method in which the long-range RPA correlation contribution is calculated in terms of local orbitals [135]. In this approach, screening techniques could be employed in order to reduce the number of excitations as described by the RPA, thus reducing the overall computational cost. The approach has been tested for a number of dimer systems, namely water, methane, formamide and benzene dimers [135]. It has been found that a direct calculation of the long-range local RPA contribution to the interaction energy can reproduce the supermolecular results based on using the canonical long-range RPA correlation approach fairly well and at a significantly reduced computational cost [135].

### 3.4.4 ACFDT Methods with Additional Kernel Correlation Terms

The adiabatic connection fluctuation dissipation theorem (ACFDT) provides an exact, yet completely different approach from standard wavefunction methods to solving the electron correlation problem. In the FDT, the internal fluctuations of a many-body system are related to the response of the system to an applied external perturbation that is chosen small enough so that the system is not excited from its ground state [136]. The underlying equation of the FDT is [136]

$$\langle \Psi_0 | (O - \langle O \rangle)^2 | \Psi_0 \rangle = -\text{Im} \int_0^\infty \frac{d\omega}{\pi} \int d\mathbf{r} O(\mathbf{r}) \chi(\mathbf{r}, \mathbf{r}, \omega) O(\mathbf{r}), \quad (3.44)$$

where  $\Psi_0$  is the ground state wavefunction,  $\chi$  is the density–density response function and  $O$  is a one-particle observable. The left-hand side is the mean square fluctuation of the one-particle observable and the right-hand side corresponds to the dissipative (frictional) part of the response function. An interpretation of the fluctuation-dissipation theorem is given in Fig. 3.9. The left panel shows randomly moving particles of the many-body system and the right panel shows an extra particle that is pulled through the system and moves the particles of the system apart. The fluctuation-dissipation theorem relates the two cases through Eq. (3.44), which can be understood qualitatively by means of the consideration that the origin of the interactions between the particles is identical for the unperturbed and the perturbed system.

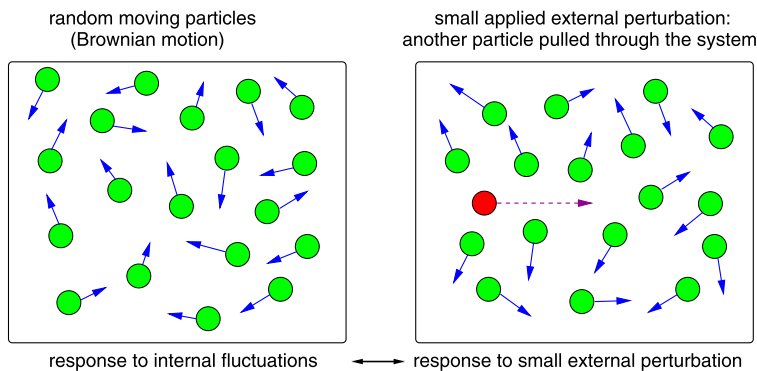


FIGURE 3.9 Illustration of the fluctuation-dissipation theorem.

While the FDT is conventionally used in statistical physics for predicting the behavior of nonequilibrium thermodynamical systems [137], Langreth and Perdew generalized this theorem to obtain an expression for the correlated part of the pair density  $P_{\alpha}^c$ , which can directly be used to calculate the correlation energy of the many-body system [59,60]. Within the ACFDT the exact correlation energy in an orbital basis set can be calculated as

$$E_c^{\text{ACFDT}} = -\frac{1}{2\pi} \int_0^1 d\alpha \int_0^{\infty} d\omega \text{Tr}(\mathbf{C}[\chi_{\alpha} + \lambda]), \quad (3.45)$$

where  $\chi_{\alpha}$  is the “exact” response matrix (in contrast to previous definitions used in the presentation of exchange RPA methods, see Section 3.4.1 and Eq. (3.30)) at coupling strength  $\alpha$ . A comparison of Eqs. (3.30) and (3.45) shows that the origin of the response matrix is the only difference between the ACFDT method and the EXX-RPA method. In fact, in case of the ACFDT method, the response matrix is defined in the same way as the EXX response matrix (Eqs. (3.28) and (3.29)), however, with the exact exchange kernel in Eq. (3.29) replaced by the full exact exchange-correlation (xc) kernel

$$K_{ia,jb}^{\text{ACFDT}} = \left[ ia \left| \frac{1}{r_{12}} + f_{xc}(\mathbf{r}_1, \mathbf{r}_2, i\omega) \right| jb \right]. \quad (3.46)$$

If the exact xc kernel were known, Eqs. (3.45), (3.28), and (3.46) would yield the exact correlation energy of the many-body interacting system. However, the exact xc kernel is unknown and must be approximated. The simplest approximation, as described in this work (Section 3.3), is to set  $f_{xc} = 0$ , which leads to the direct RPA method. As a second step, exact exchange interactions can be included in the kernel by using the second functional derivative of the exchange energy leading to the EXX-RPA method (Eq. (3.30)). In principle, the correlation kernel can be computed to any desired level, but its calculation is already very complicated and expensive if approximated at second-order [138]. The adiabatic second-order correlation kernel has been derived and tested by Bokhan and Bartlett [138] and it was found that (within this approximation) excitation energies of the neon atom do not improve compared to an exact exchange-only TDDFT calculation. Moreover, the solution of

standard equation-of-motion coupled-cluster equations is less time-consuming than solving the TDDFT eigenvalue equation using a second-order correlation kernel [138]. Therefore, while the ACFDT method can be extended in this way to approach to the exact correlation energy, in practice this route does not seem to be promising.

However, approximations to the exact nonlocal and frequency dependent kernel can also be obtained from standard DFT methods. Namely, in standard TDDFT methods using LDA or GGA approximations to the xc functional, the xc kernel is approximated as

$$f_{xc}(\mathbf{r}_1, \mathbf{r}_2, \omega) \approx f_{xc}^{\text{GGA}}(\mathbf{r}_1)\delta(\mathbf{r}_1 - \mathbf{r}_2) = \frac{\delta E_{xc}^{\text{GGA}}}{\delta\rho(\mathbf{r}_1)\delta\rho(\mathbf{r}_2)}, \quad (3.47)$$

where  $f_{xc}^{\text{GGA}}$  is the second functional derivative of a local xc functional which is generally given as

$$E_{xc}^{\text{GGA}} = \int d\mathbf{r} \rho(\mathbf{r})\varepsilon_{xc}(\rho(\mathbf{r}), \nabla\rho(\mathbf{r}), \dots), \quad (3.48)$$

where  $\varepsilon_{xc}$  is the xc energy density that depends on the density and, in case of gradient corrected functionals, density gradients. The insertion of approximate DFT kernels of the type of Eq. (3.47) in Eq. (3.46) therefore leads to an approximate ACFDT scheme in which both the exchange and the correlation contributions to the kernel are approximated by local adiabatic kernels. This so-called ACFDT-DFT method was first derived and tested by Furche and Van Voorhis [88]. While it was found that the ACFDT-DFT method improves standard DFT methods for describing the binding energy curves of rare gas dimers, the results strongly depend on the choice of the functional [88]. In the case of the helium dimer, it was found that the ACFDT-DFT used in conjunction with the BP86 xc functional [139,140] yields a repulsive potential in contrast to, for example, the results obtained using the RPA method utilizing the same xc functional.

A principal drawback of the ACFDT-DFT method is that the correlated pair density is not well defined for small electron–electron distances, and exhibits a  $1/r_{12}$  divergence to first-order in the coupling strength  $\alpha$  [88]. Consequently, the ACFDT-DFT method might even yield infinite correlation energies for larger basis sets. In order to correct for this, Olsen and Thygesen have derived a renormalized version of the adiabatic local-density (ALDA) xc kernel (rALDA) which resolves the divergence of the pair density for small electron–electron distances [98]. This method was tested for van der Waals interactions of small molecular dimers as well as bilayer graphene [99]. In both cases it was found that the RPA-rALDA method yields results that are close to RPA, indicating only a small effect of the xc kernel contribution on the interaction energy. However, Olsen et al. have argued that their plane-wave implementation is not well suited for the calculation of finite molecular systems due to the necessity to use large supercells and that, because of this, their results may not be completely converged with respect to the supercell size [99].  $C_6$  dispersion coefficients for a selection of eight atoms of the first, second and eighth group as yielded by the RPA-rALDA method were shown to be in a better agreement with accurate reference dispersion coefficients than those obtained by the direct RPA method [99].

An alternative approach for correcting the ill-defined pair function for short electron distances, as yielded by the ALDA xc kernel, has been derived in Ref. [141]. In this work, the



ACFDT-ALDA pair function is seamlessly connected with a modified RPA pair function for the short range in the following way:

$$P_c^{\text{ACFDT-ALDAcorr}}(\mathbf{r}_1, \mathbf{r}_2) = \left(1 - s(r_{12})\right) P_c^{\text{sr}}(\mathbf{r}_1, \mathbf{r}_2) + s(r_{12}) P_c^{\text{ACFDT-ALDA}}(\mathbf{r}_1, \mathbf{r}_2), \quad (3.49)$$

where  $s(r_{12})$  is a switching function that goes to zero for small distances of  $r_{12}$  and to one if  $r_{12}$  is large. The function  $s(r_{12}) = \text{erf}(\beta r_{12})$  has been utilized with  $\beta = 2$  so that  $s(r_{12}) \approx 1$  for  $r_{12} \geq 1$  bohr [141]. The pair function for the short range contribution,  $P_c^{\text{sr}}$ , has been approximated by a direct RPA method in which the Coulomb kernel is scaled by a factor of 0.6 in order to match the ACFDT-ALDA pair function at intermediate ranges [141]. The corrected ACFDT-ALDAcorr method has been shown to yield strong improvements over RPA for atomization energies, ionization potentials and intermolecular interactions [141] (see also Section 3.5).

### 3.4.5 Particle-Particle RPA

It was asserted in Section 3.4.1 that RPA methods that include exchange interactions through all orders cannot be exact in third-order perturbation theory due to the missing particle-particle (pp) and hole-hole (hh) correlation energy diagrams. In contrast to the ring form of the diagrams as yielded by particle-hole (ph) interactions described by the RPA methods, these types of diagrams have a ladder form [34] (with two particle or hole lines entering on one vertex). In Section 3.4.2 a correction method was sketched that can be applied to make RPA methods exact through third-order by adding the lowest ladder contribution to the correlation energy [125]. Yang and coworkers have developed an all-order correlation method which sums over all ladder contributions to the correlation energy [101,102,142,143]. Their approach cannot be regarded as a strict extension to the RPA because ladder contributions will only contribute to the correlation energy of an electron gas at low densities [34] (where the RPA is no longer valid, see Section 3.2) but Yang et al. nevertheless termed their method as pp-RPA. Like ph-RPA methods, it can be formulated in various ways [142]. The pp-RPA eigenvalue equation can be attained from the corresponding ph-RPA equation (Eq. (3.3)) by replacing the matrices  $\mathbf{A}$  in the diagonal blocks by [142]:

$$A_{ab,cd}^{\text{pp}} = (\varepsilon_c + \varepsilon_d)\delta_{ac}\delta_{bd} + [ac|bd] - [ad|bc], \quad (3.50)$$

$$A_{ij,kl}^{\text{hh}} = -(\varepsilon_k + \varepsilon_l)\delta_{ki}\delta_{jl} + [ik|jl] - [il|jk], \quad (3.51)$$

which are of the dimensions  $N_{\text{vir}} \times N_{\text{vir}}$  and  $N_{\text{occ}} \times N_{\text{occ}}$  ( $N_{\text{occ}}$ , number of occupied orbitals;  $N_{\text{vir}}$ , number of virtual orbitals), respectively. As in case of the ph-RPA method, a straightforward solution to the resulting pp-RPA equation would scale as  $\mathcal{N}^6$  with the system size. However, by making use of the tensor hypercontraction approach, it is possible to reduce the computational cost of the pp-RPA method to  $\mathcal{N}^4$  [144] (see also Ref. [124], which describes a corresponding approach for reducing the computational cost of ph-RPA methods). The pp-RPA method was shown to be equivalent to the ladder coupled-cluster doubles method (ladder-CCD) and thus, as the ph-RPA method, can be viewed as a restricted coupled-cluster approach [142].

The pp-RPA has the advantage over standard ph-RPA methods (including standard TDDFT methods) that it has the capability to describe double excitations if applied to study excited molecular states [143]. The method was also tested for the description of nonbonded interaction energies using both a HF and a PBE reference determinant [144]. It was found that the pp-RPA method yields smaller errors to corresponding reference interaction energies than the ph-RPA method or, more precisely, the ring coupled-cluster doubles (ring-CCD) method. However, the interaction energies were not extrapolated but evaluated using aug-cc-pVDZ (in some cases aug-cc-pVQZ) basis sets [144]. Due to the limited number of systems studied in Ref. [144], the accuracy of intermolecular interaction energies from the pp-RPA method in comparison with other ph-RPA variants has yet to be investigated.

### 3.4.6 Orbital Optimized RPA

The RPA methods described in Sections 3.3 and 3.4.1 to 3.4.5 are commonly used in conjunction with reference determinants from approximate (GGA-type) xc functionals. Often xc functionals that do not contain empirically fitted parameters are chosen so that it can be argued that the combined Kohn–Sham RPA method is fully ab initio with respect to the energy functional and with respect to the xc potential used for calculating the reference determinant.

In Section 3.4.2, it was explained that the success of Kohn–Sham-based RPA methods over corresponding RPA methods which employ Hartree–Fock reference determinants lies in the fact that the KS determinant can implicitly take into account singles excitations and therefore includes major parts of the RPA first-order density matrix [61]. If approximate (GGA-type) xc potentials are used within KS-RPA methods, however, the electron density of the reference determinant and the fully relaxed density of the KS-RPA method will in general be different, i.e., molecular properties calculated from the KS orbitals and the functional derivative of the RPA energy will differ from each other. In this sense, KS-RPA methods are not genuine KS methods and actually are closer to standard wavefunction approaches in which the true wavefunction is approximated by a sum of determinants of an “unoptimized” reference state. Moreover, the density constraint imposed in the adiabatic connection formulation (see Fig. 3.7) is not strictly fulfilled in unoptimized KS-RPA methods.

The KS-RPA method can, however, be formulated as a Kohn–Sham method by taking the functional derivative of the underlying xc functional:

$$\frac{\delta E_{xc}^{\text{EXX+RPA}}}{\delta \rho(\mathbf{r})} = \frac{\delta E_x^{\text{EXX}}}{\delta \rho(\mathbf{r})} + \frac{\delta E_c^{\text{RPA}}}{\delta \rho(\mathbf{r})} = v_x^{\text{EXX}}(\mathbf{r}) + v_c^{\text{RPA}}(\mathbf{r}), \quad (3.52)$$

yielding the KS equations

$$\left( -\frac{1}{2}\nabla^2 + v_{\text{ext}}(\mathbf{r}) + v_J(\mathbf{r}) + v_x^{\text{EXX}}(\mathbf{r}) + v_c^{\text{RPA}}(\mathbf{r}) \right) \phi_i(\mathbf{r}) = \varepsilon_i \phi_i(\mathbf{r}), \quad (3.53)$$

with  $v_{\text{ext}}$  denoting the external potential and  $v_J$  the Coulomb potential. The potentials  $v_x^{\text{EXX}}$  and  $v_c^{\text{RPA}}$  in Eqs. (3.52) and (3.53) correspond to the local exact-exchange (EXX) and the RPA correlation potential, respectively. Since both the EXX energy and the RPA energy are only implicit functionals of the density, the derivatives in Eq. (3.52) cannot be taken directly. In

case of the EXX method, a number of approaches have been derived to obtain the functional derivative of the exchange energy [145–149], most of them based on the optimized effective potential method (OEP) [150,151]. In the OEP, the local potential is expanded by a linear combination of basis functions and the energy is then minimized with respect to the expansion coefficients [145]. It should be noted that the approach can be affected by numerical instabilities, but these can be resolved with various methods [145–149].

The RPA correlation potential employing the OEP approach has been derived by several groups [85,93,152,153]. In Ref. [152] the resulting orbital-optimized RPA (ORPA) method was tested with particular focus on the description of the bond dissociations of small molecules like  $\text{H}_2$  or  $\text{LiH}$ . It was found that the ORPA method reproduces the dissociation limit in these systems correctly and separates the charges at bond dissociation by virtue of a peak at the bond midpoint, a feature it has in common with the exact correlation potential. In a work by Verma et al. it was shown for a number of atoms that the ORPA correlation potentials slightly differ from the local correlation potentials obtained from other higher-level correlation functionals, namely linearized CCD and full CCD [153]. Bleiziffer et al. derived an ORPA method which preserves the favorable  $\mathcal{N}^4$  scaling behavior of the nonoptimized RPA method, thus enabling its application to large systems [85]. In their work, the ORPA method was also tested for intermolecular interactions; see Section 3.5. Bleiziffer et al. also derived and tested the functional derivative of the EXX-RPA correlation functional within a self-consistent RPA method [87] (see also Ref. [93] for a corresponding method by Hellgren and von Barth). It turns out that the orbital optimized EXX-RPA method generally improves the description of electron correlation effects as compared to the ORPA method, but at a much higher computational cost, making this method currently impractical for the description of extended molecular systems [87].

## 3.5 INTERACTION ENERGY BENCHMARKS

### 3.5.1 S22 Benchmark

In this and in subsequent sections, we assess the performance of the different RPA methods introduced in Sections 3.3 and 3.4 for the description of intermolecular interaction energies. For this purpose, high level CCSD(T) interaction energies will be used as reference in most cases. The CCSD(T) method is exact through a fourth-order perturbation theory expansion of the correlation energy [14,154] and can be considered to be accurate to within  $\pm 0.1$  kcal/mol for the interaction energies of small to intermediate sized molecules for which the electronic structure can be well described by a single determinant.

As discussed in Section 3.4.3, large basis sets including both diffuse and high-angular momentum functions are necessary in ab initio wavefunction calculations to converge the correlation energy contribution to the complete basis set limit (see also Chapter 4). Unfortunately, the use of very large basis sets in CCSD(T) calculations is not feasible for large molecules, so an extrapolation approach to estimate the complete basis set (CBS) limit values has to be applied to describe the dynamic correlation effects accurately. Current approaches calculate the CCSD(T) interaction energy in a small basis set and estimate the basis set error

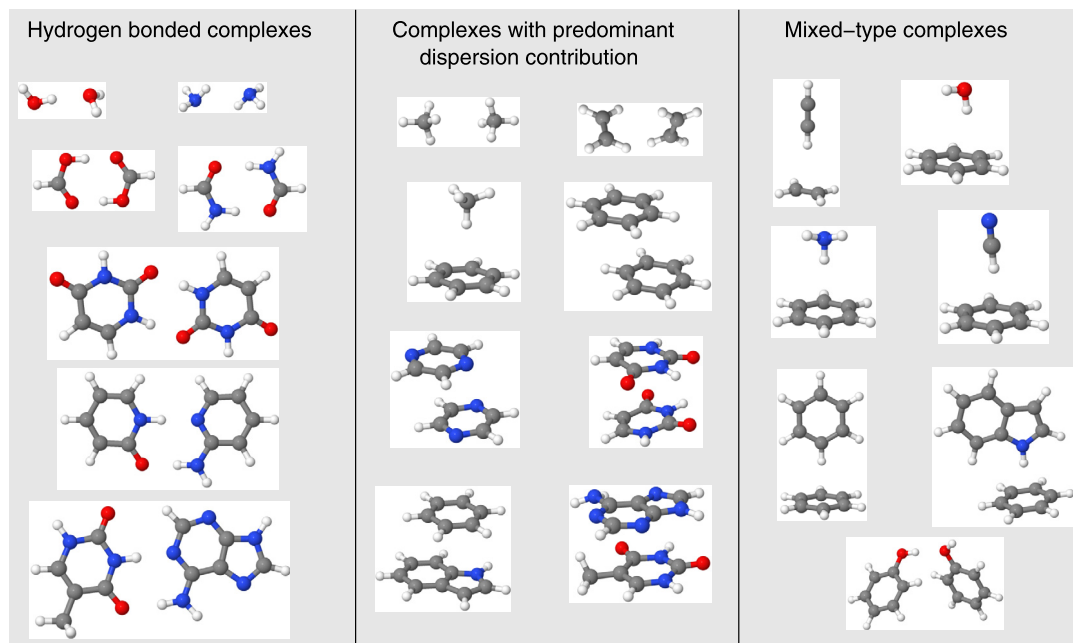


FIGURE 3.10 Dimers in the S22 benchmark set [104].

by extrapolating second-order Møller–Plesset perturbation theory (MP2) energies using [155, 156]

$$\begin{aligned}
 E_{\text{int}}^{\text{CCSD(T)}}(\text{CBS}) &\approx E_{\text{int}}^{\text{MP2}}(\text{CBS}) + \left( E_{\text{int}}^{\text{CCSD(T)}}(\text{small basis}) - E_{\text{int}}^{\text{MP2}}(\text{small basis}) \right) \\
 &\approx E_{\text{int}}^{\text{MP2}}(\text{CBS}) + \Delta(\text{CCSD(T)}).
 \end{aligned}
 \tag{3.54}$$

The correction method used in this equation is based on the idea that, while the total MP2 and CCSD(T) interaction energies depend strongly on the basis set size, their absolute difference, i.e., the term  $\Delta\text{CCSD(T)}$ , does not. Indeed, it has been found by Hobza et al. that even for fairly small basis sets the  $\Delta\text{CCSD(T)}$  correction is much less basis set dependent than the interaction energy itself [155]. Eq. (3.54) provides a route to obtaining almost converged CCSD(T)/CBS results if the  $E_{\text{int}}^{\text{MP2}}(\text{CBS})$  values are close to the complete basis set limit (as implied by the equation).

Many of the RPA methods introduced in Sections 3.3 and 3.4 have been tested for their ability to describe intermolecular interaction energies of various complexes by comparing the results to high level CCSD(T) interaction energies. A meaningful comparison of the different approaches, however, can only be made if they are applied to the same systems. Therefore, only those RPA methods that have been tested on the so-called S22 dimer benchmark set will be discussed.

The S22 benchmark data base developed by Hobza et al. contains seven dimers bound by hydrogen bonds, eight dimers in which dispersion dominates the intermolecular interaction,

and seven dimers with mixed noncovalent interactions [104] (see Fig. 3.10). All dimer geometries of this benchmark set were optimized using the MP2 method [104]. The S22 benchmark set has a balanced number of dimers within each interaction type making it particularly well-suited as a means for assessing different computational methods. Ideally, a given method should describe complexes containing strong electrostatic interactions and those containing strong dispersion interactions on an equal footing, otherwise potential energy surfaces in which both types of interactions play a role cannot be accurately described.

The original CCSD(T) reference interaction energies by Hobza et al. [104] for the S22 dimers were revised by Takatani et al. using a modified basis set extrapolation scheme for the  $\Delta$ CCSD(T) correction [157]

$$E_{\text{int}}^{\text{CCSD(T)}}(\text{CBS}) \approx E_{\text{int}}^{\text{MP2}}(\text{aVTZ} \rightarrow \text{aVQZ}) + \left( E_{\text{int}}^{\text{CCSD(T)}}(\text{aVDZ} \rightarrow \text{aVTZ}) - E_{\text{int}}^{\text{MP2}}(\text{aVDZ} \rightarrow \text{aVTZ}) \right), \quad (3.55)$$

where aVXZ represents the aug-cc-pVXZ basis set [17–20]. The  $\Delta$ CCSD(T) correction is obtained from the difference between the CBS estimates of the CCSD(T) and MP2 interaction energies using the two-point aVDZ  $\rightarrow$  aVTZ basis set extrapolation. For the smallest systems, Takatani et al. also performed aVTZ  $\rightarrow$  aVQZ extrapolations to estimate the CCSD(T) basis set limit and found deviations of 0.02 kcal/mol on average relative to the energies obtained by the extrapolation scheme of Eq. (3.55). The latter approach can therefore be considered to be close to the true CCSD(T) CBS interaction energies for the S22 dimers.

Tables 3.1 to 3.5 compile interaction energies for the S22 dimer systems obtained by the different RPA methods introduced in Sections 3.3 and 3.4, namely:

- Table 3.1: direct RPA methods (Sections 3.3 and 3.4.6).
- Table 3.2: RPA methods including exchange interactions (Section 3.4.1).
- Table 3.3: RPA methods with additional singles corrections to the correlation energy (Section 3.4.2).
- Table 3.4: range-separated RPA methods (Section 3.4.3).
- Table 3.5: ACFDT methods including approximate xc kernels (Section 3.4.4).

In all cases, unless otherwise noted, the interaction energies of the different methods were extrapolated to the complete basis set limit. The three different groups in the tables represent the hydrogen bonded, dispersion dominated, and mixed-type systems. In all cases the Boys–Bernardi counterpoise correction was used to reduce the basis set superposition error (BSSE) [158].

Along with the RPA interaction energies each table also contains the CCSD(T)/CBS estimates by Takatani et al. [157] for comparison. The mean absolute errors (MAE) relative to these reference energies are shown for the groups of individual interaction types as well as for the whole S22 set.

Table 3.1 presents the interaction energies of the direct RPA method for the S22 dimers calculated using three different reference determinants: the KS determinant calculated by the PBE functional, the EXX functional and the ORPA (optimized-orbital RPA) functional. In all cases the interaction energies for the hydrogen bonded systems are underestimated by 1 to 1.5 kcal/mol on average. The deviation relative to the CCSD(T) interaction energies is smaller

**TABLE 3.1** Interaction energies of the S22 dimer systems: direct RPA methods. The xc functional used to calculate the orbitals and orbital energies is given in square brackets. All interaction energies are extrapolated to the basis set limit (energies in kcal/mol)

Dimer	CCSD(T) [157]	RPA [71] <sup>a</sup> [PBE]	RPA [85] [EXX]	ORPA [87]
(NH <sub>3</sub> ) <sub>2</sub> (C <sub>2h</sub> )	-3.17	-2.58	-2.63	-2.65
(H <sub>2</sub> O) <sub>2</sub> (C <sub>s</sub> )	-5.02	-4.11	-4.42	-4.54
(HCOOH) <sub>2</sub> (C <sub>2h</sub> )	-18.80	-17.12	-17.03	-18.38
(CHONH <sub>2</sub> ) <sub>2</sub>	-16.12	-14.84	-14.82	-15.08
Uracil-Uracil (C <sub>2h</sub> )	-20.69	-18.76	-18.48	-19.13
C <sub>5</sub> H <sub>5</sub> ON-C <sub>5</sub> H <sub>6</sub> N <sub>2</sub>	-17.00	-15.57	-15.06	-15.78
Adenine-Thymine (WC) <sup>b</sup>	-16.74	-15.28	-14.63	-15.52
MAE		1.33	1.50	0.92
(CH <sub>4</sub> ) <sub>2</sub> (D <sub>3d</sub> )	-0.53	-0.39	-0.36	-0.37
(C <sub>2</sub> H <sub>4</sub> ) <sub>2</sub> (D <sub>2d</sub> )	-1.50	-1.12	-1.16	-1.09
Benzene-CH <sub>4</sub> (C <sub>3</sub> )	-1.45	-1.12	-1.17	-1.03
Benzene-Benzene (C <sub>2h</sub> )	-2.62	-1.87	-2.20	-1.78
Pyrazine-Pyrazine (C <sub>s</sub> )	-4.20	-3.27	-3.48	-3.18
Uracil-Uracil (C <sub>2</sub> )	-9.74	-8.60	-8.13	-8.50
Indole-Benzene (stacked)	-4.59	-3.36	-3.73	-3.39
Adenine-Thymine (stacked)	-11.66	-9.94	-10.73	-9.73
MAE		0.83	0.66	0.90
C <sub>2</sub> H <sub>4</sub> -C <sub>2</sub> H <sub>2</sub> (C <sub>2v</sub> )	-1.51	-1.16	-1.38	-1.19
Benzene-H <sub>2</sub> O (C <sub>s</sub> )	-3.29	-2.82	-2.80	-2.73
Benzene-NH <sub>3</sub> (C <sub>s</sub> )	-2.32	-1.94	-1.97	-1.85
Benzene-HCN (C <sub>s</sub> )	-4.55	-3.89	-3.83	-3.85
Benzene-Benzene (C <sub>2v</sub> )	-2.71	-2.19	-2.29	-1.96
Indole-Benzene (T-shaped)	-5.62	-4.93	-4.99	-4.90
Phenol-Phenol	-7.09	-6.08	-6.04	-6.31
MAE		0.62	0.54	0.61
MAE (total)		0.91	0.89	0.82

<sup>a</sup> *aug-cc-pV5Z basis set using counterpoise correction.*

<sup>b</sup> *Watson-Crick structure of the adenine-thymine base pair.*

for the dispersion-dominated and mixed-type systems but in these cases all direct RPA methods are underbinding. Apart from the hydrogen bonded systems, where the ORPA method yields more accurate interaction energies than the other two approaches, the reference determinant appears to have only a small effect on the accuracy of the predicted interaction energies. It should be noted here that Eshuis et al. presented direct RPA interaction energies that are much closer to the reference results than the ones given in Table 3.1, with an average error of 0.4 kcal/mol only [70]. These results were, however, not BSSE corrected and accordingly were too large in magnitude compared to the full counterpoise corrected results (see also Ref. [71] and Chapter 4).

**TABLE 3.2** Interaction energies of the S22 dimer systems: exchange RPA methods. The xc functional used to calculate the orbitals and orbital energies is given in square brackets. All interaction energies are extrapolated to the basis set limit (energies in kcal/mol)

Dimer	CCSD(T) [157]	SOSEX [100] [PBE]	EXX-RPA [87] [EXX]	EXX-RPA [87] [ORPA]	RPAX2 [64] [PBEx]
(NH <sub>3</sub> ) <sub>2</sub> (C <sub>2h</sub> )	-3.17	-2.75	-3.01	-3.02	-3.00
(H <sub>2</sub> O) <sub>2</sub> (C <sub>s</sub> )	-5.02	-4.64	-5.26	-5.33	-4.83
(HCOOH) <sub>2</sub> (C <sub>2h</sub> )	-18.80	-18.95	-19.68	-19.90	-19.13
(CHONH <sub>2</sub> ) <sub>2</sub>	-16.12	-16.02	-16.62	-16.89	-16.45
Uracil-Uracil (C <sub>2h</sub> )	-20.69	-21.26	-21.29	-21.58	-20.85
C <sub>5</sub> H <sub>5</sub> ON-C <sub>5</sub> H <sub>6</sub> N <sub>2</sub>	-17.00	-16.63	-17.03	-17.27	-17.13
Adenine-Thymine (WC)	-16.74	-16.35	-16.75	-17.01	-16.91
MAE		0.34	0.35	0.53	0.21
(CH <sub>4</sub> ) <sub>2</sub> (D <sub>3d</sub> )	-0.53	-0.40	-0.48	-0.48	-0.59
(C <sub>2</sub> H <sub>4</sub> ) <sub>2</sub> (D <sub>2d</sub> )	-1.50	-1.28	-1.48	-1.47	-1.59
Benzene-CH <sub>4</sub> (C <sub>3</sub> )	-1.45	-1.18	-1.41	-1.32	-1.47
Benzene-Benzene (C <sub>2h</sub> )	-2.62	-1.72	-2.49	-2.17	-2.37
Pyrazine-Pyrazine (C <sub>s</sub> )	-4.20	-3.21	-3.78	-3.45	-3.90
Uracil-Uracil (C <sub>2</sub> )	-9.74	-9.45	-9.19	-9.30	-10.04
Indole-Benzene (stacked)	-4.59	-3.36	-4.16	-3.78	-4.08
Adenine-Thymine (stacked)	-11.66	-10.70	-10.35	-10.61	-11.51
MAE		0.62	0.37	0.46	0.21
C <sub>2</sub> H <sub>4</sub> -C <sub>2</sub> H <sub>2</sub> (C <sub>2v</sub> )	-1.51	-1.48	-1.61	-1.58	-1.53
Benzene-H <sub>2</sub> O (C <sub>s</sub> )	-3.29	-3.05	-3.27	-3.22	-3.33
Benzene-NH <sub>3</sub> (C <sub>s</sub> )	-2.32	-2.06	-2.28	-2.20	-2.37
Benzene-HCN (C <sub>s</sub> )	-4.55	-4.50	-4.71	-4.55	-4.50
Benzene-Benzene (C <sub>2v</sub> )	-2.71	-2.36	-2.65	-2.47	-2.72
Indole-Benzene (T-shaped)	-5.62	-5.23	-5.60	-5.45	-5.68
Phenol-Phenol	-7.09	-6.70	-7.12	-7.13	-7.12
MAE		0.24	0.06	0.10	0.04
MAE (total)		0.41	0.26	0.37	0.16

In [Table 3.2](#) the S22 interaction energies of various exchange-RPA methods are shown, namely SOSEX, EXX-RPA and RPAX2. As expected, all exchange-RPA methods yield an improvement over the direct RPA results presented in [Table 3.1](#). With exception of the SOSEX method, the deviations of the interaction energies to the CCSD(T) reference values are very similar for the hydrogen bonded and dispersion-dominated systems, suggesting that exchange-RPA methods yield a more balanced description of different types of noncovalent interactions than the direct RPA method. As in case of the direct RPA method ([Table 3.1](#)), the choice of the reference determinant does not have a strong effect on the quality of the predicted interaction energies, which can be seen by comparing the EXX-RPA interaction energies using EXX orbitals and ORPA orbitals. The RPAX2 method performs best among the exchange-RPA methods, yielding an average error of only 0.16 kcal/mol. Both the EXX-RPA

**TABLE 3.3** Interaction energies of the S22 dimer systems: RPA methods including single-excitation (SE) many-body terms. The xc functional used to calculate the orbitals and orbital energies is given in square brackets. The SE-RPA energies were calculated with the NAO tier4+gaussian diffuse aug-cc-pV5Z basis set [100] (energies in kcal/mol)

Dimer	CCSD(T) [157]	RPA+SE [100] [PBE]	RPA+rSE [100] [PBE]	SOSEX+rSE [100] [PBE]
(NH <sub>3</sub> ) <sub>2</sub> (C <sub>2h</sub> )	-3.17	-3.51	-3.05	-3.21
(H <sub>2</sub> O) <sub>2</sub> (C <sub>s</sub> )	-5.02	-5.49	-4.87	-5.30
(HCOOH) <sub>2</sub> (C <sub>2h</sub> )	-18.80	-19.94	-18.99	-20.79
(CHONH <sub>2</sub> ) <sub>2</sub>	-16.12	-15.96	-15.97	-17.13
Uracil-Uracil (C <sub>2h</sub> )	-20.69	-19.65	-19.72	-22.18
C <sub>5</sub> H <sub>5</sub> ON-C <sub>5</sub> H <sub>6</sub> N <sub>2</sub>	-17.00	-17.97	-17.01	-18.03
Adenine-Thymine (WC)	-16.74	-17.64	-16.78	-17.75
MAE		0.72	0.23	0.98
(CH <sub>4</sub> ) <sub>2</sub> (D <sub>3d</sub> )	-0.53	-0.59	-0.51	-0.51
(C <sub>2</sub> H <sub>4</sub> ) <sub>2</sub> (D <sub>2d</sub> )	-1.50	-1.45	-1.34	-1.50
Benzene-CH <sub>4</sub> (C <sub>3</sub> )	-1.45	-1.28	-1.25	-1.31
Benzene-Benzene (C <sub>2h</sub> )	-2.62	-1.88	-1.98	-1.82
Pyrazine-Pyrazine (C <sub>s</sub> )	-4.20	-3.72	-3.49	-3.42
Uracil-Uracil (C <sub>2</sub> )	-9.74	-9.32	-9.18	-9.96
Indole-Benzene (stacked)	-4.59	-3.64	-3.67	-3.57
Adenine-Thymine (stacked)	-11.66	-11.61	-10.94	-11.57
MAE		0.37	0.49	0.38
C <sub>2</sub> H <sub>4</sub> -C <sub>2</sub> H <sub>2</sub> (C <sub>2v</sub> )	-1.51	-1.37	-1.36	-1.59
Benzene-H <sub>2</sub> O (C <sub>s</sub> )	-3.29	-3.40	-3.14	-3.36
Benzene-NH <sub>3</sub> (C <sub>s</sub> )	-2.32	-2.29	-2.15	-2.26
Benzene-HCN (C <sub>s</sub> )	-4.55	-4.23	-4.13	-4.71
Benzene-Benzene (C <sub>2v</sub> )	-2.71	-2.40	-2.38	-2.53
Indole-Benzene (T-shaped)	-5.62	-5.39	-5.29	-5.55
Phenol-Phenol	-7.09	-6.96	-6.75	-7.28
MAE		0.18	0.27	0.12
MAE (total)		0.42	0.34	0.49

and RPAX2 interaction energies are more accurate than those obtained using SOSEX, which demonstrates that a systematic improvement of the energy functional is also reflected in an improvement of performance.

The latter conclusion can also be drawn if the direct RPA interaction energies of Table 3.1 are compared to the RPA interaction energies which include additional singles correction terms in Table 3.3. The use of both first-order singles (RPA+SE) and of additional renormalized singles correction terms in the correlation energy (RPA+rSE) leads to a significant improvement of the reference interaction energies compared to the direct RPA results. In the case of the SOSEX method, however, the addition of the rSE correction leads to a slight deterioration of its performance: While the description of the interactions in the dispersion-



**TABLE 3.4** Interaction energies of the S22 dimer systems: range-separated RPA methods. The xc functional used to calculate the orbitals and orbital energies is given in square brackets. The RS-RPA interaction energies were calculated using the aug-cc-pVDZ basis set [96] (energies in kcal/mol)

Dimer	CCSD(T) [157]	RPA [srPBE]	SOSEX [srPBE]	RPAx [srPBE]	RPA-SO1 [srPBE]	RPA-SO2 [srPBE]
(NH <sub>3</sub> ) <sub>2</sub> (C <sub>2h</sub> )	-3.17	-2.87	-2.92	-3.07	-3.20	-3.18
(H <sub>2</sub> O) <sub>2</sub> (C <sub>s</sub> )	-5.02	-5.16	-5.23	-5.33	-5.40	-5.39
(HCOOH) <sub>2</sub> (C <sub>2h</sub> )	-18.80	-20.30	-20.55	-20.81	-20.94	-20.98
(CHONH <sub>2</sub> ) <sub>2</sub>	-16.12	-16.51	-16.68	-17.03	-17.32	-17.27
Uracil-Uracil (C <sub>2h</sub> )	-20.69	-21.03	-21.36	-21.80	-22.04	-22.15
C <sub>5</sub> H <sub>5</sub> ON-C <sub>5</sub> H <sub>6</sub> N <sub>2</sub>	-17.00	-17.07	-17.28	-17.81	-18.25	-18.20
Adenine-Thymine (WC)	-16.74	-16.53	-16.73	-17.29	-17.81	-17.69
MAE		0.42	0.53	0.83	1.06	1.05
(CH <sub>4</sub> ) <sub>2</sub> (D <sub>3d</sub> )	-0.53	-0.30	-0.31	-0.42	-0.53	-0.51
(C <sub>2</sub> H <sub>4</sub> ) <sub>2</sub> (D <sub>2d</sub> )	-1.50	-0.97	-1.02	-1.28	-1.52	-1.47
Benzene-CH <sub>4</sub> (C <sub>3</sub> )	-1.45	-0.92	-0.98	-1.23	-1.47	-1.43
Benzene-Benzene (C <sub>2h</sub> )	-2.62	-1.27	-1.38	-2.05	-2.72	-2.61
Pyrazine-Pyrazine (C <sub>s</sub> )	-4.20	-2.99	-3.10	-3.78	-4.49	-4.34
Uracil-Uracil (C <sub>2</sub> )	-9.74	-8.22	-8.46	-9.38	-10.25	-10.13
Indole-Benzene (stacked)	-4.59	-2.58	-2.75	-3.70	-4.64	-4.48
Adenine-Thymine (stacked)	-11.66	-9.38	-9.68	-10.97	-12.23	-12.02
MAE		1.21	1.08	0.44	0.20	0.14
C <sub>2</sub> H <sub>4</sub> -C <sub>2</sub> H <sub>2</sub> (C <sub>2v</sub> )	-1.51	-1.31	-1.36	-1.48	-1.58	-1.57
Benzene-H <sub>2</sub> O (C <sub>s</sub> )	-3.29	-2.90	-2.96	-3.16	-3.34	-3.30
Benzene-NH <sub>3</sub> (C <sub>s</sub> )	-2.32	-1.83	-1.88	-2.11	-2.33	-2.29
Benzene-HCN (C <sub>s</sub> )	-4.55	-4.20	-4.31	-4.54	-4.72	-4.71
Benzene-Benzene (C <sub>2v</sub> )	-2.71	-1.92	-2.00	-2.39	-2.77	-2.70
Indole-Benzene (T-shaped)	-5.62	-4.54	-4.65	-5.17	-5.66	-5.57
Phenol-Phenol	-7.09	-6.48	-6.62	-7.07	-7.49	-7.43
MAE		0.56	0.47	0.17	0.11	0.09
MAE (total)		0.75	0.71	0.48	0.45	0.41

dominated and mixed-type dimers improves with the rSE correction, the hydrogen bonded complexes are now strongly overbound by the SOSEX+rSE method. Contrary to the results obtained with the exchange-RPA methods in Table 3.1, the singles energy corrections do not lead to a balanced description of the hydrogen bonded and dispersion-dominated systems. While RPA+SE and SOSEX+rSE give mean absolute errors that are twice as large for the former group of systems, the reverse is observed in case of RPA+rSE.

Table 3.4 shows interaction energies for the S22 dimers for various range-separated RPA methods. In these cases, the short-range PBE (srPBE) functional [133] is used in conjunction with the long-range (lr) RPA correlation functional [96]. As can be seen in the table, the lr-RPA and lrSOSEX functionals underestimate the magnitude of the interaction energies for the dispersion-dominated systems by about 1.1 kcal/mol on average while producing results

**TABLE 3.5** Interaction energies of the S22 dimer systems: ACFDT methods including corrected ALDA xc kernels. The xc functional used to calculate the orbitals and orbital energies is given in square brackets. In case of rALDA a plane-wave cutoff of 600 eV was used [99]. In all other cases, the interaction energies were extrapolated to the basis set limit (energies in kcal/mol)

Dimer	CCSD(T) [157]	rALDA [99] [LDA]	ALDAcorr [141] [PBE]
(NH <sub>3</sub> ) <sub>2</sub> (C <sub>2h</sub> )	-3.17	-2.31	-3.03
(H <sub>2</sub> O) <sub>2</sub> (C <sub>s</sub> )	-5.02	-3.92	-4.81
(HCOOH) <sub>2</sub> (C <sub>2h</sub> )	-18.80		-18.92
(CHONH <sub>2</sub> ) <sub>2</sub>	-16.12	-16.37	-16.28
Uracil-Uracil (C <sub>2h</sub> )	-20.69		-20.34
C <sub>5</sub> H <sub>5</sub> ON-C <sub>5</sub> H <sub>6</sub> N <sub>2</sub>	-17.00		-17.09
Adenine-Thymine (WC)	-16.74		-16.81
MAE			0.16
(CH <sub>4</sub> ) <sub>2</sub> (D <sub>3d</sub> )	-0.53	-0.23	-0.54
(C <sub>2</sub> H <sub>4</sub> ) <sub>2</sub> (D <sub>2d</sub> )	-1.50		-1.50
Benzene-CH <sub>4</sub> (C <sub>3</sub> )	-1.45		-1.45
Benzene-Benzene (C <sub>2h</sub> )	-2.62		-2.45
Pyrazine-Pyrazine (C <sub>s</sub> )	-4.20		-3.98
Uracil-Uracil (C <sub>2</sub> )	-9.74		-9.68
Indole-Benzene (stacked)	-4.59		-4.19
Adenine-Thymine (stacked)	-11.66		-11.35
MAE			0.15
C <sub>2</sub> H <sub>4</sub> -C <sub>2</sub> H <sub>2</sub> (C <sub>2v</sub> )	-1.51		-1.49
Benzene-H <sub>2</sub> O (C <sub>s</sub> )	-3.29		-3.28
Benzene-NH <sub>3</sub> (C <sub>s</sub> )	-2.32		-2.32
Benzene-HCN (C <sub>s</sub> )	-4.55		-4.47
Benzene-Benzene (C <sub>2v</sub> )	-2.71		-2.67
Indole-Benzene (T-shaped)	-5.62		-5.61
Phenol-Phenol	-7.09		-6.93
MAE			0.04
MAE (total)			0.12

for the hydrogen bonded systems that are in a much better agreement to the reference values. The reverse trend is observed for the IrRPAx, IrRPA-SO1 and IrRPA-SO2 exchange-RPA variants, which overestimate the interaction energies of the hydrogen bonded complexes but describe the dispersion-dominated systems quite well. The latter holds true in particular for the IrRPA-SO1 and IrRPA-SO2 functionals for which the MAEs for the dispersion-dominated and the mixed-type systems are within a range of 0.1 to 0.2 kcal/mol.

In Table 3.5, results are shown for the ACFDT method employing short-range corrected ALDA xc kernels (Section 3.4.4). The third column presents, where available, results from the renormalized ALDA ACFDT method by Olsen et al. [99]. With the exception of the formamide dimer, the reference interaction energies are underestimated by Olsen et al.'s

method. It should be noted, however, that these results might not yet be fully converged with respect to the basis set size since Olsen et al. used a plane-wave basis set requiring large unit cells for the given finite systems [99]. The ACFDT interaction energies employing the ALDAcorr xc kernel shown in the last column of the table are in a very good agreement with the reference energies: The interaction energies of the hydrogen bonded and the dispersion dominated dimers have MAEs of only 0.16 kcal/mol. In case of the mixed interaction-type systems, the MAE is only 0.04 kcal/mol, which is below the estimated error of the reference CCSD(T) interaction energies.

To give an overall comparison of the performance of the different RPA functionals from Tables 3.1 to 3.5, Fig. 3.11 compiles the mean absolute deviations relative to the CCSD(T) reference interaction energies for each group of interaction types in the S22 set. Marked by the solid bars in the diagrams in Fig. 3.11 are the direct RPA methods of Table 3.1, the checked bars show the deviations of the exchange-RPA methods of Table 3.2, the brick-type bars are the deviations of the singles-corrected RPA methods of Table 3.3, the mesh-type bars the deviations for the range-separated methods of Table 3.4 and the striped bars show the errors for the ACFDT[ALDAcorr] method in Table 3.5.

Common to all of the methods presented in Fig. 3.11 is the fact that the smallest errors are obtained for the mixed interaction-type systems, as indicated in the bottom left diagram. One can also clearly see that the RPA methods that include either additional exchange contributions (checked bars), singles correlation energy terms (brick-type bars) or additional xc kernel contributions (striped bar) clearly outperform the direct RPA methods. This indicates that indeed the RPA method can be systematically improved in its ability to describe intermolecular interaction energies. A comparison of the different groups of methods indicates that the exchange-RPA methods and the ACFDT methods with additional approximate xc kernel contributions are the most consistent methods because they describe both the hydrogen bonded and dispersion-dominated systems with a similar accuracy, see top left and right diagram in Fig. 3.11.

### 3.5.2 S66×8 Benchmark

Despite the fact that the S22 set has become a standard benchmark for assessing the accuracy of quantum chemical methods for describing intermolecular interactions, it is biased toward nucleic-acid-like dimers which are present in the set as hydrogen bonded and stacked arrangements. Another potential problem of the S22 database is that all of the structures were optimized using the MP2 method. Since the MP2 method gives an unbalanced description of noncovalent interactions it can be assumed that the structures obtained by MP2 have a varying accuracy depending on the type of the interaction in the dimer. For example, the MP2 method strongly overestimates  $\pi$ - $\pi$  stacking interactions and therefore it can be expected that the distance between molecules in a stacked dimer will be underestimated by MP2. It will be shown in this section that this is indeed the case.

Due to the limitations associated with the S22 database, Hobza et al. developed a larger and more balanced database of noncovalently interacting dimers termed S66×8 (see Table 1 in Ref. [105]). In this database each of the 66 dimers is considered at 8 different intermonomer distances by scaling the distance by factors of 0.9, 0.95, 1.0, 1.05, 1.10, 1.25, 1.5, and 2.0 relative to the equilibrium structure. The first two scaling factors yield structures at smaller

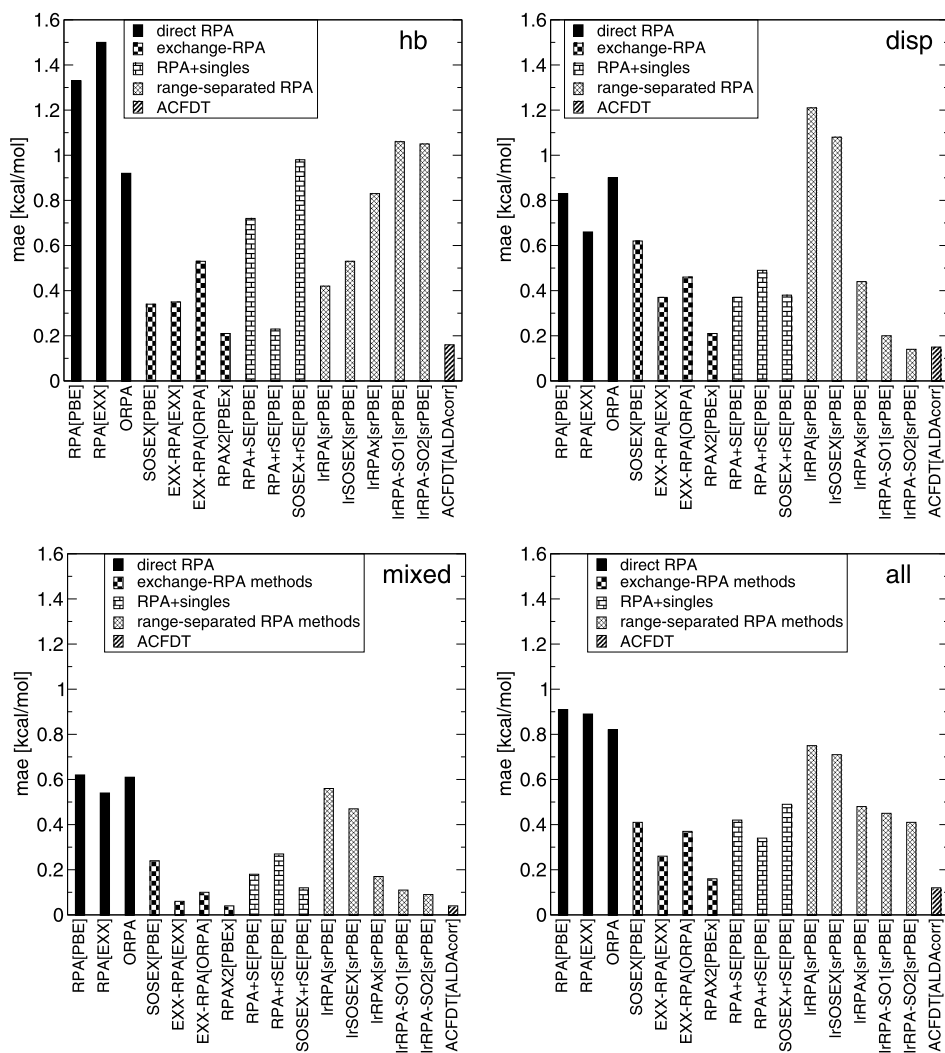


FIGURE 3.11 Mean absolute errors compared to CCSD(T) interaction energies of various RPA methods in the S22 set (solid, direct RPA methods; checked, exchange-RPA methods; brick, RPA methods including singles energy corrections; mesh, range-separated RPA methods; and striped, ACFTD methods): (top left) hydrogen-bonded dimers; (top right) dispersion-dominated dimers; (bottom left) mixed-type dimers; (bottom right) all dimers.

intermonomer distances compared to the minima, which is associated with the factor 1.0 (optimized at the MP2 level). The remaining five scaling factors yield dimer structures with larger monomer separations. The  $S66 \times 8$  benchmark set thus provides data that enable the assessment of a given method for the shorter- and longer-range regions of intermolecular potentials in noncovalently bonded systems. The  $\Delta\text{CCSD(T)}$  correction used to compute the CCSD(T)/CBS reference interaction energies was calculated using aVDZ basis sets; see

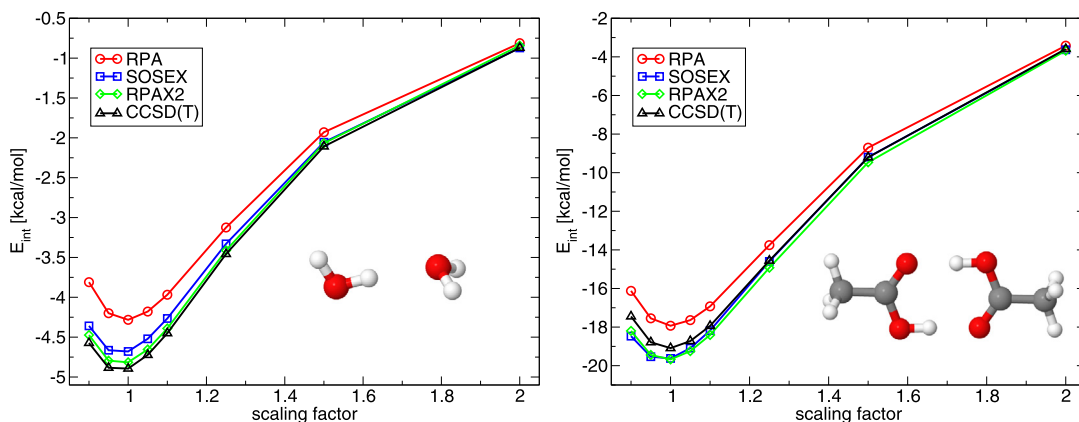
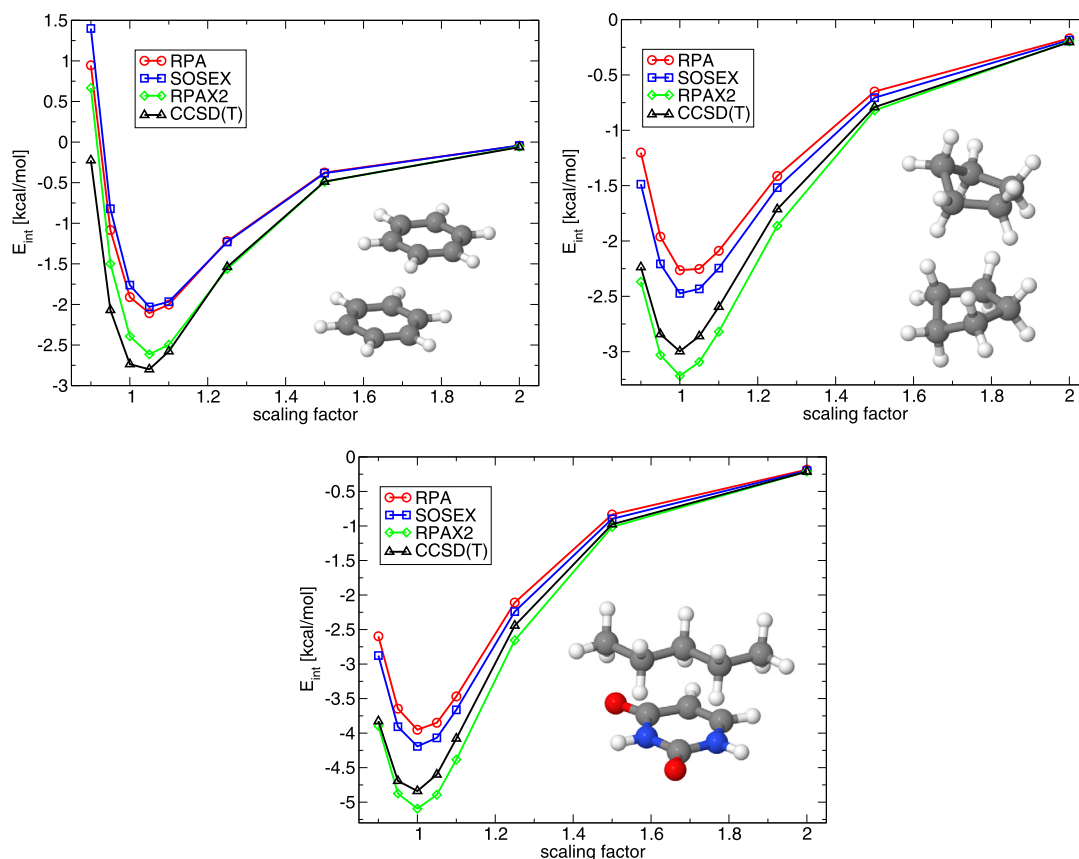


FIGURE 3.12 Interaction energy curves for two dimers from the hydrogen bonded group of complexes of the S66 $\times$ 8 database: (left) water dimer representing a system with a single O $\cdots$ H hydrogen bond; (right) acetic acid dimer representing a system with a cyclic hydrogen bond.

Eq. (3.54). The dimers in the S66 $\times$ 8 set are roughly categorized into 23 hydrogen bonded systems, 23 dispersion dominated systems and 20 “other” systems that contain mixed interactions, which cannot easily be assigned to one of the two former interaction types.

Fig. 3.12 shows the interaction energy curves for two dimers from the hydrogen bonded group of complexes from the S66 $\times$ 8 database obtained by the RPA, SOSEX, and RPAX2 method. The RPA and SOSEX methods here were used in conjunction with PBE reference states (i.e., the reference determinant was calculated using the PBE xc functional) while for RPAX2 the PBE exchange functional (PBEx) was used to determine the reference state. All of the interaction energies obtained by the various RPA functionals were extrapolated by the aVTZ $\rightarrow$ aVQZ two-point extrapolation scheme [126]. The black curves in the diagrams in Fig. 3.12 show the corresponding extrapolated CCSD(T) interaction energies from Hobza et al. [105] As one can see in the left diagram in the figure, the RPA method underestimates the water dimer interaction energy around the equilibrium region by almost 0.8 kcal/mol. This is corrected by the SOSEX method which only slightly underestimates the CCSD(T) interaction energy curve at the equilibrium distance. Another clear improvement over the SOSEX method is obtained with the RPAX2 approach, which yields an interaction energy curve that is fairly close to the CCSD(T) curve. This example again demonstrates the possibility of a systematic improvement of the RPA method by including higher-order exchange contributions. Similar improvements are observed in the different RPA methods for the acetic acid dimer, see the right-most diagram in Fig. 3.12. In this case, however, both the SOSEX and RPAX2 method underestimate the CCSD(T) reference interaction energies around the equilibrium by about  $-0.6$  kcal/mol.

Fig. 3.13 shows interaction energy curves for three different dispersion-dominated dimers for the various RPA methods. In the case of the stacked parallel displaced benzene dimer (top left), it can be seen that the minimum yielded by the CCSD(T) method is at a slightly larger intermonomer distance as compared to the MP2 structure, which is consistent with the overbinding conferred to these types of systems by the MP2 method. All three RPA methods



**FIGURE 3.13** Interaction energy curves for three dimers from the dispersion-dominated group of complexes of the S66 $\times$ 8 database: (top left) parallel displaced benzene dimer representing a  $\pi$ -stacked system; (top right) cyclopentane dimer representing a system with aliphatic dispersion interactions; (bottom) pentane–uracil dimer representing a system with  $\pi$ -aliphatic interactions.

produce minimum-energy structures that are consistent with those obtained by CCSD(T), indicating that they may be better suited than MP2 for determining the structures of dimer systems that are characterized by strong dispersion contributions. Compared to the hydrogen bonded systems, SOSEX does not clearly improve the RPA results. In contrast, the RPAX2 method provides a considerable improvement over both the RPA and the SOSEX method for all of the different interaction motifs represented by the three systems considered in Fig. 3.13. However, the deviations of the RPAX2 interaction energies from the reference values are not uniform for the different dimers. In case of the  $\pi$ -stacked benzene dimer the interaction energy is slightly underestimated as compared to the CCSD(T) values, while in case of the pure aliphatic and mixed  $\pi$ -aliphatic interaction types the interaction energy is slightly overestimated by the RPAX2 method.

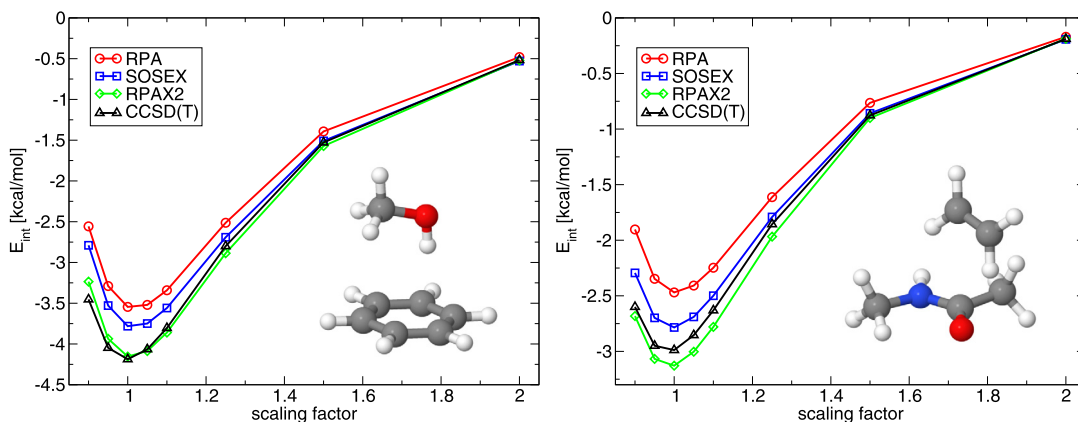
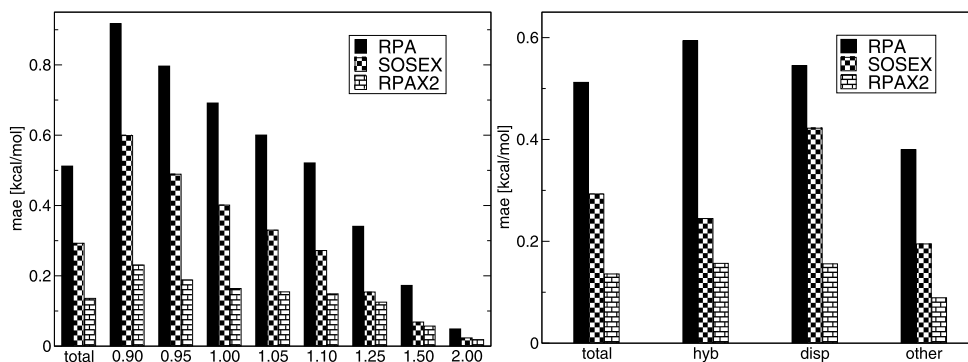


FIGURE 3.14 Interaction energy curves for two dimers from the mixed interaction group of complexes of the S66 $\times$ 8 database: (left) methanol–benzene dimer representing a system with OH $\cdots\pi$  interactions; (right) ethene–*N*-methylacetamide dimer which is characterized both by hydrogen bond and CH $\cdots\pi$  interactions.

Finally, Fig. 3.14 shows the interaction energy curves for two dimers in which the total interaction is characterized both by electrostatic interactions and dispersion interactions. The ratio of the dispersion energy over the electrostatic interaction energy (disp/elec) obtained by the DFT-SAPT method [159–162] amounts to 1.54 and 1.70 for the two types, respectively [105]. Dispersion interactions therefore dominate only slightly over the electrostatic interaction energy as compared to the three dimers considered in Fig. 3.13, for which the disp/elec ratios are larger than 3.4 [105]. For these dimers, it can be seen that the SOSEX interaction energy curves are closer to the reference curves than the RPA potentials, but still underestimate the CCSD(T) interaction energies by about 0.6 and 0.5 kcal/mol at the minimum geometries, respectively. The RPAX2 interaction energy curve for the methanol–benzene dimer is almost indistinguishable from the reference curve at all monomer distances, while in case of the ethene–methylacetamide dimer the RPAX2 potential is slightly too attractive compared to the reference.

Fig. 3.15 shows the mean absolute errors for the different RPA methods broken down by the monomer distance in the S66 $\times$ 8 set (left) and by the types of interactions (right). It can be seen that a systematic reduction of the error is obtained by including exchange interactions in the RPA functional in the order RPA $\rightarrow$ SOSEX $\rightarrow$ RPAX2. The RPAX2 method yields an average error of only 0.14 kcal/mol for all 528 systems of the database, see left brick-type bars in both diagrams in Fig. 3.15. This means that the error yielded by the RPAX2 method for the interaction energies from the S66 $\times$ 8 systems is almost within the estimated error range of the CCSD(T)/CBS values themselves. A comparison of the average errors for the different monomer distances shows that the RPAX2 interaction energies do not significantly deteriorate at shorter distances in comparison to the RPA and SOSEX methods. One can therefore expect that the RPAX2 method can also describe the repulsive part of intermolecular potentials with a very good accuracy. For larger monomer distances one can see that the errors of the RPAX2 and SOSEX method converge. This indicates that higher (than second-order) exchange contributions become less important for large distances. Intramonomer exchange



**FIGURE 3.15**  $S66\times 8$  data base: mean absolute errors of RPA, SOSEX, and RPAX2 interaction energies relative to extrapolated CCSD(T) values. In the left diagram the numbers on the abscissa refer to scaling factors for the intermolecular distance at the minimum [105]. In the right diagram the errors are broken down by the three different interaction types: hydrogen bonded interactions (hyb), dispersion interactions (disp), and other interaction types. Both diagrams show the total errors for all 528 systems for comparison.

interactions still significantly contribute to the total interaction energy at larger distances, which is evident by comparing the errors between the RPA method and the RPAX2 and SOSEX methods, see left diagram in Fig. 3.15.

The right diagram in Fig. 3.15 confirms the findings associated with the S22 benchmark (Section 3.5.1), namely that the SOSEX method improves the RPA method in both cases but yields an unbalanced description for hydrogen bonded and dispersion dominated systems. In comparison, the RPAX2 method not only yields significantly smaller errors for both interaction types, but the errors for these two cases are also almost identical and amount to about 0.16 kcal/mol. One can therefore conclude that the RPAX2 method is well suited for determining potential energy surfaces of heterogeneous dimer systems that can be stabilized both by electrostatic and dispersion interactions.

### 3.5.3 IDISP Benchmark

Long-range van der Waals interactions are important not only for the description of interaction energies between nonbonded molecules, but also for the determination of the structure of extended single molecules in which the internal interactions between their fragments may lead to a large number of different conformers. Schwabe and Grimme [106] have developed a small data base of 6 (originally 7 [106]) reactions of hydrocarbon molecules containing up to 24 carbon atoms. These comprise reactions involving the intramolecular interactions of  $\pi$ -systems, isomerization energies of branched versus unbranched alkane molecules, and conformational energy changes due to the folding of long alkane chain molecules [106] (see Fig. 3.16).

The reference reaction energies of the IDISP (intramolecular dispersion) database are shown in Table 3.6 and are partially derived from back-corrected experimental heats of formations (reactions 2 and 3) and partially calculated using different quantum chemistry methods, namely diffusion quantum Monte Carlo (DMC), QCISD(T) (quadratic configuration interac-



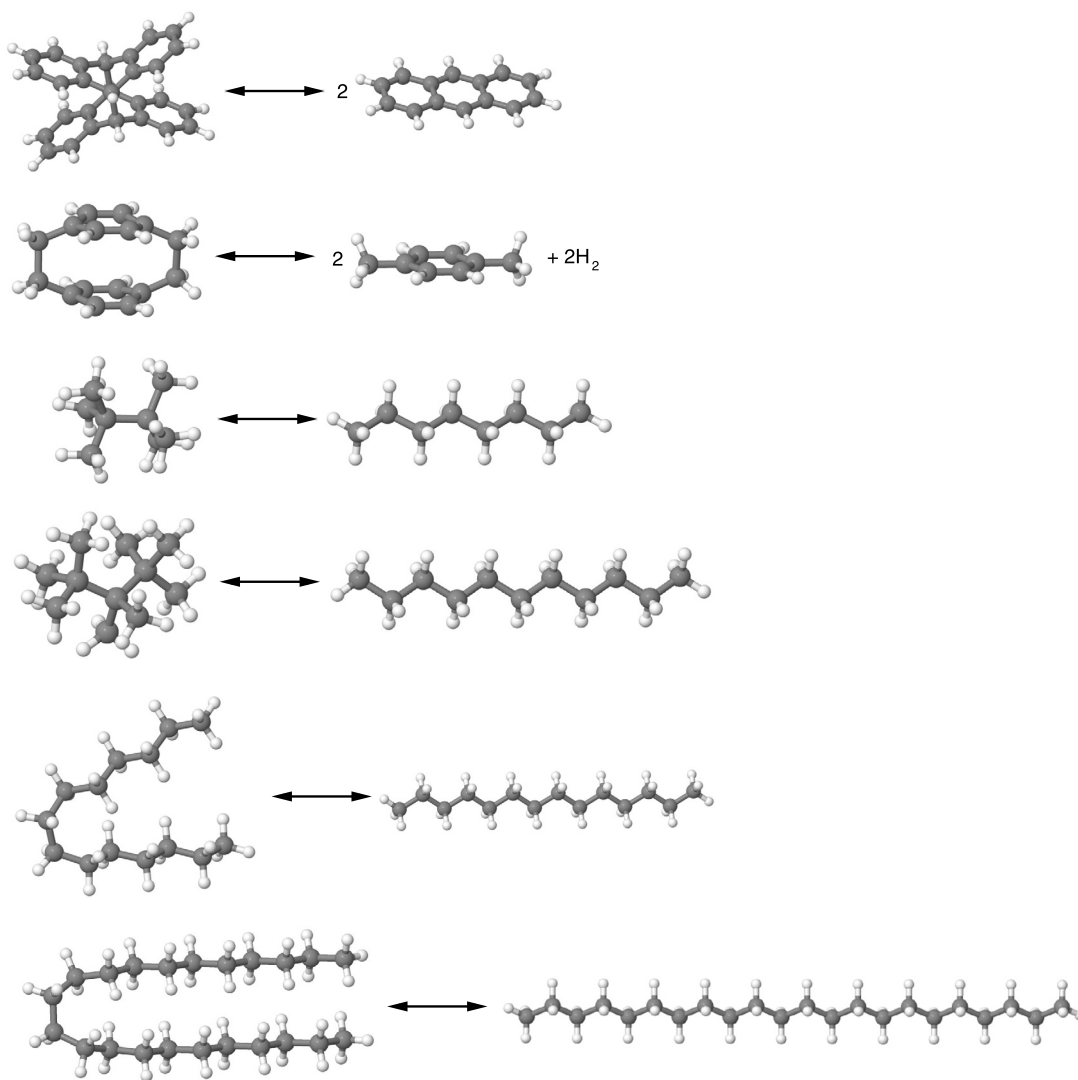


FIGURE 3.16 Reactions in the IDISP benchmark set [163,164].

tion singles doubles with perturbative triples), MP2, and MP2.5. The latter method involves an interpolation of the MP2 and MP3 correlation energy by adding the MP3 correlation energy scaled by a factor of one half to the MP2 correlation energy [165]. The rationale behind the MP2.5 approach is that often the third-order correlation energy contribution overcorrects the MP2 correlation energy compared to highly accurate correlation energies and it has been observed that a scaling by 0.5 of the third-order contributions leads to a much better description of, for example, intermolecular interactions than those obtained by the full MP3 method.

**TABLE 3.6** Reaction energies and conformation energies for the IDISP benchmark systems [106,163,164]. All energies, unless noted otherwise, are extrapolated using an aVTZ→aVQZ two-point extrapolation (kcal/mol). The reactions are listed in the order in which they appear in Fig. 3.16

Dimer	Refs. [106,163,164] <sup>a</sup>	RPA [71] <sup>b</sup> [PBE]	RPA [PBE]	SOSEX [PBE]	RPAX2 [PBEx]
Reaction 1	-9.0	-8.1	-8.11	-7.64	-6.19
Reaction 2	-58.5	-57.9	-57.16	-63.06	-60.27
Reaction 3	-1.9	-0.6	-0.88	-0.74	-1.52
Reaction 4	8.2	10.0	9.33	10.61	8.76
Reaction 5	-3.1	-3.9	-3.76	-4.09	-3.56
Reaction 6	0.4	-3.6	-3.16	-3.11	-0.95
MAE (total)		1.6	1.43	2.33	1.22

<sup>a</sup> Reaction 1, DMC and QCISD(T); Reaction 2, experimental heats-of-formation and PBE-D vibrational/thermal corrections; Reaction 3, derived from experimental heats-of-formation; Reaction 4, MP2.5/CBS estimate; Reactions 5 and 6, MP2/CBS.

<sup>b</sup> aVQZ→aV5Z extrapolation.

In case of the folding reactions of the C<sub>14</sub>H<sub>30</sub> and C<sub>22</sub>H<sub>46</sub> molecules, Schwabe et al. used the comparably cheap MP2 method because higher-level coupled cluster calculations are not feasible in this case.

Columns 3–6 in Table 3.6 show the reaction energies for the IDISP database calculated with the RPA, SOSEX, and RPAX2 method. In all cases the correlation energy contributions were extrapolated using an aVTZ→aVQZ two-point extrapolation. In the case of the RPA method, the third column of the table also displays the RPA values using an aVQZ→aV5Z extrapolation taken from Ref. [71]. As can be seen in the table, the more accurate aVQZ→aV5Z extrapolation has the largest effect on the isomerization energies of octane and undecane, leading to a change of +0.3 and +0.65 kcal/mol in favor of the branched isomer, respectively. This demonstrates that, in these particular cases, large basis sets are necessary to obtain well-converged results.

The average errors to the reference energies of the three RPA methods considered in Table 3.6 are quite similar and range between 1.2 and 2.3 kcal/mol. Notable differences among the various methods are found for the folding reaction of C<sub>22</sub>H<sub>46</sub> (reaction 6), for which MP2 predicts a small positive reaction energy (i.e., the folded conformer is stabilized relative to the unfolded conformer) while all RPA methods yield a negative reaction energy and favor the linear conformer. It cannot be ruled out here, however, that the reference value for this reaction, which has been obtained using the MP2 method (utilizing an aVTZ→aVQZ extrapolation [106]) are not more accurate than the RPA results presented in this work [71]. It is known that the MP2 method usually overestimates dispersion interactions in extended systems [166,167] and so it is likely that the reference value of 0.4 kcal/mol yielded by the MP2 method for this reaction is too large. However, it has been found in the present work that both the RPA and the SOSEX method tend to underestimate intermolecular interaction energies of systems which involve strong dispersion contributions (Tables 3.1 and 3.2). Thus it can be anticipated that the reaction energy for the folding reaction of C<sub>22</sub>H<sub>46</sub> of about -3.2 kcal/mol as predicted by the RPA and SOSEX method is too low. The reaction energy

of about  $-1.0$  kcal/mol yielded by the RPAX2 method is intermediate to the MP2 result and the RPA and SOSEX results and might therefore be a reasonable estimate.

### 3.6 RPA IN INTERMOLECULAR PERTURBATION THEORY

The two main quantum chemical approaches for determining intermolecular interaction energies are the supermolecular method and intermolecular perturbation theories. In the supermolecular approach, the interaction energy of a dimer  $AB$  is straightforwardly obtained by subtracting the monomer energies from the dimer energy:

$$E_{\text{int}} = E^{AB} - E^A - E^B. \quad (3.56)$$

Supermolecular calculations of the interaction energy can thus be performed using practically any quantum chemistry program. It should, however, be taken into account that the method used to compute the dimer and monomer energies must be size-consistent. Moreover, according to the Boys–Bernardi counterpoise correction [158], the monomer energies are usually calculated in the full dimer basis set in order to reduce the basis-set superposition error. Consequently, supermolecular methods have a less “black-box” character than might be implied by Eq. (3.56).

A completely different approach for calculating intermolecular interaction energies are intermolecular perturbation theory methods [168,169] (see also Chapters 1 and 2). In these methods, the interaction energy is determined by a perturbation theory expansion of the intermolecular interaction yielding, in each order, a number of terms which can be interpreted on a physical basis. The total interaction energy is then given directly by a sum of these terms and can generally be written as

$$E_{\text{int}} = E_{\text{elst}}^{(1)} + E_{\text{ind}}^{(2)} + E_{\text{disp}}^{(2)} + E_{\text{exch}}^{(1-2)} + \dots, \quad (3.57)$$

where  $E_{\text{elst}}^{(1)}$  denotes the electrostatic interaction energy,  $E_{\text{ind}}^{(2)}$  is the induction energy and  $E_{\text{disp}}^{(2)}$  is the dispersion energy. The corresponding order in the intermolecular interaction is given by the superscript added to each term in Eq. (3.57). The term  $E_{\text{exch}}^{(1-2)}$  comprises the so-called exchange contributions in first- and second-order and stems from a tunneling of the electrons from one monomer to the other. It should be noted that these terms can be defined differently in different intermolecular perturbation theories because they originate from a symmetry adaptation of the standard Rayleigh–Schrödinger expansion of the wavefunction [169]. The antisymmetry of the dimer wavefunction can be treated in various ways. Currently, a symmetrized Rayleigh–Schrödinger (SRS) expansion is generally used to take into account the antisymmetry of the total wavefunction with respect to exchanges of electrons among the monomers [169,170]. While this is only a weak symmetry forcing approach compared to more rigorous approaches like the Eisenschitz–London [171] or Jeziorski–Kolos methods [172], the SRS method to date is the only one that can be applied to systems with more than four electrons. Since the SRS symmetry adaptation is used in almost all applications using in-

termolecular perturbation theory, this method is commonly denoted by the more general acronym SAPT (symmetry-adapted perturbation theory).

An advantage of the SAPT method over the supermolecular approach is that each of the terms of Eq. (3.57) can be calculated using a different quantum chemistry method. They may also be written in terms of monomer properties only and so it is in principle not necessary to perform a calculation of the full dimer wavefunction for computing the interaction energy. Higher-order contributions not treated by the expansion in Eq. (3.57), however, are usually estimated using a supermolecular Hartree–Fock approach [173,174]. This correction is particularly important in cases where the monomers possess strong 0-rank (charge) or 1-rank (dipolar) multipole moments which can lead to significant high-order polarization contributions to the interaction energy.

The monomer properties defining the interaction energy contributions through a second-order expansion are:

- $E_{\text{elst}}^{(1)}$ , electron densities;
- $E_{\text{ind}}^{(2)}$ , static response functions;
- $E_{\text{disp}}^{(2)}$ , frequency-dependent response functions;
- $E_{\text{exch}}^{(1-2)}$ , density-matrix generalizations of the quantities given above.

The polarization terms in the above given list (i.e.,  $E_{\text{elst}}^{(1)}$ ,  $E_{\text{ind}}^{(2)}$  and  $E_{\text{disp}}^{(2)}$ ) can furthermore be expanded in multipole series for large intermolecular distances [169]. The interaction energy at large monomer distances could in principle be calculated exactly with the knowledge of the underlying quantities only (the exchange contributions vanish exponentially at large distances). These are:

- $E_{\text{elst}}^{(1)}$ , electric multipole moments of the monomers;
- $E_{\text{ind}}^{(2)}$ , static polarizabilities of monomer  $A/B$  and multipole moments of monomer  $B/A$ ;
- $E_{\text{disp}}^{(2)}$ , frequency-dependent polarizabilities of the monomers.

Section 3.6.1 continues with an analysis of the description of electric first- and second-order molecular properties yielded by the RPA method. In Section 3.6.2, the orbital-optimized RPA (ORP) method will be used in conjunction with the DFT-SAPT method for describing interaction energy contributions and total intermolecular interaction energies. The DFT-SAPT method is a variant of the SAPT method in which the intramolecular correlation contributions are calculated on the DFT level [159–162,175–179].

### 3.6.1 Molecular Properties

In his work “Forces in Molecules”, Feynman conjectured that “...*van der Waals’ forces can also be interpreted as arising from charge distributions with higher concentration between the nuclei. [...] It is [...] the attraction of each nucleus for the distorted charge distribution of its ‘own’ electrons that gives the attractive  $1/R^7$  force*” [180]. The conjecture was later proven by Hunt for the case of van der Waals interactions between molecular systems of arbitrary symmetries [181]. In the case of Kohn–Sham (KS) DFT methods, this description about the origin of van der Waals

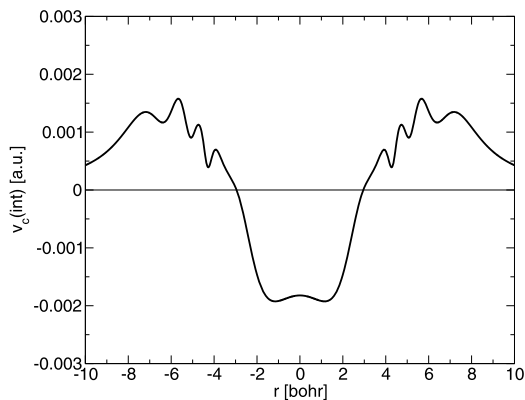


FIGURE 3.17 Interaction correlation potential of  $\text{He}_2$  calculated by the ORPA method. The potential is plotted along the He-He bond axis for  $R_{\text{He-He}} = 9.0$  bohr.

interactions, which differs from the common picture of fluctuating charge distributions, implies that the weak forces which cause the van der Waals interaction can also be calculated from the underlying KS xc, or more precisely KS correlation potential. Indeed, Allen and Tozer have proven numerically that the (practically) exact KS correlation potential for the helium dimer, in contrast to common correlation potentials from GGA functionals, describes a small, yet distinct depression between the atoms as compared to the sum of the monomer correlation potentials [182]. Correspondingly, the KS potential accumulates charge between the nuclei leading to a weak interaction even for the case of spherically symmetric atoms at a large separation. While this appears to be a classical description of van der Waals interactions, it should be noted that the origin of the modified shape of the potential, and thus the charge aggregation, originates from a quantum mechanical effect.

The question is now whether the decrease of the potential between two helium atoms at a large distance can also be observed for the ORPA correlation potential, i.e., whether the ORPA potential also contains the physics of van der Waals interactions as does the exact potential. Fig. 3.17 shows the interaction correlation potential, i.e.,

$$v_c^{\text{int}}(\text{He-He}) = v_c^{\text{ORPA}}(\text{He}_2) - 2v_c^{\text{ORPA}}(\text{He}), \quad (3.58)$$

for the helium dimer at a distance of  $R_{\text{He-He}} = 9.0$  bohr. While at this distance the atomic charges practically do not overlap, indeed one can observe a distinct negative bump in the interaction potential that is similar in shape to the KS interaction potential presented in Ref. [182], which was obtained from the BCCD(T) density using the Zhao-Morrison-Parr method [183,184]. Therefore, the RPA method describes both van der Waals interactions through the energy functional and through the underlying functional derivative.

As was described earlier in this section, intermolecular interactions can be described solely by monomer properties within the framework of intermolecular perturbation theories. Therefore, in the DFT-SAPT method one does not require knowledge of the xc functional but only knowledge of the xc potential (and higher functional derivatives) in order to compute the

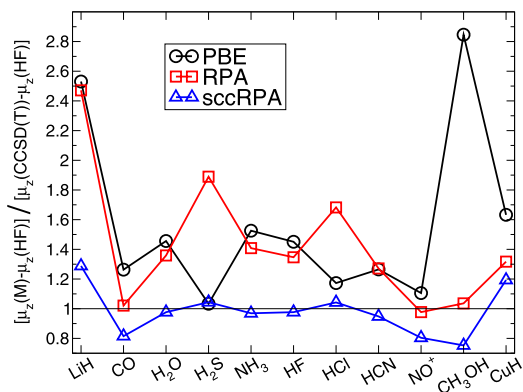


FIGURE 3.18 Molecular dipole moments: deviation of the correlation effect of various KS methods to the CCSD(T) correlation effect. The molecules were oriented according to a center of mass coordinate system (basis set, aug-cc-pVQZ).

individual interaction energy contributions. In this subsection, it will be investigated how accurate the RPA xc potential actually is for describing first- and second-order static and dynamic properties. A new method by which the direct RPA method can be improved regarding its description of molecular properties will also be introduced and tested.

Fig. 3.18 shows the deviations of correlation effects of the  $z$ -component of the dipole moment to accurate CCSD(T) values for a selection of small molecules yielded by the PBE xc functional and the ORPA functional. As can be seen, both the PBE and the ORPA functionals tend to overestimate the electron correlation effect on the dipole moment, in some cases even by more than 40%. A notable difference between PBE and ORPA can be observed for the methanol molecule, where PBE overshoots the correlation contribution by 180%, while the ORPA dipole moment agrees well with the CCSD(T) reference. Fig. 3.18 shows that the ORPA method on average does not yield more accurate dipole moments than a standard GGA-type functional.

It turns out that, in order to improve the ORPA xc potential, it is necessary to take into account electron exchange effects in the underlying correlation functional. Bleiziffer et al. developed an orbital-optimized EXX-RPA (OEXX-RPA) method that produced a potential for the neon atom that is closer to the exact KS correlation potential than the ORPA correlation potential [87]. Unfortunately, the computational expense associated with generating the OEXX-RPA correlation potential significantly exceeds the effort to compute just the corresponding ORPA correlation potential and it will not be further considered here. However, a simple empirical correction approach to the direct RPA functional and potential will be used in the following.

Recall that the exchange potential for a closed-shell two-electron system is identical to minus one half the Coulomb potential [185]:

$$v_x^{2\text{-el}}(\mathbf{r}) = -\frac{1}{2}v_J^{2\text{-el}}(\mathbf{r}), \quad (3.59)$$

so that the sum of the Coulomb and exchange kernel  $f_{\text{ux}}$  is given by [58,186]

$$f_{\text{ux}}^{2\text{-el}}(\mathbf{r}_1, \mathbf{r}_2) = \frac{1}{2r_{12}}, \quad (3.60)$$

that is, it corresponds to half the standard Coulomb kernel. An RPA method that is implemented within the ACFDT framework can thus simply be transformed into an RPA method that takes into account exchange effects exactly (like the EXX-RPA method) by scaling the Coulomb kernel with a prefactor of one half. Recall that the unphysical self-correlation contributions are corrected by this scaling of the kernel in the case of two-electron systems. Furthermore, the same holds true for the correlation potential in a corresponding ORPA method.

Based on these considerations, a simple (though inaccurate) self-correlation correction (scc) to the RPA functional and ORPA correlation potential is proposed by approximating the full Coulomb plus exchange kernel by a scaled Coulomb kernel:

$$f_{\text{ux}}^{\text{scc}}(\mathbf{r}_1, \mathbf{r}_2) \approx \kappa \frac{1}{r_{12}}. \quad (3.61)$$

While this equation holds true exactly for two-electron systems if  $\kappa = \frac{1}{2}$ , in systems with more than two electrons this would overcorrect the self-correlation error of the direct RPA method. A reasonable choice for the scaling factor of  $\kappa$  therefore would be to interpolate between  $\kappa = \frac{1}{2}$  and  $\kappa = 1$  (corresponding to the values yielding the EXX-RPA and the direct RPA methods for a two-electron system, respectively). In this work  $\kappa$  is set to  $\kappa = \frac{3}{4}$  to reduce the self-correlation error of the RPA. This correction will be referred to as sccRPA (self-correlation corrected RPA) in the following.

Fig. 3.18 shows that, with the sccRPA correction, the dipole moments for the small molecules considered in the figure improve considerably in almost all cases in comparison to the ORPA dipole moments. Mean absolute errors for the dipole moments and the quadrupole moments relative to accurate CCSD(T) reference values are shown in Fig. 3.19. Along with the RPA and sccRPA errors, the two diagrams in Fig. 3.19 also display the errors for Hartree-Fock (HF), MP2, CCSD, and the GGA and hybrid-GGA functionals PBE and PBE0. As one can see, both dipole and quadrupole moments predicted by the sccRPA method are as accurate as the corresponding results of the CCSD and the PBE0 method.

For the calculation of second-order response properties, knowledge of both the xc potential and the xc kernel is required. In the case of the ORPA method, this means that the correlation kernel would have to be calculated by taking the functional derivative of the ORPA correlation potential. This again would lead to a high computational cost compared to, for example, standard DFT response methods. It is known, however, that the accuracy of the xc kernel is comparably less important in DFT response methods than the xc potential [188]. This is confirmed in the top diagram of Fig. 3.20, which shows the mean absolute errors of the polarizabilities yielded by the RPA method relative to experimental polarizabilities for a selection of molecules using three different approximations: the uncoupled approximation (RPA/unc.) which corresponds to setting  $f_{\text{uxc}} = 0$ , the RPA xc potential used in conjunction with the RPA kernel (RPA/RPA,  $f_{\text{uxc}} = 1/r_{12}$ ) and the RPA xc potential used in conjunction with the Coulomb plus ALDA xc kernel (RPA/ALDA,  $f_{\text{uxc}} = 1/r_{12} + f_{\text{xc}}^{\text{ALDA}}$ ). One can

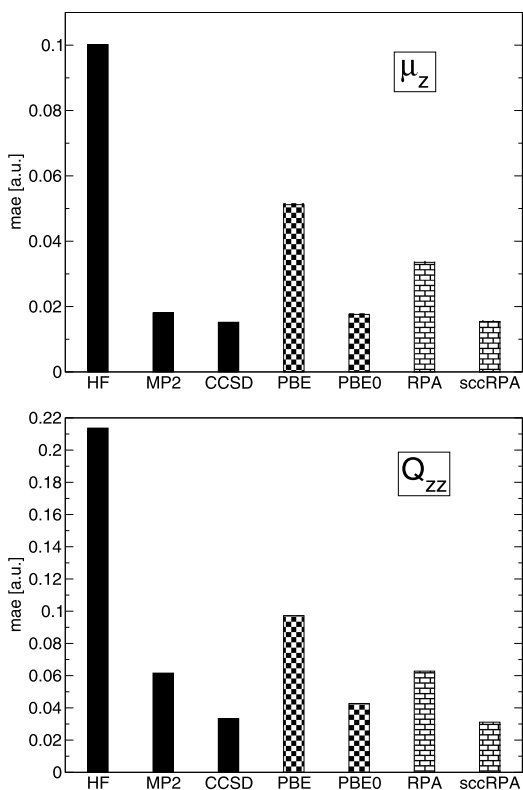


FIGURE 3.19 Mean absolute errors of the  $z$ -component of the dipole moment and the  $zz$ -component of the quadrupole moment using various methods for the molecules shown in Fig. 3.18. The CCSD(T) method was used as reference. The molecules were oriented according to a center of mass coordinate system (basis set, aug-cc-pVQZ).

see that the uncoupled approach is not very accurate since the experimental polarizabilities are significantly overestimated. A clear improvement is obtained by taking into account the Coulomb kernel in the response equations, but in this case the reference dipole polarizabilities are underestimated by about 10% on average. A further improvement is achieved by also taking into account xc contributions to the kernel using the ALDA xc kernel. Fig. 3.20 shows that the combined RPA/ALDA method is as accurate as DFT response methods using the PBE0 hybrid-GGA xc functional.

In order to investigate whether or not the RPA/ALDA polarizabilities are close to the exact RPA polarizabilities, i.e., the exact derivatives of the induced dipole moments with respect to the field strength, Table 3.7 compares the RPA/ALDA and exact RPA polarizabilities for a subset of the molecules in Fig. 3.20. The differences are obviously marginal for all molecules. This demonstrates that the ALDA xc kernel serves as a good approximation to the full ORPA xc kernel, which corresponds to the sum of the nonadiabatic and nonlocal exact exchange kernel, and the RPA correlation kernel in DFT response methods.



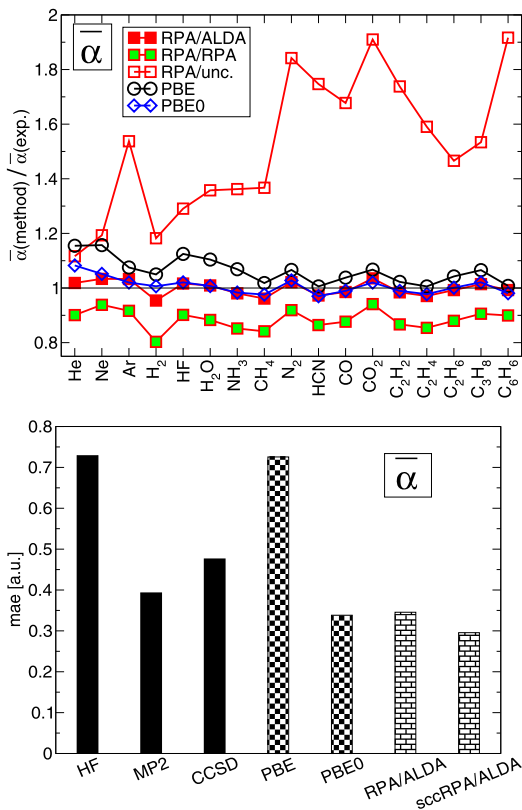


FIGURE 3.20 Average dipole–dipole polarizabilities: (top) deviation of the polarizabilities of various KS methods relative to experimental reference values (basis set, aug-cc-pVQZ); (bottom) mean absolute error of the polarizabilities of various KS methods relative to experimental reference values. The experimental polarizabilities were taken from Ref. [187].

The bottom diagram in Fig. 3.20 shows the mean absolute errors of the dipole polarizabilities relative to the experimental reference values for RPA/ALDA and a number of other methods. Here the results for the sccRPA method combined with the ALDA xc kernel (sccRPA/ALDA) are also included. In contrast to the significant improvements over the RPA method for first-order electric molecular properties (Fig. 3.19), the self-correlation correction only yields a small improvement over the direct RPA method.

Finally, Fig. 3.21 presents the errors in the leading-order isotropic  $C_6$  dispersion coefficients for the RPA method combined with the three different approximations to the response kernel, relative to accurate values derived from dipole-oscillator strength distribution results [189–191]. The isotropic  $C_6$  dispersion coefficients for two molecules  $A$  and  $B$  are defined as

$$C_6(AB) = -\frac{3}{\pi} \int_0^\infty d\omega \bar{\alpha}^A(i\omega) \bar{\alpha}^B(i\omega), \quad (3.62)$$

**TABLE 3.7** Average dipole polarizabilities (in a.u.) for a selection of small molecules computed using the ORPA xc potential and the ALDA xc kernel (RPA/ALDA), and using the exact RPA energy derivatives computed by the finite-field method

Molecule	RPA/ALDA	RPA (exact)
HF	5.68	5.71
H <sub>2</sub> O	9.67	9.74
NH <sub>3</sub>	14.19	14.22
C <sub>2</sub> H <sub>2</sub>	22.91	22.87
C <sub>3</sub> H <sub>8</sub>	39.89	39.71

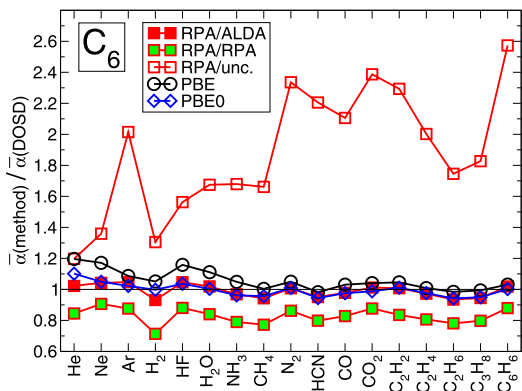


**FIGURE 3.21** Deviation of the calculated isotropic  $C_6$  dispersion coefficients using various KS methods (basis set, aug-cc-pVQZ) relative to accurate dipole oscillator strength distribution (DOSD) reference results from Refs. [189–191].

with  $\bar{\alpha}^A$  and  $\bar{\alpha}^B$  denoting the isotropic polarizabilities of the two molecules at the imaginary frequency of  $i\omega$ . The dynamic polarizabilities at imaginary frequencies monotonically decay to zero upon increase of  $\omega$  and can sometimes be estimated with knowledge of the static limit ( $\omega = 0$ ) alone [192]. Indeed, a comparison of the diagrams in Figs. 3.20 and 3.21 shows that the relative errors for the isotropic polarizabilities and the isotropic dispersion coefficients are very similar for the different methods. As in case of the dipole polarizabilities, the RPA/ALDA hybrid approach also gives a fairly good description of the  $C_6$  dispersion coefficients compared to the accurate DOSD reference values.

### 3.6.2 Symmetry-Adapted Perturbation Theory

In Section 3.6.1 it was shown that the RPA and in particular the sccRPA (Eq. (3.61)) method describes first- and second-order molecular properties fairly well. It can therefore be expected that first- and second-order intermolecular interaction energies (Eq. (3.57)) are also described with a reasonable accuracy by these RPA methods. In order to investigate this, a selection of 9 different dimers in 21 different structures were considered, see Fig. 3.22. The set of systems

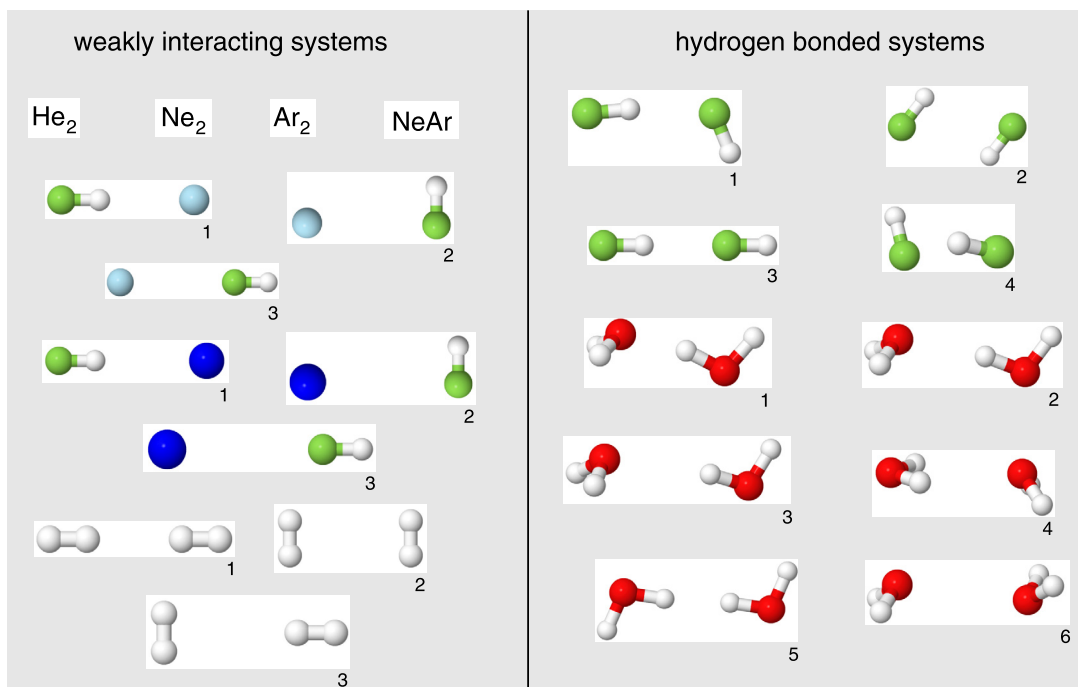


FIGURE 3.22 Dimer systems from Ref. [193]. The numeric labels displayed below the boxes correspond to the labels given in the reference and in Fig. 3.23 and Table 3.8.

comprises weakly interacting systems like rare gas dimers, rare gas atoms interacting with HF (hydrogen fluoride), the hydrogen molecule dimer, and strongly interacting hydrogen bonded systems, namely the HF dimer and the H<sub>2</sub>O dimer. The geometries are taken from Ref. [193]. The correlation contributions in this study were not extrapolated but have been estimated using the aug-cc-pVTZ basis set for the hydrogen bonded systems and using the aug-cc-pVQZ basis set for all other systems. Since the interaction energies of all methods considered in the following are affected to the same extent by the basis set truncation error, the basis sets used should enable a reasonable comparison of the different methods.

Fig. 3.23 shows the relative deviations for four different interaction energy contributions ( $E_{\text{elst}}^{(1)}$ ,  $E_{\text{exch}}^{(1)}$ ,  $E_{\text{ind}}^{(2)}$ , and  $E_{\text{disp}}^{(2)}$ ) yielded by the DFT-SAPT method using the functionals PBE0, PBE0AC, RPA and sccRPA relative to the many-body SAPT interaction energy contributions [194]. In the many-body SAPT (MB-SAPT) method, the energy terms are calculated using [195,196]:

- $E_{\text{elst}}^{(1)}$ , MP3<sub>resp</sub> (the subscript *resp* here means that the MP3 densities are calculated at the fully relaxed level);
- $E_{\text{exch}}^{(1)}$ , using a second-order expansion of the one- and two-particle density matrix employing CCSD amplitudes for the monomers;

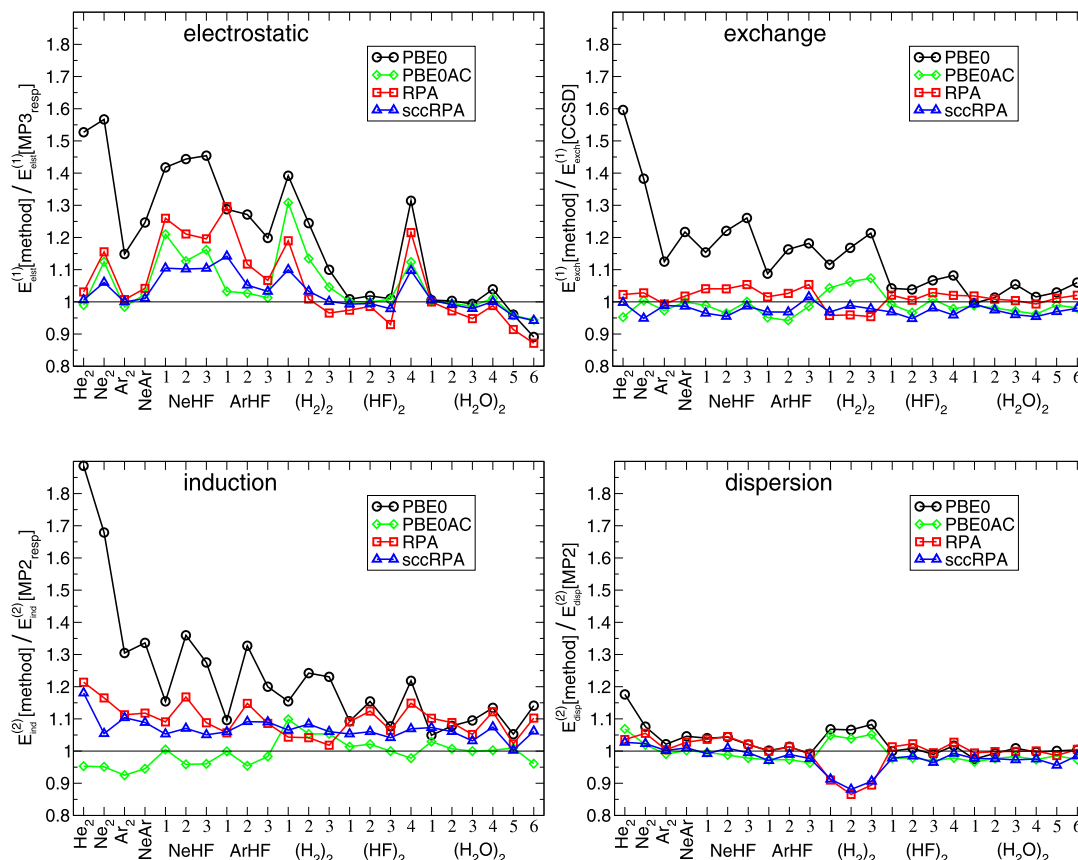


FIGURE 3.23 Intermolecular interaction energy contributions for a selection of 21 small dimer systems using various DFT-SAPT methods relative to many-body SAPT interaction energies: (top left) electrostatic; (top right) first-order exchange; (bottom left) second-order induction; (bottom right) second-order dispersion.

- $E_{\text{ind}}^{(2)}$ , MP2<sub>resp</sub>;
- $E_{\text{disp}}^{(2)}$ , MP2.

It should be noted that the methods given in this list are used to describe the *intramolecular* correlation effects. For example, the dispersion energy given by MB-SAPT actually takes into account quadruple excitations (double excitations on each monomer) and thus the dispersion energy calculated at the MP2 level should not be confused with the dispersion interaction energy described by the supermolecular MP2 method, which involves only single excitations on each monomer and therefore does not take into account intramolecular correlation.

In the PBE0AC DFT method, whose performance is shown along with the results for the standard PBE0 hybrid-GGA functional, the xc potential is asymptotically corrected to reproduce the exact  $-1/r$  behavior of the exact xc potential at large distances from the molecule [197,198]. Fig. 3.23 shows that the asymptotic correction of the xc potential is crucial

**TABLE 3.8** Total interaction energies (in kcal/mol) of many-body SAPT and DFT-SAPT employing different approximations to the xc potential (shown in square brackets) for the set of 21 small dimer systems in Fig. 3.22. The first column contains supermolecular CCSD(T) reference interaction energies

Dimer	Struct.	CCSD(T)	MB-SAPT	DFT-SAPT			
				[PBE0]	[PBE0AC]	[ORPA]	[sccRPA]
He <sub>2</sub>	5.5 a <sub>0</sub>	-0.018	-0.018	-0.008	-0.022	-0.018	-0.018
Ne <sub>2</sub>	6.0 a <sub>0</sub>	-0.067	-0.065	-0.051	-0.067	-0.070	-0.071
Ar <sub>2</sub>	7.0 a <sub>0</sub>	-0.225	-0.260	-0.207	-0.250	-0.257	-0.257
NeAr	6.5 a <sub>0</sub>	-0.102	-0.110	-0.078	-0.106	-0.110	-0.111
NeHF	1	-0.200	-0.193	-0.137	-0.184	-0.178	-0.190
	2	-0.060	-0.058	-0.026	-0.058	-0.057	-0.064
	3	-0.101	-0.106	-0.080	-0.099	-0.101	-0.103
ArHF	1	-0.457	-0.459	-0.415	-0.444	-0.442	-0.448
	2	-0.163	-0.174	-0.146	-0.166	-0.166	-0.168
	3	-0.187	-0.203	-0.177	-0.194	-0.188	-0.190
(H <sub>2</sub> ) <sub>2</sub>	1	0.998	0.847	1.023	0.866	0.824	0.862
	2	0.500	0.410	0.562	0.459	0.452	0.476
	3	-0.039	-0.082	-0.012	-0.063	-0.053	-0.051
(HF) <sub>2</sub>	1	-4.19	-4.27	-3.75	-3.98	-3.74	-4.11
	2	-3.28	-3.29	-2.94	-3.14	-2.98	-3.23
	3	-3.32	-3.56	-3.58	-3.35	-3.00	-3.33
	4	0.57	0.60	0.77	0.63	0.63	0.57
(H <sub>2</sub> O) <sub>2</sub>	1	0.95	-0.09	1.23	1.07	1.37	0.37
	2	-4.82	-4.98	-4.49	-4.66	-4.40	-4.75
	3	-3.53	-3.62	-3.45	-3.51	-3.34	-3.49
	4	-1.26	-1.39	-1.13	-1.27	-1.13	-1.34
	5	4.92	5.07	4.65	4.98	4.86	4.98
	6	2.63	2.60	2.78	2.67	2.60	2.62
MAE			0.10	0.13	0.05	0.12	0.05

for the description of all interaction energy contributions, see also Refs. [159,175–177] and the recent review by Jansen [162] for an explanation of this important detail that has to be taken into account in DFT-SAPT methods. Compared to this, both the RPA and sccRPA functionals describe first-order exchange interactions exactly and thus the underlying xc potential exhibits the correct Coulombic decay as the exact xc potential [197,199]. Fig. 3.23 shows that both the PBE0AC method and the two RPA methods accurately reproduce the reference interaction energy contributions. The largest errors are obtained for the electrostatic interaction energies of the weakly interacting systems NeHF and (H<sub>2</sub>)<sub>2</sub>, with deviations of 10 to 30% for the different methods. With the exception of the (H<sub>2</sub>)<sub>2</sub> dimer, an excellent agreement with the reference values is obtained for the dispersion energies (bottom right of Fig. 3.23).

Table 3.8 shows the total interaction energies for the different SAPT approaches compared to the CCSD(T) reference energies. The last line in the table shows the mean absolute errors.

It can be seen that all SAPT approaches yield total interaction energies that agree with the reference values. The only cases where some larger errors are found is the third T-shaped structure of the  $\text{H}_2$  dimer and the first structure of the water dimer. The latter corresponds to the minimum structure of  $(\text{H}_2\text{O})_2$ , but with a reduced distance between the two water molecules [200]. It should be noted that for very short monomer distances the SAPT method cannot be considered very accurate due to the fact that some exchange contributions are calculated within the so-called  $S^2$  approximation [195], and more generally because the standard SAPT method uses a weak symmetry forcing approach. It is remarkable, however, that all DFT-SAPT methods are more accurate than MB-SAPT for these systems and reproduce the correct sign of the interaction energy for the first structure of the water dimer. Since the repulsive exchange interaction energy contributions depend on density matrices of the monomers they can generally not be expected to be described well by DFT-SAPT methods even if the exact xc potentials were used to obtain the monomer orbitals. This holds true because the exact KS orbitals yield the exact density but not, in general, the exact  $n$ -particle density matrices [201].

A comparison between the different SAPT methods shows that the highest accuracy is obtained with the PBE0AC and sccRPA functionals. While the improvement of DFT-SAPT/PBE0AC over DFT-SAPT/PBE0 can be attributed to the asymptotic correction in the PBE0AC xc potential, the improvement of DFT-SAPT/sccRPA compared to DFT-SAPT/RPA may also originate from a more accurate description of the electron density in the core region (see Section 3.6.1). As an example, in most of the  $(\text{HF})_2$  and  $(\text{H}_2\text{O})_2$  dimer structures, DFT-SAPT/sccRPA clearly outperforms DFT-SAPT/RPA while for all other dimers both methods yield interaction energies that are very close. Since the total interaction in the  $(\text{HF})_2$  and  $(\text{H}_2\text{O})_2$  dimers is dominated by electrostatic interactions, the results for first-order properties (Section 3.6.1) can rationalize the differences found for the total interaction energies of DFT-SAPT obtained by the RPA and sccRPA xc potentials. For example, for the minimum-energy structure of the water dimer (structure 2) the DFT-SAPT/RPA method yields an electrostatic interaction energy which is 0.14 kcal/mol higher than the corresponding results of the DFT-SAPT/sccRPA method. In summary the results of Table 3.8 show that the DFT-SAPT method is systematically improvable by increasing the accuracy of the xc potentials for the monomers.

A comparison based on Table 3.8 of the DFT-SAPT method using the PBE0AC or sccRPA functionals shows that it outperforms MB-SAPT. This demonstrates that the DFT-SAPT method, depending on the choice of the underlying xc potential used, is not only a computationally inexpensive alternative to MB-SAPT, but can also describe total intermolecular interaction energies with a high accuracy.

### 3.7 $\sigma$ -STACKING VERSUS $\pi$ -STACKING INTERACTIONS

Until recently, stacking interactions between  $\sigma$  systems have been considered of secondary importance compared to the stacking interactions between  $\pi$  electronic systems. However, the strength of the interaction between  $\sigma$ -stacked cyclohexane molecules and  $\pi$ -stacked benzene molecules calculated with high level correlated quantum chemistry methods are almost equal in magnitude [202,203]. An interesting question is thus how both types of interactions

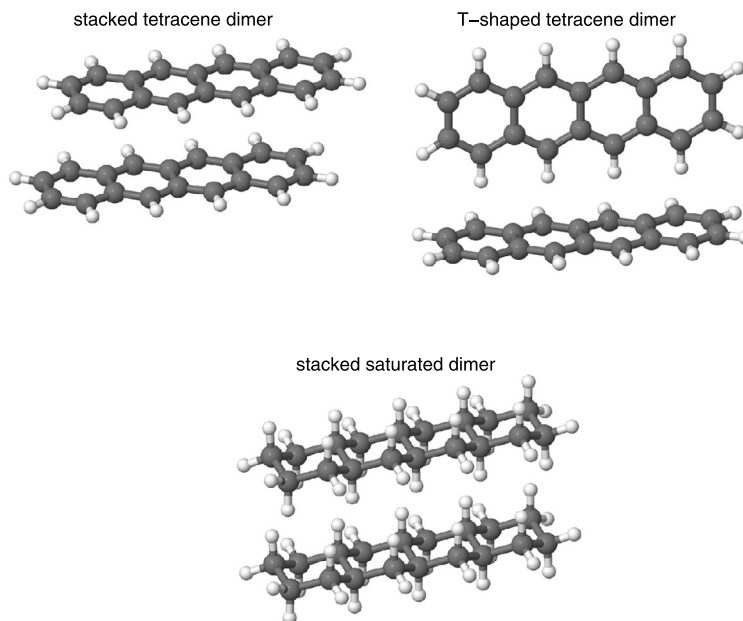
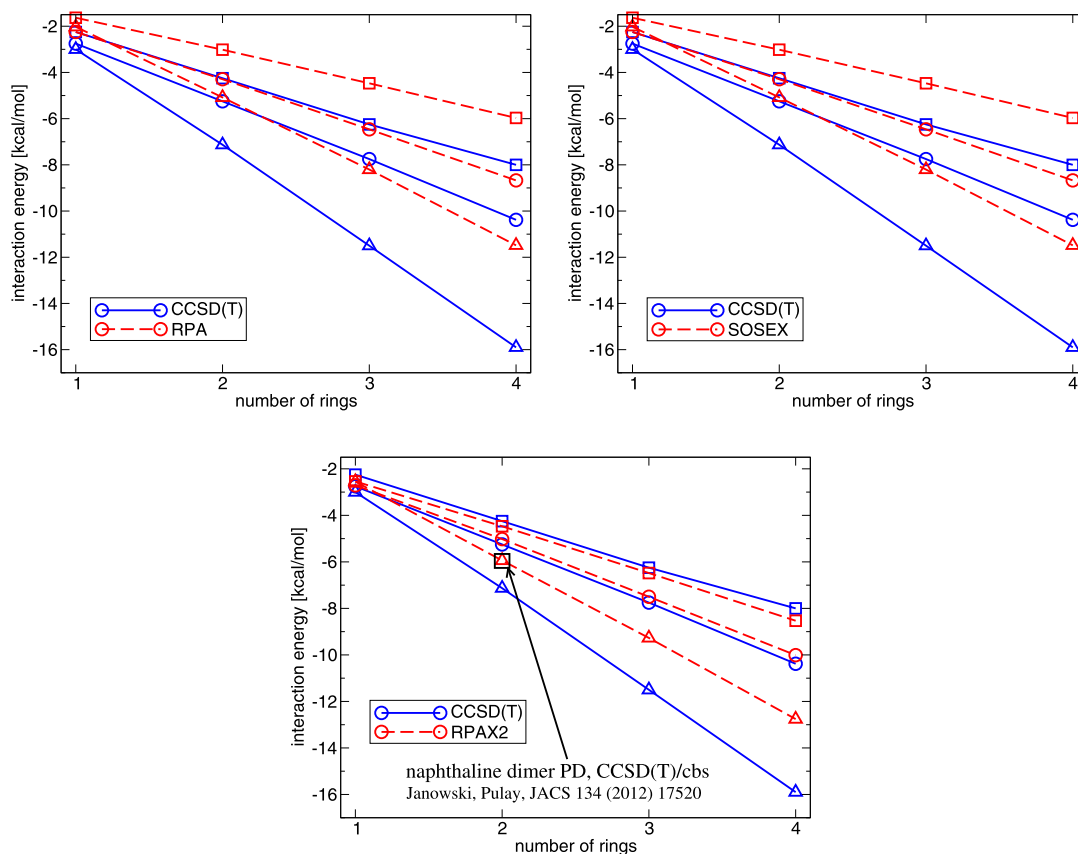


FIGURE 3.24  $\pi$ -stacked tetracene dimer (top left), T-shaped tetracene dimer (top right), and stacked octadecahydro-tetracene dimer (bottom).

relate to each other in extended molecular systems. More precisely, how do  $\sigma$ - and  $\pi$ -stacking interactions increase with the size of the system?

In order to answer this question, Grimme et al. considered the three structural types shown for the 4-ring structures in Fig. 3.24, namely stacked linear acene dimers, stacked linear perhydrogenated acene dimers and T-shaped acene dimers, each incrementally extended from one to four rings [202,203]. For the stacked acene dimers the interaction is dominated by the attractive dispersion interaction between the  $\pi$  systems while in the case of the saturated stacked dimers the  $\sigma$ - $\sigma$  stacking motif occurs. The T-shaped acene dimer systems can be considered as an intermediate between the  $\sigma$ - and  $\pi$ -stacking, and contains CH- $\pi$  interaction motifs. The geometries for these three structure types (12 systems in total) were optimized using dispersion-corrected DFT employing the TPSS functional [203].

In order to obtain estimates for the CCSD(T) interaction energies at the complete basis set limit, Grimme et al. used aVTZ $\rightarrow$ aVQZ extrapolated MP2 interaction energies corrected by the  $\Delta$ CCSD(T) term [202,203] (Eq. (3.54)) calculated at the VDZ level (VXZ will be used as abbreviation for the cc-pVXZ basis set in the rest of the chapter). Larger basis sets for the CCSD(T) correction for the largest systems considered here (with up to 276 electrons) were not technically possible. These restrictions do not apply to the RPA methods, where calculations using large aVQZ basis sets were performed. The RPA, SOSEX, and RPAX2 interaction energies were obtained from an aVTZ $\rightarrow$ aVQZ basis set extrapolation and can be assumed to be almost converged with respect to the basis set size. The interaction energies for the



**FIGURE 3.25** Interaction energies of acenes and corresponding saturated molecules, see Fig. 3.24, as a function of the number of rings for RPA (top left), SOSEX (top right) and RPAX2 (bottom). Circles, T-shaped dimers; squares, saturated dimers; triangles, stacked dimers. The CCSD(T) reference interaction energies (solid curves) are taken from Ref. [203]. The CCSD(T) reference interaction energy for the stacked naphthalene dimer (marked square in the bottom diagram) is taken from Ref. [204]

different RPA methods along with the CCSD(T) reference values by Grimme are shown in Fig. 3.25.

The figure shows that all methods predict a  $\pi$ -stacking > T-shaped > saturated stability order upon increasing the number of rings. This clearly demonstrates that in case of extended molecular structures  $\pi$ -stacking can indeed be considered as special in comparison to other interaction motifs. The question is, however, whether the relative importance of  $\pi$ -stacking is accurately quantified by the interaction energies in Fig. 3.25? For the 4-ring systems the CCSD(T) method yields an interaction energy for the  $\pi$ -stacked dimer which is almost twice as large as for the  $\sigma$ -stacked one. A similar relation between the two types for the 4-ring dimers is also obtained by RPA and SOSEX. However, both methods significantly under-



estimate the total magnitude of the CCSD(T) interaction energies. A much smaller ratio of the interaction energy of the tetracene dimer and perhydro-tetracene dimer of about 1.5 is found for the RPAX2 method, see bottom diagram in Fig. 3.25. Thus, RPAX2 still favors the  $\pi$ -stacking interaction with increasing system size but to a lesser extent than predicted by CCSD(T).

A direct comparison between the RPAX2 and CCSD(T) interaction energies (bottom diagram in Fig. 3.25) shows a good agreement for the saturated and the T-shaped dimers of all sizes. In contrast, the CCSD(T) interaction energies increase much more quickly than the RPAX2 interaction energies with respect to the number of rings for the stacked polyacenes. The question is whether this difference originates from missing correlation effects in the RPAX2 method which are described by the CCSD(T) method, or whether it stems from a basis set incompleteness of the  $\Delta$ CCSD(T) scheme used by Grimme? There is some evidence that the latter is true. Marshall et al. studied the accuracy of the  $\Delta$ CCSD(T) correction for a number of benchmark data bases, including the S22 systems [156] (see also Section 3.5). They showed that the omission of diffuse functions for the correction can lead to an underestimation of this term by about 8% on average for the dispersion dominated structures of the S22 systems [156]. For the hydrogen bridged and mixed type systems errors of only 3% and 2% were found [156]. As an example, for the stacked benzene dimer the  $\Delta$ CCSD(T) correction deviates by almost 19% from the corresponding aVDZ result when calculated with the VDZ basis set, while for the T-shaped benzene dimer an error of only 4% was found [156]. If an augmented aVDZ basis set is used for the correction, the error reduces to 2.9% for the former and to 1.0% for the latter. This shows that the CCSD(T)/CBS estimates by Grimme for the acene dimers are likely not very accurate, in particular for the  $\pi$ -stacked systems.

This conclusion is also supported by a study of Janowski and Pulay which also analyzes the role of  $\pi$ -stacking interactions in comparison to  $\sigma$ -stacking for a number of systems [204]. In their work, the  $\Delta$ CCSD(T) correction was calculated for the  $\pi$ -stacked naphthalene dimer using a half-augmented aVDZ basis set, i.e., diffuse functions were set on every second carbon atom of naphthalene. While the structures for the naphthalene dimers of Refs. [203,204] are certainly different, the structures in the work of Janowski and Pulay have been optimized at the CCSD(T) level using the half-augmented basis set and thus can be regarded as being fairly close to true minimum-energy gas-phase structures. The estimated CCSD(T) interaction energy for the naphthalene dimer from the work of Janowski and Pulay has been added to the bottom diagram in Fig. 3.25 (marked square). It can be observed that it is significantly lower in magnitude than the CCSD(T)/CBS estimate by Grimme. In fact, the estimated CCSD(T)/CBS interaction energy from Janowski et al. agrees well with the RPAX2 result. This suggests that the rise in the interaction energy for the  $\pi$ -stacked acene systems with an increasing number of rings is well described by the RPAX2 method.

In summary, the RPA methods favor  $\pi$ -stacking interactions over  $\sigma$ -stacking interactions with an increasing system size, in line with higher-level coupled-cluster calculations. The RPA and SOSEX interaction energies underestimate the CCSD(T) reference interaction energies for larger ring numbers in the considered systems, while the RPAX2 interaction energies appear to be in a good agreement with CCSD(T)/CBS values. To obtain accurate estimates for the latter, however, diffuse functions should be used for the  $\Delta$ CCSD(T) correction [156].

## 3.8 INTERACTION ENERGIES FOR LARGE ORGANIC COMPLEXES

### 3.8.1 S12L Benchmark Database: Introduction

The increasing efficiency of computer hardware and the development of improved computational algorithms has allowed the calculation of intermolecular interaction energies for systems containing  $\sim 1000$  electrons using quantum chemistry methods. This, however, only applies to methods that possess a moderate scaling behavior with respect to the molecular size, such as MP2 ( $\mathcal{N}^5$ ) or RPA ( $\mathcal{N}^4$ ), as well as a number of RPA variants described in Section 3.4, which can be implemented with  $\mathcal{N}^{4-5}$  scaling algorithms. The CCSD(T) method, which is the method of choice for providing reference-level intermolecular interaction energies, is not feasible for systems with more than about 50 nonhydrogen atoms, at least not if used in conjunction with reasonably large basis sets.

Grimme et al. [205,206] developed the S12L benchmark database composed of six large molecular hosts, each containing two different guest molecules, giving 12 supermolecular complexes. They circumvented the need for calculating CCSD(T)/CBS reference interaction energies for the S12L set by back-correcting experimentally measured free energies for the effects of solvent and thermal effects to yield intermolecular interaction energies. The complexes of the S12L set are shown in Fig. 3.26.

The S12L database contains two tweezer complexes with tetracyanoquinone and 1,4-dicyanobenzene (**2a,b**), two pincer complexes of organic  $\pi$  systems (**3a,b**),  $C_{60}$  and  $C_{70}$  complexed by a bulky catcher molecule (**4a,b**), an amide macrocycle binding benzoquinone and glycine anhydride (**5a,b**), cucurbit[6]uril cation complexes of  $BuNH_4$  and  $PrNH_4$  (**6a,b**) and two cucurbit[7]uril inclusion complexes with dicationic and neutral ferrocene derivatives (**7a,b**).

The free energy of association in solution  $\Delta G_a$  for these complexes relates to the gas-phase interaction energy  $\Delta E_{\text{bind}}$  in the following way:

$$\Delta G_a = \Delta E_{\text{bind}} + \Delta G_{\text{vib}}^T + \Delta \delta G_{\text{solv}}^T(X), \quad (3.63)$$

where  $\Delta G_{\text{vib}}^T$  is the vibrational contribution to the free enthalpy and  $\Delta \delta G_{\text{solv}}^T(X)$  is the free energy of solvation. Eq. (3.63) implies that by a knowledge of the last two contributions, the binding energy  $\Delta E_{\text{bind}}$  could be directly obtained from experimental  $\Delta G_a$  values. Thus Eq. (3.63) yields a possible route to obtaining reference interaction energies for large complexes for which high-level wavefunction methods are not feasible.

The accuracy of this method, however, critically depends on the accuracy of the terms  $\Delta G_{\text{vib}}^T$  and  $\Delta \delta G_{\text{solv}}^T(X)$ . Grimme has applied the rigid-rotor-harmonic-oscillator (RRHO) approximation including the zero-point vibrational energy for each species in the gas phase for the former and the COSMO-RS continuum solvation model [207,208] for the latter quantity [205]. While the vibrational frequencies can principally be calculated with standard DFT methods even for such large systems, the calculation of the vibrational spectrum in order to obtain thermodynamic properties is cumbersome for large systems, and Grimme opted to use the semiempirical SCC-DFTB [209] and PM6 [210] methods to approximate the  $\Delta G_{\text{vib}}^T$  values (finding deviations in  $\Delta G_{\text{vib}}^T$  between these two methods of up to 3 kcal/mol for complex 6b).

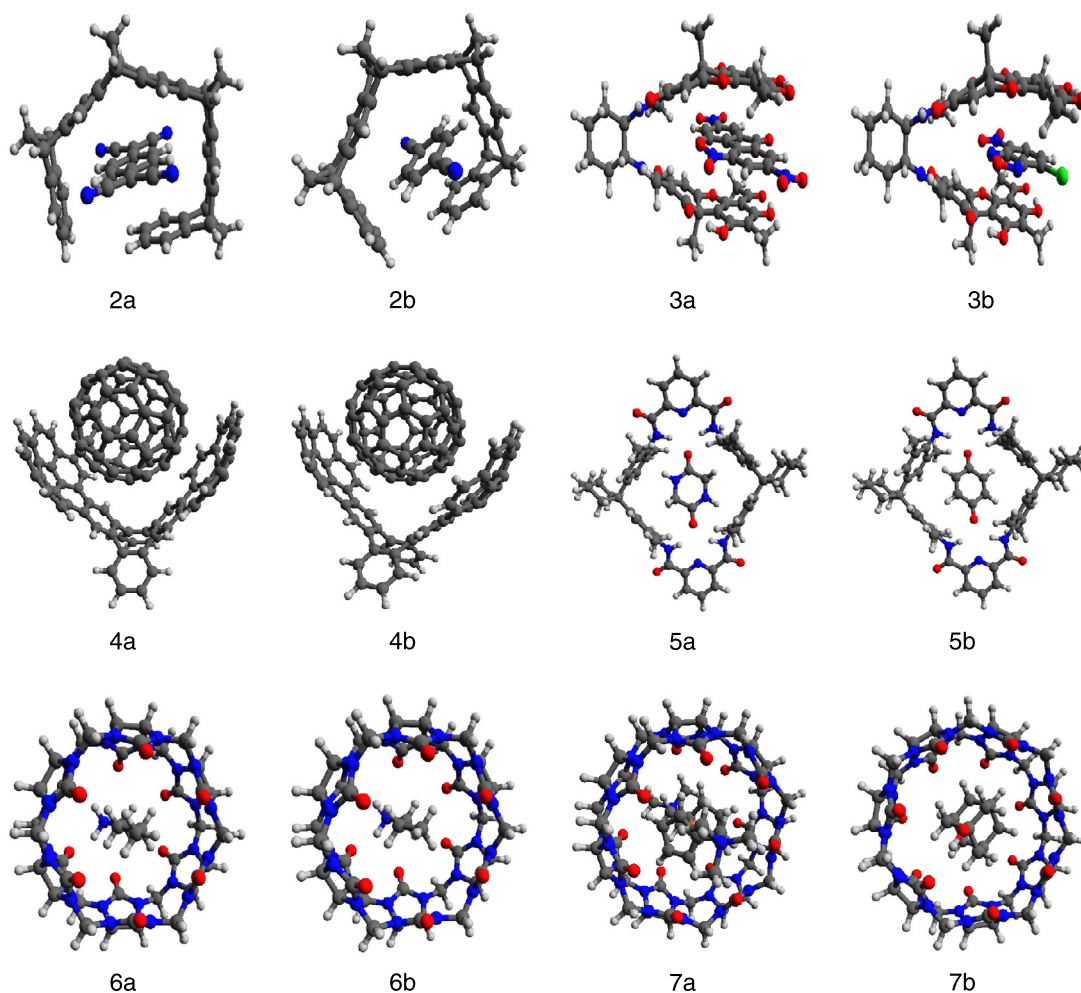


FIGURE 3.26 Supramolecular complexes in the S12L database [205,206].

The BP86 [139,140] standard GGA DFT functional was used for the single-point energy computations to estimate the electrostatic solute-solvent interaction energy. It was estimated that this approach will give an error of 0.5 to 1 kcal/mol in the solvation energies for neutral systems [205].

### 3.8.2 Basis Set Extrapolation Scheme for Large Systems

It is well known that intermolecular interaction energies strongly depend on the presence of diffuse functions in the basis sets employed (Section 3.7). They are particularly important for converging the dispersion interaction contribution to the intermolecular correlation inter-

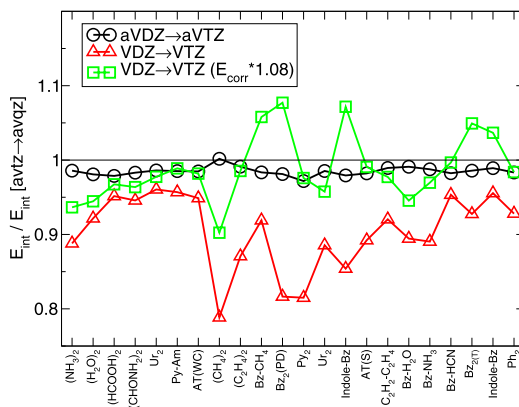


FIGURE 3.27 Deviation of the interaction energies calculated using several basis set extrapolation schemes compared to the aVTZ→aVQZ extrapolated results for the S22 dimer systems. The RPAX2 method has been used.

action energy. A neglect of diffuse functions can lead to an underestimation of 20% or more in dispersion dominated dimers [211]. However, in large molecules, diffuse basis functions become almost linearly dependent and this hampers the convergence of self-consistent field (SCF) calculations. In Ref. [211], an approach for correcting interaction energies obtained by utilizing basis sets without diffuse functions through a two-point VDZ→VTZ extrapolation was described. While this approach was used in conjunction with the DFT-SAPT method in Ref. [211], it will be used here for the extrapolations of RPA interaction energies.

Fig. 3.27 compares several basis set extrapolation schemes against the aVTZ→aVQZ extrapolated RPAX2 interaction energies for the S22 dimer systems. The corresponding aVDZ→aVTZ extrapolated energies (circles) slightly underestimate the aVTZ→aVQZ results by 1–2%, indicating that the aVTZ→aVQZ interaction energies are fairly close to the complete basis set limit. In contrast, the VDZ→VTZ extrapolation using nonaugmented basis sets (triangles) leads to an underestimation of up to 20% of the interaction energies, in particular for the dispersion dominated systems. Thus it is clear that VDZ→VTZ extrapolations are not sufficient for reducing the basis set error in the prediction of intermolecular interaction energies.

It was found in case of a DFT-SAPT interaction energy decomposition that all first-order contributions and the second-order induction and exchange-induction interaction energies deviate by less than about 5% from the CBS limit when using the VDZ→VTZ extrapolation [211]. Only the dispersion and exchange-dispersion contributions (i.e., the intermolecular correlation contributions) are strongly affected by the neglect of diffuse functions in the basis set. Using this fact, the sum of the extrapolated dispersion and exchange-dispersion energies was scaled by a factor that was obtained by a fit to the CBS results for the S22 dimers [211]. The same approach will be applied here, but now scaling the “complete” correlation energy contribution:

$$E_{\text{int}}^{\text{CBS}} \approx E_{\text{int}}^{\text{VTZ}}(\text{Ref}) + \alpha E_{\text{int}}^{\text{VDZ} \rightarrow \text{VTZ}}(\text{corr}), \quad (3.64)$$

where VDZ→VTZ is a short-hand notation for the cc-pVDZ→cc-pVTZ two-point basis set extrapolation [126] and  $E_{\text{int}}(\text{Ref})$  and  $E_{\text{int}}(\text{corr})$  denote the interaction energy of the reference determinant and the correlation contribution to the interaction energy, respectively.

The scaling parameter  $\alpha$  was fitted to the CBS results for the interaction energies of the S22 systems. Interestingly, the optimal value of  $\alpha = 1.08$  obtained in this way for the extrapolation of the RPAX2 interaction energies is identical to the optimum for the scaling parameter in a corresponding DFT-SAPT analysis [211]. The deviations of the RPAX2 interaction energies obtained by the corrected extrapolation scheme of Eq. (3.64) to the aVTZ→aVQZ (practically CBS) results are shown in Fig. 3.27 (squares). As can be seen in the figure, in almost all cases the interaction energies obtained by the modified extrapolation approach of Eq. (3.64) deviate by no more than  $\pm 5\%$  from the CBS energies. Larger deviations are observed only for  $(\text{CH}_4)_2$  ( $-10\%$ ), benzene- $\text{CH}_4$  ( $+6\%$ ), benzene<sub>2</sub>(PD) ( $+8\%$ ) and indole-benzene(stacked) ( $+7\%$ ). All these systems belong to the group of dispersion dominated complexes. One therefore should be aware of the possibility that the use of the correction scheme of Eq. (3.64) for extrapolating RPA interaction energies can overshoot the basis set error stemming from the neglect of diffuse functions.

### 3.8.3 S12L Benchmark Database: Binding Energies

In order to calculate the total binding energies of large dimer complexes, it has to be taken into account that they contain, in addition to the interaction energy, the deformation energies associated with the changes in the geometry upon the complex formation of the two monomers  $A$  and  $B$  relative to their isolated gas-phase structures:

$$\Delta E_{\text{bind}} = E_{\text{int}}(AB) + E_{\text{deform}}(A) + E_{\text{deform}}(B). \quad (3.65)$$

In small systems the structural changes due to the complexation are usually small and the deformation energy  $E_{\text{deform}} = E_{\text{deform}}(A) + E_{\text{deform}}(B)$  can be neglected. However, in large complexes like those from the S12L database, the deformation energy can be a substantial positive (i.e., repulsive) contribution to the binding energy.

In Fig. 3.28 the total deformation energies for the S12L complexes calculated with MP2, spin-component scaled MP2 (SCS-MP2) [212], and the RPA methods RPA, SOSEX and RPAX2 are shown. As can be seen, the deformation energy can become quite large. This is in particular observed for the pincer complex (C3a,b), where the strongest contribution to the deformation energy likely originates from the attractive  $\pi$ - $\pi$  interaction between the pincer arms in the monomer structure excluding the guest molecules. Except for the pincer complexes, all methods yield deformation energies which are fairly close to each other. This indicates that the  $E_{\text{deform}}$  values are not strongly dependent on the level of electron correlation employed, except for the pincer complexes for which the MP2 deformation energies are almost 8 kcal/mol larger than with the other methods. The reason for this can be understood by the known fact that the MP2 method strongly overestimates long-range dispersion interaction energies because it does not take into account intrasystem correlation contributions (that is, it describes long-range correlation interactions at the uncoupled level) [166,213,214].

The total binding energies of the S12L dimer systems were calculated with the direct RPA method as well as the exchange RPA methods SOSEX (Eq. (3.25)) and RPAX2 (Eq. (3.27)). In

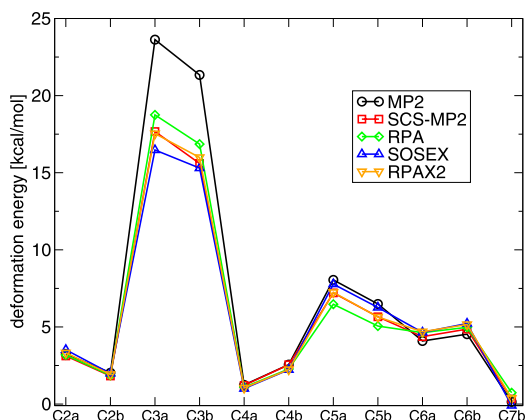


FIGURE 3.28 Deformation energies for the complexes of the S12L database calculated with MP2, SCS-MP2 and various RPA methods (the VDZ→VTZ basis set extrapolation was used).

TABLE 3.9 Binding energies (in kcal/mol) of the complexes from the S12L benchmark set using various RPA methods. A standard VDZ→VTZ two-point extrapolation was used to estimate the basis set limit. The first column in the table contains the empirical reference energies from Ref. [205]

Dimer	Empir. [205]	RPA [PBE]	SOSEX [PBE]	RPAX2 [PBE]	RPAX2 [PBEx]
C2a	-29.9	-24.8	-27.9	-28.0	-29.1
C2b	-20.5	-16.0	-17.4	-17.9	-18.7
C3a	-24.3	-11.4	-15.9	-15.7	-17.2
C3b	-20.4	-9.3	-13.2	-12.9	-13.8
C4a	-27.5	-29.7	-29.9	-31.9	-32.1
C4b	-28.7	-30.3	-30.5	-32.6	-32.8
C5a	-34.8	-29.7	-33.6	-33.1	-35.1
C5b	-21.3	-16.9	-20.2	-19.9	-21.6
C6a	-77.4	-80.5	-84.5	-83.7	-86.1
C6b	-77.0	-77.7	-81.1	-80.4	-82.3
C7b	-22.6	-22.9	-25.4	-25.7	-28.6
MAE		4.6	3.7	4.1	4.2

all cases the PBE xc potential was used to compute the reference determinant. In the case of RPAX2, the PBEx (PBE exchange) potential was also used in order to highlight the influence of the orbitals on the interaction energies. In case of the C7a complex the iterative RPA amplitude update failed to converge. This complex will therefore be omitted in the following analysis.

Table 3.9 shows the binding energies for the different RPA methods obtained by the standard VDZ→VTZ basis set extrapolation, i.e., without using the correction method of Eq. (3.64). The binding energies therefore likely underestimate the true CBS results of  $E_{\text{bind}}$

**TABLE 3.10** Binding energies (in kcal/mol) of the S12L complexes using various RPA methods. The modified (VDZ→VTZ)×1.08 basis set extrapolation approach was used to estimate the basis set limit. The first column contains the empirical reference energies [205] and the second column, where available, the DQMC interaction energies of Ambrosetti et al. [215] along with the statistical sampling uncertainties given in parenthesis. The third and fourth column contain the DFT-SAPT and MP2C interaction energies [211] for comparison

Dimer	Empir. [205]	DQMC [215]	DFT-SAPT [211]	MP2C [211]	RPA [PBE]	SOSEX [PBE]	RPAX2 [PBE]	RPAX2 [PBEx]
C2a	-29.9	-27.2 (0.3)	-32.0	-33.6	-28.1	-31.5	-31.6	-32.7
C2b	-20.5	-17.2 (1.0)	-21.0	-23.1	-18.4	-20.0	-20.5	-21.4
C3a	-24.3		-18.7	-23.2	-16.1	-20.8	-20.6	-22.1
C3b	-20.4		-15.9	-17.3	-12.4	-16.5	-16.2	-17.1
C4a	-27.5	-25.8 (1.5)	-36.0	-41.5	-35.0	-35.1	-37.4	-37.7
C4b	-28.7		-37.1	-42.3	-35.9	-36.1	-38.4	-38.9
C5a	-34.8	-33.4 (1.0)	-33.8	-37.2	-32.1	-36.4	-35.8	-37.7
C5b	-21.3		-23.1	-25.2	-19.3	-22.9	-22.5	-24.2
C6a	-77.4	-81.0 (1.6)	-82.6	-85.2	-82.2	-86.5	-85.7	-87.9
C6b	-77.0		-79.1	-81.5	-79.0	-82.7	-81.9	-83.8
C7b	-22.6	-24.1 (1.8)	-27.0	-28.2	-25.9	-28.6	-29.0	-31.7
MAE			4.0	5.7	4.5	4.4	4.6	5.6

(see also Fig. 3.27). The first column in the table shows the empirical reference values by Grimme obtained using the combined experimental plus semiempirical approach described above. The mean absolute errors of the RPA binding energies for the different RPA methods are 4–4.5 kcal/mol, see last line in Table 3.9. The largest deviations from the reference values are found for the pincer complexes (C3a,b) for which both RPA and exchange-RPA methods predict binding energies that are underestimated by 50% and 30%, respectively. For all other complexes the agreement between the binding energies from the RPA methods and the empirical results is fairly good on average. One can observe that the  $E_{\text{bind}}$  values from all exchange RPA methods are slightly more attractive than the direct RPA values. A comparison of the RPAX2 results using the PBE orbitals and the PBEx orbitals shows that the latter are again somewhat more attractive than the former.

Note, however, that the binding energies shown in Table 3.9 can be expected to be too small compared to the true CBS results. Table 3.10 shows the RPA binding energies obtained by the modified extrapolation method of Eq. (3.64) which can be expected to be closer to the true CBS results on average. Also shown in the table are the diffusion quantum Monte Carlo (DQMC) estimates by Ambrosetti et al. [215] as well as the MP2 coupled (MP2C) [167,216] and DFT-SAPT interaction energies [211]. It can be seen that the mean absolute errors for the different RPA methods are not significantly different from the MAEs for the standard VDZ→VTZ extrapolation, and are of the order of 4.5 to 5.5 kcal/mol. The application of Eq. (3.64) yields errors for the binding energies which are significantly smaller in case of the pincer complexes (C3a,b). However, the  $E_{\text{bind}}$  energies for the bucky catcher complexes (C4a,b) are much larger in magnitude compared to the uncorrected values and deviate from the reference energies by up to -10 kcal/mol, irrespective of the type of the RPA method. Since the C4a and C4b com-

plexes are strongly dominated by dispersion interactions [211], and due to the behavior of the corrected extrapolation method (Fig. 3.27), it cannot be ruled out that the binding energies of the RPA methods for the bucky catcher systems are too high. It can, however, be stated with some degree of certainty that the RPA binding energies of Table 3.9, which are already larger in magnitude than the reference values, are underestimating the true CBS values. Accordingly, even if the VDZ $\rightarrow$ VTZ( $\times 1.08$ ) extrapolation overcorrects the basis set error due to the neglect of diffuse functions in this case, both direct RPA as well as SOSEX and RPAX2 will significantly overestimate the binding energies for the (C4a,b) systems at the CBS limit. Relatively large overestimations of about 5 to 9 kcal/mol of the RPA values to the reference binding energies can also be observed for the charged complex C6a and the complex C7b.

The DQMC results from Ambrosetti et al. presented in the second column in Table 3.10 are, where available, quite close to the empirical estimates by Grimme and therefore the above relations between the RPA results and the empirical energies hold true, too, if the DQMC binding energies are taken as reference. The only notable exception to this is the (C6a) complex where the DQMC energy is larger by 3.6 kcal/mol than the corresponding empirical value. In this case, the DQMC binding energy is in a quite good agreement with the direct RPA binding energy of  $-82$  kcal/mol. A fairly good agreement is observed between the RPA, SOSEX and RPAX2 energies and the DFT-SAPT and MP2C energies. The DFT-SAPT and MP2C values were obtained by practically the same extrapolation approach, applied, however, only to the (exchange-)dispersion contribution to the interaction energy. This strongly implies that the level of electron correlation, which is different for all methods of Table 3.10, appears to be sufficient for the description of the binding energies in these large complexes.

---

### 3.9 SUMMARY

---

This work summarized the recent progress of Kohn–Sham RPA correlation methods for describing intermolecular interaction energies. Since the RPA method itself was developed by Bohm and Pines for describing the collective motion of electrons in the homogeneous electron gas at high density [28–31], it is surprising that this method can also be used with some success for molecular systems in which the electrons are much more weakly coupled. It is, however, not so much the description of short-range electron–electron interactions which manifests the advance of the RPA method in the molecular world, but its ability to describe long-range electron correlation interactions with a fairly good accuracy. A range of new computational algorithms that reduce the computational cost to less than that of a standard second-order perturbation theory calculation [63–65] may lead to a further increase in the popularity of the RPA method. Compared to standard DFT correlation functionals, however, the RPA correlation energy depends strongly on the basis set size [55,71,77,127,141] and thus the basis set error of finite-basis set RPA methods needs to be properly corrected in practical calculations [71,77,127].

In this work also a number of recently developed extensions to the RPA which improve the performance of the RPA method for molecular and bulk systems (Section 3.4) have been presented. It has been observed that the inclusion of additional exchange interactions in second and higher orders in a perturbation theory expansion of the correlation energy (Section 3.4.1)



allow for a systematic improvement of the RPA method for the description of intermolecular interactions. This was shown for a number of benchmark sets in Section 3.5 as well as for extended van der Waals complexes in Sections 3.7 and 3.8. This shows that KS-RPA correlation methods can be systematically improved in contrast to standard density functional theory methods that are based on the generalized gradient approximation. As was demonstrated in Section 3.1, this property can be very useful for estimating the correlation contribution to intermolecular interaction energies. Due to the advantageous relation between the high accuracy and moderate computational cost of the RPA and some of its extensions, it can therefore be expected that KS-RPA methods will evolve as a new standard for the accurate description of intermolecular interactions of extended systems for which high-level coupled cluster methods are not feasible.

## List of Acronyms

- AC** Adiabatic connection  
**ACFDT** Adiabatic-connection fluctuation dissipation theorem  
**ALDA** Adiabatic local density approximation  
**aVXZ** ( $X = D, T, Q, 5, \dots$ ) Augmented correlation-consistent valence double/triple/quadruple/pentuple... basis set with polarization functions and additional diffuse functions (aug-cc-pVXZ) by Dunning et al. [17–20]  
**AXK** Adiabatic exchange kernel [86]  
**BCCD(T)** Brueckner coupled-cluster singles doubles with perturbative triples  
**BP86** Becke exchange and Perdew correlation functional [139,140]  
**CCD** Coupled-cluster doubles  
**CCSD** Coupled-cluster singles doubles  
**CCSD(T)** Coupled-cluster singles doubles with perturbative triples  
**CPU** Central processing unit  
 **$\Delta$ CCSD(T)** Incremental CCSD(T) correlation correction to lower-level correlation methods (Refs. [155,156] and Eq. (3.54))  
**DFT** Density-functional theory  
**DFT-SAPT** (Intermolecular) symmetry-adapted perturbation theory including intramolecular correlation corrections from static and time-dependent DFT monomer properties [160–162]  
**DOSD** Dipole-oscillator strength distribution  
**DQMC** Diffusion quantum Monte-Carlo  
**EXX** Exact-exchange (usually in the context of DFT to denote the exact-exchange DFT functional)  
**EXX-RPA** Random-phase approximation with exchange [83]  
**drCCD** Direct ring coupled-cluster doubles  
**FCI** Full configuration interaction  
**FDT** Fluctuation-dissipation theorem [136]  
**GGA** Generalized-gradient approximation (to the exchange-correlation density functional)  
**HF** Hartree-Fock  
**IDISP** Benchmark database by Grimme et al. for studying intramolecular dispersion effects [106]  
**KS** Kohn-Sham  
**LCCD** Linearized coupled-cluster doubles  
**LDA** Local density approximation  
**lr** Long-range  
**MB-SAPT** Many-body symmetry-adapted perturbation theory [169,195]  
**MP2** Second-order Møller-Plesset perturbation theory  
**MP3** Third-order Møller-Plesset perturbation theory  
**OEP** Optimized-effective potential method [150,151]  
**ORPA** Orbital optimized random-phase approximation [65,152,153]  
**PBE** Perdew-Burke-Ernzerhof exchange-correlation functional [56]

**PBEx** Perdew–Burke–Ernzerhof exchange functional [56]  
**PBE0** Hybrid Perdew–Burke–Ernzerhof exchange–correlation functional [217]  
**PBE0AC** Hybrid Perdew–Burke–Ernzerhof exchange–correlation functional with asymptotic correction [175]  
**ph-RPA** Particle–hole random-phase approximation  
**pp-RPA** Particle–particle random-phase approximation [142]  
**rALDA** Renormalized adiabatic local density approximation  
**RPA** Random-phase approximation  
**RPA+SE** Random-phase approximation augmented with singles excitations [100]  
**RPA+rSE** Random-phase approximation augmented with renormalized singles excitations [100]  
**RPA-SO1** Random-phase approximation with exchange according to the first method proposed by Szabo and Ostlund [44]  
**RPA-SO2** Random-phase approximation with exchange according to the second method proposed by Szabo and Ostlund [44]  
**RPax** Random-phase approximation with exchange [89]  
**RPAX2** Random-phase approximation with exchange [64]  
**RS-DFT** Range-separated density-functional theory  
**RSH** Range-separated hybrid (DFT functional)  
**S12L** Benchmark database by Grimme containing 12 supramolecular complexes [205,206]  
**S22** Benchmark database by Hobza et al. containing 22 different dimer systems [104]  
**S66x8** Benchmark database by Hobza et al. containing 528 dimer systems [105]  
**SAPT** (Intermolecular) symmetry-adapted perturbation theory [169,194]  
**scc** Self-correlation correction (Section 3.6.1)  
**sr** Short-range  
**SOSEX** Second-order screened exchange random-phase approximation correlation method [81]  
**TDA** Tamm–Dancoff approximation (Eq. (3.13))  
**VXZ** ( $X = D, T, Q, 5, \dots$ ) Correlation-consistent valence double/triple/quadruple/pentuple... basis set with polarization functions (cc-pVXZ) by Dunning et al. [17–20]  
**WC** Watson–Crick (structure of the adenine–thymine base pair)  
**xc** Exchange–correlation

## Acknowledgments

Financial support of this work through the DFG (Deutsche Forschungsgemeinschaft) priority program SPP1807 (“Control of London dispersion interactions in molecular chemistry”) is gratefully acknowledged. I would like to thank Julien Toulouse, Henk Eshuis, Patrick Bleiziffer, and Xinguo Ren for useful hints and for providing me with reference interaction energies for their different RPA methods.

I dedicate this work to my colleague and good friend Janos Angyan who unexpectedly died recently at the age of 60. Janos has shown me the grace of faith and the beauty of science. I am in his debt forever.

## References

- [1] E. Schrödinger, *Ann. Phys.* 79 (1926) 361.
- [2] M. Born, W. Heisenberg, P. Jordan, *Z. Phys.* 35 (1926) 557.
- [3] Here and in the following, for the sake of describing the different quantum chemistry methods, it is assumed that electrons follow certain paths or that they can be associated with certain positions. This disregards the uncertainty principle for quantum particles and is thus not completely correct.
- [4] D.R. Hartree, *Proc. Camb. Philos. Soc.* 24 (1928) 89.
- [5] S.M. Blinder, *Am. J. Phys.* 33 (1965) 431.
- [6] V. Fock, *Z. Phys.* 61 (1930) 126.
- [7] J.C. Slater, *Phys. Rev.* 32 (1928) 339.
- [8] J.C. Slater, *Phys. Rev.* 34 (1929) 1293.
- [9] J.C. Slater, *Phys. Rev.* 35 (1930) 210.

- [10] A. Szabo, N.S. Ostlund, *Modern Quantum Chemistry*, Dover Press, 1996.
- [11] E.J. Baerends, O.V. Gritsenko, *J. Phys. Chem. A* 101 (1997) 5383.
- [12] F.E. Harris, H.J. Monkhorst, D.L. Freeman, *Algebraic and Diagrammatic Methods in Many-Fermion Theory*, Oxford University Press, 1992.
- [13] T. Korona, H.L. Williams, R. Bukowski, B. Jeziorski, K. Szalewicz, *J. Chem. Phys.* 106 (1997) 5109.
- [14] I. Shavitt, R.J. Bartlett, *Many-Body Methods in Chemistry and Physics: MBPT and Coupled-Cluster Theory*, Cambridge University Press, 2009.
- [15] I. Lindgren, *Atomic Many-Body Theory*, Springer, 1986.
- [16] T. van Mourik, T.H. Dunning Jr., *J. Chem. Phys.* 111 (1999) 9248.
- [17] T.H. Dunning, *J. Chem. Phys.* 90 (1989) 1007.
- [18] R.A. Kendall, T.H. Dunning Jr., R.J. Harrison, *J. Chem. Phys.* 96 (1992) 6796.
- [19] D. Woon, T.H. Dunning Jr., *J. Chem. Phys.* 98 (1993) 1358.
- [20] D. Woon, T.H. Dunning Jr., *J. Chem. Phys.* 100 (1994) 2975.
- [21] T. Kato, *Commun. Pure Appl. Math.* 10 (1957) 151.
- [22] W. Klopper, *R12 Methods, Gaussian Geminals. Modern Methods and Algorithms of Quantum Chemistry*, John von Neumann Institute for Computing, Jülich, 2000.
- [23] T. Korona, D. Kats, M. Schütz, T.B. Adler, Y. Liu, H.-J. Werner, in: *Challenges and Advances in Computational Chemistry and Physics*, vol. 13, Springer, 2011, p. 345.
- [24] L. Kong, F.A. Bischoff, E.F. Valeev, *Chem. Rev.* 112 (2012) 75.
- [25] A.D. Becke, *J. Chem. Phys.* 140 (2014) 18A301.
- [26] S. Grimme, A. Hansen, J.G. Brandenburg, C. Bannwarth, *Chem. Rev.* 116 (2016) 5105.
- [27] E.R. Johnson, I.D. Mackie, G.A. DiLabio, *J. Phys. Org. Chem.* 22 (2009) 1127.
- [28] D. Bohm, D. Pines, *Phys. Rev.* 82 (1951) 625.
- [29] D. Pines, D. Bohm, *Phys. Rev.* 85 (1952) 338.
- [30] D. Bohm, D. Pines, *Phys. Rev.* 92 (1953) 609.
- [31] D. Pines, *Phys. Rev.* 92 (1953) 626.
- [32] D. Pines, P. Nozieres, *The Theory of Quantum Liquids*, vol. I: Normal Fermi Liquids, W.A. Benjamin, New York, Amsterdam, 1966.
- [33] C.J. Powell, J.B. Swan, *Phys. Rev.* 115 (1959) 869.
- [34] R.D. Mattuck, *A Guide to Feynman Diagrams in the Many-Body Problem*, Dover Press, 1992.
- [35] E.P. Wigner, *Phys. Rev.* 46 (1934) 1002.
- [36] J. Hubbard, *Proc. R. Soc. Lond. A* 240 (1957) 539.
- [37] J. Hubbard, *Proc. R. Soc. Lond. A* 243 (1958) 336.
- [38] P. Nozieres, D. Pines, *Nuovo Cimento* 9 (1958) 470.
- [39] P. Nozieres, D. Pines, *Phys. Rev.* 109 (1958) 762.
- [40] H. Ehrenreich, M.H. Cohen, *Phys. Rev.* 115 (1959) 786.
- [41] M.A. Ball, A.D. MacLachlan, *Mol. Phys.* 7 (1964) 501.
- [42] A.D. MacLachlan, M.A. Ball, *Rev. Mod. Phys.* 36 (1964) 844.
- [43] A.D. MacLachlan, R.D. Gregory, M.A. Ball, *Mol. Phys.* 7 (1964) 119.
- [44] A. Szabo, N.S. Ostlund, *J. Chem. Phys.* 67 (1977) 4351.
- [45] A. Szabo, N.S. Ostlund, *Int. J. Quant. Chem.* S11 (1977) 389.
- [46] J. Oddershede, *Adv. Quantum Chem.* 11 (1978) 275.
- [47] G. Chambaud, B. Levy, P. Millie, *Theor. Chim. Acta* 48 (1978) 103.
- [48] H. Weiss, R. Ahlrichs, M. Häser, *J. Chem. Phys.* 99 (1993) 1262.
- [49] G.D. Purvis, R.J. Bartlett, *J. Chem. Phys.* 76 (1982) 1910.
- [50] R.J. Bartlett, N. Musial, *Rev. Mod. Phys.* 79 (2007) 291.
- [51] J.M. Pitarke, A.G. Eguiluz, *Phys. Rev. B* 57 (1998) 6329.
- [52] J.F. Dobson, J. Wang, *Phys. Rev. Lett.* 82 (1999) 2123.
- [53] S. Kurth, J.P. Perdew, *Phys. Rev. B* 59 (1999) 10461.
- [54] Z. Yan, J.P. Perdew, S. Kurth, *Phys. Rev. B* 61 (2000) 430.
- [55] F. Furche, *Phys. Rev. B* 64 (2001) 195120.
- [56] J.P. Perdew, K. Burke, M. Ernzerhof, *Phys. Rev. Lett.* 77 (1996) 3865.
- [57] M. Fuchs, Y.-M. Niquet, X. Gonze, K. Burke, *J. Chem. Phys.* 122 (2005) 094116.
- [58] A. Heßelmann, A. Görling, *Phys. Rev. Lett.* 106 (2011) 093001.

- [59] D.C. Langreth, J.P. Perdew, *Solid State Commun.* 17 (1975) 1425.
- [60] D.C. Langreth, J.P. Perdew, *Phys. Rev. B* 15 (1977) 2884.
- [61] A. Heßelmann, in: *Density Functionals: Thermochemistry*, in: Springer Series in Topics in Current Chemistry, Springer, Heidelberg, 2014.
- [62] F. Furche, *J. Chem. Phys.* 129 (2008) 114105.
- [63] H. Eshuis, J. Yarkony, F. Furche, *J. Chem. Phys.* 132 (2010) 234114.
- [64] A. Heßelmann, *Phys. Rev. A* 85 (2012) 012517.
- [65] P. Bleiziffer, A. Heßelmann, A. Görling, *J. Chem. Phys.* 139 (2013) 084113.
- [66] M. Kallay, *J. Chem. Phys.* 142 (2015) 204105.
- [67] H.-V. Nguyen, S. de Gironcoli, *Phys. Rev. B* 79 (2009) 205114.
- [68] X. Ren, P. Rinke, C. Joas, M. Scheffler, *J. Mater. Sci.* 47 (2012) 7447.
- [69] D. Rocca, *J. Chem. Phys.* 140 (2014) 18A501.
- [70] H. Eshuis, F. Furche, *J. Phys. Chem. Lett.* 2 (2011) 983.
- [71] H. Eshuis, F. Furche, *J. Chem. Phys.* 136 (2012) 084105.
- [72] A.E. Kerdawy, J.S. Murray, P. Politzer, P. Bleiziffer, A. Heßelmann, A. Görling, T. Clark, *J. Chem. Theory Comput.* 9 (2013) 2264.
- [73] J. Harl, G. Kresse, *Phys. Rev. B* 77 (2008) 045136.
- [74] J. Harl, G. Kresse, *Phys. Rev. Lett.* 103 (2009) 056401.
- [75] D. Lu, D.Y.L. Rocca, G. Galli, *Phys. Rev. Lett.* 102 (2009) 206411.
- [76] X. Ren, P. Rinke, M. Scheffler, *Phys. Rev. B* 80 (2009) 045402.
- [77] J. Harl, L. Schimka, G. Kresse, *Phys. Rev. B* 81 (2010) 115126.
- [78] S. Lebegue, J. Harl, T. Gould, J.G. Angyan, G. Kresse, J.F. Dobson, *Phys. Rev. Lett.* 105 (2010) 196401.
- [79] H.-V. Nguyen, G. Galli, *J. Chem. Phys.* 132 (2010) 044109.
- [80] Y. Li, D. Lu, H.-V. Nguyen, G. Galli, *J. Phys. Chem. A* 114 (2010) 1944.
- [81] A. Grüneis, M. Marsman, J. Harl, L. Schimka, G. Kresse, *J. Chem. Phys.* 131 (2009) 154115.
- [82] J. Paier, B.G. Janesko, T.M. Henderson, G.E. Scuseria, A. Grüneis, G. Kresse, *J. Chem. Phys.* 132 (2010) 094103, Erratum: *J. Chem. Phys.* 133 (2010) 179902.
- [83] A. Heßelmann, A. Görling, *Mol. Phys.* 108 (2010) 359.
- [84] A. Heßelmann, A. Görling, *Mol. Phys.* 109 (2011) 2473.
- [85] P. Bleiziffer, A. Heßelmann, A. Görling, *J. Chem. Phys.* 136 (2012) 134102.
- [86] J.E. Bates, F. Furche, *J. Chem. Phys.* 139 (2013) 171103.
- [87] P. Bleiziffer, M. Krug, A. Görling, *J. Chem. Phys.* 142 (2015) 244108.
- [88] F. Furche, T. Van Voorhis, *J. Chem. Phys.* 122 (2005) 164106.
- [89] J. Toulouse, I.C. Gerber, G. Jansen, A. Savin, J.G. Angyan, *Phys. Rev. Lett.* 102 (2009) 096404.
- [90] B.G. Janesko, T.M. Henderson, G.E. Scuseria, *J. Phys. Chem.* 130 (2009) 081105.
- [91] B.G. Janesko, G.E. Scuseria, *J. Chem. Phys.* 131 (2009) 154106.
- [92] X. Ren, A. Tkatchenko, P. Rinke, M. Scheffler, *Phys. Rev. Lett.* 106 (2011) 153003.
- [93] M. Hellgreen, U. von Barth, *J. Chem. Phys.* 132 (2010) 044101.
- [94] W. Zhu, J. Toulouse, A. Savin, J.G. Angyan, *J. Chem. Phys.* 132 (2010) 244108.
- [95] T.M. Henderson, G.E. Scuseria, *Mol. Phys.* 108 (2010) 2511.
- [96] J. Toulouse, W. Zhu, A. Savin, G. Jansen, J.G. Angyan, *J. Chem. Phys.* 135 (2011) 084119.
- [97] J. Angyan, R.-F. Liu, J. Toulouse, G. Jansen, *J. Chem. Theory Comput.* 7 (2011) 3116.
- [98] T. Olsen, K.S. Thygesen, *Phys. Rev. B* 86 (2012) 081103(R).
- [99] T. Olsen, K.S. Thygesen, *Phys. Rev. B* 88 (2013) 115131.
- [100] X. Ren, P. Rinke, G.E. Scuseria, M. Scheffler, *Phys. Rev. B* 88 (2013) 035120.
- [101] H. van Aggelen, Y. Yang, W. Yang, *Phys. Rev. A* 88 (2013) 030501(R).
- [102] Y. Yang, H. van Aggelen, S.N. Steinmann, D. Peng, W. Yang, *J. Chem. Phys.* 139 (2013) 174110.
- [103] H. Eshuis, J.E. Bates, F. Furche, *Theor. Chem. Acc.* 131 (2012) 1084.
- [104] P. Jurečka, J. Šponer, J. Černý, P. Hobza, *Phys. Chem. Chem. Phys.* 8 (2006) 1985.
- [105] J. Rezac, K.E. Riley, P. Hobza, *J. Chem. Theory Comput.* 7 (2011) 2427.
- [106] T. Schwabe, S. Grimme, *Phys. Chem. Chem. Phys.* 9 (2007) 3397.
- [107] J. Oddershede, P. Jørgensen, D.L. Yeager, *Comput. Phys. Rep.* 2 (1984) 33.
- [108] R. McWeeny, *Methods of Molecular Quantum Mechanics*, Academic Press, 1996.
- [109] D.B. Cook, *Handbook of Computational Quantum Chemistry*, Dover Press, 2004.

- [110] N. Ostlund, M. Karplus, *Chem. Phys. Lett.* 11 (1971) 450.
- [111] M.E. Casida, in: D.P. Chong (Ed.), *Recent Advances in Density Functional Methods*, vol. I, World Scientific, Singapore, 1995, p. 155.
- [112] P. Jørgensen, *Annu. Rev. Phys. Chem.* 26 (1975) 359.
- [113] S. Hirata, M. Head-Gordon, *Chem. Phys. Lett.* 314 (1999) 291.
- [114] M. Huix-Rotllant, B. Natarajan, A. Ipatov, C.M. Wawire, T. Deutsch, M.E. Casida, *Phys. Chem. Chem. Phys.* 12 (2010) 12811.
- [115] G.E. Scuseria, T.M. Henderson, D.C. Sorensen, *J. Chem. Phys.* 129 (2008) 231101.
- [116] G. Jansen, R.-F. Liu, J.G. Angyan, *J. Chem. Phys.* 133 (2010) 154106.
- [117] A. Görling, *Int. J. Quant. Chem.* 69 (1998) 265.
- [118] P. Mori-Sanchez, Q. Wu, W. Yang, *J. Chem. Phys.* 123 (2005) 062204.
- [119] H. Jiang, E. Engel, *J. Chem. Phys.* 125 (2006) 184108.
- [120] A. Heßelmann, *J. Chem. Phys.* 122 (2005) 244108.
- [121] A. Heßelmann, *Phys. Chem. Chem. Phys.* 8 (2006) 563.
- [122] N.C. Handy, J.A. Pople, K. Raghavachari, G.W. Trucks, *Chem. Phys. Lett.* 164 (1989) 185.
- [123] C. Hampel, K. Peterson, H.-J. Werner, *Chem. Phys. Lett.* 190 (1992) 1.
- [124] J.E. Moussa, *J. Chem. Phys.* 140 (2014) 014107.
- [125] A. Heßelmann, *J. Chem. Phys.* 134 (2011) 204107.
- [126] K.L. Bak, P. Jørgensen, J. Olsen, T. Helgaker, W. Klopper, *J. Chem. Phys.* 112 (2000) 9229.
- [127] E. Fabiano, F. Della Sala, *Theor. Chem. Acc.* 131 (2012) 1278.
- [128] J. Toulouse, F. Colonna, A. Savin, *Phys. Rev. A* 70 (2004) 062505.
- [129] K.S. Singwi, M.P. Tosi, R.H. Land, A. Sjölander, *Phys. Rev.* 176 (1968) 1968.
- [130] Z. Yan, J.P. Perdew, S. Kurth, *Phys. Rev. B* 61 (2000) 16430, Erratum: *Phys. Rev. B* 81 (2010) 169902(E).
- [131] I. Røeggen, L. Veseth, *Int. J. Quant. Chem.* 101 (2005) 201.
- [132] K.T. Tang, J.P. Toennies, *J. Chem. Phys.* 118 (2003) 4976.
- [133] E. Goll, H.-J. Werner, H. Stoll, *Phys. Chem. Chem. Phys.* 7 (2005) 3917.
- [134] C. Sosa, J. Noga, R.J. Bartlett, *J. Chem. Phys.* 88 (1988) 5974.
- [135] E. Chermak, B. Mussard, J.G. Angyan, P. Reinhardt, *Chem. Phys. Lett.* 550 (2012) 162.
- [136] H.B. Callen, T.A. Welton, *Phys. Rev.* 83 (1951) 34.
- [137] L.D. Landau, J.M. Lifschitz, *Statistische Physik*, Harri Deutsch, 1987.
- [138] D. Bokhan, R.J. Bartlett, *Phys. Rev. A* 73 (2006) 022502.
- [139] A.D. Becke, *Phys. Rev. A* 38 (1988) 3098.
- [140] J.P. Perdew, *Phys. Rev. B* 33 (1986) 8822.
- [141] A. Heßelmann, A. Görling, *J. Chem. Theory Comput.* 9 (2013) 4382.
- [142] D. Peng, S.N. Steinmann, H. van Aggelen, W. Yang, *J. Chem. Phys.* 139 (2013) 104112.
- [143] Y. Yang, H. van Aggelen, W. Yang, *J. Chem. Phys.* 139 (2013) 224105.
- [144] N. Shenvi, H. van Aggelen, Y. Yang, W. Yang, *J. Chem. Phys.* 141 (2014) 024119.
- [145] S. Hirata, S. Ivanov, I. Grabowski, R. Bartlett, K. Burke, J.D. Talman, *J. Chem. Phys.* 115 (2001) 1635.
- [146] Q. Wu, W. Yang, *J. Theor. Comput. Chem.* 2 (2003) 627.
- [147] S. Kümmel, J.P. Perdew, *Phys. Rev. Lett.* 90 (2003) 043004.
- [148] T. Heaton-Burgess, F.A. Bulat, W. Yang, *Phys. Rev. Lett.* 98 (2007) 256401.
- [149] A. Heßelmann, A.W. Götz, F. Della Sala, A. Görling, *J. Chem. Phys.* 127 (2007) 054102.
- [150] R.T. Sharp, G.K. Horton, *Phys. Rev.* 90 (1953) 317.
- [151] J.D. Talman, W.F. Shadwick, *Phys. Rev. A* 14 (1976) 36.
- [152] M. Hellgren, D.R. Rohr, E.K.U. Gross, *J. Chem. Phys.* 136 (2012) 034106.
- [153] P. Verma, R.J. Bartlett, *J. Chem. Phys.* 136 (2012) 044105.
- [154] K. Raghavachari, J.A. Pople, E.S. Replogle, M. Head-Gordon, N.C. Handy, *Chem. Phys. Lett.* 167 (1990) 115.
- [155] P. Jurecka, P. Hobza, *Chem. Phys. Lett.* 365 (2002) 89.
- [156] M.S. Marshall, L.A. Burns, C.D. Sherrill, *J. Chem. Phys.* 135 (2011) 194102.
- [157] T. Takatani, E.G. Hohenstein, M. Malagoli, M.S. Marshall, C.D. Sherrill, *J. Chem. Phys.* 132 (2010) 144104.
- [158] S.F. Boys, F. Bernadi, *Mol. Phys.* 19 (1970) 553.
- [159] A. Misquitta, K. Szalewicz, *Chem. Phys. Lett.* 357 (2002) 301.
- [160] A. Heßelmann, G. Jansen, *Phys. Chem. Chem. Phys.* 5 (2003) 5010.
- [161] A. Heßelmann, G. Jansen, M. Schütz, *J. Chem. Phys.* 122 (2005) 014103.

- [162] G. Jansen, *WIREs Comput. Mol. Sci.* 4 (2013) 127.
- [163] S. Goerigk, S. Grimme, *J. Chem. Theory Comput.* 7 (2011) 291.
- [164] S. Goerigk, S. Grimme, *Phys. Chem. Chem. Phys.* 13 (2011) 6670.
- [165] M. Pitonak, P. Neogrady, J. Cerny, S. Grimme, P. Hobza, *Chem. Phys. Chem.* 10 (2009) 282.
- [166] S.M. Cybulski, M.L. Lytle, *J. Chem. Phys.* 127 (2007) 141102.
- [167] M. Pitonak, A. Heßelmann, *J. Chem. Theory Comput.* 6 (2010) 168.
- [168] P. Arrighini, *Intermolecular Forces and Their Evaluation by Perturbation Theory*, Lecture Notes in Chemistry, vol. 25, Springer, 1981.
- [169] B. Jeziorski, R. Moszynski, K. Szalewicz, *Chem. Rev.* 94 (1994) 1887.
- [170] T. Cwiok, B. Jeziorski, W. Kolos, R. Moszynski, K. Szalewicz, *J. Chem. Phys.* 97 (1992) 7555.
- [171] R. Eisenschitz, F. London, *Z. Phys.* 60 (1930) 491.
- [172] B. Jeziorski, W. Kolos, *Int. J. Quant. Chem.* 12 (1977) 91.
- [173] M. Jeziorska, B. Jeziorski, J. Cizek, *Int. J. Quant. Chem.* 32 (1987) 149.
- [174] R. Moszynski, T.G.A. Heijmen, B. Jeziorski, *Mol. Phys.* 88 (1996) 741.
- [175] A. Heßelmann, G. Jansen, *Chem. Phys. Lett.* 357 (2002) 464.
- [176] A. Heßelmann, G. Jansen, *Chem. Phys. Lett.* 362 (2002) 325.
- [177] A. Heßelmann, G. Jansen, *Chem. Phys. Lett.* 367 (2003) 778.
- [178] R. Bukowski, R. Podeszwa, K. Szalewicz, *Chem. Phys. Lett.* 414 (2005) 111.
- [179] R. Podeszwa, K. Patkowski, K. Szalewicz, *Phys. Chem. Chem. Phys.* 12 (2010) 5974.
- [180] R.P. Feynman, *Phys. Rev.* 56 (1939) 340.
- [181] K.L.C. Hunt, *J. Chem. Phys.* 92 (1990) 1180.
- [182] M.J. Allen, D.J. Tozer, *J. Chem. Phys.* 117 (2002) 11113.
- [183] Q. Zhao, R.C. Morrison, R.G. Parr, *Phys. Rev. A* 50 (1994) 2138.
- [184] D.J. Tozer, V.E. Ingamells, N.C. Handy, *J. Chem. Phys.* 105 (1996) 9200.
- [185] M.E. Mura, P.J. Knowles, C.A. Reynolds, *J. Chem. Phys.* 106 (1997) 9659.
- [186] T. Gimon, A. Ipatov, A. Heßelmann, A. Görling, *J. Chem. Theory Comput.* 5 (2009) 781.
- [187] D.R. Lide (Ed.), *CRC Handbook of Chemistry and Physics*, 77th ed., CRC Press, Florida, 1997.
- [188] S.J.A. van Gisbergen, F. Kootstra, P.R.T. Schipper, O. Gritsenko, J.G. Snijders, E.J. Baerends, *Phys. Rev. A* 57 (1998) 2556.
- [189] G.D. Zeiss, W.J. Meath, *Mol. Phys.* 33 (1977) 1155.
- [190] A. Kumar, W.J. Meath, *Mol. Phys.* 54 (1985) 823.
- [191] S.M. Cybulski, T.P. Haley, *J. Chem. Phys.* 121 (2004) 7711.
- [192] T.P. Haley, E.P. Graybill, S.M. Cybulski, *J. Chem. Phys.* 124 (2006) 204301.
- [193] A. Heßelmann, G. Jansen, *J. Chem. Phys.* 112 (2000) 6949.
- [194] K. Szalewicz, *WIREs Comput. Mol. Sci.* 2 (2012) 254.
- [195] S. Rybak, B. Jeziorski, K. Szalewicz, *J. Chem. Phys.* 95 (1991) 6576.
- [196] B. Jeziorski, R. Moszynski, A. Ratkiewicz, S. Rybak, K. Szalewicz, H.L. Williams, in: E. Clementi (Ed.), *Methods and Techniques in Computational Chemistry: METECC-94*, vol. B, STEF, Cagliari, 1993, p. 79.
- [197] C.-O. Almbladh, U. von Barth, *Phys. Rev. B* 31 (1985) 3231.
- [198] D.J. Joubert, *Phys. Rev. A* 76 (2007) 012501.
- [199] F. Della Sala, A. Görling, *J. Chem. Phys.* 115 (2001) 5718.
- [200] M. Torheyden, G. Jansen, *Theor. Chim. Acta* 104 (2000) 370.
- [201] R.M. Dreizler, E.K.U. Gross, *Density Functional Theory*, Springer, Heidelberg, 1990.
- [202] S. Grimme, *Angew. Chem. Int. Ed.* 47 (2008) 3430.
- [203] S. Ehrlich, J. Moellmann, S. Grimme, *Acc. Chem. Res.* 46 (2013) 916.
- [204] T. Janowski, P. Pulay, *J. Am. Chem. Soc.* 134 (2012) 17520.
- [205] S. Grimme, *Chem. Eur. J.* 18 (2012) 9955.
- [206] T. Risthaus, S. Grimme, *J. Chem. Theory Comput.* 9 (2013) 1580.
- [207] A. Klamt, *J. Phys. Chem.* 99 (1995) 2224.
- [208] F. Eckert, A. Klamt, *AIChE J.* 48 (2002) 369.
- [209] B. Aradi, B. Hourahine, T. Frauenheim, *J. Phys. Chem. A* 111 (2007) 5678.
- [210] J.J.P. Stewart, *J. Mol. Model.* 13 (2007) 1173.
- [211] A. Heßelmann, T. Korona, *J. Chem. Phys.* 141 (2014) 094107.
- [212] S. Grimme, *J. Chem. Phys.* 118 (2003) 9095.

- [213] G. Chalasinski, M.M. Szczesniak, *Mol. Phys.* 63 (1987) 205.
- [214] S.M. Cybulski, G. Chalasinski, R. Moszynski, *J. Chem. Phys.* 92 (1990) 4357.
- [215] A. Ambrosetti, D. Alfe, R.A. DiStasio Jr., A. Tkatchenko, *J. Phys. Chem. Lett.* 5 (2014) 849.
- [216] A. Heßelmann, *J. Chem. Phys.* 128 (2008) 144112.
- [217] C. Adamo, V. Barone, *Chem. Phys. Lett.* 274 (1997) 242.

# Wavefunction Theory Approaches to Noncovalent Interactions

*C. David Sherrill*

Center for Computational Molecular Science and Technology, School of Chemistry and Biochemistry, and School of Computational Science and Engineering, Georgia Institute of Technology, Atlanta, GA, USA

## 4.1 THE CHALLENGES OF MODELING NONCOVALENT INTERACTIONS

### 4.1.1 The Electron Correlation Challenge

To illustrate the difficulties in obtaining accurate quantum chemical results for noncovalent interactions, consider the case of H<sub>2</sub>S interacting with benzene, as illustrated in Fig. 4.1. This complex might be considered as a simple prototype of sulfur- $\pi$  interactions, which have long been considered as stabilizing elements in proteins [1–3]. Perhaps surprisingly, the general features of the potential energy landscape of the simple H<sub>2</sub>S··benzene system correlate well [4] with observed geometrical preferences of sulfur- $\pi$  interactions in the Protein Data-bank [5]. The convergence of the interaction energy of this complex with respect to electron correlation treatment and basis set has previously been reported [6].

Fig. 4.1 illustrates the interaction energy between the H<sub>2</sub>S and benzene molecules, with the two hydrogens of H<sub>2</sub>S pointed down toward the benzene ring; the two molecules are kept rigid, and the distance between their centers of mass is varied. Here we are plotting the interaction energy, defined as

$$\Delta E_{\text{IE}} = E_{\text{AB}}^{\text{AB}} - E_{\text{A}}^{\text{AB}} - E_{\text{B}}^{\text{AB}}, \quad (4.1)$$

where the subscripts denote the identity of the molecular system whose energy is being evaluated (dimer AB or monomers A or B), and the superscripts AB indicate that the interaction energy is computed with all species at the geometry they adopt in the dimer. For example,  $E_{\text{A}}^{\text{AB}}$  means the energy of monomer A at the geometry it adopts while in the dimer. Negative interaction energies correspond to attractive interactions, while positive interaction energies correspond to repulsive interactions. Note that an interaction energy neglects the energy



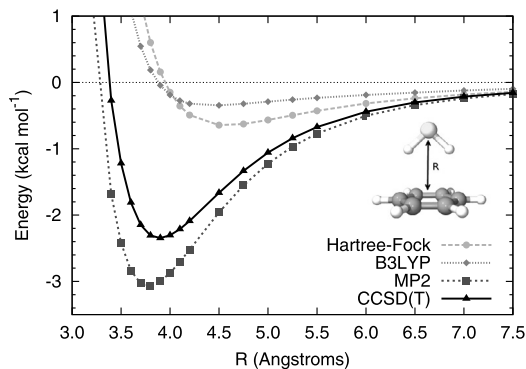


FIGURE 4.1 Interaction energies for the  $\text{H}_2\text{S}\cdots\text{benzene}$  complex as a function of the intermolecular separation (rigid monomers, aDZ basis, with counterpoise correction). Data from Ref. [6].

penalty required to deform the monomers into the geometries they adopt in the dimer,

$$\Delta E_{\text{def}} = \left( E_{\text{A}}^{\text{AB}} - E_{\text{A}}^{\text{A}} \right) + \left( E_{\text{B}}^{\text{AB}} - E_{\text{B}}^{\text{B}} \right). \quad (4.2)$$

Thus a more chemically relevant quantity, the binding energy, can be defined as

$$\Delta E_{\text{bind}} = -(\Delta E_{\text{IE}} + \Delta E_{\text{def}}), \quad (4.3)$$

where the sign convention is opposite that of  $\Delta E_{\text{IE}}$ . Theoretical studies often examine  $\Delta E_{\text{IE}}$  for convenience, and in the case of rigid monomers  $\Delta E_{\text{def}} = 0$  and hence  $\Delta E_{\text{bind}} = -\Delta E_{\text{IE}}$ . A molecule can deform significantly when it interacts with another molecule in a van der Waals complex if the interaction is strong (e.g., hydrogen bonding), but in more weakly bound complexes (e.g., benzene dimer, benzene $\cdots\text{H}_2\text{S}$ , methane dimer) the monomer geometries hardly change, and hence a rigid monomer approximation is appropriate.

Fig. 4.1 shows interaction energies computed using the medium-sized aug-cc-pVDZ basis set, which is Dunning's "correlation-consistent" polarized-valence double- $\zeta$  basis [7] (cc-pVDZ), augmented (the "aug-" prefix) by a set of diffuse  $s$ ,  $p$ , and  $d$  functions [8]. A basis set of this size will typically give reasonably accurate results in quantum chemistry (although it is often not good enough for high-accuracy applications like comparing to spectroscopic experiments). We discuss basis sets in more detail in the next subsection. At large distances, the interaction energy approaches zero because the two molecules are too far apart to interact significantly. At shorter distances, there is a serious disagreement between the interaction energies computed by the various methods. Hartree-Fock molecular orbital theory fails for this problem when compared to a truly high-accuracy method like coupled-cluster with singles, doubles, and perturbative triple substitutions [CCSD(T)] [9]. The Hartree-Fock potential curve is substantially underbound, predicting an attraction of only 0.6 kcal/mol between the two molecules, whereas CCSD(T) determines an attraction of 2.3 kcal/mol at 3.9 Å separation. Second-order Møller-Plesset perturbation theory (MP2), also called second-order many-body perturbation theory, yields results much closer to CCSD(T) than does Hartree-Fock.

However, the MP2 interaction energies are still not particularly accurate, overestimating the attraction by 0.8 out of 2.3 kcal/mol (a 35% error), and underestimating the equilibrium intermolecular separation by about 0.1 Å. This performance is perhaps not as good as one might have expected, given that MP2, as the least costly correlated wavefunction method, was widely used for many applications prior to the broad adoption of density functional theory.

The primary difficulty in obtaining accurate interaction energies for weakly bound van der Waals complexes like H<sub>2</sub>S⋯benzene is that London dispersion forces (see Chapter 1) constitute a significant fraction of the intermolecular interaction. These forces are often introduced in general chemistry textbooks as arising from a temporary fluctuation of electrons leading to an “instantaneous” dipole moment, which then induces a complementary dipole moment on the other monomer (“instantaneous-dipole”/“induced-dipole” interactions). The physics of this interaction is governed by the correlated motions of electrons, which makes it difficult to model. Hartree–Fock molecular orbital theory is a model in which each electron experiences only the *average* charge cloud of the other electrons, so that there is no opportunity for electrons on one monomer to respond to an instantaneous fluctuation of the electron density on the other monomer; in this sense, Hartree–Fock is said to lack electron correlation (although to be precise, it does contain some degree of correlation between electrons with the same spin, due to the fact that a Slater determinant obeys the antisymmetry principle) [10]. The large difference between the Hartree–Fock and CCSD(T) results in Fig. 4.1 indicates that electron correlation effects are quite important in this system; primarily, they lead to London dispersion interactions that CCSD(T) can capture and that Hartree–Fock cannot. The fact that Hartree–Fock is still weakly attractive indicates that part of the attraction comes from favorable electrostatic and/or polarization (induction) interactions, which can be captured by Hartree–Fock with reasonable accuracy. Exchange-repulsion (steric repulsion) is also captured reasonably well by Hartree–Fock. The small net attraction means that at the Hartree–Fock level, the sum of the favorable electrostatics and polarization is larger in magnitude than the unfavorable exchange-repulsion. It can be very helpful in studies of intermolecular interactions to explicitly compute the fraction of the attraction between two molecules due to London dispersion forces, electrostatics, and polarization, and also the opposing exchange-repulsion energy. This is possible using methods like symmetry-adapted perturbation theory (SAPT), discussed below in Section 4.4.4 and more fully in Chapter 2.

In the H<sub>2</sub>S⋯benzene system, there is a favorable electrostatic interaction because the hydrogens of H<sub>2</sub>S bear a partial positive charge (they are less electronegative than sulfur), and the  $\pi$  cloud of benzene bears a partial negative charge. The close contact of these opposite charges leads to a favorable electrostatic interaction. Additionally, the  $\pi$  cloud of benzene is polarizable, and the partial positive hydrogens can pull some of the  $\pi$  electron density toward them, leading to further stabilization via induction/polarization. Because Hartree–Fock often describes electrostatics, induction, and exchange-repulsion fairly accurately [11], the large difference between Hartree–Fock and CCSD(T) suggests that for H<sub>2</sub>S⋯benzene the London dispersion forces (the only interaction missing from Hartree–Fock) must be substantial. In charged systems, or systems with significant hydrogen bonding, electrostatic and polarization terms will often become more important than London dispersion terms, meaning that Hartree–Fock becomes less unreliable. However, even in such systems, the magnitude of the London dispersion forces increases for larger systems. In addition, even in systems with

strong electrostatic interactions like small doubly hydrogen-bonded dimers, the London dispersion forces can remain nonnegligible [12].

MP2 is considered the simplest wavefunction-based method that incorporates a reasonable model of electron correlation effects: each electron's motion is allowed to respond to the motion of each other electron, taken a pair at a time. However, the model is imperfect because it ignores any correlation between more than two electrons at a time. Fig. 4.1 shows that MP2 is much more accurate than Hartree–Fock, although London dispersion forces are overestimated, leading to a too-strong attraction between the molecules.

Finally, for comparison purposes, we also plot the interaction energy computed using the very popular B3LYP method from density functional theory (DFT) [13,14]. Although B3LYP incorporates electron correlation via the Lee–Yang–Parr (LYP) functional [15], it seems to suffer essentially the same challenges as uncorrelated Hartree–Fock theory, dramatically underestimating the strength of attraction between H<sub>2</sub>S and benzene. This is because standard density functional approximations are short-ranged and cannot capture electron correlation effects beyond a few Å [16–18]. By now it is widely appreciated that standard density functionals are not appropriate for systems where London dispersion interactions are significant (which would include essentially all organic molecules except those that are very small or that have essentially 1D or 2D shapes). Chapters 5 to 8 describe improvements to density functional approximations that allow them to accurately model such systems.

### 4.1.2 The Basis Set Challenge

We saw in the previous section that the computed strength of a noncovalent interaction can be very sensitive to the choice of theoretical method used, even when all of the methods considered are of Hartree–Fock quality or better. Unfortunately, interaction energies can also be quite sensitive to the choice of basis set. Fig. 4.2 illustrates this for the H<sub>2</sub>S··benzene complex using the MP2 method and a series of augmented correlation-consistent basis sets (aug-cc-pVXZ) ranging in size from the modest aug-cc-pVDZ basis up to the very large aug-cc-pV5Z basis set. We will follow common practice and abbreviate these basis sets by the shorthand aXZ (e.g., aDZ for aug-cc-pVDZ). The figure contains two sets of curves: one set of standard computations denoted by open symbols, and another set using the Boys–Bernardi counterpoise (CP) correction, denoted by closed symbols. We discuss the standard computations first, followed by a brief discussion of the CP correction and an analysis of the CP results. Typically, basis set convergence of post-Hartree–Fock methods will be qualitatively similar to the MP2 trends discussed here.

In the cc-pVXZ correlation-consistent basis sets, each time one goes to a higher  $\zeta$ -level (e.g., double- $\zeta$  to triple- $\zeta$ ), one increases the maximum angular momentum in the basis set by one, and then adds an additional set of basis functions for every angular momentum in the basis. For example, improving the basis from cc-pVDZ to cc-pVTZ increases the maximum angular momentum from  $d$  to  $f$ , and adds a set of  $f$  functions, a set of  $d$  functions, a set of  $p$  functions, and an  $s$  function. When diffuse functions are added to yield the “augmented” correlation-consistent basis sets (aug-cc-pVXZ), the basis sets are enlarged by an additional set of diffuse functions for every angular momentum in the basis. This means that basis sets like aQZ or a5Z are enormous in size and are infeasible in computations except for small systems and/or at lower levels of theory like Hartree–Fock or perhaps MP2. For the small

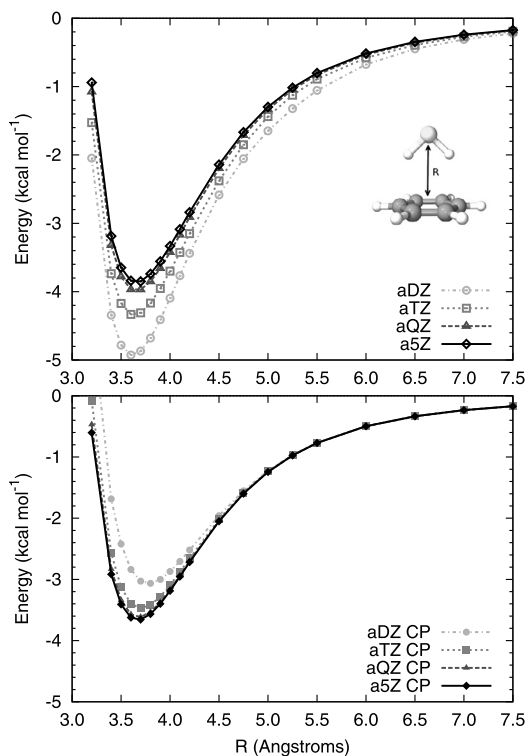


**FIGURE 4.2** Interaction energies for the  $\text{H}_2\text{S}\cdots\text{benzene}$  complex as a function of the intermolecular separation (rigid monomers) computed using the MP2 method and a series of aug-cc-pVXZ (aXZ) basis sets, with (solid symbols, bottom panel) and without (open symbols, top panel) counterpoise correction. Data from Ref. [20].

$\text{H}_2\text{S}\cdots\text{benzene}$  complex, the number of basis functions in the aDZ, aTZ, aQZ, and a5Z basis sets is 237, 510, 932, and 1533, respectively.

This rapid growth in the number of basis functions is problematic because the computational cost of standard quantum wavefunction methods grows nonlinearly with the number of basis functions. Unless various numerical approximations are employed, the time required to compute a Hartree–Fock energy scales approximately as  $\mathcal{O}(N^4)$ , where  $N$  is the number of basis functions. The computational scaling grows to  $\mathcal{O}(oN^4)$  for MP2, where  $o$  is the number of occupied orbitals. Thus, for Hartree–Fock or MP2, one might expect that doubling the size of the basis will increase the computation time by a factor of  $2^4 = 16$ . In practice, actual computational costs do not always follow these formal scalings, especially if one applies screening techniques, local correlation approximations, etc. Using the very efficient density fitting approximation (see Section 4.2.4 below), MP2 dimer computations (including program startup, the Hartree–Fock component, etc.) require 7, 31, 132, and 586 seconds in the aDZ, aTZ, aQZ, and a5Z basis sets, respectively, on a 4-core Intel i7-3770K computer using Psi4 [19]. While none of these computations take very long, the series illustrates the rapid growth in computer

time with the number of basis functions, which can make large basis sets like aQZ and a5Z infeasible for larger molecular systems.

Fig. 4.2 shows a very large discrepancy between the aDZ and aTZ potential curves (open circles and open squares, respectively). The aDZ curve yields an interaction energy of  $-4.9$  kcal/mol at its potential energy minimum ( $3.6$  Å), whereas the aTZ curve yields an interaction energy of only  $-4.3$  kcal/mol at the same intermonomer separation. The interaction energy continues to decrease in magnitude upon using larger basis sets, becoming  $-4.0$  and  $-3.9$  with the aQZ and a5Z basis sets. Additionally, the minimum-energy distance shifts to  $3.7$  Å for the latter two basis sets. Overall, the predicted interaction energy changes by an entire kcal/mol as one progresses from the aDZ to the a5Z basis set.

### Counterpoise Corrections

The substantial overbinding by the smaller basis sets seen in Fig. 4.2 for  $\text{H}_2\text{S} \cdots \text{benzene}$  is typical for van der Waals dimers, as is the monotonic convergence of the interaction energy from below as the basis set size is increased. This overbinding is ascribed to “basis set superposition error” (BSSE), which refers to the imbalanced way in which interaction energies are computed in a finite basis set when using Eq. (4.1). In the dimer, each monomer is able to benefit not only from its own basis functions, but also from the basis functions of the other monomer, if the monomers are close to each other. Access to additional basis functions provides additional flexibility which necessarily lowers the energy in any variational computations (and typically lowers the energy in nonvariational computations, as well). However, when the monomer energies are computed in Eq. (4.1), each monomer has access to only its own basis functions. Thus, the dimer is treated preferentially with respect to its basis set, and it is overstabilized relative to the monomers, leading to overbinding. The extent of this overstabilization is referred to as the BSSE. As the size of the basis set is increased, the extent of this imbalance is reduced, and in the complete basis set (CBS) limit, the monomers are described just as well as the dimer, meaning that the BSSE becomes zero.

Boys and Bernardi [21] introduced the “counterpoise” (CP) correction, which is meant to remove this overbinding due to BSSE. In their scheme, the BSSE in a finite basis set is computed as the extent to which monomer A gains extra stabilization from the basis set of monomer B in the dimer, plus the corresponding extra stabilization of B in the dimer by basis functions from A:

$$E_{\text{BSSE}} = \left( E_{\text{A}}^{\text{AB}}(\text{AB}) - E_{\text{A}}^{\text{AB}}(\text{A}) \right) + \left( E_{\text{B}}^{\text{AB}}(\text{AB}) - E_{\text{B}}^{\text{AB}}(\text{B}) \right). \quad (4.4)$$

Here, subscripts denote the molecular species, superscripts indicate the geometry at which the energies are evaluated, and symbols in parentheses denote the basis set used. The superscripts are all AB, indicating that the counterpoise correction is evaluated at the geometries the monomers have within the dimer. So,  $E_{\text{A}}^{\text{AB}}(\text{A})$  denotes the energy of monomer A computed in its own basis set (at its geometry within the dimer), and  $E_{\text{A}}^{\text{AB}}(\text{AB})$  denotes the energy of monomer A computed using all the functions from monomers A and B. When we perform a computation using the basis functions of monomer B but not the nuclear charges or electrons of monomer B, as we do when computing  $E_{\text{A}}^{\text{AB}}(\text{AB})$ , this is called using the “ghost functions” of monomer B. As mentioned above,  $E_{\text{A}}^{\text{AB}}(\text{AB}) < E_{\text{A}}^{\text{AB}}(\text{A})$  (in practice, and necessarily for variational methods), and likewise for monomer B. Thus,  $E_{\text{BSSE}} < 0$ , consistent with

the overstabilization of dimers in finite basis sets. To apply the counterpoise correction, we subtract this error from the interaction energy as computed by Eq. (4.1), to yield:

$$\begin{aligned} \Delta E_{\text{IE}}^{\text{CP}} &= E_{\text{AB}}^{\text{AB}}(\text{AB}) - E_{\text{A}}^{\text{AB}}(\text{A}) - E_{\text{B}}^{\text{AB}}(\text{B}) - E_{\text{BSSE}} \\ &= E_{\text{AB}}^{\text{AB}}(\text{AB}) - E_{\text{A}}^{\text{AB}}(\text{A}) - E_{\text{B}}^{\text{AB}}(\text{B}) - \left( E_{\text{A}}^{\text{AB}}(\text{AB}) - E_{\text{A}}^{\text{AB}}(\text{A}) \right) - \left( E_{\text{B}}^{\text{AB}}(\text{AB}) - E_{\text{B}}^{\text{AB}}(\text{B}) \right) \\ &= E_{\text{AB}}^{\text{AB}}(\text{AB}) - E_{\text{A}}^{\text{AB}}(\text{AB}) - E_{\text{B}}^{\text{AB}}(\text{AB}). \end{aligned} \quad (4.5)$$

As a reminder, to compute energies relative to monomers in their equilibrium geometries, we would also need to add monomer deformation energies (Eq. (4.2)) to the above expression (if we assume rigid monomers, these terms are zero). Returning to Fig. 4.2, we see that the CP-corrected potential curves converge to the CBS limit from above, opposite to the behavior of the uncorrected curves. For the  $\text{H}_2\text{S} \cdots$  benzene system, at least, convergence of the CP-corrected curves is more rapid than that of the uncorrected curves. However, superior performance of CP-corrected energies is not guaranteed. For hydrogen-bonded systems, uncorrected values with modest basis sets like aDZ can be relatively close to the CBS limit, and the CP correction can make them substantially underbound; on the other hand, for these systems the CP-corrected series often converges more smoothly and more rapidly to the CBS limit as larger basis sets are employed [22,23]. Because CP-corrected and uncorrected values tend to bracket the CBS limit, numerous authors have tested and advocated using the average of these results [22–25].

## 4.2 DEFINITIVE RESULTS USING COUPLED-CLUSTER THEORY

### 4.2.1 The Reliability of Coupled-Cluster with Perturbative Triples, CCSD(T)

The previous section demonstrates that noncovalent interaction energies are very sensitive both to the theoretical method and also to the basis set. On the face of it, this would appear to create a dilemma about what method and basis set to use. Fortunately, however, wavefunction methods of the configuration interaction or coupled-cluster type are “convergent” *ab initio* methods, meaning that one can and should expect more accurate results as one includes successively higher excitations. Assuming one avoids systems with near-degeneracies among the electron configurations (e.g., diradicals, systems with unfilled *d* or *f* shells, unimolecular bond dissociation reactions, etc.), the coupled-cluster methods are rapidly convergent with respect to the excitation level included, and only singles, doubles, and a perturbative estimate of triples (i.e., CCSD(T)) is sufficient to obtain a nearly converged treatment of electron correlation [26]; for this reason, CCSD(T) is often referred to as a “gold standard” of quantum chemistry. Specifically for the case of noncovalent interaction energies, the neglect of electron correlation effects beyond the CCSD(T) level causes errors on the order of a few hundredths of one kcal/mol for small van der Waals dimers [27–29]. Core correlation effects are also of this size and can also be neglected in most applications [30,31].

Thus we can achieve high-accuracy results using CCSD(T) in conjunction with large basis sets. Indeed, this is the desired approach when the molecular system is small enough for the computations to be feasible. Unfortunately, the computational cost of canonical CCSD(T)

scales steeply as  $\mathcal{O}(o^3v^4)$ , where  $o$  and  $v$  are the number of occupied and virtual (unoccupied) orbitals, respectively [9]. Hence, very large basis sets like aug-cc-pV5Z are currently infeasible in conjunction with CCSD(T) except for small systems with only a few atoms.

### 4.2.2 Basis Set Extrapolation

Dunning’s correlation-consistent basis sets (cc-pVXZ), including their augmented variants (aug-cc-pVXZ), are specifically designed to converge smoothly toward the complete basis set limit as one progresses to larger basis sets in the series. This allows for the possibility of extrapolating a series of results to the CBS limit. Basis set convergence behavior of the Hartree–Fock energy is somewhat different than that of the electron correlation energy, so they are often extrapolated separately. The Hartree–Fock energy is often [32–34] fit to an exponential series in  $X$ , the cardinal number of the basis set (D: 2, T: 3, Q: 4, etc.), although Halkier et al. [33] suggest simply using the unextrapolated Hartree–Fock energy for  $X > 4$ . Moreover, for the case of interaction energies, the aQZ basis is already sufficient for convergence of the Hartree–Fock contribution, with a mean absolute error (MAE) of only 0.001 kcal/mol compared to Hartree–Fock/a6Z results for the 9 members of the A24 test set where we have computed them ( $\text{NH}_3 \cdots \text{H}_2\text{O}$ ,  $(\text{H}_2\text{O})_2$ ,  $(\text{HCN})_2$ ,  $(\text{HF})_2$ ,  $(\text{NH}_3)_2$ ,  $\text{CH}_4 \cdots \text{HF}$ ,  $\text{H}_2\text{O} \cdots \text{CH}_4$ ,  $\text{CH}_4 \cdots \text{Ar}$ , and  $\text{C}_2\text{H}_4 \cdots \text{Ar}$ ) [23].

Although correlation energies are smaller in magnitude than Hartree–Fock energies, their errors with respect to the CBS limit tend to be larger. Additionally, their rate of convergence to the CBS limit is slower, exhibiting a power-law rather than an exponential dependence. Hence, extrapolation provides a more noticeable improvement for correlation energies than for Hartree–Fock energies. The correlation energy is often fit to a function

$$E_X^{\text{corr}} = E_\infty^{\text{corr}} + AX^{-3}, \quad (4.6)$$

which, after some rearrangement, allows one to perform the extrapolation based on correlation energies from only two basis sets (a “two-point” extrapolation):

$$E_{XY}^\infty = \frac{E_X^{\text{corr}}X^3 - E_Y^{\text{corr}}Y^3}{X^3 - Y^3}, \quad (4.7)$$

as proposed by Helgaker and coworkers [35]. Numerous alternative extrapolation schemes exist (see, e.g., Refs. [36–39]).

Table 4.1 compares the basis set convergence of conventional CCSD(T) against two-point extrapolations of the correlation energy using Eq. (4.7) and a pair of sequential basis sets, a(X-1)Z and aXZ (the Hartree–Fock energy is not extrapolated and is evaluated in the larger aXZ basis). Also presented are focal-point and explicitly correlated results, discussed below. Compared to conventional CCSD(T) using an aXZ basis set, a two-point extrapolation using the a(X-1)Z and aXZ basis sets reduces the error by a factor of two or more. Indeed, this extrapolation yields errors as good as conventional CCSD(T) with the a(X+1)Z basis set, at least for this test case. Given the rapid growth of the number of basis functions with respect to the cardinal number  $X$  (discussed in Section 4.1.2), in conjunction with the high computational scaling of CCSD(T) with respect to the number of basis functions, these extrapolation

**TABLE 4.1** Errors in the CCSD(T) interaction energy (kcal/mol) vs. the CBS limit for the CH<sub>4</sub>⋯HF dimer<sup>a,b</sup>

Conventional	Extrapolated		Focal-point <sup>c</sup>		Explicitly correlated <sup>d</sup>				
					F12a	F12b	F12c		
aDZ	0.62		aTQZ + $\delta$ /aDZ	0.05	aDZ	0.10	0.14	0.12	
aTZ	0.11	aDTZ	-0.04	aTQZ + $\delta$ /aTZ	-0.01	aTZ	-0.02	0.00	0.01
aQZ	0.04	aTQZ	-0.02	aQ5Z + $\delta$ /aQZ	-0.01	aQZ	-0.01	0.00	0.00
a5Z	0.02	aQ5Z	0.00	a56Z + $\delta$ /a5Z	-0.01	a5Z	-0.01	0.00	0.00
a6Z	0.01	a56Z	0.00						

<sup>a</sup> At the C<sub>3v</sub> geometry from the A24 test set (Ref. [31]).

<sup>b</sup> Data from Ref. [23]. All values counterpoise-corrected. Estimated CBS limit of -1.66 kcal/mol.

<sup>c</sup> Focal-point methods are discussed in Section 4.2.3. Here, aTQZ +  $\delta$ /aTQZ denotes MP2/aTQZ +  $\delta_{\text{MP2}}^{\text{CCSD(T)}}$ /aDZ, etc.

<sup>d</sup> Explicitly correlated methods are discussed in Section 4.2.5.

schemes seem very advantageous. Whereas an aQZ basis is required to reduce the conventional CCSD(T) error below 0.1 kcal/mol, this can be achieved by an aDTZ extrapolation. Hence, if we want to reduce the basis set error in CCSD(T) so that it is comparable to the errors from neglect of quadruple excitations or core correlation (typically both in the hundredths of kcal/mol), this can be achieved by using a basis set of aQZ size or larger, or a basis set extrapolation of at least aDTZ quality.

Although the aDTZ extrapolation works well here, in other systems, it can provide less reliable results than the unadulterated aTZ because substantial errors in the aDZ energies can lead to overshooting the CBS limit [23,35,40]. So long as the smallest basis set is of triple- $\zeta$  quality or better, two-point extrapolations seem generally reliable.

Burns et al. [20] present a systematic study of the performance of various wavefunction methods for noncovalent interaction energies, based on benchmark-quality results for the S22 [40,41], NBC10 [40], HBC6 [12,40], and HSG [40,42] databases (see Section 4.4.1 for a discussion of these and other benchmark databases for van der Waals dimers). Averaged over these databases (which include complexes with much stronger interactions than the CH<sub>4</sub>⋯HF complex in Table 4.1), CCSD(T) exhibits MAE for interaction energies of 0.96 and 0.35 kcal/mol in the aDZ and aTZ basis sets, respectively. On average, the aDTZ extrapolation is an improvement over aTZ, yielding an MAE of 0.11 kcal/mol. Extrapolations of CCSD(T) with larger basis sets were not considered in this study because the aQZ basis is too large for the required computations to be feasible. Many of the benchmark values were estimated using focal-point approximations, discussed below, that avoided explicit CCSD(T)/aQZ computations.

### 4.2.3 Focal-Point Analysis

Fortunately, it has been known for some time that higher-order electron correlation effects are generally well described by smaller basis sets. That is, the difference in the correlation energy between a sophisticated method like CCSD(T) and a more basic method like MP2 is fairly insensitive to the basis set used. This means that one can compute this difference in a small basis, and add it as a correction to the basic method as computed in a large basis set. This



**TABLE 4.2** Basis set convergence of  $\delta_{\text{MP2}}^{\text{CCSD(T)}}$  (kcal/mol) for the sandwich (S), T-shaped (T), and parallel-displaced (PD) configurations of the benzene dimer, with and without counterpoise (CP) correction<sup>a</sup>

Basis	no CP			CP		
	S	T	PD	S	T	PD
DZ	1.20	0.70	1.58	1.12	0.70	1.48
aDZ	1.34	0.62	1.69	1.41	0.76	1.84
aTZ	1.51	0.85	1.98	1.46	0.79	1.90
aDTZ	1.58	0.94	2.10	1.47	0.80	1.93
aQZ	1.57	0.91		1.49		
aTQZ	1.62	0.96		1.51		

<sup>a</sup> Data from Ref. [51].

kind of “focal-point” approach has been popular in quantum chemistry for many years [43, 44], and it is natural to apply it in the context of noncovalent interactions [45–48]. In particular, we have advocated [40,47,49] the following approach to estimate the CCSD(T)/CBS limit:

$$E_{\text{CCSD(T)}}^{\text{CBS}} \approx E_{\text{MP2}}^{\text{CBS}} + \delta_{\text{MP2}}^{\text{CCSD(T)}}, \quad (4.8)$$

$$\delta_{\text{MP2}}^{\text{CCSD(T)}} = E_{\text{CCSD(T)}}^{\text{small}} - E_{\text{MP2}}^{\text{small}}. \quad (4.9)$$

Accurate estimates of the MP2/CBS limit may be obtained using a two-point Helgaker extrapolation [35] of the correlation energies obtained with the aTZ and aQZ basis sets, using Eq. (4.7). When used in conjunction with counterpoise correction, MP2/aTQZ and MP2/aQ5Z are essentially converged with respect to the CBS limit, with both having mean absolute errors of 0.01 kcal/mol for the A24 test set [23].

Table 4.2 demonstrates the basis set convergence of  $\delta_{\text{MP2}}^{\text{CCSD(T)}}$  for three configurations of the benzene dimer. For this challenging test case, where electron correlation effects are fairly large, we found [49] that polarized double- $\zeta$  basis sets like cc-pVDZ are not large enough to provide reliable estimates of  $\delta_{\text{MP2}}^{\text{CCSD(T)}}$ . Most of the error for the benzene dimer is eliminated when one adds diffuse functions via the aDZ basis [49], but even this is not quite sufficient to reduce the error in  $\delta_{\text{MP2}}^{\text{CCSD(T)}}$  to less than 0.1 kcal/mol [50], as might be desired for obtaining benchmark-quality results. The table indicates that the CP-corrected values converge more quickly and more smoothly than the uncorrected values, at least for this system, and that with CP correction, the aTZ values appear to be nearly converged.

For the A24 test set,  $\delta_{\text{MP2}}^{\text{CCSD(T)}}$  is nearly always converged within 0.05 kcal/mol of its CBS limit with an aTZ basis set or larger, although the quantity does not converge smoothly and exhibits small oscillations as the basis set is increased [23]. For this test set,  $\delta_{\text{MP2}}^{\text{CCSD(T)}}$  is more reliably computed using the aTZ basis than using an aDTZ extrapolation [23].

The reliable estimation of the MP2/CBS limit by a two-point aTQZ extrapolation and the reliable computation of  $\delta_{\text{MP2}}^{\text{CCSD(T)}}$  by an aDZ or, when feasible, aTZ basis suggests that focal-point schemes using these ingredients should be worthwhile in estimating the CCSD(T)/CBS limit. Table 4.1 shows errors vs. CCSD(T)/CBS for several focal-point schemes. MP2/aTQZ

+  $\delta_{\text{MP2}}^{\text{CCSD(T)}/\text{aDZ}}$  exhibits an error for this test case of 0.05 kcal/mol, whereas MP2/aTQZ +  $\delta_{\text{MP2}}^{\text{CCSD(T)}/\text{aTZ}}$  or better is essentially converged.

Burns et al. [23] have examined focal-point schemes of the type MP2/aTQZ +  $\delta_{\text{MP2}}^{\text{CCSD(T)}/\text{aDZ}}$  and MP2/aQ5Z +  $\delta_{\text{MP2}}^{\text{CCSD(T)}/\text{aTZ}}$ , with and without counterpoise correction, and they find that for the A24 test set, any variation on these approaches provides an MAE across the test set of less than 0.1 kcal/mol. Using MP2/aTQZ +  $\delta_{\text{MP2}}^{\text{CCSD(T)}/\text{aDZ}}$ , MAE for A24 ranged from 0.03 to 0.08 kcal/mol, depending on the counterpoise treatment, whereas MAE for MP2/aQ5Z +  $\delta_{\text{MP2}}^{\text{CCSD(T)}/\text{aTZ}}$  ranged from 0.02 to 0.03 kcal/mol. For the larger systems of the S22 test, larger errors are expected and observed. Compared to the best available data from the S22B benchmark values [40], MAE for MP2/aTQZ +  $\delta_{\text{MP2}}^{\text{CCSD(T)}/\text{aDZ}}$  range from 0.06–0.18 kcal/mol, depending on counterpoise treatment. It is difficult to evaluate the reliability of the more complete MP2/aQ5Z +  $\delta_{\text{MP2}}^{\text{CCSD(T)}/\text{aTZ}}$  treatment for S22, because not all of the benchmark values are of demonstrably higher quality. For the smallest 10 members of S22 for which higher-quality data are available, MP2/aQ5Z +  $\delta_{\text{MP2}}^{\text{CCSD(T)}/\text{aTZ}}$  exhibits MAE in the range of 0.01–0.04 kcal/mol, consistent with the A24 results.

Altogether, these data suggest that a focal-point approach using (CP-corrected)  $\delta_{\text{MP2}}^{\text{CCSD(T)}/\text{aDZ}}$  and an MP2/CBS estimate of aTQZ quality or better should provide interaction energies accurate to around 0.1 kcal/mol for small van der Waals dimers, whereas similar approaches using a  $\delta_{\text{MP2}}^{\text{CCSD(T)}/\text{aTZ}}$  should be accurate to several hundredths of one kcal/mol for these same systems. Due to the high efficiency of modern MP2 programs using density fitting (see next section), typically the coupled-cluster correction  $\delta_{\text{MP2}}^{\text{CCSD(T)}}$  is the most time-consuming step of such focal-point computations. Using the density-fitting and frozen natural orbital approximations (see next section) available in Psi4 [19], a CCSD(T)/aDZ computation on the benzene trimer required 39 hours on a 6-core Intel i7-3930K overclocked to 4.0 GHz [52]. Using a similar 6-core Intel i7-4930K clocked at 3.7 GHz, a CCSD(T)/aDZ computation on a 45-atom transition state in the proline-catalyzed aldol reaction between benzaldehyde and cyclohexanone required about 9 days [53]. Due to its unfavorable computational scaling, only slightly larger molecular systems are presently accessible for CCSD(T)/aDZ without resorting to additional approximations or utilizing large computer clusters. CCSD(T) computations in the larger aTZ basis of course take even longer to perform, making them difficult for systems much larger than the benzene dimer.

#### 4.2.4 Density Fitting, Cholesky Decomposition, and Frozen Natural Orbitals

Nearly all *ab initio* quantum chemical methods are formulated in terms of the one- and two-electron integrals. The two-electron integrals [10], also called electron repulsion integrals (ERIs), are defined as

$$(pq|rs) = \int \phi_p(\mathbf{r}_1)\phi_q(\mathbf{r}_1) \frac{1}{r_{12}} \phi_r(\mathbf{r}_2)\phi_s(\mathbf{r}_2) d\mathbf{r}_1 d\mathbf{r}_2, \quad (4.10)$$

where the  $\phi$ 's denote orbitals (which we have assumed are real, not complex functions),  $\mathbf{r}_1$  and  $\mathbf{r}_2$  denote the 3D positions of electrons 1 and 2, and  $r_{12}$  is the distance between the two

electrons. These ERIs can be represented by a 4-index tensor that formally has  $N^4$  elements ( $N^4/8$  for large  $N$ , if we take advantage of permutational symmetry), where  $N$  is the number of basis functions. In a basis of atom-centered Gaussian functions (commonly employed in quantum chemistry), the integral will become very small if  $\phi_p(\mathbf{r})$  and  $\phi_q(\mathbf{r})$  are centered on atoms that are very far apart: this means that their product  $\phi_p(\mathbf{r})\phi_q(\mathbf{r})$  will be near zero. Of course, the same holds true if  $\phi_r(\mathbf{r})$  and  $\phi_s(\mathbf{r})$  are far apart. These very small integrals can be neglected through various screening techniques, meaning that the 4-index tensor has many elements that are set to zero (we say that the tensor is sparse). However, even taking this into account, the rapid growth of the ERI tensor with the number of basis functions is one of the bottlenecks of quantum chemical methods: the tensor is typically too large to store in main memory, necessitating storage on attached hard disks or regeneration on the fly by repeated computations (“integral direct” algorithms). The former solution is undesirable because reading and writing the integrals is time-consuming, and the disk access speed does not increase as we add compute cores to a node. The latter solution is undesirable as it takes a long time (even on a multicore node) to recompute the ERIs in every iteration of the algorithm.

For these reasons, there has been intense recent interest in methods that factorize the 4-index ERIs as products of lower-rank tensors that are easier to compute, store, and process. The most popular such approach is density fitting (DF), also known as resolution of the identity (RI) [54–61]. Although this approach has been around for decades, its utility in accelerating quantum chemistry methods has become widely appreciated only in the past several years. The orbital product (“generalized density”)  $\phi_p(\mathbf{r})\phi_q(\mathbf{r})$  is approximated by a linear combination of  $N_{\text{aux}}$  auxiliary functions  $\{\chi_Q(\mathbf{r})\}$ ,

$$\phi_p(\mathbf{r})\phi_q(\mathbf{r}) \approx \sum_Q^{N_{\text{aux}}} d_Q^{pq} \chi_Q(\mathbf{r}). \quad (4.11)$$

By minimizing the error of the electrostatic potential of this density, one obtains [55,62] the expansion coefficients as

$$d_Q^{pq} = \sum_P (pq|P)[\mathbf{J}^{-1}]_{PQ}, \quad (4.12)$$

where  $(pq|P)$  and  $(Q|rs)$  are three-index electron repulsion integrals defined as

$$(pq|P) = \int \phi_p(\mathbf{r}_1)\phi_q(\mathbf{r}_1) \frac{1}{r_{12}} \chi_P(\mathbf{r}_2) d\mathbf{r}_1 d\mathbf{r}_2, \quad (4.13)$$

and  $J_{PQ}$  is just the Coulomb metric evaluated in the auxiliary basis,

$$J_{PQ} = \int \chi_P(\mathbf{r}_1) \frac{1}{r_{12}} \chi_Q(\mathbf{r}_2) d\mathbf{r}_1 d\mathbf{r}_2. \quad (4.14)$$

Utilizing this expansion results the following approximation for the ERIs:

$$(pq|rs) \approx \sum_{PQ}^{N_{\text{aux}}} (pq|P)[\mathbf{J}^{-1}]_{PQ}(Q|rs). \quad (4.15)$$

The auxiliary basis set is typically optimized for a given level of theory (e.g., Hartree–Fock (HF) [59] or MP2 [63,64]). We can use a symmetric expression which splits the matrix  $\mathbf{J}^{-1}$  into a product  $\mathbf{J}^{-1/2}\mathbf{J}^{-1/2}$  to write

$$(pq|rs) \approx \sum_{PQR} (pq|P)[\mathbf{J}^{-1/2}]_{PQ}[\mathbf{J}^{-1/2}]_{QR}(R|rs). \quad (4.16)$$

This form is advantageous because it factorizes as

$$(pq|rs) \approx \sum_Q b_{pq}^Q b_{rs}^Q, \quad (4.17)$$

where

$$b_{pq}^Q = \sum_P (pq|P)[\mathbf{J}^{-1/2}]_{PQ}. \quad (4.18)$$

If the system studied is not so large that the 4-index ERI tensor becomes very sparse, the 3-index intermediates, having a smaller dimension than the original 4-index ERIs, require less storage. The integral  $(pq|Q)$  retains a permutational symmetry between the  $p$  and  $q$  indices, so that it requires  $N^2 N_{\text{aux}}/2$  elements in the absence of sparsity, which is a factor of  $N^2/4N_{\text{aux}}$  smaller than the original (dense) 4-index ERI tensor. Typically, even very accurate density fitting requires a basis set of auxiliary functions  $\{\chi_Q(\mathbf{r})\}$  that is only  $\sim 2$ – $4$  times larger than the primary basis set, so that storage is reduced by something like a factor of  $N/10$ . Even for modest systems ( $N \sim 1000$ ), this is a dramatic reduction in the size of the tensor. For smaller molecules, the 3-index intermediates may even fit in main memory, eliminating any input/output (I/O) associated with the ERIs. For larger molecules, there is still a large reduction in the size of the tensor stored on disk, and an associated reduction in the I/O costs. In addition to these advantages, the introduction of a new tensor index  $Q$  allows more flexibility in arranging the order of the tensor multiplications, and sometimes this can lead to reduced computational cost [65,66].

With appropriately chosen auxiliary basis sets, the errors introduced are quite modest, and they tend to cancel almost exactly when computing energy differences such as noncovalent interaction energies. For example, applying density fitting to the integrals used for the MP2 correlation energy introduces an error of  $-0.0001$  kcal/mol for the interaction energy of the sandwich benzene dimer [51], and density fitting the Hartree–Fock part of the computation increases this to only  $0.005$  kcal/mol, using the recommended auxiliary basis sets. However, density fitting substantially speeds up the MP2 procedure [61,67], as well as the Hartree–Fock procedure [59].

Cholesky decomposition (CD) is a technique from linear algebra to decompose a Hermitian, positive semidefinite matrix into a product of a lower triangular matrix and its conjugate transpose,  $\mathbf{A} = \mathbf{L}\mathbf{L}^\dagger$ . When  $\mathbf{A}$  is sparse, one can approximate it through an incomplete CD with a reduced number of columns in  $\mathbf{L}$ . That is,

$$A_{ij} \approx \sum_{Q=1}^K L_i^Q L_j^Q, \quad (4.19)$$

where  $K$  is the number of “Cholesky vectors” used (if we keep a number equal to the dimension of  $\mathbf{A}$ , then this is a complete CD and we recover  $\mathbf{A}$  exactly). We can apply these techniques to the ERI tensor if we consider  $(pq|rs)$  to be a 2D matrix with the row denoted by the composite index  $pq$  and the column to be denoted by the composite index  $rs$  [68–71]. This then results in a decomposition with the same form as Eq. (4.17), but with the three-index intermediates  $b_{pq}^Q$  now obtained from the CD procedure rather than from density fitting, and with  $Q$  indexing a Cholesky vector rather than an auxiliary basis function. The advantage of CD is that it can be carried to arbitrary precision. However, to achieve a comparable accuracy, typically about the same number of Cholesky vectors are needed as auxiliary basis functions in the density fitting approach. The recently introduced tensor hypercontraction (THC) approximation is similar in spirit to density fitting but it uses even lower-rank intermediates; it expresses the ERI tensor as a product of 5 rank-2 tensors [66,72,73].

Density fitting and related approaches have been effective for some of the lower-scaling quantum chemistry methods, including Hartree–Fock [59,70], density functional theory, second-order perturbation theory [56,70,74], and symmetry-adapted perturbation theory [11,75–77]. Until recently, such approaches have not been as commonly used for higher-scaling methods like coupled-cluster theory. DF/CD approaches do not reduce the computational scaling of coupled-cluster with single and double excitations (CCSD), but they remain promising for the possibility of reducing storage and file I/O costs for the ERIs. Several works [78–81] have examined the CD approximation in favor of the DF approximation because of the lack of RI auxiliary basis sets specific to coupled-cluster methods. For example, Boström used a CD factorization of the ERIs in conjunction with CCSD(T) to compute interaction energies for some of the S22 test set, finding errors on the order of 0.001 kcal/mol with a CD threshold of  $10^{-4}$ . DePrince and Sherrill [52] examined DF-CCSD using existing auxiliary basis sets and found it quite accurate, giving errors similar to those of CD with a  $10^{-4}$  cutoff, but with a slightly smaller number of auxiliary basis functions. Krylov and coworkers also examined DF/CD-CCSD, and they extended the DF/CD approaches to equation-of-motion CCSD for excited or ionized states [82].

Although DF/CD-CCSD reduces I/O costs substantially, this cost saving is partially counteracted by the repeated formation of the 4-virtual ERIs  $(ab|cd)$ , according to Eq. (4.17), as part of the rate-determining step of CCSD. With the ERIs available, the overall computational cost of this term is  $\mathcal{O}(\rho^2 v^4)$ . However, in density fitting, the cost of generating the  $(ab|cd)$  integrals with all virtual indices is  $\mathcal{O}(v^4 N_{\text{aux}})$ , which is quite costly for an overall  $\sim \mathcal{O}(N^5)$  step (for larger basis sets,  $v$  can be much larger than  $\rho$ , and can approach  $N$ ). Hence, DF/CD-CCSD is not necessarily faster than conventional CCSD on machines with fast local disks, e.g., two or more disks striped together (this is called a “redundant array of inexpensive disks” at level zero, RAID0).

However, an alternative approximation works very synergistically with DF/CD-CCSD: frozen natural orbitals. Natural orbitals (NOs) are those that diagonalize the one-particle density matrix [10], typically taken from a correlated computation like MP2. NOs corresponding to large eigenvalues contribute significantly to the correlation energy, whereas NOs with small eigenvalues contribute very little to the correlation energy. Indeed, a group of NOs with the smallest eigenvalues will contribute much less to the correlation energy than the same number of the highest-lying virtual molecular orbitals. Hence, NOs are a more suitable

basis set than MOs for truncating unimportant virtual orbitals with minimal errors in the energy [83–85]. “Frozen” natural orbitals are those where the occupied orbitals are fixed in their MO form: only the virtual orbitals are changed, by diagonalizing just the virtual–virtual block of the one-particle density matrix. Keeping canonical Hartree–Fock MOs for the occupied orbitals simplifies many-body perturbation theory or the calculation of the perturbative triples in CCSD(T). As an alternative to FNOs, the optimized virtual orbital space (OVOS) approach also provides compact virtual orbital spaces [86–88].

With FNOs, a significant fraction of the virtual orbitals can be eliminated while introducing very minor errors in the energy. Indeed, truncating NOs corresponding to eigenvalues of  $10^{-5}$  or less, and approximating the energy due to the deleted virtuals by their contributions to the MP2 energy, resulted in a mean absolute error of only 0.012 kcal/mol for  $\delta_{\text{MP2}}^{\text{CCSD(T)}}$ /aug-cc-pVDZ computations of the S22 test set [89]. However, this led to a 1.6x speedup for adenine–thymine dimer, and almost a 6x speedup for computations of the monomers in the dimer basis, as required for counterpoise correction. The latter speedup is larger because most of the ghost functions do not contribute significantly to the correlation energy, meaning they have very small eigenvalues and are deleted in the FNO procedure. Bigger speedups are possible with less conservative NO cutoffs; with a cutoff of  $10^{-4}$  for the eigenvalues, the MAE is still only 0.025 kcal/mol for the S22 test set, but the adenine–thymine speedups become 2.6x for the dimer and 6.7x for each of the monomers in the dimer basis.

FNOs therefore substantially boost the utility of the DF/CD approximations for coupled-cluster computations, because they significantly cut down the number of virtual orbitals and therefore the number of  $(ab|cd)$  integrals that need to be formed. Because the DF/CD errors are so tiny, the errors of the combined DF-FNO-CCSD(T) approach are typically dominated by the (small and controllable) FNO errors [52]. Even with a very conservative FNO cutoff of  $10^{-6}$ , the DF-FNO-CCSD(T)/aug-cc-pVDZ computation of the three-body contribution to the interaction energy of benzene trimer was 4x faster while yielding an error of only 0.0016 kcal/mol compared to the conventional CCSD(T) result [52]. An additional speedup of  $\sim 2$ – $3$ x is possible using graphics processing units (GPUs) [90]. These faster coupled-cluster algorithms helped enable the first definitive computation of three-body contributions to the lattice energy of crystalline benzene [91].

### 4.2.5 Explicitly Correlated Methods

Standard wavefunction methods have a hard time accurately representing the behavior of the many-electron wavefunction as two of the electrons (let us label them as electrons 1 and 2) begin to approach each other, i.e., when  $r_{12} \approx 0$ . One consequence of this is that highly accurate results can require large basis sets and/or large numbers of Slater determinants. Kato worked out how the wavefunction should behave at these Coulomb singularities, yielding the so-called cusp conditions [92]. In these regions, the wavefunction involves terms that are linear in  $r_{12}$  (as well as higher powers of  $r_{12}$ ). Such terms, as well as terms involving  $r_1 + r_2$  and  $r_1 - r_2$ , are also present in the highly accurate Hylleraas treatment of the helium atom [93]. Such work inspired the exploration of “explicitly correlated” methods that include interatomic distances like  $r_{12}$  in the expansion of the wavefunction. These methods are also known as R12 methods, or more recently, as F12 methods to emphasize the utility of going

beyond  $r_{12}$  to general functions of  $r_{12}$ , particularly short-range ones like the simple Slater correlation factor  $f_{12}(r_{12}) = e^{-\beta r_{12}}$  [94].

Introducing F12 factors into the wavefunction leads to rather complex expressions, and for a practical implementation, a number of approximations need to be made, such as the reduction of three- and four-electron integrals into products of two-electron integrals via the resolution of the identity in an auxiliary basis set [95,96]. Various choices for the additional approximations necessary lead to the variety of R12/F12 *ansätze* currently available. Explicitly correlated versions of many quantum chemistry methods have been developed, as discussed in recent review articles [97–99]. The main advantage of modern R12/F12 methods is that they substantially accelerate convergence toward the complete basis set limit, such that even relatively modest basis sets exhibit only small basis set errors.

Because MP2 can exhibit substantial errors for noncovalent interactions (see Section 4.1.1), F12 versions of standard MP2 are not especially helpful for high-accuracy studies. Indeed, for  $\pi$  interactions, MP2 interaction energy errors tend to *increase* as larger basis sets are used, so that acceleration to the CBS limit by F12 techniques is actually detrimental. F12 versions of more sophisticated MP2 techniques can be helpful, as discussed further below in Section 4.4.2.

More interesting are F12 versions of coupled-cluster methods [100–107]. In particular, the CCSD-F12a and CCSD-F12b approximations [103,105], and the CCSD(F12\*) approximation (also called CCSD-F12c) [107], have become popular in recent years. These methods are all very similar, and differ in details such as exactly how the F12 terms are allowed to couple to the equations determining the cluster amplitudes [105]. As with MP2, canonical CCSD is not especially accurate for noncovalent interactions, and hence approximating the CCSD/CBS limit via CCSD-F12 methods is not necessarily helpful (although it can be helpful for modified CCSD methods like spin-component-scaled CCSD, see Section 4.4 below). Unfortunately, at present there is not a widely available extension of F12 methods for the (T) perturbative triples correction. On the other hand, because (T) is just a single noniterative step performed after the CCSD equations are converged, one can still use CCSD-F12 and then perform a conventional (T) correction on top of it, to yield CCSD(T)-F12. To approximately account for the lack of explicit correlation in the (T) term, Werner and coworkers [105,108] introduced an improved triples correction that they call (T\*). This correction assumes that explicit correlation would magnify the conventional (T) correction by the same ratio as it magnifies the MP2 correlation energy:

$$E_{\text{corr}}^{(\text{T}^*)} = E_{\text{corr}}^{(\text{T})} \frac{E_{\text{corr}}^{\text{MP2-F12}}}{E_{\text{corr}}^{\text{MP2}}}. \quad (4.20)$$

In the context of computing noncovalent interaction energies, to preserve size-consistency it is helpful to use the same scaling ratio for monomer A, monomer B, and the dimer [108]; we denote the use of the dimer ratio for each component by (T\*\*). Although such scaling leads to high-quality estimates of the CCSD(T)/CBS limit, the lack of explicit correlation in the (T) term appears to be one of the largest sources of error in CCSD(T\*)-F12 or CCSD(T\*\*)-F12 [109,110].

In an early application of CCSD(T\*\*)-F12a, Marchetti and Werner [108] demonstrated interaction energies within 0.2 kcal/mol of the CCSD(T) limit using only an aDZ basis. Comparing to more accurate benchmark energies from the S22B revision of the data [40],

the mean absolute errors for CCSD(T\*\*) with F12a and F12b are only about 0.1 kcal/mol in this basis set [40]. In the aDZ basis, F12a tends to be slightly better than F12b for hydrogen bonded systems, whereas the reverse is true for dispersion-dominated or systems of mixed interaction type. This inspired the introduction of a “dispersion weighted” (DW) CCSD(T\*\*)-F12 that combines F12a and F12b results in a way that minimizes errors on average [111] (analogous to Marchetti and Werner’s dispersion-weighted MP2-F12 method [108] that mixes MP2-F12 with spin-component-scaled MP2-F12). For the S22B test set, the MAE of DW-CCSD(T\*\*)-F12/aDZ is only 0.05 kcal/mol.

Several additional works have examined the performance of CCSD(T)-F12 for noncovalent interactions in various test sets of van der Waals dimers [109,110,112,113]. Perhaps surprisingly, even though the cc-pVXZ-F12 basis sets of Peterson and coworkers [110,114,115] were developed specifically for use in post-Hartree–Fock F12 methods, interaction energies seem to be more accurately computed using the standard aug-cc-pVXZ basis sets [109,113]. CCSD(T)-F12a works well with an aDZ basis set, but for larger basis sets, it is inferior to F12b or F12c for interaction energies [109,113]. F12b and F12c tend to perform very similarly [109, 112,113].

Table 4.1 presents errors for CCSD(T\*\*)-F12 for the CH<sub>4</sub>...HF dimer. The F12a, F12b, and F12c approximations yield similar errors for the aDZ basis set (0.10–0.14 kcal/mol), which are much smaller than the conventional CCSD(T)/aDZ error of 0.62 kcal/mol. However, these errors are not as small as that of MP2/aTQZ +  $\delta_{\text{MP2}}^{\text{CCSD(T)}}$ /aDZ, which is 0.05 kcal/mol. On the other hand, for larger basis sets, the CCSD(T\*\*)-F12 errors essentially vanish, the one with the largest magnitude being –0.02 kcal/mol for CCSD(T\*\*)-F12a/aTZ. At least for this test case, CCSD(T\*\*) with the F12b or F12c approximations is just as good in the aTZ basis set as the MP2/aTQZ +  $\delta_{\text{MP2}}^{\text{CCSD(T)}}$ /aTZ focal-point estimate, but without the need for the MP2/aTQZ computations. This is very advantageous for the CCSD(T\*\*)-F12 approach, because the computation typically takes only around 30% longer than a conventional CCSD(T) computation when using the MOLPRO program [116]. Moreover, the CCSD(T\*\*)-F12a/b values in the aTZ basis are also better than a CCSD(T)/aTQZ extrapolation, which would be much more computationally expensive because it requires a CCSD(T) computation in the much larger aQZ basis set.

More generally, for the A24 test set [31], the MAE for CCSD(T\*\*) with any of the F12a, F12b, or F12c *ansätze* are in the range 0.04–0.06 kcal/mol for the aDZ basis set, and these all drop to 0.02 or less for the aTZ basis set [113]. By contrast, conventional CCSD(T) in these basis sets yields MAE of 0.38 and 0.12 kcal/mol for aDZ and aTZ, respectively, demonstrating the power of explicit correlation.

### 4.3 COUPLED-CLUSTER APPROACHES FOR LARGER SYSTEMS

Absent any complicating factors like partially filled *d* subshells that could lead to near-degeneracies among multiple electron configurations, CCSD(T) in a large basis set will yield reliable results for noncovalent interactions. As discussed above, focal-point approximations, explicitly correlated methods, and/or natural orbitals allow one to reduce the basis set requirements for the CCSD(T) computation, and density fitting can further speed up the



computation by reducing heavy I/O costs associated with the electron repulsion integrals. Nevertheless, these kinds of computations will still only be possible for small complexes (say, 60 atoms or less) unless more drastic approximations are employed.

### 4.3.1 Local Correlation Methods

Local correlation methods seek to reduce computational costs by transforming the Hartree–Fock orbitals to a spatially localized representation [117–120] and then asserting that electron motions should only be correlated for electrons that are near each other in space. Thus, for a double excitation  $ij \rightarrow ab$ , one requires that the occupied orbitals  $i$  and  $j$  are spatially close to each other. The Coulomb operator  $r_{ij}^{-1}$  that mediates the interaction between excitations  $i \rightarrow a$  and  $j \rightarrow b$  is sufficiently long-range that the energetic contributions for these double excitations do not start to vanish until around 15 bohr or more [61]. For shorter distances, one can use a hierarchy of approximations [121–123]: the closest pairs can be treated with a reliable level of theory such as coupled-cluster, more distant pairs can be treated by MP2, and even more distant pairs can be treated with multipole approximations to the relevant electron-repulsion integrals [124]. (More recent work suggests that using distances between occupied orbitals to decide whether to treat a pair with coupled-cluster, MP2, or multipoles is not as good as deciding this based on estimates of the pair correlation energy [123].) In addition to these approximations based on the proximity of local occupied orbitals  $i$  and  $j$ , one can also take advantage of the fact that the virtual orbitals  $a$  and  $b$  must also be close to  $i$  and  $j$ . (One might also attempt to take only  $a$  close to  $i$  and  $b$  close to  $j$ , but this neglects some ionic or charge-transfer contributions that can be important at about 8 bohr or less [124,125].)

Pulay and Saebø made seminal contributions to local electron correlation models in the 1980s and 1990s [121,125–127]. Their approach utilizes atomic orbitals for the virtual orbitals, which are already spatially localized; to keep the virtual orbital space orthogonal to the occupied orbital space, the occupied orbitals are projected out of the virtuals, leading to so-called “projected atomic orbitals” (PAOs) for the virtuals. These early studies indicated that the local correlation model tends to eliminate excitations that contribute to BSSE [128].

Due to the success of the Pulay–Saebø models, several other theorists contributed to local correlation and related methods in the 1990s and beyond (see, e.g., Refs. [129–132]). In particular, Werner, Schütz, and coworkers (sometimes in collaboration with Pulay) vigorously pursued computationally efficient local correlation approximations to MP2, CCSD, and CCSD(T) [123,124,133,134], including methods whose computational cost increases only linearly with the system size [122,135–137]. Many of these approaches have been combined with density fitting and/or Cholesky decomposition, and indeed often these approximations are synergistic (see, e.g., Ref. [61]).

As discussed above, natural orbitals (NOs) can be very helpful in reducing the size of the virtual space in coupled-cluster computations, and they can also be applied to local coupled-cluster methods. Neese and coworkers [138] revived the pair natural orbital (PNO) approach [139], which obtains natural orbitals for each pair of correlated electrons. This yields a highly compact virtual correlation space that is ultimately even more compact than the set of PAOs belonging to the pair domain in local methods of the Pulay–Saebø type. This “local pair natural orbital” (LPNO) approach, which couples local occupied orbitals with

PNOs for the virtual space of each pair, was introduced [138] for the coupled-electron pair approximation (CEPA) and quickly extended to CCSD [140]. Similar ideas were utilized in the “orbital-specific virtual” (OSV) scheme [141,142], which defines the virtual space for each individual orbital rather than for each pair of orbitals—this leads to certain simplifications, particularly in the integral transformation. While OSV-based local coupled-cluster was found to work well for barrier heights or reaction energies, it was noted that it is not necessarily more efficient than PAO-based local coupled-cluster when tight cutoffs are used, as can be required for applications to noncovalent interaction energies [141,142]. In addition, OSV-based local coupled-cluster seems to exhibit larger BSSE than when using PAOs [141,142].

Recently, the efficiency of LPNO-CC has been increased by generating the PNOs in the local pair domain of PAOs for each pair, rather than in the basis of the delocalized Hartree–Fock canonical orbitals. This yields the “domain-based” local pair natural orbital (DLPNO) approach, which was introduced in 2013 for CCSD and CCSD(T) [143,144]. Single excitations are truncated according to singles-specific NOs, and pairs are prescreened using a multipole expansion of a pair energy estimate based on OSVs. In a very impressive application, the DLPNO-CCSD(T) method was demonstrated for an entire protein, crambin [144].

Noncovalent interactions are particularly challenging for reduced-scaling CCSD(T) methods, because often the approximations one makes to reduce the computational costs are particularly deleterious for a subtle property like an interaction energy, which is typically a small number (several kcal/mol) resulting as the difference between very large total electronic energies (Eq. (4.1)). Even worse, the small, long-range pair energies eliminated in local correlation methods can be important contributors to the London dispersion forces between two molecules. It is hard to assess how well the local CCSD(T) methods perform for large complexes, because it is difficult or impossible to obtain conventional CCSD(T) results for comparison. For small systems, electron pairs may be too close to adequately test some of the local correlation approximations. Nevertheless, limited studies confirm that one must be cautious in attempting to employ local correlation models to interaction energies. In principle, accurate results can be recovered by using tighter cutoff values, but doing so of course increases the cost of the approach.

As discussed above, MP2 can substantially overbind in noncovalent interactions, particularly those involving aromatic rings. Hence, using MP2 to approximate more weakly correlated electron pairs can be problematic unless the interaction between pairs is quite weak. Schütz, Masur, and Usvyat reported large errors in the correlation contributions to interaction energies of  $\pi$ -stacked systems, and they proposed an alternative, more robust approximation for weak pairs that includes higher-order terms and more accurately reproduces results obtained when all pairs are treated at the local CCSD level [145].

DLPNO-CCSD(T) has also been examined, at least partially, for its ability to provide accurate noncovalent interaction energies. The method involves numerous approximations that may affect the quality of interaction energies. First, the triples correction mimics the “ $T_0$ ” treatment [136], which replaces the orbital energies of the occupied orbitals in the energy denominators with the diagonal Fock matrix elements  $F_{ii}$  (neglecting occupied–occupied couplings that arise in the local basis). This leads to small deviations for noncovalent interactions; the mean absolute error is 0.06 kcal/mol for the S66 test set with a cc-pVTZ basis without diffuse functions, although the differences approach 0.2 kcal/mol for some dimers [146]. Additionally, with the default thresholds for keeping PNOs or for assign-

ing a pair as a “strong pair” (to be computed using coupled-cluster instead of MP2), and other associated default thresholds, a standard deviation of 0.37 kcal/mol is observed for DLPNO-CCSD(T)/cc-pVTZ results vs. CCSD(T)<sub>0</sub>/cc-pVTZ results for S66. Using tighter cutoffs reduces this to 0.06 kcal/mol (with an MAE of 0.1 kcal/mol), but with an increase in computational cost of about 6 times for the case of pentane...neopentane [146]. It is not yet clear how discrepancies between DLPNO-CCSD(T) and canonical CCSD(T) might grow for larger systems.

Finally, various local correlation methods have also been combined with explicitly correlated methods discussed in Section 4.2.5 (typically also in concert with density fitting approximations). These include various types of density-fitted, F12-based local MP2 (DF-LMP2-F12) [147,148], F12-based local CCSD (LCCSD-F12) [149], and density-fitted local CCSD(T) using the T<sub>0</sub> approximation and the F12a and F12b *ansätze* (DF-LCCSD(T)<sub>0</sub>-F12a,b) [150]. An impressive application to the lattice energy of crystalline benzene by Chan and coworkers utilized an OSV-based LCCSD(T)<sub>0</sub>-F12 approach [151]. As in the nonlocal methods, the F12 terms accelerate convergence toward the complete basis set limit and provide greater accuracy for a given basis set.

### 4.3.2 The Many-Body Expansion

So far, we have been concerned with accurate computations of weakly interacting dimers. In principle, methods that work well for dimer interaction energies should also work well to describe the properties of single molecules that feature important noncovalent interactions. Indeed, the thermodynamics of hydrocarbon reactions seem to be predicted much more accurately by models capable of describing London dispersion forces [152]. However, methods specifically parameterized to reproduce dimer interaction energies, such as MP2 and CCSD using spin-component-scaling for molecular interactions (SCS(MI)) [153,154] (see Sections 4.4.2 and 4.4), could conceivably suffer degraded accuracy for single-molecule properties.

One might also wish to compute the energetics of clusters involving more than two monomers (or even lattice energies of molecular crystals, see Chapter 10). Suppose we have a trimer. The total energy of the trimer is approximately the sum of the monomer energies, plus the interaction energies between each pair of monomers. However, the energy is not quite pairwise-additive in this way. Usually the largest non-pairwise-additive effect is many-body induction/polarization (see Chapter 1). Monomer A may polarize monomer B, and that polarization can in turn affect the polarization of monomer B by monomer C, etc., so that in principle one must solve for polarization terms by a self-consistent procedure including coupling between all the pairwise polarizations. The part of a trimer energy that is not pairwise-additive is called the three-body contribution, and it is defined such that the total energy of the trimer is obtained as an identity:

$$E_{ABC}^{ABC} = \sum_A E_A^{ABC} + \sum_{A<B} \Delta E_{AB}^{ABC} + \Delta E_{ABC}^{ABC}, \quad (4.21)$$

where, as before, the superscripts denote that we are evaluating energies at the trimer geometry, and the subscripts denote the species for which the energy is evaluated, with  $A, B \in \{A, B, C\}$ .

The dimer interaction energies are defined, analogously to Eq. (4.1), as

$$\Delta E_{AB}^{ABC} = E_{AB}^{ABC} - E_A^{ABC} - E_B^{ABC}, \quad (4.22)$$

and the (nonadditive) three-body interaction then must be

$$\Delta E_{ABC}^{ABC} = E_{ABC}^{ABC} - \sum_A E_A^{ABC} - \sum_{A<B} \Delta E_{AB}^{ABC} \quad (4.23)$$

to recover the total energy of the trimer exactly. If we define the trimer interaction energy as the difference in energy between the trimer and the sum of the monomers,

$$\Delta E_{IE,ABC} = E_{ABC}^{ABC} - \sum_A E_A^{ABC}, \quad (4.24)$$

then the nonadditive three-body interaction energy is just the part of the overall interaction energy  $\Delta E_{IE,ABC}$  that does not come from the pairwise interactions,

$$\Delta E_{ABC}^{ABC} = \Delta E_{IE,ABC} - \sum_{A<B} \Delta E_{AB}^{ABC}. \quad (4.25)$$

Here we have ignored counterpoise corrections, but various schemes for counterpoise correction of clusters with three or more monomers have been proposed [155,156].

We can generalize our expression for trimers to a cluster of arbitrary size as

$$E_{ABC\dots D}^{ABC\dots D} = \sum_A E_A^{ABC\dots D} + \sum_{A<B} \Delta E_{AB}^{ABC\dots D} + \sum_{A<B<C} \Delta E_{ABC}^{ABC\dots D} + \dots + \Delta E_{ABC\dots D}^{ABC\dots D}, \quad (4.26)$$

where  $A, B, C \in \{A, B, C, \dots, D\}$ . Such an expansion is called the “many-body expansion,” which dates back to at least 1940 [157], and this or related “fragment methods” are currently being investigated by numerous researchers (see Chapter 14 and recent reviews in Refs. [158, 159]).

For molecular clusters, so long as polarization effects are not very large, it is generally thought that truncating this many-body expansion to include only monomers, dimers, and trimers is sufficient to yield fairly accurate results. In the event that four-body or higher effects are important, these would typically be polarization effects that should be adequately modeled at a low level of theory like Hartree–Fock, DFT, or even a polarizable force field (see Chapter 14). For high-accuracy work, it is desirable to use CCSD(T) if possible for the trimers; three-body dispersion is not captured by Hartree–Fock, DFT, or even by MP2 (although any of these models will reasonably capture three-body polarization, see Chapter 5). If CCSD(T) is not feasible for the trimers, then some other model of three-body dispersion should be employed, such as Axilrod–Teller–Muto expressions [160,161], if the monomers are close enough for three-body dispersion effects to be significant (although note that the approximate models can break down at sufficiently short distances).

Many-body expansions have been applied to estimate high-quality CCSD(T) results for energies and vibrational frequencies of clusters [162,163], and lattice energies of crystals [91, 151], among other applications.

## 4.4 EVALUATING APPROXIMATE METHODS

One of the benefits of highly accurate CCSD(T)/CBS interaction energies is that they may be used to assess and/or parameterize more efficient computational methods.

### 4.4.1 Databases of Benchmark Interaction Energies

To date, the majority of published benchmark-quality CCSD(T)/CBS interaction energies have been estimated using focal point approaches as described in Section 4.2.3. Initially these benchmarks utilized aDZ basis sets for the  $\delta_{\text{MP2}}^{\text{CCSD(T)}}$  correction, until it was shown [50,51] that this led to an error of nearly 0.1 kcal/mol for the parallel-displaced benzene dimer. Two-point extrapolations using the aDZ and aTZ basis sets were used in the S22A revision [164] of the interaction energies for the S22 test set [41], and this  $\delta_{\text{MP2}}^{\text{CCSD(T)}}$ /aDTZ scheme was adopted in a revision [165] of the energies for the popular S66 test set [166]. However, given occasional overestimations of correlation energies by the aDTZ extrapolation (because of the limited quality of the aDZ basis), unextrapolated  $\delta_{\text{MP2}}^{\text{CCSD(T)}}$ /aTZ values have since been recommended [40]. These corrections, added to MP2/aTQZ or MP2/aQ5Z estimates of the MP2/CBS limit, are expected to reduce errors vs. true CCSD(T)/CBS to less than 0.1 kcal/mol for small systems (errors will inevitably grow for larger systems).

There are several published test sets of small van der Waals complexes where the interaction energies have been computed using focal-point schemes similar to MP2/aTQZ +  $\delta_{\text{MP2}}^{\text{CCSD(T)}}$ /aTZ or better, which we will consider for the present discussion to be of “benchmark quality.” The S22 test set of Hobza and coworkers [41] collects 22 van der Waals dimers of various types and sizes, from water dimer to adenine...thymine. Although the original data used various approximations for the MP2 and CCSD(T) components of the energy due to limitations in software and hardware in 2006, the energies have since been revised [30, 40,164] to benchmark quality. The S66 test set, also by Hobza and coworkers [166], is similar in spirit to the S22 test set, but is expanded to 66 test cases; the revised energies [165] are also of benchmark quality. Several other test sets of similar quality have been published. The HBC6 test set [12,40] provides potential energy curves for six doubly hydrogen-bonded complexes with rather strong interaction energies. The NBC10 test set [40,51,167,168] provides potential energy curves for more weakly interacting systems like the benzene dimer, or benzene...methane. For the HSG test set [40,42] the complexes were taken directly from close contacts between the ligand indinavir and HIV-II protease. The A24 test set [31] consists of 24 very small complexes (e.g., water dimer), and very highly converged values are available for it, using basis sets larger than aTZ for the CCSD(T) computations, and with corrections for quadruple excitations, etc. The A21 test set of Patkowski and coworkers is similar but evaluates quadruple excitations in larger basis sets [28].

More recently, given the very good performance of explicitly correlated methods in smaller basis sets, some benchmarks have been established based on CCSD(T)-F12. As discussed in Section 4.2.5, even CCSD(T)-F12 cannot quite converge values within 0.1 kcal/mol of the CCSD(T)/CBS limit when using an aDZ basis set. However, dispersion weighting of the F12a and F12b values via DW-CCSD(T<sup>\*\*</sup>)-F12/aDZ appears to be able to do this in just an aDZ basis [111,113]. When CCSD(T)-F12 computations are possible with an aTZ basis or larger, they

should be of truly high quality (and indeed may be better than focal-point estimates based on  $\delta_{\text{MP2}}^{\text{CCSD(T)}/\text{aTZ}}$ ). DW-CCSD(T<sup>\*\*</sup>)-F12/aDZ has been used to efficiently compute high-quality benchmark energies for the 3380 members of the sidechain–sidechain (SSI) database [169]. Like the HSG database, the interacting fragments in SSI are taken directly from crystal structures—in this case, from contacts between sidechains in proteins. Smith and Patkowski [170] have presented focal-point benchmarks using  $\text{MP2/aTQZ} + \delta_{\text{MP2}}^{\text{CCSD(T}^{**}\text{)-F12b}/\text{aDTZ}}$  for methane interacting with benzene and naphthalene. Martin and coworkers [112] have obtained CCSD(T<sup>\*</sup>)-F12b/cc-pV5Z-F12 results for 7 of the smallest members of the S22×5 test set (based on S22, but with the monomers displaced at 0.9, 1.0, 1.2, 1.5, and 2.0 times the equilibrium intermonomer separation) [171]. Similarly, that group has also reported [172] CCSD(T)-F12 revisions of the S66×8 test set, which is S66 at 8 different intermolecular separations. Both of the latter studies also investigated possible combinations of CCSD(T)-F12 with focal-point schemes.

## 4.4.2 Methods Based on Møller–Plesset Perturbation Theory

### **Canonical MP2**

As seen in Section 4.1.1, MP2 can exhibit substantial errors for interaction energies, and it often overbinds complexes involving  $\pi$ -interactions. This has motivated substantial interest in MP2-like theories that might exhibit higher accuracy for noncovalent interactions while retaining a relatively low computational cost, at least compared to methods like CCSD(T). Table 4.3 presents mean absolute errors vs. the most accurate available data for the S22, NBC10, HBC6, and HSG test sets [40]. Consistent with our earlier discussion, Hartree–Fock and MP2 exhibit substantial errors. The Hartree–Fock errors are around 4 kcal/mol and are not improved with larger basis sets. The MP2 errors do improve somewhat with basis set, but remain 0.6 kcal/mol for aQZ; an MAE of this size is disappointing given the  $\mathcal{O}(N^5)$  computational cost of MP2 and the typically small values of the interaction energy. Additionally, errors for individual complexes can be substantially larger than this. MP2-F12 achieves MP2/aQZ quality using only an aDZ basis, and the MAE values are essentially identical when larger basis sets are used.

### **Spin-Component-Scaled MP2**

Grimme’s spin-component-scaled (SCS) MP2 [173] was initially greeted with significant optimism as a way to improve MP2 for a variety of properties, including interaction energies. This approach introduces separate scale factors for the correlation energy contributions coming from same-spin electrons and opposite-spin electrons, with the scale factors fitted to high-quality reaction energies. SCS-MP2 very impressively corrected the significant overbinding of the benzene dimer by MP2 [173], but later it was found to increase errors for systems that were treated well by canonical MP2, such as the methane dimer [167,174]. On average, SCS-MP2 is actually worse than MP2 for the test sets in Table 4.3. Although the errors are reduced by the use of large basis sets and/or F12 terms, they remain larger than the corresponding MP2 MAE values.

Other researchers reasoned that SCS parameters determined specifically for interaction energies would improve results. This led to the introduction of parameters optimized for

**TABLE 4.3** Mean absolute error (kcal/mol) for the interaction energy of MP2-based methods averaged over the S22, NBC10, HBC6, and HSG test sets<sup>a</sup>

Method X	aDZ	aTZ	MP2/aTQZ + $\delta_{\text{MP2}}^{\text{X}}/\text{aTZ}$	aQZ
HF	3.97	3.92		3.90
MP2	0.89	0.65		0.59
SCS-MP2	1.44	0.96		0.79
SCS(N)-MP2	0.33	0.32		0.37
SCS(MI)-MP2 <sup>b</sup>		0.29		0.26
DW-MP2	0.90	0.43		0.30
MP2C	0.89	0.28	0.14	0.15
MP3	1.30	0.73	0.46	
MP2.5	0.82	0.32	0.16	
MP2-F12	0.58	0.58		0.59
SCS-MP2-F12	0.71	0.69		0.68
SCS(N)-MP2-F12	0.38	0.38		0.38
SCS(MI)-MP2-F12 <sup>b</sup>		0.42		
DW-MP2-F12	0.27	0.25		0.25
MP2C-F12	0.13			

<sup>a</sup> All results counterpoise corrected. Each test set given equal weight. Data from Ref. [20].

<sup>b</sup> Using the cc-pVXZ basis sets rather than aug-cc-pVXZ. Not defined for cc-pVDZ.

nucleobase stacking (SCS(N)-MP2) [175], or for the S22 test set of molecular interactions (SCS(MI)-MP2) [153]. The latter method was parameterized specifically for nonaugmented cc-pVXZ basis sets, and only for cc-pVTZ or larger. Table 4.3 shows that, unlike the original parameters of SCS-MP2, the new parameters in SCS(N)-MP2 or SCS(MI)-MP2 are substantial improvements on average over MP2, leading to MAE of 0.3–0.4 kcal/mol. The parameterization makes these methods insensitive to basis set; indeed, F12 terms do not offer any improvement on average.

### Dispersion-Weighted MP2

Marchetti and Werner introduced “dispersion-weighted” (DW) MP2, which mixes MP2 and SCS-MP2 according to the type of intermolecular interaction [108]. For dispersion-dominated systems like the benzene dimer where SCS-MP2 provides substantial improvements, the SCS-MP2 interaction energy is weighted more heavily. Interaction type is quantified by the ratio of the Hartree–Fock and MP2 interaction energies, which will deviate from one as the dispersion contribution becomes larger. Table 4.3 shows that this approach is quite poor in the aDZ basis but becomes rather good with larger basis sets, achieving an MAE of 0.30 kcal/mol in the aQZ basis set. Given the basis set sensitivity of this approach and its improvement for larger basis sets, it is a good candidate for pairing with F12 techniques. The DW-MP2-F12 MAE are all 0.27–0.25 kcal/mol, and hence the aDZ basis seems sufficient. This makes DW-MP2-F12/aDZ competitive with SCS(N)-MP2 and SCS(MI)-MP2.

### Coupled MP2

The significant overbinding by MP2 for some polarizable systems like  $\pi$ -stacked systems has been attributed to the fact that the MP2 dispersion energy can be rewritten as an integral over frequency-dependent response functions for the monomers, and that these response functions are effectively determined for MP2 at the relatively unsophisticated uncoupled Hartree–Fock level [176]. Coupled response functions would be considerably more reliable. The “coupled” MP2 method (MP2C) computes independently the intermolecular dispersion part of an MP2 interaction energy (using symmetry-adapted perturbation theory), subtracts it from the MP2 interaction energy, and replaces it with a more reliable estimate based on time-dependent density functional theory [177]. Table 4.3 shows that very low MAEs are achieved if one uses basis sets larger than aDZ, reaching 0.28 and 0.15 kcal/mol for the aTZ and aQZ basis sets, respectively. It is possible to reach aQZ quality by a focal-point approach that uses MP2/CBS estimates based on an aTQZ extrapolation and then adds the difference between MP2 and MP2C as computed in an aTZ basis set (third numerical column of Table 4.3). Alternatively, F12 techniques are very effective for MP2C, and an MAE of only 0.13 kcal/mol is achieved for MP2C-F12/aDZ. This is the lowest MAE in Table 4.3.

### MP2.5

As MP2 tends to overbind van der Waals complexes, MP3 tends to underbind them. This inspired the introduction [178] of “MP2.5,” which is a simple average of the MP2 and MP3 interaction energies. MP3 is more expensive than MP2, with a computational cost of  $\mathcal{O}(N^6)$ , which is the same as that of CCSD except that MP3 is noniterative. Table 4.3 shows that MP2.5 is accurate for aTZ or larger basis sets, with focal-point estimates using a  $\delta_{\text{MP2}}^{\text{MP2.5}}/\text{aTZ}$  correction giving a very low MAE of 0.16 kcal/mol. This makes the approach competitive with some CCSD-based methods, discussed in the next section.

### 4.4.3 Methods Based on Coupled-Cluster Theory

CCSD, although it presents a substantially more sophisticated model of electron correlation than MP2, does not necessarily lead to improved interaction energies. Indeed, just as MP2 often overbinds dispersion-dominated complexes, CCSD can underbind by just as much. Additionally, both MP2 and CCSD often underbind hydrogen-bonded or other electrostatically dominated complexes [20]. Hence, analogous to efforts to improve MP2, investigations have sought to improve CCSD for noncovalent interactions. Table 4.4 presents MAE for some coupled-cluster based approaches for the S22, NBC10, HBC6, and HSG test sets [40].

From the Table we see that canonical CCSD is uniformly poor, even worse on average than canonical MP2. It is quite sensitive to basis set, but even focal-point estimates yield an MAE of 0.68 kcal/mol.

### Spin-Component-Scaled CCSD

Takatani et al. [179] introduced spin-component scaling techniques into coupled-cluster singles and doubles, yielding the SCS-CCSD method. They obtained parameters by fitting to reaction energies, as done originally by Grimme for SCS-MP2 [173]. SCS-CCSD is quite good as part of a focal point scheme, with  $\text{MP2/aTQZ} + \delta_{\text{MP2}}^{\text{SCS-CCSD}}/\text{aTZ}$  yielding an MAE of



**TABLE 4.4** Mean absolute error (kcal/mol) for the interaction energy of coupled-cluster methods averaged over the S22, NBC10, HBC6, and HSG test sets<sup>a</sup>

Method X	aDZ	aTZ	MP2/aTQZ + $\delta_{MP2}^X/aTZ$
CCSD	1.55	1.03	0.68
SCS-CCSD	1.16	0.53	0.20
SCS(MI)-CCSD	0.96	0.37	0.06
CCSD(T)	0.96	0.35	0.01 <sup>b</sup>
CCSD-F12a	0.71		
CCSD-F12b	0.84		
SCS-CCSD-F12a	0.18		
SCS-CCSD-F12b	0.31		
SCS(MI)-CCSD-F12a	0.04		
SCS(MI)-CCSD-F12b	0.16		
CCSD(T**)-F12a	0.10		
CCSD(T**)-F12b	0.09		
DW-CCSD(T**)-F12	0.05		

<sup>a</sup> All results counterpoise corrected. Each test set given equal weight. Data from Ref. [20].

<sup>b</sup> This is essentially the level of theory used for the benchmarks (except for some higher-quality data for S22B). See Ref. [40].

only 0.20 kcal/mol, which is surpassed only by the very best MP2-type methods in Table 4.3. However, it is quite sensitive to basis set, giving much larger errors for the aDZ and aTZ basis sets (1.16 and 0.53 kcal/mol, respectively). It is a good candidate for explicit correlation techniques, and we see that SCS-CCSD-F12a and -F12b yield MAE of 0.18 and 0.31 kcal/mol, respectively, using the modest aDZ basis set.

Much as SCS(N)-MP2 and SCS(MI)-MP2 improved over SCS-MP2 by obtaining parameters from interaction energies rather than from reaction energies, Hobza and coworkers reparameterized SCS-CCSD to reproduce interaction energies for the S22 database, yielding the SCS(MI)-CCSD approach [154]. Of course, fitting the parameters to interaction energies may degrade the accuracy of these methods for other properties, such as reaction energies. Table 4.4 shows significant improvements of SCS(MI)-CCSD vs. the original parameters of SCS-CCSD when computing interaction energies over a diverse set of interaction motifs. Focal point estimates of SCS(MI)-CCSD/CBS give an incredibly low MAE of 0.06 kcal/mol, and explicit correlation using the F12a or F12b methods gives MAE of 0.04 and 0.16 kcal/mol, respectively, in the aDZ basis set. Hence, any of these approaches seems quite reliable for interaction energies.

### Canonical CCSD(T)

Table 4.4 displays the previously discussed basis set sensitivity of CCSD(T), with an MAE of nearly 1 kcal/mol for the aDZ basis, and 0.35 kcal/mol for the aTZ basis. Hence, approximate methods like MP2C or MP2.5 can actually be more reliable than CCSD(T) unless the CCSD(T) computations use a basis set better than aTZ (or, alternatively, focal-point tech-

**TABLE 4.5** Mean absolute error (kcal/mol) for the interaction energy of SAPT and DFT methods averaged over the S22, NBC10, HBC6, and HSG test sets<sup>a</sup>

Method	aDZ	aTZ
sSAPT0/jaDZ	0.44	
SAPT2+(3) $\delta$ MP2	0.52	0.16
B97-D3	0.49	0.28
B3LYP-D3	0.72	0.36
M06-2X	0.50	0.34
$\omega$ B97X-D	0.79	0.34

<sup>a</sup> No counterpoise correction applied. Data from Ref. [20].

niques, basis set extrapolation, or explicit correlation). However, CCSD(T\*\*) with F12a or F12b yields quite low MAE of about 0.1 kcal/mol in just the aDZ basis set.

### Dispersion-Weighted CCSD(T)

The previously discussed DW-CCSD(T\*\*)-F12 approach further improves over CCSD(T\*\*)-F12a and CCSD(T\*\*)-F12b for the test sets considered in Table 4.4, yielding a very impressive MAE of 0.05 kcal/mol in the aDZ basis.

## 4.4.4 Comparison to Density-Functional Theory and Symmetry-Adapted Perturbation Theory

To conclude this chapter, it is interesting to compare some of the best wavefunction-based approaches to some of the best approaches from DFT or SAPT. DFT has a significant speed advantage over most of the methods discussed in this chapter, and SAPT has the advantage that it provides not just the interaction energy, but also its breakdown into electrostatics, dispersion, induction/polarization, and exchange-repulsion. These approaches are further discussed in Chapters 2, 5, 6, and 8.

Table 4.5 presents MAEs for some of the better DFT and SAPT methods for the same test sets used in Tables 4.3 and 4.4. SAPT0/jaDZ denotes Hartree–Fock-based SAPT plus second-order dispersion and exchange-dispersion; jaDZ is a shorthand for the jun-cc-pVDZ basis [180], which is aug-cc-pVDZ minus diffuse functions on hydrogen and diffuse *d* functions on heavy atoms. This basis set was found to exhibit surprisingly good error cancellation with SAPT0. The “s” prefix in sSAPT0 denotes “scaled” SAPT [181], where we have scaled the exchange-dispersion and exchange-induction cross-terms by a factor meant to correct for errors in the so-called  $S^2$  or “single-exchange” approximation. We see that sSAPT0/jaDZ provides an MAE of 0.44 kcal/mol for this test set, not among the lowest MAE, but better than many more costly wavefunction methods. It is certainly sufficient for meaningful energy component analysis, and is quite good when considering that SAPT0, when based on density fitting, is extremely efficient and can be applied to at least 400 atoms on a single workstation [182]. SAPT2+(3) $\delta$ MP2 denotes a high-order SAPT method with an MP4-like treatment of intramolecular correlation, and some intermolecular terms included through third order;  $\delta$ MP2 corrects the MP2-analogous portion to exactly reproduce the MP2 interaction energy,

which implicitly includes some higher-order terms [65,181]. This SAPT approach is sensitive to the basis set, and the aDZ results are actually not as good on average as the much simpler sSAPT0/jaDZ results. However, for the aTZ basis, quite accurate results are obtained (MAE 0.16 kcal/mol).

The selected dispersion-corrected density functional theory methods are competitive with many of the much more expensive wavefunction methods considered in this chapter, with MAE of 0.5–0.8 kcal/mol for aDZ and 0.3–0.4 kcal/mol for aTZ. While not ultimately as accurate as the very best wavefunction methods (and hence not suitable for benchmarking purposes), these methods should be quite suitable for routine applications to noncovalent interactions.

## Acknowledgments

The author thanks Dr. Lori Burns, Dr. Ryan Richard, Dominic Sirianni, and Trent Parker for assistance in preparing this chapter. He also gratefully acknowledges support from the U.S. National Science Foundation through grant CHE-1566192.

## References

- [1] R.S. Morgan, C.E. Tatsh, R.H. Gushard, J.M. Mcadon, P.K. Warne, *Int. J. Pept. Protein Res.* 11 (1978) 209–217.
- [2] R.J. Zauhar, C.L. Colbert, R.S. Morgan, W.J. Welsh, *Biopolymers* 53 (2000) 233–248.
- [3] K.S.C. Reid, P.F. Lindley, J. Thornton, *FEBS Lett.* 190 (1985) 209–213.
- [4] A.L. Ringer, A. Senenko, C.D. Sherrill, *Protein Sci.* 16 (2007) 2216–2223.
- [5] H.M. Berman, J. Westbrook, Z. Feng, G. Gilliland, T.N. Bhat, H. Weissig, I.N. Shindyalov, P.E. Bourne, *Nucleic Acids Res.* 28 (2000) 235–242.
- [6] T.P. Tauer, M.E. Derrick, C.D. Sherrill, *J. Phys. Chem. A* 109 (2005) 191–196.
- [7] T.H. Dunning, *J. Chem. Phys.* 90 (1989) 1007–1023.
- [8] R.A. Kendall, T.H. Dunning, R.J. Harrison, *J. Chem. Phys.* 96 (1992) 6796–6806.
- [9] K. Raghavachari, G.W. Trucks, J.A. Pople, M. Head-Gordon, *Chem. Phys. Lett.* 157 (1989) 479–483.
- [10] A. Szabo, N.S. Ostlund, *Modern Quantum Chemistry: Introduction to Advanced Electronic Structure Theory*, McGraw-Hill, New York, 1989.
- [11] E.G. Hohenstein, C.D. Sherrill, *J. Chem. Phys.* 133 (2010) 014101.
- [12] K.S. Thanthiriwatte, E.G. Hohenstein, L.A. Burns, C.D. Sherrill, *J. Chem. Theory Comput.* 7 (2011) 88–96.
- [13] A.D. Becke, *J. Chem. Phys.* 98 (1993) 1372–1377.
- [14] P.J. Stephens, F.J. Devlin, C.F. Chabalowski, M.J. Frisch, *J. Phys. Chem.* 98 (1994) 11623–11627.
- [15] C. Lee, W. Yang, R.G. Parr, *Phys. Rev. B* 37 (1988) 785–789.
- [16] S. Kristyán, P. Pulay, *Chem. Phys. Lett.* 229 (1994) 175–180.
- [17] S. Tsuzuki, H.P. Lüthi, *J. Chem. Phys.* 114 (2001) 3949–3957.
- [18] E.R. Johnson, R.A. Wolkow, G.A. DiLabio, *Chem. Phys. Lett.* 394 (2004) 334–338.
- [19] J.M. Turney, et al., *WIREs Comput. Mol. Sci.* 2 (2012) 556–565.
- [20] L.A. Burns, M.S. Marshall, C.D. Sherrill, *J. Chem. Phys.* 141 (2014) 234111.
- [21] S.F. Boys, F. Bernardi, *Mol. Phys.* 19 (1970) 553–566.
- [22] A. Halkier, W. Klopper, T. Helgaker, P. Jørgensen, P.R. Taylor, *J. Chem. Phys.* 111 (1999) 9157–9167.
- [23] L.A. Burns, M.S. Marshall, C.D. Sherrill, *J. Chem. Theory Comput.* 10 (2014) 49–57.
- [24] K.S. Kim, B.J. Mhin, U.-S. Choi, K. Lee, *J. Chem. Phys.* 97 (1992) 6649–6662.
- [25] I.D. Mackie, G.A. DiLabio, *J. Chem. Phys.* 135 (2011) 134318.
- [26] T.J. Lee, G.E. Scuseria, in: S.R. Langhoff (Ed.), *Quantum Mechanical Electronic Structure Calculations with Chemical Accuracy*, Kluwer Academic Publishers, Dordrecht, 1995, pp. 47–108.
- [27] B.W. Hopkins, G.S. Tschumper, *J. Phys. Chem. A* 108 (2004) 2941–2948.
- [28] D.G.A. Smith, P. Jankowski, M. Slawik, H.A. Witek, K. Patkowski, *J. Chem. Theory Comput.* 10 (2014) 3140.

- [29] J. Řezáč, M. Dubecký, P. Jurečka, P. Hobza, *Phys. Chem. Chem. Phys.* 17 (2015) 19268.
- [30] R. Podeszwa, K. Patkowski, K. Szalewicz, *Phys. Chem. Chem. Phys.* 12 (2010) 5974–5979.
- [31] J. Řezáč, P. Hobza, *J. Chem. Theory Comput.* 9 (2013) 2151–2155.
- [32] D. Feller, *J. Chem. Phys.* 98 (1993) 7059–7071.
- [33] A. Halkier, T. Helgaker, P. Jørgensen, W. Klopper, J. Olsen, *Chem. Phys. Lett.* 302 (1999) 437–446.
- [34] F. Jensen, *Theor. Chem. Acc.* 113 (2005) 267.
- [35] A. Halkier, T. Helgaker, P. Jørgensen, W. Klopper, H. Koch, J. Olsen, A.K. Wilson, *Chem. Phys. Lett.* 286 (1998) 243–252.
- [36] M.R. Nynden, G.A. Petersson, *J. Chem. Phys.* 75 (1981) 1843.
- [37] J.M.L. Martin, *Chem. Phys. Lett.* 259 (1996) 669.
- [38] D.G. Truhlar, *Chem. Phys. Lett.* 294 (1998) 45–48.
- [39] J.G. Hill, K.A. Peterson, G. Knizia, H.-J. Werner, *J. Chem. Phys.* 131 (2009) 194105.
- [40] M.S. Marshall, L.A. Burns, C.D. Sherrill, *J. Chem. Phys.* 135 (2011) 194102.
- [41] P. Jurečka, J. Šponer, J. Černý, P. Hobza, *Phys. Chem. Chem. Phys.* 8 (2006) 1985–1993.
- [42] J.C. Faver, M.L. Benson, X. He, B.P. Roberts, B. Wang, M.S. Marshall, M.R. Kennedy, C.D. Sherrill, K.M. Merz, *J. Chem. Theory Comput.* 7 (2011) 790–797.
- [43] A.L.L. East, W.D. Allen, *J. Chem. Phys.* 99 (1993) 4638–4650.
- [44] A.G. Császár, W.D. Allen, H.F. Schaefer, *J. Chem. Phys.* 108 (1998) 9751–9764.
- [45] H. Koch, B. Fernández, O. Christiansen, *J. Chem. Phys.* 108 (1998) 2784–2790.
- [46] S. Tsuzuki, K. Honda, T. Uchimaru, M. Mikami, K. Tanabe, *J. Am. Chem. Soc.* 124 (2002) 104–112.
- [47] M.O. Sinnokrot, E.F. Valeev, C.D. Sherrill, *J. Am. Chem. Soc.* 124 (2002) 10887–10893.
- [48] P. Jurečka, P. Hobza, *Chem. Phys. Lett.* 365 (2002) 89–94.
- [49] M.O. Sinnokrot, C.D. Sherrill, *J. Phys. Chem. A* 108 (2004) 10200–10207.
- [50] T. Janowski, P. Pulay, *Chem. Phys. Lett.* 447 (2007) 27–32.
- [51] C.D. Sherrill, T. Takatani, E.G. Hohenstein, *J. Phys. Chem. A* 113 (2009) 10146–10159.
- [52] A.E. DePrince, C.D. Sherrill, *J. Chem. Theory Comput.* 9 (2013) 2687–2696.
- [53] B.W. Bakr, C.D. Sherrill, *Phys. Chem. Chem. Phys.* 18 (2016) 10297–10308.
- [54] J.L. Whitten, *J. Chem. Phys.* 58 (1973) 4496–4501.
- [55] B.I. Dunlap, J.W.D. Connolly, J.R. Sabin, *J. Chem. Phys.* 71 (1979) 3396–3402.
- [56] M. Feyereisen, G. Fitzgerald, A. Komornicki, *Chem. Phys. Lett.* 208 (1993) 359–363.
- [57] O. Vahtras, J. Almlöf, M.W. Feyereisen, *Chem. Phys. Lett.* 213 (1993) 514–518.
- [58] A.P. Rendell, T.J. Lee, *J. Chem. Phys.* 101 (1994) 400–408.
- [59] F. Weigend, *Phys. Chem. Chem. Phys.* 4 (2002) 4285–4291.
- [60] A. Sodt, J.E. Subotnik, M. Head-Gordon, *J. Chem. Phys.* 125 (2006) 194109.
- [61] H.-J. Werner, F.R. Manby, P.J. Knowles, *J. Chem. Phys.* 118 (2003) 8149–8160.
- [62] B.I. Dunlap, J.W.D. Connolly, J.R. Sabin, *Int. J. Quantum Chem. Symp.* 11 (1977) 81.
- [63] F. Weigend, M. Haser, H. Patzelt, R. Ahlrichs, *Chem. Phys. Lett.* 294 (1998) 143–152.
- [64] F. Weigend, A. Köhn, C. Hättig, *J. Chem. Phys.* 116 (2002) 3175–3183.
- [65] E.G. Hohenstein, C.D. Sherrill, *WIREs Comput. Mol. Sci.* 2 (2012) 304–326.
- [66] E.G. Hohenstein, R.M. Parrish, T.J. Martínez, *J. Chem. Phys.* 137 (2012) 044103.
- [67] R.A. Kendall, H.A. Fruchtl, *Theor. Chem. Acc.* 97 (1997) 158–163.
- [68] N.H.F. Beebe, J. Linderberg, *Int. J. Quant. Chem.* 12 (1977) 683–705.
- [69] I. Roeggen, E. Wisloff-Nilssen, *Chem. Phys. Lett.* 132 (1986) 154–160.
- [70] H. Koch, A.S. de Meras, T.B. Pedersen, *J. Chem. Phys.* 118 (2003) 9481–9484.
- [71] F. Aquilante, T.B. Pedersen, R. Lindh, *J. Chem. Phys.* 126 (2007) 194106.
- [72] R.M. Parrish, E.G. Hohenstein, T.J. Martínez, C.D. Sherrill, *J. Chem. Phys.* 137 (2012) 224106.
- [73] E.G. Hohenstein, R.M. Parrish, C.D. Sherrill, T.J. Martínez, *J. Chem. Phys.* 137 (2012) 221101.
- [74] D.E. Bernholdt, R.J. Harrison, *Chem. Phys. Lett.* 250 (1996) 477–484.
- [75] A. Heßelmann, G. Jansen, M. Schütz, *J. Chem. Phys.* 122 (2005) 014103.
- [76] A.J. Misquitta, R. Podeszwa, B. Jeziorski, K. Szalewicz, *J. Chem. Phys.* 123 (2005) 214103.
- [77] E.G. Hohenstein, C.D. Sherrill, *J. Chem. Phys.* 132 (2010) 184111.
- [78] T.B. Pedersen, A.M.J. Sánchez de Merás, H. Koch, *J. Chem. Phys.* 120 (2004) 8887–8897.
- [79] M. Pitonak, F. Aquilante, P. Hobza, P. Neogrady, J. Noga, M. Urban, *Collect. Czechoslov. Chem. Commun.* 76 (2011) 713–742.

- [80] F. Aquilante, L.D. Vico, N. Ferre, G. Ghigo, P. Malmqvist, P. Neogrady, T.B. Pedersen, M. Pitonak, M. Reiher, B.O. Roos, L. Serrano-Andres, M. Urban, V. Veryazov, R. Lindh, *J. Comput. Chem.* 31 (2010) 224–247.
- [81] J. Boström, M. Pitoňák, F. Aquilante, P. Neogrady, T.B. Pedersen, R. Lindh, *J. Chem. Theory Comput.* 8 (2012) 1921–1928.
- [82] E. Epifanovsky, D. Zuev, X. Feng, K. Khistyayev, Y. Shao, A.I. Krylov, *J. Chem. Phys.* 139 (2013) 134105.
- [83] C. Sosa, J. Geersten, G.W. Trucks, R.J. Bartlett, J.A. Franz, *Chem. Phys. Lett.* 159 (1989) 148–154.
- [84] W. Klopper, J. Noga, H. Koch, T. Helgaker, *Theor. Chem. Acc.* 97 (1997) 164–176.
- [85] A.G. Taube, R.J. Bartlett, *Collect. Czechoslov. Chem. Commun.* 70 (2005) 837–850.
- [86] L. Adamowicz, R.J. Bartlett, *J. Chem. Phys.* 86 (1987) 6314–6324.
- [87] P. Neogrady, M. Pitoňák, M. Urban, *Mol. Phys.* 103 (2005) 2141–2157.
- [88] P. Dedíková, M. Pitoňák, P. Neogrady, I. Černušák, M. Urban, *J. Phys. Chem. A* 112 (2008) 7115–7123.
- [89] A.E. DePrince, C.D. Sherrill, *J. Chem. Theory Comput.* 9 (2013) 293–299.
- [90] A.E. DePrince, M.R. Kennedy, B.G. Sumpter, C.D. Sherrill, *Mol. Phys.* 112 (2014) 844–852.
- [91] M.R. Kennedy, A. Ringer McDonald, A.E. DePrince, M.S. Marshall, R. Podeszwa, C.D. Sherrill, *J. Chem. Phys.* 140 (2014) 121104.
- [92] T. Kato, *Commun. Pure Appl. Math.* 10 (1957) 151–177.
- [93] E.A. Hylleraas, *Z. Phys.* 54 (1929) 347.
- [94] S. Ten-no, *Chem. Phys. Lett.* 398 (2004) 56–61.
- [95] W. Kutzelnigg, W. Klopper, *J. Chem. Phys.* 94 (1991) 1985–2001.
- [96] W. Klopper, C.C.M. Samson, *J. Chem. Phys.* 116 (2002) 6397–6410.
- [97] L. Kong, F.A. Bischoff, E.F. Valeev, *Chem. Rev.* 112 (2012) 75–107.
- [98] J. Noga, W. Klopper, W. Kutzelnigg, in: R.J. Bartlett (Ed.), *Recent Advances in Coupled-Cluster Methods*, in: *Recent Advances in Computational Chemistry*, vol. 3, World Scientific, Singapore, 1997, pp. 1–48.
- [99] W. Klopper, F.R. Manby, S. Ten-no, E.F. Valeev, *Int. Rev. Phys. Chem.* 25 (2006) 427–468.
- [100] J. Noga, W. Kutzelnigg, W. Klopper, *Chem. Phys. Lett.* 199 (1992) 497–504.
- [101] J. Noga, W. Kutzelnigg, *J. Chem. Phys.* 101 (1994) 7738–7762.
- [102] H. Fliegl, W. Klopper, C. Hättig, *J. Chem. Phys.* 122 (2005) 084107.
- [103] T.B. Adler, G. Knizia, H.-J. Werner, *J. Chem. Phys.* 127 (2007) 221106.
- [104] J. Noga, S. Kedzuch, J. Simunek, S. Ten-no, *J. Chem. Phys.* 128 (2008) 174103.
- [105] G. Knizia, T.B. Adler, H.-J. Werner, *J. Chem. Phys.* 130 (2009) 054104.
- [106] T. Shiozaki, E.F. Valeev, S. Hirata, *J. Chem. Phys.* 131 (2009) 044118.
- [107] C. Hättig, D.P. Tew, A. Kohn, *J. Chem. Phys.* 132 (2010) 231102.
- [108] O. Marchetti, H.-J. Werner, *J. Phys. Chem. A* 113 (2009) 11580–11585.
- [109] K. Patkowski, *J. Chem. Phys.* 138 (2013) 154101.
- [110] K.A. Peterson, M.K. Kesharwani, J.M.L. Martin, *Mol. Phys.* 113 (2015) 1551–1558.
- [111] M.S. Marshall, C.D. Sherrill, *J. Chem. Theory Comput.* 7 (2011) 3978–3982.
- [112] B. Brauer, M.K. Kesharwani, J.M.L. Martin, *J. Chem. Theory Comput.* 10 (2014) 3791–3799.
- [113] D.A. Sirianni, L.A. Burns, C.D. Sherrill, *J. Chem. Theory Comput.* 13 (2017) 86–99.
- [114] K.A. Peterson, T.B. Adler, H.-J. Werner, *J. Chem. Phys.* 128 (2008) 084102.
- [115] J.G. Hill, S. Mazumder, K.A. Peterson, *J. Chem. Phys.* 132 (2010) 054108.
- [116] H.-J. Werner, P.J. Knowles, F.R. Manby, M. Schütz, P. Celani, G. Knizia, T. Korona, R. Lindh, A. Mitrushenkov, G. Rauhut, T.B. Adler, R.D. Amos, A. Bernhardsson, A. Berning, D.L. Cooper, M.J.O. Deegan, A.J. Dobbyn, F. Eckert, E. Goll, C. Hampel, A. Hesselmann, G. Hetzer, T. Hrenar, G. Jansen, C. Köppl, Y. Liu, A.W. Lloyd, R.A. Mata, A.J. May, R. Tarroni, T. Thorsteinsson, M. Wang, A. Wolf, MOLPRO, version 2010.1, a package of ab initio programs, see <http://www.molpro.net>.
- [117] S.F. Boys, in: P.-O. Löwdin (Ed.), *Quantum Theory of Atoms, Molecules, and the Solid State*, Academic Press, New York, 1966, pp. 253–262.
- [118] J. Pipek, P.G. Mezey, *J. Chem. Phys.* 90 (1989) 4916–4926.
- [119] C. Edmiston, K. Ruedenberg, *J. Chem. Phys.* 43 (1965) S097–S116.
- [120] G. Knizia, *J. Chem. Theory Comput.* 9 (2013) 4834–4843.
- [121] S. Saebø, P. Pulay, *J. Chem. Phys.* 86 (1987) 914–922.
- [122] M. Schutz, G. Hetzer, H.-J. Werner, *J. Chem. Phys.* 111 (1999) 5691–5705.
- [123] M. Schwilk, D. Usvyat, H.-J. Werner, *J. Chem. Phys.* 142 (2015) 121102.
- [124] G. Hetzer, P. Pulay, H.-J. Werner, *Chem. Phys. Lett.* 290 (1998) 143–149.

- [125] S. Saebø, P. Pulay, *Chem. Phys. Lett.* 113 (1985) 13–18.
- [126] P. Pulay, *Chem. Phys. Lett.* 100 (1983) 151–154.
- [127] S. Saebø, P. Pulay, *Annu. Rev. Phys. Chem.* 44 (1993) 213–236.
- [128] S. Saebø, W. Tong, P. Pulay, *J. Chem. Phys.* 98 (1993) 2170–2176.
- [129] P.E. Maslen, M. Head-Gordon, *Chem. Phys. Lett.* 283 (1998) 102–108.
- [130] G.E. Scuseria, P.Y. Ayala, *J. Chem. Phys.* 111 (1999) 8330–8343.
- [131] T.S. Chwee, A.B. Szilva, R. Lindh, E.A. Carter, *J. Chem. Phys.* 128 (2008) 224106.
- [132] J.J. Eriksen, P. Baudin, P. Ettenhuber, K. Kristensen, T. Kjaergaard, P. Jørgensen, *J. Chem. Theory Comput.* 11 (2015) 2984–2993.
- [133] C. Hampel, H.-J. Werner, *J. Chem. Phys.* 104 (1996) 6286–6297.
- [134] G. Rauhut, P. Pulay, H.-J. Werner, *J. Comput. Chem.* 19 (1998) 1241–1254.
- [135] G. Hetzer, M. Schütz, H. Stoll, H.-J. Werner, *J. Chem. Phys.* 113 (2000) 9443–9455.
- [136] M. Schütz, *J. Chem. Phys.* 113 (2000) 9986–10001.
- [137] M. Schütz, H.-J. Werner, *J. Chem. Phys.* 114 (2001) 661–681.
- [138] F. Neese, F. Wennmohs, A. Hansen, *J. Chem. Phys.* 130 (2009) 114108.
- [139] C. Edmiston, M. Krauss, *J. Chem. Phys.* 42 (1965) 1119–1120.
- [140] F. Neese, A. Hansen, D.G. Liakos, *J. Chem. Phys.* 131 (2009) 064103.
- [141] J. Yang, G.K.L. Chan, F.R. Manby, M. Schütz, H.-J. Werner, *J. Chem. Phys.* 136 (2012) 144105.
- [142] M. Schütz, J. Yang, G.K.L. Chan, F.R. Manby, H.-J. Werner, *J. Chem. Phys.* 138 (2013) 054109.
- [143] C. Riplinger, F. Neese, *J. Chem. Phys.* 138 (2013) 034106.
- [144] C. Riplinger, B. Sandhoefer, A. Hansen, F. Neese, *J. Chem. Phys.* 139 (2013) 134101.
- [145] M. Schütz, O. Masur, D. Usvyat, *J. Chem. Phys.* 140 (2014) 244107.
- [146] D.G. Liakos, M. Sparta, M.K. Kesharwani, J.M.L. Martin, F. Neese, *J. Chem. Theory Comput.* 11 (2015) 1525–1539.
- [147] F.R. Manby, H.-J. Werner, T.B. Adler, A.J. May, *J. Chem. Phys.* 124 (2006) 094103.
- [148] T.B. Adler, H.-J. Werner, F.R. Manby, *J. Chem. Phys.* 130 (2009) 054106.
- [149] T.B. Adler, H.-J. Werner, *J. Chem. Phys.* 130 (2009) 241101.
- [150] T.B. Adler, H.-J. Werner, *J. Chem. Phys.* 135 (2011) 144117.
- [151] J. Yang, W. Hu, D. Usvyat, D. Matthews, M. Schuetz, G.K. Chan, *Science* 345 (2014) 640–643.
- [152] S.N. Steinmann, M.D. Wodrich, C. Corminboeuf, *Theor. Chem. Acc.* 127 (2010) 429–442.
- [153] R.A. Distasio, M. Head-Gordon, *Mol. Phys.* 105 (2007) 1073–1083.
- [154] M. Pitoňák, J. Řezáč, P. Hobza, *Phys. Chem. Chem. Phys.* 12 (2010) 9611–9614.
- [155] B.H. Wells, S. Wilson, *Chem. Phys. Lett.* 101 (1983) 429–434.
- [156] P. Valiron, I. Mayer, *Chem. Phys. Lett.* 275 (1997) 46–55.
- [157] J.E. Mayer, M.G. Mayer, *Statistical Mechanics*, John Wiley & Sons, Inc., London, England, 1940.
- [158] R.M. Richard, J.M. Herbert, *J. Chem. Phys.* 137 (2012) 064113.
- [159] M.S. Gordon, D.G. Fedorov, S.R. Pruitt, L.V. Slipchenko, *Chem. Rev.* 112 (2012) 632–672.
- [160] B.M. Axilrod, E. Teller, *J. Chem. Phys.* 11 (1943) 299–300.
- [161] Y. Muto, *J. Phys.-Math. Soc. Jpn.* 17 (1943) 629.
- [162] S. Yoo, E. Aprà, X.C. Zeng, S.S. Xantheas, *J. Phys. Chem. Lett.* 1 (2010) 3122–3127.
- [163] J.C. Howard, G.S. Tschumper, *J. Chem. Theory Comput.* 11 (2015) 2126–2136.
- [164] T. Takatani, E.G. Hohenstein, M. Malagoli, M.S. Marshall, C.D. Sherrill, *J. Chem. Phys.* 132 (2010) 144104.
- [165] J. Řezáč, K.E. Riley, P. Hobza, *J. Chem. Theory Comput.* 7 (2011) 3466–3470.
- [166] J. Řezáč, K.E. Riley, P. Hobza, *J. Chem. Theory Comput.* 7 (2011) 2427–2438.
- [167] T. Takatani, C.D. Sherrill, *Phys. Chem. Chem. Phys.* 9 (2007) 6106–6114.
- [168] E.G. Hohenstein, C.D. Sherrill, *J. Phys. Chem. A* 113 (2009) 878–886.
- [169] L.A. Burns, J.C. Faver, Z. Zheng, M.S. Marshall, D.G.A. Smith, K. Vanommeslaeghe, A.D. MacKerell, K.M. Merz, C.D. Sherrill, submitted for publication.
- [170] D.G.A. Smith, K. Patkowski, *J. Chem. Theory Comput.* 9 (2013) 370–389.
- [171] L. Gráfová, M. Pitoňák, J. Řezáč, P. Hobza, *J. Chem. Theory Comput.* 6 (2010) 2365–2376.
- [172] B. Brauer, M.K. Kesharwani, S. Kozuch, J.M.L. Martin, *Phys. Chem. Chem. Phys.* 472 (2016) 72–80.
- [173] S. Grimme, *J. Chem. Phys.* 118 (2003) 9095–9102.
- [174] J. Antony, S. Grimme, *J. Phys. Chem. A* 111 (2007) 4862–4868.
- [175] J.G. Hill, J.A. Platts, *J. Chem. Theory Comput.* 3 (2007) 80–85.

- [176] S.M. Cybulski, M.L. Lytle, *J. Chem. Phys.* 127 (2007) 141102.
- [177] A. Hesselmann, *J. Chem. Phys.* 128 (2008) 144112.
- [178] M. Pitoňák, P. Neogrady, J. Černý, S. Grimme, P. Hobza, *ChemPhysChem* 10 (2009) 282–289.
- [179] T. Takatani, E.G. Hohenstein, C.D. Sherrill, *J. Chem. Phys.* 128 (2008) 124111.
- [180] E. Papajak, J. Zheng, X. Xu, H.R. Leverentz, D.G. Truhlar, *J. Chem. Theory Comput.* 7 (2011) 3027–3034.
- [181] T.M. Parker, L.A. Burns, R.M. Parrish, A.G. Ryno, C.D. Sherrill, *J. Chem. Phys.* 140 (2014) 094106.
- [182] E.G. Hohenstein, R.M. Parrish, C.D. Sherrill, J.M. Turney, H.F. Schaefer, *J. Chem. Phys.* 135 (2011) 174107.

# The Exchange-Hole Dipole Moment Dispersion Model

*Erin R. Johnson*

Department of Chemistry, Dalhousie University, Halifax, NS, Canada

## 5.1 THE PERTURBATION THEORY OF DISPERSION

### 5.1.1 The London and Salem Models

Fritz London presented his theory of the dispersion interaction in 1930 [1]. This classic model is based on the picture of weakly-interacting instantaneous dipole moments in the electron distribution of separated atoms or molecules. London's dispersion model, together with a later theory from Salem [2], form the historical underpinnings of the exchange-hole dipole moment (XDM) dispersion model.

Consider two spherically symmetric atoms, *A* and *B*, separated by a large internuclear distance *R*. Due to the motion of the electrons, instantaneous dipole moments will arise in the electron distribution of each atom, as shown in Fig. 5.1. The dipoles in atoms *A* and *B* are aligned along the vectors  $\mathbf{r}_A$  and  $\mathbf{r}_B$ , respectively, defined relative to the atomic nuclei. The radial components of these dipole moments are given by  $M_1(r_A)$  and  $M_1(r_B)$ .

The interaction energy can be evaluated using perturbation theory, with the noninteracting atomic wavefunctions as the unperturbed reference state. The reader is directed to Chapter 1 for an in-depth discussion of the perturbation theory of intermolecular interactions. In the present case, the perturbation is given in terms of the magnitudes of the two dipole moments and is dependent on their relative orientations,

$$V_{1,1} = \frac{M_1(r_A)M_1(r_B)}{R^3} (\hat{\mathbf{r}}_A \cdot \hat{\mathbf{r}}_B - 3 \cos \theta_A \cos \theta_B), \quad (5.1)$$

where  $\hat{\mathbf{r}}_A$  and  $\hat{\mathbf{r}}_B$  are the unit vectors in the directions of the two dipoles and  $\theta_A$  and  $\theta_B$  are the angles of these vectors with respect to the line A–B between the two nuclei. The first-order energy correction is zero for neutral, spherically-symmetric charge distributions (see Chapter 1). Using second-order perturbation theory, the leading-order contribution to the



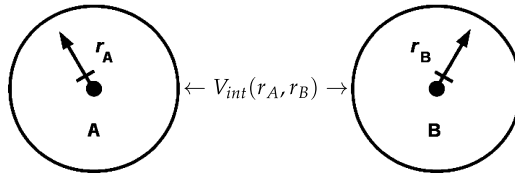


FIGURE 5.1 Interacting instantaneous dipoles in separated atoms.

dispersion energy is

$$E_{\text{disp}} = -\frac{C_6}{R^6}. \quad (5.2)$$

The closure approximation is made to avoid an explicit sum over excited atomic states. Within this approximation, the  $C_6$  dispersion coefficient is given in terms of expectation values of the instantaneous dipole moments and average atomic excitation energy ( $\epsilon$ ) denominators:

$$C_6 = \frac{2}{3} \frac{\langle M_1^2 \rangle_A \langle M_1^2 \rangle_B}{\epsilon_A + \epsilon_B}. \quad (5.3)$$

The average excitation energy, for each atom (A or B) is formally

$$\epsilon = \sum_{i=1}^N \frac{\epsilon_i}{N}, \quad (5.4)$$

where the sum runs over all possible atomic excitations. The dipole-moment expectation values are integrals evaluated over the atomic charge distribution for each atom,

$$\langle M_1^2 \rangle = \sum_{\sigma} \int \rho_{\sigma}(\mathbf{r}) M_1^2(r) d\mathbf{r}, \quad (5.5)$$

where  $\rho_{\sigma}$  is the  $\sigma$ -spin electron density.

Within the closure approximation, second-order perturbation theory also provides an analogous expression for the polarizability of an isolated atom in terms of the same dipole-moment integral and average atomic excitation energy:

$$\alpha = \frac{2}{3} \frac{\langle M_1^2 \rangle}{\epsilon}. \quad (5.6)$$

London used this result to eliminate the moments from Eq. (5.3) to obtain a formula for the interatomic  $C_6$  dispersion coefficient in terms of the free atomic polarizabilities and average excitation energies, which were taken to be equal to the atomic ionization potentials:

$$C_6 = \frac{3}{2} \alpha_A \alpha_B \left( \frac{\epsilon_A \epsilon_B}{\epsilon_A + \epsilon_B} \right). \quad (5.7)$$

This model performs reasonably well for atomic dispersion coefficients and results for noble-gas dimers will be compared with those from more recently-developed models in Section 5.1.3.

In 1960, Salem presented an alternative dispersion model in which the second-order perturbation theory of polarizability is used to eliminate the average excitation energies from Eq. (5.3) in favor of the dipole moments [2]. The magnitude of instantaneous dipole moment, written as  $\mu$  in this model, is simply evaluated as the distance between the reference electron and the nucleus, or  $\mu = -r$ , and the required  $\langle M_1^2 \rangle$  integral becomes

$$\langle \mu^2 \rangle = \sum_{\sigma} \int \rho_{\sigma}(\mathbf{r}) r^2 d\mathbf{r}. \quad (5.8)$$

The resulting expression for the  $C_6$  dispersion coefficient is

$$C_6 = \frac{\alpha_A \alpha_B \langle \mu^2 \rangle_A \langle \mu^2 \rangle_B}{\alpha_A \langle \mu^2 \rangle_B + \alpha_B \langle \mu^2 \rangle_A}, \quad (5.9)$$

and this formula can be evaluated for isolated atoms or molecules given only the electron density and either computed or reference polarizabilities.

Despite its theoretical elegance, the Salem model provides significantly worse dispersion coefficients than the original London model, as will be seen in Section 5.1.3. However, the formalism of the Salem model invites the question of whether one could propose an improved definition of the instantaneous dipole moments in order to obtain improved dispersion coefficients.

### 5.1.2 The Exchange-Hole Dipole Moment Model

The key idea behind the XDM model is that the dipole moment between a reference electron and its corresponding exchange hole is taken as the source of the instantaneous dipole moments that give rise to dispersion interactions [3,4].

The exchange hole is a fundamental construct in density-functional theory (DFT) [5]. The hole describes the depletion in density associated with finding a second same-spin electron (at position  $\mathbf{r}_2$ ) in the vicinity of a reference electron (at position  $\mathbf{r}_1$ ), relative to a classical electronic distribution:

$$h_{X\sigma}(\mathbf{r}_1, \mathbf{r}_2) = -\frac{1}{\rho_{\sigma}(\mathbf{r}_1)} \sum_{ij} \psi_{i\sigma}(\mathbf{r}_1) \psi_{j\sigma}(\mathbf{r}_1) \psi_{i\sigma}(\mathbf{r}_2) \psi_{j\sigma}(\mathbf{r}_2). \quad (5.10)$$

This equation is valid for a single-Slater-determinant reference state and the sum runs over the occupied,  $\sigma$ -spin Hartree-Fock (HF) or Kohn-Sham orbitals,  $\psi_{i,\sigma}$ .

The exchange hole arises from the Pauli exclusion principle and ensures that there is zero probability of finding a second same-spin electron at the reference point:

$$h_{X\sigma}(\mathbf{r}_1, \mathbf{r}_1) = -\rho_{\sigma}(\mathbf{r}_1). \quad (5.11)$$

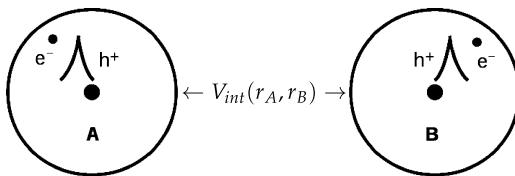


FIGURE 5.2 Interacting exchange-hole dipoles in separated atoms.

The exchange hole is normalized to  $-1$  electron,

$$\int h_{X\sigma}(\mathbf{r}_1, \mathbf{r}_2) d\mathbf{r}_2 = -1, \quad (5.12)$$

but is not spherically symmetric, in general. Thus, taken together, the reference electron and the exchange hole have zero net charge but a nonzero dipole moment.

Consider the behavior of the exchange hole for a reference electron in an isolated atom [6]. In the high-density core regions, the exchange hole will be centered near the reference electron, although it will be displaced slightly toward the nucleus, where the density is highest. In regions of low density, more distant from the nucleus, the exchange hole will remain centered on the atom and this will give rise to a significant dipole moment between the electron and hole, as sketched in Fig. 5.2. The interaction between such moments in two separated atoms will result in dispersion attraction.

The exchange-hole dipole moment at each reference point,  $\mathbf{r}_1$ , in space is obtained by integrating Eq. (5.10) over the coordinate  $\mathbf{r}_2$ :

$$\mathbf{d}_{X\sigma}(\mathbf{r}_1) = \left[ \frac{1}{\rho_{\sigma}(\mathbf{r}_1)} \sum_{ij} \psi_{i\sigma}(\mathbf{r}_1) \psi_{j\sigma}(\mathbf{r}_1) \int \mathbf{r}_2 \psi_{i\sigma}(\mathbf{r}_2) \psi_{j\sigma}(\mathbf{r}_2) d\mathbf{r}_2 \right] - \mathbf{r}_1. \quad (5.13)$$

Using this model, the  $\langle M_1^2 \rangle$  expectation values appearing in the definition of the  $C_6$  dispersion coefficient (Eq. (5.3)) are now replaced with the corresponding expectation values involving the exchange-hole dipole moment:

$$\langle d_X^2 \rangle = \sum_{\sigma} \int \rho_{\sigma}(\mathbf{r}) d_{X\sigma}^2(\mathbf{r}) d\mathbf{r}. \quad (5.14)$$

This gives a formula for the dispersion coefficient that is analogous to Eq. (5.9), with the classical dipole moments,  $\mu$ , replaced by the exchange-hole dipole moments,  $d_X$ :

$$C_6 = \frac{\alpha_A \alpha_B \langle d_X^2 \rangle_A \langle d_X^2 \rangle_B}{\alpha_A \langle d_X^2 \rangle_B + \alpha_B \langle d_X^2 \rangle_A}. \quad (5.15)$$

This model allows the dispersion coefficients to be computed for any atom or molecule given only the occupied atomic orbitals and polarizabilities.

**TABLE 5.1** Comparison of  $C_6$  dispersion coefficients, in atomic units, for selected homoatomic pairs. Reference atomic ionization potentials and polarizabilities are used [10]. Values of the moments were computed from fully-numerical Hartree–Fock calculations on the atoms [4]. Reference dispersion coefficients were taken from Ref. [11], except for H and He, the values for which were taken from Refs. [12] and [13], respectively

Atom pairs	London Eq. (5.7)	Salem Eq. (5.9)	XDM Eq. (5.15)	Reference value
H <sub>2</sub>	7.59	6.75	6.75	6.49
He <sub>2</sub>	1.29	1.64	1.64	1.46
Ne <sub>2</sub>	4.24	12.5	5.83	6.55
Ar <sub>2</sub>	53.42	144.4	62.73	64.54
Kr <sub>2</sub>	108.6	331.7	132.1	135.1
Xe <sub>2</sub>	249.5	855.8	304.7	302.3
MA%E <sup>a</sup>	19.7	93.2	5.5	—

<sup>a</sup> The MA%E is the mean absolute percent error.

XDM can be viewed as a semiclassical model of dispersion. The interaction is treated using a classical multipole expansion, but the values of the multipole moments are determined quantum mechanically, rather than classically, as in Salem’s model. The use of the exchange hole in the definition of the moments builds in the effect of Pauli repulsion, which accounts for the majority of the exchange-correlation effects between same-spin electrons [4]. Since the exchange hole integrates to  $-1$  electron, while the correlation hole integrates to zero [5], the exchange hole is the dominant contribution to the full atomic exchange-correlation hole and is therefore expected to be the dominant contribution to the dipole moment of the exchange-correlation hole as well [4].

Since the initial proposal of XDM, Angyan [7], Ayers [8], and Heßelmann [9] have each derived a formula for the dispersion coefficient in terms of the exchange hole from first principles that is similar in form to Eqs. (5.9) and (5.15). However, the derived result is intermediate between the XDM and Salem dispersion models, such that the multipole moments are given by  $\langle \mu d_X \rangle$  rather than  $\langle d_X^2 \rangle$ . Thus, while there is some rigorous theoretical justification for taking the exchange-hole dipole moment as the source of the dispersion interaction, the XDM formulae have not yet been derived from first principles and this approach remains a model, albeit one with a strong physical motivation.

### 5.1.3 Comparison of Atomic Dispersion Coefficients

To compare the performance of the London, Salem, and XDM models for atomic dispersion coefficients, the homoatomic  $C_6$  coefficients for hydrogen and the noble gas atoms are shown in Table 5.1.

The London model is found to overestimate the  $C_6$  for hydrogen and underestimate the dispersion coefficients for the noble gases. This is to be expected due to the assumption that the average atomic excitation energies could be approximated by the ionization potential. For hydrogen, there are many bound excited states with energies lower than the ionization

potential. However, for the noble-gas atoms, the average excitation energies will be higher than the ionization potential due to contributions from the excitations of core electrons.

The Salem and XDM models, which use dipole-moment integrals rather than ionization potentials in computation of the dispersion coefficients, give identical results for hydrogen and helium. For hydrogen specifically, the Hartree–Fock density used for the calculations will be exact, so the only approximation made in determination of the  $C_6$  is the closure (Un-söld) approximation. The result of 6.75 a.u. is in good agreement with the reference value of 6.49 a.u., but is not exact, implying that improvements to the XDM model could still be made if the closure approximation were avoided.

Beyond helium, the Salem model gives very poor dispersion coefficients that are much worse than the London model, while XDM maintains good performance. To understand the divergence between the Salem and XDM models beyond helium, consider the differences in definition of the dipole moments. In the Salem model, an electron at a distance  $r$  from the nucleus gives a dipole moment of  $\mu = -r$ . This can be viewed as the dipole moment for classical or uncorrelated electrons, since the distribution of the remaining electrons in the atom is not taken into account. Conversely, in XDM, the use of the exchange hole in the definition of the multipole moments introduces the quantum-mechanical effect of exchange on the electron distribution [4]. Both models necessarily give the same results for atoms with only  $s$  electrons because there is only a single electron of a given spin. In this case, the exchange hole remains centered at the nucleus regardless of the choice of reference point and  $\mu = d_X$ . However, for atoms with electrons of higher angular momenta, the density maximum is displaced from the nucleus. Consequently, the exchange hole will also be displaced from the nucleus and centered closer to the reference electron, so  $|d_X| < |\mu|$ . Thus, going down the group of noble gases, the uncorrelated moments become much larger than the XDM moments. The latter is clearly a better approximation, since using the uncorrelated moments causes increasing overestimation of the  $C_6$  coefficients for heavier atoms.

#### 5.1.4 Exact Versus Density-Functional Hole Models

In the preceding description of the XDM model, the exact (or Hartree–Fock) exchange hole was used to generate the dipole and higher-order multipole moments responsible for dispersion. The exact exchange hole,  $h_{X\sigma}(\mathbf{r}_1, \mathbf{r}_2)$ , is an inherently nonlocal function of two electron coordinates and involves a summation over all of the occupied atomic or molecular orbitals. While the exact exchange-hole dipole moment is simple to compute for small molecules, the nonlocality of the hole makes its evaluation impractical for very large molecules or periodic systems. As such, replacing the use of the exact exchange hole in XDM with a semi-local density-functional exchange-hole model greatly eases computations, in particular for solid-state applications.

Preliminary tests of the XDM model used the exact (Hartree–Fock) exchange hole [3,14–17], while subsequent work used the Becke–Roussel [6] (BR) exchange-hole model [18–29]. The latter is a density-functional model of the spherically-averaged exchange hole that depends on the electron density ( $\rho_\sigma$ ), the density gradient ( $\nabla\rho_\sigma$ ) and Laplacian ( $\nabla^2\rho_\sigma$ ), and the kinetic-

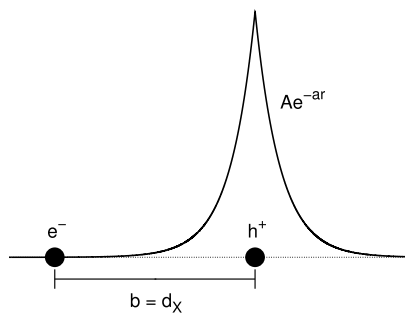


FIGURE 5.3 Sketch of the BR exchange hole.

energy density ( $\tau_\sigma$ ), which is given in terms of the occupied orbitals,

$$\tau_\sigma = \sum_i |\nabla\phi_{i,\sigma}|^2, \quad (5.16)$$

and is defined without the  $1/2$  factor. The energy functional resulting from the BR model can be classified as a meta-GGA functional.

With the BR functional, the (spherically-averaged) exchange hole is modeled as an off-center exponential function of the form  $Ae^{-ar}$  centered a distance  $b$  from the position of the reference electron, as shown in Fig. 5.3. The BR exchange hole is exact for the hydrogen atom by construction because, for single-electron atoms, the exchange hole will be the negative of the atomic density, which has the form of a single exponential function. The BR model has also been demonstrated to be an excellent approximation to the exact exchange hole for many-electron atoms [6].

In this model, the values of the three parameters, the exponent  $a$ , normalization  $A$ , and displacement  $b$ , must be determined for each reference point by imposing three known constraints on the hole. The three constraints selected [6] are that the model hole must:

1. Be normalized to  $-1$  electron (Eq. (5.12)),
2. Deplete to the spin density at the reference point (Eq. (5.11)),
3. Have the same curvature as the exact exchange hole at the reference point, which is given by [6]

$$Q_\sigma = \frac{1}{6} \left[ \nabla^2 \rho_\sigma - 2\tau_\sigma + \frac{1}{2} \frac{(\nabla \rho_\sigma)^2}{\rho_\sigma} \right]. \quad (5.17)$$

The normalization constraint fixes the value of  $A$ ,

$$A = -\frac{a^3}{8\pi}, \quad (5.18)$$

while the density constraint gives

$$\rho_\sigma = \frac{a^3}{8\pi} e^{-ab}, \quad (5.19)$$

and the curvature constraint gives

$$Q_\sigma = \frac{\rho_\sigma}{6b} (a^2b - 2a). \quad (5.20)$$

The values of  $a$  and  $b$  are fixed by solving the nonlinear equation resulting from combining Eqs. (5.19) and (5.20) for  $x = ab$ ,

$$\frac{x e^{-2x/3}}{(x-2)} = \frac{2}{3} \pi^{2/3} \frac{\rho_\sigma^{5/3}}{Q_\sigma}, \quad (5.21)$$

following which  $b$  is obtained from a rearrangement of Eq. (5.19),

$$b^3 = \frac{x^3 e^{-x}}{8\pi\rho_\sigma}. \quad (5.22)$$

As shown in Fig. 5.3 the exchange hole dipole moment is simply the distance between the reference electron and the center of the hole, which is equal to  $b$  in this model. In general, the exchange-hole dipole moment should never exceed the value of the uncorrelated moment, or  $b \leq r$ . Spuriously high values of the exchange-hole dipole moment, such that  $b > r$ , can occasionally be obtained, and these are replaced with  $b = r$  as the appropriate limiting value [26].

Like all density-functional exchange models, the BR approach captures some effects of electron correlation by assuming that the exchange hole is localized to a region of roughly atomic size [30]. In contrast, the exact exchange hole is delocalized over all the constituent atoms [31]. As such, using the BR exchange hole may offer a better approximation to the atomic contributions to the combined exchange-correlation-hole dipole moment in molecules, and hence an improved description of atom-in-molecule dispersion coefficients. However, for isolated atoms, the exact exchange hole is already localized and the resulting moments should offer the more accurate dispersion coefficients.

### 5.1.5 The dDsC Exchange-Hole Model

A method related to XDM is the density-dependent correction (dDsC) model of Steinmann and Corminboeuf [32–34]. This model is based on a simplification of the Becke–Roussel exchange hole that involves only the electron density and gradient and does not require the Laplacian or kinetic-energy density. This further simplifies the computation of the exchange-hole dipole moments used in the definition of the XDM dispersion coefficients.

The starting point of the dDsC model is the definition of the BR exchange-hole dipole moment, given by taking the cube root of Eq. (5.22):

$$b = \frac{x e^{-x/3}}{(8\pi\rho_\sigma)^{1/3}}. \quad (5.23)$$

Rather than using an explicitly asymmetric exchange hole that recovers the curvature of the exact hole, this model makes use of an interpolation between the symmetric exchange hole resulting from the local-density approximation (for zero density gradient) and a modified BR

hole at large density gradients [32]. The expression for the exchange-hole dipole moment is rewritten in terms of the Wigner–Seitz radius,

$$r_s = \left( \frac{3}{4\pi\rho} \right)^{\frac{1}{3}}, \quad (5.24)$$

and the reduced density gradient,

$$s = \frac{1}{2(3\pi^2)^{1/3}} \frac{|\nabla\rho|}{\rho^{4/3}}, \quad (5.25)$$

by assuming a linear relation between the parameter  $x$  and the reduced density gradient,  $x = C \cdot s$ . Because atomic densities are piecewise exponential, the reduced density gradient typically increases as the reference point moves away from a molecule. Similarly, the exchange hole dipole moment will increase for reference points farther away from a molecule since the exchange hole will remain centered near regions of high electron density. Making the assumption of a linear relation between  $x$  and  $s$  in Eq. (5.22) gives the following result for the exchange-hole dipole moment:

$$b = Ar_s s e^{-Bs}, \quad (5.26)$$

where  $A$  and  $B$  are constants that are treated as empirical parameters in the model [32]. The assumed linear relation between  $x$  and  $s$  transforms the BR model into a simpler GGA model that permits evaluation of the exchange-hole dipole moment from only the electron density and its reduced gradient. The resulting  $b$  values may then be used directly in the XDM equations ((5.14) and (5.15)) to obtain the multipole-moment integrals and dispersion coefficients.

The values of  $A$  and  $B$  were fit to minimize the errors in the computed  $C_6$  dispersion coefficients for the homoatomic noble-gas pairs (He–Kr). The resulting values were quite close to  $A = 2$  and  $B = 1$ , so these integer values were adopted in the model [32]. One consequence of treating these constants as empirical parameters is that it causes the density constraint to be relaxed and the model hole will no longer deplete to the spin density at the reference point. While adding empiricism, the relaxation of this constraint could allow the dDsC hole model to capture some further effects of electron correlation, which serve to further deepen and localize the hole. The dDsC model was demonstrated to perform well for molecular  $C_6$  dispersion coefficients and was extensively benchmarked for both intra- and intermolecular dispersion interactions [33].

## 5.2 THE XDM DISPERSION ENERGY

### 5.2.1 Higher-Order Dispersion Coefficients

The XDM model can easily be generalized to describe higher-order terms in the dispersion-energy expansion by including interactions beyond dipole–dipole [4,15]. For the moment, it is assumed that the two interacting atoms are infinitely-separated, although finite separations will be considered when interacting atoms within molecules are discussed in Section 5.2.2. In



the extended perturbation-theory treatment, as described in Chapter 1, the interaction,  $V_{AB}$ , between atoms  $A$  and  $B$  is given by a sum of dipole–dipole and higher-order multipole–multipole interactions:

$$V_{AB} = V_{1,1} + V_{1,2} + V_{2,1} + V_{1,3} + V_{3,1} + V_{2,2} + \dots \quad (5.27)$$

This sum can be expressed simply as a multipolar expansion over the two atomic sites [35]:

$$V_{AB}(\mathbf{r}_A, \mathbf{r}_B) = \sum_{l_A l_B=1}^{\infty} \frac{V_{l_A l_B}(\mathbf{r}_A, \mathbf{r}_B)}{R^{l_A+l_B+1}}. \quad (5.28)$$

The subscripts on each term  $V_{l_A, l_B}$  indicate interactions between the  $l_A$ -pole moments in atom  $A$  and the  $l_B$ -pole moments in atom  $B$ . All terms that contribute to orders  $R^{-3}$ ,  $R^{-4}$ , and  $R^{-5}$  are explicitly included in Eq. (5.27). Even higher-order terms beyond  $R^{-5}$  can also be modeled, but are generally neglected in XDM since they do not contribute significantly to the dispersion energy [24]. The individual terms in  $V_{AB}$  depend on the magnitudes of the instantaneous dipole ( $M_1$ ), quadrupole ( $M_2$ ), and octopole ( $M_3$ ) moments, for each atom, as well as their relative orientations.

The second-order perturbation-theory treatment gives the following sum-over-states expression for the dispersion energy,

$$E_{\text{disp}}^{(2)} = - \sum_{mn \neq 0} \frac{\langle 00 | V_{AB} | mn \rangle \langle mn | V_{AB} | 00 \rangle}{\varepsilon_A^m + \varepsilon_B^n}, \quad (5.29)$$

where  $m$  and  $n$  run over the possible excited states of atoms  $A$  and  $B$ , with excitation energies  $\varepsilon_A^m$  and  $\varepsilon_B^n$ , respectively. Using the closure (Unsöld) approximation, in which the individual atomic excitation energies are replaced by average energies  $\varepsilon_A$  and  $\varepsilon_B$ , Eq. (5.29) reduces to [35]

$$E_{\text{disp}}^{(2)} = - \frac{1}{\varepsilon_A + \varepsilon_B} \sum_{l_A l_B=1}^{\infty} \frac{\lambda_{l_A l_B} \langle M_{l_A}^2 \rangle_A \langle M_{l_B}^2 \rangle_B}{R^{2(l_A+l_B+1)}}. \quad (5.30)$$

The subscripts  $l_A$  and  $l_B$  again refer to the order of the multipole and the coefficients are

$$\lambda_{l_A, l_B} = \frac{(2l_A + 2l_B)!}{(2l_A + 1)(2l_B + 1)(2l_A)!(2l_B)!}. \quad (5.31)$$

As noted previously, the second-order perturbation theory of polarizability can be used to replace the excitation-energy denominators, using Eq. (5.6). This gives the usual XDM formulae [4] for the pairwise  $C_6$ ,  $C_8$ , and  $C_{10}$  dispersion coefficients between atoms  $A$  and  $B$ :

$$C_6^{AB} = \alpha_A \alpha_B \frac{\langle M_1^2 \rangle_A \langle M_1^2 \rangle_B}{\alpha_B \langle M_1^2 \rangle_A + \alpha_A \langle M_1^2 \rangle_B}, \quad (5.32)$$

$$C_8^{AB} = \frac{3}{2} \alpha_A \alpha_B \frac{\langle M_1^2 \rangle_A \langle M_2^2 \rangle_B + \langle M_2^2 \rangle_A \langle M_1^2 \rangle_B}{\alpha_B \langle M_1^2 \rangle_A + \alpha_A \langle M_1^2 \rangle_B}, \quad (5.33)$$

$$C_{10}^{AB} = \alpha_A \alpha_B \frac{2\langle M_1^2 \rangle_A \langle M_3^2 \rangle_B + 2\langle M_3^2 \rangle_A \langle M_1^2 \rangle_B + \frac{21}{5}\langle M_2^2 \rangle_A \langle M_2^2 \rangle_B}{\alpha_B \langle M_1^2 \rangle_A + \alpha_A \langle M_1^2 \rangle_B}. \quad (5.34)$$

As described above, the reference electron and its corresponding exchange hole generate a dipole with two unit point charges of opposite sign. The reference electron and the center of the exchange hole lie at distances of  $r$  and  $(r - d_{X\sigma})$  from the atomic nucleus, respectively. Since the exchange-hole dipole is directed toward, but displaced from, the atomic nucleus (taken as the origin), it also has nonzero quadrupole, octopole, and higher-order  $l$ -pole moments. The magnitude of each of these moments is given by  $r^l - (r - d_{X\sigma})^l$ . Thus, the expression for the multipole-moment integrals, analogous to Eq. (5.5) is

$$\langle M_l^2 \rangle = \sum_{\sigma} \int \rho_{\sigma}(\mathbf{r}) [r^l - (r - d_{X\sigma})^l]^2 d\mathbf{r}, \quad (5.35)$$

and this result is used to evaluate all integrals involving higher-order multipole moments in the computation of the XDM dispersion coefficients.

The initial XDM model used only the leading-order  $C_6$  contribution to the dispersion energy [14,18]. However, the resulting intermolecular dispersion energies did not provide sufficient binding for two  $\pi$ -stacked orientations of the benzene dimer [18]. This shortcoming of the model prompted consideration of the contributions of the higher-order  $C_8$  and  $C_{10}$  terms to the dispersion energy [15,16]. Inclusion of the dipole–quadrupole  $C_8$  term was found to be essential for a reliable treatment of the binding in  $\pi$ -stacked systems. Overall, for a set of small-molecule dimers, the  $C_6$  term is responsible for roughly 60% of the overall dispersion energy. The  $C_8$  and  $C_{10}$  terms contribute roughly 30% and 10% of the dispersion energy, respectively [16], while the effects of higher-order terms beyond  $C_{10}$  are negligible [24].

Table 5.2 illustrates the importance of the higher-order dispersion terms in computing the binding energies of a reference set of 49 intermolecular complexes for which highly-accurate coupled-cluster binding energies are available. This data set, referred to as the KB49 (Kannemann–Becke set of 49 small intermolecular complexes) [25] includes complexes bound by dispersion,  $\pi$ -stacking, dipole-induced-dipole, dipole–dipole, and hydrogen-bonding interactions. Results are presented for XDM in conjunction with several popular density-functional methods (the extension of XDM to molecular dimers will be discussed in the remainder of Section 5.2). As shown in the table, unacceptably large errors are obtained if only the leading-order  $C_6$  contribution to the dispersion energy is included for all functionals except LC- $\omega$ PBE. However, when all three ( $C_6$ ,  $C_8$ , and  $C_{10}$ ) dispersion-energy terms are included in the XDM model, very good performance is obtained with the majority of the functionals considered, emphasizing the importance of including these higher-order interactions.

Finally, the XDM model was also generalized to include the 3-atom Axilrod–Teller–Muto [47,48] dispersion term [24], which is also discussed in Chapters 1, 4, 6, and 10. This term is dependent on the relative orientations of the three interacting atoms,  $A$ ,  $B$ , and  $C$ , and is given by

$$E_{\text{disp}}^{(3)} = (1 + 3 \cos \theta_A \cos \theta_B \cos \theta_C) \frac{C_9}{R_{AB}^3 R_{BC}^3 R_{AC}^3}, \quad (5.36)$$

**TABLE 5.2** Mean absolute errors for the KB49 set (in kcal/mol) with selected functionals depending on the number of terms included in the dispersion-energy series expansion. All calculations were performed with Gaussian 09 [36] and the postg program [37], using the aug-cc-pVTZ basis set. The  $C_9$  term was evaluated using a damping function consisting of the product of three  $f_6$  damping functions (Eq. (5.46)) as recommended in Ref. [38]

Functional	$C_6$	$C_6, C_8$	$C_6, C_8, C_{10}$	$C_6, C_8, C_{10}, C_9$
BLYP [39,40]	1.04	0.41	0.28	0.30
B3LYP [40,41]	0.76	0.32	0.25	0.26
BH&HLYP [40,42]	0.61	0.37	0.32	0.33
PW86PBE [43,44]	0.53	0.40	0.39	0.39
PBE [44]	0.63	0.51	0.48	0.49
PBE0 [45]	0.53	0.41	0.40	0.41
LC- $\omega$ PBE [46]	0.25	0.23	0.24	0.24

where  $\theta_A$  is the angle at vertex  $A$  for the triangle formed by the three atoms (i.e., the  $B - A - C$  angle). As such, if the atoms are in a linear arrangement, the interaction will be maximally attractive. Conversely, if the atoms form an equilateral triangle, the interaction will be maximally repulsive. The  $C_9$  dispersion coefficient arises from nonadditive interactions between the instantaneous dipole moments in the electron distribution of the three atoms:

$$C_9 = \frac{4}{9} \frac{\varepsilon_A + \varepsilon_B + \varepsilon_C}{(\varepsilon_A + \varepsilon_B)(\varepsilon_B + \varepsilon_C)(\varepsilon_A + \varepsilon_C)} \langle M_1^2 \rangle_A \langle M_1^2 \rangle_B \langle M_1^2 \rangle_C. \quad (5.37)$$

The  $\varepsilon$  are the average atomic excitation energies, which can be eliminated in favor of the atomic polarizabilities using Eq. (5.6) as was done for  $C_6$  coefficient. The  $C_9$  coefficients can be evaluated with XDM by using the exchange-hole dipole to evaluate the moment integrals. The resulting  $C_9$  values for atomic trimers consisting of hydrogen and the noble gases are again in good agreement with reference data [24]. However, inclusion of the  $C_9$  term does not contribute significantly to the dispersion binding of intermolecular complexes with XDM [24]. As shown in Table 5.2, it either has no effect on the binding-energy statistics or causes the error to increase slightly. This is most likely because exchange-repulsion errors from the base density functional are typically an order of magnitude larger than the 3-body dispersion energies for molecular clusters [49]. Thus, the  $C_9$  term is omitted from the canonical implementation of the XDM method.

### 5.2.2 Decomposition into Atomic Contributions

Up to this point, only dispersion interactions between infinitely-separated atoms have been considered. A generalization of the dispersion model is necessary to describe both intermolecular and intramolecular interactions. In order to compute the dispersion energy for interacting molecules, the overall molecular polarizabilities and exchange-hole dipole moments must be partitioned into individual atomic contributions.

For two infinitely-separated molecules, the dispersion energy is

$$E_{\text{disp}} = - \sum_{n=6,8,10} \sum_{\substack{i \in A \\ j \in B}} \frac{C_{n,ij}}{R_{ij}^n}. \quad (5.38)$$

The first sum represents the orders in the multipolar expansion of the dispersion energy, or  $2(l_A + l_B + 1)$  as in Eq. (5.30). The second sum runs over all atoms  $i$  in the first molecule and all atoms  $j$  in the second molecule. To evaluate the dispersion coefficients for each atomic pair, atom-in-molecule contributions to the moments and polarizabilities must be defined. For the exchange-hole multipole moments, this is straightforward. Any reasonable partitioning scheme can be used by inserting integration weights,  $w_i(\mathbf{r})$ , in the integrand of Eq. (5.35):

$$\langle M_l^2 \rangle_i = \sum_{\sigma} \int w_i(\mathbf{r}) \rho_{\sigma}(\mathbf{r}) \left[ r^l - (r - d_{X\sigma})^l \right]^2 d\mathbf{r}. \quad (5.39)$$

The Hirshfeld partitioning scheme, which uses a sum of spherical free-atomic densities, was adopted for use in the XDM model. The Hirshfeld weights for atom  $i$  are defined by taking the ratio of the atomic density relative to the “promolecular” density (the sum of all atomic densities):

$$w_i(\mathbf{r}) = \frac{\rho_i(\mathbf{r})}{\sum_j \rho_j(\mathbf{r})}. \quad (5.40)$$

The weight function  $w_i(\mathbf{r})$  has a value close to 1 near atom  $i$  and close to 0 everywhere else in the molecule. Also, the total electron density must be recovered from the sum of the atomic pieces, so the sum of weight functions is  $\sum_i w_i(\mathbf{r}) = 1$  at all points in space. Tests have shown that the moments and dispersion coefficients are quite insensitive to the partitioning scheme chosen [32].

Evaluation of the atom-in-molecule polarizabilities is more challenging since this quantity is not well defined. As discussed in Chapter 1, atomic polarizabilities are not strictly additive since the response of each component atomic density to a field will be strongly affected by polarization of the neighboring atoms. The first test of XDM for intermolecular binding energies [14] involved partitioning the overall molecular polarizability into atomic contributions, but this is complicated by having first to compute the molecular polarizability, which is not possible to do “on-the-fly” during an electronic-structure calculation. A more generally-applicable approach to obtain atom-in-molecule polarizabilities was therefore sought. The polarizability definition now used in XDM was inspired by the work of Brinck, Murray, and Politzer [50], who demonstrated an excellent linear relationship between polarizability and volume that can be physically motivated based on a conducting-sphere model. The atom-in-molecule polarizability is therefore defined as the free-atomic polarizability scaled by a ratio of the atom-in-molecule ( $V_i$ ), to free-atomic ( $V_{i,\text{free}}$ ) volumes [15,51]:

$$\alpha_i = \frac{V_i}{V_{i,\text{free}}} \alpha_{i,\text{free}}. \quad (5.41)$$

Tabulated free-atomic polarizabilities [10] are thus used as reference data in all XDM calculations. The atom-in-molecule volumes are computed using Hirshfeld partitioning [52] of the electron density:

$$V_i = \langle r^3 \rangle_i = \int w_i(\mathbf{r}) \rho(\mathbf{r}) r^3 d\mathbf{r}. \quad (5.42)$$

The atom-in-molecule polarizabilities from Eq. (5.41) and moments from Eq. (5.39) are then used directly in Eqs. (5.32)–(5.34) to evaluate the dispersion coefficients for each atomic pair. The resulting atom-in-molecule dispersion coefficients are sensitive to changes in local atomic environment, such as charge and coordination [53,54].

The definition of the atom-in-molecule polarizabilities in terms of free-atomic quantities is a fairly drastic approximation made to extend the applicability of the XDM model to molecular calculations. Nevertheless, the model performs quite well, giving a mean absolute error of 9.1% for a benchmark set of intermolecular  $C_6$  dispersion coefficients [15]. More sophisticated treatments could conceivably be adopted, in which the free-atomic polarizabilities and volumes are interpolated between different reference atomic charge states. This would likely make the model more accurate for ionic systems, but introduces further empiricism and has not yet been pursued.

The relationship between polarizability and volume of Eq. (5.41) has also been successfully adopted for use in the Tkatchenko–Scheffler (TS) dispersion model [55]. The TS atomic dispersion coefficients are defined using the following combination rule:

$$C_6^{AB} = \frac{2C_6^{AA}C_6^{BB}}{\frac{\alpha_B}{\alpha_A}C_6^{AA} + \frac{\alpha_A}{\alpha_B}C_6^{BB}}, \quad (5.43)$$

where the homoatomic dispersion coefficients are evaluated through volume scaling of the corresponding free-atomic values,

$$C_6^{AA} = \left( \frac{V_A}{V_{A,\text{free}}} \right)^2 C_{6,\text{free}}^{AA}. \quad (5.44)$$

The atom-in-molecule volumes are obtained using Hirshfeld partitioning [52], as in Eq. (5.42), in the same manner as with XDM.

### 5.2.3 Dependence on the Chemical Environment

Because the XDM dispersion coefficients are evaluated from properties of the density and the exchange hole, they can vary significantly depending on the local chemical environment of an atom. XDM results for some selected molecules and solids are shown in Table 5.3. The effect of changing chemical environment on  $C_6$  coefficients is also discussed in terms of a dependence on atomic coordination numbers for the DFT-D3 [56] dispersion model in Chapter 6.

In general, the charge state strongly affects both the exchange-hole dipole moment and the atomic volume, and hence the polarizability. This is illustrated by the  $\text{Li}_2$ ,  $\text{LiH}$ , and  $\text{LiF}$  series in Table 5.3 where both the moments and volumes decrease by a factor of roughly a third as

**TABLE 5.3** Exchange-hole dipole moment integrals, atomic volumes, and homoatomic  $C_6$  dispersion coefficients for carbon, lithium, and silver atoms, all in atomic units. Finite-molecule calculations were performed with B3LYP/6-31+G\* using Gaussian 09 [36] and postg [37]. Periodic-boundary calculations were performed with B86bPBE using Quantum ESPRESSO [57]. The calculation for the Ag atom was performed by placing an isolated, spin-averaged atom within a large supercell

Finite	$\langle M_1^2 \rangle$	$V$	$C_6$	Periodic	$\langle M_1^2 \rangle$	$V$	$C_6$
C <sub>2</sub> H <sub>2</sub>	6.02	32.7	32.7	Graphite	3.45	33.7	17.8
C <sub>2</sub> H <sub>4</sub>	5.17	30.9	26.5	Diamond	2.61	35.1	14.1
C <sub>2</sub> H <sub>6</sub>	4.45	29.1	21.5	Ag atom	15.64	115	351
Li <sub>2</sub>	12.48	83.2	960	AgCl bulk	9.79	118	226
LiH	6.71	41.4	257	Ag surface	9.19	123	221
LiF	3.60	26.4	87.7	Ag bulk	7.36	126	178

the atom bound to the lithium becomes more electronegative and the Li charge increases from 0 to 0.6. Conversely, changes in coordination tend to have smaller effects on the volume than on the exchange-hole dipole moment integrals. This can be seen from the acetylene, ethylene, and ethane series in Table 5.3, as well as from a comparison of graphite and diamond.

For solids, there is typically a much smaller change in atomic volumes than seen in gas-phase molecules and most of the variation between dispersion coefficients for the free atoms and bulk solids arises from the moment integrals. This is illustrated for silver in Table 5.3 by comparing the dispersion coefficient for the free atom with analogous values for the metal surface, bulk metal, and bulk metal chloride. The changes in the silver dispersion coefficients are due to large differences in the distribution of the exchange hole, relative to the reference point, and hence the exchange-hole dipole moment for each solid.

For a reference electron far from an isolated atom, the exchange hole remains localized on the atom, so the exchange-hole dipole moment is large. This conceptual picture is also applicable to the metal chloride, but the more positive charge on the silver atom in the salt results in a reduced moment integral, similar to that seen for LiF relative to Li<sub>2</sub>. Conversely, for the bulk metal, the density in the interstitial region is very flat [58] and resembles a uniform electron gas. This causes the hole to be localized near the reference electron and the exchange-hole dipole moment is small, resulting in a large reduction of the moment integral for the bulk metal relative to both the free atom and the salt, despite maintaining an overall neutral charge. Finally, the dispersion coefficient for atoms at the surface of a four-layer silver slab [54] are intermediate between those seen for the free atom and bulk metal. This demonstrates the high sensitivity of the dispersion coefficients to the extent of the exchange hole and the importance of incorporating this physics into any dispersion model.

### 5.2.4 The Damping Function

The final step in the development of the XDM model is evaluation of the dispersion energy from the interatomic dispersion coefficients. The expression for the dispersion energy given in Eq. (5.38) is valid in the limit of infinite separations. For finite separations, a damping function is used to prevent divergence of the dispersion energy at small internuclear distances and also

serves to correct for errors in the multipolar expansion [59,60]. The expression for the damped dispersion energy is

$$E_{\text{disp}} = - \sum_{n=6,8,10} \sum_{i < j} \frac{C_{n,ij} f_n(R_{ij})}{R_{ij}^n}, \quad (5.45)$$

where  $i$  and  $j$  now run over all atoms (regardless of to which molecule they belong). The multiplicative function  $f_n(R_{ij})$  damps the dispersion energy at small internuclear separations,  $R_{ij}$ .

Many forms for the damping functions,  $f_n(R_{ij})$ , have been proposed in the literature and one of the most popular is the exponential damping function of Wu and Yang [61], used in Grimme's DFT-D2 and D3 dispersion models [56,62], as well as in the original Tkatchenko–Scheffler [55] model. The Tang–Toennies damping function [63] is also quite popular and is used in a later variant of the TS model [64] and in dDsC [33]. Both of these damping functions cause the limiting value of the dispersion energy to approach zero for small internuclear distances. The disadvantage of this is that requiring the dispersion energy to be zero in the united-atom limit introduces a nonphysical, repulsive dispersion force at small internuclear distances. In the development of XDM, it was argued that the dispersion force should approach zero at small separations, so the dispersion energy should instead approach a constant, nonzero value. This is consistent with the perturbation-theory result for two hydrogen atoms, which demonstrates that the dispersion energy should indeed be nonzero in the limit of small interatomic separation [65].

In the initial XDM model, which used only the leading-order  $C_6$  contribution to the dispersion energy, the damping function was defined in terms of the atomic correlation energies of the interacting atoms [14,18]. However, all subsequent implementations of XDM involving the  $C_6$ ,  $C_8$ , and  $C_{10}$  dispersion-energy terms use a damping function based on the atomic radii [16]. Now commonly referred to as Becke–Johnson damping [66], this function is given by

$$f_n(R_{ij}) = \frac{R_{ij}^n}{R_{ij}^n + (a_1 R_{c,ij} + a_2)^n}. \quad (5.46)$$

In this equation,  $R_{c,ij}$  denotes a “critical” separation for interactions between atoms  $i$  and  $j$  that describes the distance range at which the multipolar expansion breaks down and successive terms in the series expansion of the dispersion energy become equal, rather than decreasing in magnitude. This behavior is illustrated in Fig. 5.4, which shows the component terms of the undamped dispersion energy for the neon dimer. At an internuclear separation of ca. 2.16 Å the three curves cross. In practice, there are three possible choices for  $R_c$ , depending on which two terms in the dispersion expansion are related:

$$R_{c,ij} = \left\{ \left( \frac{C_{8,ij}}{C_{6,ij}} \right)^{\frac{1}{2}}, \left( \frac{C_{10,ij}}{C_{8,ij}} \right)^{\frac{1}{2}}, \left( \frac{C_{10,ij}}{C_{6,ij}} \right)^{\frac{1}{4}} \right\}. \quad (5.47)$$

In the XDM model, the average of these three values is used to define the critical separation, although the simple  $(C_{8,ij}/C_{6,ij})^{1/2}$  ratio was adopted in Grimme's DFT-D3 model when Becke–Johnson damping is used [66].

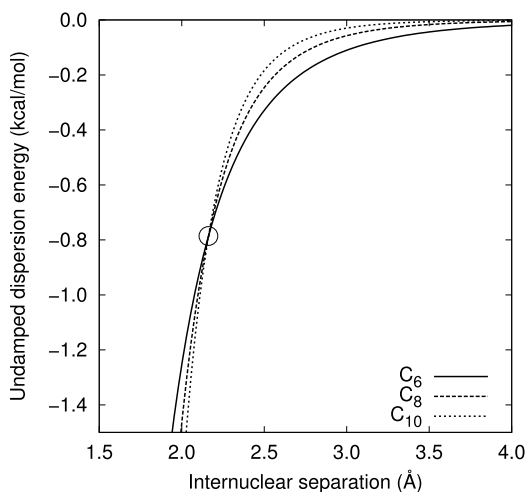


FIGURE 5.4 Component  $C_6$ ,  $C_8$ , and  $C_{10}$  dispersion-energy terms for the neon dimer. The critical separation (circled in the plot) is defined as the internuclear distance at which these curves intersect.

Finally, in addition to the critical separations, there are two empirical parameters,  $a_1$  and  $a_2$ , in the definition of the damping function given in Eq. (5.46). The two parameters should be fit for use with a particular density-functional method. The damping parameters are commonly optimized by minimizing the binding-energy errors for the KB49 set [25]. This set can be expanded to 65 complexes (KB65), as presented in the work of Kannemann and Becke [22], by including additional complexes involving noble-gas atoms.

Readers are strongly cautioned against using the reported damping parameter values from preliminary calculations [16] with HF exchange and BR correlation [67] in production calculations, even though they are the default in the Q-chem implementation of XDM [68]. The optimal damping parameter values for GGA or hybrid functionals are very different than with full HF exchange [29]. Appropriate damping parameters should always be selected to match the underlying base exchange-correlation functional used in the calculations. The effect of the base functional on the performance for intermolecular interactions will be discussed in detail in the following section.

Most XDM calculations have employed aug-cc-pVTZ basis sets for all atoms, except noble gases, where the larger aug-cc-pV5Z sets are used [22,25], in order to provide results that are close to the basis-set limit. However, for production calculations, smaller basis sets are desired and can be employed quite successfully, with minimal losses in accuracy provided that diffuse functions are present [69,70]. The  $a_1$  and  $a_2$  parameters should be refit if smaller basis sets are to be used, in order to take advantage of error cancellation between the damping function and basis-set incompleteness. Although counterpoise corrections [71] can be used in conjunction with XDM [70], they are not included in the canonical implementation of XDM in order to treat intermolecular and intramolecular interactions on equal footing and to avoid increasing the computational complexity. It should be noted that the damping also corrects



for deficiencies in the base density functional, as well as in the basis set, and this will be discussed in the next section.

### 5.3 THE ROLE OF THE BASE FUNCTIONAL

The XDM dispersion energy is typically an *a posteriori* correction that is added to the self-consistent DFT energy obtained with some base density functional. Thus, the total (base plus dispersion) energy is given by

$$E = E_{\text{base}} + E_{\text{disp}}. \quad (5.48)$$

The dispersion energy correction is evaluated using the self-consistent electron density and Kohn–Sham orbitals. While implementations in which the dispersion energy is evaluated at each step of the SCF procedure have been considered, dispersion interactions do not strongly affect the electron density [72] and the much more complicated SCF implementation is not necessary for either XDM [68] or dDsC [34]. Similar findings were also obtained for a self-consistent implementation of a nonlocal van der Waals functional [73]. With the post-SCF implementation, XDM can be used for single-point energy calculations, geometry optimizations, and frequency calculations in conjunction with the Gaussian electronic-structure package [36] using the postg program [37]. Additionally, postg can be used to evaluate XDM dispersion energies with any electronic structure program capable of producing a wavefunction (wfn, wfx, molden) file.

The performance of the XDM method is strongly dependent on the choice of the base density functional. This is because the underlying base functional must give an accurate treatment of all interactions with the exception of dispersion, including exchange-repulsion, electrostatics, and induction. Only the exchange-repulsion term need be considered for non-polar, dispersion-bound complexes [49], but the electrostatic and induction terms are critical for stronger interactions, such as hydrogen-bonding [49] and halogen-bonding [29].

The performance of a base functional for exchange-repulsion is typically assessed by how accurately the method is able to reproduce exact exchange-only repulsion curves for noble-gas dimers and is elegantly explained in terms of the behavior of the exchange enhancement factor in the limit of large reduced density gradients [21,26,74–76]. To understand the importance of the large reduced-gradient limit, consider two separated atoms (or molecules). The electron density of each atom is piecewise exponential. The reduced density gradient is given by Eq. (5.25) and increases exponentially far from each atom or molecule in all directions. When an intermolecular complex is formed from the separated monomers, some of the large-reduced-gradient region is replaced by a “noncovalent” region of low reduced gradient, directly between the two interacting atoms or molecules [77]. This is illustrated in Fig. 5.5 for triplet  $\text{H}_2$  at its equilibrium geometry.

For generalized-gradient-approximation (GGA) functionals, the exchange energy is evaluated as

$$E_X^{\text{GGA}} = -\frac{3}{2} \left( \frac{3}{4\pi} \right)^{\frac{1}{3}} \sum_{\sigma} \int \rho_{\sigma}^{4/3} F(s_{\sigma}) d\mathbf{r}, \quad (5.49)$$

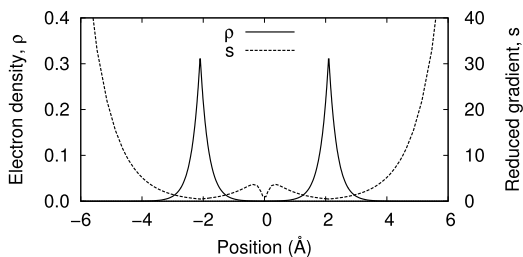


FIGURE 5.5 Electron density and reduced density gradient along the internuclear axis for the triplet state of  $\text{H}_2$ , with the center-of-mass at the origin. The internuclear distance corresponds to the equilibrium value of  $4.2 \text{ \AA}$ .

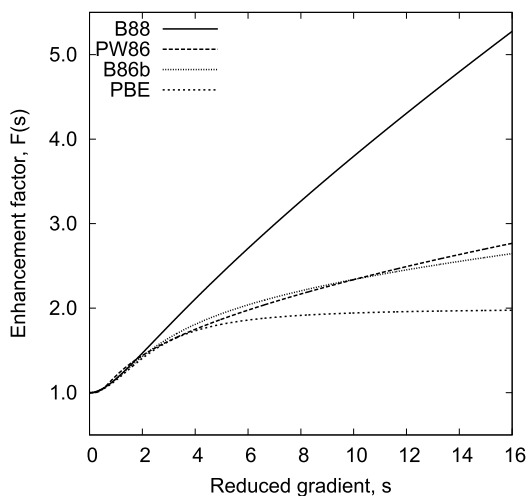


FIGURE 5.6 Plot of the exchange enhancement factor for four selected GGA functionals.

where  $F(s)$  is termed the enhancement factor. This factor approaches unity in the limit of low reduced density gradient (i.e.,  $s \rightarrow 0$ ) in order to recover the uniform-electron-gas limit. In regions of large  $s$ , far from the molecule as on either side of Fig. 5.5, this factor serves to enhance the contribution to the exchange energy beyond what is obtained with the local spin-density approximation, resulting in vastly improved atomic exchange energies [39,78]. The precise form of the enhancement factor depends on the particular functional.

Plots of  $F(s)$  for four selected GGAs are given in Fig. 5.6. The B88 [39], PBE [44], and PW86 [43] functionals are all implemented in the Gaussian 09 [36] electronic-structure program although, unfortunately, B86b [78] is not. All four functionals are available in the Quantum ESPRESSO program [57] used for the periodic-boundary implementation of XDM to be discussed in Section 5.4.

As seen in Fig. 5.6, the enhancement factors of these common GGAs differ greatly in the limit of large reduced density gradient. It can be shown [78] that  $F(s)$  should be proportional to  $s^{2/5}$  as  $s \rightarrow \infty$ , a limit that is obeyed by only the PW86 [43] and B86b [78] functionals.

**TABLE 5.4** Mean absolute errors for the S22 [80], S66 [81], HSG [82], and XB18 [79] noncovalent interaction benchmark sets (in kcal/mol) with selected XDM-corrected functionals. All data is taken from Ref. [25], except for the halogen-bonded XB18 set, where the data was taken from Ref. [29]

Functional	S22	S66	HSG	XB18
BLYP [39,40]	0.22	0.22	0.20	1.17
B3LYP [40,41]	0.31	0.25	0.12	0.54
BH&HLYP [40,42]	0.47	0.34	0.18	0.21
PW86PBE [43,44]	0.35	0.29	0.17	1.51
PBE [44]	0.57	0.41	0.16	1.74
PBE0 [45]	0.53	0.39	0.15	0.68
LC- $\omega$ PBE [46]	0.31	0.20	0.23	0.66

These are the same two GGAs that best reproduce the exchange-only repulsion curves for the noble-gas dimers [21,26]. For comparison, the B88 functional has an enhancement factor that diverges more rapidly as  $s \rightarrow \infty$ , causing a contribution to the exchange energy for the large-gradient regions that is too large in magnitude. As a result, B88 exchange over-stabilizes the separated monomers, underbinds the intermolecular complex, and typically provides potential-energy curves that are overly repulsive. Conversely, the PBE enhancement factor approaches a constant as  $s \rightarrow \infty$ , causing too small a contribution to the exchange energy for the large-gradient regions. Consequently, PBE exchange destabilizes the separated monomers, overbinds the intermolecular complex relative to exact exchange, and typically provides potential-energy curves that are overly attractive, even in the absence of a dispersion correction. Thus, the difference in contribution to the exchange energy between the high-gradient regions in the separated-atom limit and the low-gradient noncovalent regions in the intermolecular complex explains the observed binding-energy trends with each GGA functional [21,74–76].

Only exchange functionals, like PW86, that give exchange repulsion behavior similar to exact exchange perform well for the noble gas dimers. Interestingly, for this particular base functional, Kannemann showed that fitting to reference data for only the noble-gas dimers [70] provides a set of XDM damping parameters that is transferable to all other elements and types of intermolecular interactions, including  $\pi$ -stacking and hydrogen bonding [22,23]. However, most other popular density functionals do not reproduce exact exchange-repulsion behavior sufficiently well to provide reasonable binding energies for complexes involving noble-gas atoms when used in conjunction with XDM. In these cases, the damping parameters are fit to the KB49 data set [25] and the damping function serves to partially offset errors in the exchange-repulsion energy from the base functional.

Beyond the treatment of exchange repulsion, various functionals will have differing performance for intermolecular complexes depending on their treatment of electrostatic and induction interactions, which are strongly affected by the fraction of exact-exchange mixing [29,49]. Error statistics obtained with XDM and several base density functionals for selected standard noncovalent interactions benchmark sets are collected in Table 5.4. The results for the halogen-bonded XB18 set [79] are particularly sensitive to the choice of base functional and only BH&HLYP, which provides the best description of the induction terms [29,49], is

able to give reliable results. For the remaining noncovalent benchmarks sets [80–84], which primarily involve dispersion and hydrogen-bonding interactions, all of the base functionals provide reasonable performance when combined with XDM. The greatest spread in error statistics is seen for the S22 set, which involves the strongest hydrogen bonding.

In some cases, particularly for halogen-bonding [29] and other charge-transfer complexes [85–87], the base functional alone can overbind even without the dispersion contribution, so adding a dispersion correction will actually degrade the performance. However, this is not due to errors in the dispersion treatment, but rather arises from inherent delocalization error (also called self-interaction or charge-transfer error) [88–92] in the base functional. In the particular case of PBE, the combination of overly-attractive exchange-repulsion behavior and delocalization error causes some hydrogen-bonded complexes to be too strongly bound, even in the absence of a dispersion correction, explaining the relatively poor performance of XDM when paired with PBE relative to the other base functionals considered in Table 5.4. Good performance can only be expected when a dispersion model is paired with a base functional that gives a reliable description of all the other components to the intermolecular interaction except for dispersion.

Once the XDM damping parameters are fit for use with a reliable base functional, the method is highly transferable to systems that exhibit different chemistry from those included in the training set. Parameterization to only the KB49 set of intermolecular complexes has allowed successful application of XDM to more challenging classes of noncovalent interactions well outside the scope of the reference data set. Notable examples include metallophilic interactions [28], halogen bonding [29], and radical-addition transition states [93]. Additionally, XDM has also been recently applied to small-molecule clusters [49], and to supermolecular chemistry [94], both of which are subject to subtle interplay between the exchange-repulsion behavior, exact-exchange mixing, and electron-correlation treatment of the base functional.

## 5.4 THE SOLID STATE: XDM FOR PERIODIC SYSTEMS

The original development of XDM was entirely focused on finite molecular systems. However, dispersion interactions are ubiquitous in the study of molecular crystals, layered materials, and surface adsorption, to list a few solid-state examples. In order to extend the utility of XDM to periodic systems, the method was implemented in the open-source, planewave/pseudopotential Quantum ESPRESSO program [57].

The solid-state implementation does require a few slight differences in the details of the XDM model. The first of these is that, in the evaluation of the dispersion energy, the summation of Eq. (5.45) must now run over all atoms in the unit cell and atoms in neighboring, periodic images. Thus, the dispersion energy for a periodic lattice is given by

$$E_{\text{disp}} = -\frac{1}{2} \sum_{n=6,8,10} \sum_{\mathbf{L}} \sum_{ij} \frac{C_{n,ij} f_n(R_{ij,\mathbf{L}})}{R_{ij,\mathbf{L}}}, \quad (5.50)$$

where  $\mathbf{L}$  indicates the lattice vector. The final sum excludes the  $i = j$  term for  $\mathbf{L} = \mathbf{0}$ , but this term is included for all other replicated cells. To evaluate the dispersion energy, a distance

**TABLE 5.5** Mean absolute errors for the KB49 molecular set and the X23 set of sublimation energies (in kcal/mol) for the XDM dispersion model paired with selected base functionals. All calculations were performed with version 5.3.0 of the Quantum ESPRESSO program [57]

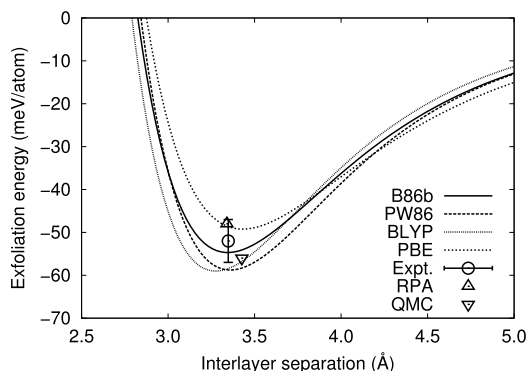
Functional	$a_1$	$a_2$ (Å)	KB49	X23
B86bPBE [44,78]	0.6512	1.4633	0.41	0.85
PW86PBE [43,44]	0.6836	1.5045	0.41	0.88
BLYP [39,40]	0.4502	1.6210	0.43	1.31
PBE [44]	0.3275	2.7673	0.50	1.11

cut-off, chosen based on the maximum interatomic  $C_6$  coefficient, is used to truncate this summation to a more localized atomic region surrounding the central unit cell.

This implementation uses planewave basis sets for the valence electrons and pseudopotentials to represent the core electrons. With the projector augmented wave (PAW) method [95], it is possible to use core-reconstruction to obtain all-electron densities, which are used to determine the Hirshfeld weights and atomic volumes needed to evaluate the XDM dispersion coefficients. However, the exchange-hole dipole moment, and higher-order multipole moments, are evaluated using the valence electron density and kinetic-energy densities without core reconstruction. This is done for simplicity since, in the core shells, the exchange hole will be centered very near the reference electron. Thus, in these regions, the exchange-hole dipole will not have a significant value, and will have effectively zero contribution to the expectation values of Eq. (5.39). Finally, in solid-state calculations, the expectation values are evaluated using uniform three-dimensional integration grids that span the unit cell rather than the usual atom-centered integration grids used in molecular calculations.

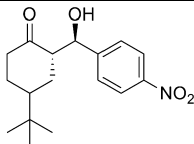
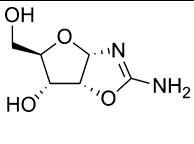
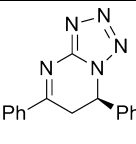
The main limitation of planewave/pseudopotential calculations is that only local and semi-local base functionals can be used, since the computational cost of the double integrals over orbital products needed to evaluate the exact exchange energy is extremely high. Thus, only GGA functionals are used in production calculations on periodic systems with the XDM dispersion model. Fitting of the damping parameters for use with the various GGA base functionals was still performed using the KB49 set, with the molecules or complexes placed at the center of a large supercell, surrounded on all sides by vacuum [26]. Mean absolute errors for the KB49 set are shown in Table 5.5 and are only slightly worse than the analogous results for our molecular implementation using Gaussian 09 and postg, shown in Table 5.2. The lowest errors are obtained with the B86bPBE and PW86PBE base functionals; however, the 1/15 exponent used in the definition of the PW86 exchange enhancement factor [43] causes numerical noise and makes SCF convergence problematic with this functional. As such, B86bPBE is the recommended base functional for use in all production XDM calculations for periodic systems.

While coupled-cluster reference data is readily available for small intermolecular complexes (see Chapter 4), similar highly-accurate data is not generally available for van der Waals interactions in solids. At the time when XDM was first implemented for periodic systems, one of the only reliable benchmarks was the exfoliation energy of graphite [26]. Fig. 5.7 shows the calculated exfoliation energy as a function of interlayer separation for XDM with four base functionals. Reference data from experiment [96] or high-level theory, using either



**FIGURE 5.7** Exfoliation energy of graphite as a function of the interlayer separation for four XDM-corrected density functionals [26]. Reference data from experiment [96] and high-level theory (RPA [97] or QMC [98]) is given for comparison.

**TABLE 5.6** Comparison of calculated and experimental enantiomeric excess values (%) for selected chiral compounds

Molecule			
Experiment	34 [100]	62 [100,101]	>99.9 [102]
B86bPBE-XDM	35.5	51.3	>99.9

random-phase approximation (RPA) [97] or quantum Monte Carlo (QMC) [98] calculations, is shown for comparison. The results confirm that XDM describes the interlayer binding in graphite quite accurately and that the best performance is again obtained with the B86bPBE base functional.

For molecular crystals, the first benchmark of DFT dispersion models consisted of 21 experimental sublimation enthalpies back-corrected to account for thermal effects (the C21 set) [27]. This benchmark was later expanded by the addition of two further crystals and revision of the thermal correction to give the X23 set [99]. Statistics for the X23 set, using the XDM dispersion correction paired with selected base functionals, are shown in Table 5.5. As for the original C21 set, B86bPBE-XDM gives the best performance for the expanded X23 set of sublimation enthalpies, with an MAE of 0.85 kcal/mol per molecule in the unit cell. Additionally, the mean absolute errors obtained with all XDM corrected functionals are somewhat lower than obtained with PBE using the more-complex many-body dispersion (MBD) correction (1.41 kcal/mol) [99].

Beyond lattice energies, a great number of applications in solid-state chemistry depend on the relative energies of differing crystal forms of a given compound; however, such energies are quite difficult to determine experimentally. For the specific case of chiral compounds, the relative energies between the homochiral and heterochiral crystal forms can be directly

related to their relative solubilities, which are easily quantified by the solution-phase enantiomeric excess (e.e.) at the chiral eutectic point. The relative solubilities can be measured experimentally with much greater precision than is possible for calorimetric measurements on each separate crystal form. A benchmark for chiral crystals was assembled using the relative solubilities for 10 of the naturally-occurring amino acids [103]. This is a particularly sensitive test of computational methods since the range of possible enantiomeric excess values covers a very small energy range, due to the exponential dependence of the e.e. on the energy difference. The B86bPBE-XDM method was found to predict the e.e. to within 10% of experiment, on average [103]. Analogous calculations have since been performed on three additional compounds, with differing chemical functionality. As shown in Table 5.6, the results were again found to be in good agreement with experimental measurements.

## 5.5 CONCLUSIONS

---

In summary, the XDM dispersion model performs extremely well for both molecular and solid-state applications. Without any reparameterization of the damping function, the method is transferable to such diverse chemical systems as molecular crystals [27,103], layered materials [26,104], metal halides [28], and metal surfaces [54]. Successes of the model include the exfoliation [26] or surface energy [104] of graphite, molecular physisorption on noble metal surfaces [54], metallophilic effects [28], sublimation enthalpies of molecular crystals [27], and relative solubilities of homochiral and heterochiral crystal phases [103]. Due to the dependence of the XDM model on the exchange-hole, the resulting dispersion coefficients respond to changes in the local chemical environment [53,54]. As such, the XDM model provides a highly-general treatment of dispersion that can reliably be applied to an extremely broad range of chemical systems.

## Acknowledgments

The author gratefully acknowledges the contributions of Axel D. Becke and Alberto Otero-de-la-Roza to the development and implementation of the XDM model; this work was only possible thanks to their efforts.

## References

- [1] F. London, *Z. Phys.* 63 (1930) 245–279.
- [2] L. Salem, *Mol. Phys.* 3 (1960) 441–452.
- [3] A.D. Becke, E.R. Johnson, *J. Chem. Phys.* 122 (2005) 154104.
- [4] A.D. Becke, E.R. Johnson, *J. Chem. Phys.* 127 (2007) 154108.
- [5] A.D. Becke, *J. Chem. Phys.* 140 (2014) 18A301.
- [6] A.D. Becke, M.R. Roussel, *Phys. Rev. A* 39 (1989) 3761–3767.
- [7] J.G. Ángyán, *J. Chem. Phys.* 127 (2007) 024108.
- [8] P.W. Ayers, *J. Math. Chem.* 46 (2009) 86–96.
- [9] A. Heßelmann, *J. Chem. Phys.* 130 (2009) 084104.
- [10] D. Lide, W. Haynes (Eds.), *CRC Handbook of Chemistry and Physics*, 90th edition, CRC Press, 2010.
- [11] A.J. Thakkar, H. Hattema, P.E.S. Wormer, *J. Chem. Phys.* 97 (1992) 3252–3257.
- [12] A.J. Thakkar, *J. Chem. Phys.* 89 (1988) 2092–2098.

- [13] A.J. Thakkar, *J. Chem. Phys.* 75 (1981) 4496–4501.
- [14] E.R. Johnson, A.D. Becke, *J. Chem. Phys.* 123 (2005) 024101.
- [15] A.D. Becke, E.R. Johnson, *J. Chem. Phys.* 124 (2006) 014104.
- [16] E.R. Johnson, A.D. Becke, *J. Chem. Phys.* 124 (2006) 174104.
- [17] E.R. Johnson, A.D. Becke, *Chem. Phys. Lett.* 432 (2006) 600–603.
- [18] A.D. Becke, E.R. Johnson, *J. Chem. Phys.* 123 (2005) 154101.
- [19] A.D. Becke, E.R. Johnson, *J. Chem. Phys.* 127 (2007) 124108.
- [20] E.R. Johnson, A.D. Becke, *J. Chem. Phys.* 128 (2008) 124105.
- [21] F.O. Kannemann, A.D. Becke, *J. Chem. Theory Comput.* 5 (2009) 719–727.
- [22] F.O. Kannemann, A.D. Becke, *J. Chem. Theory Comput.* 6 (2010) 1081–1088.
- [23] A.D. Becke, A.A. Arabi, F.O. Kannemann, *Can. J. Chem.* 88 (2010) 1057–1062.
- [24] A. Otero-de-la-Roza, E.R. Johnson, *J. Chem. Phys.* 138 (2013) 054103.
- [25] A. Otero-de-la-Roza, E.R. Johnson, *J. Chem. Phys.* 138 (2013) 204109.
- [26] A. Otero-de-la-Roza, E.R. Johnson, *J. Chem. Phys.* 136 (2012) 174109.
- [27] A. Otero-de-la-Roza, E.R. Johnson, *J. Chem. Phys.* 137 (2012) 054103.
- [28] A. Otero-de-la-Roza, J.D. Mallory, E.R. Johnson, *J. Chem. Phys.* 140 (2014) 18A504.
- [29] A. Otero-de-la-Roza, E.R. Johnson, G.A. DiLabio, *J. Chem. Theory Comput.* 10 (2014) 5436–5447.
- [30] A.D. Becke, *J. Chem. Phys.* 119 (2003) 2972–2977.
- [31] M.A. Buijse, E.J. Baerends, *Mol. Phys.* 100 (2002) 401–421.
- [32] S.N. Steinmann, C. Corminboeuf, *J. Chem. Phys.* 134 (2011) 044117.
- [33] S.N. Steinmann, C. Corminboeuf, *J. Chem. Theory Comput.* 7 (2011) 3567–3577.
- [34] E. Brémond, N. Golubev, S.N. Steinmann, C. Corminboeuf, *J. Chem. Phys.* 140 (2014) 18A516.
- [35] A. Dalgarno, W.D. Davison, *Adv. At. Mol. Phys.* 2 (1966) 1–32.
- [36] M.J. Frisch, et al., *Gaussian 09 Revision A.1*, Gaussian Inc., Wallingford, CT, 2009.
- [37] The postg program is available from <http://schooner.chem.dal.ca>.
- [38] Y.H. Huang, G.J.O. Beran, *J. Chem. Phys.* 143 (2015) 044113.
- [39] A.D. Becke, *Phys. Rev. A* 38 (1988) 3098–3100.
- [40] C. Lee, W. Yang, R.G. Parr, *Phys. Rev. B* 37 (1988) 785.
- [41] A.D. Becke, *J. Chem. Phys.* 98 (1993) 5648–5652.
- [42] A. Becke, *J. Chem. Phys.* 98 (1993) 1372.
- [43] J. Perdew, W. Yue, *Phys. Rev. B* 33 (1986) 8800.
- [44] J. Perdew, K. Burke, M. Ernzerhof, *Phys. Rev. Lett.* 77 (1996) 3865–3868.
- [45] C. Adamo, V. Barone, *J. Chem. Phys.* 110 (1999) 6158–6170.
- [46] O.A. Vydrov, G.E. Scuseria, *J. Chem. Phys.* 125 (2006) 234109.
- [47] B.M. Axilrod, E. Teller, *J. Chem. Phys.* 11 (1943) 299–300.
- [48] Y. Muto, *J. Phys. Math. Soc. Jpn.* 17 (1943) 629.
- [49] A. Otero-de-la-Roza, G.A. DiLabio, E.R. Johnson, *J. Chem. Theory Comput.* 12 (2016) 3160–3175.
- [50] T. Brinck, J.S. Murray, P. Politzer, *J. Chem. Phys.* 98 (1993) 4305–4306.
- [51] F.O. Kannemann, A.D. Becke, *J. Chem. Phys.* 136 (2012) 034109.
- [52] F.L. Hirshfeld, *Theor. Chim. Acta* 44 (1977) 129–138.
- [53] E.R. Johnson, *J. Chem. Phys.* 135 (2011) 234109.
- [54] M.S. Christian, A. Otero-de-la-Roza, E.R. Johnson, *J. Chem. Theory Comput.* 12 (2016) 3305–3315.
- [55] A. Tkatchenko, M. Scheffler, *Phys. Rev. Lett.* 102 (2009) 073005.
- [56] S. Grimme, J. Antony, S. Ehrlich, H. Krieg, *J. Chem. Phys.* 132 (2010) 154104.
- [57] P. Giannozzi, S. Baroni, et al., *J. Phys. Condens. Matter* 21 (2009) 395502.
- [58] P. Mori-Sánchez, A. Martín Pendás, V. Luaña, *J. Am. Chem. Soc.* 124 (2002) 14721–14723.
- [59] A. Dalgarno, J. Lewis, *Proc. Phys. Soc. A* 69 (1955) 57.
- [60] A. Stone, A. Misquitta, *Int. Rev. Phys. Chem.* 26 (2007) 193–222.
- [61] Q. Wu, W. Yang, *J. Chem. Phys.* 116 (2002) 515.
- [62] S. Grimme, *J. Comput. Chem.* 27 (2006) 1787–1799.
- [63] K. Tang, J.P. Toennies, *J. Chem. Phys.* 80 (1984) 3726–3741.
- [64] O.A. von Lilienfeld, A. Tkatchenko, *J. Chem. Phys.* 132 (2010) 234109.
- [65] A. Koide, *J. Phys. B* 9 (1976) 3173–3183.
- [66] S. Grimme, S. Ehrlich, L. Goerigk, *J. Comput. Chem.* 32 (2011) 1456–1465.



- [67] A.D. Becke, *Int. J. Quant. Chem.* S28 (1994) 625–632.
- [68] J. Kong, Z.T. Gan, E. Proynov, M. Freindorf, T.R. Furlani, *Phys. Rev. A* 79 (2009) 042510.
- [69] E.R. Johnson, A. Otero-de-la-Roza, S.G. Dale, G.A. DiLabio, *J. Chem. Phys.* 139 (2013) 214109.
- [70] F.O. Kannemann, Development and Benchmarking of a Semilocal Density-Functional Approximation Including Dispersion, PhD thesis, Dalhousie University, 2013, available from <http://hdl.handle.net/10222/21434>.
- [71] S. Boys, F. Bernardi, *Mol. Phys.* 19 (1970) 553–566.
- [72] M.J. Allen, D.J. Tozer, *J. Chem. Phys.* 117 (2002) 11113–11120.
- [73] T. Thonhauser, V.R. Cooper, S. Li, A. Puzder, P. Hyldgaard, D.C. Langreth, *Phys. Rev. B* 76 (2007) 125112.
- [74] J.M. Perez-Jorda, A.D. Becke, *Chem. Phys. Lett.* 233 (1995) 134–137.
- [75] Y. Zhang, W. Pan, W. Yang, *J. Chem. Phys.* 107 (1997) 7921–7925.
- [76] D.J. Lacks, R.G. Gordon, *Phys. Rev. A* 47 (1993) 4681.
- [77] E.R. Johnson, S. Keinan, P. Mori-Sánchez, J. Contreras-García, A.J. Cohen, W. Yang, *J. Am. Chem. Soc.* 132 (2010) 6498–6506.
- [78] A. Becke, *J. Chem. Phys.* 85 (1986) 7184.
- [79] S. Kozuch, J.M.L. Martin, *J. Chem. Theory Comput.* 9 (2013) 1918–1931.
- [80] P. Jurečka, J. Šponer, J. Černý, P. Hobza, *Phys. Chem. Chem. Phys.* 8 (2006) 1985–1993.
- [81] J. Řezáč, K.E. Riley, P. Hobza, *J. Chem. Theory Comput.* 7 (2011) 2427–2438.
- [82] J.C. Faver, M.L. Benson, X. He, B.P. Roberts, B. Wang, M.S. Marshall, M.R. Kennedy, C.D. Sherrill, K.M. Merz, *J. Chem. Theory Comput.* 7 (2011) 790–797.
- [83] M.S. Marshall, L.A. Burns, C.D. Sherrill, *J. Chem. Phys.* 135 (2011) 194102.
- [84] G.A. DiLabio, E.R. Johnson, A. Otero-de-la-Roza, *Phys. Chem. Chem. Phys.* 15 (2013) 12821–12828.
- [85] E. Ruiz, D.R. Salahub, A. Vela, *J. Phys. Chem.* 100 (1996) 12265–12276.
- [86] S.N. Steinmann, C. Piemontesi, A. Delacht, C. Corminboeuf, *J. Chem. Theory Comput.* 8 (2012) 1629–1640.
- [87] E.R. Johnson, M. Salamone, M. Bietti, G.A. DiLabio, *J. Phys. Chem. A* 117 (2013) 947–952.
- [88] Y. Zhang, W. Yang, *J. Chem. Phys.* 109 (1998) 2604–2608.
- [89] D.J. Tozer, *J. Chem. Phys.* 119 (2003) 12697–12699.
- [90] A. Ruzsinszky, J.P. Perdew, G.I. Csonka, O.A. Vydrov, G.E. Scuseria, *J. Chem. Phys.* 125 (2006) 194112.
- [91] A.J. Cohen, P. Mori-Sánchez, W. Yang, *Science* 321 (2008) 792.
- [92] M.-C. Kim, E. Sim, K. Burke, *Phys. Rev. Lett.* 111 (2013) 073003.
- [93] E.R. Johnson, O. Clarkin, S.G. Dale, G.A. DiLabio, *J. Phys. Chem. A* 119 (2015) 5883–5888.
- [94] A. Otero-de-la-Roza, E.R. Johnson, *J. Chem. Theory Comput.* 11 (2015) 4033–4040.
- [95] P.E. Blöchl, *Phys. Rev. B* 50 (1994) 17953.
- [96] R. Zacharia, H. Ulbricht, T. Hertel, *Phys. Rev. B* 69 (2004) 155406.
- [97] S. Lebègue, J. Harl, T. Gould, J.G. Ángyán, G. Kresse, J.F. Dobson, *Phys. Rev. Lett.* 105 (2010) 196401.
- [98] L. Spanu, S. Sorella, G. Galli, *Phys. Rev. Lett.* 103 (2009) 196401.
- [99] A.M. Reilly, A. Tkatchenko, *J. Chem. Phys.* 139 (2013) 024705.
- [100] J.E. Hein, Unpublished results.
- [101] J.E. Hein, E. Tse, D.G. Blackmond, *Nat. Chem.* 3 (2011) 704–706.
- [102] I.K. Price, Investigation and Application of Crystal Phase Behavior to Obtain Enantiopure Chemicals, MSc thesis, University of California, Merced, 2014, available from <http://eprints.cdlib.org/uc/item/24r9v8mc>.
- [103] A. Otero-de-la-Roza, B.H. Cao, I.K. Price, J.E. Hein, E.R. Johnson, *Angew. Chem. Int. Ed.* 53 (2014) 7879–7882.
- [104] Z. Ye, A. Otero-de-la-Roza, E.R. Johnson, A. Martini, *Nanotechnology* 25 (2014) 425703.

## 6

# A Comprehensive Overview of the DFT-D3 London-Dispersion Correction

*Lars Goerigk*

School of Chemistry, The University of Melbourne, Melbourne, Australia

## 6.1 INTRODUCTION

In the mid 1990s, it became evident that conventional Kohn–Sham density functional theory [1] (KS-DFT) approximations do not properly describe London-dispersion interactions [2–5], which are nonlocal in nature and asymptotically governed by the well-known relation [6]:

$$E_{\text{disp}} \propto -\frac{C_6}{R^6}. \quad (6.1)$$

Eq. (6.1) shows that in the long-range regime—where we expect negligible overlap between the electron clouds of two molecular or atomic fragments—the dispersion energy  $E_{\text{disp}}$  depends to the sixth power on the distance  $R$  between those fragments, with  $C_6$  being the sixth-order dispersion coefficient. It turns out that due to their semilocal nature, common density functional approximations (DFAs) do not capture this long-range tail of the dispersion energy. This posed a particular dilemma, given that KS-DFT had become a central methodology in Quantum Chemistry and that London dispersion is ubiquitous and very important in chemical processes. Therefore, it is not surprising that a great deal of effort has been put into solving the dispersion problem for conventional DFAs. As reviewed in detail elsewhere [7–9], the resulting dispersion-corrected KS-DFT techniques are numerous and they can be divided into four categories:

1. Semilocal functionals that have been fitted to noncovalent interactions [10].
2. Effective one-electron potentials optimized to reproduce interaction energies in noncovalently bound dimers (see Chapter 7) [11,12].
3. Van der Waals (vdW) DFAs that contain a nonlocal kernel that enforces the correct long-range behavior (see Chapter 8) [13,14].

4. Additive corrections that can be solely pairwise-additive in nature or that can also contain many-body terms (see below as well as Chapter 5) [15–24].

The above list only covers approaches that are easily applicable to both inter- and intramolecular dispersion; for a review of other DFT-based approaches for intermolecular interaction energies only, see Refs. [8] and [9]. The aforementioned additive corrections, together with some category-3 methods, have the advantage that they can be combined with nearly any semilocal DFA. As the name implies, the dispersion correction is usually obtained in a separate calculation after the conventional KS-DFT step and then added to the KS-DFT result. This is sometimes done self-consistently or after the KS-DFT calculation has converged. Very important, however, is that this separate evaluation of the London-dispersion contribution is carried out in only a fraction of the time needed for the underlying KS-DFT calculation, which makes additive corrections valuable tools in the efficient treatment of large systems.

It is worthwhile to note that the idea of additive dispersion corrections dates back to the 1970s, with the main focus being on Hartree–Fock (HF) wave-function theory [25,26]. Empirical additive corrections for KS-DFT have initially been tested in the 1990s [27], however, the development of more accurate and applicable semiclassical corrections only took off in the mid and late 2000s. As examples of these modern approaches, we want to particularly acknowledge Grimme’s DFT-D3 correction [22], the Tkatchenko–Scheffler model (DFT+TS) [21], as well as Johnson and Becke’s exchange-hole-dipole moment model (XDM) [16–18,20]. While the XDM and DFT+TS methods have been reviewed in Chapters 5 and 9, this chapter focusses on Grimme’s DFT-D3 approach.

Grimme developed two variants in 2010 [22] and 2011 [24], which can be considered refinements of his earlier works on the simpler versions DFT-D1 [15] (2004) and DFT-D2 [19] (2006). These additive corrections, in particular the DFT-D3 variants, have made a large impact [28] and they have become standard tools in quantum-chemical applications.

In the following, we provide a comprehensive overview of DFT-D3. First, we establish the theoretical context by briefly reviewing its predecessor DFT-D2, before we describe the DFT-D3 framework in detail. In 2015 the second DFT-D3 variant was further modified by Schwabe and coworkers [29]. For the sake of completeness we also present this modification briefly. In Section 6.3, we provide an overview of software that allows using DFT-D3, before we round off our review by discussing different aspects of this correction, including its accuracy and usefulness in applications.

---

## 6.2 THEORETICAL BACKGROUND

---

### 6.2.1 The DFT-D2 Correction

Before we proceed with a detailed explanation of the DFT-D3 approach, it is worthwhile to give a brief introduction to its predecessor DFT-D2 [19]. Published in 2006, this correction includes one multipole-term that depends to the sixth order on the distance  $R_{AB}$  between two atoms  $A$  and  $B$ . In other words, DFT-D2 considers all possible atom pairs in a given chemical system and attributes a dispersion contribution to each pair according to London’s formula (Eq. (6.1)). These atom-pair contributions are then added to obtain the molecular dispersion

correction:

$$E_{\text{disp}}^{\text{DFT-D2}} = -\frac{1}{2}s_6 \sum_{A \neq B} \frac{C_6^{AB}}{R_{AB}^6} f_{\text{damp}}^{\text{DFT-D2}}(R_{AB}), \quad (6.2)$$

where  $C_6^{AB}$  denotes the averaged, isotropic sixth-order dispersion coefficient for atom pair  $AB$ ,  $f_{\text{damp}}^{\text{DFT-D2}}$  is a damping function and  $s_6$  is a global scaling parameter. The prefactor of one half is needed to avoid double counting.

While DFT-D2 ensures a sixth-order decay of the dispersion contribution in the asymptotic long-range region, it has to be taken into account that the short-range region (overlapping electron clouds of the noncovalently bound fragments) is mostly governed by the underlying DFA. To avoid any double counting in that region, the DFT-D2 contribution needs to be damped. Moreover, a seamless connection has to be established in the region between the short- and long-range parts, which we call “medium-range region” in the following. Both of these conditions are achieved with a damping function  $f_{\text{damp}}^{\text{DFT-D2}}$ , which has the form:

$$f_{\text{damp}}^{\text{DFT-D2}}(R_{AB}) = \frac{1}{1 + e^{-20(R_{AB}/R_r - 1)}}, \quad (6.3)$$

where  $R_r$  is the sum of vdW radii, which were determined from restricted-open-shell HF density contour plots and subsequently scaled by a factor of 1.10. This value was chosen to improve intermolecular distances, particularly between systems containing heavier atoms. The exponent of 20 in Eq. (6.3) was chosen to provide larger corrections at intermediate distances, as compared to the predecessor DFT-D1 (see Ref. [19] for details). More details on damping functions and representative plots are provided in the next section.

Every DFA behaves differently in the short- to medium-range regimes. Some functionals, such as PBE [30] or PW91 [31], are attractive, which initially led to the assumption that they could be used for the calculation of noncovalent interaction energies [32]. On the other hand, some functionals can also be repulsive, such as BLYP [33,34] or B3LYP [35,36]. To take these functional-specific characteristics into account, the global scaling factor  $s_6$  in Eq. (6.2) needs to be adjusted for every DFA, which is done by empirical fitting to a set of noncovalent interaction energies. Attractive DFAs have a smaller  $s_6$  value and repulsive functionals a value larger than unity. Note that in a modification of the DFT-D2 idea, Jurečka et al. pointed out that using a global scale factor  $s_6$  also affects the dispersion strength far from the overlap region between the electron clouds of two noncovalently bound fragments. However, that region should not be affected at all by the choice of DFA, and therefore they suggested to set  $s_6$  to unity and to adjust the scaling of the vdW radii instead [37].

The  $C_6^{AB}$  dispersion coefficients in DFT-D2 are empirical in nature and they are obtained from element-specific coefficients ( $C_6^A$  and  $C_6^B$ ) as a geometric mean:

$$C_6^{AB} = \sqrt{C_6^A C_6^B}. \quad (6.4)$$

These element-specific dispersion coefficients were obtained from atomic ionization potentials  $IP^A$  and static dipole polarizabilities  $\alpha^A$ :

$$C_6^A = 0.05N \times IP^A \times \alpha^A, \quad (6.5)$$

where  $N$  can be 2, 10, 18, 36, or 54, depending on the respective element's row in the periodic table.  $IP^A$  and  $\alpha^A$  were obtained from unrestricted PBE0 [38,39] calculations.

It is without doubt that DFT-D2 can be regarded as a seminal contribution to the DFT community [28]. Despite some empirical elements, it provided a straightforward means to treat noncovalent interactions at the KS-DFT level, as it was easy to use also for nonexpert users without much technical effort. Not only has it enabled a better description of noncovalent interactions, but more importantly, findings obtained from DFT-D2-corrected treatments have helped to elucidate the importance of London dispersion in general thermochemistry and helped slowly change a common misconception that dispersion effects are small and therefore negligible [40].

Nevertheless, shortcomings of this approach also need to be taken into consideration. Van der Waals radii and  $C_6$  coefficients were only determined for the main-group elements up to xenon. All 3d transition metals have been assigned the values for scandium and all 4d metals those for yttrium. Moreover, despite being adjusted by scaling factors in Eq. (6.5), the element-specific  $C_6$  coefficients are essentially based on free-atom calculations in the gas phase. It is known, however, that  $C_6$  coefficients also depend on effects such as hybridization or oxidation states [41]. Some problems have also been reported for charged and neutral alkaline metal compounds [22]. These issues have ultimately motivated the development of the DFT-D3 correction, as outlined in the next section.

### 6.2.2 The DFT-D3 Correction

DFT-D3 is a refined version of DFT-D2. It is applicable to the first 94 elements of the periodic table and, contrary to DFT-D2, main-group elements and transition metals are now treated on an equal footing. The biggest difference with its predecessor is that its dispersion coefficients are fully flexible and system dependent. For the reader's convenience, Table 6.1 lists the main differences between DFT-D2 and the different DFT-D3 variants.

The first version of DFT-D3 was published in 2010 [22], and a modified variant followed in 2011 [24]. As we will see below, both variants are based on the same underlying framework, but they make use of two different damping functions. The 2010 version is nowadays called the "zero-damping" version and in this chapter we will therefore adopt the acronym "DFT-D3(0)." However, it is important to bear in mind that particularly between 2010 and 2012, authors often simply referred to this method as "DFT-D3." Herein, however, we try to avoid this confusion and whenever we use "DFT-D3" we mean the general underlying framework regardless of the type of damping function. The 2011 variant is called the "Becke–Johnson-damping" version "DFT-D3(BJ)." In 2015, Schwabe and coworkers modified the DFT-D3(BJ) variant further and dubbed this approach "DFT-D3(CSO)" [29].

In the following three subsections, we will describe the similarities and differences between these three approaches. The information covered should be sufficient for a general understanding of the DFT-D3 idea. The fourth subsection then describes in detail how the dispersion coefficients for DFT-D3 were derived.

#### **The DFT-D3(0) Variant**

The remainder of Section 6.2.2 only considers two-body (atom-pair) contributions to the dispersion correction of a molecular system, similarly to our previous discussion of DFT-D2.

**TABLE 6.1** Comparison between DFT-D2 and the three DFT-D3 variants

	DFT-D2	DFT-D3(0)	DFT-D3(BJ)	DFT-D3(CSO)
Multipole terms	$R_{AB}^{-6}$	$R_{AB}^{-6}$ and $R_{AB}^{-8}$	$R_{AB}^{-6}$ and $R_{AB}^{-8}$	$R_{AB}^{-6}$
Can be used for	The first 34 main-group elements; limited applicability to 3d and 4d metals	The first 94 elements in the periodic table		
Dispersion coefficients	Empirical; fixed for each element	Based on fractional atomic coordination numbers; Flexible and system dependent		
vdW/cut-off radii	Fixed for each element	Fixed for each atom pair	Tabulated for each element; Based on calculated dipole- and quadrupole-moment expectation values	
Fit parameters	1 <sup>a</sup>	2 <sup>b</sup>	3 <sup>c</sup>	1 <sup>d</sup>

<sup>a</sup>  $s_6$  in Eq. (6.2).

<sup>b</sup>  $s_8$  in Eq. (6.6) and  $s_{r,6}$  in Eq. (6.7).

<sup>c</sup>  $s_8$  in Eq. (6.11), and  $a_1$  and  $a_2$  in Eq. (6.12).

<sup>d</sup>  $c_1$  in Eq. (6.15).

Three-body effects within the DFT-D3 framework and the extension of DFT-D3 to treat periodic structures are discussed separately in Sections 6.2.4 and 6.2.5. The atomic pairwise DFT-D3(0) dispersion correction is described as:

$$E_{\text{disp}}^{\text{DFT-D3(0)}} = -\frac{1}{2} \sum_{A \neq B} \sum_{n=6,8} s_n \frac{C_n^{AB}}{R_{AB}^n} f_{\text{damp},n}^{\text{DFT-D3(0)}}(R_{AB}). \quad (6.6)$$

While formally similar to the DFT-D2 expression (Eq. (6.2)), the first noticeable difference is that DFT-D3(0) depends on two multipole terms. The first is the familiar sixth-order term with isotropic dispersion coefficients  $C_6^{AB}$  for each atom pair, while the second is of eighth order with dispersion coefficients  $C_8^{AB}$ . This term begins to decay toward zero at shorter interatomic distances and it is designed to take into account medium-range effects. Both terms are scaled, with scaling parameters  $s_6$  and  $s_8$ , respectively. During the development stage of DFT-D3(0), higher order terms were tested. However, it was reported these were negligible in this correction, and could even lead to instabilities [22]. Instead, any errors from missing higher-order terms were absorbed into the  $s_8$  scale factor. How these scale factors were determined, is discussed separately in Section 6.2.3.

DFT-D3(0) uses damping functions  $f_{\text{damp},n}^{\text{DFT-D3(0)}}(R_{AB})$  that were originally proposed by Chai and Head-Gordon for a modified DFT-D2 variant used in conjunction with their  $\omega$ -B97X hybrid functional [42]. According to Grimme and coworkers, this function is particularly well suited for DFT-D3(0) due to its numerical stability for higher-order multipole terms [22]. For

the long-range (sixth-order) term, the damping function is

$$f_{\text{damp},6}^{\text{DFT-D3(0)}}(R_{AB}) = \frac{1}{1 + 6(R_{AB}/(s_{r,6}R_0^{AB}))^{-\alpha_6}}, \quad (6.7)$$

where  $s_{r,6}$  is a scale factor (see Section 6.2.3) and  $R_0^{AB}$  is the cut-off radius for the  $AB$  atom pair.  $\alpha_6$  determines the steepness of the damping function. It was adjusted manually to a value of 14 such that the dispersion correction is smaller than 1% of the maximal dispersion energy of a given system whenever  $R_{AB}$  approaches values of typical covalent bond lengths [22]. In this way it was ensured that the dispersion correction does not interfere with covalent bond lengths. The factor of 6 in the denominator has originally been chosen by Chai and Head-Gordon for their  $\omega$ -B97X-D method (see Ref. [42] for technical details). The damping function for the eight-order term assumes a slightly modified form:

$$f_{\text{damp},8}^{\text{DFT-D3(0)}}(R_{AB}) = \frac{1}{1 + 6(R_{AB}/R_0^{AB})^{-(\alpha_6+2)}}. \quad (6.8)$$

The cut-off radii  $R_0^{AB}$  in the previous two equations were derived from PBE0/QZVP calculations for every possible atom-pair combination of the first 94 elements, leading to a total of 4465 values and a higher flexibility of DFT-D3 compared to DFT-D2, which only depends on a limited number of density-contour-based radii (see previous discussion of DFT-D2) [22]. Note that these cut-off radii should not be confused with the common term “vdW radii,” which would describe the minimum of a potential energy curve. We refer the interested reader to the original publication for a more detailed discussion on this topic [22].

Fig. 6.1 shows how these damping functions influence the sixth- and eighth-order DFT-D3 dispersion-correction contributions for a pair of two argon atoms. For long distances, we observe how the  $R^{-6}$  and  $R^{-8}$  terms decay, with the latter approaching the asymptotic limit at shorter distances. In the medium-range regime, the absolute energy contributions reach maxima before they are damped down at shorter distances. This latter behavior explains why this correction has been dubbed “zero damping.”

We have already mentioned that the derivation of the dispersion coefficients can be seen as the major difference between DFT-D2 and DFT-D3. While we refer the interested reader to a later section for a detailed discussion of this derivation, it suffices to say that the pair coefficients  $C_6^{AB}$  are calculated from atomic  $C_6$  coefficients that are uniquely determined on the fly by taking into account the chemical environment of the relevant atoms. In other words, the dispersion coefficients in DFT-D3 are system dependent, which makes DFT-D3 overall more robust and broadly applicable to a variety of different systems compared to its predecessors. The  $C_8^{AB}$  coefficients are calculated according to the recursive relation [44]:

$$C_8^{AB} = 3C_6^{AB} \sqrt{Q_A Q_B}, \quad (6.9)$$

with

$$Q_A = \frac{1}{2} \sqrt{Z_A} \frac{\langle r^4 \rangle_A}{\langle r^2 \rangle_A}, \quad (6.10)$$

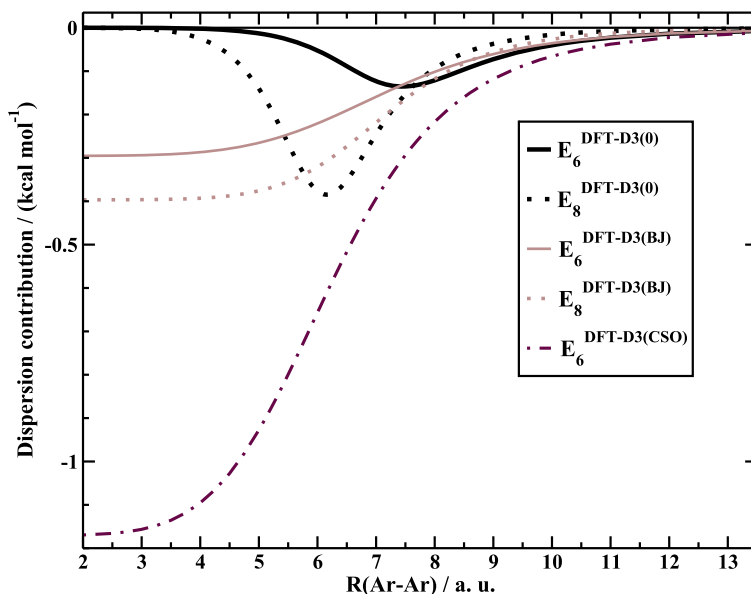


FIGURE 6.1 Sixth- and eighth-order contributions ( $E_6$  and  $E_8$ ) to the dispersion correction in the argon dimer at different Ar–Ar distances for the zero-damping, Becke–Johnson, and C-six-only variants of DFT-D3. The DFT-D3 parameters for the TPSS [43] DFA were used in this example. The behavior of these curves is similar for other DFAs.

where  $Z$  is the nuclear charge,  $\langle r^4 \rangle$  are the quadrupole- and  $\langle r^2 \rangle$  are the dipole-moment-type expectation values derived from atomic densities (see Ref. [22] for more details). They were calculated once for every element and then tabulated. Obtaining higher-order coefficients recursively from lower-order ones is an established strategy, not unique to DFT-D3 [41,44–46]. Employing such techniques was shown to provide a very good estimate for the higher-order coefficients, within a few per cent of their accurate values [41,47]. The two subsequent DFT-D3 variants make use of the same dispersion coefficients and they differ merely in their damping functions.

### The DFT-D3(BJ) Variant

The DFT-D3(BJ) [24] variant published in 2011 employs a rational (finite) damping function proposed by Becke and Johnson for the XDM dispersion model (see Chapter 5) [16–18]:

$$E_{\text{disp}}^{\text{DFT-D3(BJ)}} = -\frac{1}{2} \sum_{A \neq B} \sum_{n=6,8} s_n \frac{C_n^{AB}}{R_{AB}^n + [f_{\text{damp}}^{\text{DFT-D3(BJ)}}(R_{\text{BJ}}^{AB})]^n}, \quad (6.11)$$

with  $s_n$  and  $C_n^{AB}$  being similar to DFT-D3(0), while the damping function is

$$f_{\text{damp}}^{\text{DFT-D3(BJ)}}(R_{\text{BJ}}^{AB}) = a_1 R_{\text{BJ}}^{AB} + a_2. \quad (6.12)$$



The parameters  $a_1$  and  $a_2$  are adjustable and they control the dispersion correction in the short- to medium-range regimes (see Section 6.2.3). The influence of this rational damping function on the sixth- and eighth-order dispersion-correction contributions in a pair of argon atoms is shown in Fig. 6.1 and compared with the zero-damping variant. While the tail of the function is again governed by  $R^{-6}$  and  $R^{-8}$  terms, the DFT-D3(BJ) correction approaches a constant, attractive value for a spatially close pair of atoms. Note that Fig. 6.1 only shows the dispersion correction and that, when adding the contribution from the DFA, the overall dissociation curve will be highly repulsive in the short-range regime. It has to be pointed out that this form of damping function is, in fact, physically more sound than the zero-damping form. In theoretical considerations, Koide showed in 1976 that there is an attractive dispersion contribution even at the unified atom limit [48].

In DFT-D3(BJ),  $R_{\text{BJ}}^{AB}$  in Eq. (6.12) replaces the cut-off radii from DFT-D3(0), while establishing a direct connection with the dispersion coefficients:

$$R_{\text{BJ}}^{AB} = \sqrt{\frac{C_8^{AB}}{C_6^{AB}}}. \quad (6.13)$$

By using Eqs. (6.9) and (6.10), we see that  $R_{\text{BJ}}^{AB}$  can be expressed with the already tabulated multipole-type expectation values needed to obtain  $C_8^{AB}$ , thus lowering the number of tabulated parameters compared to DFT-D3(0):

$$R_{\text{BJ}}^{AB} = \sqrt{\frac{3}{2} \sqrt{\sqrt{Z_A} \frac{\langle r^4 \rangle_A}{\langle r^2 \rangle_A} \sqrt{Z_B} \frac{\langle r^4 \rangle_B}{\langle r^2 \rangle_B}}}. \quad (6.14)$$

### The DFT-D3(CSO) Variant

In 2015, Schwabe and coworkers investigated the influence of the  $R^{-8}$  term in DFT-D3(BJ) and concluded that its main purpose is not only to improve interaction energies, but also to provide the flexibility needed to adjust DFT-D3(BJ) to a given DFA [29]. In other words, the  $R^{-8}$  term can be seen as an interpolation function connecting the dispersion correction with the DFA. Schwabe and coworkers argued that such an interpolation could also be done using a sigmoidal damping function, thus completely eliminating the need for an  $R^{-8}$  term. This resulting variant has been dubbed the ‘‘C-six-only’’ version (CSO). DFT-D3(CSO) adopts the form:

$$E_{\text{disp}}^{\text{DFT-D3(CSO)}} = -\frac{1}{2} \sum_{A \neq B} \left[ s_6 + \frac{c_1}{1 + \exp\left(R_{AB} - 2.5R_{\text{BJ}}^{AB}\right)} \right] \frac{C_6^{AB}}{R_{AB}^6 + (2.5^2)^6}, \quad (6.15)$$

where  $R_{\text{BJ}}^{AB}$  are the same radii used in DFT-D3(BJ).  $c_1$  is an adjustable scaling parameter. Note, that in the original publication this parameter had been named  $a_1$ . However, to avoid confusion with the parameter of the same name in Eq. (6.12), we have adopted a different nomenclature. In DFT-D3(CSO), the short-range behavior of DFT-D3(BJ) is maintained and the overall shape of the resulting curve for the argon-dimer dispersion correction in Fig. 6.1

is very similar to that of DFT-D3(BJ). As DFT-D3(CSO) only depends on one multipole term, its dispersion contribution must be at least the same as the sum of the sixth- and eighth-order DFT-D3(BJ) terms. In fact, at short distances, the absolute value of the DFT-D3(CSO) contribution is even larger (Fig. 6.1), with the exact meaning of this observation still being unexplored. As of July 2016, only a limited number of results have been published for DFT-D3(CSO), but it has been reported that they were very similar to those of DFT-D3(BJ) [29]. Due to the lack of experience with this variant, the majority of the subsequent discussions will deal mostly with DFT-D3(0) and DFT-D3(BJ).

### The System-Dependent $C_6$ Coefficients in DFT-D3

In the previous section, we have mentioned that one reason for the success of DFT-D3 is the way in which its dispersion coefficients had been derived. Also, we have stated that, contrary to DFT-D2, the DFT-D3 dispersion coefficients are system dependent and, thus, offer a route to broader applicability and higher robustness. Having system-dependent dispersion coefficients is by far not unique to the DFT-D3 scheme; for instance, the XDM model uses electron-density dependent  $C_6$  coefficients [16–18,20]. The uniqueness of DFT-D3, however, is that its coefficients depend on the given molecular geometry only. This is achieved by introducing the concept of fractional coordination numbers (CNs), which are obtained for each atom  $A$  in the system by the formula

$$\text{CN}^A = \sum_{B \neq A} \frac{1}{1 + e^{-16(4(R_{A,\text{cov}} + R_{B,\text{cov}})/(3R_{AB}) - 1)}}, \quad (6.16)$$

where the covalent radii  $R_{\text{cov}}$  are based on a self-consistent additive procedure derived from theoretical and experimental data by Pyykkö and Atsumi [49]. Obviously, the fractional coordination number for a given atom is mainly determined by the atoms in its immediate vicinity. Fig. 6.2 shows some examples for fractional CNs in a folded phenylalanyl-glycylglycine conformer. For this geometry, all H atoms have CNs close to unity, C atoms vary between 3.13 and 4.13, N atoms have values of around 3.07, and O atoms range from 1.06 to 2.04. All fractional CNs therefore make sense from a chemical perspective.

The sixth-order pair coefficients  $C_6^{AB}$  in DFT-D3 depend on the fractional CNs of atoms  $A$  and  $B$ . In general,  $C_6^{AB}$  pair coefficients can be obtained from their averaged dipole polarizabilities  $\alpha(i\omega)$  at imaginary frequency  $\omega$  using the Casimir and Polder formula [50]

$$C_6^{AB} = \frac{3}{\pi} \int_0^\infty \alpha_A(i\omega) \alpha_B(i\omega) d\omega. \quad (6.17)$$

However, instead of relating the pair coefficients to atomic dipole polarizabilities, Grimme argued that a much more intuitive way to obtaining system-dependent coefficients is to base them on a set of reference coefficients for different CNs. These coefficients  $C_{6,\text{ref}}^{AB}$  were calculated by employing a variation of the Casimir–Polder equation

$$C_{6,\text{ref}}^{AB}(\text{CN}^A, \text{CN}^B) = \frac{3}{\pi} \int_0^\infty d\omega \frac{1}{m} \left[ \alpha_{A_m H_n}(i\omega) - \frac{n}{2} \alpha_{H_2}(i\omega) \right] \times \frac{1}{k} \left[ \alpha_{B_k H_l}(i\omega) - \frac{l}{2} \alpha_{H_2}(i\omega) \right], \quad (6.18)$$

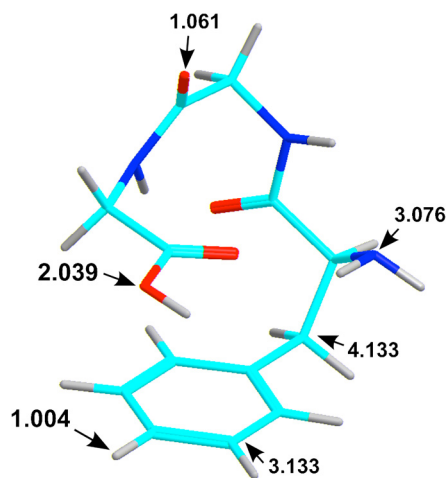


**FIGURE 6.2** Fractional coordination numbers obtained according to Eq. (6.16) for a folded phenylalanyl-glycylglycine conformer.

where  $A_m H_n$  and  $B_k H_l$  are element hydrides with specific CNs used as reference compounds. The dipole polarizabilities  $\alpha$  of these reference compounds are then related to those of  $H_2$ . The  $m$ ,  $n$ ,  $l$ , and  $k$  in the previous equation are stoichiometric coefficients.

The chosen reference compounds reflect typical bonding situations for the underlying elements. For example, to obtain a reference value for carbon with a CN of 1, one needs to obtain a reference dispersion coefficient from the dipole polarizability of CH, while a calculation of the dipole polarizability of  $CH_4$  is needed to obtain a reference value for carbon with a CN of 4.

The dipole polarizabilities of the element hydrides and  $H_2$  were obtained at the time-dependent DFT level with a modified PBE0 functional containing 3/8 Fock exchange instead of the usual 25% (PBE38) [22]. Eq. (6.18) implies that  $C_{6,ref}^{AB}$  must be computed for every possible pair combination between the first 94 elements in the periodic table for different coordination numbers. While one can argue that, as a consequence of this procedure, DFT-D3 contains a large number of tabulated reference coefficients, these tabulated values only serve as a means to obtain system-specific coefficients in the actual DFT-D3 treatment. This is in contrast to DFT-D2, where all coefficients were predetermined and the same for a given atom, regardless of its environment.

In the following, we use “ $C_6^{AB}(CN^A, CN^B)$ ” to label the atom-pair dispersion coefficients used in the actual DFT-D3 calculation, to indicate that the coefficient depends on the CNs of the two atoms in this pair. In Fig. 6.2, we saw that the actual CNs are fractional. For instance, the N atoms shown therein have CN values slightly larger than 3. The pre-calculated pair coefficients  $C_{6,ref}^{AB}$ , however, are based only on integer values of CN. In our example, it is therefore not feasible to use the tabulated  $C_{6,ref}^{AB}$  values for which N has a CN of 3. Instead, the actual  $C_6^{AB}(CN^A, CN^B)$  must reflect that the N atoms have a value somewhere between 3 and 4. As a practical solution, we have to interpolate between these tabulated values. As the

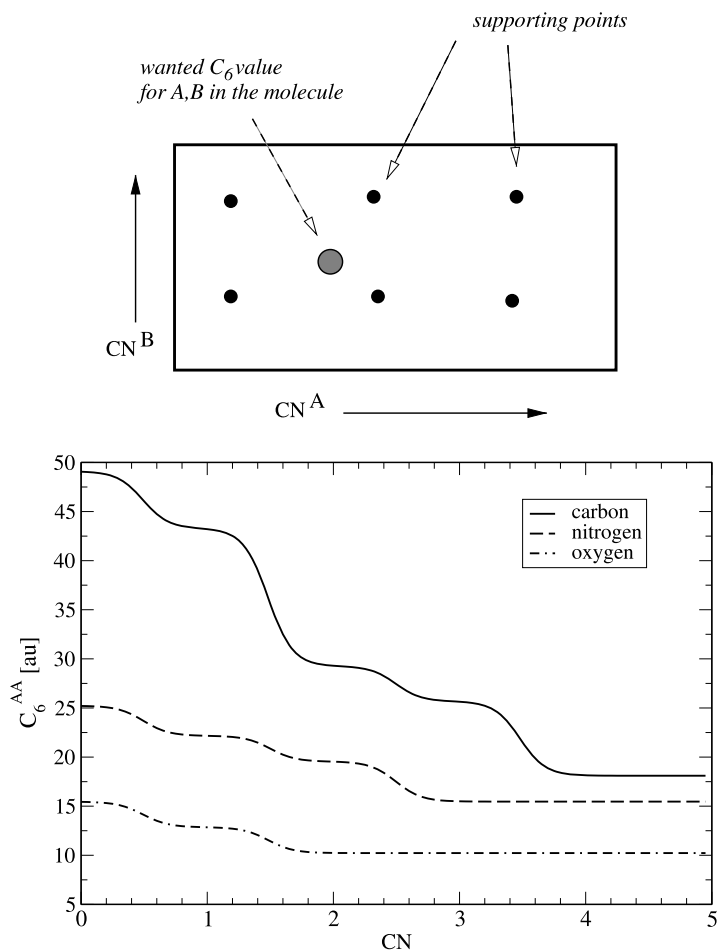


**FIGURE 6.3** 2D interpolation scheme for the dispersion coefficients (top) and cut through the surface for C–C, N–N, and O–O atom pairs with  $CN^A = CN^B = CN$ . Note the mentioned increase in the  $C_6$  value for decreasing  $CN$ . Reprinted with permission from Ref. [22]. Copyright 2010 AIP Publishing.

dispersion coefficient depends on two atoms, such interpolation also needs to be carried out for the second atom that N may be bound to in our example. Also, that atom has a fractional  $CN$ . Consequently, a two-dimensional interpolation is chosen.

The top part of Fig. 6.3 depicts such an interpolation. The smaller black circles stand for the tabulated reference coefficients  $C_{6,\text{ref}}^{AB}$ . These coefficients are discrete supporting points in a two-dimensional grid spanned by  $CN^A$  and  $CN^B$ . The larger, gray circle in the top part of Fig. 6.3 stands for the actual  $C_6^{AB}(CN^A, CN^B)$  that has to be calculated for a given atom pair A and B in the system. It lies somewhere between the supporting points. Therefore, a two-dimensional interpolation is required to determine its value. The interpolation formula

used in this procedure is

$$C_6^{AB}(\text{CN}^A, \text{CN}^B) = \frac{\sum_i^{N_A} \sum_j^{N_B} C_{6,\text{ref}}^{AB}(\text{CN}_i^A, \text{CN}_j^B) L_{ij}}{\sum_i^{N_A} \sum_j^{N_B} L_{ij}}, \quad (6.19)$$

where  $N_A$  and  $N_B$  represent the number of supporting points  $i, j$ —the tabulated  $C_{6,\text{ref}}^{AB}$  values—in this two-dimensional grid.  $L_{ij}$  stands for a Gaussian-type distance between these supporting points and the actual location of the current  $\text{CN}^A$  and  $\text{CN}^B$  in the two-dimensional grid:

$$L_{ij} = e^{-4[(\text{CN}^A - \text{CN}_i^A)^2 + (\text{CN}^B - \text{CN}_j^B)^2]}. \quad (6.20)$$

While for typical main group elements, supporting points with CNs of up to 5 were calculated, heavier elements normally require only supporting points up to  $\text{CN} = 2$ . Consequently, the initial DFT-D3 implementation contained 227 of such supporting points covering the first 94 elements in the periodic table. However, according to the authors, more supporting points would be added to the code on a regular basis [22].

The lower part of Fig. 6.3 demonstrates how the  $C_6$  coefficients of C–C, N–N and O–O pairs depend on the coordination numbers. A free atom has the largest dispersion coefficient. With an increasing CN, the dispersion coefficients decrease. We will discuss this trend again in Section 6.4.1 [22].

### 6.2.3 Combining DFT-D3 with Quantum-Chemical Approaches

We now turn our attention to making the DFT-D3 correction work together with electronic-structure methods. Table 6.2 supports this discussion and gives an overview of the compatibility of DFT-D3 with typical approaches. The first four rows in Table 6.2 deal with conventional KS-DFT approaches. The reader unfamiliar with DFT may want to familiarize themselves with the common terminology used in this field [51], which we will adopt in this section. As mentioned earlier in Section 6.2.2, every DFA behaves differently in the short- and medium-range regimes, with some DFAs being more attractive and others more repulsive. Due to their already strong over-binding tendency, it was recommended that local-density approximation (LDA) functionals should not be combined with DFT-D3 [52]. Conventional generalized-gradient-approximation (GGA), meta-GGA and global hybrid functionals, on the other hand, work with all three variants. The same is also true for range-separated hybrid functionals, as they only exhibit an improved description of the exchange energy, while the correlation contribution is usually that of a conventional DFA. As London dispersion itself is an electron-correlation effect, range-separated DFs therefore also benefit from dispersion corrections, as demonstrated in Ref. [52].

To take into account the different behavior in the short- and medium range regimes, each DFT-D3 variant comes with a number of parameters that have to be adjusted for each DFA. Given that all other internal parameters have been derived from first principles, only these adjustable parameters can be considered as the truly empirical parts in the DFT-D3 methodology. The number of adjustable parameters for each variant is also shown in Table 6.1 and compared with DFT-D2.

TABLE 6.2 Compatibility of the DFT-D3 variants with quantum-chemical methods

Methodology	Value of $s_6$	Compatible with		
		DFT-D3(0)?	DFT-D3(BJ)?	DFT-D3(CSO)
LDA DFAs	$\times$	$\times$	$\times$	$\times$
(Meta-)GGA DFAs	1	✓	✓	✓
Global hybrid DFAs	1	✓	✓	✓
Range-separated DFAs	1	✓	✓	? <sup>a</sup>
Minnesota DFAs	1	✓	$\times/\sqrt{}^b$	?
Double-hybrid DFAs	<1 <sup>c</sup>	✓	✓	✓
Semiempirical MO theory	1	✓	✓	?
HF theory	1	✓	✓	?
MP2-type methods	<1 <sup>d</sup>	✓	✓	?

<sup>a</sup> As of July 2016, no parameters have been determined.

<sup>b</sup> Depending on the functional.

<sup>c</sup> Usually between 0.5 and 0.8.

<sup>d</sup> Between  $-0.04$  and  $0.3$ .

In principle, the first parameter that would be adjustable is the scaling factor for the long-range multipole term ( $s_6$ ). Contrary to DFT-D2, however, it is kept fixed at unity for (meta-)GGA and hybrid functionals. The related scale parameter  $s_8$ , on the other hand, needs to be empirically adjusted because it determines the strength of the medium-range  $R_{AB}^{-8}$  term that may already interfere with the underlying DFA. This is, of course, only the case for the DFT-D3(0) and DFT-D3(BJ) variants, as the DFT-D3(CSO) approach does not rely on such a term.

The three different versions all contain additional empirical parameters in their damping functions. In the case of DFT-D3(0), this is the parameter  $s_{r,6}$ , which scales the atom-pair specific cut-off radii  $R_0^{AB}$  in Eq. (6.7). Thus, DFT-D3(0) has a total of two adjustable parameters for conventional DFAs. The damping function for DFT-D3(BJ) contains the parameters  $a_1$  and  $a_2$  that control the steepness of the damping function and the magnitude of the constant dispersion contribution at short inter-fragment distances (Eq. (6.12)). Therefore, a total of three parameters have to be fitted for DFT-D3(BJ). DFT-D3(CSO) only contains one adjustable parameter, called  $c_1$  in Eq. (6.15).

It was suggested that the two DFT-D3(0) and the three DFT-D3(BJ) parameters be determined using a least-squares fit to a set of 130 noncovalent interaction energies based on reference values with at least CCSD(T) quality extrapolated to the complete basis set limit [22,24]. This set involves rare-gas dimers [22,53,54], as well as the 22 noncovalently bound dimers at their equilibrium geometries known as “S22” test set [55]. Furthermore, the complexes in S22 are also considered at nonequilibrium geometries to allow a better adjustment of the DFT-D3 parameters in the short- and long-range regimes (S22+ set) [22]. Also, intramolecular interactions are taken into consideration in the form of relative energies in alkane, sugar, tripeptide and cysteine conformers (ACONF, SCONF, PCONF, and CYCONF sets) [22,53,54]. With this training set, DFT-D3 parameters have been determined for more than 60 DFAs, with the majority of these published in Refs. [22,24,52,56], as well as on the Grimme research website [57]. In 2016, Smith et al. suggested increasing the training set to 1526 data points and they presented refitted DFT-D3(0) and DFT-D3(BJ) parameters for eight DFAs [58]. The

authors used the acronyms “D3M” and “D3M(BJ)” to distinguish these refitted variants from the originally proposed parameters. In their DFT-D3(CSO) version, Schwabe and coworkers fitted the  $c_1$  parameter of eight DFAs to the S66 [59] set of noncovalent interaction energies in 66 dimers at their equilibrium geometries [29].

The fifth and sixth rows of Table 6.2 single out two special classes of DFAs. The first class consists of Truhlar’s highly popular Minnesota density functionals [10]. While these can also be described as (meta-)GGA, global or range-separated methods, they are distinguished from conventional DFAs by the large number of parameters in their construction, which have been fitted to reproduce noncovalent interaction energies as well as “covalent” properties. Therefore, they formally belong to the first category of dispersion-corrected DFAs listed in Section 6.1. However, while it has been argued that such an approach may be reasonable for structures near their vdW minima, the correct long-range asymptotic behavior of the dispersion energy with distance cannot be recovered by this approach. This was first demonstrated in 2011 for the M05 and M06 classes of Minnesota functionals [60].

Later, it was shown for newer Minnesota classes that the strategy of fitting DFA parameters to noncovalent interaction energies can also cause unphysical behavior near vdW minima. A detailed discussion of this problem is beyond the scope of this chapter and the interested reader is referred to Ref. [56]. However, it has been shown that their description of noncovalent interaction energies improves by coupling Minnesota functionals with dispersion corrections, both in the inter- and intramolecular case. DFT-D3 parameters for these methods have been determined accordingly [52,56]. Contrary to common DFAs, where DFT-D3(0) and DFT-D3(BJ) can both be used without problems, double-counting effects in the short-range region and unphysical values for the fit parameters have been observed for the majority of Minnesota functionals when combined with DFT-D3(BJ). The likely reason for this is the large number of functional-inherent parameters that have already been fitted to noncovalent interaction energies. While the M05 [61], SOGGA11-X [62], M11 [63], MN12-L [64], N12-SX [65], and MN12-SX [65] DFAs can be used with DFT-D3(BJ), the zero-damping version was recommended for most other Minnesota methods [52,56]. We would like to reemphasize that, regardless of the chosen damping function, adding a DFT-D3-type correction to Minnesota functionals corrects for their wrong long-range asymptotic behavior. In fact, improvement of up to 50% or more have been reported when a DFT-D3-type correction was applied [52,56,60]. In this context, vdW-DFA-type corrections have also been combined with DFT-D3 methods and the findings are very similar to those described above—including double-counting effects in the short range [56].

Another special class of DFAs are double-hybrid DFAs, which contain a portion of nonlocal MP2-type perturbative correlation [66]. In 2007, it was observed that due to this nonlocal contribution, long-range dispersion effects are partially described by double-hybrids and that, consequently, the magnitude of the DFT-D2 correction has to be smaller than for conventional DFAs [67]. For DFT-D3, this is reflected in an  $s_6$  parameter smaller than unity (Table 6.2). While in the first DFT-D3 publication the same  $s_6$  value as in DFT-D2 has been adopted for some double hybrids [22], Goerigk and Grimme later proposed evaluating this parameter by adjusting it to the interaction energies in the three rare gas dimers,  $\text{Ne}_2$ ,  $\text{Ar}_2$ , and  $\text{Kr}_2$ , at large interatomic distances at which only long-range dispersion plays a role [54]. According to this scheme, the  $s_6$  value can vary between 0.5 and 0.8 depending on the underlying double hybrid [66].

Finally, as Table 6.2 shows, the DFT-D3 scheme is not only limited to KS-DFT methods, but the D3(0) and D3(BJ) corrections have both been combined with other methods, in particular with semiempirical molecular-orbital (MO) methods (e.g., PM6, RM1, OM3, PM3, AM1, and DFTB) [68–72], and with HF theory [22,24]. In addition, they have also been refitted for specialized, DFT- and wave-function-based small-basis-set approaches for usage in large systems [71]. The D3(BJ) scheme has also been used in the context of molecular-mechanics force-fields [73].

Less known is the fact that D3 and D3(BJ) parameters have also been determined for MP2 and its spin-scaled [74] variants SCS-MP2 and SOS-MP2. While these parameters are not used in practice, it is interesting to note that the  $s_6$  for MP2 has been determined to be  $-0.04$ , an indication of its tendency to overestimate dispersion effects, while those of the spin-scaled variants were determined to be around 0.2 and 0.3, indicating that they slightly underbind dispersion effects [75]. These under- and overbinding tendencies are well known for these methods (see Chapter 4) [74], and the  $s_6$  values are therefore in line with these observations.

### 6.2.4 Three-Body Effects in DFT-D3

So far, we have only discussed the DFT-D3 correction as an atomic pairwise approach. While such two-body terms form the main contribution to the total dispersion correction, many-body contributions become important in larger systems (see Chapters 1, 4, and 14). In this chapter, we are solely concerned with the DFT-D3 approach, but we note that other dispersion corrections, such as the XDM (see Chapter 5) or the Tkatchenko–Scheffler models, have been extended to treat such many-body effects [76–78]. A three-body term for DFT-D3 was introduced in Grimme’s 2010 publication, and it can be optionally combined with any of the three two-body variants [22]. It makes use of the expression derived by Axilrod, Teller and Muto (ATM) for the interaction of three fragments  $A$ ,  $B$  and  $C$  [79,80]:

$$E_{\text{ATM}}^{ABC} = \frac{C_9^{ABC} (3 \cos \theta_a \cos \theta_b \cos \theta_c + 1)}{(R_{AB} R_{BC} R_{CA})^3}, \quad (6.21)$$

where the  $\theta$ s represent internal angles in a triangle spanned by the vectors representing the three inter-fragment distances  $R_{AB}$ ,  $R_{BC}$ , and  $R_{CA}$ . The coefficient  $C_9^{ABC}$  is called the “triple-dipole constant” and, similarly to the  $C_6$  coefficient, it can be obtained from dipole polarizabilities (compare with Eq. (6.17)):

$$C_9^{ABC} = \frac{3}{\pi} \int_0^\infty \alpha^A(i\omega) \alpha^B(i\omega) \alpha^C(i\omega) d\omega. \quad (6.22)$$

Given that the three-body contribution typically amounts to around 5–10% or less of the total dispersion correction, Grimme suggested to approximate the  $C_9$  coefficient as a geometric mean from the already calculated  $C_6$  coefficients:

$$C_9^{ABC} \approx -\sqrt{C_6^{AB} C_6^{BC} C_6^{CA}}. \quad (6.23)$$



The three-body contribution with DFT-D3 is then calculated as

$$E^{\text{D3}(3)} = - \sum_{ABC} f_{\text{damp}}(\bar{R}_{ABC}) E_{\text{ATM}}^{ABC}. \quad (6.24)$$

Regardless of the chosen damping function for the DFT-D3 two-body term, the three-body term exclusively makes use of the zero-damping function presented for DFT-D3(0) with  $\bar{R}_{ABC}$  being the geometric mean over the distances  $R_{AB}$ ,  $R_{BC}$ , and  $R_{CA}$ . The  $E^{\text{D3}(3)}$  contribution is added to one of the previously presented two-body contributions. In the literature, DFT-D3 energies that include a three-body term have been dubbed “DFT-D3<sup>ATM</sup>”.

## 6.2.5 DFT-D3 for Periodic Systems

To apply DFT-D3 to periodic systems, an additional summation has to be performed over the system’s unit-cell translation vectors  $\mathbf{T}$ . While this extension is straightforward to all three flavors of DFT-D3, we only demonstrate this for the Becke–Johnson-damping version [81,82]:

$$E_{\text{disp}} = -\frac{1}{2} \sum_{AB} \sum_{n=6,8} \sum_{\mathbf{T}} s_n \frac{C_n^{AB}}{|\mathbf{R}_{AB} + \mathbf{T}|^n + (a_1 R_{\text{BJ}}^{AB} + a_2)^n}, \quad (6.25)$$

where  $\mathbf{R}_{AB}$  denotes the vector between atoms  $A$  and  $B$  within the same unit cell. The definition of the remaining parameters and variables is identical to those described earlier for the molecular case. The extension of DFT-D3 to periodic system made a slight modification of the coordination-number formula (Eq. (6.16)) necessary. The attentive reader may have noticed that for an infinite distance between two atoms, the equation converges to a small, albeit nonzero, contribution ( $1.1 \times 10^{-7}$ ). For most applications, particularly in the molecular case, this has no implications because this small contribution does not affect the final CN for an atom. Moreover, it is much smaller than the uncertainty from other technical settings, e.g., the quadrature-grid choice of the underlying KS-DFT treatment. Nevertheless, to ensure proper convergence of the CN in periodic systems, it was suggested to modify Eq. (6.16) with an additional damping factor; see Ref. [81] for these technical details.

---

## 6.3 AVAILABILITY OF DFT-D3

The DFT-D3(0) and DFT-D3(BJ) methods, including the ATM three-body corrections and analytical gradients, were first implemented in the standalone program `dftd3`, whose source code and binaries are freely available for download [57]. The DFT-D3 scheme has also been incorporated into various quantum-chemical software packages. Some of these programs are freely available for the academic user, while others require a license fee. Table 6.3 lists these programs and provides details on which DFT-D3 variants they include and whether they allow for calculations beyond single-point energies, i.e., analytical gradients or Hessians. The table also shows if users are allowed to set their own DFT-D3 parameters or whether the correction can only be used with a pre-defined set of DFAs. For usage of DFT-D3(CSO), we recommend contacting the authors directly [29].

TABLE 6.3 Details on DFT-D3 implementations in current versions of quantum-chemical software<sup>a</sup>

Program	D3(0)	D3(BJ)	ATM	User-defined parameters	Energy	Gradient	Hessian
Gaussian09 E.01 [83]	✓	✓	✗	✓	✓	✓	✓
TURBOMOLE 7.0 [84]	✓	✓	✓	✓	✓	✓	✓
ORCA 3.0.3 [85]	✓	✓	✓	✓	✓	✓	✓
QCHEM 4.4 [86]	✓	✗	✓	✓	✓	✓	✓
GAMESS-US 2014 [87]	✓	✗ <sup>b</sup>	✓	✓	✓	✓	✗
NWCHEM 6.6 [88]	✓	✗	✗	✗	✓	✓	✓
ADF [89]	✓	✓	✗	✓	✓	✓	✓
PSI4 [90]	✓	✓	✗	✓	✓	✓	✗
MOLPRO 2015.1 [91]	✓	✗	✗	✗	✓	✗	✗
Dalton 2016 [92]	✓	✓	✓	✓	✓	✓	✗
VASP 5.3.4 [93]	✓	✓	✗	✓	✓	✓	✗
Jaguar [94]	✓	✗	✗	✗	✓	✗	✗
Spartan14 [95]	see QCHEM4.4						

<sup>a</sup> As of July 2016.

<sup>b</sup> Will be included in the 2016/2017 release of GAMESS-US.

## 6.4 DISCUSSION AND EXAMPLES

We will present a selection of DFT-D3 applications in this section to provide usage guidelines and general recommendations. For more detailed examples, we recommend the reviews by Grimme and coworkers [7,8].

### 6.4.1 On the Accuracy of DFT-D3 Dispersion Coefficients

In the last part of Section 6.2.2, we have outlined that DFT-D3 features flexible  $C_6$  coefficients that adjust for every system due to their fractional, atomic CNs. We would like to emphasize that this dependency is a geometrical one, but that, nevertheless, the resulting dispersion coefficients are chemically more reasonable than the empirical coefficients in DFT-D2. We have already seen in Fig. 6.3 that the  $C_6$  value is largest for a free atom and it decreases with increasing CN. Indeed, atoms in different hybridization states have different chemical environments and, thus, different CNs. This connection is therefore indirectly represented in DFT-D3. For example, Grimme reported that the DFT-D3 coefficient for an atom pair consisting of two sp-hybridized C-atoms is 29.3 atomic units (a.u.) compared to an experimental value of 29.7 a.u. [22]. The DFT-D3 values for pairs of two sp<sup>2</sup> and sp<sup>3</sup> atoms are 25.7 and 18.1 a.u., respectively, compared to experimental values of 27.4 and 22.4 a.u. [22]. A comparison of molecular DFT-D3  $C_6$  coefficients with 174 experimental pair coefficients showed that DFT-D3 coefficients had a mean absolute deviation (MAD) of about 8% [22]. A subsequent more extensive study on 1225 molecules ranging from small systems, such as dihydrogen, to medium-sized ones, such as octane, revealed even better results with an MAD of less than 5% [7]. This suggests that one of the main reasons for DFT-D3's success is the accuracy of its system-dependent dispersion coefficients.

### 6.4.2 Typical Noncovalent Interactions

Compared to DFT-D2, initial results showed only minor improvements of 0.8 kJ/mol for an MAD averaged over nine DFT-D3(0)-corrected DFAs for the S22 set of noncovalently bound dimers at their equilibrium geometries [22]. However, a much more significant error reduction was observed for rare-gas dimers and for dimers including heavy (3rd- or 4th-row) elements, which demonstrates the broader applicability and robustness of the DFT-D3 scheme. While those examples covered interaction energies in noncovalently bound systems, the main advantage of DFT-D3(0) over DFT-D2 became apparent for intramolecular dispersion effects in conformers. For instance, averaged over nine DFAs, DFT-D2 showed a large MAD of more than 4 kJ/mol for relative energies in tripeptide conformers, which dropped to 2.4 kJ/mol for DFT-D3. For a set of alkane conformers the MAD dropped from 2 kJ/mol to only 0.4 kJ/mol, which is within the accuracy of the high-level *ab initio* reference data [22].

The DFT-D3(BJ) correction introduced further improvement over earlier DFT-D versions and it is now the recommended default approach [24], with the exception of those Minnesota functionals that only work in combination with DFT-D3(0) [52,56]. It was also shown that DFT-D3(BJ)-corrected functionals can outperform more costly vdW-DFAs [96,97], which makes DFT-D3(BJ) particularly interesting in the application to systems that are prohibitively large for vdW-DFAs.

A more thorough analysis with about 45 DFAs was conducted in 2011 with the large GMTKN30 [53,54] database for general main-group thermochemistry, kinetics and noncovalent interactions [52]. One third of GMTKN30 contains noncovalent-interaction-energy test sets. For the noncovalent-interaction sets, it was demonstrated how DFT-D3-corrected double-hybrid DFAs describe inter- and intramolecular interactions not only on an equal footing, but also with errors close or below the accuracy threshold of high-level *ab initio* coupled-cluster methods, therefore outperforming DFAs from lower rungs of the Jacob's Ladder [52]. In the same study, dispersion-corrected double-hybrids had average errors that were smaller by at least 50% compared to the average errors of wave-function MP2-type methods [52]. Double-hybrids are conceptually equivalent to MP2 strategies and they require similar computing time. Therefore, dispersion-corrected double-hybrids are a useful alternative to conventional MP2 treatments of noncovalent interactions. The study concluded by recommending dispersion-corrected double hybrids for routine DFT applications of noncovalent interaction energies, provided that the system size allows it [52].

The DFT-D3 variants have also been assessed for nonequilibrium geometries. Extended studies of Hobza's S66x8 set [59] with 66 dimers at eight different intermolecular distances showed that in the long-range regime, DFT-D3 corrected functionals, particularly double hybrids, recover the interaction energies within an error margin of  $\pm 10$ –15% [60]. Also, we note that DFAs parametrized to treat noncovalent interactions, such as the popular Minnesota functionals, underbind those dimers by 25–50% [56,60].

The DFT-D3<sup>ATM</sup> approach has been shown to be useful in the treatment of larger systems. The initial DFT-D3(0) paper showed that the three-body contribution to the dissociation energy of two graphene layers—based on interpolation from graphene model systems—is about 8% and, thus, significant [22]. Benchmark studies with test sets for large supramolecular compounds—called S12-L [98] and S30-L [99]—showed that for some DFAs the ATM correction contributed to up to 15 % of the binding energy.

### 6.4.3 Intramolecular Dispersion Effects in Thermochemistry and Kinetics

London dispersion is ubiquitous and as such it also influences general thermochemistry and kinetics. Many examples with DFT-D3 (and other dispersion corrections) have demonstrated over the years that any computational treatment of, for instance, reaction energies or barrier heights should therefore include a dispersion correction by default. Extensive studies on GMTKN30 showed that dispersion effects in typical reactions involving medium-sized organic molecules can influence reaction energies and barrier heights by 8 kJ/mol or more [24,52]. Adding a dispersion correction to a reliable DFA therefore improves the description of these, with DFT-D3(BJ) being more robust and accurate than DFT-D3(0) [24], and DFT-D3(CSO) being very similar to DFT-D3(BJ) [29]. Again, DFT-D3-corrected double hybrids turned out to be the best-performing DFAs, also outperforming MP2-type wavefunction approaches [52,54]. Note that in the unimolecular case, dispersion effects are also sizable (more than 8 kJ/mol) like, for instance, in the case of inversion and racemization barriers [100]. DFT-D3(BJ)-corrected DFAs have also been shown to be competitive with vdW-DFAs and other dispersion-corrected approaches in thermochemical benchmark studies, including atomization energies, reaction energies and barrier heights of organic and inorganic reactions, mostly taken from the aforementioned GMTKN30 benchmark database [96,97].

The importance of London-dispersion has also been exemplified in the context of typical computational organic chemistry applications. In this field, the B3LYP/6-31G\* level of theory is probably the most applied by far. This popularity stems from the fact that missing dispersion effects in B3LYP are partially compensated by incompleteness effects from the relatively small 6-31G\* atomic-orbital basis set. One portion of this incompleteness error is called the “basis-set superposition error” (BSSE), which leads to an artificial overestimation of noncovalent interactions. Due to BSSE, a dispersion-uncorrected method may appear to provide improved interaction energies when combined with a small basis set (see Chapter 4). Kruse et al., however, clearly showed that this error compensation between BSSE and missing dispersion cannot be controlled and instead they provided recommendations on how to fix this apparent problem without compromising the relatively low computational cost of B3LYP/6-31G\* [101]. Using DFT-D3(BJ) constitutes an important component in this improved alternative.

Using DFT-D3<sup>ATM</sup> to treat thermochemistry of larger systems was suggested in a thermochemical protocol presented in Ref. [102], where the ATM contribution made up about 5% of the reaction energies of large systems for most tested DFAs.

### 6.4.4 DFT-D3 and Geometries

It will not come as a surprise that London dispersion affects geometries, not only those of noncovalently bound complexes, but also of single molecules. DFT-D3 geometry optimizations can be routinely carried out with a number of programs, as shown in Table 6.3. The usefulness of DFT-D3 in geometry optimizations has been pointed out for the BJ-damping variant in particular, where this version led to an improved description of notoriously difficult systems, such as the ring–ring distance in 2,2-paracyclophane or the S–S distances in the cyclic S<sub>8</sub><sup>2+</sup> ion (Fig. 6.4) [24]. The same was verified two years later in a more extended benchmark study on rotational constants of 25 molecules in the gas phase, which reflect the

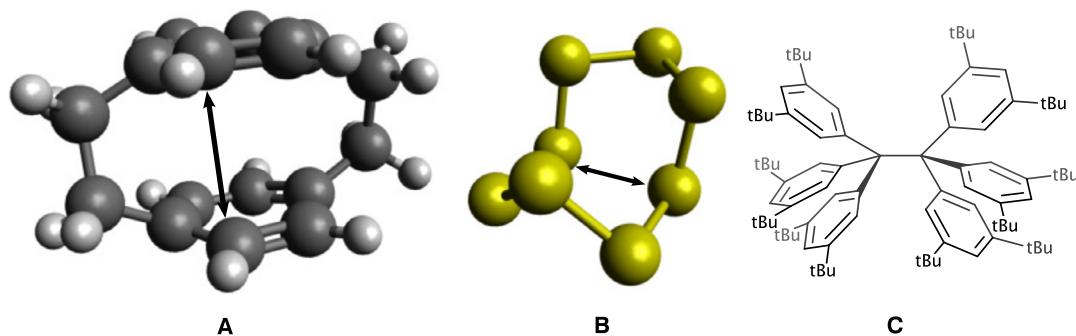


FIGURE 6.4 Structures of 2,2-paracyclophane (A),  $S_8^{2+}$  (B), and an all-meta-*tert*-butyl substituted hexaphenylethane (C). The arrows indicate the interatomic distances influenced by intramolecular London dispersion in A and B.

quality of their geometries. Again, DFT-D3(BJ) was found to be accurate, with errors in the 0.5–1% range for most corrected DFAs and with dispersion-corrected double-hybrids being accurate to 0.25% [103]. A second comprehensive benchmark study revealed that DFT-D3(BJ) is also competitive with vdW-DFAs for geometry optimizations [104]. Another noteworthy example is all-meta-*tert*-butyl-substituted hexaphenylethane (Fig. 6.4). This molecule is particularly puzzling, as it was found to be stable, contrary to common textbook knowledge, which suggest the opposite due to steric hindrance between the bulky substituents. With the help of DFT-D3, however, it was shown that the central C–C bond in this system is indeed stabilized by the dispersion correction, and detailed analysis showed that this is due to the description of London-dispersion interactions between those bulky groups [105].

D3(BJ) geometry optimizations in combination with HF theory have also been described in the literature. The first DFT-D3(BJ) study indicated that HF-D3(BJ) structures were comparable with some dispersion-corrected DFA ones [24]. Later, Goerigk and Reimers showed that, indeed, HF-D3(BJ) is more accurate than dispersion-corrected hybrid DFAs for gas-phase peptide structures [106] and protein-crystal fragments [107,108]. Gordon also confirmed that HF-D3(BJ) is a useful alternative to dispersion-corrected DFAs for structures of noncovalently bound dimers [109]. The good performance of HF-D3(BJ) can be explained with the finite damping function; due to its constant contribution at short distances, the D3(BJ) correction mimics short-range electron correlation effects missing in HF theory. Note, however, that HF-D3(BJ)'s accuracy for noncovalent interaction energies is of GGA-D3(BJ) quality only (with an average error of 4 kJ/mol for the noncovalent interaction sets in GMTKN30) [52].

### 6.4.5 DFT-D3 for Bulk Solids and Surfaces

As shown in Section 6.2.5, DFT-D3 has been extended to periodic systems. Single-point calculations and geometry optimizations are possible with the popular solid-state code VASP (see Table 6.3). The first application in this area was carried out by Moellmann and Grimme in 2010, where they showed that the DFT-D3(0) correction gave accurate crystal structures in a bis-thiophene derivative, outperforming the uncorrected PBE functional, which is the usual

method of choice in this field [110]. A more comprehensive study by the same authors was published in 2014 [82]. In the latter, they applied the DFT-D3(BJ) correction with and without the three-body correction to accurately reproduce cohesive energies and lattice parameters in rare-gas crystals and for the X23 [111,112] set of organic crystals. Other examples of successful descriptions of packing effects with DFT-D3(BJ) include organometallic ruthenium [113] and zirconium compounds [114], as well as ice polymorphs [115].

Brandenburg and Grimme also showed that HF-D3(BJ) was competitive with DFT-based methods [116]. We also note that a variety of low-cost wave-function and semiempirical MO methods were suggested as alternatives for the treatment of crystal structures, due to their lower computing time [71,116].

While bulk materials imply a three-dimensional periodicity, DFT-D3(BJ) has also been used in the context of two-dimensional periodic systems in the modeling of adsorption processes on surfaces. One impressive example is the work by Reimers et al., which described the formation of polymorphic, self-assembled monolayers of tetra-alkyl porphyrins on graphite surfaces, demonstrating that this dispersion-driven process involves monolayer-surface dispersion interactions of up to 600 kJ/mol [117]. Reimers' optimized monolayer structures could be verified with scanning tunneling microscopy, thus demonstrating the predictive value of DFT-D3-corrected treatments (see Chapter 13).

#### 6.4.6 Modified DFT-D3 Dispersion Coefficients in the Literature

As outlined in Section 6.2.2, the pair coefficients are derived from neutral hydrides as reference compounds. The effect of oxidation states on the dynamic polarizabilities and, hence, the dispersion coefficients are therefore not covered. In a limited number of studies, special adjustments to the tabulated reference pair coefficients were made. In 2011, Grimme and coworkers treated sodium chloride and magnesium oxide in the bulk and as substrates for the adsorption of organic molecules [118]. For this specialized case, new  $C_6$  coefficients for  $\text{Na}^+$  and  $\text{Mg}^{2+}$  were calculated with electrostatically embedded NaCl and MgO clusters as reference compounds. Later, a similar approach was chosen to obtain coefficients for  $\text{Ti}^{4+}$  to describe the structural and energetic properties of  $\text{TiO}_2$  in the bulk phase [119].

In 2014, Grimme and coworkers reported that interactions in some transition metal complexes were overestimated [120]. Also here, alternative  $C_6$  coefficients for positively charged transition metal atoms were derived, with chlorides used as reference compounds. Indeed, the resulting  $C_6$  coefficients were smaller than for neutral atoms and they allowed a better description of the related dispersion effects. This modified approach was dubbed "DFT-D3M<sup>+</sup>." We also note that in larger organometallic complexes, the main stabilizing (dispersive) interaction takes place between the organic ligands, for which the originally derived dispersion coefficients are sufficient. Presumably, this is the reason why this modification has not appeared again. Indeed, based on our own experience and on a large number of data reported by different groups over the years, one can conclude that the originally implemented dispersion coefficients are sufficiently reliable for routine applications, particularly in computational organic and inorganic chemistry.

## 6.5 SUMMARY

The DFT-D3 approach for the efficient treatment of London-dispersion interactions has without doubt made an impressive impact on modern computational chemistry. Herein, we first outlined how it is a conceptual extension of the equally popular DFT-D2 scheme. Like its predecessor, DFT-D3 calculates the dispersion correction from the molecular geometry only. This correction is then added to the result of a conventional KS-DFT method and also other mean field approaches. It is, thus, a correction to the total energy, but as such it also influences geometries and frequencies, as these are connected to the first and second derivatives of the energy with respect to the atomic coordinates. DFT-D3 does not influence other electronic properties directly, but rather indirectly, for instance if that property is sensitive to structural changes induced by the correction. One main advantage of DFT-D3, however, is that it is obtained at negligible computational cost, which makes it particularly attractive in applications to large systems.

The main change compared to DFT-D2 is that in DFT-D3 the dispersion coefficients are system dependent and that it is applicable to the first 94 elements of the periodic table. DFT-D3 is therefore not only more accurate, but also more flexible and it allows application to a broader range of elements in the periodic table.

The DFT-D3 correction comes in three flavors, with the DFT-D3(0) variant depending on two fit parameters that have to be adjusted for every underlying method, while DFT-D3(BJ) includes three and DFT-D3(CSO) depends on only one method-specific fit parameter. The first two variants have been implemented in a variety of codes and, therefore, can be routinely used by a broad community. The input is straightforward and, thus, the hurdle to change to DFT-D3-based computational protocols is low. Our review aimed at lowering this hurdle even more and we encourage the reader to test DFT-D3 in one of their next studies.

## Acknowledgments

L.G. is the recipient of an Australian Research Council Discovery Early Career Researcher Award (project number DE140100550). L.G. would like to thank Prof. Tobias Schwabe for his program version of DFT-D3(CSO) to generate parts of the plot in [Fig. 6.1](#). L.G. also thanks Prof. Stefan Grimme for a high-resolution version to reprint [Fig. 6.3](#).

## References

- [1] W. Kohn, L.J. Sham, *Phys. Rev.* 140 (1965) A1133–A1138.
- [2] J.M. Perez-Jorda, A.D. Becke, *Chem. Phys. Lett.* 233 (1995) 134–137.
- [3] S. Kristyán, P. Pulay, *Chem. Phys. Lett.* 229 (1994) 175–180.
- [4] P. Hobza, J. Šponer, T. Reschel, *J. Comput. Chem.* 16 (1995) 1315–1325.
- [5] J. Šponer, J. Leszczynski, P. Hobza, *J. Comput. Chem.* 17 (1996) 841–850.
- [6] F. London, *Z. Phys.* 63 (1930) 245–279.
- [7] S. Grimme, *WIREs Comput. Mol. Sci.* 1 (2011) 211–228.
- [8] S. Grimme, A. Hansen, J.G. Brandenburg, C. Bannwarth, *Chem. Rev.* 116 (2016) 5105–5154.
- [9] G.A. DiLabio, A. Otero-de-la-Roza, *Reviews in Computational Chemistry*, John Wiley & Sons, 2016, pp. 1–97.
- [10] R. Peverati, D.G. Truhlar, *Philos. Trans. R. Soc. Lond. A* 372 (2014) 20120476.
- [11] O.A. von Lilienfeld, I. Tavernelli, U. Rothlisberger, D. Sebastiani, *Phys. Rev. Lett.* 93 (2004) 153004.
- [12] E. Torres, G.A. DiLabio, *J. Phys. Chem. Lett.* 3 (2012) 1738–1744.
- [13] M. Dion, H. Rydberg, E. Schröder, D.C. Langreth, B.I. Lundqvist, *Phys. Rev. Lett.* 92 (2004) 246401.

- [14] O.A. Vydrov, T. Van Voorhis, *J. Chem. Phys.* 133 (2010) 244103.
- [15] S. Grimme, *J. Comput. Chem.* 25 (2004) 1463–1473.
- [16] A.D. Becke, E.R. Johnson, *J. Chem. Phys.* 122 (2005) 154104.
- [17] A.D. Becke, E.R. Johnson, *J. Chem. Phys.* 123 (2005) 154101.
- [18] E.R. Johnson, A.D. Becke, *J. Chem. Phys.* 124 (2006) 174104.
- [19] S. Grimme, *J. Comput. Chem.* 27 (2006) 1787–1799.
- [20] A.D. Becke, E.R. Johnson, *J. Chem. Phys.* 127 (2007) 154108.
- [21] A. Tkatchenko, M. Scheffler, *Phys. Rev. Lett.* 102 (2009) 073005.
- [22] S. Grimme, J. Antony, S. Ehrlich, H. Krieg, *J. Chem. Phys.* 132 (2010) 154104.
- [23] S.N. Steinmann, C. Corminboeuf, *J. Chem. Theory Comput.* 7 (2011) 3567–3577.
- [24] S. Grimme, S. Ehrlich, L. Goerigk, *J. Comput. Chem.* 32 (2011) 1456–1465.
- [25] J. Hepburn, G. Scoles, R. Penco, *Chem. Phys. Lett.* 36 (1975) 451–456.
- [26] R. Ahlrichs, R. Penco, G. Scoles, *Chem. Phys.* 19 (1977) 119–130.
- [27] F.A. Gianturco, F. Paesani, M.F. Laranjeira, V. Vassilenko, M.A. Cunha, A.G. Shashkov, A.F. Zolotoukhina, *Mol. Phys.* 92 (1997) 957–972.
- [28] See, e.g., Thomson Reuter's Web of Science Core Collection, <http://apps.webofknowledge.com/>.
- [29] H. Schröder, A. Creon, T. Schwabe, *J. Chem. Theory Comput.* 11 (2015) 3163–3170.
- [30] J.P. Perdew, K. Burke, M. Ernzerhof, *Phys. Rev. Lett.* 77 (1996) 3865–3868.
- [31] J.P. Perdew, in: P. Ziesche, H. Eschrig (Eds.), *Proceedings of the 21st Annual International Symposium on the Electronic Structure of Solids*, Akademie Verlag, Berlin, 1991, p. 11.
- [32] T.A. Wesolowski, O. Parisel, Y. Ellinger, J. Weber, *J. Phys. Chem. A* 101 (1997) 7818–7825.
- [33] A.D. Becke, *Phys. Rev. A* 38 (1988) 3098–3100.
- [34] C. Lee, W. Yang, R.G. Parr, *Phys. Rev. B* 37 (1988) 785–789.
- [35] A.D. Becke, *J. Chem. Phys.* 98 (1993) 5648–5652.
- [36] P.J. Stephens, F.J. Devlin, C.F. Chabalowski, M.J. Frisch, *J. Phys. Chem.* 98 (1994) 11623–11627.
- [37] P. Jurečka, J. Černý, P. Hobza, D.R. Salahub, *J. Comput. Chem.* 28 (2007) 555–569.
- [38] C. Adamo, V. Barone, *J. Chem. Phys.* 110 (1999) 6158–6170.
- [39] M. Ernzerhof, G.E. Scuseria, *J. Chem. Phys.* 110 (1999) 5029–5036.
- [40] S. Grimme, J. Antony, T. Schwabe, C. Mück-Lichtenfeld, *Org. Biomol. Chem.* 5 (2007) 741–758.
- [41] A. Stone, *The Theory of Intermolecular Forces*, 2nd ed., Oxford University Press, 2013.
- [42] J.-D. Chai, M. Head-Gordon, *Phys. Chem. Chem. Phys.* 10 (2008) 6615–6620.
- [43] J. Tao, J.P. Perdew, V.N. Staroverov, G.E. Scuseria, *Phys. Rev. Lett.* 91 (2003) 146401.
- [44] G. Starkschall, R.G. Gordon, *J. Chem. Phys.* 56 (1972) 2801–2806.
- [45] K.T. Tang, J.P. Toennies, *J. Chem. Phys.* 80 (1984) 3726–3741.
- [46] A.J. Thakkar, H. Hettema, P.E.S. Wormer, *J. Chem. Phys.* 97 (1992) 3252–3257.
- [47] A.J. Thakkar, *J. Chem. Phys.* 89 (1988) 2092–2098.
- [48] A. Koide, *J. Phys. B* 9 (1976) 3173–3183.
- [49] P. Pyykkö, M. Atsumi, *Chem. Eur. J.* 15 (2009) 186–197.
- [50] H.B.G. Casimir, D. Polder, *Phys. Rev.* 73 (1948) 360–372.
- [51] S.M. Bachrach, *Computational Organic Chemistry*, 2nd ed., John Wiley & Sons, Hoboken, 2014.
- [52] L. Goerigk, S. Grimme, *Phys. Chem. Chem. Phys.* 13 (2011) 6670–6688.
- [53] L. Goerigk, S. Grimme, *J. Chem. Theory Comput.* 6 (2010) 107–126.
- [54] L. Goerigk, S. Grimme, *J. Chem. Theory Comput.* 7 (2011) 291–309.
- [55] P. Jurečka, J. Šponer, J. Černý, P. Hobza, *Phys. Chem. Chem. Phys.* 8 (2006) 1985–1993.
- [56] L. Goerigk, *J. Phys. Chem. Lett.* 6 (2015) 3891–3896.
- [57] Grimme Research Web Site, <http://www.thch.uni-bonn.de/tc/index.php?section=downloads&subsection=DFT-D3&lang=english>.
- [58] D.G.A. Smith, L.A. Burns, K. Patkowski, C.D. Sherrill, *J. Phys. Chem. Lett.* 7 (2016) 2197–2203.
- [59] J. Řezáč, K.E. Riley, P. Hobza, *J. Chem. Theory Comput.* 7 (2011) 2427–2438.
- [60] L. Goerigk, H. Kruse, S. Grimme, *ChemPhysChem* 12 (2011) 3421–3433.
- [61] Y. Zhao, N.E. Schultz, D.G. Truhlar, *J. Chem. Phys.* 123 (2005) 161103.
- [62] R. Peverati, D.G. Truhlar, *J. Chem. Phys.* 135 (2011) 191102.
- [63] R. Peverati, D.G. Truhlar, *J. Phys. Chem. Lett.* 2 (2011) 2810–2817.
- [64] R. Peverati, D.G. Truhlar, *Phys. Chem. Chem. Phys.* 14 (2012) 13171–13174.



- [65] R. Peverati, D.G. Truhlar, *Phys. Chem. Chem. Phys.* 14 (2012) 16187–16191.
- [66] L. Goerigk, S. Grimme, *WIREs Comput. Mol. Sci.* 4 (2014) 576–600.
- [67] T. Schwabe, S. Grimme, *Phys. Chem. Chem. Phys.* 9 (2007) 3397–3406.
- [68] J. Řezáč, P. Hobza, *J. Chem. Theory Comput.* 8 (2012) 141–151.
- [69] J.C. Kromann, A.S. Christensen, C. Steinmann, M. Korth, J.H. Jensen, *PeerJ* 2 (2014) e449.
- [70] J.G. Brandenburg, S. Grimme, *J. Phys. Chem. Lett.* 5 (2014) 1785–1789.
- [71] J.G. Brandenburg, M. Hochheim, T. Bredow, S. Grimme, *J. Phys. Chem. Lett.* 5 (2014) 4275–4284.
- [72] A.S. Christensen, T. Kubar, Q. Cui, M. Elstner, *Chem. Rev.* 116 (2016) 5301–5337.
- [73] S. Grimme, *J. Chem. Theory Comput.* 10 (2014) 4497–4514.
- [74] S. Grimme, L. Goerigk, R.F. Fink, *WIREs Comput. Mol. Sci.* 2 (2012) 886–906.
- [75] L. Goerigk, *Density Functional Theory Approximations: Development and Evaluation for Electronic Ground and Excited States*, PhD thesis, Westfälische Wilhelms-Universität Münster, 2011.
- [76] A. Otero-de-la-Roza, E.R. Johnson, *J. Chem. Phys.* 138 (2013) 054103.
- [77] O. Anatole von Lilienfeld, A. Tkatchenko, *J. Chem. Phys.* 132 (2010) 234109.
- [78] A. Tkatchenko, R.A. DiStasio, R. Car, M. Scheffler, *Phys. Rev. Lett.* 108 (2012) 236402.
- [79] B.M. Axilrod, E. Teller, *J. Chem. Phys.* 11 (1943) 299–300.
- [80] Y. Muto, *Proc. Phys. Math. Soc. Jpn.* 17 (1943) 629–631.
- [81] W. Reckien, F. Janetzko, M.F. Peintinger, T. Bredow, *J. Comput. Chem.* 33 (2012) 2023–2031.
- [82] J. Moellmann, S. Grimme, *J. Phys. Chem. C* 118 (2014) 7615–7621.
- [83] M.J. Frisch, G.W. Trucks, H.B. Schlegel, G.E. Scuseria, M.A. Robb, J.R. Cheeseman, G. Scalmani, V. Barone, B. Mennucci, G.A. Petersson, et al., *Gaussian 09 Revision E.01*, Gaussian, Inc., Wallingford, CT, 2009.
- [84] R. Ahlrichs, M. Bär, M. Häser, H. Horn, C. Kölmel, *Chem. Phys. Lett.* 162 (1989) 165–169.
- [85] F. Neese, *WIREs Comput. Mol. Sci.* 2 (2012) 73–78.
- [86] Y. Shao, Z. Gan, E. Epifanovsky, A.T.B. Gilbert, M. Wormit, J. Kussmann, A.W. Lange, A. Behn, J. Deng, X. Feng, et al., *Mol. Phys.* 113 (2015) 184–215.
- [87] M.W. Schmidt, K.K. Baldridge, J.A. Boatz, S.T. Elbert, M.S. Gordon, J.H. Jensen, S. Koseki, N. Matsunaga, K.A. Nguyen, S. Su, T.L. Windus, M. Dupuis, J.A. Montgomery, *J. Comput. Chem.* 14 (1993) 1347–1363.
- [88] M. Valiev, E. Bylaska, N. Govind, K. Kowalski, T. Straatsma, H.V. Dam, D. Wang, J. Nieplocha, E. Apra, T. Windus, W. de Jong, *Comput. Phys. Commun.* 181 (2010) 1477–1489.
- [89] G. te Velde, F.M. Bickelhaupt, E.J. Baerends, C. Fonseca Guerra, S.J.A. van Gisbergen, J.G. Snijders, T. Ziegler, *J. Comput. Chem.* 22 (2001) 931–967.
- [90] J.M. Turney, A.C. Simmonett, R.M. Parrish, E.G. Hohenstein, F.A. Evangelista, J.T. Fermann, B.J. Mintz, L.A. Burns, J.J. Wilke, M.L. Abrams, et al., *WIREs Comput. Mol. Sci.* 2 (2012) 556–565.
- [91] H.-J. Werner, P.J. Knowles, G. Knizia, F.R. Manby, M. Schütz, *WIREs Comput. Mol. Sci.* 2 (2012) 242–253.
- [92] K. Aidas, C. Angeli, K.L. Bak, V. Bakken, R. Bast, L. Boman, O. Christiansen, R. Cimiraglia, S. Coriani, P. Dahle, et al., *WIREs Comput. Mol. Sci.* 4 (2014) 269–284.
- [93] G. Kresse, J. Hafner, *Phys. Rev. B* 47 (1993) 558–561.
- [94] A.D. Bochevarov, E. Harder, T.F. Hughes, J.R. Greenwood, D.A. Braden, D.M. Philipp, D. Rinaldo, M.D. Halls, J. Zhang, R.A. Friesner, *Int. J. Quant. Chem.* 113 (2013) 2110–2142.
- [95] See Spartan Web Site, <https://www.wavefun.com/products/spartan.html>.
- [96] W. Hujo, S. Grimme, *J. Chem. Theory Comput.* 7 (2011) 3866–3871.
- [97] L. Goerigk, *J. Chem. Theory Comput.* 10 (2014) 968–980.
- [98] T. Risthaus, S. Grimme, *J. Chem. Theory Comput.* 9 (2013) 1580–1591.
- [99] R. Sure, S. Grimme, *J. Chem. Theory Comput.* 11 (2015) 3785–3801.
- [100] L. Goerigk, R. Sharma, *Can. J. Chem.* 94 (2016) 1133–1143.
- [101] H. Kruse, L. Goerigk, S. Grimme, *J. Org. Chem.* 77 (2012) 10824–10834.
- [102] M. Steinmetz, A. Hansen, S. Ehrlich, T. Risthaus, S. Grimme, in: R.E. Johnson (Ed.), *Density Functionals: Thermochemistry*, Springer International Publishing, Cham, 2015, pp. 1–23.
- [103] S. Grimme, M. Steinmetz, *Phys. Chem. Chem. Phys.* 15 (2013) 16031–16042.
- [104] W. Hujo, S. Grimme, *J. Chem. Theory Comput.* 9 (2013) 308–315.
- [105] S. Grimme, P.R. Schreiner, *Angew. Chem. Int. Ed.* 50 (2011) 12639–12642.
- [106] L. Goerigk, J.R. Reimers, *J. Chem. Theory Comput.* 9 (2013) 3240–3251.
- [107] L. Goerigk, O. Falklöff, C.A. Collyer, J.R. Reimers, in: J. Zeng, R.-Q. Zhang, H.R. Treutlein (Eds.), *Quantum Simulations of Materials and Biological Systems*, Springer, Dordrecht, 2012, pp. 87–120.

- [108] L. Goerigk, C.A. Collyer, J.R. Reimers, *J. Phys. Chem. B* 118 (2014) 14612–14626.
- [109] J.A. Conrad, M.S. Gordon, *J. Phys. Chem. A* 119 (2015) 5377–5385.
- [110] J. Moellmann, S. Grimme, *Phys. Chem. Chem. Phys.* 12 (2010) 8500–8504.
- [111] A. Otero-de-la-Roza, E.R. Johnson, *J. Chem. Phys.* 137 (2012) 054103.
- [112] A.M. Reilly, A. Tkatchenko, *J. Chem. Phys.* 139 (2013) 024705.
- [113] J. Moellmann, S. Grimme, *Organometallics* 32 (2013) 3784–3787.
- [114] J.G. Brandenburg, G. Bender, J. Ren, A. Hansen, S. Grimme, H. Eckert, C.G. Daniliuc, G. Kehr, G. Erker, *Organometallics* 33 (2014) 5358–5364.
- [115] J.G. Brandenburg, T. Maas, S. Grimme, *J. Chem. Phys.* 142 (2015) 124104.
- [116] J.G. Brandenburg, S. Grimme, in: S. Atahan-Evrenk, A. Aspuru-Guzik (Eds.), *Prediction and Calculation of Crystal Structures: Methods and Applications*, Springer International Publishing, Cham, 2014, pp. 1–23.
- [117] J.R. Reimers, D. Panduwinata, J. Visser, Y. Chin, C. Tang, L. Goerigk, M.J. Ford, M. Santic, T.-J. Sum, M.J.J. Coenen, et al., *Proc. Natl. Acad. Sci. USA* 112 (2015) E6101–E6110.
- [118] S. Ehrlich, J. Moellmann, W. Reckien, T. Bredow, S. Grimme, *Chem. Phys. Chem.* 12 (2011) 3414–3420.
- [119] J. Moellmann, S. Ehrlich, R. Tonner, S. Grimme, *J. Phys. Condens. Matter* 24 (2012) 424206.
- [120] A. Hansen, C. Bannwarth, S. Grimme, P. Petrović, C. Werlé, J.-P. Djukic, *ChemistryOpen* 3 (2014) 177–189.

# Atom-Centered Potentials for Noncovalent Interactions and Other Applications

---

*Gino A. DiLabio*

Department of Chemistry, The University of British Columbia, Kelowna, BC, Canada

## 7.1 INTRODUCTION

---

It has been well-known since the earliest days of the application of quantum mechanics to chemical systems that the time-independent Schrödinger equation (SE) can only be solved exactly for single-electron systems and nearly exactly for two electron systems. For molecules, the exact solution to the SE requires the use of infinitely large (i.e., complete) basis sets coupled with a full correlation treatment. Full correlation refers to the expansion of a wavefunction representative of the system of interest, such as one obtained using Hartree–Fock (HF) theory, with electronic configurations obtained by exciting all of the electrons of the system into all of the unoccupied orbitals. Since the exact solution requires the use of basis sets of infinite size, the number of unoccupied orbitals is likewise infinite, making the full correlation impossible, and therefore the use of approximate methods to solve the SE is necessary. Applied quantum mechanics nevertheless works despite the need to apply approximate methods because the exact solution to the SE is seldom required in order to obtain insight into problems of chemical or physical interest. This fact has underpinned the development of a wide range of approximations to solving the SE, including compact basis sets, limited correlation treatments, and, separately, density-functional theory methods. Furthermore, the difficulties associated with the computational modeling of many-electron systems have often been alleviated through the judicious application of chemical/physical intuition.

One simple, but powerful, example of the use of intuition in the simplification of modeling is that core electrons participate very little (if at all) in most chemical processes. As a consequence of this simplification, all of the electronic configurations generated from the excitation of core electrons into unoccupied orbitals can be omitted from correlation calculations. That is, an HF calculation is performed on the entire system with all of its electrons, following which only the valence electrons are subjected to excitations in order to develop a correlated wavefunction. This is generally referred to as the “frozen core” approximation and it is

commonly used in most computational chemistry programs by default. Although the energy obtained from a correlated wavefunction using the frozen core approximation will be higher (i.e., farther away from the exact energy) than that obtained by correlating the core and valence electrons, the difference between these two energies will almost completely cancel-out when they are used to calculate properties of relevance in chemistry (e.g., bond strengths, barrier heights, etc.).

Similar in philosophy to the frozen core correlation approach is the effective-core approximation, which completely removes core electrons from the calculation altogether. This is achieved by replacing the core electrons and the corresponding nuclear charges with a spherical potential that mimics their effects. In the earliest days of applied quantum mechanics, the use of atom-centered potentials (ACPs) in the form of effective core potentials (ECPs) allowed for the efficient calculation of chemical species that reside in the lower rows of the periodic table by removing a large number of electrons that are not relevant to the chemistry of those elements. By making use of Gaussian-type function expansions to the potential, the number of electrons that enter HF and subsequent correlation calculations can be greatly reduced.

Another advantage to the use of ECPs is that they can, to some extent, incorporate the effects of relativity. Relativistic effects arise as a consequence of large nuclear charges, like those in heavy elements such as gold and lead. When nuclear charges become large, electrons close to the core, like those in a  $1s$  orbital in heavy elements, travel close to the speed of light. This causes electron mass to increase and a consequent decrease in the radius of their orbits. In order to maintain orthogonality,  $s$ - and  $d$ -type orbitals with higher  $n$  quantum numbers must also contract, while  $p$ -orbitals extend farther into space. To obtain reasonable valence properties like bond lengths and bond energies for chemical systems containing heavy elements, scalar relativistic effects must be incorporated [1]. For example, when heavy systems (e.g., TIH) are treated without the inclusion of scalar relativistic effects, computed bond lengths can be in error by as much as  $+0.3 \text{ \AA}$ , depending on the system [2].

Since core orbitals are removed from atoms in the course of applying the ECP approach, it is necessary to generate new valence orbitals, called "pseudo-orbitals". As a simple example, consider the carbon atom, which has an electronic configuration  $1s^2 2s^2 2p^2$  and for which an ECP may replace the electrons in the  $1s$  orbital. The  $1s$  and  $2p$  orbitals are nodeless outside of the nucleus, while the  $2s$  orbital has a single node. Replacement of the electrons in the  $1s$  orbital necessitates that the  $2s$  orbital be reformulated so that it is smooth and nodeless from the nucleus out into the valence region while retaining its valence properties. In general, the variety of effective core potentials available today differ from each other in the way that the pseudo-orbitals are generated. Although the methods for generating pseudo-orbitals are theoretically motivated in general, there is no ideal approach, and the one taken relies to some extent on what works best.

In addition to how the pseudo-orbitals are formulated, the impact ECPs have on the accuracy of results depends on the number of core electrons replaced (often referred to as the "size" of the core). For a heavy element, it is fairly intuitive that errors will decrease with decreasing core size. This is particularly the case when an atom with a core represented by ECPs engages in strong polarizing interactions, on account of which polarization of the core electrons may contribute to bonding (or other) interactions in the valence. Since ECPs are fixed functions, they are unable to respond to polarization effects and strong interactions of this type could lead to errors. It is also possible that the penetration of the electron density of

an atom bonded to another with an ECP representing a large core could lead to the erroneous shielding of bonding electron density and incorrectly predicted molecular properties [3].

## 7.2 A BRIEF THEORETICAL BACKGROUND ON EFFECTIVE CORE POTENTIALS

ECPs are normally generated by solving the HF equations (or Dirac–Hartree–Fock equations in order to capture relativistic effects) for an atom in a particular electronic state. The potentials are determined from solutions of the Fock equations as given by

$$\left[ -\frac{1}{2}\nabla^2 - \frac{Z_{\text{eff}}}{r} + U_l + W_l \right] \chi_l = \varepsilon_l \chi_l, \quad (7.1)$$

where  $Z_{\text{eff}}$  is the effective nuclear charge, which is usually equal to the number of valence electrons since the valence shell is shielded from the nucleus by the electrons in the core.  $W_l$  incorporates the Coulomb and exchange interactions between the valence electrons as computed from the pseudo-orbitals,  $\chi_l$ .  $r$  represents the electron–nuclear distance,  $l$  is the angular momentum associated with the orbital, and  $\varepsilon_l$  are the orbital energies. The choice of the electronic state used for the all-electron calculation is chosen by the ECP developer, and the choice is sometimes made based on the nature of the electronic state (e.g., occupation of certain orbitals) or the desired application of the ECPs. This choice introduces some level of empiricism in ECP development.

In Eq. (7.1),  $U_l$  replaces the core–valence Coulomb and exchange interaction potentials associated with the all-electron systems and therefore the corresponding operators in the Fock equations. It is important to note that  $U_l$  also corrects for the deficiencies in the representation of the potential due to the core that arise from the use of pseudo-orbitals and as a consequence of reducing the charge of the nucleus. Inversion of Eq. (7.1) allows for the solution of  $U_l$ , which requires that  $\chi_l$ s be nodeless in order to avoid discontinuities in the solutions.

The ECPs have the form

$$U^{\text{ECP}} = U_L(r) + \sum_{l=0}^{L-1} [U_l(r) - U_L(r)] |l\rangle\langle l|, \quad (7.2)$$

where  $L$  is usually one higher than the highest angular momentum quantum number  $l$  representing electrons in the core. These  $L$  potentials are often referred to as “local” potentials, and they act on all orbitals.  $|l\rangle\langle l|$  is an operator that projects the potential onto the specific orbitals associated with  $l$  quantum numbers. These functions are called “nonlocal potentials” in the literature.

For  $l$  corresponding to occupied core orbitals,  $U_l$  will also include a Pauli repulsion term that prevents the collapse of valence orbitals into the core. In practice, for  $l$  greater than the highest  $l$  in the core ( $L - 1$ ), the  $U_l$  are reduced to simple shielding-type potentials, which suggests that the  $l$  expansion in Eq. (7.2) can be truncated at  $L$  without significant error. The

individual  $U_l$  are fitted to Gaussian expansions according to

$$U_l(r) = r^{-2} \sum_{i=1} c_{li} r^{n_{li}} e^{-\zeta_{li} r^2}, \quad (7.3)$$

where the coefficients,  $c_{li}$ , control the magnitude and the exponents,  $\zeta_{li}$ , control the spatial extent of the potentials. The value of  $n_{li}$  is an integer quantity, usually set to 0, 1 or 2, which determines how quickly the potential goes to zero as a function of  $r$ . As described above, the ECP approach requires the reduction of the nuclear charge by an amount that corresponds to the number of electrons represented by the core potential. However, this charge is not completely screened by the core electrons. Consequently, ECPs usually have  $U_L$  potentials with  $c_L < 0$  that compensate for the missing attractive interactions between the valence electrons and the nucleus.

### 7.3 BEYOND POTENTIALS REPRESENTING CORE ELECTRONS: ACPS FOR APPLICATION IN QMMM CALCULATIONS

The utility of atom-centered potentials extends beyond the representation of core electrons. In the late 1990s and early 2000s, researchers recognized that ACPs could be used to tackle problems associated with the simulation of large systems through the application of hybrid quantum mechanics–molecular mechanics (QMMM) techniques. QMMM approaches allow the simulation of large systems by dividing them into a small, computationally manageable QM region and an MM region containing the remainder of the system. Since MM methods treat atoms as point charges, QMMM allows the electronic density of the QM system to respond to the presence of the field created by the atoms in the MM region. Similarly, the MM system responds to the charge distribution of the QM region through changes in atomic positions. Chapter 12 describes the technical details associated with the simulation of systems in which the QM region is not chemically bonded to the remainder of the system.

QMMM approaches benefit from the application of chemical intuition. Like the effective core approximation, where it was recognized that core electrons do not participate in the chemistry of an atom, likewise in large systems such as an enzyme only a subset of its component atoms are involved in the reactions they catalyze. Therefore, QMMM techniques can be used to efficiently simulate the chemistry occurring in an enzyme active site by treating the bulk of the protein that is far away from the active site using computationally inexpensive MM. However, an important technical issue arises in the application of QMMM in cases where the QM component is covalently bonded to the MM region. These cases requires “cutting” the bonds that connect the QM and MM regions. This process can introduce perturbations to the QM system of such an extent that its electron density no longer resembles that of the real system.

To address the problems associated with the truncation of QM systems and the subsequent creation of dangling bonds (i.e., uncapped quantum mechanical bonds), a number of approaches have been devised, and the interested reader is directed toward the brief review in Ref. [4]. The simplest approach is to cap the dangling bond created by truncating the QM

region with hydrogen atoms [5]. If the bonds connecting the QM and MM regions is one between two  $sp^3$  carbon atoms, the capping of the QM carbon “dangling” bond with a hydrogen atom introduces small perturbations because of the small electronegativity difference between C and H. In general, carbon–carbon single bonds connecting the QM and MM regions are cut: The low polarity of these bonds minimizes the perturbation associated with their truncation. This “link atom” approach remains in extensive use today.

Several research groups have used ACPs having the form of ECPs to tackle the dangling bond problem in QMMM calculations. One of the earliest such approaches was the “pseudobond” approach developed by Yang’s group [6] wherein the atom used to cap the QM dangling bond is a pseudohalogen atom, although the method was designed to be applied to capping truncated C–C bonds. That is, an ACP was designed so that the capping atom has seven valence electrons and a corresponding nuclear charge of +7. In order to apply the pseudohalogen to cap a carbon–carbon bond, the effective potential terms must be optimized to mimic the features of the C–C bond. Yang and coworkers fit the terms of the  $U_l(r)$  Gaussian expansion in order to reproduce some of the properties of ethane, including bond lengths and angles, the C–C bond dissociation energy and Mulliken charges. The result was a fairly compact ACP and a robust approach to the capping problem. Importantly, the approach allows for the utilization of ECP computational “machinery” which is available in virtually every conventional computational chemistry program. Furthermore, the approach is independent of the type of force field parameters used to describe the MM region.

A few years later, DiLabio et al. developed the quantum capping potential (QCP) approach to deal with the dangling bond in QMMM treatments [7]. The QCP approach is similar in nature to the pseudobond approach. However, it was recognized that the use of seven-electron capping atoms could significantly increase the computational expense associated with modeling the QM region when the number of capping atoms increases, i.e., when the QM region becomes large. QCPs were designed as single-electron atoms for capping truncated C–C bonds. The driving notion was that if core and valence electrons are separable as in ECP theory, then it should be possible to likewise separate valence electrons.

The first QCPs were developed for using ethane as a testbed. Starting from a carbon two-electron effective core potential, an initial simple QCP for one of the  $-\text{CH}_3$  groups was generated by: (i) removing the hydrogen atoms from the group; (ii) reducing the nuclear charge by 3 and moving three valence electrons into the core; (iii) adding a single, local (i.e., “shielding”) potential with the form of  $\approx 3/r$ . The coefficients and exponent in Eq. (7.3) were then adjusted in order to approximately reproduce the ethane HF/6-31G(d,p) Mulliken charges on the carbon and hydrogen atoms of the all-electron  $-\text{CH}_3$  group, see Fig. 7.1.

The initial QCP was able to reproduce the ethane C–C bond length but not the HCC bond angles. The angles were found to be too low by about  $4^\circ$ , which was most likely due to the loss of the repulsive interactions between C–H bonds because of the removal of three carbon valence electrons and their associated hydrogen atoms. In order to improve the HCC bond angles, repulsive Pauli potentials were incorporated into the QCP (referred to as “QCP4” in Ref. [7]). Although more complex, this revised QCP is able reproduce the ethane HCC bond angles to within about  $2^\circ$ . In QMMM tests, the QCP generally performed better than the hydrogen link atom approach. For example, QCPs were able to better reproduce the all-electron protonation energy in a model of histidine (see Fig. 7.2). They were later successfully applied to compute nuclear magnetic resonance shielding tensors in QMMM model systems [8].

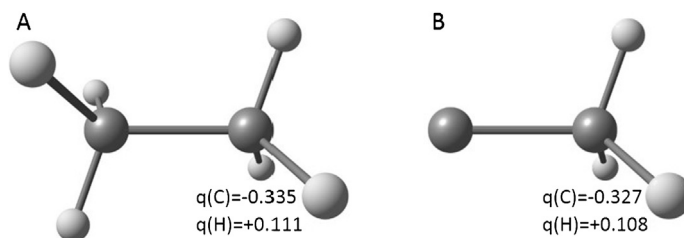


FIGURE 7.1 (A) All-electron ethane molecule. (B) Ethane molecule with the  $-\text{CH}_3$  group on the left replaced by a simple carbon quantum capping potential. The exponent and coefficient of the local potential on the QCP carbon were adjusted to approximate the ethane Mulliken charges ( $q$ , in electrons) of the atoms of the all-electron  $-\text{CH}_3$  group. Key: light spheres, hydrogen; dark spheres, carbon.

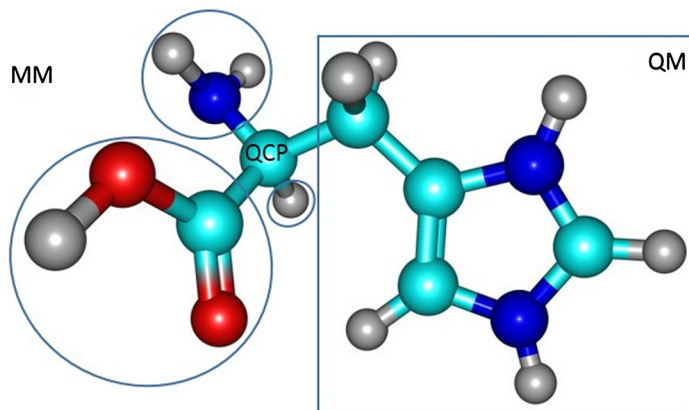


FIGURE 7.2 Application of QCPs to histidine. The  $\text{C}_\alpha$  is replaced by a QCP representation of a one-electron carbon atoms. The atoms outlined by the square are treated quantum mechanically, as is the QCP carbon center. The atoms in the ovoids are treated with molecular mechanics as point charges. Key (online color only): red, oxygen; gray, hydrogen; light blue, carbon; dark blue, nitrogen.

DiLabio et al. later developed a QCP for a one-electron representation of the silicon atom in order to facilitate the simulation of chemical reactions on bulk silicon(100) [9]. At the time, the common practice for the simulation of chemical processes on silicon surfaces was to model systems using a finite-size cluster wherein the Si-Si bonds connecting the cluster to the bulk were capped by hydrogen atoms whose positions were kept fixed in space. This approach generally failed to reproduce some of the key properties of silicon. In addition, the fixed atom hydrogen capping approach does not allow for the calculation of vibration frequencies since clusters capped in this fashion are not genuine energy minima. This means that the vibration/thermal contributions to reactions energies could not be determined using a silicon cluster approach. DiLabio et al. demonstrated that Si QCPs allow for the prediction of ionization potentials, electron affinities and the energy difference between the highest occupied and lowest unoccupied molecular orbitals (the HOMO-LUMO gap) for small silicon clusters that are in much better agreement with those obtained for large clusters than those obtained



using hydrogen atom-capped clusters of the same size. Furthermore, the Si QCP approach allows for full geometry optimization that produces structures that closely resemble bulk silicon. The QCP approach thereby allowed for the calculation of vibration frequencies of these clusters and therefore the determination of their reaction enthalpies and free energies. Later efforts by Raghavachari's group extend the QCP concept to a two electron Si atom [10].

Other groups have developed ACPs that were similar in design philosophy and purpose to QCPs. For example, Martinez's group developed a QCP-type, one electron carbon atom ACP called multicenter valence electron effective potential using the properties of ethane for fitting purposes [11]. Jardillier and Goursoot developed a QCP for the oxygen atom developed a QCP for the oxygen atom [12]. Rothlisberger et al. developed carbon capping potentials for use in plane wave calculations [13] (in this context, ACPs are referred to as pseudopotentials). An interesting aspect of Rothlisberger et al.'s work is that they developed potentials for use with the BLYP density functional [14,15] to reproduce the results obtained using B3LYP [15,16], which is many times more computationally intensive than is BLYP in plane wave simulations.

What is evident from the work on capping potentials is that the scope of ACPs is wider than just the representation of core electrons. The use of ACPs to create new atoms types, as in the pseudobond or QCP approaches, or to simulate the properties of systems that are consistent with those obtained from more accurate methods but using a less computationally intensive techniques, underscores the utility of ACPs. Indeed, some of the earliest work on the development of pseudopotentials for plane-wave modeling work used experimental data to fit the potentials, rather than relying solely on fitting to potentials derived from ab initio calculations [17]. In the following sections of this chapter, approaches related to the use of ACPs to correct for the deficiencies in conventional density-functional theory (DFT) will be presented.

## 7.4 ACPS FOR IMPROVING DFT IN NONCOVALENTLY INTERACTING SYSTEMS

---

Other chapters in this book describe the shortcomings of conventional DFT-based methods with respect to the prediction of noncovalent interactions (see Chapters 4, 5, and 6). Conventional DFT-based methods do not contain the correct physics to describe dispersion interactions and therefore fail when applied to problems in which dispersion plays an important role. This is illustrated in Fig. 7.3, which shows results obtained for 28 dimers where the dominant interactions are dispersion (14 dimers), dipole-induced dipole (6 dimers), dipole-dipole (3 dimers), and hydrogen bonded (5 dimers) [18]. The data shown in the figure were obtained at dimer geometries that correspond to their energetic minima using the indicated functional or second-order Møller–Plesset perturbation theory (MP2, an ab initio wavefunction approach) using 6-311++G(3df,3pd) basis sets and counterpoise corrections [19]. Mean absolute percent errors (MAPEs) were obtained by comparing to CCSD(T) binding energies.

Although the number of dimers examined in Ref. [18] is not exhaustive, the data demonstrate the weakness of conventional DFT-base methods for noncovalent interactions. B3LYP,

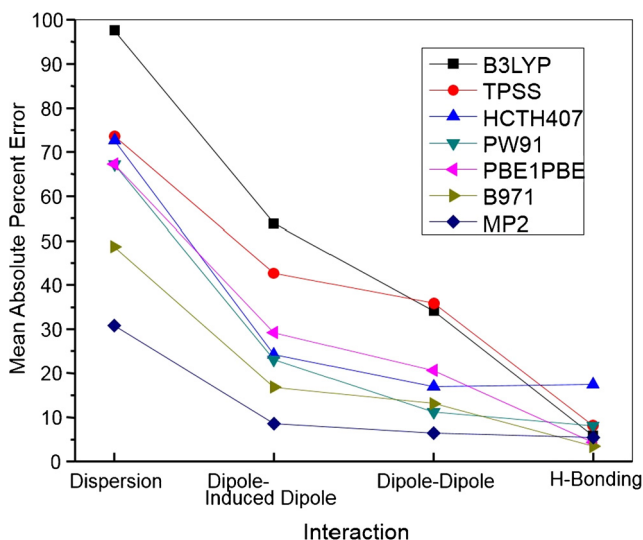
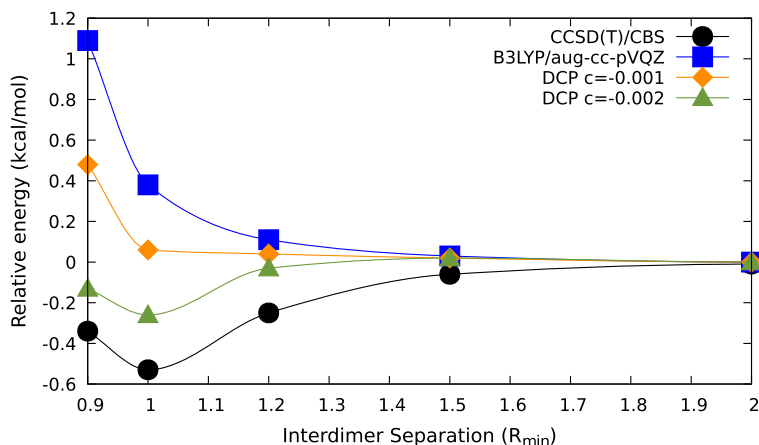


FIGURE 7.3 Mean absolute errors in predicted binding energies of noncovalently interacting dimers. Reprinted from *Chem. Phys. Lett.* 419 (2006) 333. Copyright 2006, with permission from Elsevier.

which remains the most widely used density functional, is the worst functional when it comes to all van der Waals interactions, but not hydrogen bonding. The data reflect the fact that longer-range interactions (i.e., those beyond the covalent bonding regime) are overly repulsive using this functional: Species interacting principally by dispersion tend to be completely unbound. As the strength of the electrostatic interactions increases (from left to right on the  $x$ -axis in Fig. 7.3), the MAPEs associated with the predicted binding energies decrease. Most of the functionals examined in the study display behavior that is similar to that of B3LYP, that is, they are overly repulsive, although the errors in predicted binding energies vary in magnitude. The poor performance of the MP2 was interesting in the context of the study: At the time, MP2 was used extensively to model noncovalently bonded systems but nearly similar or better quality results could be obtained by DFT approaches for interactions in which electrostatics play a significant role, particularly for hydrogen bonding.

Around the time that Ref. [18] was published, there were very few generally available dispersion-corrected DFT-based methods. The success and flexibility of the QCP approach motivated the development of an easily implemented method for correcting the poor performance of DFT-based methods for the treatment of noncovalent interactions. This led to studies to assess the capabilities of ACPs in this connection. The approach was eventually described as “dispersion-correcting potentials” (DCPs) [20–23]. The promise of the DCP-type approach was explored prior to this work via a similar plane wave approach that was put forward by von Lilienfeld [24], which is referred to as dispersion-correcting atom centered potentials (DCACPs).

Fig. 7.4 demonstrates how DCPs might be effective in correcting for the lack of dispersion in DFT for methane dimer. The curve marked with circles in the figure represents the weakly attractive PES obtained using estimated complete basis set CCSD(T) [25]. Using nearly com-



**FIGURE 7.4** Noncovalently bonded methane dimer potential energy surfaces. Circles represent the CCSD(T) estimated complete basis set values and squares represent the B3LYP/aug-cc-pVQZ potential without corrections for dispersion. The curves labeled “DCP” were calculated using a single local DCP function as indicated in Eq. (7.3) on each carbon atom with  $\zeta = 0.08$  and coefficients  $c = -0.001$  or  $c = -0.002$ . Negative energies represent binding interactions.

plete basis set B3LYP, the potential energy curve for the dimer is completely repulsive, as can be seen by the PES indicated with squares. The addition of a single local attractive function of the type shown in Eq. (7.3) with  $n_L = 2$ ,  $c_L = -0.001$ , and  $\zeta_L = 0.08$  (closed circles) to the B3LYP calculation reduces the repulsion near the dimer minimum to the extent that a small minimum results. Increasing the magnitude of  $c_L$  to  $-0.002$  deepens the potential even further, resulting in a PES that more closely resembles that obtained with the high-level wavefunction method. Note that because the DCPs do not replace any electrons, the electron density can respond as a consequence of polarization, unlike core electrons in the ECP approach.

The initial DCP development was almost as straightforward as the example shown in Fig. 7.4. Since most DFT-based methods are overly repulsive in the dimer binding regime, a particular problem in hydrocarbon-containing species, a local attractive potential could be applied to carbon atoms to correct for this shortcoming. The potential would act on all electrons in the system, meaning that they would not be used to replace electrons at all. An additional requirement imposed during their development was that the DCPs be applied in conjunction with small basis sets, initially 6-31+G(d,p), so that calculations would be as low cost as possible. The first carbon DCPs used a single Gaussian function (see Eq. (7.3)) with  $c_{L1} \approx -0.00015$  and  $\zeta_{L1} = 0.08$ . A second, repulsive Gaussian function with  $c_{L2} \approx +0.00035$  and  $\zeta_{L2} = 0.12$  was added in order to prevent over-binding at short  $r$ . In both cases,  $n_L$  was set to 2.

The coefficients varied slightly depending on the type of DFT-based method, and this kind of minor functional dependence is expected on the basis of the different degrees to which functionals display repulsive behavior in dispersion interactions. These DCP exponents and coefficients are several orders of magnitude smaller than those used for ECP applications, and

reasonably so: The potentials associated with the removal of core electrons are expected to be much stronger than the comparatively subtle potentials needed to adjust for the weak interactions associated with noncovalent bonding. The performance of this first simple approach to DCPs was surprisingly good. For seven hydrocarbon dimers (including methane dimer) in 12 configurations, the errors in binding energies obtained with B97 [26]/6-31+G(d,p) were reduced from a mean absolute error of 1.34 kcal/mol to just 0.13 kcal/mol, in other words by more than an order of magnitude. Similar results were obtained using the other two functionals in the study, PBE [27] and PW91 [28]. Although this approach to DCPs was entirely empirical, it was not completely divorced from some of the empirical principles involved in the development of ECPs, and it provided an efficient means to capture dispersion behavior. In later work, an additional diffuse local function ( $\zeta_{L3} = 0.009$ ,  $c_{L3} = -0.0000042$ ) was added to obtain the correct longer-range (ca. 5–10 Å) behavior [22].

As described in Chapters 3 and 4, incomplete basis sets can result in erroneous over-binding in noncovalently bonded systems. Therefore, in addition to correcting for the lack of dispersion physics in DFT-based methods, the first carbon DCPs also performed a second valuable function—they corrected the effects associated with the use of small basis sets. It turns out that the ability of ACPs to mitigate the errors that arise from using incomplete basis sets is a potentially valuable attribute. This will be discussed in a later section of this chapter.

The first generation of DCPs were applied to study a number of problems. One of the more interesting ones was the determination of the structure of a model for Maya asphaltenes. Asphaltenes are large, mostly organic molecules, usually composed of several polycyclic aromatic hydrocarbons (PAHs) linked together by saturated hydrocarbon chains and containing heteroatoms such as N, S, and O. Asphaltenes are present in heavy oil deposits (e.g., in Alberta Oil Sands) and create significant technical difficulties for the oil upgrading process. For some time, the structure of Maya asphaltene was described as an open structure, that is, one where the PAH moieties were not interacting with each other. Modeling work [29] predicted that the lowest energy structure for the Maya asphaltene model was in fact a closed structure in which all of the PAH moieties were stacked; see Fig. 7.5.

The predicted structure of Maya asphaltenes led to the hypothesis that asphaltenes in general may be suitable for application in organic electronics because of the large extent of  $\pi$ -stacking and  $\pi$ -electron delocalization that is present in the asphaltenes (see, for example, Chapter 9). Testing of the conductivity of isolated asphaltenes showed some hysteresis in the current–voltage (I–V) behavior, which increased dramatically when the samples were exposed to air; see Fig. 7.6. These measurements supported the hypothesis that asphaltenes may be useful as components of organic electronic devices and allowed a patent to be published [30].

Simple Si DCPs that were similar in construction to those of carbon were later developed. In combination with the carbon DCPs, they provided the opportunity to perform modeling studies of processes involving hydrocarbons on silicon surfaces using DFT-based techniques [31]. Hybrid organic–silicon systems are of interest because of the potential to marry the diversity of properties that can be built into organic molecules through synthesis with the functionality of semiconducting silicon. It was demonstrated that benzene displayed binding to the corrugated hydrogen-terminated silicon surface (H–Si(100)-2 × 1) that is on the order of about 5.5 kcal/mol and that the barrier to lateral diffusion on the surface was quite low

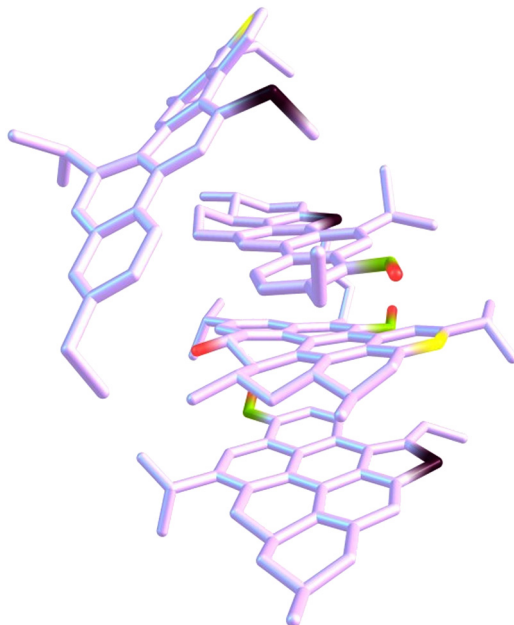


**FIGURE 7.5** Perspective views of the minimum energy structure of a Maya asphaltene model, as predicted by PBE-DCP/6-31+G(d,p). The folded structure pictured here is predicted to be ca. 9 kcal/mol lower in energy than the open structure, which was believed to be the lowest energy structure. For clarity, hydrogen atoms are not shown in the model. The light-colored components are carbon atoms and the darker colors are used to represent heteroatoms (N, S, O). Adapted, with permission, from I.D. Mackie, G.A. DiLabio, *Energy Fuels* 24 (2010) 6468. Copyright 2010 American Chemical Society.

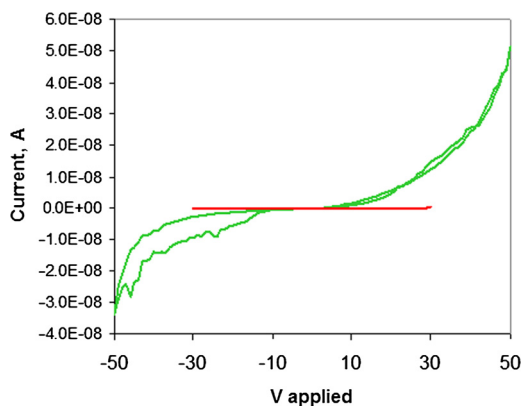


**FIGURE 7.6** Current–voltage (I–V) curve for asphaltenes obtained by precipitation from a solution of bitumen in pentane. The curves were obtained by depositing the asphaltenes on an interdigitated electrode device. The nearly horizontal line shows the I–V behavior for undoped asphaltenes and the hysteresis curve shows the I–V behavior for asphaltenes doped through exposure to air.

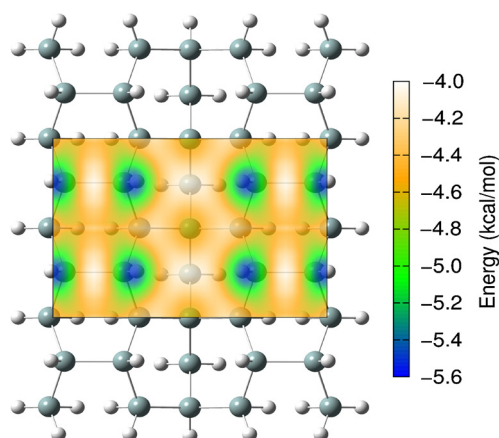


**FIGURE 7.7** Potential energy surface for benzene on the H-Si(100)- $2 \times 1$  surface calculated using B971/6-31+G(d,p) with dispersion-correcting potentials on the carbon and silicon atoms. The potentials were generated with the benzene molecule constrained to lie parallel to, and at a fixed height of 4.0 Å over the surface. The potential is associated with the placement of the benzene center-of-mass at different positions over the surface. The energy scale is in kcal/mol. Reprinted with permission from E.R. Johnson, G.A. DiLabio, *J. Phys. Chem. C* 113 (2009) 5681. Copyright 2009 American Chemical Society.

(Fig. 7.7). More interesting was the fact that the calculations pointed to a clear anisotropy associated with lateral diffusion, with migration of benzene along the so-called “dimer rows” of the silicon surface being more facile than that in a direction perpendicular to the rows. The anisotropic diffusion behavior on H-Si(100)- $2 \times 1$  was later demonstrated for styrene using scanning tunneling microscopy (STM) experiments and DCP-based Monte Carlo simulations [32]. DCPs were also used to suggest that conclusions derived from STM experiments that apparently showed that pentacene diffusion in H-Si(100)- $2 \times 1$  was facile at a temperature of 5 K [33] were likely incorrect. The modeling work led to the hypothesis that the inability to capture images of the molecule on flat terraces of the surface were not because of facile lateral diffusion but were likely a consequence of diffusion induced by the tunneling current emanating from the microscope tip [34].

Subsequent development work was done to expand the range of atoms that could be treated using DCPs [23]. The need to fit the functions described by Eq. (7.3) to describe non-covalent binding energies accurately is a severe shortcoming of the DCP approach and limits the number of atoms for which DCPs can be developed because of the lack of availability of these data. Nevertheless, very good reference data were available for dimers containing the H, C, N, and O atoms and this enabled the development of DCPs for those atoms. The focus was placed on the development of DCPs for the B3LYP [15,16] functional because of its widespread use and with 6-31+G(2d,p) basis sets. Although these basis sets are larger than those that were previously used for DCPs, they were chosen because they are roughly midway between compact and nearly complete basis sets. The expectation was that DCPs developed for use with 6-31+G(2d,p) basis sets could be applied with smaller or larger basis with minimal degradation in performance.

Unlike the first generation of potentials, the DCPs developed in Ref. [23] used three Gaussian functions to define the local ( $L$  in Eq. (7.3)) potential and one function for angular momentum  $l$ . That is, for the H atom, the DCP was designed with 3  $p$ - and 1  $s$ -function, while C, N, O had 3  $f$ -functions, 1  $s$ -, 1  $p$ -, and 1  $d$ -function. A random-walk-based search method was used for the optimization. This started with a guess of the form of the initial DCPs. The quality of the generated DCP was then evaluated by a cost function computed as the weighted average of the absolute error of the DCP-computed binding energies relative to the data in a fitting set. The final set of DCPs were obtained when the average error was minimized. The fitting set was composed a small number of accurate (estimated complete basis set CCSD(T)) noncovalent binding energies and their associated structures. The set included four to six points on the potential energy surfaces for five dimers containing carbon and hydrogen, four nitrogen-, and four oxygen-containing dimers. Three dimers containing all four elements were also included in the fitting set. The H and C DCPs were developed concurrently, and these were then used to develop the O and, separately, the N DCPs. All of the fitting data were then used to simultaneously optimize the DCPs for all four atoms. The optimized DCPs are can be found in Ref. [23] with a sample input for the Gaussian program [35] provided in the Supporting Information of that paper.

Tests of the B3LYP-DCP approach were performed on a number of benchmark data sets including the “S66” [36] and “S22” [37] sets, which are comprised of 66 and 22 dimers, respectively, in which the interactions are dominated by hydrogen bonding, dispersion and a mix of van der Waals interactions (see also Chapter 3). The results are summarized in Table 7.1. The B3LYP-DCPs were found to perform well, giving mean absolute errors of 0.37 kcal/mol or less, depending on the basis set and benchmark set. The best performance was achieved with B3LYP-DCP/6-31+G(2d,2p), giving MAEs of 0.18 and 0.22 kcal/mol for the S66 and S22 sets, respectively. In the absence of DCPs, the errors obtained with B3LYP/6-31+G(2d,2p) on these sets are more than 15 times larger.

Additional testing of the B3LYP-DCP/6-31+G(2d,2p) approach was performed on the HSG-A benchmark set of noncovalently bonded dimers and trimers. This set is composed of 21 neutral and charged fragments taken from the HIV-II protease crystal structure with a bound inhibitor called indinavir. Marshall et al. computed CCSD(T)/CBS-level binding energies for the HSG-A set [38]. The DCP approach produces binding energies for the HSG-A set with an MAE of 0.15 kcal/mol. Burns et al. reported MAEs for the M06-2X,  $\omega$ B97X-D, and B3LYP-D3 methods with aug-cc-pVTZ of 0.47, 0.32, and 0.48 kcal/mol, respectively [39].

Although the B3LYP DCPs described above perform quite well for noncovalent interactions, they were later found to adversely affect covalent properties. For example, the application of the B3LYP-DCP/6-31+G(2d,2p) approach to the C–C bond-breaking process that occurs in the unimolecular  $\beta$ -scission of the cumyloxyl radical, i.e.,  $\text{C}_6\text{H}_5\text{C}(\text{CH}_3)_2\text{O}\cdot \rightarrow \text{C}_6\text{H}_5\text{C}(=\text{O})\text{CH}_3 + \cdot\text{CH}_3$ , it was found that the predicted barrier height was 20.8 kcal/mol, which is about 8 kcal/mol higher than would be expected on the basis of the experimental rate constant. Additional testing on the strengths of representative X–Y covalent bonds (X,Y = C, N, O) showed that the DCPs predicted C–C, C–N, and C–O bond strengths that were too high by about 17, 9, and 6 kcal/mol, respectively, higher than the corresponding B3LYP/6-31+G(2d,2p) predicted values [40]. It was therefore clear that, although the DCPs were designed to correct for errors in noncovalently interactions, they also impacted bond strengths. This prompted the revision of the carbon DCPs [40].

**TABLE 7.1** Mean absolute errors (mean absolute percent errors) of binding energies for the noncovalently bonded dimers of the S66<sup>a</sup> and S22<sup>b</sup> sets calculated using selected density-functional theory (DFT) based methods, relative to estimated complete basis set CCSD(T) values<sup>c</sup>

Dispersion-correcting potentials: B3LYP/basis set				
Basis set	S66		S22	
6-31+G(d,p)	0.32	(7.5)	0.29	(8.2)
aug-cc-pVDZ	0.35	(9.7)	0.23	(7.4)
6-31+G(2d,p) <sup>d</sup>	0.19	(5.0)	0.28	(6.9)
6-31+G(2d,2p) <sup>e</sup>	0.18	(4.7)	0.22	(6.3)
6-311+G(2d,2p)	0.22	(5.7)	0.30	(6.0)
aug-cc-pVTZ	0.24	(6.0)	0.37	(6.9)
Other DFT/6-31+G(2d,2p)				
Method	S66		S22	
B3LYP	3.06	(82.6)	3.35	(78.0)
B97-D	0.39	(9.6)	0.45	(9.3)
M06-2X	0.25	(5.8)	0.43	(6.0)
$\omega$ B97XD	0.30	(8.2)	0.58	(13.3)
Other DFT/def2-QZVP				
Method	S66		S22	
BLYP-D3 <sup>f,g</sup>	0.39 <sup>h</sup>		0.24	
B3LYP-D3 <sup>f,g</sup>	0.40 <sup>i</sup>		0.36	
M06-2X <sup>f</sup>	0.28		0.40	

<sup>a</sup> Ref. [36].

<sup>b</sup> Ref. [37].

<sup>c</sup> The units for MAE and MAPE are kcal/mol and %, respectively.

<sup>d</sup> Basis set used to optimize the DCPs.

<sup>e</sup> Basis set recommended for the general use with the B3LYP-DCP approach.

<sup>f</sup> Ref. [23].

<sup>g</sup> Using the original damping function implementation of D3, see Chapter 6.

<sup>h</sup> MAEs decrease to 0.19 when the damping function of Beck and Johnson (see Chapter 5) is used.

<sup>i</sup> MAEs decrease to 0.28 when the damping function of Beck and Johnson (see Chapter 5) is used.

The negative impact that DCPs may have on properties for which they are not intended to treat demonstrates an important shortcoming of this (and all empirical) approaches. Unless a large collection of properties are included into the fitting process, one can never be entirely certain that any sort of empirical correction scheme will not make some properties worse in the course of improving others. Despite the foregoing, the fact that DCPs can impact covalent properties such as bond strengths in addition to improving noncovalent interactions encouraged the development of DCPs that could improve the description of both covalent to van der Waals bonding.



## 7.5 ACPS FOR IMPROVED DESCRIPTIONS OF COVALENT BONDS AND NONCOVALENT INTERACTIONS

Subsequent efforts to develop DCPs for application to covalent bonds and noncovalent interactions [41] focused on their use with the LC- $\omega$ PBE functional [42]. The two main reasons for selecting this functional were: (i) It predicts bond dissociation enthalpies that are in better agreement with experimental values than many other functionals, including the popular B3LYP, and (ii) As a range-separated DFT-based method (i.e., one that utilized different degrees of Hartree–Fock exchange as a function of distance from the nuclei), it predicts binding energies for noncovalently bound charge-transfer complexes better than functionals with little or no Hartree–Fock exchange. For example, a functional like B3LYP over-binds noncovalent bound complexes involving halogen bonding [43]. The over-binding gets worse with the application of dispersion corrections to B3LYP, such as D3 or DCP, because these corrections uniformly increase the binding energies of all noncovalently bonded complexes to which they are applied.

The fitting of H, C, N, and O DCPs for the LC- $\omega$ PBE functional with 6-31+G(2d,2p) basis sets used the accurate bond energies for 11 representative bonds (C–H, O–H, N–H, C–C, C–O, C–N), and the potential energy surfaces for 16 noncovalently bonded systems whose interactions span the range of dispersion to hydrogen bonding. The optimized DCPs are presented in Ref. [41].

These DCPs predict the binding energies for the S66 and HSG-A sets of noncovalently interacting systems with MAEs of 0.21 and 0.28 kcal/mol, respectively, which represents an improvement of about a factor of 10 over LC- $\omega$ PBE/6-31+G(2d,2p) without any corrections. This level of performance is comparable to that associated with the use of the D3 dispersion correction, which gives MAEs of 0.39 (S66) and 0.17 (HSG-A) kcal/mol. For the S12L set of large dimer complexes [44] (see also Chapter 4), the DCP approach predicts binding energies with an MAE of 3.4 kcal/mol and significantly outperforms the D3 approach which gives an MAE of 11.9 kcal/mol. Some representative PESs predicted using LC- $\omega$ PBE/6-31+G(2d,2p) with and without dispersion corrections are shown in Fig. 7.8.

The DCPs were also tested on a database of 44 experimentally-determined X–H and X–Y (X,Y = C, N, O) bond dissociation enthalpies in common organic molecules [45]. Without dispersion corrections, LC- $\omega$ PBE/6-31+G(2d,2p) predicts an MAE of 3.7 kcal/mol. This error drops to 3.0 kcal/mol with the inclusion of the D3 correction, and to 1.8 kcal/mol with the use of DCPs.

A broader assessment of the ability of the DCPs to predict general molecular properties and reaction energies was made by testing the approach on benchmark data subsets taken from the large GMTKN30 database compiled by Goerigk and Grimme [46] (see Ref. [41] for the details of the subsets used). This assessment revealed that LC- $\omega$ PBE-DCP/6-31+G(2d,2p) performs, on average, better than LC- $\omega$ PBE/6-31+G(2d,2p) alone and about the same as LC- $\omega$ PBE-D3/6-31+G(2d,2p). It should be pointed out that D3 dispersion corrections were developed for use with large, quadruple-zeta basis sets, and their use in conjunction with 6-31+G(2d,2p) basis sets, which were used for comparisons to the DCP results, may erode the performance of LC- $\omega$ PBE-D3.

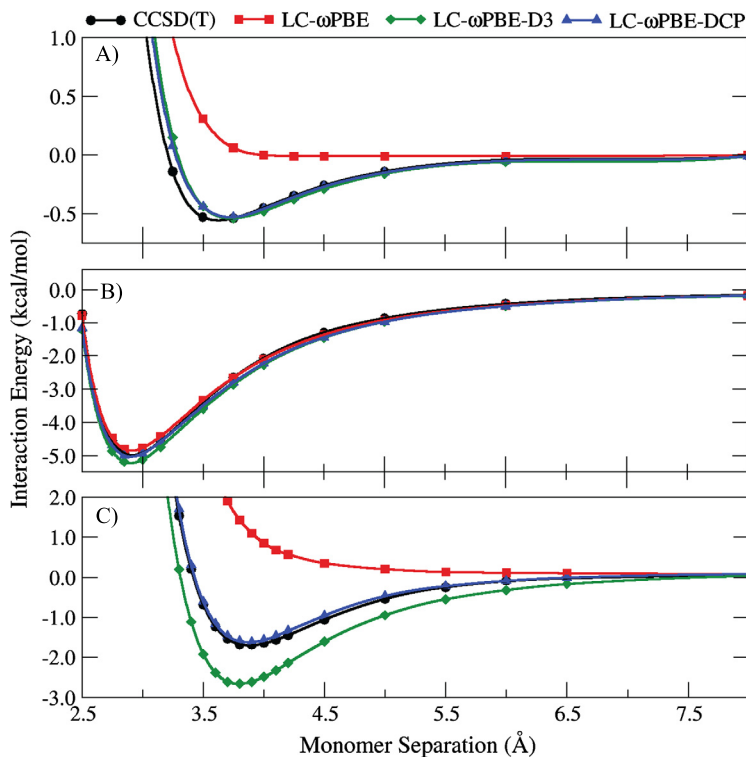


**FIGURE 7.8** Potential energy surfaces for (A) the methane dimer, (B) the water dimer, and (C) the stacked (or “sandwich”) benzene dimer. The surfaces were computed using monomers frozen at the LC- $\omega$ PBE-DCP/6-31+G(2d,2p) optimized geometry. For (A) and (B), CCSD(T)/aug-cc-pVQZ was used to obtain the high-level PES. For (C), the high-level data were taken from Ref. [38]. Reused, with permission, from G.A. DiLabio, M. Koleini, *J. Chem. Phys.* 140 (2014) 18A542. Copyright 2014 AIP Publishing LLC.

For a few of the reference datasets tested, including Diels–Alder reaction barrier heights, proton affinities, and isomerization energies of large organic molecules, uncorrected LC- $\omega$ PBE outperforms both the D3- and DCP-corrected methods. This indicates that the functional may be predicting some properties quite well, such as proton affinities, or underestimated properties, such as barrier heights, and the inclusion of dispersion corrections reduces agreement with the accepted values. With respect to the latter property, the inclusion of pairwise-type dispersion corrections in particular will always decrease the predicted barrier associated with a bi-molecular reaction because the dispersion energy in the separated reactants will necessarily be lower than that of the transition state complex. This is so because the number of pairwise interactions is larger in the transition state structure than the sum of the number of pairwise interactions in the reactants. In any case, as the general quality of functionals improves, one can expect that molecular properties will be predicted with more uniform accuracy, and that the accuracy will be improved through the inclusion of dispersion corrections.

Overall, the DCPs developed for use with the LC- $\omega$ PBE functional along with 6-31+G(2d,2p) basis sets appear to be capable of simultaneously improving predicted noncovalent binding energies in noncovalently bound dimer complexes and general improvements to bond dissociation enthalpies and other properties in molecules. This demonstrates that atom-centered potentials, although empirical, are quite flexible and may be used to mitigate many of the deficiencies in the underlying computational methodology.

## 7.6 ACPs FOR BASIS SET INCOMPLETENESS

As described in previous section, DCPs were developed for use with basis sets that range in size from 6-31+G(d) to 6-31+G(2d,2p). These basis sets are fairly compact and incomplete, in particular when compared to correlation-consistent basis sets, such as aug-cc-pVTZ, and the incompleteness will lead to overestimation in predicted noncovalent binding energies (see Chapters 3 and 4). The fact that DCPs perform well for noncovalently bonded dimers despite the fact that they were developed for use in conjunction with small basis sets indicates that they are mitigating the effects of basis set incompleteness.

The ability of ACPs to correct for the effects of basis set incompleteness was examined in Ref. [47]. The study was performed using the BLYP/6-31+G(2d,2p) approach with the inclusion of the D3 dispersion correction, and fitting a set of ACPs for the H, C, N, and O atoms to accurate noncovalent binding energies and bond dissociation energies. The principal notion behind this effort was that if the D3 correction largely accounts for dispersion interactions, the ACPs would then account for the basis set incompleteness. There does remain underlying deficiencies in the functional and the D3 correction scheme, and optimized ACPs would also account for these deficiencies. Nevertheless, the study represents a first step toward a new approach to correcting for the errors that arise from the use of small basis sets.

Similar to what was done in previous DCP-related development work, the ACPs were optimized using a small set of 11 bond dissociation energies and the potential energy surfaces for 16 noncovalently bonded dimers. The good performance of the optimized potentials in representative dimer systems is illustrated in Fig. 7.9. The ACPs produce quite good results for the S66 reference set of noncovalently interacting dimers, giving an MAE of 0.21 kcal/mol, which is about half the MAE obtained without the potentials and a factor of 18 lower than uncorrected BLYP/6-31+G(2d,2p). With a complete basis set, BLYP-D3 without ACPs gives an error of 0.19 kcal/mol. The excellent agreement between the MAEs obtained with BLYP-D3-ACP/6-31+G(2d,2p) and with BLYP-D3/CBS indicates that the ACPs are effectively mitigating the errors associated with basis set incompleteness in noncovalent binding energies. Similarly good performance was observed for bond dissociation energies, which were generally improved with the application of the ACPs.

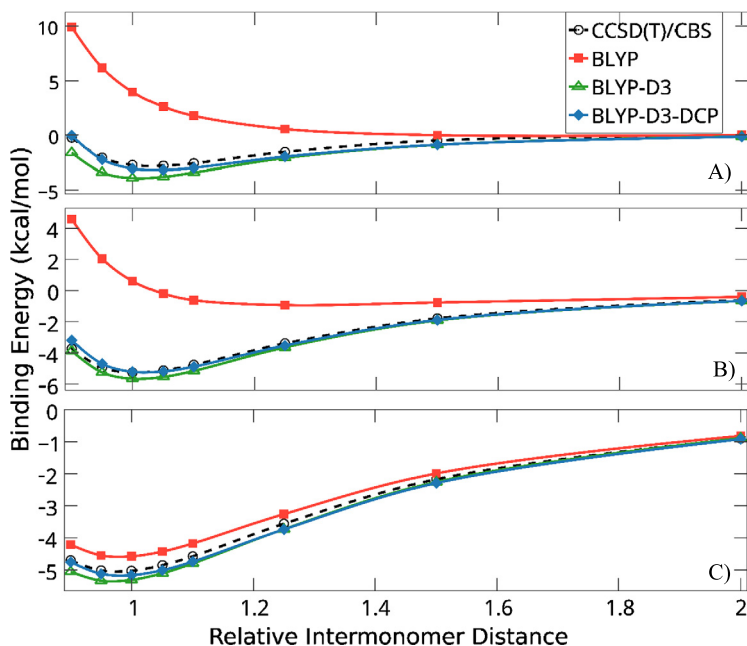


FIGURE 7.9 Potential energy surfaces of the (A)  $\pi$ -stacked benzene dimer, (B) benzene-peptide ( $N-H \pi$ ) dimer, and (C) water dimer. The reference CCSD(T)/CBS PESs and their associated structures were obtained from the S66 $\times$ 8 set. Relative intermonomer distance is defined by the scaling factor applied to the intermonomer separation of the dimer minimum structure. All BLYP calculations utilized 6-31+G(2d,2p) basis sets. Reused, with permission, from J.A. van Santen, G.A. DiLabio, *J. Phys. Chem. A* 119 (2015) 6703. Copyright 2015 American Chemical Society.

## 7.7 SUMMARY AND OUTLOOK

Atom-centered potentials (ACPs) were originally developed in the context of effective core potentials for the purpose of speeding-up calculations involving atoms in the lower rows of the periodic table and as an efficient means to introduce scalar relativistic effects. Later work showed that the ACP approach could be applied to the link atom problem in QMMM work by creating one-electron carbon atoms to cap the dangling bond at the interface between the quantum mechanical and molecular mechanics regions in a protein, and as a one-electron silicon atom to cap the Si-Si bonds in a finite cluster representation of bulk silicon. This was achieved by developing potentials that move all but one valence electron into the “core” and adjusting the parameters of the ACP functions to account for the loss of the valence electrons. Although these one-electron atoms represent an unconventional use of ACPs, they demonstrate the flexibility that ACPs have in addressing applications for which they were not originally intended. Furthermore, because virtually every computational chemistry program can use ECPs, any ACP-based approach can be applied directly and without the need for programming.

The success associated with the extension of ACPs to address the absence of dispersion physics in conventional density-functional theory methods, through the development of dispersion-correcting potentials, is a further demonstration of the flexibility of the ACP approach. Despite the inherent empiricism associated with the development of DCPs, they represent a simple way to correct for major deficiencies inherent in DFT-based methods. The results obtained using DCPs to predict noncovalent binding energies are on-par with many other semiempirical techniques in common use today. However, the need to fit the DCPs to CCSD(T)/CBS quality reference data, which generally available only for common atoms like H, C, N, and O is a serious shortcoming. It is conceivable that DCPs for a broader range of atoms can be developed as more reference data become available, but this is unlikely to happen given the quality of the results predicted by currently available dispersion-corrected DFT-based methods.

The results derived from DCPs demonstrate that certain other deficiencies in applied DFT-based methods could also be addressed, the most significant of which is the use of incomplete basis sets. The errors that arise from the use of small basis sets are pronounced in noncovalent interactions, and DCPs designed for use with small basis sets correct for basis set incompleteness in addition to the lack of dispersion. Furthermore, the ability of DCPs to improve covalent properties, like bond dissociation enthalpies, is another avenue worthy of exploration.

Our future work on ACPs will leverage the ease of application and accuracy of pairwise dispersion corrections, such as D3 (Chapter 6) and XDM (Chapter 5), in conjunction with potentials designed solely to mitigate basis set incompleteness. We expect to develop a general approach for the accurate prediction of molecular properties, including noncovalent binding energies and structures, at an order of magnitude or less computational cost compared to current methods.

## References

- [1] Spin-orbit splitting is another relativistic effect that become important as atom weight increase. Most ECPs that are generated for heavy elements incorporate scalar relativistic effects but not spin-orbit effects.
- [2] P. Pyykkö, *Chem. Rev.* 88 (1988) 563–594.
- [3] S. Wildman, G. DiLabio, P. Christiansen, *J. Chem. Phys.* 107 (1997) 9975–9979.
- [4] H. Lin, D.G. Truhlar, *Theor. Chem. Acc.* 117 (2007) 185–199.
- [5] U.C. Singh, P.A. Kollman, *J. Comput. Chem.* 7 (1986) 718–730.
- [6] Y. Zhang, T.-S. Lee, W. Yang, *J. Chem. Phys.* 110 (1999) 46–54.
- [7] G.A. DiLabio, M.M. Hurley, P.A. Christiansen, *J. Chem. Phys.* 116 (2002) 9578–9584.
- [8] S. Moon, P.A. Christiansen, G.A. DiLabio, *J. Chem. Phys.* 120 (2004) 9080–9086.
- [9] G.A. DiLabio, R.A. Wolkow, E.R. Johnson, *J. Chem. Phys.* 122 (2005) 044708.
- [10] B.C. Gamoke, U. Das, H.P. Hratchian, K. Raghavachari, *J. Chem. Phys.* 139 (2013) 164708.
- [11] P. Slaviček, T.J. Martínez, *J. Chem. Phys.* 124 (2006) 084107.
- [12] N. Jardillier, A. Goursot, *Chem. Phys. Lett.* 454 (2008) 65–69.
- [13] O.A. von Lilienfeld, I. Tavernelli, U. Rothlisberger, D. Sebastiani, *J. Chem. Phys.* 122 (2005) 014113.
- [14] A.D. Becke, *Phys. Rev. A* 38 (1988) 3098.
- [15] C. Lee, W. Yang, R.G. Parr, *Phys. Rev. B* 37 (1988) 785.
- [16] A.D. Becke, *J. Chem. Phys.* 98 (1993) 5648–5652.
- [17] M.L. Cohen, V. Heine, in: H. Ehrenreich, F. Seitz, D. Turnbull (Eds.), *Solid State Physics*, vol. 24, Academic Press, New York, 1970, pp. 37–246.
- [18] E.R. Johnson, G.A. DiLabio, *Chem. Phys. Lett.* 419 (2006) 333–339.

- [19] S.F. Boys, F.D. Bernardi, *Mol. Phys.* 19 (1970) 553–566.
- [20] G.A. DiLabio, *Chem. Phys. Lett.* 455 (2008) 348–353.
- [21] I.D. Mackie, G.A. DiLabio, *J. Phys. Chem. A* 112 (2008) 10968–10976.
- [22] I.D. Mackie, G.A. DiLabio, *Phys. Chem. Chem. Phys.* 12 (2010) 6092–6098.
- [23] E. Torres, G.A. DiLabio, *J. Phys. Chem. Lett.* 3 (2012) 1738–1744.
- [24] O.A. Von Lilienfeld, I. Tavernelli, U. Rothlisberger, D. Sebastiani, *Phys. Rev. Lett.* 93 (2004) 153004.
- [25] L. Gráfová, M. Pitonak, J. Rezac, P. Hobza, *J. Chem. Theory Comput.* 6 (2010) 2365–2376.
- [26] F.A. Hamprecht, A.J. Cohen, D.J. Tozer, N.C. Handy, *J. Chem. Phys.* 109 (1998) 6264–6271.
- [27] J.P. Perdew, K. Burke, M. Ernzerhof, *Phys. Rev. Lett.* 77 (1996) 3865.
- [28] K. Burke, J.P. Perdew, Y. Wang, in: J.F. Dobson, G. Vignale, M.P. Das (Eds.), *Electronic Density Functional Theory: Recent Progress and New Directions*, Plenum, 1998.
- [29] I.D. Mackie, G.A. DiLabio, *Energy Fuels* 24 (2010) 6468–6475.
- [30] G.A. DiLabio, I. MacKie, H.D. Dettman, *Asphaltene components as organic electronic materials*, US Patent 9,065,059, 2015.
- [31] E.R. Johnson, G.A. DiLabio, *J. Phys. Chem. C* 113 (2009) 5681–5689.
- [32] S. Sinha, G. DiLabio, R. Wolkow, *J. Phys. Chem. C* 114 (2009) 7364–7371.
- [33] A. Bellec, F. Ample, D. Riedel, G. Dujardin, C. Joachim, *Nano Lett.* 9 (2008) 144–147.
- [34] G.A. DiLabio, E.R. Johnson, J. Pitters, *J. Phys. Chem. C* 113 (2009) 9969–9973.
- [35] M.J. Frisch, et al., *Gaussian 09 Revision A.1*, Gaussian Inc., Wallingford, CT, 2009.
- [36] J. Rezac, K.E. Riley, P. Hobza, *J. Chem. Theory Comput.* 7 (2011) 2427–2438.
- [37] P. Jurečka, J. Šponer, J. Černý, P. Hobza, *Phys. Chem. Chem. Phys.* 8 (2006) 1985–1993.
- [38] M.S. Marshall, L.A. Burns, C.D. Sherrill, *J. Chem. Phys.* 135 (2011) 194102.
- [39] L.A. Burns, Á. Vázquez-Mayagoitia, B.G. Sumpter, C.D. Sherrill, *J. Chem. Phys.* 134 (2011) 084107.
- [40] G.A. DiLabio, M. Koleini, E. Torres, *Theor. Chem. Acc.* 132 (2013) 1–13.
- [41] G.A. DiLabio, M. Koleini, *J. Chem. Phys.* 140 (2014) 18A542.
- [42] O.A. Vydrov, G.E. Scuseria, *J. Chem. Phys.* 125 (2006) 234109.
- [43] A. Otero-de-la-Roza, E.R. Johnson, G.A. DiLabio, *J. Chem. Theory Comput.* 10 (2014) 5436–5447.
- [44] S. Grimme, *Chem. Eur. J.* 18 (2012) 9955–9964.
- [45] E.R. Johnson, O.J. Clarkin, G.A. DiLabio, *J. Phys. Chem. A* 107 (2003) 9953–9963.
- [46] L. Goerigk, S. Grimme, *Phys. Chem. Chem. Phys.* 13 (2011) 6670–6688.
- [47] J.A. Van Santen, G.A. DiLabio, *J. Phys. Chem. A* 119 (2015) 6703–6713.

# The vdW-DF Family of Nonlocal Exchange-Correlation Functionals

Elsebeth Schröder<sup>\*</sup>, Valentino R. Cooper<sup>†</sup>, Kristian Berland<sup>‡</sup>,  
Bengt I. Lundqvist<sup>§</sup>, Per Hyldgaard<sup>\*</sup>, Timo Thonhauser<sup>¶,||</sup>

<sup>\*</sup>Microtechnology and Nanoscience, MC2, Chalmers University of Technology, Göteborg, Sweden <sup>†</sup>Materials Science and Technology Division, Oak Ridge National Laboratory, Oak Ridge, TN, USA <sup>‡</sup>Centre for Materials Science and Nanotechnology, SMN, University of Oslo, Oslo, Norway <sup>§</sup>Department of Physics, Chalmers University of Technology, Göteborg, Sweden <sup>¶</sup>Department of Physics, Wake Forest University, Winston-Salem, NC, USA <sup>||</sup>Department of Chemistry, Massachusetts Institute of Technology, Cambridge, MA, USA

## 8.1 WHY A NONLOCAL CORRELATION DENSITY FUNCTIONAL?

Van der Waals (vdW) forces—also called dispersion forces—are ever-present and generally attractive interactions that arise due to correlated charge fluctuations [1]. While mostly thought of as fairly weak long-range interactions with macroscopic consequences—e.g., enabling geckos to run up vertical surfaces—van der Waals forces are in fact one of the most important and strongest interactions just beyond the covalent-binding separation regime, crucial for, e.g., the physisorption of molecules on surfaces and the binding of layered materials. Such systems are often small enough that density functional theory (DFT) can be used to investigate their ground-state properties [2,3]. DFT is traditionally used in problems ranging from solids and surfaces to atoms and molecules [4,5]. However, it is only more recently that it has also been used for sparse matter, i.e., materials characterized by regions of low electron density, where not all components are rigidly linked to each other via chemical bonds.

In DFT the electron density  $\rho(\mathbf{r})$  is the key variable [2,3]. How a given DFT model makes use of this density also serves as a measure of its sophistication and level of approximation. The local density approximation (LDA) [3,6], describing many-electron effects in terms of a functional depending only on the density  $\rho(\mathbf{r})$ , has been indispensable for the description and understanding of, for instance, semiconductors. The semilocal, generalized gradient approximation (GGA) [7] goes one step further by including a dependence on the density gradient  $\nabla\rho(\mathbf{r})$ , which significantly improves the description of the binding of molecules—thereby

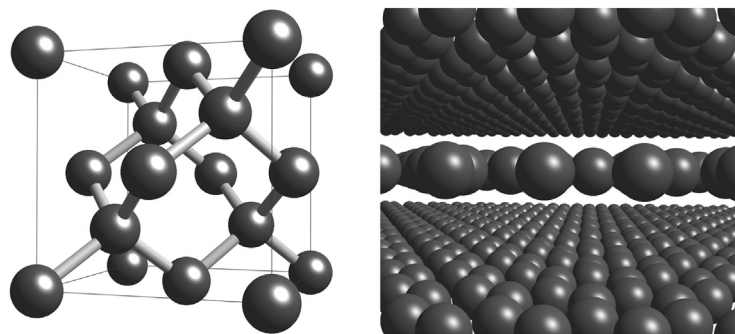


FIGURE 8.1 (Left) Diamond, with strong covalent bonding between all atoms. (Right) Graphene sheets in graphite, with strong covalent bonding between atoms in the same layer and weak van der Waals bonding between the layers, which are separated by low density regions.

making it popular among chemists as well as physicists. However, the description of sparse matter requires an even more sophisticated, nonlocal dependence on the charge density  $\rho(\mathbf{r})$ .

To illustrate the need for a nonlocal description of many-electron interactions, one can contrast diamond with graphite, shown in Fig. 8.1. Although both systems are composed solely of carbon, they form quite different solids. Whereas the layered material graphite is soft, diamond is hard; graphite is opaque and black, but pure diamond is transparent and colorless; graphite is a conductor, while diamond is an insulator. DFT's ability to describe different kinds of covalent bonds, both those of diamond and those within a single layer of graphite (called graphene), is one reason why DFT in the LDA and GGA is so popular. However, the description of the interactions between graphene sheets, which are separated by very low density regions, demands that a functional is aware of the correlation between well separated densities giving rise to vdW interactions and demands a nonlocal dependence on the density. In other words, a local or semilocal functional simply does not contain the information required to be fully aware of the presence of other graphene sheets in close proximity. In this respect, it is interesting to review the DFT literature on layered graphitic systems prior to the turn of the century, studied with the then standard GGA. Only a few results can be found, which is surprising considering how important this material is for a wide range of applications including fuel cells, sealing materials, powdered metallurgy, friction products, steel-mill and foundry products, lubricants, and plastics, not to mention pencils. The results that were presented were often contradictory and unphysical [8–10]. However, more disappointing was the lack of public discussion of the problems encountered when using GGA. This precarious situation may be due to the fact that early DFT results using LDA—with its local dependence on  $\rho(\mathbf{r})$  and thus without any proper description of vdW forces—often gave reasonable equilibrium separations [10–13]. Perhaps the good numbers had a blinding effect, obscuring how fortuitous they were and not giving sufficient impetus for further theory development. In hindsight, it is not surprising that an exchange-correlation functional such as LDA, derived from a homogeneous electron gas, is not suitable for sparse matter with its extremely inhomogeneous densities.



## 8.2 EXCHANGE AND CORRELATION IN DFT

Before deriving a formalism to capture vdW forces through a nonlocal exchange-correlation functional in DFT, it is helpful to review the basics of DFT in general and the definition and constraints of the exchange-correlation functional in particular. Some of these concepts have already been introduced in Chapter 5.

In principle, DFT can give an exact description of ground-state properties of many-electron systems [2,3]. In practice, however, the goal is to find approximations that best mimic the important interactions for the system of interest. Hohenberg and Kohn proved that all ground-state properties of an interacting many-body system are uniquely determined by the ground-state electron density and can be viewed as a functional of  $\rho(\mathbf{r})$  [2]. In particular, the total energy of the system is also a functional of the density, i.e.,  $E = E[\rho(\mathbf{r})]$ . By varying the density  $\rho(\mathbf{r})$ , one can minimize  $E[\rho(\mathbf{r})]$  and the correct ground-state density is the one that gives the global minimum of  $E[\rho(\mathbf{r})]$ . It is advantageous to express this energy functional as a sum of four terms,

$$E[\rho(\mathbf{r})] = T[\rho(\mathbf{r})] + \int d^3r \rho(\mathbf{r}) \left[ V_{\text{ext}}(\mathbf{r}) + \frac{1}{2} V_{\text{Coulomb}}(\mathbf{r}) \right] + E_{\text{xc}}[\rho(\mathbf{r})], \quad (8.1)$$

where  $T[\rho(\mathbf{r})]$  is the kinetic-energy functional of noninteracting electrons in an effective potential,  $V_{\text{ext}}(\mathbf{r})$  is the external potential,  $V_{\text{Coulomb}}(\mathbf{r})$  is the classical Coulomb potential for the electrons, and  $E_{\text{xc}}[\rho(\mathbf{r})]$  is the exchange-correlation (XC) energy, which contains the many-electron interactions. Within Kohn–Sham (KS) theory [3], the large contributions  $T[\rho(\mathbf{r})]$ ,  $V_{\text{ext}}(\mathbf{r})$ , and  $V_{\text{Coulomb}}(\mathbf{r})$  can be treated exactly and only the usually small  $E_{\text{xc}}[\rho(\mathbf{r})]$  requires approximations.

A set of single-particle Schrödinger-type equations, the so-called KS equations [3], can be obtained by minimizing Eq. (8.1) through a functional derivative with respect to the KS orbitals  $\psi_i(\mathbf{r})$ . Using atomic units, one finds

$$\left[ -\frac{1}{2} \nabla^2 + V_{\text{ext}}(\mathbf{r}) + V_{\text{Coulomb}}(\mathbf{r}) + V_{\text{xc}}(\mathbf{r}) \right] \psi_i(\mathbf{r}) = \epsilon_i \psi_i(\mathbf{r}), \quad (8.2)$$

where the XC potential is given by

$$V_{\text{xc}}(\mathbf{r}) = \frac{\delta E_{\text{xc}}[\rho(\mathbf{r})]}{\delta \rho(\mathbf{r})}, \quad (8.3)$$

and the density is calculated from the occupied KS orbitals as

$$\rho(\mathbf{r}) = \sum_{i=1}^{\text{occ}} |\psi_i(\mathbf{r})|^2. \quad (8.4)$$

If the exact  $E_{\text{xc}}[\rho(\mathbf{r})]$  were known and used in Eq. (8.3), these equations would give the exact ground-state energy and density, including all many-electron effects. In practice, however, approximations must be made, which determine the accuracy of all DFT calculations.

The XC energy functional  $E_{\text{xc}}[\rho(\mathbf{r})]$  can be defined through Eq. (8.1) as the difference between the exact energy and the contributions that can be calculated exactly. Compared with the total energy, the XC term is small, yet it often plays a key role in weak bonding and the utility of DFT hinges on a careful handling of this term. But, even if the exact XC functional is not known, there are ways to get insight into its properties. It is useful to consider a Hamiltonian where one can gradually, i.e., adiabatically, turn on Coulomb interactions  $\lambda V(\mathbf{r} - \mathbf{r}') = \lambda |\mathbf{r} - \mathbf{r}'|^{-1}$  between electrons via a coupling constant  $0 \leq \lambda \leq 1$ ,

$$H_\lambda = T + V_{\text{ext},\lambda} + \lambda V, \quad (8.5)$$

where  $\lambda = 1$  corresponds to the fully interacting system with  $V_{\text{ext},\lambda=1} \equiv V_{\text{ext}}$  and  $\lambda = 0$  corresponds to noninteracting electrons in an effective potential  $V_{\text{ext},\lambda=0}$ . The interaction is assumed to be switched on and off adiabatically such that the effective potential  $V_{\text{ext},\lambda}$  adjusts to keep the density  $\rho(\mathbf{r})$  fixed to that of the fully interacting system. At every  $\lambda$  one can then define an external-field response function  $\chi(\mathbf{r}, \mathbf{r}'; \omega)$  that relates the changes in the potential  $\delta V_{\text{ext}}(\mathbf{r}'; t')$  at one point  $\mathbf{r}'$  to the density changes  $\delta\rho$  at another point,

$$\delta\rho(\mathbf{r}; t) = \int d^3r' \int_0^\infty \frac{dt'}{2\pi} \chi(\mathbf{r}, \mathbf{r}'; t - t') \delta V_{\text{ext}}(\mathbf{r}'; t'). \quad (8.6)$$

Since ground-state DFT describes steady-state behavior, the density response is often described in the frequency domain

$$\delta\rho(\mathbf{r}; \omega) = \int d^3r' \chi(\mathbf{r}, \mathbf{r}'; \omega) \delta V_{\text{ext}}(\mathbf{r}'; \omega). \quad (8.7)$$

The vdW interactions are caused by charge fluctuations  $\delta\rho(\mathbf{r}; t)$  in one part of a system that correlate with fluctuations  $\delta\rho(\mathbf{r}'; t')$  in another part. The response function  $\chi(\mathbf{r}, \mathbf{r}'; \omega)$  is a key ingredient to describe such situations. In fact,  $\chi(\mathbf{r}, \mathbf{r}'; \omega)$  is simply a formal expression of all the density–density correlations in the electron system [6,14,15].

Using the Hellmann–Feynman theorem and integrating  $\lambda$  from 0 to 1, one finds a formally exact expression for the XC energy—also called the adiabatic connection formula (ACF)—which provides a rigorous basis for the design of approximate XC functionals in DFT [6,14,15]:

$$\begin{aligned} E_{\text{xc}}[\rho(\mathbf{r})] &= - \int_0^1 d\lambda \int_0^\infty \frac{du}{2\pi} \text{Tr} \{ \chi_\lambda(iu) V \} - \frac{1}{2} \text{Tr} \{ \rho V \} \\ &= - \int_0^1 d\lambda \int_0^\infty \frac{du}{2\pi} \int d^3r d^3r' \chi_\lambda(\mathbf{r}, \mathbf{r}'; iu) V(\mathbf{r}' - \mathbf{r}) \\ &\quad - \frac{1}{2} \int d^3r d^3r' \rho(\mathbf{r}) \delta(\mathbf{r} - \mathbf{r}') V(\mathbf{r} - \mathbf{r}'). \end{aligned} \quad (8.8)$$

The last term on the right side of Eq. (8.8) is the so-called Coulomb self-energy  $E_{\text{self}}$  of the electrons. It is a term that is convenient to retain while performing many-body calculations (of the density–density correlation function  $\chi$ ) but which must be subtracted when extracting, for example, results for XC functional approximations [15].

The response function  $\chi_\lambda(\mathbf{r}, \mathbf{r}'; \omega)$  has poles in the complex frequency plane corresponding to important excitations of the electron gas. The use of an imaginary-frequency integration  $\omega \equiv iu$  in Eq. (8.8) enables the ACF to pick up all contributions from various excitations, while keeping the integrations tractable. It is convenient to define an XC hole [6]

$$\rho_{xc}(\mathbf{r}, \mathbf{r}') = -\frac{2}{\rho(\mathbf{r})} \int_0^1 d\lambda \int_0^\infty \frac{du}{2\pi} \chi_\lambda(\mathbf{r}, \mathbf{r}'; iu) - \delta(\mathbf{r} - \mathbf{r}') \quad (8.9)$$

as the charge depletion that arises around an electron at position  $\mathbf{r}$  due to both Pauli exclusion and electron–electron interaction effects. The formal XC energy evaluation in Eq. (8.8) can then be expressed as the Coulomb interaction of the electrons and their associated holes

$$E_{xc}[\rho(\mathbf{r})] = \frac{1}{2} \int d^3r \int d^3r' \frac{\rho(\mathbf{r}) \rho_{xc}(\mathbf{r}, \mathbf{r}')}{|\mathbf{r} - \mathbf{r}'|}. \quad (8.10)$$

The importance of XC holes was also discussed in Chapter 5. In essence, the search for approximations to the XC energy in Eq. (8.8) consists of making physically motivated approximations for the XC hole in Eq. (8.9).

The XC hole has a positive charge density, the total charge being equal to the electron charge unit

$$\int d^3r' \rho_{xc}(\mathbf{r}, \mathbf{r}') = -1. \quad (8.11)$$

The XC hole has several properties [6,16,17] that provide a basis for finding good approximations for the XC energy functional. The sum rule in Eq. (8.11) states that the XC hole integrates to  $-1$ . For the individual exchange and correlation parts one finds

$$\int d^3r' \rho_x(\mathbf{r}, \mathbf{r}') = -1, \quad (8.12)$$

and

$$\int d^3r' \rho_c(\mathbf{r}, \mathbf{r}') = 0. \quad (8.13)$$

Finally, the exchange hole is nonpositive, i.e.,

$$\rho_x(\mathbf{r}, \mathbf{r}') \leq 0. \quad (8.14)$$

An important observation is that the XC energy depends only on the spherical average of the XC hole, not on the finer details of the hole [6]. This averaging effect has been used as an argument for the unphysical and surprising ability of LDA to sometimes give reasonable results also in inhomogeneous density situations [6]. This argument might explain why LDA has been in popular use in calculations on bulk semiconductors, but it is certainly insufficient for situations with electron densities close to zero, like that between the layers in graphite and for a multitude of other noncovalently bound systems. Such situations strongly motivate developing density functionals that properly include vdW interactions.

### 8.3 LEARNING FROM THE ASYMPTOTIC LIMIT

The vdW-DF family of functionals use a systematic approach that adheres closely to physical conservation rules. It has its roots in many-body theory (MBT) and uses the ACF from Eq. (8.8) as its starting point. This section illustrates early ideas in the systematic development of vdW-DF. It first shows explicitly for three model systems—two neutral atoms, an atom on a surface, and two parallel surfaces—that vdW interactions are present in the exact density functional [18]. Then, the asymptotic limit for large separations is analyzed, providing a simple functional form. This functional form itself was used in the vdW-DF method [19–21], although (as discussed in the following sections) further enhanced by electron-response insight. This insight gives vdW-DF a seamless integration with a GGA-type description of exchange effects and permits vdW-DF to describe interactions across length scales [19–23].

When describing long-range interactions, it is natural to divide the system into subsystems or fragments [24]. The fragments are characterized by a macroscopic electric charge, but the vdW interactions will also be present when the fragments are neutral. While the neutral-fragment case is the focus in this discussion, the vdW-DF method works also in the general case. With two fragments  $a$  and  $b$ , one can define the response function  $\chi_{ab}(\mathbf{r}, \mathbf{r}'; \omega)$ , which carries the same meaning as defined in Eq. (8.6), but  $\mathbf{r}$  and  $\mathbf{r}'$  are restricted to the fragments indicated by the subscripts. Writing the density as  $\rho(\mathbf{r}) = \rho_a(\mathbf{r}) + \rho_b(\mathbf{r})$  [24], the original Hamiltonian can be split into separate parts  $H = H_a + H_b + V_{ab}$ , which naturally allows for switching  $V_{ab}$  on and off via the coupling constant  $\lambda$ , as done in Eq. (8.5). Following Ref. [18], Eq. (8.8) is applied to the fragments using the relation

$$\chi = \chi^{\text{bare}} + \chi^{\text{bare}} V \chi, \quad (8.15)$$

where  $\chi^{\text{bare}}$  is the density response description that arises in the absence of any electron–electron interaction, i.e., the bare susceptibility that defines the starting point of the random phase approximation (RPA), as discussed in Chapter 3. When expanded to second order in  $V_{ab}$  this leads to

$$E_{\text{xc}}[\rho(\mathbf{r})] = E_{\text{xc}}^{\infty} + \frac{1}{2\pi i} \int_C d\omega \text{Tr}\{V_{ab} \chi_{bb} V_{ba} \chi_{aa}\} + \mathcal{O}(V_{ab}^3). \quad (8.16)$$

Here,  $C$  is an integration contour across the real axis enclosing the upper half-plane and the superscript  $\infty$  denotes the value when fragments  $a$  and  $b$  are infinitely separated. Present-day vdW-DF does not rely on a study of an RPA-type  $\chi^{\text{bare}}$ , but builds instead on a screening account extracted from the response behavior that underpins GGA [20,22,23]. The details of the expansion used in Eq. (8.16)—for separate fragments as well as for weakly overlapping fragments—are included and discussed in Ref. [22] as part of an interpretation of the vdW-DF method. That interpretation paper also takes the expansion to third order, noticing that the vdW-DF framework can be seen as a systematic extension of RPA, an extension that seeks to capture screening also when relying on a finite-order expansion [22].

Application of Eq. (8.16) to the case of two neutral atoms in their ground state separated by a distance  $R$  gives

$$E_{\text{xc}}[\rho(\mathbf{r})] = E_{\text{xc}}^{\infty} - \frac{3}{\pi R^6} \int_0^{\infty} du P_a(iu) P_b(iu), \quad (8.17)$$

where

$$P(\omega) = 2 \sum_n \frac{2\omega_{n0} | \langle 0|z|n \rangle |^2}{\omega_{n0}^2 - \omega^2} \quad (8.18)$$

is the frequency-dependent polarizability of an atom, as derived in Chapter 5 [25]. If one single dipole moment  $\langle 0|z|n \rangle$  dominates for each of the atoms  $a$  and  $b$  with frequencies  $\omega_a$  and  $\omega_b$ , respectively, then  $P(\omega)$  can be expressed in terms of their numbers of electrons  $N_a$  and  $N_b$ . The energy then reduces to the simple London formula [26]

$$E_{\text{vdW}}(R) = -\frac{1}{R^6} \frac{3}{2} \frac{N_a N_b}{\omega_a \omega_b (\omega_a + \omega_b)} \equiv -\frac{C_6}{R^6}. \quad (8.19)$$

The interaction between an atom and a surface can also be obtained from the second-order expansion in  $V_{ab}$ , Eq. (8.16). For the case of a neutral atom outside a surface, this expression is the starting point of Zaremba and Kohn's derivation [27,28] of the Lifshitz formula [29]. For two extended objects, such as two parallel surfaces at large separations, the simple second-order expansion is not sufficient. Eq. (8.16) is only a second-order expansion without inclusion of screening effects and effects of  $V_{ab}$  must be included to infinite order. For two parallel plates a distance  $d$  apart, the Lifshitz result [29] (as derived by van Kampen et al.) gives [30]

$$E_{\text{vdW}}(d) = \frac{A}{32\pi d^2} \int_C \frac{d\omega}{2\pi i} \int_0^{\infty} \frac{x^2 dx}{e^x/\alpha^2 - 1}, \quad (8.20)$$

where  $\alpha = (1 - \epsilon)/(1 + \epsilon)$ ,  $\epsilon$  is the dielectric function, and  $A$  is the surface area. The need to include all orders in  $V_{ab}$  suggests that methods using atom-pair potential corrections are inadequate. In summary, for all three model systems, DFT in combination with the ACF leads to the well-known analytical expressions for vdW interactions, proving that these interactions are present in the exact density functional.

The external-field response function  $\chi$  in Eq. (8.6) describes excitations such as electron-hole pairs [31], plasmons [32], and polarization waves [33]. The behavior of plasmons in turn underpins both traditional DFT in the LDA and GGA and vdW forces, as further discussed and summarized in, for example, Ref. [23]. Electron-hole excitations play a central role in applications of the free-electron gas model. This model is not only useful for describing almost free electron-hole pairs in the conduction-electron regions, but can also be an important component in describing localized pairs involving  $d$ -electrons at the atomic sites. Maggs and Ashcroft revitalized this thinking by finding new diagrams with leading contributions to the cohesion of such systems [34]. MBT can describe the dynamics of particles and fields in graphical Feynman-type diagrams, with straight arrows describing particles and wavy lines describing interactions such as  $\chi$ . When lines cross, physical conservation laws are taken

care of at each vertex. The systematic tool of MBT—the so-called Dyson equation for  $\chi$ —automatically incorporates screening of the Coulomb interaction in the electron system. MBT has been applied to many model systems, producing valuable results when the system is simple enough to allow an analytical or accurate numerical solution, such as for the homogeneous electron gas. These results are most valuable for alkali and alkaline metals, but they do also provide insight for more complicated systems, such as transition metals. Nonetheless, MBT studies of the many-body effects in the slightly inhomogeneous electron gas, like those of Langreth and Vosko (LV) [35] and Rapcewicz and Ashcroft (RA) [36], have provided an excellent starting point for vdW-DF.

The next step in the development of a vdW-including functional is to find a simple calculational scheme in the spirit of LDA and GGA, but extended to include the necessary physical nonlocal dependence on the density  $\rho(\mathbf{r})$ . The Andersson–Langreth–Lundqvist (ALL) functional [37] is used to calculate the leading term in the interaction between two neutral monomers separated by  $R$ . It is an asymptotic functional designed to use the monomer electron density distributions and it leads to mutual attraction that reflects the expected vdW form  $-C_6/R^6$ . This functional was inspired by a similar functional by Rapcewicz and Ashcroft [36], which had certain formal shortcomings, for instance being inconsistent with the famous London results for  $C_6$  coefficients in Eq. (8.19). The ALL theory gave credible frequency dependent atomic polarizabilities and  $C_6$  coefficients for a host of small molecule pairs that were remarkably accurate (10–20%), considering the simplicity of the method [37, 38]. A more complete description of the method is given in Ref. [39]. The ALL functional has found many applications, for instance, in combination with empirical damping functions, and provides one of the foundations of the general-geometry vdW-DF functional developed a decade later [19–21].

Analyzing the diagrams for high frequencies and small momenta, RA find a limiting behavior that leads to a long-range behavior of the electron–electron interaction of the form

$$\phi^{\text{RA}}(\mathbf{r}, \mathbf{r}') = -\frac{3}{4} \frac{1}{(\omega_{\text{p}}(\mathbf{r}, \mathbf{r}'))^3 |\mathbf{r} - \mathbf{r}'|^6}, \quad (8.21)$$

where  $\omega_{\text{p}}(\mathbf{r}, \mathbf{r}') = \sqrt{4\pi\rho_{\text{eff}}(\mathbf{r}, \mathbf{r}')}$  is a plasmon frequency defined by an effective (nonlocal) density  $\rho_{\text{eff}}^{\text{RA}}(\mathbf{r}, \mathbf{r}')$ . With the motivation to get both the homogeneous-gas and the separated-atom limits to agree with independently derived exact results, the ALL chooses the effective density

$$\rho_{\text{eff}}^{\text{ALL}}(\mathbf{r}, \mathbf{r}') = \left[ \sqrt{\rho_a(\mathbf{r}) \rho_b(\mathbf{r}')} \left( \sqrt{\rho_a(\mathbf{r})} + \sqrt{\rho_b(\mathbf{r}')} \right) \right]^{2/3}. \quad (8.22)$$

The choice is different than what is used in the RA description, but the choice in Eq. (8.22) makes it possible to express the interaction contributions in terms of the local value of the classical plasmon frequency  $\omega_{\text{p}}(\mathbf{r}) = \sqrt{4\pi\rho(\mathbf{r})}$ . The vdW interaction energy between two atoms separated by a large distance  $R$  takes the form

$$E_{\text{vdW}}^{\text{ALL}} = \int_a d^3r \int_b d^3r' \rho(\mathbf{r}) \phi^{\text{ALL}}(\mathbf{r}, \mathbf{r}') \rho(\mathbf{r}'), \quad (8.23)$$

given by a kernel

$$\phi^{\text{ALL}}(\mathbf{r}, \mathbf{r}') = -\frac{3}{2} \frac{1}{\omega_{\text{p}}(\mathbf{r})\omega_{\text{p}}(\mathbf{r}') [\omega_{\text{p}}(\mathbf{r}) + \omega_{\text{p}}(\mathbf{r}')] } \cdot \frac{1}{|\mathbf{r} - \mathbf{r}'|^6}, \quad (8.24)$$

that represents the effective electron–electron interaction in a form that is consistent with the London formula in Eq. (8.19). The functional form Eq. (8.23) is similar to the one used in present-day vdW-DF. In fact, it provided an important limiting behavior which guided some of the assumptions made in designing vdW-DF [20].

ALL uses fairly simple approximations for the electrodynamical screening in its account of the electrodynamical coupling between plasmons  $\omega_{\text{p}}(\mathbf{r})$  at different density points [37]. Thus, after the ALL development a description having a self-consistent and unified treatment of the electrodynamical screening was sought that was applicable to atoms, molecules, and other objects [40]. These so-called unified functional descriptions are ALL-functional extensions that are still developed for asymptotic separations, but they account for screening effects by solving for the electrodynamical coupling as it emerges in the specific electron-density variation.

The original ALL functional computes the frequency-dependent molecular polarizability as a perturbation in the applied electric field. With the unified functional approach, the results for the  $C_6$  coefficients between a few closed-shell atoms and small molecules show some, but not substantial, improvement over the non-self-consistent theory, a result that was useful in the design of a general-purpose functional, namely the present-day vdW-DF method [20,21,23]. The unified functional approach has also been applied to other atoms and molecules [38,40–43], such as the low-index faces of Al. The unified description provides accurate results for the so-called vdW image plane, for example, of relevance for an accurate description of  $\text{H}_2$  adsorption [44,45]. Interactions between  $\text{C}_{60}$  molecules [38] have also been studied with the unified functional approach, here finding that it is important to retain a self-consistent account for an accurate description at asymptotic separations. The relevance of image-plane or screening effects on interactions for both the binding and asymptotic regions have also been analyzed in the framework of the modern vdW-DF versions, for example, in studies of graphite and carbon nanotube bundles [46–48].

---

## 8.4 DERIVATION OF VDW-DF

---

The vdW-DF family of truly nonlocal functionals represent a systematic extension of the semilocal XC functional description. As shown in Eq. (8.10), the XC energy can be expressed in terms of the XC hole  $\rho_{\text{xc}}$ , describing the charge depletion around a given electron [6,15]. LDA and the constraint-based GGAs result from making consistent approximations for the shape of the XC holes as defined in the homogeneous or in the weakly perturbed electron gas and as treated in a semilocal framework [6,15,49,50]. Such semilocal functionals work well for molecules or solids, but they are incapable of describing vdW interactions. To understand those GGA shortcomings, note that the set of electrons with surrounding semilocal XC holes are themselves quantum systems with zero-point vibrations, and that there must be

an electrodynamical coupling between such virtual charge fluctuation via the RA mechanism discussed in the previous section. Recognizing the importance of this mutual coupling led directly to the construction of the (asymptotic) ALL and unified functionals and of truly non-local functionals for all separations, including a functional for layered systems [46] and the set of modern vdW-DF versions [20,21,51,52]. The importance of a mutual XC hole coupling is also recognized in the Becke–Johnson formulation of a functional description of vdW interaction, discussed in Chapter 5. The discussion focuses on the most recent, general-geometry vdW-DF versions [20,51,53] that have seamless integration with a traditional GGA-type description and which can be used for all types of system geometries.

The vdW-DF method provides a succinct determination of the total energy shift that arises from the above-mentioned electrodynamical coupling among electrons and the XC hole associated with an internal semilocal functional  $E_{xc}^0$  of GGA type [22,53]. The vdW-DF method provides this determination in an electron-based description that is also computationally efficient and as fast as GGA calculations in plane-wave codes. Nevertheless, the zero-point vibrations of the electron relative to semilocal XC holes remain a central ingredient of the vdW-DF method. As such, vdW-DF connects [20,22,23,46,54] to the London picture of dispersive interactions between atoms or molecules [26,55,56] and provides a bridge between the electron-gas picture used by condensed-matter physicists [18,23,34,36,37,39,57,58] and more traditional descriptions of vdW interactions.

### 8.4.1 The Coupling Constant Integration

vdW-DF rests on the ACF, an expression for the XC energy in terms of a coupling-constant integration in Eq. (8.8). It is convenient to define an effective dielectric function  $\kappa_{ACF}$  that automatically enforces current conservation [22] and which reflects the coupling-constant integration that underpins the formally exact ACF expression in Eq. (8.8):

$$\kappa_{ACF}(iu) \equiv \exp \left[ - \int_0^1 d\lambda \chi_\lambda(iu) V \right]. \quad (8.25)$$

This expression must be understood as a matrix form with a corresponding real-space evaluation given by

$$A(\mathbf{r}, \mathbf{r}') = \langle \mathbf{r} | A | \mathbf{r}' \rangle, \quad (8.26)$$

$$\langle \mathbf{r} | A B | \mathbf{r}' \rangle = \int d^3 r'' A(\mathbf{r}, \mathbf{r}'') B(\mathbf{r}'', \mathbf{r}'). \quad (8.27)$$

The right-hand side of Eq. (8.25) can thus be expressed as

$$\langle \mathbf{r} | \ln \kappa_{ACF}(iu) | \mathbf{r}' \rangle \equiv - \int_0^1 d\lambda \int d^3 r'' \chi_\lambda(\mathbf{r}, \mathbf{r}''; iu) V(\mathbf{r}'' - \mathbf{r}'), \quad (8.28)$$



and the logarithm of the left-hand side must also be expanded before evaluation. With this definition of  $\kappa_{\text{ACF}}(iu)$ , one can recast the ACF evaluation in Eq. (8.8) as

$$E_{\text{xc}}[\rho] = \int_0^\infty \frac{du}{2\pi} \int d^3r \langle \mathbf{r} | \ln \kappa_{\text{ACF}}(iu) | \mathbf{r} \rangle - E_{\text{self}}. \quad (8.29)$$

This expression has the advantage that the explicit coupling-constant integration is avoided, working instead with a  $\lambda$ -averaged response that is expressed in  $\kappa_{\text{ACF}}(iu)$ . The main goal now becomes to find suitable approximations for  $\kappa_{\text{ACF}}(iu)$ .

The first major step in the vdW-DF formulation is to write  $\kappa_{\text{ACF}}$  in such a form that it serves as an appropriate description of the electrodynamic coupling of the electron gas. If  $\epsilon(iu)$  represents an approximation for the dielectric tensor, one can extract the relevant longitudinal projection by writing [20,22,23,46,54]

$$\kappa_{\text{ACF}}(\mathbf{r}, \mathbf{r}'; iu) = - \int d^3r'' \nabla \cdot \boldsymbol{\epsilon}(\mathbf{r}, \mathbf{r}''; iu) \cdot \nabla' V(\mathbf{r}'' - \mathbf{r}') / 4\pi. \quad (8.30)$$

This projection ensures that the screening description is consistent with the continuity equation, i.e., with current conservation [20,22]. The quality of functional approximations that can be constructed from Eq. (8.30) will, of course, depend on the choice of the dielectric tensor  $\boldsymbol{\epsilon}(\mathbf{r}, \mathbf{r}'; iu)$ ; in practice it is sufficient to work with a scalar approximation [19]. A key trick of the vdW-DF method is to assert the form of the  $\lambda$ -averaged dielectric function  $\kappa_{\text{ACF}}(iu)$  by using a semilocal GGA-type internal functional  $E_{\text{xc}}^0$  to fix the form of  $\boldsymbol{\epsilon}(\mathbf{r}, \mathbf{r}'; iu)$  [20,22,23,46,54], so that the resulting screening description is automatically consistent with the continuity equation, i.e., with current conservation [20,22].

The next major step in the formulation of the vdW-DF method is to link  $\boldsymbol{\epsilon}(\mathbf{r}, \mathbf{r}'; iu)$  to a GGA starting point [20,23,59], i.e., an internal functional  $E_{\text{xc}}^0$  of the GGA type [22,53]. The term *internal* refers to the fact that it will parametrize the nonlocal correlation energy as opposed to contributing directly to the total energy functional. The underlying idea is that the vdW-DF total XC energy density functional

$$E_{\text{xc}}[\rho] = E_{\text{xc}}^0[\rho] + E_{\text{c}}^{\text{nl}}[\rho] \quad (8.31)$$

extends the lowest order GGA-type term  $E_{\text{xc}}^0[\rho]$  by a truly nonlocal correlation term  $E_{\text{c}}^{\text{nl}}[\rho]$ . To have a practical  $\boldsymbol{\epsilon}(\mathbf{r}, \mathbf{r}'; iu)$  specification, the so-called plasmon-pole response description [23]

$$S_{\text{xc}}(\mathbf{r}, \mathbf{r}'; iu) \equiv \langle \mathbf{r} | \ln \epsilon(iu) | \mathbf{r}' \rangle \quad (8.32)$$

is introduced. The form in Eq. (8.32) is closely related to the plasmon propagator  $S = 1 - \epsilon^{-1}$  that was analyzed to yield input for both early LDA [6,60] and the first formulations of vdW-DF [46,54]. The vdW-DF method assumes that the term linear in  $S_{\text{xc}}$  must correspond to a semilocal GGA type functional lacking nonlocal correlations [20,22,23],

$$E_{\text{xc}}^0[\rho] = \int_0^\infty \frac{du}{2\pi} \int d^3r \langle \mathbf{r} | \ln \epsilon(iu) | \mathbf{r} \rangle - E_{\text{self}}. \quad (8.33)$$

With Eq. (8.32) the screening set by  $\epsilon(iu) = e^{S_{xc}(iu)} = 1 + S_{xc}(iu) + \frac{S_{xc}(iu)^2}{2!} + \frac{S_{xc}(iu)^3}{3!} + \dots$  is given by the GGA-type input  $E_{xc}^0$ . This screening description is in turn sufficient to complete the vdW-DF approximation for the total  $\lambda$ -averaged dielectric function in Eq. (8.30) that also enters in the full functional specification (8.29).

The resulting truly nonlocal functional is given by Eq. (8.31). One separates the descriptions of nonlocal correlation plus exchange, captured by  $E_{xc}^0$ , and of nonlocal correlations captured by

$$E_c^{\text{nl}}[\rho] = \int_0^\infty \frac{du}{2\pi} \int d^3r \{ \langle \mathbf{r} | \ln \kappa_{\text{ACF}}(iu) | \mathbf{r} \rangle - \langle \mathbf{r} | \ln \epsilon(iu) | \mathbf{r} \rangle \}. \quad (8.34)$$

A strictly nonempirical determination of  $E_c^{\text{nl}}[\rho]$  follows simply by keeping higher-order terms in  $S_{xc}$ . The procedure can be shown to collect all the zero-point energy shifts that arise from a mutual electrodynamical coupling among electron-hole pairs [22]. It describes dispersive interactions because it is a practical implementation of the RA mechanism discussed in the previous section [22,23,36].

In practice, the vdW-DF method uses a single plasmon-pole approximation to represent the variation of  $S_{xc}$ . For a given density, the nonlocal variation of  $S_{xc}$  is specified in terms of its Fourier components

$$S_{xc}(\mathbf{q}, \mathbf{q}'; iu) = \frac{1}{2} \left[ \tilde{S}_{\mathbf{q}, \mathbf{q}'}(iu) + \tilde{S}_{-\mathbf{q}', -\mathbf{q}}(iu) \right], \quad (8.35)$$

$$\tilde{S}_{\mathbf{q}, \mathbf{q}'}(iu) = \int d^3r \frac{4\pi\rho(\mathbf{r}) e^{-i(\mathbf{q}-\mathbf{q}')\cdot\mathbf{r}}}{(iu + \omega_q(\mathbf{r}))(-iu + \omega_{q'}(\mathbf{r}))}. \quad (8.36)$$

Here,  $4\pi\rho(\mathbf{r})$  is the value of the classical plasmon frequency  $\omega_p(\mathbf{r})$  squared (see below Eq. (8.22)) while  $\omega_q(\mathbf{r})$  corresponds to the assumed form of the plasmon dispersion, discussed below. This vdW-DF choice for  $S_{xc}(\mathbf{r}, \mathbf{r}'; iu)$  ensures compliance with a set of constraints for a plasmon description of the screening response [20,23]:

1. *F*-sum rule,  $S_{xc}(\mathbf{q}, \mathbf{q}'; \omega) \rightarrow -4\pi \rho_{q-q'}/\omega^2$  in the large- $\omega$  limit;
2. Approaching a free-electron response behavior,  $\int_{-\infty}^\infty du S_{xc}(\mathbf{q}, \mathbf{q}'; iu) \rightarrow 8\pi^2 N/q^2$  for large  $q$ , where  $N$  is the total number of electrons;
3. Time-reversal symmetry,  $S_{xc}(\mathbf{q}, \mathbf{q}'; \omega) = S_{xc}(-\mathbf{q}', -\mathbf{q}; \omega)$ ;
4. Charge conservation, finite  $S_{xc}(\mathbf{q}, \mathbf{q}'; \omega)$  for  $\mathbf{q} = 0$  or  $\mathbf{q}' = 0$  for  $\omega \neq 0$  (and for all complex  $\omega$  in the upper right quadrant).

vdW-DF provides a nonempirical specification of the assumed plasmon dispersion  $\omega_q(\mathbf{r})$  in Eq. (8.36) (and hence of  $S_{xc}$ ), which follows from the analysis of the spatial variation of a semilocal XC hole  $\rho_{xc}^0(\mathbf{r}, \mathbf{r}')$ , as discussed elsewhere [20,22,23,53]. In making this choice, LDA exchange and correlation components are kept together [15] and gradient corrections are restricted to exchange effects [20,59], as vdW-DF captures all nonlocal correlation corrections in  $E_c^{\text{nl}}[\rho]$ . To obtain the dispersion  $\omega_q(\mathbf{r})$  of the plasmons entering  $S_{xc}$  one can study the Fourier transform  $\rho_{xc}(\mathbf{r}, q)$  of the XC hole corresponding to the internal GGA-type functional  $E_{xc}^0$  [20,22]. For simplicity, a Gaussian form  $\rho_{xc}^0 \equiv -\exp[-\gamma(q/q_0(\mathbf{r}))^2]$  is assumed where  $q_0(\mathbf{r})$  is set by the local energy-per-particle value  $\epsilon_{xc}^0(\mathbf{r})$  of the internal functional

$E_{xc}^0 = \int d^3r \rho(\mathbf{r}) \varepsilon_{xc}^0(\mathbf{r})$  [20,22,23,53,59]. Specifically, the  $q_0(\mathbf{r})$  value depends on the local density and its gradient and it is given by

$$q_0(\mathbf{r}) = \frac{\varepsilon_{xc}^0(\mathbf{r})}{\varepsilon_x^{\text{LDA}}(\mathbf{r})} k_F(\mathbf{r}), \quad (8.37)$$

where  $k_F(\mathbf{r}) = (3\pi^2\rho(\mathbf{r}))^{1/3}$  and  $\varepsilon_x^{\text{LDA}} = -3k_F/4\pi$  denotes the energy per particle of LDA exchange. In effect, the function  $q_0(\mathbf{r})$  takes the form of the Fermi wavevector  $k_F(\mathbf{r})$  multiplied by the so-called enhancement factor [50]  $F_{xc}^0(\rho, s)$  for the GGA-type  $E_{xc}^0$  input; here  $s = |\nabla\rho|/2k_F\rho$  is the reduced gradient.

The present-day vdW-DF versions [20,22,53] are all strictly nonempirical, having no free parameters at all. This follows because they specify

$$q_0 = -\frac{4\pi}{3} \varepsilon_c^{\text{LDA}} - \left(1 - \frac{Z_{ab}}{9} s^2\right) \frac{4\pi}{3} \varepsilon_x^{\text{LDA}}, \quad (8.38)$$

from LDA and from approximations for gradient-corrected exchange that are themselves given by results from MBT or from high-density scaling analysis [20,23,53,59]. In the first general-geometry vdW-DF version [20] and in the new consistent-exchange vdW-DF-cx [51], the value  $Z_{ab} = -0.8491$  is extracted from a diagram analysis of gradient corrections to screened exchange [20,59].

With the specification of  $q_0(\mathbf{r})$  and  $\omega_q(\mathbf{r})$  also follows a full determination of  $S_{xc}$  via Eqs. (8.35) and (8.36). The value of the function  $q_0(\mathbf{r})$  determines the spatially dependent roll-over in the response description  $S_{xc}$ , changing it from a plasmon-type behavior at small wavevector to the free-electron behavior that must emerge at long wavevectors and high frequencies. The description therefore respects criterion “1” (formulated above) for a valid plasmon-response description (as well as all other criteria). An example vdW-DF study shows that both types of response behaviors are relevant in a general discussion of molecular adsorption on a surface [61].

The fact that vdW-DF is explicitly designed to be anchored in constraint-based GGAs is a key strength. The immense success of the GGAs can in part be traced to the soundness of its XC-hole description [62] and it is clear that such GGAs already capture a large part of the many-body screening and response effects for bulk materials, surfaces, and individual molecules [62,63]. This insight is ported into vdW-DF as a starting point via  $S_{xc}$  and the introduction of an internal functional [20,22,23,53].

## 8.4.2 The Universal-Kernel Evaluation

Having assembled all the different pieces that go into vdW-DF, one can now derive the standard general-geometry formulation of vdW-DF. The starting point is Eq. (8.34), which contains all orders of  $S_{xc}$ . To second order in  $S_{xc}$  one finds

$$E_c^{\text{nl}}[\rho] \approx \int \frac{du}{4\pi} \text{Tr} \left\{ S_{xc}^2 - (\nabla S_{xc} \cdot \nabla V/4\pi)^2 \right\} \quad (8.39)$$

$$= \frac{1}{2} \int d^3r d^3r' \rho(\mathbf{r}) \phi[\rho](\mathbf{r}, \mathbf{r}') \rho(\mathbf{r}'). \quad (8.40)$$

The second-order expression for  $E_c^{\text{nl}}[\rho]$  can be written to take the form of an effective interaction between two densities (as expressed in Eq. (8.40)), with an interaction strength given by a universal two-point kernel  $\phi$  [20]. This particular form was inspired by the form of the ALL functional in Eq. (8.23).

Eq. (8.39) is written as compact matrix notation and an explicit evaluation would correspond to both integrating over the frequency and six dimensions in momentum space (as given by the matrix product and the trace) as well as six additional spatial dimensions coming from the expressions for  $S_{\text{xc}}$ . Thus, with only six spatial integrals, Eq. (8.40) represents a drastic reduction of complexity, which is achieved by the use of a universal-kernel  $\phi(\mathbf{r}, \mathbf{r}') = \phi(d, d')$  formulation [20], with arguments given by

$$d = q_0(\mathbf{r})|\mathbf{r} - \mathbf{r}'|, \quad (8.41a)$$

$$d' = q_0(\mathbf{r}')|\mathbf{r} - \mathbf{r}'|. \quad (8.41b)$$

Here,  $d$  and  $d'$  can be understood as effective dimensionless separations, with  $q_0(\mathbf{r})$  parameterizing the strength of the interaction, defined in terms of the local density and its gradient as discussed in the previous section. A small value of  $q(\mathbf{r})$  corresponds to a shorter dimensionless separation  $d$  and hence, in the vdW regime, a stronger vdW interaction.

To derive the universal kernel formulation, a key observation is that Eqs. (8.35) and (8.36) can be recast

$$S_{\text{xc}}(\mathbf{q}, \mathbf{q}'; iu) = \int d^3r e^{-i(\mathbf{q}-\mathbf{q}')\cdot\mathbf{r}} f(q, q', \mathbf{r}; \omega) \rho(\mathbf{r}), \quad (8.42)$$

$$f(q, q', \mathbf{r}; \omega) = 2\pi \frac{\omega_q(\mathbf{r})\omega_{q'}(\mathbf{r}) - \omega^2}{(\omega_q^2(\mathbf{r}) - \omega^2)(\omega_{q'}^2(\mathbf{r}) - \omega^2)}, \quad (8.43)$$

so that  $S_{\text{xc}}$  comprises a frequency-dependent part  $f(q, q', \mathbf{r}; \omega)$ , independent of the direction of the momentum, and a frequency-independent part. Moving the spatial integration to the outside, in the expression for the nonlocal correlation in Eq. (8.39) an expression for the kernel can be identified and written as

$$\phi(\mathbf{r}, \mathbf{r}') = \int d^3q d^3q' \left[1 - (\hat{\mathbf{q}} \cdot \hat{\mathbf{q}}')^2\right] e^{-i(\mathbf{q}-\mathbf{q}')\cdot(\mathbf{r}-\mathbf{r}')} I_{\text{freq}}(q, q', \mathbf{r}, \mathbf{r}'), \quad (8.44)$$

$$I_{\text{freq}}(q, q', \mathbf{r}, \mathbf{r}') = \int_0^\infty \frac{du}{2\pi} f(q, q', \mathbf{r}; iu) f(q', q, \mathbf{r}'; iu). \quad (8.45)$$

It is possible to evaluate the frequency integral analytically, resulting in

$$I_{\text{freq}}(q, q', \mathbf{r}, \mathbf{r}') = 2(2\pi)^2 T[\omega_q(\mathbf{r}), \omega_{q'}(\mathbf{r}), \omega_q(\mathbf{r}'), \omega_{q'}(\mathbf{r}')], \quad (8.46)$$

$$T(w, x, y, z) = \frac{1}{2} \left[ \frac{1}{w+x} + \frac{1}{y+z} \right] \left[ \frac{1}{(x+z)(w+y)} + \frac{1}{(x+y)(w+z)} \right]. \quad (8.47)$$

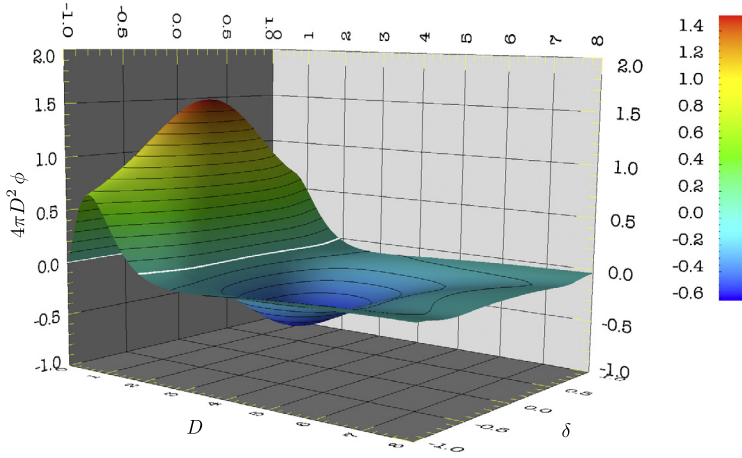


FIGURE 8.2 The kernel  $\phi$ , plotted as a function of  $D = (d + d')/2$  and  $\delta = (d - d')/(d + d')$ , where  $0 \leq D < \infty$  and  $0 \leq |\delta| < 1$ . Isolines are separated by kernel values of 0.1 and the  $\phi = 0$  isosurface is plotted in white.

The angular integration can also be evaluated and the kernel takes the form of a double integral

$$\phi(\mathbf{r}, \mathbf{r}') = \frac{2}{\pi^2} \int_0^\infty da a^2 \int_0^\infty db b^2 W(a, b) T[v(a), v(b), v'(a), v'(b)], \quad (8.48)$$

where  $v(a) = a^2/[2h(a/d)]$ ,  $v'(a) = a^2/[2h(a/d')]$ , and  $W(a, b)$  is a simple algebraic function [20]

$$W(a, b) = \frac{2}{a^3 b^3} \left[ (3 - a^2)b \cos b \sin a + (3 - b^2)a \cos a \sin b + (a^2 + b^2 - 3) \sin a \sin b - 3ab \cos a \cos b \right]. \quad (8.49)$$

The form in Eq. (8.48) lends itself to a numerical evaluation and can be tabulated once and for all. The kernel  $\phi$  is plotted in Fig. 8.2.

The real-space kernel evaluation, as described above, was used extensively in the early vdW-DF studies [20,64–66]. It is naturally suitable to the study of nonperiodic systems, but it has also been applied to periodic structures [48,67–70]. In computational schemes, it can then be useful to separate the evaluation into interactions arising from intra- or inter-unit cell contribution [71]. However, with its six spatial integrations, numerically evaluating Eq. (8.40) is quite costly. A great speedup was achieved by writing  $E_c^{\text{nl}}[\rho]$  as a set of convolutions [72], which was made possible by using a numerical interpolation technique to approximate the kernel as

$$\begin{aligned} \phi(\mathbf{r}, \mathbf{r}') &= \phi(q_0(\mathbf{r}), q_0(\mathbf{r}'), |\mathbf{r} - \mathbf{r}'|) \\ &\approx \sum_{\alpha\beta} \phi(q_\alpha, q_\beta, |\mathbf{r} - \mathbf{r}'|) p_\alpha(q_0(\mathbf{r})) p_\beta(q_0(\mathbf{r}')). \end{aligned} \quad (8.50)$$

Here,  $q_\alpha$  are a set of fixed  $q_0$  values and  $p_\alpha$  are cubic splines. Eq. (8.40) can then be expressed as

$$\begin{aligned} E_c^{\text{nl}}[\rho] &= \frac{1}{2} \sum_{\alpha\beta} \int d^3r d^3r' \theta_\alpha(\mathbf{r}) \phi_{\alpha\beta}(|\mathbf{r} - \mathbf{r}'|) \theta_\beta(\mathbf{r}') \\ &= \frac{1}{2} \sum_{\alpha\beta} \int d^3k \theta_\alpha^*(\mathbf{k}) \phi_{\alpha\beta}(k) \theta_\beta(\mathbf{k}), \end{aligned} \quad (8.51)$$

where  $\theta_\alpha(\mathbf{r}) = \rho(\mathbf{r}) p_\alpha(q_0(\mathbf{r}))$  and  $\theta_\alpha(\mathbf{k})$  is its Fourier transform. In the same sense,  $\phi_{\alpha\beta}(k)$  is the Fourier transform of  $\phi_{\alpha\beta}(r) \equiv \phi(q_\alpha, q_\beta, |\mathbf{r} - \mathbf{r}'|)$ . The original six-dimensional integral for  $E_c^{\text{nl}}[\rho]$  has now been replaced by Eq. (8.51), i.e., a three-dimensional integral over Fourier transformed quantities, which in plane-wave DFT codes benefits from highly optimized and readily available fast-Fourier transforms. This replacement has accelerated (fully self-consistent) vdW-DF calculations in plane-wave codes to the extent that for large systems there is only an insignificant difference in computational cost relative to GGA.

Finally, it is important to note that  $E_c^{\text{nl}}[\rho]$  is able to capture many different physical effects, more than one would expect from its seemingly simple form. Examples include the image-plane effects that can significantly affect the vdW-type bonding of molecules on surfaces. These effects arise because the low-density regions outside surfaces and molecules are more polarizable than the high-density regions. The image-plane effects are specific examples of multipole effects in dispersive interactions [46] and they are important for both adsorption and intermolecular interactions [48,73]. They are screening effects on vdW forces and they are accurately captured because vdW-DF tracks energy effects from couplings among XC holes, themselves nonlocal objects that reflect screening effects [22,36].

### 8.4.3 Further Developments: Self-Consistency and Spin

The XC potential  $V_{\text{xc}}(\mathbf{r})$  from Eq. (8.3) represents the central input to the KS scheme. Since  $E_{\text{xc}}$  within vdW-DF is nonlocal, evaluating it is more complicated than for GGA-type functionals and the proper XC potential was not developed until 2007 [59]. A fully self-consistent solution to the KS equations is important because of accuracy and because it makes it possible to calculate atomic forces and the stress tensor via the Hellmann–Feynman theorem [59,74,75], essential for structural relaxations. Moreover, the fully self-consistent solution also allows for studying the nature of the van der Waals binding itself, as described in ground-state DFT. In DFT studies one generally uses the Born–Oppenheimer approximation, treating the nuclei as classical objects. As such, the nuclei can exclusively react to electrostatic forces, defined by changes visible in the electron density distribution. As vdW-DF provides a successful inclusion of vdW forces in ground-state DFT, it is clear that this capacity must be reflected in an electrostatic signature, i.e., the changes in the electron density distribution.

Fig. 8.3 shows this electrostatic signature of the van der Waals bond of an Ar noble-gas dimer, obtained from the first fully self-consistent vdW-DF calculations as described in Ref. [59]. Even if the charge density rearrangement due to vdW interactions in the Ar dimer is small—as it is in many vdW bounded systems—it is entirely responsible for the binding by pulling charge in-between the two nuclei. Thus, such a study of the electrostatic signature

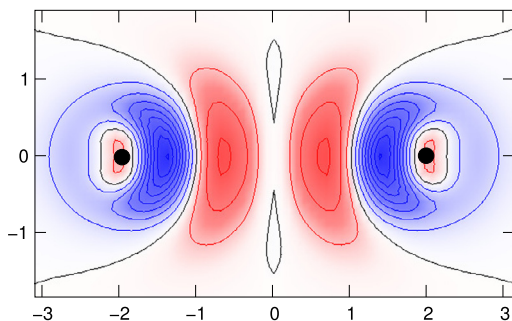


**FIGURE 8.3** Bonding charge (i.e., difference in induced electron density) of the Ar dimer. The black disks mark the position of the nuclei; the scale is in Å. The zero isoline is shown as black contour; increments between isolines are  $5 \times 10^{-5}$  electrons/Å<sup>3</sup>. Red/blue (light/dark gray) areas represent regions that gain/lose electron density when the nonlocal part is included. Reprinted with permission from Ref. [59], <http://dx.doi.org/10.1103/PhysRevB.76.125112>. Copyright 2007 American Physical Society.

provides insight, based on quantitative results, into the nature of the vdW bond as described in ground-state DFT [59].

A more recent development concerns the proper inclusion of spin in vdW-DF. The nonlocal exchange-correlation functional  $E_c^{\text{nl}}[\rho]$  in Eq. (8.40) is not spin dependent, i.e., it is expressed purely in terms of the total electron charge density  $\rho(\mathbf{r})$  [20,23]. It is problematic to use the original  $E_c^{\text{nl}}[\rho]$  version to describe systems where spin polarization plays a significant role. Still, the fact that vdW-DF lacked a spin polarized generalization for over a decade caused the development of various pragmatic approximations to treat spin, such as ignoring the effect of spin on the nonlocal correlation or estimating the effect using the semilocal correlation of PBE [76–78]. Some DFT codes (like VASP) permit an approximate approach to include spin by computing  $E_c^{\text{nl}}$  with the total electron density and not the spin-polarized electron densities, which ignores the effect of spin polarization on the plasmon dispersion.

A fully consistent vdW-DF extension, called svdW-DF, for spin-polarized systems was derived in 2015 [52]. This extension notes that the vdW-DF design philosophy completely specifies spin effects on the internal functional and hence on the  $E_c^{\text{nl}}[\rho]$  term. Using  $\rho_\uparrow$  and  $\rho_\downarrow$  to denote the up- and down-spin densities, the proper spin extension is dictated by the exact spin scaling of exchange [49], i.e.,  $E_x[\rho_\uparrow, \rho_\downarrow] = E_x[2\rho_\uparrow]/2 + E_x[2\rho_\downarrow]/2$ , and the well-established spin-dependence of the local correlation [79]. The spin-scaling of exchange results in a spin-dependent response  $S_{xc}$ , Eqs. (8.35) and (8.36), in which spin enters exclusively in the denominator through  $\omega_q(\mathbf{r})$  in Eq. (8.36). The numerator in that equation describes instead just a classical plasmon and thus depends only on the total electron density  $\rho$ . The spin extension of vdW-DF can therefore use the same universal kernel  $\phi$  from Eq. (8.48). The only thing that changes is the form of the effective response parameter  $q_0$  in Eq. (8.38), which now becomes  $q_0[\rho] \rightarrow \tilde{q}_0[\rho_\uparrow, \rho_\downarrow]$  to reflect the explicit spin dependence of the plasmon dispersion [52].

### 8.4.4 Related Approaches: Vydrov–Van Voorhis Functionals

The vdW-DF framework has also been exploited for alternative formulations by Vydrov and Van Voorhis. They first designed a functional called vdW-DF-09 [80] that also introduced an optimization of the nonlocal correlation part by evaluating the results for a set of reference systems. That functional is not as closely connected to GGA as the vdW-DFs, but it does retain all the essential constraints of vdW-DF.

Soon thereafter, Vydrov and Van Voorhis developed offsprings from vdW-DF called VV09 [81] and VV10 [82], and the VV family of functionals inherits many of the features of vdW-DF. Although these functionals adhere to fewer exact constraints [83], they include additional arguments concerning the description of screening. They improve the description of long-range interactions between small molecules by using optimization to reference systems in order to parameterize one (two) fixed parameters in VV09 (VV10). VV09 has a construction that is more closely related to vdW-DF, whereas VV10 strongly emphasizes simplicity in its design. The latter is the version presently recommended by the VV authors.

Central in the design of both VV09 and VV10 is the introduction of a spatially varying gap  $\omega_g(\mathbf{r})$ , given by [81,84]

$$\omega_g^2(\mathbf{r}) = C \left| \frac{\nabla \rho}{\rho(\mathbf{r})} \right|^4. \quad (8.52)$$

The parameter  $C$  is fitted to optimize the  $C_6$  coefficients that describe the long-range interaction between molecules in VV09 or VV10.

VV09 builds upon a plasmon propagator  $S$  defined from its Fourier components as

$$\tilde{S}_{\mathbf{q},\mathbf{q}'}(iu) = \int d^3r e^{-i\mathbf{r}\cdot(\mathbf{q}-\mathbf{q}')} \frac{\omega_p^2(\mathbf{r})}{\omega_0(\mathbf{r})^2 + u^2} F_{\mathbf{q},\mathbf{q}'}(\mathbf{r}), \quad (8.53)$$

in analogy with the vdW-DF use of  $S \approx S_{xc} = \ln(\epsilon)$ . In Eq. (8.53) the plasmon poles are given by

$$\omega_0^2(\mathbf{r}) = \omega_g^2(\mathbf{r}) + \omega_p^2(\mathbf{r})/3, \quad (8.54)$$

where  $\omega_p(\mathbf{r}) = \sqrt{4\pi\rho(\mathbf{r})}$  is the classical plasma frequency. The factor of 1/3 is motivated by the Clausius–Mossotti relation and it is a strong trait of VV09 and VV10 that they use the appropriate screening relation for jellium spheres [81].

VV09 differs from vdW-DF in that its description of plasmon poles in Eq. (8.54) is independent of the wavevector. Using  $k_F$  and the spin-scaling factor

$$\xi = \frac{1}{2} \left[ (1 + \zeta)^{2/3} + (1 - \zeta)^{2/3} \right], \quad (8.55)$$

where  $\zeta = (\rho_\uparrow - \rho_\downarrow)/\rho$  is the relative spin polarization, VV09 uses instead a damping factor  $F_{\mathbf{q},\mathbf{q}'} = \exp[-(q^2 + q'^2)/(k_{TF}^2 \xi^2)]$  to reduce the weight of dispersive states in the low-density regions [81]. This choice causes VV09 to break charge conservation, whereas this constraint is emphasized in vdW-DF [20,83].

The VV10 construction gives up the vdW-DF and VV09 idea of seeking to approximate the evaluation of the ACF and focuses instead directly on improving the content in the universal



kernel  $\phi$  in Eq. (8.40). The existence of the VV10 kernel is motivated by the vdW-DFs and VV09 developments, but it is given simply by the ansatz

$$\phi^{\text{VV10}}(\mathbf{r}, \mathbf{r}', R = |\mathbf{r} - \mathbf{r}'|) = -\frac{3}{2gg'(g + g')}. \quad (8.56)$$

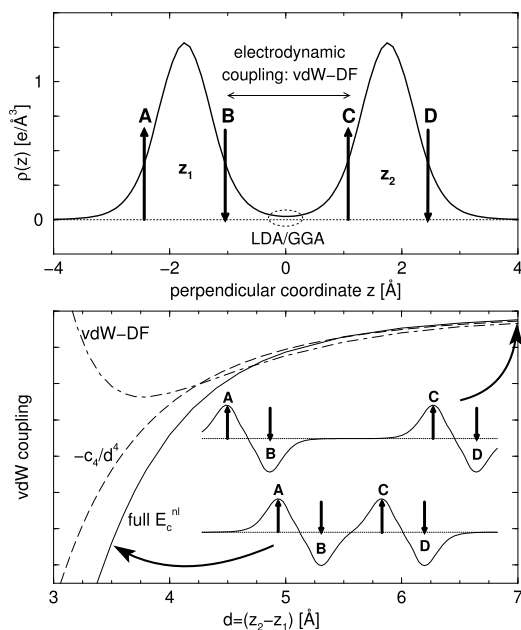
Here,  $R = |\mathbf{r} - \mathbf{r}'|$  is the separation and a damping function  $\kappa$  enters in the specification of two characteristic plasmon frequencies  $g = \omega_0(\mathbf{r})R^2 + \kappa(\mathbf{r})$  and  $g' = \omega_0(\mathbf{r}')R^2 + \kappa(\mathbf{r}')$ . The damping exists to limit the nonlocal correlation-energy contributions at shorter separations and  $\kappa$  depends on a scaling parameter  $b$ , which is fixed for a given semilocal partner by optimizing binding energies to the S22 benchmark [85]. Introducing a small modification to the VV10 kernel [86], it is possible to also accelerate the evaluation of the nonlocal correlation energy in VV10 using fast-Fourier transforms [72], similar to those introduced for vdW-DF in Section 8.4.2. By design, the VV10 kernel has the same asymptotic form as that of VV09.

## 8.5 IMPORTANCE OF BEING ELECTRON FOCUSED

A unique characteristic of the vdW-DF method is that it is derived from the ACF in Eq. (8.8), having a screening—and therefore XC-energy—description that is directly linked to the response behavior of the electron gas. In fact, one can think of vdW-DF as a generalization of RPA [22], a description discussed in Chapter 3. In particular, this electron-gas foundation ensures that the vdW-DF method has seamless integration [20,22,23,46,47]. The same logic that determines the lowest-order component  $E_{\text{xc}}^0[\rho]$  is also used to formulate the truly nonlocal correlation part  $E_{\text{c}}^{\text{nl}}[\rho]$ , see Eq. (8.31). Accordingly, there is no need for fitting a damping function to avoid double counting of the semilocal and truly nonlocal vdW correlations—in contrast to vdW-DF alternatives, where instead an atom-centered response description of the vdW binding is added to a semilocal XC choice. The electron focus also gives the vdW-DF method some practical advantages, for example, that the method includes a proper framework to handle and capture image-plane effects and multipolar-response components in the description of physisorption and van der Waals interactions [45,73]. Image-plane effects have long been known to play a crucial role in the case of molecular physisorption on metals [27,28], and the ability of vdW-DF to accurately describe the physisorption of hydrogen molecules has been documented [45,73]. Physisorption is also discussed in Chapter 13.

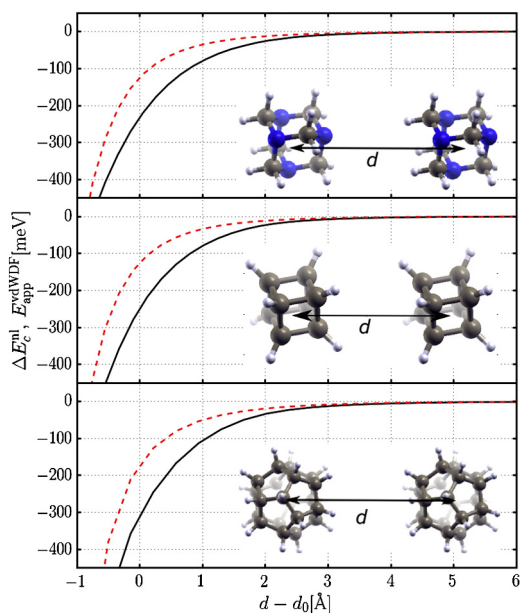
The vdW-inclusive DFT formulations are often used to compute the interactions between molecular, one-dimensional, or layered fragments and it is clear that each fragment itself must have an electron-distribution surface, and in particular, an electron-tail region that dominates the electrodynamic-response description [87]. Such electrodynamic responses are central in the Rapcewicz–Ashcroft picture [36] of dispersive interactions and it is important that vdW-inclusive DFT accounts provide an accurate description of the associated multipole interactions effects. Being electron-based, the vdW-DF method has the correct ingredients to capture such image-type effects, even when they emerge in molecular-type interactions [46, 48,70].

Fig. 8.4 highlights the electrodynamic nature of the nonlocal correlation (or van der Waals) binding between two parallel graphene sheets. Here the numbers are obtained from



**FIGURE 8.4** Electrodynamic nature (top panel) and multipole enhancement consequences (bottom panel): vdW binding between two graphene sheets [46]. The top panel shows the computed electron-density variation (in the direction perpendicular to the graphene sheets) and emphasizes that the intersheet attraction arises from the mutual electrodynamic coupling, not from the electron overlap that would describe binding in the LDA/GGA. The panel further illustrates how a spontaneous polarization in one sheet with electron enhancement (depletion) at upward (downward) arrow A (B) induces density changes (represented by C and D arrows) in the second sheet. The arrows are placed at the positions of the largest density response to external fields and they are not at the positions  $z_1$  and  $z_2$  of the carbon atoms. The bottom panel shows results for the intersheet binding energies as a function of sheet separation  $d = |z_2 - z_1|$ . The panel shows the results of a full vdW-DF calculation (dashed-dotted curve) and the contribution arising from just the  $E_c^{nl}[\rho]$  term (solid curve). The panel documents clear multipole enhancements in the  $E_c^{nl}[\rho]$  relative to an asymptotic determination (dashed curve). Finally, the insert interprets this enhancement in terms of image-plane effects: As the graphene sheets are pulled to binding separations, the distance between response-region C (on the second sheet) and response-region B (on the first sheet) becomes comparable to the A–B and C–D separations, and a simple binding description in terms of a dipole–dipole coupling is no longer sufficient. Reprinted with permission from Ref. [46], <http://dx.doi.org/10.1103/PhysRevLett.91.126402>. Copyright 2003 American Physical Society.

the early layered-geometry vdW-DF formulation [46], but the discussion is generic to the vdW-DF method and applies also to the general-geometry vdW-DF versions that are now in mainstream usage. The top panel of Fig. 8.4 shows the spatial variation of the density distribution (averaged over the in-sheet directions) at binding separations and identifies qualitative differences in the LDA/GGA and vdW-DF descriptions. As indicated by the dotted oval, the traditional local and semilocal XC functionals seek to capture a would-be binding from the density overlap, a strategy which is doomed to fail in the case of GGA [46], and which can easily be shown to lack robustness and transferability in the case of LDA [61]. On the other hand, the vdW-DF method emphasizes a description of the electrodynamic coupling be-



**FIGURE 8.5** Multipole enhancement effects in the nonlocal correlation or van der Waals binding for a set of simple organic crystals: hexamine (top panel), cubane (middle panel), and dodecahedrane (bottom panel) [70]. The relevant crystal geometries in these simple cases can be fully parameterized in terms of an intermolecular separation  $d$ , and the figure shows the variation in the  $E_c^{\text{nl}}[\rho]$  contributions to the binding relative to vdW-DF result for the binding separation (denoted  $d_0$ ). As in Fig. 8.4, the solid curves show the results of a full vdW-DF calculation whereas the dashed curves show the results obtained with an approximation, here denoted  $E_{\text{app}}^{\text{vdW-DF}}$ , that reflects the logic of treating the vdW interactions in atom-centered descriptions. Specifically, that approximation consists of expressing the vdW-DF electron (plasmon-pole) description of response as if it arose entirely as an effective average per-atom susceptibility that is also centered on the atom [46,48]. Reprinted from Ref. [70], <http://dx.doi.org/10.1063/1.3366652>, with the permission of AIP Publishing.

tween the external-field response behavior of the individual sheets. As indicated by upward and downward arrows, an external field (representing the temporal fluctuations relevant for the vdW binding mechanism) will induce both local electron accumulations and local electron deficiencies; these have a mutual coupling that produces a nonlocal correlation binding in the Ashcroft–Rapcewicz picture on which vdW-DF builds [22,23,36].

The bottom panel of Fig. 8.4 documents and explains that the multipole effects have significant consequences on the strength of intersheet cohesion at binding separations [46]. The panel shows the variation (with binding separation  $d$ ) in the binding energy (dashed–dotted curve) obtained with this layered-geometry vdW-DF implementation and in part defined by the corresponding evaluation of the  $E_c^{\text{nl}}[\rho]$  functional component. The  $E_c^{\text{nl}}[\rho]$  binding component is evaluated both in a full calculation (solid curve) and using an asymptotically-valid approximation given by  $-C_4/d^4$  (dashed curved). The asymptotic behavior can readily be derived by assuming an atom-centered dipole description given by the vdW-DF method [20,48,70]. However, the full density variation relevant to a temporal density fluctuation (that under-

pins dispersion forces) will have a distributed charge relocation; this is indicated in the insert by pairs of up/down arrows. The spatial distribution of the per-fragment electrodynamic response plays an increasing role as the interacting fragments approach the separations relevant for materials binding. While an atom-centered vdW-DF approximation [20,48,70] yields the asymptotic  $d^{-4}$  interaction variation for sheets, it is also clear that the details of the screening, including multipole effects, can enhance the nonlocal correlation interactions at smaller separations [20,48,70]. The bottom panel of Fig. 8.4 demonstrates that the resulting enhancements are significant in the binding of two graphene sheets [46].

Fig. 8.5 shows that the vdW-DF description also produces a corresponding multipole enhancement of the  $E_c^{\text{nl}}[\rho]$  interaction for molecules; in this case, a set of platonic or platonic-like organic crystals investigated with vdW-DF [70]. The same enhancement is also found for the binding between parallel carbon nanotubes (CNTs) as described in vdW-DF [48]. For CNT dimers the discussion can be taken further with access to analytic results for the interaction, subject to the assumption that the per-CNT electrodynamic response originates from a cylindrical shell [41–43]. This made it possible to directly interpret the multipole enhancement for CNT dimers as an effective image-plane effect. As expected, this vdW-DF study also confirmed that it is the electron tails that define the per-CNT response and hence the total CNT binding [48].

## 8.6 OVERVIEW OF NONLOCAL FUNCTIONAL RELEASES AND VARIANTS

Many nonlocal correlation functionals now exist that are either direct offsprings of—or strongly inspired by—the original vdW-DF introduced in 2004. In general, new developments have been driven by the desire to reach chemical accuracy or to simplify the functional form in order to reduce computational demands. In the vdW-DF framework the XC energy is split into a semilocal contribution  $E_{xc}^0[\rho]$  and the nonlocal contribution  $E_c^{\text{nl}}[\rho]$ , as can be seen in Eq. (8.31). Although the framework provides an exact expression for the semilocal exchange-correlation energy in Eq. (8.33), it cannot be expected from the simple plasmon-pole model—which was introduced to give a good description for the nonlocal part—to also give a good description for the semilocal part. In practical implementations the semilocal part thus has to be approximated. The vdW-DF method therefore provides a natural framework for sequential improvements spanning two main categories: (i) modification of the expression for  $E_c^{\text{nl}}[\rho]$  or (ii) the creation or optimization of semilocal functionals that approximate the internal functional, with a special focus on semilocal exchange. It is interesting to note that, when new expressions for the nonlocal correlation term were developed, the form of the semilocal exchange needed adjustment—implying the need for consistency between the exchange functional and the nonlocal correlation form. The performance of the variants discussed in this section (benchmarked on the S22 [85,88] set of noncovalently bonded molecular dimers interacting through hydrogen-bonding, dispersion forces, and a mixture thereof) is compiled in Table 8.1.

Given the number of possible combinations of exchange and nonlocal correlation functionals that go into making a particular vdW-DF variant, it is necessary to outline a naming

**TABLE 8.1** Performance of the vdW-DF variants discussed throughout Section 8.6. Mean absolute deviation (MAD) and mean absolute relative deviation (MARD) are given where appropriate. For the binding energies of the S22 set [85,88], the performance is divided into systems where the binding is dominated by hydrogen bonds (hyd.), dispersion interactions (disp.), and a mixture thereof (mix.). For the bulk lattice constants, the benchmark studies do not use the same data sets or the same codes, so estimates of the MAD are provided. For weak chemisorption, “good” simply means that it typically can get the right binding nature, where as “unreliable” means that there are clear examples of failures in the literature

Functional	Fitted	S22 (MAD kcal/mol) (hyd., disp., mix., tot.)	Layer sep. <sup>c</sup> (MAD Å)	Layer energy (MARD <sup>c</sup> %)	Bulk lattice (MAD estimate)	Weak chemisorp.	Asymptote <sup>g</sup> C <sub>6</sub> (MARD %)
vdW-DF1	N	2.12, 0.32, 0.46, 0.92 <sup>a</sup>	0.47	21	too large $\sim 0.1$ Å <sup>a</sup>	unreliable <sup>a,f</sup>	18.5
vdW-DF2	N	1.20, 0.25, 0.46, 0.62 <sup>a</sup>	0.40	15	too large 0.1–0.2 Å <sup>a,c</sup>	unreliable <sup>a,f</sup>	60.9
vdW-DF1-C09	N	0.51, 0.60, 0.09, 0.42 <sup>a</sup>	0.1	46	$< 0.05$ Å <sup>a</sup>	good <sup>a</sup>	18.5
vdW-DF1-cx	N	0.46, 0.18, 0.18, 0.30 <sup>a</sup>	0.06	22	0.05–0.1 Å <sup>a</sup>	good <sup>a</sup>	18.5
vdW-DF1-B88	Y	0.30, 0.23, 0.16, 0.23 <sup>b</sup>	0.14	22	0.05–0.1 Å <sup>c</sup>	good <sup>a</sup>	18.5
vdW-DF1-optB86b	N	0.30, 0.37, 0.14, 0.28 <sup>c</sup>	0.07	27	$< 0.05$ Å <sup>c</sup>	good <sup>d</sup>	18.5
vdW-DF2-B86R	N	0.44, 0.37, 0.46, 0.42 <sup>d</sup>	0.07	16	$< 0.05$ Å <sup>d</sup>	good <sup>d</sup>	60.9
VV10	Y	0.69, 0.09, 0.16, 0.30 <sup>e</sup>	0.12	52 <sup>c</sup>	0.05–0.1 Å <sup>e,c</sup>	unknown	10.7

<sup>a</sup> Refs. [51,75].

<sup>b</sup> Ref. [91].

<sup>c</sup> Refs. [92–94].

<sup>d</sup> Ref. [95].

<sup>e</sup> Ref. [82].

<sup>f</sup> Refs. [96–98].

<sup>g</sup> Ref. [99].

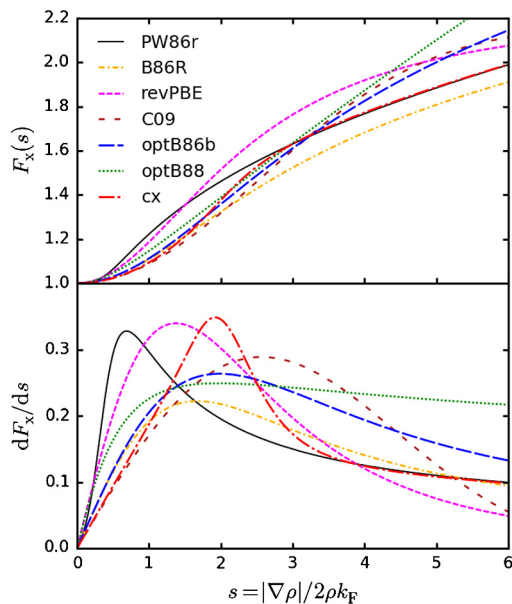


FIGURE 8.6 (Top) Exchange enhancement factors  $F_x(s)$  for a variety of exchange functionals used in conjunction with vdW-DF1 [51,89,91,92,100] and vdW-DF2 [90,95]. (Bottom) Derivative of the exchange enhancement factor, i.e.,  $dF_x/ds$ , indicating how repulsive a given exchange functional is for different values of  $s$ .

convention. As such, the following is suggested: vdW-DF $n$ - $E_x$ , where  $n$  indicates the version of the nonlocal correlation functional and  $E_x$  names the specific exchange functional used. For historical purposes, the original nonlocal correlation functional of Dion et al. [20] (nominally vdW-DF1-revPBE [20,89]) is simply referred to as vdW-DF1 and the nonlocal correlation functional of Lee et al. [53] (nominally vdW-DF2-PW86r [53,90]) is denoted vdW-DF2.

For a semilocal exchange functional of the GGA type the exchange energy  $E_x[\rho(\mathbf{r})]$  can be written as a function of the enhancement factor  $F_x(s)$ , where  $s$  is the reduced gradient introduced below Eq. (8.37),

$$E_x[\rho(\mathbf{r})] = \int d^3r \rho(\mathbf{r}) F_x(s). \quad (8.57)$$

Fig. 8.6 shows the functional form and corresponding derivative of several  $F_x(s)$  used in conjunction with the vdW-DF nonlocal correlation functionals. The implications of their differences will be discussed below. However, it is worth noting that many of the more successful variants have very similar forms of  $F_x(s)$ .

### 8.6.1 vdW-DF1

When the original vdW-DF1 was released in 2004 [20], it was a major breakthrough. Differing from atomistic correction schemes that were undergoing development at the time [101],

it was a proper density functional derived from physical laws and MBT, as described in Section 8.4. Unlike its predecessor [46], which was specifically developed for layered geometries, vdW-DF1 has no such restriction and can be applied to general geometries. Initial results demonstrated good agreement between calculated binding energies and experimental data as well as higher-accuracy methods applied to aromatic molecules and the adsorption of these molecules on surfaces.

In assessing the success and utility of vdW-DF1, as compared to more recent variants, it is important to keep in mind that it was never intended to describe anything but van der Waals bonded systems. At the time it was constructed, there were also still some misconceptions as to whether LDA or GGA could capture some vdW interactions—whereas now it is evident that they can not. Nevertheless, to demonstrate that the vdW forces in vdW-DF1 originate purely from the nonlocal correlation term  $E_c^{\text{nl}}[\rho(\mathbf{r})]$ , it was paired with the repulsive revPBE [89] exchange functional, which seemingly did not exhibit any of the spurious binding effects typically observed in other exchange functionals, such as LDA in particular [90]. The repulsive nature of revPBE is reflected in the large value of  $dF_x/ds$  for a wide range of  $s$  values in Fig. 8.6.

However, this choice led to one of its most crucial weaknesses. Early on it was noted that vdW-DF1 had a tendency to overestimate binding separations between fragments of van der Waals bonded systems [59], such as interlayer separations of layered materials like graphite [76]. For purely van der Waals bonded systems, this overestimation is typically around 0.2–0.3 Å. For systems characterized by competing interactions [75], in particular those with so-called incipient covalency or weak chemisorption, this overestimation can be more severe. Some of these systems have very shallow binding energy curves, while others are characterized by competing minima where a small change in the functional description can tip the balance in favor of pure physisorption, resulting in underestimated binding energies as well [96]. In addition, a careful analysis of binding energies showed an overestimation of the binding energies of small nonpolar molecules, while underestimating hydrogen bond strengths [53]. Bulk lattice constants of coinage metals and some other solids are overestimated as well [51,92].

Despite its shortcomings, vdW-DF1 has had its share of successes, yielding many accurate predictions for a variety of systems [23]. vdW-DF1 also turns out to be one of the most accurate functionals for dense hydrogen and helium, which is relevant for the simulation of gas giants [102,103]. The functional can also produce molecular atomization energies comparable to PBE, when combined with a proper spin treatment [52]. However, vdW-DF1 is not recommended as the primary tool for modeling general material systems, as later refinements have addressed many of its shortcomings [23].

### 8.6.2 vdW-DF2

vdW-DF2 [53] was developed as a successor of vdW-DF1 with an emphasis on improving the performance in molecular systems. Like the original vdW-DF1, it relies on nonempirical criteria, but with conditions chosen to better represent the properties of molecular systems. Initial concerns regarding the overly repulsive nature of the revPBE exchange functional in vdW-DF1, thought to be the origin of the overestimation of separation distances, inspired the redesign and development of a number of new exchange functionals.

An analysis of the Hartree–Fock exchange from quantum-chemical calculations for many molecular [90] and rare-gas [104] dimers at different separations suggested that the enhancement factor  $F_x(s)$  should be proportional to  $s^{5/2}$  at large  $s$ . This factor also arises in the numerical GGA construction [49,105] and, with an enhancement factor that increases with  $s$ , one also avoids spurious binding effects on formal grounds. Murray et al. demonstrated that the Hartree–Fock exchange interaction energy could be sufficiently reproduced for a test set of molecular dimers through a refitted PW86 exchange functional [49], referred to as PW86r [90]. For binding between molecules, which are characterized by  $s$  values ranging from 1 to 3, PW86r is generally less repulsive than revPBE, as can be seen in the smaller derivatives in the lower panel of Fig. 8.6. Ultimately, this choice results in a significant reduction in the overestimation of binding separations of molecular dimers.

To account for the large change in the enhancement factor  $F_x(s)$  of PW86r compared to revPBE, Lee et al. modified vdW-DF1 to create a new nonlocal correlation functional, i.e., vdW-DF2. They noted that, to achieve better consistency between the PW86r exchange and the nonlocal part, it was necessary to scale the gradient correction to the screened exchange term,  $Z_{ab}$  in Eq. (8.38), from  $-0.8491$  in vdW-DF1 to  $-1.887$  in vdW-DF2. Although the nonlocal correlation energy in vdW-DF2 has a very similar form compared to vdW-DF1, the coupling between different density regions (i.e., between  $\rho(\mathbf{r})$  and  $\rho(\mathbf{r}')$ ) is far more aggressive and therefore provides a more appropriate parametrization for molecules than the slowly-varying electron-gas limit used in vdW-DF1. However, this choice results in significantly underestimated  $C_6$  values for all but helium [99]. One might think that this would worsen the potential energy curves in the vdW-dominated region beyond binding separations—since in this region the curves are dominated by nonlocal correlation contributions—yet, the opposite occurs for the S22 set [85,88]. This is due to the fact that a typical asymptotic form is not reached until about 4–5 Å beyond the binding separations and at shorter separations the multiple effects and image-plane built into vdW-DF still contribute significantly to the binding curves [71].

While vdW-DF2 generally reduces the overestimation of vdW-DF1 and improves the performance for small molecules and hydrogen-bonded systems, it still struggles with systems exhibiting incipient covalency and bulk lattice constants are overestimated even more than in vdW-DF1. Both these issues can be related to the fact that for  $s$  values between 0.1 and 1.0 the  $dF_x(s)/ds$  values of PW86r are even larger than those of revPBE [51]. This is reflected by the fact that vdW-DF2 overestimates covalent bond-lengths of solids somewhat more than vdW-DF1. Furthermore, in layered systems—which are characterized by somewhat smaller  $s$  values than molecular dimers—vdW-DF2 also overestimates separations. As most of the issues of vdW-DF1 and vdW-DF2 are linked to the exchange functional, emphasis was shifted to further refining this part of the exchange-correlation functional.

### 8.6.3 Exchange Functionals

Since vdW-DF1 provides reasonable binding energies while binding separations are typically too large, a key challenge was to fix the former without ruining the latter. In this regard, major efforts focused on optimizing the form of the semilocal exchange while leaving the nonlocal correlation term as it is. Initial efforts found that simply replacing for instance



revPBE [89] with PBE [50], could reduce separations but typically increased binding energies. As such, the need to develop and/or optimize new functionals became a vibrant line of research that can be divided into two groups: (i) reference system optimization and (ii) first-principles development. The first kind adjusts the enchantment factors to obtain good performance for particular reference sets, whereas the latter attempts to rely solely on derived conditions or results in special limits to construct the functionals. The previously discussed PW86r falls into the latter category, as it was designed based on the first-principles construction of a numerical hole model. However, the distinction between the two categories is in practice not always clear. A poorly performing derived functional is less likely to be published and while some functionals are derived explicitly others are designed only to observe certain limits.

Using reference-system optimization, Klimeš et al. [91,92] designed several exchange functionals. For example, the functionals optPBE and optB88 were found by adjusting the parameters of PBE and B88 until the interaction energies of fixed (unrelaxed) dimer pairs were optimized for the S22 dataset. Strikingly, this optimization did not only improve performance for molecular dimers, of which the reference set consisted, but the functionals also exhibited good performance for a wide range of systems, including solids, layered systems, and adsorption systems. vdW-DF1-optPBE often gives good energies for vdW-bonded systems, but their separations can be somewhat too large. After much benchmarking, it has also become evident that vdW-DF1-optB88 is a good all-round variant, working well for many different systems, as can be seen in Table 8.1. Klimeš et al. also designed a third exchange functional called optB86b by simply setting the low- $s$  limit of B86b to that of the gradient expansion  $\mu_{\text{GEA}}$  used in PBEsol; the second parameter  $\kappa$  was set to 1 to make the functional minimalistic and well suited for solids. vdW-DF1-optB86b seems to exhibit very good performance not only for covalent solids but also for a wide range of sparsely packed molecular systems.

Alternatively to the reference-system optimization, new functionals can also be constructed based on first-principles observations. A key step in this direction was the construction of a new exchange functional for vdW-DF1 called C09 [100]. This exchange functional has a small  $s$  form similar to the gradient-expansion result for the homogeneous electron gas. But, at larger  $s$  values, it goes over to a revPBE form, as shown in Fig. 8.6. The former choice was motivated by the fact that it improves lattice constants of solids [106] compared to, e.g., PBE, whereas by going over to the revPBE exchange at large  $s$  values one could retain the good energies of vdW-DF1 for van der Waals bonded systems. The new functional combination improved upon vdW-DF1 for many different systems. After several tests, it was found that vdW-DF1-C09 sometimes over-corrected vdW-DF1, producing slightly too short binding separations and too large binding energies. Furthermore, the analysis of Murray et al. [90] indicated that revPBE was not—from a theoretical point of view—the best functional for larger  $s$  values, as it has traces of spurious binding mechanisms of the same kind exhibited strongly by LDA and weakly by PBE [90].

The question whether the plasmon-pole model of vdW-DF1 is sufficiently robust to describe the entire exchange-correlation energy motivated Berland and Hyldgaard to design a new functional, termed vdW-DF1-cx [51]. This development aimed at improving the consistency between the semilocal exchange and the vdW-DF1 internal functional in Eq. (8.31), similar to the efforts used to develop vdW-DF2. The form of this consistent exchange, cx, allows vdW-DF1-cx to avoid a hidden correction, namely a cross-over term [51]  $\delta E_{\text{xc}}$ , representing

the difference between the functional  $E_{xc}^0$  and the internal functional used to determine the nonlocal correlation term in vdW-DF1. Specifically, in vdW-DF1-cx there are no contributions to the cross-over term  $\delta E_{xc}$  from density regions with  $s$ -values up to approximately 2 (for  $s$  larger than 2, the exchange part of vdW-DF1-cx takes the form of the exchange functional used in vdW-DF2). A concern driving the development of vdW-DF1-cx was that at smaller  $s$  the term  $\delta E_{xc}$  does not necessarily retain all the constraints of the vdW-DF framework. vdW-DF1-cx [51] accounts for this correction and contains a nonempirical exchange functional that is consistent with the ACF for small to medium  $s$ , and at the same time achieves an accuracy similar to vdW-DF1-optB86b and vdW-DF1-optB88. As seen in the lower panel of Fig. 8.6, this new exchange functional generally has somewhat larger  $dF_x(s)/ds$  values up to  $s \approx 3$ , indicating that it is a little more repulsive than C09, but at the same time far more attractive than revPBE.

Finally, it is interesting to note that most functional releases have been based on finding a suitable exchange partner for vdW-DF1. Hamada instead focused on finding a suitable exchange functional for vdW-DF2. This work was inspired by earlier testing, which indicated that using vdW-DF1-C09 could give too large physisorption energies for graphene and molecules on coinage metals (also see Chapter 13) [107,108], whereas replacing the correlation with that of vdW-DF2 could improve performance for those particular systems. Another reason for starting from vdW-DF2 was that for molecular dimers the tests of Lee et al. [53] indicated that the vdW-DF2 contribution to the nonlocal binding contribution was of a reasonable magnitude. Hamada reparameterized the enhancement factor of B86b to arrive at the new functional B86R with the same small- $s$  form as the GEA limit, just as for optB86b. Further, they designed it to approximately take the large- $s$  form of B86b [109], a functional designed for highly inhomogeneous systems. Despite inheriting the poor asymptotes of vdW-DF2, the resulting vdW-DF2-B86R [107] has an impressive overall performance, often similar to that of vdW-DF1-cx and similar variants as, for instance, seen in Table 8.1. In particular, this functional can describe small molecules better due to the lower vdW contribution to binding in those cases. The fact that vdW-DF1-cx and vdW-DF2-B86R often have similar binding energies, despite the fact that the former has much larger nonlocal correlation contributions to the binding, is linked to the enhancement factor of B86R, which is the least steep of all functionals in Fig. 8.6, making it the least repulsive and compensating for the smaller nonlocal correlation contribution to the binding. Both vdW-DF1-cx and vdW-DF2-B86R are still relatively new and it remains to be seen how well they perform for a wide range of systems.

A recent attempt has been to incorporate uncertainty quantification to determine the dispersion interaction contributions. The BEEF-vdW approach estimates the reliability of DFT energies by using an ensemble of XC functionals and a Bayesian error estimation to provide “error bars” for computed energies. While it still remains to be seen whether such an approach has long term success, it has already yielded some good results with regards to modeling dispersion bound complexes [110,111].

#### 8.6.4 VV Family and Variants

The Vydrov–Van Voorhis functionals [81–83], even if strongly inspired by vdW-DF, differ significantly on a formal level, emphasizing good asymptotes and molecular interactions over adhering to vdW-DF’s exact conditions. Like some dispersion-corrected DFT methods,

VV10 is in principle reference-system optimized, but it is done with minimal empiricism. It has no need for an external damping function for nonlocal correlation and it has just two input parameters,  $C$  in Eq. (8.52) and  $b$  entering  $\kappa$  below Eq. (8.56). The latter makes VV10 highly flexible as it is set (once) for whatever specific choice of exchange partner is chosen to be combined with the VV10 evaluation. Accordingly, VV10 can also serve to give a determination of the many coefficients in an ordinary dispersion-corrected DFT formulation [99] and can readily be used also with, e.g., meta-GGAs [112] and (range-separated) hybrid functionals [82,113,114].

VV10 has been tested on many types of problems including noble-gas and molecular systems, traditional bulk materials, and layered vdW systems [86,93,94,115–117]. VV10 works extremely well for interactions between small molecules [82,114,115], with binding energies for the S22 set similar to those of the more recent vdW-DF variants as listed in Table 8.1. VV10 also has better  $C_6$  coefficients than vdW-DF for such systems, which determines the long-range interactions between molecules. However, results for layered systems indicate that VV10's transferability across length scales may be inferior to that of vdW-DF [94,116], with a typical overestimation of interlayer binding energies of about 50% compared to an RPA estimate, as detailed in Table 8.1; the vdW-DF variants typically have an overestimation of around 20%.

Still, the VV10 framework is highly flexible and can be adapted to accurately describe special classes of systems, for example, as has been done with Björkman's design of VV10sol for layered systems [93]. On the other hand, one can in general expect some limitations on transferability across systems with varying binding separations, given that VV10 has only a simple semiempirical mechanism to saturate vdW forces, unlike the mechanisms in vdW-DF which arise directly from fundamental constraints. At shorter binding separations it lacks vdW-DF's ability to ensure a seamless integration to traditional semilocal functionals by the wavevector dependence of plasmon poles [20]. A recent vdW-DF analysis shows that the details of this dispersion are important when the binding separations fall in the range between those of vdW and stronger bonds [61]. An accurate description of this binding region is, for example, relevant for understanding how weak chemisorption affects molecular functionality [118,119]. In general, all nonlocal functionals should be tested on this class of important problems.

Finally, the success of VV09 and VV10, together with that of vdW-DF, illustrates the usefulness of emphasizing a density-functional framework for including van der Waals forces. The VV and vdW-DF family of functionals are close in nature such that, by comparing their functionality for specific classes of materials, one can hope to correlate performance differences with differences in design emphasis, stimulating further improvements for truly nonlocal correlation density functionals.

## 8.7 CURRENT STATUS AND FUTURE DEVELOPMENTS

The previous section gave an overview of the type of systems that the set of specific vdW-DF versions and variants can be used for; a more comprehensive list is available in reviews and perspectives [23,87,120,121]. These applications show that the vdW-DF method

is emerging as a general-purpose approach for parameter-free materials characterization [75], and it is nowadays regularly used to study a broad range of materials. It has, for example, been used successfully to study intermolecular binding [102,122–126], water and its adsorption [127–131], chemical-fuel storage and pollution capture [53,132–138], organic crystals and their optical and vibrational behavior [70,71,78,139–141], polymers and nanotubes [48,68,72], biomolecular interactions [65,66,142–144], organics-based solar harvesting [75,145,146], hard materials including oxides [75,147–149], two-dimensional and layered materials [46,51,64,117,150–155], graphene and molecular electronics [118,119], intercalation [69], adsorption in metal organic frameworks [156–161], surfaces and coatings [67,96,107,162–166], as well as to discuss the crossover between physisorption behavior [45,73] (for very small molecules) and weak chemisorption behavior (for larger molecules) [52,61,98,108,167–172]. There is now an awareness that the traditional semilocal XC formulation is not capable of describing materials where sparseness in the electron distribution is generally important [87]. Also, the set of recent vdW-DF consistent-exchange versions and related variants are proving successful in providing a highly accurate description of materials behavior, in general. It can also be expected that the inherent logic of the method will lead to the development of new, truly nonlocal density functionals based on the electron-gas tradition [75].

A continued development of vdW-DF can follow different tracks. It is, for example, interesting to check the present design of vdW-DF versions (building from a second-order expansion form in Eq. (8.39)) by computing the full  $E_c^{\text{nl}}[\rho]$  evaluation in Eq. (8.34), an approach that was used and discussed in the first version for general separations [46,47]. This early vdW-DF version automatically keeps track of all screening effects, effects that are now also called many-body dispersion effects. The so-called TS-MBD formulation starts from an analysis of harmonic oscillators [173]. However, within the vdW-DF framework the inclusion of higher-order expansion effects will have other implications, as screening at the GGA level is already build into the plasmon-pole approximation  $S_{xc}$ . The vdW-DF method aims to describe the region near binding separations and tests will verify whether or not inclusion of higher-order terms [22] will affect that important region.

vdW-DF in various recent versions and variants will likely remain a workhorse in DFT for years to come. By now many of its strengths and weaknesses have been uncovered. A deeper theoretical insight into the method has also been achieved. One can therefore expect new and exciting developments to emerge in the coming years.

## Acknowledgments

We would like to emphasize the central role Prof. David Langreth played in the development of density functionals in general and nonlocal functionals that can capture van der Waals interactions in particular. David passed away on 27 May 2011. VRC was supported by the US Department of Energy, Office of Science, Basic Energy Sciences, Materials Sciences and Engineering Division. KB acknowledges support from the Research Council of Norway (No. 250346). PH and ES were supported by the Swedish Research Council (VR) and the Chalmers Area of Advance Materials. TT acknowledges support from the US National Science Foundation award No. DMR-1145968 for providing a wealth of data that led to the improvement of vdW-DF. Finally, TT also acknowledges generous support from the Simons Foundation through grant No. 391888.

## References

- [1] J.D. van der Waals, *Over de Continuïteit van den Gas- en Vloeistofoestand (On the Continuity of the Gas and Liquid State)*, PhD thesis, University of Leiden, Leiden, The Netherlands, 1873.
- [2] P. Hohenberg, W. Kohn, *Phys. Rev.* 136 (1964) B864.
- [3] W. Kohn, L.J. Sham, *Phys. Rev.* 140 (1965) A1133.
- [4] R.O. Jones, O. Gunnarsson, *Rev. Mod. Phys.* 61 (1989) 689.
- [5] J.N. Israelachvili, *Intermolecular and Surface Forces*, 3rd ed., Academic Press, New York, 2011.
- [6] O. Gunnarsson, B.I. Lundqvist, *Phys. Rev. B* 13 (1976) 4274.
- [7] J.P. Perdew, J.A. Chevary, S.H. Vosko, K.A. Jackson, M.R. Pederson, D.J. Singh, C. Fiolhais, *Phys. Rev. B* 46 (1992) 6671.
- [8] K.R. Kganyago, P.E. Ngoepe, *Phys. Rev. B* 68 (2003) 205111.
- [9] I.-H. Lee, R.M. Martin, *Phys. Rev. B* 56 (1997) 7197.
- [10] G. Kern, J. Hafner, *Phys. Rev. B* 58 (1998) 13167.
- [11] H.J.F. Jansen, A.J. Freeman, *Phys. Rev. B* 35 (1987) 8207.
- [12] M.C. Schabel, J.L. Martins, *Phys. Rev. B* 46 (1992) 7185.
- [13] J.-C. Charlier, X. Gonze, J.-P. Michenaud, *Europhys. Lett.* 29 (1995) 43.
- [14] D.C. Langreth, J.P. Perdew, *Solid State Commun.* 17 (1975) 1425.
- [15] D.C. Langreth, J.P. Perdew, *Phys. Rev. B* 15 (1977) 2884.
- [16] O. Gunnarsson, M. Jonson, B.I. Lundqvist, *Phys. Rev. B* 20 (1979) 3136.
- [17] J.M. Seminario, in: J.M. Seminario, P. Politzer (Eds.), *Modern Density Functional Theory: A Tool for Chemistry*, in: *Theoretical and Computational Chemistry*, vol. 2, 1995, p. 1.
- [18] B.I. Lundqvist, Y. Andersson, H. Shao, S. Chan, D.C. Langreth, *Int. J. Quant. Chem.* 56 (1995) 247.
- [19] H. Rydberg, *Nonlocal Correlations in Density Functional Theory*, PhD thesis, Department of Applied Physics, Chalmers University of Technology, Göteborg, Sweden, 2001.
- [20] M. Dion, H. Rydberg, E. Schröder, D.C. Langreth, B.I. Lundqvist, *Phys. Rev. Lett.* 92 (2004) 246401.
- [21] M. Dion, H. Rydberg, E. Schröder, D.C. Langreth, B.I. Lundqvist, *Phys. Rev. Lett.* 95 (2005) 109902.
- [22] P. Hyldgaard, K. Berland, E. Schröder, *Phys. Rev. B* 90 (2014) 075148.
- [23] K. Berland, V.R. Cooper, K. Lee, E. Schröder, T. Thonhauser, P. Hyldgaard, B.I. Lundqvist, *Rep. Prog. Phys.* 78 (2015) 066501.
- [24] J. Harris, *Phys. Rev. B* 31 (1985) 1770.
- [25] H. Margenau, N.R. Kestner, *Theory of Interatomic Forces*, 2nd ed., Pergamon Press, Oxford, 1969.
- [26] R. Eisenshitz, F. London, *Z. Phys.* 60 (1930) 491.
- [27] E. Zaremba, W. Kohn, *Phys. Rev. B* 13 (1976) 2270.
- [28] E. Zaremba, W. Kohn, *Phys. Rev. B* 15 (1977) 1769.
- [29] E.M. Lifshitz, *Zh. Eksp. Teor. Fiz.* 29 (1955) 94, translated in *Sov. Phys. JETP* 2 (1956) 73.
- [30] N. Van Kampen, B. Nijboer, K. Schram, *Phys. Lett. A* 26 (1968) 307.
- [31] P. Nozières, *The Theory of Interacting Fermion Systems*, Benjamin, New York, 1963.
- [32] D. Bohm, D. Pines, *Phys. Rev.* 92 (1953) 609.
- [33] S. Lundqvist, A. Sjölander, *Ark. Fys.* 26 (1964) 17.
- [34] A.C. Maggs, N.W. Ashcroft, *Phys. Rev. Lett.* 59 (1987) 113.
- [35] D.C. Langreth, S.H. Vosko, *Adv. Quantum Chem.* 21 (1990) 175.
- [36] K. Rapcewicz, N.W. Ashcroft, *Phys. Rev. B* 44 (1991) 4032.
- [37] Y. Andersson, D.C. Langreth, B.I. Lundqvist, *Phys. Rev. Lett.* 76 (1996) 102.
- [38] Y. Andersson, H. Rydberg, *Phys. Scr.* 60 (1999) 211.
- [39] Y. Andersson, E. Hult, H. Rydberg, P. Apell, B.I. Lundqvist, D.C. Langreth, in: J.F. Dobson, G. Vignale, M.P. Das (Eds.), *Electronic Density Functional Theory: Recent Progress and New Directions*, Plenum Press, Berlin, 1997.
- [40] E. Hult, H. Rydberg, B.I. Lundqvist, D.C. Langreth, *Phys. Rev. B* 59 (1999) 4708.
- [41] E. Schröder, P. Hyldgaard, *Surf. Sci.* 532–535 (2003) 880.
- [42] E. Schröder, P. Hyldgaard, *Mater. Sci. Eng. C* 23 (2003) 721.
- [43] J. Kleis, P. Hyldgaard, E. Schröder, *Comput. Mater. Sci.* 33 (2005) 192.
- [44] E. Hult, *Van der Waals Interactions in Density Functional Theory*, PhD thesis, Chalmers University of Technology, Göteborg, Sweden, 1999.
- [45] K. Lee, K. Berland, M. Yoon, S. Andersson, E. Schröder, P. Hyldgaard, B.I. Lundqvist, *J. Phys. Condens. Matter* 24 (2012) 424213.

- [46] H. Rydberg, M. Dion, N. Jacobson, E. Schröder, P. Hyldgaard, S.I. Simak, D.C. Langreth, B.I. Lundqvist, *Phys. Rev. Lett.* 91 (2003) 126402.
- [47] D.C. Langreth, M. Dion, H. Rydberg, E. Schröder, P. Hyldgaard, B.I. Lundqvist, *Int. J. Quant. Chem.* 101 (2005) 599.
- [48] J. Kleis, E. Schröder, P. Hyldgaard, *Phys. Rev. B* 77 (2008) 205422.
- [49] J.P. Perdew, Y. Wang, *Phys. Rev. B* 33 (1986) 8800.
- [50] J.P. Perdew, K. Burke, M. Ernzerhof, *Phys. Rev. Lett.* 77 (1996) 3865.
- [51] K. Berland, P. Hyldgaard, *Phys. Rev. B* 89 (2014) 035412.
- [52] T. Thonhauser, S. Zuluaga, C.A. Arter, K. Berland, E. Schröder, P. Hyldgaard, *Phys. Rev. Lett.* 115 (2015) 136402.
- [53] K. Lee, È.D. Murray, L. Kong, B.I. Lundqvist, D.C. Langreth, *Phys. Rev. B* 82 (2010) 081101.
- [54] H. Rydberg, B.I. Lundqvist, D.C. Langreth, M. Dion, *Phys. Rev. B* 62 (2000) 6997.
- [55] F. London, *Z. Phys.* 63 (1930) 245.
- [56] F. London, *Z. Phys. Chem.* 33 (1937) 8, English translation in: H. Hettema (Ed.), *Quantum Chemistry, Classic Scientific Papers*, World Scientific, Singapore, 2000.
- [57] A.D. Becke, E.R. Johnson, *J. Chem. Phys.* 123 (2005) 154101.
- [58] A.D. Becke, E.R. Johnson, *J. Chem. Phys.* 127 (2007) 154108.
- [59] T. Thonhauser, V.R. Cooper, S. Li, A. Puzder, P. Hyldgaard, D.C. Langreth, *Phys. Rev. B* 76 (2007) 125112.
- [60] L. Hedin, B.I. Lundqvist, *J. Phys. C* 4 (1971) 2064.
- [61] K. Berland, P. Hyldgaard, *Phys. Rev. B* 87 (2013) 205421.
- [62] K. Burke, *J. Chem. Phys.* 136 (2012) 150901.
- [63] A.D. Becke, *J. Chem. Phys.* 140 (2014) 18A301.
- [64] B.I. Lundqvist, et al., *Surf. Sci.* 493 (2001) 253.
- [65] V.R. Cooper, T. Thonhauser, A. Puzder, E. Schröder, B.I. Lundqvist, D.C. Langreth, *J. Am. Chem. Soc.* 130 (2008) 1304.
- [66] V.R. Cooper, T. Thonhauser, D.C. Langreth, *J. Chem. Phys.* 128 (2008) 204102.
- [67] S.D. Chakarova-Käck, E. Schröder, B.I. Lundqvist, D.C. Langreth, *Phys. Rev. Lett.* 96 (2006) 146107.
- [68] J. Kleis, B.I. Lundqvist, D.C. Langreth, E. Schröder, *Phys. Rev. B* 76 (2007) 100201.
- [69] E. Ziambaras, J. Kleis, E. Schröder, P. Hyldgaard, *Phys. Rev. B* 76 (2007) 155425.
- [70] K. Berland, P. Hyldgaard, *J. Chem. Phys.* 132 (2010) 134705.
- [71] K. Berland, Ø. Borck, P. Hyldgaard, *Comput. Phys. Commun.* 182 (2011) 1800.
- [72] G. Román-Pérez, J.M. Soler, *Phys. Rev. Lett.* 103 (2009) 096102.
- [73] K. Lee, B. Kolb, T. Thonhauser, D. Vanderbilt, D.C. Langreth, *Phys. Rev. B* 86 (2012) 104102.
- [74] R. Sabatini, E. Küçükbenli, B. Kolb, T. Thonhauser, S. de Gironcoli, *J. Phys. Condens. Matter* 24 (2012) 424209.
- [75] K. Berland, C.A. Arter, V.R. Cooper, K. Lee, B.I. Lundqvist, E. Schröder, T. Thonhauser, P. Hyldgaard, *J. Chem. Phys.* 140 (2014) 18A539.
- [76] E. Ziambaras, J. Kleis, E. Schröder, P. Hyldgaard, *Phys. Rev. B* 76 (2007) 155425.
- [77] M. Obata, M. Nakamura, I. Hamada, T. Oda, *J. Phys. Soc. Jpn.* 82 (2013) 093701.
- [78] M. Obata, M. Nakamura, I. Hamada, T. Oda, *J. Phys. Soc. Jpn.* 84 (2015) 024715.
- [79] J.P. Perdew, Y. Wang, *Phys. Rev. B* 45 (1992) 13244.
- [80] O.A. Vydrov, T. Van Voorhis, *J. Chem. Phys.* 130 (2009) 104105.
- [81] O.A. Vydrov, T. Van Voorhis, *Phys. Rev. Lett.* 103 (2009) 063004.
- [82] O.A. Vydrov, T. Van Voorhis, *J. Chem. Phys.* 133 (2010) 244103.
- [83] D.C. Langreth, B.I. Lundqvist, *Phys. Rev. Lett.* 104 (2010) 099303.
- [84] C. Gutle, A. Savin, J.B. Krieger, J. Chen, *Int. J. Quant. Chem.* 75 (1999) 885.
- [85] P. Jurecka, J. Sponer, J. Cerny, P. Hobza, *Phys. Chem. Chem. Phys.* 8 (2006) 1985.
- [86] R. Sabatini, T. Gorni, S. de Gironcoli, *Phys. Rev. B* 87 (2013) 041108(R).
- [87] D.C. Langreth, et al., *J. Phys. Condens. Matter* 21 (2009) 084203.
- [88] T. Takatani, E.G. Hohenstein, M. Malagoli, M.S. Marshall, C.D. Sherrill, *J. Chem. Phys.* 132 (2010) 144104.
- [89] Y. Zhang, W. Yang, *Phys. Rev. Lett.* 80 (1998) 890.
- [90] È.D. Murray, K. Lee, D.C. Langreth, *J. Chem. Theory Comput.* 5 (2009) 2754.
- [91] J. Klimeš, D.R. Bowler, A. Michaelides, *J. Phys. Condens. Matter* 22 (2010) 022201.
- [92] J. Klimeš, D.R. Bowler, A. Michaelides, *Phys. Rev. B* 83 (2011) 195131.
- [93] T. Björkman, *Phys. Rev. B* 86 (2012) 165109.
- [94] T. Björkman, A. Gulans, A.V. Krasheninnikov, R.M. Nieminen, *Phys. Rev. Lett.* 108 (2012) 235502.

- [95] I. Hamada, *Phys. Rev. B* 89 (2014) 121103.
- [96] J. Carrasco, W. Liu, A. Michaelides, A. Tkatchenko, *J. Chem. Phys.* 140 (2014) 084704.
- [97] W. Liu, J. Carrasco, B. Santra, A. Michaelides, M. Scheffler, A. Tkatchenko, *Phys. Rev. B* 86 (2012) 245405.
- [98] H. Yildirim, T. Greber, A. Kara, *J. Phys. Chem. C* 117 (2013) 20572.
- [99] O.A. Vydrov, T. Van Voorhis, *Phys. Rev. A* 81 (2010) 062708.
- [100] V.R. Cooper, *Phys. Rev. B* 81 (2010) 161104.
- [101] X. Wu, M.C. Vargas, S. Nayak, V. Lotrich, G. Scoles, *J. Chem. Phys.* 115 (2001) 8748.
- [102] R.C. Clay, J. McMinis, J.M. McMahon, C. Pierleoni, D.M. Ceperley, M.A. Morales, *Phys. Rev. B* 89 (2014) 184106.
- [103] R.C. Clay, M. Hotzmann, D.M. Ceperley, M.A. Morales, *Phys. Rev. B* 93 (2016) 035121.
- [104] F.O. Kannemann, A.D. Becke, *J. Chem. Theory Comput.* 5 (2009) 719.
- [105] J.P. Perdew, K. Burke, Y. Wang, *Phys. Rev. B* 54 (1996) 16533.
- [106] J.P. Perdew, A. Ruzsinszky, G.I. Csonka, O.A. Vydrov, G.E. Scuseria, L.A. Constantin, X. Zhou, K. Burke, *Phys. Rev. Lett.* 100 (2008) 136406.
- [107] I. Hamada, M. Otani, *Phys. Rev. B* 82 (2010) 153412.
- [108] I. Hamada, M. Tsukada, *Phys. Rev. B* 83 (2011) 245437.
- [109] A.D. Becke, *J. Chem. Phys.* 85 (1986) 7184.
- [110] J. Wellendorff, K.T. Lundgaard, A. Møgelhøj, V. Petzold, D.D. Landis, J.K. Nørskov, T. Bligaard, K.W. Jacobsen, *Phys. Rev. B* 85 (2012) 235149.
- [111] A.J. Medford, J. Wellendorff, A. Vojvodic, F. Studt, F. Abild-Pedersen, K.W. Jacobsen, T. Bligaard, J.K. Nørskov, *Science* 345 (2014) 197.
- [112] H. Peng, Z.-H. Yang, J. Sun, J.P. Perdew, arXiv:1510.05712, 2016.
- [113] W. Hujó, S. Grimme, *J. Chem. Theory Comput.* 7 (2011) 3866.
- [114] O.A. Vydrov, T. Van Voorhis, *J. Chem. Theory Comput.* 8 (2012) 1929.
- [115] F. Tran, J. Hutter, *J. Chem. Phys.* 138 (2013) 204103.
- [116] T. Björkman, A. Gulans, A.V. Krasheninnikov, R.M. Nieminen, *J. Phys. Condens. Matter* 24 (2012) 424218.
- [117] T. Björkman, *J. Chem. Phys.* 141 (2014) 074708.
- [118] A. Bergvall, K. Berland, P. Hyldgaard, S. Kubatkin, T. Löfwander, *Phys. Rev. B* 84 (2011) 155451.
- [119] B. Borca, V. Schendel, R. Petuya, I. Pentegov, T. Michnowicz, U. Kraft, H. Klauk, A. Arnau, P. Wahl, U. Schlickum, K. Kern, *ACS Nano* 9 (2015) 12506.
- [120] O.A. Vydrov, T. Van Voorhis, in: M.A.L. Marques, N. Maitra, F. Nogueira, E.K.U. Gross, A. Rubio (Eds.), *Fundamentals of Time-Dependent Density Functional Theory*, Springer, Berlin, 2012, p. 443.
- [121] J. Klimeš, A. Michaelides, *J. Chem. Phys.* 137 (2012) 120901.
- [122] S.D. Chakarova, E. Schröder, *Mater. Sci. Eng. C* 25 (2005) 787.
- [123] S.D. Chakarova, E. Schröder, *J. Chem. Phys.* 122 (2005) 054102.
- [124] A. Puzder, M. Dion, D.C. Langreth, *J. Chem. Phys.* 124 (2006) 164105.
- [125] S. Li, V.R. Cooper, T. Thonhauser, A. Puzder, D.C. Langreth, *J. Phys. Chem. A* 112 (2008) 9031.
- [126] S.D. Chakarova-Käck, A. Vojvodic, J. Kleis, P. Hyldgaard, E. Schröder, *New J. Phys.* 12 (2010) 013017.
- [127] A.K. Kelkkanen, B.I. Lundqvist, J.K. Nørskov, *J. Chem. Phys.* 131 (2009) 046102.
- [128] I. Hamada, *J. Chem. Phys.* 133 (2010) 214503.
- [129] A. Møgelhøj, A.K. Kelkkanen, K.T. Wikfeldt, J. Schiøtz, J.J. Mortensen, L.G.M. Pettersson, B.I. Lundqvist, K.W. Jacobsen, A. Nilsson, J.K. Nørskov, *J. Phys. Chem. B* 115 (2011) 14149.
- [130] I. Hamada, K. Lee, Y. Morikawa, *Phys. Rev. B* 81 (2010) 115452.
- [131] E. Schröder, *J. Nanomater.* 2013 (2013) 871706.
- [132] Q. Li, B. Kolb, G. Román-Pérez, J.M. Soler, F. Yndurain, L. Kong, D.C. Langreth, T. Thonhauser, *Phys. Rev. B* 84 (2011) 153103.
- [133] A. Bil, B. Kolb, R. Atkinson, D.G. Pettifor, T. Thonhauser, A.N. Kolmogorov, *Phys. Rev. B* 83 (2011) 224103.
- [134] V.R. Cooper, Y. Ihm, J.R. Morris, *Phys. Proc.* 34 (2012) 34.
- [135] R. Poloni, B. Smit, J.B. Neaton, *J. Phys. Chem. A* 116 (2012) 4957.
- [136] R. Poloni, B. Smit, J.B. Neaton, *J. Am. Chem. Soc.* 134 (2012) 6714.
- [137] J. Åkesson, O. Sundborg, O. Wahlström, E. Schröder, *J. Chem. Phys.* 137 (2012) 174702.
- [138] R. Poloni, K. Lee, R.F. Berger, B. Smit, J.B. Neaton, *J. Phys. Chem. Lett.* 5 (2014) 861.
- [139] C. Ambrosch-Draxl, D. Nabok, P. Puschnig, C. Meisenbichler, *New J. Phys.* 11 (2009) 125010.
- [140] T. Rangel, K. Berland, S. Sharifzadeh, F. Brown-Altwater, K. Lee, P. Hyldgaard, L. Kronik, J.B. Neaton, *Phys. Rev. B* 93 (2016) 115206.

- [141] F. Brown-Altwater, T. Rangel, J.B. Neaton, *Phys. Rev. B* 93 (2016) 195206.
- [142] K. Berland, S.D. Chakarova-Käck, V.R. Cooper, D.C. Langreth, E. Schröder, *J. Phys. Condens. Matter* 23 (2011) 135001.
- [143] D. Le, A. Kara, E. Schröder, P. Hyldgaard, T.S. Rahman, *J. Phys. Condens. Matter* 24 (2012) 424210.
- [144] M. Rosa, S. Corni, R.D. Felice, *J. Chem. Theory Comput.* 10 (2014) 1707.
- [145] L. Romaner, D. Nabok, P. Puschnig, E. Zojer, C. Ambrosch-Draxl, *New J. Phys.* 11 (2009) 053010.
- [146] M. Kuisma, A.M. Lundin, K. Moth-Poulsen, P. Hyldgaard, P. Erhart, *J. Phys. Chem. C* 120 (2016) 3635.
- [147] E. Londero, E. Schröder, *Phys. Rev. B* 82 (2010) 054116.
- [148] E. Londero, E. Schröder, *Comput. Phys. Commun.* 182 (2011) 1805.
- [149] B. Sun, H. Liu, H. Song, G. Zhang, H. Zheng, X.-G. Zhao, P. Zhang, *J. Chem. Phys.* 140 (2014) 164709.
- [150] H. Rydberg, N. Jacobson, P. Hyldgaard, S.I. Simak, B.I. Lundqvist, D.C. Langreth, *Surf. Sci.* 532–535 (2003) 606.
- [151] J. Rohrer, P. Hyldgaard, *Phys. Rev. B* 83 (2011) 165423.
- [152] X. Luo, M.B. Sullivan, S.Y. Quek, *Phys. Rev. B* 86 (2012) 184111.
- [153] P. Erhart, P. Hyldgaard, D.O. Lindroth, *Chem. Mater.* 27 (2015) 5511.
- [154] H. Sadeghi, S. Santarash, C.J. Lambert, *Sci. Rep.* 5 (2015) 9514.
- [155] M. Mehboudi, A.M. Dorio, W. Zhu, A. van der Zande, H.O.H. Churchill, A.A. Pacheco-Sanjuan, E.O. Harris, P. Kumar, S. Baraza-Lopez, *Nano Lett.* 16 (2016) 1704.
- [156] S. Zuluaga, E.M.A. Fuentes-Fernandez, K. Tan, F. Xu, J. Li, Y.J. Chabal, T. Thonhauser, *J. Mater. Chem. A* 4 (2016) 5176.
- [157] P. Canepa, K. Tan, Y. Du, H. Lu, Y.J. Chabal, T. Thonhauser, *J. Mater. Chem. A* 3 (2015) 986.
- [158] K. Tan, S. Zuluaga, Q. Gong, P. Canepa, H. Wang, J. Li, Y.J. Chabal, T. Thonhauser, *Chem. Mater.* 26 (2014) 6886.
- [159] P. Canepa, C.A. Arter, E.M. Conwill, D.H. Johnson, B.A. Shoemaker, K.Z. Soliman, T. Thonhauser, *J. Mater. Chem. A* 1 (2013) 13597.
- [160] P. Canepa, N. Nijem, Y.J. Chabal, T. Thonhauser, *Phys. Rev. Lett.* 110 (2013) 026102.
- [161] N. Nijem, H. Wu, P. Canepa, A. Marti, K.J. Balkus, T. Thonhauser, J. Li, Y.J. Chabal, *J. Am. Chem. Soc.* 134 (2012) 15201.
- [162] K. Berland, T.L. Einstein, P. Hyldgaard, *Phys. Rev. B* 80 (2009) 155431.
- [163] D. Sun, D.-H. Kim, D. Le, Ø. Borck, K. Berland, K. Kim, W. Lu, Y. Zhu, M. Luo, J. Wyrick, Z. Cheng, T.L. Einstein, T.S. Rahman, P. Hyldgaard, L. Bartels, *Phys. Rev. B* 82 (2010) 201410.
- [164] J. Wyrick, D.-H. Kim, D. Sun, Z. Cheng, W. Lu, Y. Zhu, K. Berland, Y.S. Kim, E. Rotenberg, M. Luo, P. Hyldgaard, T.L. Einstein, L. Bartels, *Nano Lett.* 11 (2011) 2944.
- [165] M. Amft, S. Lebégue, O. Eriksson, N.V. Skorodumova, *J. Phys. Condens. Matter* 23 (2011) 395001.
- [166] G. Li, I. Tamblyn, V.R. Cooper, H.-J. Gao, J.B. Neaton, *Phys. Rev. B* 85 (2012) 121409.
- [167] S.D. Chakarova-Käck, Ø. Borck, E. Schröder, B.I. Lundqvist, *Phys. Rev. B* 74 (2006) 155402.
- [168] K. Toyoda, Y. Nakano, I. Hamada, K. Lee, S. Yanagisawa, Y. Morikawa, *Surf. Sci.* 603 (2009) 2912.
- [169] J. Björk, F. Hanke, C.-A. Palma, P. Samori, M. Cecchini, M. Persson, *J. Phys. Chem. Lett.* 1 (2010) 3407.
- [170] A.K. Kelkkanen, B.I. Lundqvist, J.K. Nørskov, *Phys. Rev. B* 83 (2011) 113401.
- [171] M. Callsen, N. Atodiresei, V. Caciuc, S. Blügel, *Phys. Rev. B* 86 (2012) 085439.
- [172] J. Björk, S. Stafström, *Chem. Phys. Chem.* 15 (2014) 2851.
- [173] A. Tkatchenko, R.A. DiStasio, R. Car, M. Scheffler, *Phys. Rev. Lett.* 108 (2012) 236402.



# Noncovalent Interactions in Organic Electronic Materials

---

*Mahesh Kumar Ravva\**, *Chad Risko†*, *Jean-Luc Brédas\**

\*Laboratory for Computational and Theoretical Chemistry of Advanced Materials, Division of Physical Science and Engineering, King Abdullah University of Science and Technology, Thuwal, Saudi Arabia †Department of Chemistry and Center for Applied Energy Research, University of Kentucky, Lexington, KY, USA

## 9.1 INTRODUCTION

---

Organic semiconductors, electronically and optically active materials derived from  $\pi$ -conjugated molecules and polymers, have attracted major academic and industrial attention over the past three decades. The potential for large-scale and low-cost device fabrication, distinctive device form factors that arise from the inherent mechanical flexibility of thin-film “plastic” materials, and the ability to readily tune the material electronic and optical properties through well-established synthetic chemistry principles, have driven the development of thousands of organic materials [1–6]. To date, organic semiconductors have been exploited in a wide range of applications, from light-emitting diodes for displays and solid-state lighting, solar cells, field-effect transistors, all-optical switches, or biosensors, and represent already a multibillion dollar market [7–22].

Advances in organic synthesis and molecular design, along with considerable improvement in the understanding of how to control the processing of these thin-film materials, have resulted in continued enhancement of device performance over the years [23–25]. However, organic semiconductors still suffer from numerous drawbacks when compared to their inorganic counterparts. A key parameter in many of these applications is the ability to effectively transport charges, either holes or electrons, or both in the case of ambipolar materials. Efficient charge-carrier transport, along with aspects of the optical response, strongly depends on the electronic couplings among neighboring molecules or chain segments, factors that are directly contingent on the solid-state molecular packing arrangements. Hence, there is growing interest in how to design the chemical composition of molecules and polymers to dictate not only the electronic and optical response of the isolated molecules, but also the noncovalent interactions that direct molecular packing [26–38].

Prime examples of how changes in chemical structure impact molecular packing and, in turn, the material electrical response can be found in the oligoacene family, a set of linearly fused aromatic hydrocarbons. If we take the examples of tetracene and its derivative rubrene (5,6,11,12-tetra[phenyl]tetracene)—the latter of which is discussed in more detail in Section 9.3.2 of this chapter [39,40]—we find that crystalline tetracene packs in the edge-to-face herringbone configuration typical of most oligoacenes. On the other hand, the tetraphenyl substitution along the long axis of the tetracene core in rubrene transforms the preferred packing configuration to one where the tetracene backbones are arranged in a slipped, face-to-face, often referred to as “ $\pi$ -stacked”, configuration. This configuration in rubrene leads to substantial spatial overlap of the tetracene backbones and wavefunction overlap of the tetracene-based frontier  $\pi$  orbitals, resulting in large intermolecular electronic couplings and record-high charge-carrier mobilities (up to  $40 \text{ cm}^2 \text{ V}^{-1} \text{ s}^{-1}$ ) in single-crystal field-effect transistors [39–41]. As a point of reference, electron mobilities in amorphous silicon range from  $10^{-3}$  to  $10 \text{ cm}^2 \text{ V}^{-1} \text{ s}^{-1}$  [42,43], depending on sample preparation and doping. Chemical functionalization of rubrene has achieved varying success in attempting to improve crystal packing. Such results, as we will discuss, are in fact highly dependent on the noncovalent interactions that exist in these materials [44–47].

Variations in processing can also be used to enhance the material charge-carrier transport properties. Recent advances in solution processing techniques, such as drop casting, spin coating, or meniscus-guided coating, have been developed with a view to direct the solid-state morphology of organic semiconductors [48]. These advances will not be discussed here and the interested reader is directed to recent reviews on the subject [23–25]. However, noncovalent interactions in the ink (i.e., solution) formulations of solution-processable semiconductors are critical; we will show some initial attempts to understand how such interactions in the solution environment can seed the development of the thin-film morphology of organic semiconductors.

To this point, we have discussed noncovalent intermolecular interactions in a rather general way. Building on previous chapters in this book (see, for instance, Chapter 1), we now briefly reintroduce the key interactions, as these definitions will serve an essential role in the discussion that follows:

- *Electrostatic interactions* arise from interactions among unperturbed charge distributions on neighboring molecules. The charge distributions on a molecule can be expressed in the form of a multipole expansion, i.e., monopole (charge), dipole, quadrupole, etc., starting with the lowest-order permanent multipole moment. The interactions arising from these multipoles include monopole–monopole, monopole–dipole, monopole–quadrupole, dipole–dipole, dipole–quadrupole, quadrupole–quadrupole, etc. It is important to bear in mind that such a multipole expression is valid only if the two monomers are separated by distances that are typically over  $4 \text{ \AA}$  (see Chapter 1 for further details on the convergence of the multipolar expansion). When the molecules are brought close together, the monomer charge densities start to overlap significantly, with the charge density on one molecule experiencing attraction from the nuclei of the other molecule. This increased electrostatic attraction results in an extra stabilization referred to as charge penetration [49–51]. In many relevant organic semiconductors, the plane-to-plane distance is typically less than  $4 \text{ \AA}$ . Hence, significant charge penetration effects can be present.

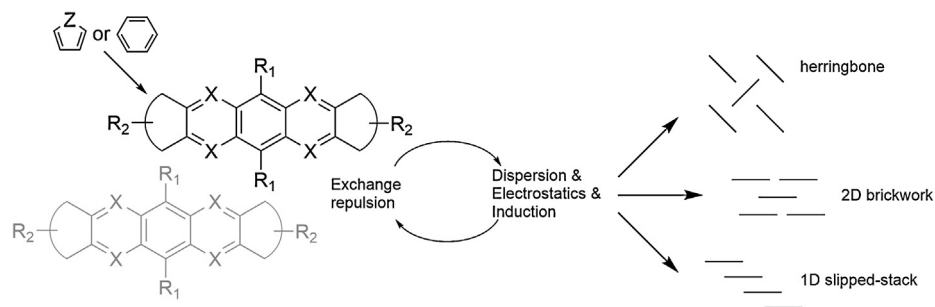


**FIGURE 9.1** Using oligoacenes as a model, modifications to the length of the  $\pi$ -conjugated framework, substitutions (X) within the framework, or moieties substituted along the periphery (R1 and R2) not only will affect the molecular redox and (opto)electronic characteristics, but also the nature and strength of the noncovalent intermolecular interactions (exchange repulsion, dispersion, electrostatics, and induction) that energetically drive certain molecular packing configurations in the solid state. Here, the nature and strength of the noncovalent interactions between two molecules—one in gray and one in black—can lead to numerous ordered packing configurations, including herringbone, one-dimensional (1D) slipped-stack, or two-dimensional (2D) brickwork, to name but a few.

- *Induction* can be understood as the energy stabilization due to the electronic relaxation of the charge distribution on one molecule in response to the presence of another molecule. In other words, induction is the stabilization due to the induced electrostatic moments on one molecule owing to the presence of permanent multipole moments of the other. In the case of  $\pi$ -conjugated organic materials, the contribution from induction is generally small in magnitude, except when dealing with charged monomers.
- *Dispersion* is a dominant contributor to intermolecular stabilization in many  $\pi$ -conjugated molecular materials. Dispersion arises from instantaneous charge fluctuations (induced dipoles) in the electron density on each interacting molecule.
- *Exchange repulsion* is the consequence of Pauli's exclusion principle, which prevents two electrons (fermions) from occupying the same quantum state and therefore the same region of space [52,53]. Exchange-repulsion physically balances the attractive forces, with the repulsion between electrons from adjacent molecules limiting the degree of contact.

The electronic and optical properties of organic semiconductors can be tuned by changing the respective contributions from these interactions as illustrated in Fig. 9.1, and this ability to tune properties paves the way to the design of new functional materials with desired physicochemical properties. The relative importance of the noncovalent interactions strongly depends on the molecular chemical composition and architecture, with multiple terms often playing critical roles that ultimately determine intermolecular packing. In the following sections, we begin by providing a brief overview of some of the chemical design principles that are used to direct the (opto)electronic characteristics of organic semiconductors. We then showcase examples where theory and computation have driven a deeper understanding of how chemical changes impact the preference for molecular packing configurations in the solid state, therefore enabling some of the considerations that are required to develop new generations of organic semiconductors.

## 9.2 MATERIALS DESIGN MOTIFS

In this section, we elaborate on some strategies that have been used to design  $\pi$ -conjugated molecular and polymeric materials. We begin with a very short overview of the connections between charge-carrier transport and molecular packing in the solid state. We then briefly describe how heteroatoms incorporated into the  $\pi$ -conjugated backbone and halogen atoms attached to the periphery of the backbone can influence molecular packing. We finally emphasize the importance of alkyl side-chains with respect to solubility, packing, and the resulting device performance. This overview is by no means exhaustive given the thousands of organic semiconductors that have been synthesized.

We note that discussions centering on  $\pi$ - $\pi$  interactions are omnipresent in the organic semiconductor literature, as the building blocks of these materials contain a conjugated backbone, often with one or more aromatic rings. Quantum-chemical calculations with energy decomposition analysis (EDA) provide insight into defining these interactions, even though a complete physical picture still needs to be reached (see Chapter 2) [50,51,54].

### 9.2.1 Charge-Carrier Transport in Organic Semiconductors: Dependence on the Intermolecular Electronic Coupling

Given the dependence of the charge-carrier transport characteristics of organic semiconductors on the noncovalent interactions that in part define molecular packing in the solid state, it is not surprising that definitive models to describe these molecular-scale processes are still under development. Interested readers are referred to detailed reviews we have published on this topic [55–57]. In general, charge-carrier transport in organic materials can be described in two limited regimes: band transport or thermally activated hopping. The band transport model is applicable to instances where the molecular wavefunctions delocalize over many sites (or molecules) in the solid-state material and form electronic bands; evidence for band transport has only been observed in highly pure molecular crystals [58]. Band transport implies very strong intermolecular electronic couplings among nearest neighbors. These couplings are directly related to the wavefunction overlap of the relevant frontier molecular orbitals (for instance, in the case of holes (electrons), the electronic coupling depends on the overlap between the HOMO (LUMO) on one molecule and the HOMO (LUMO) on the neighboring molecule). As a result, molecular arrangements in the solid state (i.e., the relative intermolecular distances, orientations, and translations) have a tremendous influence on the magnitude of these electronic couplings.

In many instances, the weak noncovalent interactions in organic semiconductors, as opposed to the covalent bonds among atoms in inorganic (semi)conductors, result in relatively large intermolecular separations (greater than 3.2 Å) when compared to a covalent bond and large degrees of intrinsic disorder (related to thermal fluctuations) and extrinsic disorder (grain boundaries, impurities). These attributes, in turn, lead to wavefunction (or charge) localization on a single or just a few molecules. Then, the transport of charge carriers corresponds to a thermally activated hopping process, where the carriers move, or hop, from one molecule or chain segment to the next.

## 9.2.2 Heteroatoms Within the $\pi$ -Conjugated Backbone

Heteroatom substitution within the  $\pi$ -conjugated backbone has been widely used to alter the electronic characteristics of molecules and polymers. The impact of heteroatoms on these characteristics comes from changing the spatial extent of the  $\pi$ -electron cloud and the polarizability of the aromatic systems. As a result, the magnitudes of the interactions (especially when the molecule is made to become noncentrosymmetric) can be greatly affected, which in turn influences the preferred packing configurations when compared to their hydrocarbon counterparts. Sulfur [59–68] and nitrogen [69–71] atoms are widely substituted into the  $\pi$ -conjugated frameworks, with oxygen, selenium, and germanium also finding greater use. We provide later on a more detailed discussion of how heteroatom substitution influences the electronic coupling between adjacent molecules.

## 9.2.3 Halogen Substituents on the $\pi$ -Conjugated Backbone Periphery

A number of halogen-substituted  $\pi$ -conjugated small molecules and polymers have garnered attention as efficient materials for thin-film transistors and solar cells, with the halogenation employed to alter the redox stability of organic semiconductors. The strong electron-withdrawing character of halogen atoms makes them particularly useful in the design of n-type semiconductors due to their ability to lower the reduction potential (i.e., increase the electron affinity). The electronegative nature of halogen atoms leads to molecules with very polar bonds. Halogen atoms decline in electron-withdrawing strength as one moves down the periodic table from fluorine to iodine. These polar bonds can play a considerable role in defining the nature of the noncovalent interactions that drive molecular packing [72–75].

Fluorine is among the most widely used halogen atoms in organic semiconductors. Fluorination of aromatic rings can lead to a reversal of the characteristics of the  $\pi$ -electron density above and below on aromatic ring. Perfluorinated aromatic rings lead to large, positive quadrupole moments, with positive poles above and below the rings (and negative poles in the plane of the nuclei), while the opposite is true for unsubstituted rings [76]. Hence, upon fluorination, the drive to maximize the electrostatic interactions and reduce the exchange-repulsion term can lead to very different packing motifs [77]. For example, appending fluorine atoms to pentacene converts the crystal packing from herringbone to a  $\pi$ -stacked motif (Fig. 9.2) [78,79].

The degree of halogenation can also play a role. For example, 5-chlorotetracene derivatives pack in a herringbone geometry whereas 5,11-dichlorotetracene and 5,6,11,12-tetrachlorotetracene both arrange in face-to-face, slip-stacked configurations, with intermolecular distances of 3.48 and 3.56 Å, respectively [80,81]. Anthony and coworkers synthesized fluorinated 6,13-triisopropylsilylethynyl (TIPS)-pentacene derivatives, where the number of fluorine atoms on the peripheral rings shifts the intermolecular stacking distance. This distance goes from 3.43 Å in the unsubstituted parent molecule to 3.36 Å for the tetrafluoro structure to 3.28 Å for the octafluoro structure [82]. Perfluorination can also take place on the solubilizing alkyl side chains, which not only alters material miscibility but also influences the preferential charge-carrier transport in the molecular semiconductor. For instance, perfluoroalkyl functionalized oligothiophenes are n-type materials, whereas their alkyl cousins are p-type [83].

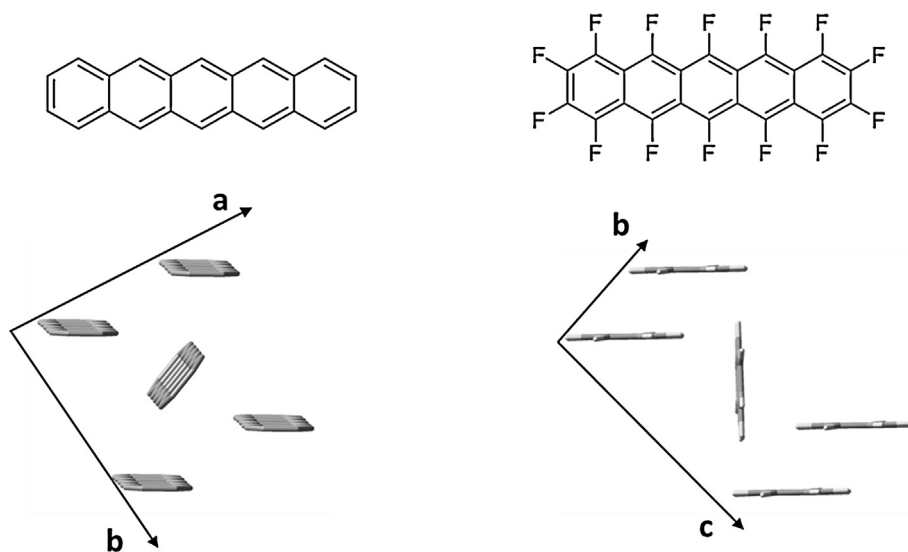
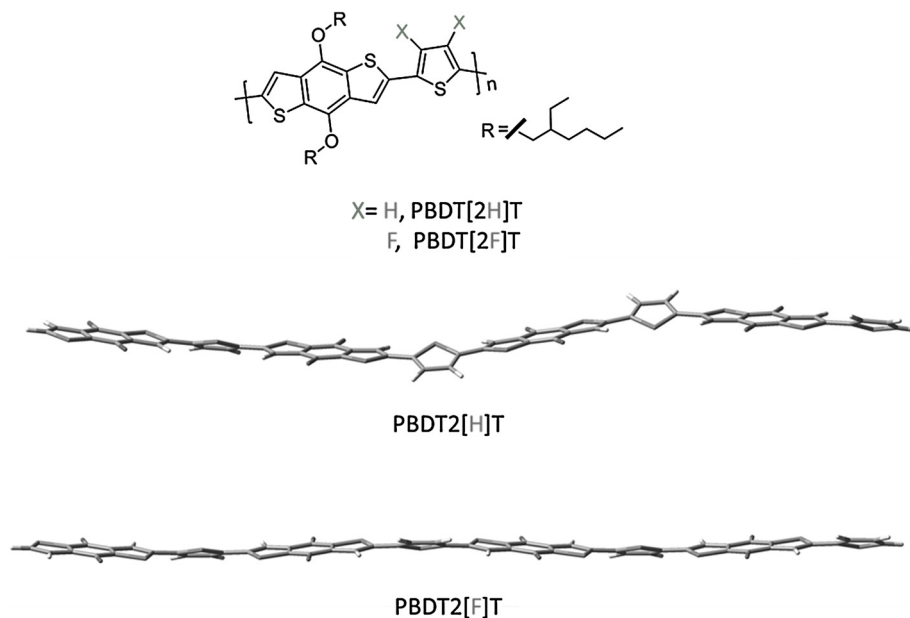


FIGURE 9.2 Chemical structures of pentacene (top, left) and perfluoropentacene (top, right) and illustrations of the crystal structure packing of pentacene [78] (bottom, left) and perfluoropentacene [79] (bottom, right).

Fluorine atom substitution has also been widely used to alter the solid-state morphology of  $\pi$ -conjugated polymers. Appropriate placement of fluorine atoms along the backbone can induce increased backbone planarity, which in turn can allow for tighter interchain packing, while the increased rigidity can enhance the charge-carrier transport properties along the chain [84–86]. Fluorination has been carried out on a wide variety of building blocks used in the synthesis of polymers, including thiophenes, carbazoles, thienothiophenes, benzothiadiazoles, benzotriazoles, benzodithiophenes, indacenodithiophenes, and anthradithiophenes [87–96]. Recently, we have shown in the case of poly(4,8-bis((2-ethylhexyl)oxy)-benzo[1,2-b:4,5-b']dithiophene-thiophene) (PBDT[2H]T) and its 3,4-difluorothiophene analog (PBDT[2F]T) polymers that fluorination induces greater planarity, enhanced chain stacking in the solid state [97], and larger interchain electronic couplings (Fig. 9.3). Though halogenation is a widely used method to modify the redox and (opto)electronic properties of organic semiconductors, an a priori insight into how halogen substituents direct solid-state packing in organic semiconductors has still to be developed [89,95].

#### 9.2.4 The Role of Alkyl Chains: From Solubility to Steric Bulk

Alkyl chains substituted on the periphery of the  $\pi$ -conjugated system are appended mainly to impart solubility and improve solution processing, but also greatly impact solid-state packing [37,98–100]. Alkyl chains are (mostly) electronically inert. However, since they play an important role in determining the intermolecular packing, their presence influences the (opto)electronic properties of the organic semiconductor. Alkyl functionalization can help



**FIGURE 9.3** Chemical structures of the PBDT[2X]T polymers and illustrations of the backbone conformations of PBDT[2H]T and PBDT[2F]T oligomers [97].

overcome the repulsive exchange interactions between  $\pi$ -conjugated moieties by shifting the balance between dispersion and exchange interactions.

The idea of attaching bulky substituents has also been widely used to control the packing of small molecules [101–103]. In particular, attaching bulky triisopropylsilyl (TIPS) groups via ethynyl linkers to the periphery of pentacene triggers the herringbone packing configuration of pentacene to transform into a 2D-brickwork packing arrangement [101]. For benzothieno[3,2-*b*]benzothiophene (BTBT), octyl chains appended along the molecular long axis leads to packing configurations that make BTBT a champion charge-carrier transport material in single-crystal field-effect transistors [104].

For polymer-based materials, aliphatic alkyl side-chains appended to rigid polymer backbones modulate the solid-state morphology [37,98–100]. In the case of PBDTTPD polymers (composed of alternating thieno[3,4-*b*]thiophene-pyrrole-4,6-dione and benzodithiophene units), crystallite formation and relative backbone orientations strongly depend on the pattern of alkyl chains along the polymer backbone [105]. For instance, the PBDTTPD polymer with branched ethyl-hexyl (EH) chains on the benzodithiophene (BTD) units and linear alkyl side-chain (C8) on the thieno[3,4-*c*]pyrrole-4,6-dione (TPD) units forms crystallites with face-on orientation relative to substrate. On the other hand the PBDTTPD polymer with C8 substituents on BDT and EH substituents on TPD has an edge-on orientation relative to substrate (Fig. 9.4). In addition, changes in the nature and positions of the alkyl chains have been shown to influence the efficiency of solar cells based on PBDTTPD polymers with fullerene acceptors [106,107]. When TPD moieties carry linear alkyl side-chains and the BDT moieties

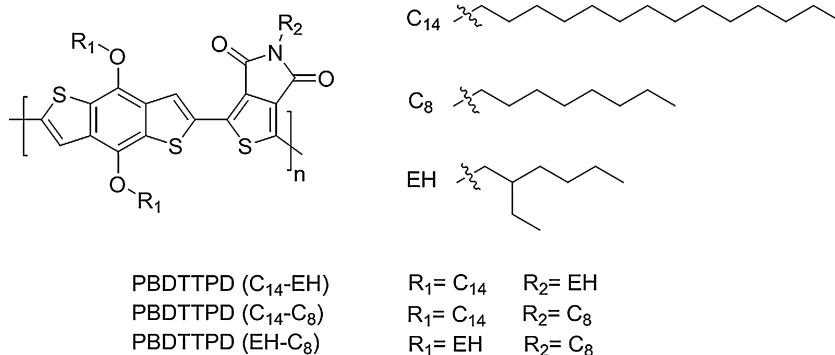


FIGURE 9.4 Chemical structures of PBDTTPD with the three side-chain patterns.

carry branched side-chains, the fullerene molecules are expected to sit preferentially over the TPD segments of the polymer chain. This arrangement leads to much better solar cell performance compared to the polymer backbone where TPD units carry branched side-chains and BDT units carry linear side-chains.

### 9.3 NONCOVALENT INTERACTIONS IN MOLECULAR MATERIALS

As can be seen from the above discussion, there is a wide range of chemistries that can be used to tune the electronic and optical characteristics of organic semiconductors, in part by controlling the ways in which  $\pi$ -conjugated molecules and polymers pack in the solid state. We now turn our attention to the results of specific studies of  $\pi$ -conjugated molecules and polymers, both in neat (pure, single-component materials) and blend (multicomponent) forms, to show how computation and theory are driving the understanding required to a priori direct molecular packing and control materials-scale properties.

#### 9.3.1 The Oligoacene Series

To set a baseline for the discussion, we begin by examining the noncovalent interactions for the oligoacene series (i.e., benzene through hexacene,  $n_{\text{rings}} = 1-6$ , Fig. 9.5) [51], as these fused aromatic systems can be considered as templates from which most molecular organic semiconductor materials are constructed. There exist a number of investigations exploring the nature and strength of the noncovalent interactions in these systems, which provide further reference [38,50,108–117]: Grimme considered benzene through tetracene [118] and Sherrill studied benzene through pentacene [119], with both studies focusing on a few, ideal dimer configurations, while Podeszwa and Szalewicz developed comprehensive potential energy surfaces for benzene through anthracene [120–122]. Here, we will briefly discuss how the nature of the noncovalent interactions changes by starting with eclipsed cofacial arrange-



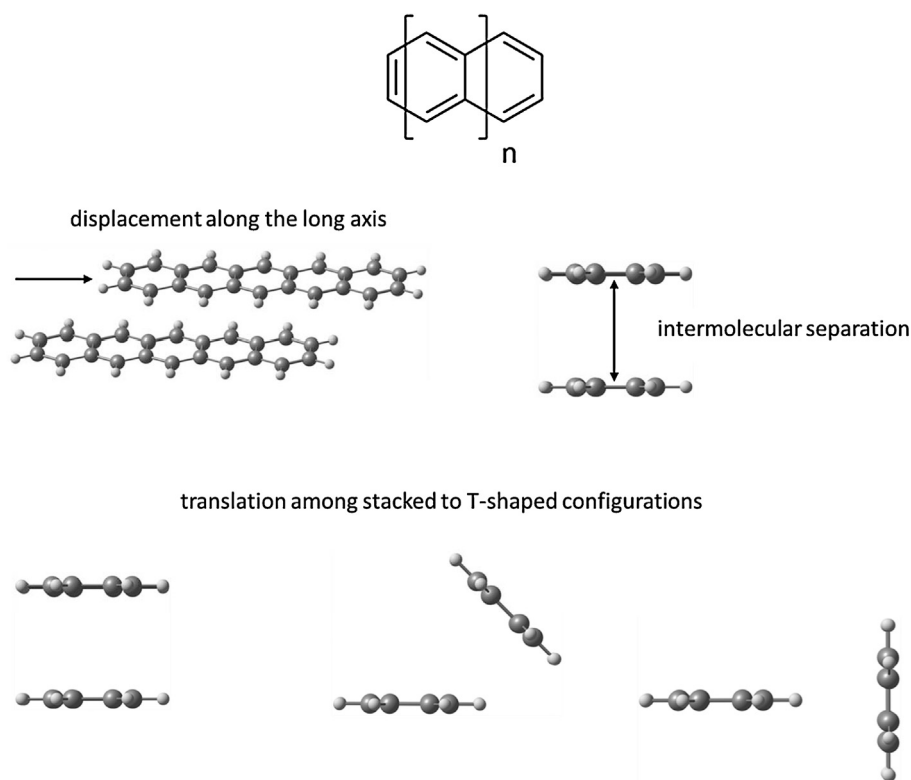


**FIGURE 9.5** Chemical structures of linear oligoacenes, where  $n$  is the number of fused rings:  $n = 0$  for benzene and  $n = 5$  for hexacene, and illustrations of pentacene dimers as a function of displacement along the long axis, varying intermolecular separation, and translation from stacked to T-shaped arrangements.

ments and then considering long-axis translation and rotation about the long-molecular axis (Fig. 9.5).

Using symmetry-adapted perturbation theory (SAPT) calculations at the SAPT0/jun-cc-pvdz level (here after simply denoted SAPT0, see Chapter 4 for further details) [123], full potential-energy surfaces for different oligoacene dimers under varying transformations were constructed [51]. For cofacial stacking configurations, the total SAPT0 interaction energies fall off quickly, as expected, as the intermolecular distances move beyond ca. 3.5 Å [124]. The exchange term decreases fastest [125], followed by the electrostatic and induction interactions, and then dispersion interactions. Notably, dispersion is the dominant attractive interaction at intermediate intermolecular separations (i.e., greater than 4.5 Å), though at even larger separations (i.e., larger than 7 Å) electrostatic interactions dominate. This is due to the distance dependence of the quadrupole–quadrupole interactions compared to the approximately distance dependence of dispersion.

Starting with cofacial dimers and slipping one molecule along the long axis (Fig. 9.5) to create a two-dimensional potential energy surface reveals large fluctuations of the total

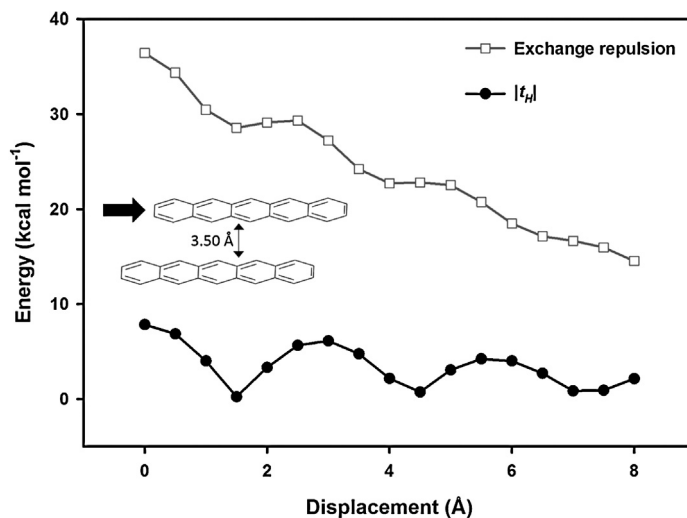


FIGURE 9.6 Intermolecular electronic couplings ( $t_H$ , closed circles), determined from the absolute value of the HOMO:HOMO overlap at the B3LYP/cc-pVDZ level of theory, and exchange-repulsion energies (open squares), determined at the SAPT0/jun-cc-pVDZ level of theory, for a pentacene dimer with an intermolecular separation of 3.5 Å. Starting from a perfectly cofacial configuration, the top molecule is gradually displaced along the molecular long axis, in the direction indicated by the large arrow. Adapted with permission from Ref. [38]. Copyright 2016 American Chemical Society.

interaction energies [51]. The number of peaks and valleys of the fluctuations for the total interaction, exchange, and induction energies correspond with the number of fused rings (i.e., one maximum/minimum for benzene and five maxima/minima for pentacene), while the electrostatic energy displays maxima and minima opposite the other contributions. The interaction energy minima are found to correspond with staggered arrangements, where bridging carbon-carbon bonds are above the rings of the adjacent molecule.

At this stage we can make an important connection between the noncovalent interactions discussed above and the expected electronic characteristics of molecular organic semiconductors [38,126]. Using a pentacene dimer with an intermolecular separation of 3.5 Å as reference, one can readily draw direct connections between the exchange energy and the intermolecular electronic coupling, a key parameter used to describe the charge-carrier transport properties of organic electronic materials (as was mentioned in Section 9.2.1). As shown in Fig. 9.6, a perfect cofacial stacking arrangement leads to the largest overlap of the highest-occupied molecular orbitals (HOMOs) on each molecule and, hence, the largest HOMO:HOMO electronic couplings [127] and exchange repulsion (see Chapter 1) [126,128]. The electronic coupling and exchange repulsion generally decrease as one molecule is slipped along the long axis at fixed 3.5 Å intermolecular separation. Both physical properties show an oscillatory pattern that correlates with the nodal pattern of the pentacene HOMO. It is useful to recall that the electronic coupling, as previously demonstrated for sexithienyl [127], goes to zero at varying molecular displacements, even though there remains considerable spatial overlap of the pentacene backbones. On the other hand, the exchange-repulsion energy in these systems

remains large in magnitude for all displacements considered at the 3.5 Å intermolecular separation, which arises from the fact that the exchange energy is determined from the overlap among all occupied orbitals, and is dominated by the electrons in the  $\sigma$  framework.

Concurrent consideration of increased intermolecular separation and long-axis translation leads to fairly complex three-dimensional surfaces [51]. For benzene, there is only one minimum in the potential energy surface, while for tetracene and beyond, multiple minima in the potential energy surfaces become apparent, in line with the two-dimensional potential energy surfaces. These extra minima are even more apparent for the longer oligoacenes (e.g., hexacene). For each of these situations, the low energy structures correspond to staggered cofacial arrangements that are reminiscent of TIPS-pentacene, where the bridging carbon-carbon bonds of one molecule are interacting with the face of the fused rings on the adjacent molecule [101,102]. While it is generally accepted that the TIPS groups dominate the packing, the nonbonded pentacene interactions act to fine tune the packing to result in the staggered, parallel-displaced arrangement (including a degree of slip along the short axis that is not considered here) of the  $\pi$ -conjugated systems.

In addition to long-axis translation, it is also of interest to explore the impact of rotating one of the molecules in the dimer, as it provides a preview of the expected intermolecular interactions observed in the herringbone packing configurations found for oligoacenes in the solid state [51]. Starting with rotation of one of the co-facial molecules by either 45° or 90° (T-shaped) and adjusting the intermolecular separation, it is found that the 45° dimer is the least stable configuration considered for all acenes in the series, though as the acene length increases, the most stable configuration changes. For benzene, the T-shaped dimer is the most stable, with 45° and eclipsed dimers being approximately equally unfavorable. In anthracene, the eclipsed dimer is intermediate of the 45° and 90° dimers, while for pentacene the eclipsed dimer is slightly more stable than the 90° dimer. Rotation of the one of the molecules in the dimer from 0° to 90° at fixed intermolecular separations (Fig. 9.5) reveals that for all systems the evolution of the total intermolecular interaction energy follows qualitatively those of exchange and electrostatics; minima are found at 20° and 90°, with a maximum at about 60° (i.e., exchange is more repulsive when electrostatics are more attractive). Here, electrostatics are dominated by charge penetration at the intermolecular distances considered. Thus, both exchange and electrostatics are dependent on the extent of orbital overlap with their contributions being of opposite sign. We note that the intermolecular angles found in the oligoacene crystal structures (approximately 50° to 80° depending on the oligoacene) lie near the least stable intermolecular interaction energies. This points to a limitation in the current analysis, suggesting that important terms are not fully accounted for in a two-body SAPT0 approach [129–132]. Thus, models aiming to predict crystal packing need to go beyond such approaches [133].

The analysis of the noncovalent interaction energies of oligoacene dimers reveals the complexity of molecular crystal engineering, with the small energy differences among rather different configurations providing a clear picture of why polymorphism is such a common phenomenon in these systems [51]. We now turn to studies on functionalized oligoacenes to highlight how chemical substitution can impart novel molecular packing in the solid state and, in turn, electronic properties.

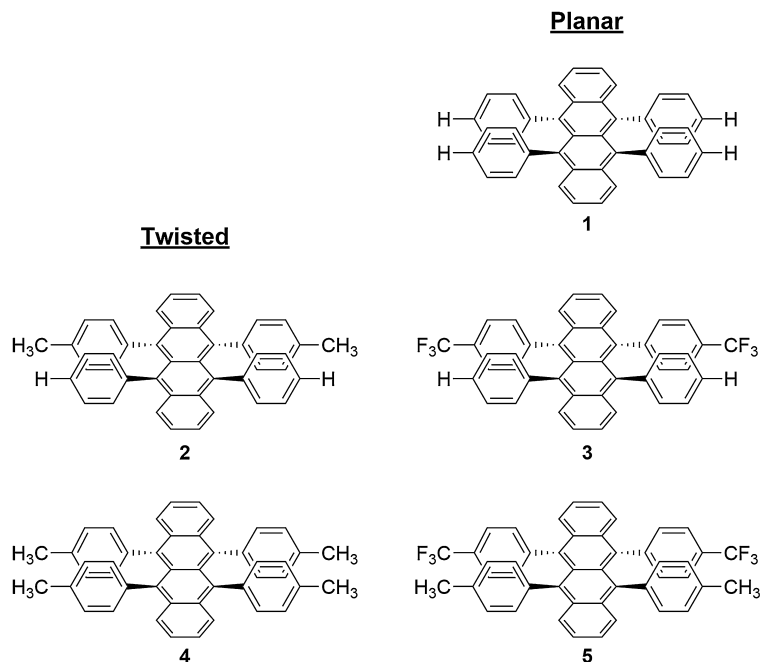


FIGURE 9.7 Chemical structures of rubrene **1** [144] and representative rubrene derivatives **2–5** [46]. **1**, **3**, and **5** possess planar tetracene backbones in their reported crystal structures, while **2** and **4** are twisted. Adapted with permission from Ref. [126]. Copyright 2015 American Chemical Society.

### 9.3.2 Rubrene: Solid-State Structure Determined by a Balance of Intramolecular and Intermolecular Noncovalent Interactions

As noted in the introduction, rubrene (labeled **1** in Fig. 9.7) is an exemplar molecular organic semiconductor in terms of measured charge-carrier transport characteristics. It also provides an important example of how chemical substitution can impact in significant ways the solid-state molecular packing not only at the intermolecular level but also at the intramolecular level. For rubrene, large hole mobilities (as high as  $40 \text{ cm}^2 \text{ V}^{-1} \text{ s}^{-1}$ ) [39] arise from strong intermolecular electronic couplings [128,134–136] that are a result, in part, of the tetracene backbones being planar in the solid state [137,138]. Fig. 9.7 illustrates that the tetracene backbone in rubrene is substituted along the periphery by four phenyl groups. Electronic-structure calculations on isolated rubrene molecules show that these phenyl rings make the tetracene backbone of an isolated rubrene molecule preferentially twist ( $\sim 40^\circ$ ) [139–142], a result confirmed by experimental evidence of twisted conformations both in solution [44,140] and in thin films [139,143]. Hence, for future materials design, there is interest in understanding why the tetracene backbone twists when rubrene is isolated and [66] what intermolecular interactions in the solid state might lead to the planarization of the backbone [126].

To explore these questions, a large series of rubrene derivatives were studied, five of which are shown in Fig. 9.7 [126]. For all rubrene derivatives considered, rubrene conformations with a twisted tetracene core (with twists of  $30^\circ$  to  $40^\circ$  in a helical-like fashion) are favored by

ca. 2 to 4 kcal/mol over rubrenes where the tetracene backbone is constrained to be planar. These results are consistent with previous theoretical studies [44,139–142]. For an isolated tetracene molecule, the planar conformation is nearly 5 kcal/mol more stable than conformations with twists similar to those in rubrene [145]. Hence, the tetracene backbone finds itself in a highly unfavorable conformation in rubrene. The nearly equivalent stabilization induced by twisting the tetracene backbone across the series indicates that the exact nature and positions of the substituents on the phenyl rings have only a small effect on the energetics of the molecular structure.

For isolated rubrene molecules, it is noncovalent intramolecular interactions between phenyl groups on the same side of the molecule that are responsible for the twisting. The phenyl pairs anchored to the central rings of the tetracene backbone are constrained to an intermolecular separation (based on interatomic distances) of approximately 3 Å at their closest point of contact.

To explore the impact of this close contact, phenyl pairs were extracted from the rubrene structures (with the broken carbon–carbon bond replaced by a carbon–hydrogen bond) and the noncovalent intermolecular interactions of the phenyl pair evaluated at the SAPT0 level of theory. The analysis reveals that, to minimize the unfavorable exchange interactions at such a close distance, the phenyl rings move away from the cofacial arrangement of a perfect  $D_{2h}$  conformation, resulting in a torque in the tetracene backbone. The repulsive exchange energy in these phenyl pairs is ca. +20 to +23 kcal/mol, an energy that is nearly twice as large as the dispersion and three times as large as the electrostatic energies. While these relative values are consistent with those for the benzene dimers at 3 Å, they are in absolute values about half as large as those for the fully eclipsed ( $D_{2h}$ ) benzene dimer at 3 Å [50].

Given that rubrene wants to maintain a twisted tetracene core, the question arises as to why some rubrene derivatives pack with a planar tetracene core in the solid state. The answer to this question is complex, and there remain many issues to address to provide a full understanding. However, a key outcome of the SAPT0 investigation is that interactions both within the plane, where the tetracene cores overlap, and between these planes, where the phenyl rings directly interact, assist in the planarization of the tetracene core [126].

### 9.3.3 Azapentacenes and Benzodithiophene as Model Systems to Investigate the Impacts of Heteroatom Substitution

The query now turns to how heteroatom substitution impacts noncovalent interactions in these materials and, in turn, the intermolecular electronic couplings. We start with a series of azapentacenes (Fig. 9.8) to explore how nitrogen-atom substitution modulates the characteristics set forth by the oligoacenes [38]. SAPT0 results for cofacial configurations at an intermolecular distance of 3.50 Å generally confirm predictions from experiment and previous calculations on small model systems: Introducing nitrogen into the  $\pi$ -conjugated backbone reduces the exchange repulsion, with each successive substitution of two nitrogen atoms for two –CH groups (e.g., from pentacene to the diazapentacenes and tetraazapentacenes) lowering the exchange repulsion by 2.5 to 4.7 kcal/mol. The reduction in the exchange repulsion (arising from smaller wavefunction overlap with increasing nitrogen content) is evidence for

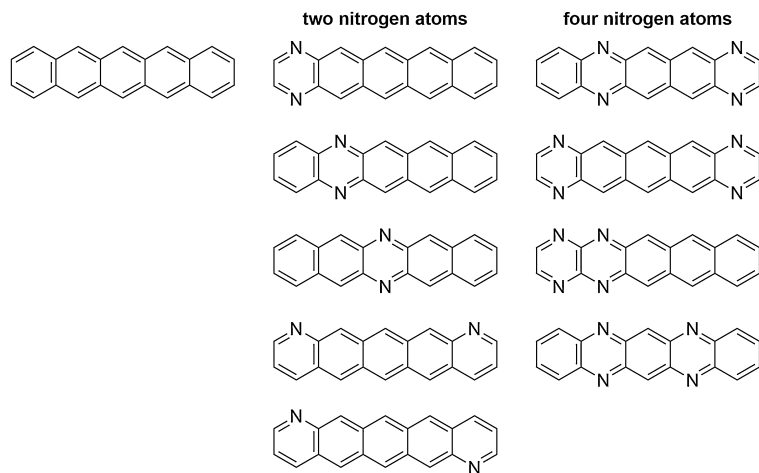


**FIGURE 9.8** Chemical structures of pentacene (left) and select diazapentacenes (middle) and tetraazapentacenes (right). Adapted with permission from Ref. [38]. Copyright 2016 American Chemical Society.

contracted electron density in the *N*-heteropentacenes. The dispersion and electrostatic energies are also generally reduced with nitrogen substitution. Hence, even though the molecules in the model series are iso-electronic and the same intermolecular separations are considered, the nature and strength of the intermolecular interactions vary in important ways with the rather subtle changes in chemistry.

Likewise, the electronic couplings are found to decrease with nitrogen substitution, with the exact decrease depending on the specific location of functionalization and orientation of the molecules in the azapentacene pairs [38]. As with pentacene, the azapentacenes show the expected correlation between exchange-repulsion and intermolecular electronic coupling, as both factors depend on the degree of wavefunction overlap. The scale of these energies, however, is considerably altered by the preferred molecular orientation. Due to dipole moments that arise from asymmetric nitrogen substitution, increased electrostatic interactions favor dimer configurations with less spatial overlap among the majority aromatic hydrocarbon components of the molecular structures, resulting in smaller electronic couplings.

Positional disorder of thiophene atoms in thienoacenes, and specifically in anthradithiophenes (ADT), has been related to the varying charge-carrier transport characteristics of the molecular materials derived from these systems [146,147]. As thin films of the molecular organic semiconductor materials are generally disordered, pathways of consistent molecular alignments that mitigate the impact of charge trapping sites (e.g., defect sites within the material that lead to electronic disorder) are necessary to provide efficient charge-carrier transport conduits through the active layer. From a materials design standpoint, it is important to realize that the substitution of thiophene into an acene structure can lead to an isomeric mixture of products [146,148–150]. In addition to isomeric purity, molecular symmetry can play a role. For molecules with low degrees of symmetry, adjacent molecules can pack in a disordered manner despite the molecules being isomerically equivalent. For isomerically pure ADTs, the

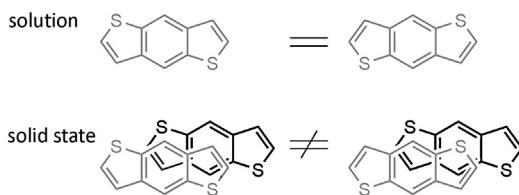


**FIGURE 9.9** Illustration of the disordermer concept for anti-benzodithiophene (BDT). The gray structures in solution (top row) are equivalent due to their averaged molecular motions. In the solid state (bottom row), the molecular positions are fixed so that the molecules cannot reorient. In this case, there are two possible disordermers with respect to the black BDT molecules. *Adapted from Ref. [147] by permission of The Royal Society of Chemistry.*

anti-isomer shows the lowest degree of thiophene positional disorder in the experimental crystal structures [146,149], which could lead to more homogeneous charge-carrier transport pathways and offers a plausible explanation for the larger hole mobilities determined from transistor studies.

To discuss the effects of disorder in a more descriptive manner, the concept of the disordermer—a form of intermolecular dissimilarity between regiochemically identical molecules due to disorder in the crystalline state—was recently introduced [147]. Fig. 9.9 demonstrates this concept with anti-benzodithiophene (BDT). We note that the syn configuration of BDT is one in which the sulfur atoms in the thiophene rings lie on the same side of the molecule. In solution, the two BDT configurations drawn at the top of Fig. 9.9, due to their averaged motion, are equivalent. However, in the solid state, the orientational disorder of the gray molecules can be seen with respect to the black BDT molecules. Since the positions of the molecules in the solid state are fixed (i.e., translation and rotational motion of the molecule are prevented), there appears two disordermers.

SAPT0 and density functional theory (DFT) calculations of syn and anti-BDT disordermers reveal important differences in the noncovalent interactions and subsequent intermolecular electronic couplings as a function of the disordermer [147]. In general, contacts where sulfur atoms are in close proximity are less energetically favorable than those where the sulfur atoms are further away from each other, due to large exchange-repulsion energies, while the electronic couplings tend to be larger when direct sulfur contacts are present. These results can be related back to the characteristics of isomerically pure ADT molecular materials. Analysis of the ADT crystal structures [146,148–150] shows that the dominant disordermers tend to minimize sulfur contacts among nearest neighbors: The anti-ADT isomer is able to sustain a pattern of minimal sulfur contacts in the solid state, while the symmetry of the syn ADT isomer does not allow this to occur, resulting in the presence of much more disorder in the crystal. The larger degree of disorder in syn ADT appears to be the reason behind the worse transistor performance when compared to transistors using anti-ADT as the active layer. Thus, while heteroatoms are widely used in the design of organic semiconductors, making seemingly subtle changes in the chemistry of the  $\pi$ -conjugated backbone through heteroatom substitution to alter the redox and (opto)electronic characteristics, can have wide ranging materials implications.

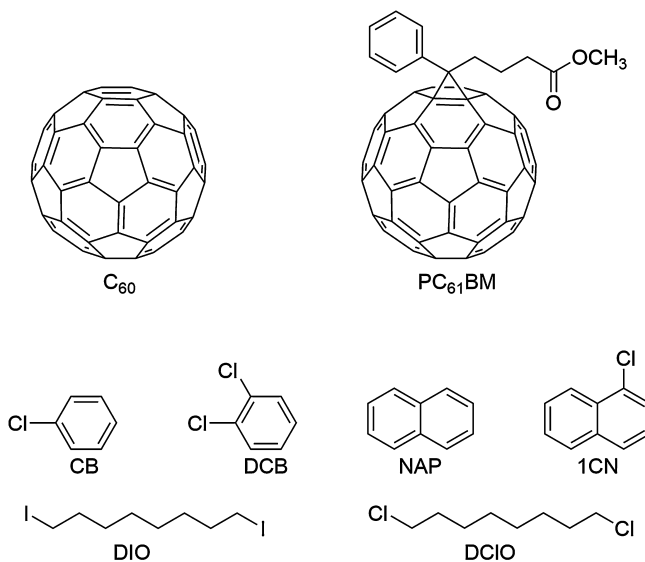


FIGURE 9.10 Chemical structures of C<sub>60</sub>, PC<sub>61</sub>BM (phenyl-C<sub>61</sub>-butyric acid methyl ester), chlorobenzene (CB), *o*-dichlorobenzene, naphthalene (NAP), 1-chloronaphthalene (1CN), 1,8-diiodooctane (DIO), and 1,8-dichlorooctane (DCIO).

### 9.3.4 Noncovalent Interactions in Fullerenes and Polymer:Fullerene Blends: Implications for Processing and Solar Cells

To this point, we have considered only neat, or pure, materials. However, ink formulations from which organic semiconductors are deposited are generally multicomponent systems. One of the more promising applications for organic semiconductors, as solar cells, requires a blend of at least two materials in the active layer. Hence, there is a need to understand how variations in noncovalent interactions can impact multicomponent systems across the field of organic electronics.

We start with an analysis of fullerenes, namely PC<sub>61</sub>BM (phenyl-C<sub>61</sub>-butyric acid methyl ester, Fig. 9.10), in solution [151]. In combination with chlorinated solvents, high-boiling point solvent additives are typically used during the solution processing of organic photovoltaic (OPV) active-layer formulations to impact the morphological/topological features of the bulk heterojunction (BHJ) multicomponent thin film. However, little is known as to how and why these additives affect solubility.

The unsubstituted fullerene, C<sub>60</sub>, can be used as a baseline to understand PC<sub>61</sub>BM solubility [151]. Potential energy surfaces were computed at the SAPT0 level of theory for C<sub>60</sub>-solvent (either chlorobenzene [CB] or *o*-dichlorobenzene [DCB]) and C<sub>60</sub>-additive interactions. The results indicate that the C<sub>60</sub>-DCB interaction is 0.5 kcal/mol more stable than C<sub>60</sub> with CB, a consequence of the extra chlorine atom in DCB, which increases each of the three stabilizing (electrostatic, dispersion, induction) terms. For the C<sub>60</sub>-additive interactions, the strengths of the interactions follow: 1-chloronaphthalene (1CN) > unsubstituted naphthalene (NAP) > 1,8-dichlorooctane (DCIO). Though DCIO lacks  $\pi$ -character, when compared



to DCB (with two chlorine atoms), the two systems show similar dispersion interactions with  $C_{60}$ , while the centrosymmetric nature of DCIO (and the resulting zero dipole moment) leads to limited electrostatic and induction interactions. The exchange-repulsion interactions increase for the  $C_{60}$ -solvent interactions in identical ways for both CB and DCB, while the increase is steeper for 1CN and NAP due to greater number electrons (including the aromatic  $\pi$  electrons) that increase the exchange term.

For the  $PC_{61}BM$ -solvent interactions, the repulsive wall of the potential energy surface rises at a smaller interaction distance (6.4 Å) when compared to the  $C_{60}$ -solvent interactions (6.8 Å). These differences are indicative of effects due to the fullerene adduct, and correlate with the higher solubility of  $PC_{61}BM$  in these solvents, especially for  $PC_{61}BM$  in CB. Turning to the  $PC_{61}BM$ -additive interactions, while DCIO reveals a tendency for much weaker binding with  $PC_{61}BM$  when compared to CB and DCB, 1CN and NAP interact rather strongly and at similar center-of-mass distances, results that are in line with those of  $C_{60}$ . Across the solvents and additives considered, the intermolecular interactions tend to be stronger with  $PC_{61}BM$  when compared to  $C_{60}$ , a factor directly attributable to the adduct.

The SAPT0-derived noncovalent intermolecular interactions can be related, in part, to the widely used Hildebrand and Hansen solubility parameters [151–153]. The Hildebrand parameter ( $\delta_T$ ) corresponds to the square-root of the cohesive energy density, i.e., the intermolecular interaction energy in the solid state per unit volume. Hansen further separated the Hildebrand parameter into three intermolecular contributions (which are referred to as the Hansen solubility parameters): dispersion ( $\delta_D$ ), Coulombic or dipole-dipole ( $\delta_P$ ), and hydrogen-bonding ( $\delta_H$ ) interactions. Moreover, we have shown with molecular dynamics (MD) simulations using the OPLS-AA force field the ability to evaluate Hildebrand and Hansen parameters for  $PC_{61}BM$ ,  $PC_{71}BM$  (phenyl- $C_{71}$ -butyric acid methyl ester), DCB, and CB with good semiquantitative agreement with experiment. In this context, the comparisons made here are qualitative, and provide an upper bound for the noncovalent intermolecular interactions that are critical to determining the solubility parameters.

Having gained insight into how the substituent appended to the fullerene cage can affect solubility, we now describe how the substituent on the fullerene can impact interactions with  $\pi$ -conjugated polymers and, in turn, the mechanical properties as considered through the cohesive energies (i.e., a measure of the noncovalent interactions holding together molecular and polymer-based materials in the solid state). Here, we focus on two fullerenes— $PC_{61}BM$  and ICMA (indene- $C_{60}$ -mono adduct, Fig. 9.11)—and the widely studied  $\pi$ -conjugated polymer poly(3-hexylthiophene) (P3HT).

The Hildebrand parameters computed from MD simulations using the OPLS-AA force field for  $PC_{61}BM$  (10.7 (cal/cc)<sup>1/2</sup>) [154], ICMA (10.0 (cal/cc)<sup>1/2</sup>), and P3HT (9.2 (cal/cc)<sup>1/2</sup>) compare very favorably with experimental data [155,156]. Decomposition of the total interaction energy into dispersive, electrostatic, and hydrogen-bonded interactions yields the Hansen miscibility parameters [153]: The dispersion parameters [153] ( $\delta_D$ ) are identical for the two fullerenes (9.8 and 9.9 (cal/cc)<sup>1/2</sup> for ICMA and  $PC_{61}BM$ , respectively). The contribution from electrostatic interactions, however, is reduced in ICMA when compared with  $PC_{61}BM$ , as the combined hydrogen-bond plus electrostatic term ( $\delta_P + \delta_H$ ) is 4.0 (cal/cc)<sup>1/2</sup> in  $PC_{61}BM$  and only 2.0 (cal/cc)<sup>1/2</sup> in ICMA. The same term in P3HT is 3.0 (cal/cc)<sup>1/2</sup>. The Hansen parameters arising from the simulations suggest that the larger ( $\delta_P + \delta_H$ ) term in  $PC_{61}BM$ , a direct function of the polar nature of the side chain, could lead to a smaller driving

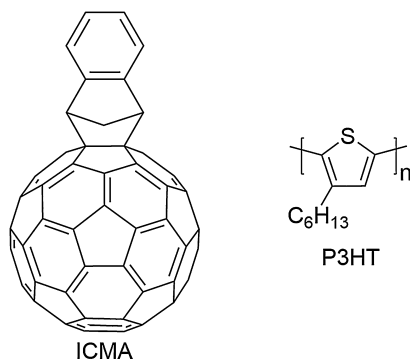


FIGURE 9.11 Chemical structures of ICMA (indene-C<sub>60</sub>-mono adduct) and poly(3-hexylthiophene) (P3HT).

force for mixing with P3HT when compared to ICMA, even though both fullerene derivatives lie within the solubility sphere of P3HT [157]. This hypothesis is consistent with the experimental observation of the formation of fullerene clusters in P3HT:PC<sub>61</sub>BM mixtures [158,159] and the improved miscibility of P3HT:indene-C<sub>60</sub>-bis-adduct (ICBA) blends when compared to P3HT:PCBM [159].

Turning to the mechanical properties of the pure materials, the calculated uniaxial elongation/tensile moduli for an elastic material, a measure of stiffness for the substituted fullerenes, are determined to be  $8.1 \pm 0.01$  GPa for PC<sub>61</sub>BM and  $8.3 \pm 0.01$  GPa for ICMA; the 0.2 GPa larger modulus for ICMA is a function of the shorter adducts that result in closer packing and higher density [160]. While the differences in tensile modulus might at first appear to be minor, extremely small error bars suggest that this is a notable difference. The cohesion energy obtained from MD deformation simulations for ICMA is  $0.36 \pm 0.05$  J m<sup>-2</sup>, a result that is somewhat larger than the experimental value ( $0.23$  J m<sup>-2</sup>) [160]. Notably, ICMA clusters are formed during film formation from deposition with chlorobenzene, the solvent used in the corresponding experimental investigation, which could reduce the film cohesion measured experimentally [161]. The calculated cohesion energy for PC<sub>61</sub>BM is  $0.50 \pm 0.05$  J m<sup>-2</sup>, a result that is in very close agreement with the experimental result of  $0.51 \pm 0.07$  J m<sup>-2</sup> [160]. These results provide confidence that the fullerene intermolecular interactions are well described by the force field.

Deformation simulations, where the simulation box was elongated in one direction to induce strain on the system, were carried out at the MD level for pure P3HT and 1:1 weight-percent mixtures of P3HT:PC<sub>61</sub>BM and P3HT:ICMA for 50-monomer (8.3 kDa) and 200-monomer (33.2 kDa) P3HT. The pure polymer simulations, as expected, show very different behavior, with the higher-molecular-weight polymer able to handle more strain, a result directly attributable to the presence of substantial entanglements in the higher-molecular-weight system [160]. The addition of the fullerene derivatives to low-molecular-weight P3HT results in no plateau with strain. In contrast, the 200-monomer P3HT:fullerene blends do show a stress plateau past 100% strain. For ICMA:P3HT mixtures, a slightly larger stress is observed at strains greater than 200%, indicative of a greater degree of entanglements in this blend compared to the P3HT:PC<sub>61</sub>BM mixtures. Upon elongation, due to stronger intermolec-

ular interactions, P3HT:ICMA mixtures tend to form thick, intermixed fibrillar structures, in contrast to independent P3HT fibrils with fewer bound PC<sub>61</sub>BM molecules in the case of P3HT:PC<sub>61</sub>BM mixtures [160]. Moreover, simulations of polymer/fullerene bilayers show that fracture tends to occur within the ICMA layer for the P3HT/ICMA bilayer, whereas the fracture occurs at the interface for a P3HT/PC<sub>61</sub>BM bilayer. Hence, relatively modest changes in fullerene chemistry can lead to rather important effects on the mechanical properties of BHJ active layers in OPV.

Our final example concerns how noncovalent interactions, driven by a combination of the chemistry of  $\pi$ -conjugated polymer backbones and variations in the chemistry of the alkyl chains appended to the backbone, drive the preferred configurations between fullerenes and copolymers based on alternating electron-rich and electron-poor moieties. A recent study by Graham and coworkers showed that, in the case of the PBDTTPD (composed of alternating thieno[3,4-b]thiophene-pyrrole-4,6-dione and benzodithiophene units) family of polymers, see Fig. 9.4, changes in the nature and positions of the alkyl side-chains affect the efficiency of solar cells with fullerene acceptors to a very significant extent [106]. As we discussed in Section 9.2.4, the locations of the fullerene molecules over the conjugated polymer backbones depend on the nature and position of the alkyl side-chains [162]. Furthermore, intermolecular interactions between polymer chains and fullerene molecules are known to play crucial roles on the electron-transfer rates [163], exciton binding energies [164], and processes of charge separation and charge recombination [163]. Hence, the performance of OPV devices does depend on the intermolecular arrangements and resulting energy landscapes at the interfaces between the polymer and fullerene phases.

As a first step, it was of interest to determine whether, in the absence of any side-chains, a fullerene molecule has a preference to locate over the electron-rich or electron-poor moieties of the copolymer. Thus, we considered a PBDTTPD oligomer without side-chains interacting with C<sub>60</sub> in two (face-on and edge-on) orientations, see Fig. 9.12 (all calculations were carried out at the  $\omega$ B97XD/6-31G(d,p) level of theory, with the coordinates of the oligomer frozen during geometry optimizations of the complexes to limit reconfiguration of the backbone). The difference in interaction energies ( $\omega$ B97XD/6-31G(d,p)) when C<sub>60</sub> sits on top of the electron-rich (BDT) unit with respect to when it sits on top of the electron-poor (TPD) unit is in fact within thermal energy at room temperature (0.4 kcal/mol) [165]. Hence, in the absence of alkyl side chains, C<sub>60</sub> has no preference on top of the backbone. Edge-on conformations are, however, much less favorable.

Addition of the phenyl butyric acid methyl ester functional group to C<sub>60</sub> to form PC<sub>61</sub>BM makes the nature of the interactions between polymer and fullerene more complex. The functional group introduces a dipole moment [166,167] that adds a significant electrostatic component to the interactions, in addition to the larger dispersion forces. The presence of the attachment of the functional group to the fullerene cage also induces more positional disorder as many orientations of the functional groups are possible, examples of which are shown in Fig. 9.13 [168].

MD simulations of the pure phases of the polymers of Fig. 9.4 using the OPLS-AA force field, reveal that linear alkyl side chains on the PBDTTPD backbone tend to extend away from the polymer backbone, while the bulkier branched side-chains remain in closer proximity [168]. Thus, on average, moieties with linear chains will have more room to accommodate fullerenes than those with branched side-chains. For the blends, the probabilities of finding

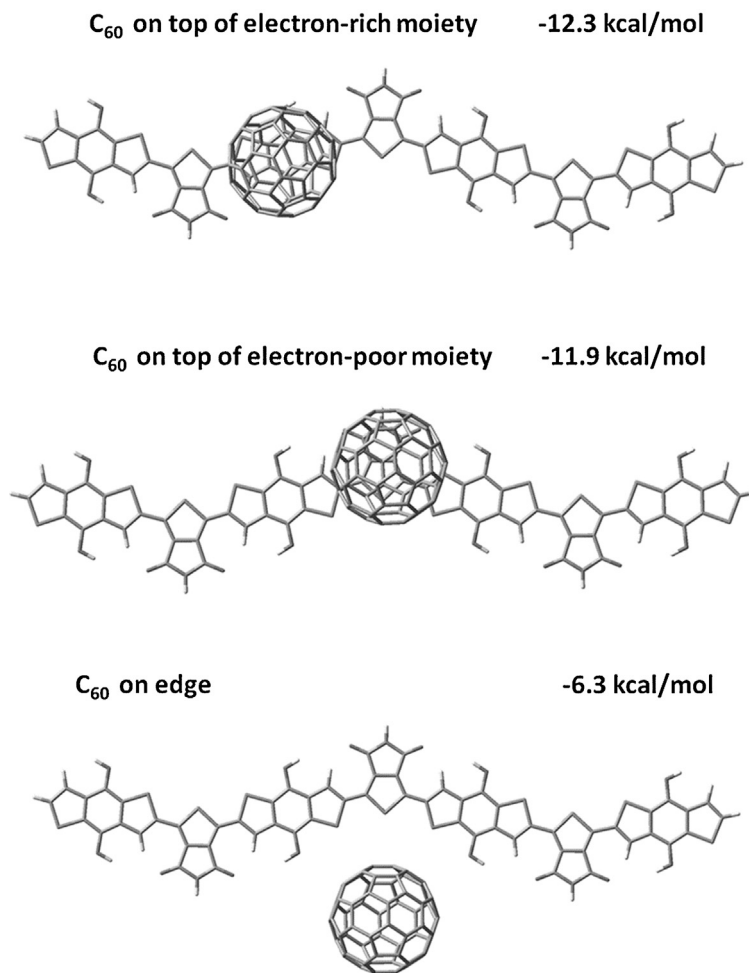


**FIGURE 9.12** Illustration of the optimized geometries for two face-on configurations and an edge-on configuration of the poly-benzo[1,2-b:4,5-b']dithiophene-thieno[3,4-c]pyrrole-4,6-dione (PBDTTPD) oligomer–fullerene complex at the  $\omega$ B97XD/6-31G(d,p) level of theory. The calculated counterpoise-corrected interaction energies at  $\omega$ B97XD/6-31G(d,p) level of theory are also given [165].

PC<sub>61</sub>BM close to the BDT and TPD moieties can be extracted from the snapshots of the MD simulations. In going from branched side-chains on the TPD moieties [PBDTTPD(C14-EH)] to all linear side-chains [PBDTTPD(C14-C8)] and then to branched side-chains on the BDT moieties [PBDTTPD(EH-C8)], see Fig. 9.4, an increase in the probability of finding PC<sub>61</sub>BM close to the TPD moieties is observed (34.1%, 42.3%, and 47.2%, respectively) [168]. The probability of finding PC<sub>61</sub>BM close to the BDT or TPD moiety is mainly determined by interactions between PBDTTPD and PC<sub>61</sub>BM, while the orientations of the PC<sub>61</sub>BM on top of the conjugated polymer backbone depend on both PBDTTPD–PC<sub>61</sub>BM and PC<sub>61</sub>BM–PC<sub>61</sub>BM interactions.

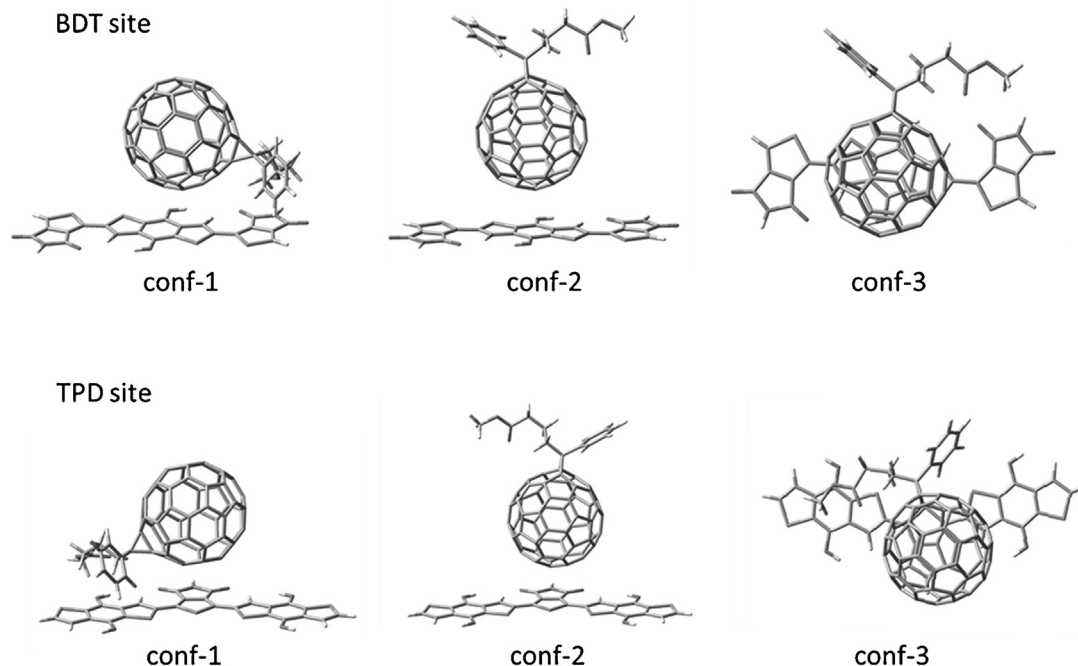


FIGURE 9.13 Illustration of three typical orientations of PC<sub>61</sub>BM relative to the PBDTTPD backbone, i.e., conf-1, conf-2, and conf-3. The BDT site and TPD site sections correspond to the cases of PC<sub>61</sub>BM close to either the BDT or TPD moiety of PBDTTPD, respectively. The side-chains of PBDTTPD are not shown for the sake of clarity [168].

## 9.4 SYNOPSIS

We are at the very initial stages of developing the quantum-chemical foundation needed for an a priori computational design of organic semiconductors. The chemistry used to develop organic electronic materials is vast. As highlighted throughout this chapter, seemingly subtle changes in molecular chemical composition and architecture to alter the redox or (opto)electronic properties of isolated molecules can greatly impact the nature and strength of the noncovalent interactions that are important to solubility, solid-state packing, and the macroscopic materials characteristics. We are therefore faced with the significant challenge to develop the multiscale models and methods necessary to enable chemical control of these features, in order to improve the design of these important electronically and optically active materials.

### Acknowledgments

This work has been supported in part by King Abdullah University of Science and Technology (KAUST), the KAUST Competitive Research Grant Program, and the Office of Naval Research Global (Award N62909-15-1-2003). We acknowledge the IT Research Computing Team and Supercomputing Laboratory at King Abdullah University of Science & Technology (KAUST) for providing computational and storage resources. The work at the University of

Kentucky was supported by a seed grant from the Center for Applied Energy Research (CAER) and start-up funds provided by the University of Kentucky Vice President for Research. We gratefully thank Drs. Sean Ryno, Naga Rajesh Tummala, and Chris Sutton for stimulating discussions.

## References

- [1] P.T. Herwig, K. Müllen, *Adv. Mater.* 11 (1999) 480–483.
- [2] D. Fournier, R. Hoogenboom, U.S. Schubert, *Chem. Soc. Rev.* 36 (2007) 1369–1380.
- [3] C.J. Hawker, K.L. Wooley, *Science* 309 (2005) 1200–1205.
- [4] Y.-J. Cheng, S.-H. Yang, C.-S. Hsu, *Chem. Rev.* 109 (2009) 5868–5923.
- [5] A.C. Grimsdale, K. Leok Chan, R.E. Martin, P.G. Jokisz, A.B. Holmes, *Chem. Rev.* 109 (2009) 897–1091.
- [6] J.W. Colson, W.R. Dichtel, *Nat. Chem.* 5 (2013) 453–465.
- [7] M. Pope, H.P. Kallmann, P. Magnante, *J. Chem. Phys.* 38 (1963) 2042–2043.
- [8] D.L. Morel, A.K. Ghosh, T. Feng, E.L. Stogryn, P.E. Purwin, R.F. Shaw, C. Fishman, *Appl. Phys. Lett.* 32 (1978) 495–497.
- [9] C.W. Tang, *Appl. Phys. Lett.* 48 (1986) 183–185.
- [10] C.W. Tang, S.A. VanSlyke, *Appl. Phys. Lett.* 51 (1987) 913–915.
- [11] H. Koezuka, A. Tsumura, T. Ando, *Synth. Met.* 18 (1987) 699–704.
- [12] J.H. Burroughes, D.D.C. Bradley, A.R. Brown, R.N. Marks, K. Mackay, R.H. Friend, P.L. Burns, A.B. Holmes, *Nature* 347 (1990) 539–541.
- [13] M. Hiramoto, H. Fujiwara, M. Yokoyama, *Appl. Phys. Lett.* 58 (1991) 1062–1064.
- [14] F. Garnier, R. Hajlaoui, A. Yassar, P. Srivastava, *Science* 265 (1994) 1684–1686.
- [15] J.J.M. Halls, C.A. Walsh, N.C. Greenham, E.A. Marseglia, R.H. Friend, S.C. Moratti, A.B. Holmes, *Nature* 376 (1995) 498–500.
- [16] G. Yu, J. Gao, J.C. Hummelen, F. Wudl, A.J. Heeger, *Science* 270 (1995) 1789–1791.
- [17] R.H. Friend, R.W. Gymer, A.B. Holmes, J.H. Burroughes, R.N. Marks, C. Taliani, D.D.C. Bradley, D.A.D. Santos, J.L. Brédas, M. Logdlund, W.R. Salaneck, *Nature* 397 (1999) 121–128.
- [18] G. Horowitz, *J. Mater. Chem.* 9 (1999) 2021–2026.
- [19] J.M. Hales, J. Matichak, S. Barlow, S. Ohira, K. Yesudas, J.-L. Brédas, J.W. Perry, S.R. Marder, *Science* 327 (2010) 1485–1488.
- [20] R.L. Gieseking, S. Mukhopadhyay, C. Risko, S.R. Marder, J.-L. Brédas, *Adv. Mater.* 26 (2014) 68–84.
- [21] R.L. Gieseking, S. Mukhopadhyay, S.B. Shiring, C. Risko, J.-L. Brédas, *J. Phys. Chem. C* 118 (2014) 23575–23585.
- [22] S. Barlow, J.-L. Brédas, Y.A. Getmanenko, R.L. Gieseking, J.M. Hales, H. Kim, S.R. Marder, J.W. Perry, C. Risko, Y. Zhang, *Mater. Horiz.* 1 (2014) 577–581.
- [23] A.C. Arias, J.D. MacKenzie, I. McCulloch, J. Rivnay, A. Salleo, *Chem. Rev.* 110 (2010) 3–24.
- [24] I. McCulloch, et al., *Adv. Mater.* 21 (2009) 1091–1109.
- [25] P.J. Diemer, C.R. Lyle, Y. Mei, C. Sutton, M.M. Payne, J.E. Anthony, V. Coropceanu, J.-L. Brédas, O.D. Jurchescu, *Adv. Mater.* 25 (2013) 6956–6962.
- [26] P.G. Karamertzanis, G.M. Day, G.W.A. Welch, J. Kendrick, F.J.J. Leusen, M.A. Neumann, S.L. Price, *J. Chem. Phys.* 128 (2008) 244708.
- [27] S.L. Price, *Acc. Chem. Res.* 42 (2009) 117–126.
- [28] A.A. Virkar, S. Mannsfeld, Z. Bao, N. Stingelin, *Adv. Mater.* 22 (2010) 3857–3875.
- [29] S. Wen, G.J.O. Beran, *J. Chem. Theory Comput.* 8 (2012) 2698–2705.
- [30] H. Li, B.C.K. Tee, G. Giri, J.W. Chung, S.Y. Lee, Z. Bao, *Adv. Mater.* 24 (2012) 2588–2591.
- [31] H. Li, B.C.K. Tee, J.J. Cha, Y. Cui, J.W. Chung, S.Y. Lee, Z. Bao, *J. Am. Chem. Soc.* 134 (2012) 2760–2765.
- [32] R. Li, H.U. Khan, M.M. Payne, D.-M. Smilgies, J.E. Anthony, A. Amassian, *Adv. Funct. Mater.* 23 (2013) 291–297.
- [33] Y. Diao, B.C.K. Tee, G. Giri, J. Xu, D.H. Kim, H.A. Becerril, R.M. Stoltenberg, T.H. Lee, G. Xue, S.C.B. Mannsfeld, Z. Bao, *Nat. Mater.* 12 (2013) 665–671.
- [34] R. Noriega, J. Rivnay, K. Vandewal, F.P.V. Koch, N. Stingelin, P. Smith, M.F. Toney, A. Salleo, *Nat. Mater.* 12 (2013) 1038–1044.
- [35] J.W. Ward, R. Li, A. Obaid, M.M. Payne, D.-M. Smilgies, J.E. Anthony, A. Amassian, O.D. Jurchescu, *Adv. Funct. Mater.* 24 (2014) 5052–5058.

- [36] K. Wei Chou, H. Ullah Khan, M.R. Niazi, B. Yan, R. Li, M.M. Payne, J.E. Anthony, D.-M. Smilgies, A. Amassian, *J. Mater. Chem. C* 2 (2014) 5681–5689.
- [37] S. Himmelberger, D.T. Duong, J.E. Northrup, J. Rivnay, F.P.V. Koch, B.S. Beckingham, N. Stingelin, R.A. Segalman, S.C.B. Mannsfeld, A. Salleo, *Adv. Funct. Mater.* 25 (2015) 2616–2624.
- [38] C. Sutton, C. Risko, J.-L. Brédas, *Chem. Mater.* 28 (2015) 3–16.
- [39] J. Takeya, M. Yamagishi, Y. Tominari, R. Hirahara, Y. Nakazawa, T. Nishikawa, T. Kawase, T. Shimoda, S. Ogawa, *Appl. Phys. Lett.* 90 (2007) 102120.
- [40] V. Podzorov, V.M. Pudalov, M.E. Gershenson, *Appl. Phys. Lett.* 82 (2003) 1739–1741.
- [41] N. Karl, in: *Proceedings of the Yamada Conference LVI. The Fourth International Symposium on Crystalline Organic Metals, Superconductors and Ferromagnets, ISCOM 2001*, vols. 133–134, 2003, pp. 649–657.
- [42] P.G. Le Comber, A. Madan, W.E. Spear, *J. Non-Cryst. Solids* 11 (1972) 219–234.
- [43] A.R. Moore, *Appl. Phys. Lett.* 31 (1977) 762–764.
- [44] A.S. Paraskar, A.R. Reddy, A. Patra, Y.H. Wijsboom, O. Gidron, L.J.W. Shimon, G. Leitius, M. Bendikov, *Chem. Eur. J.* 14 (2008) 10639–10647.
- [45] N. Stingelin-Stutzmann, E. Smits, H. Wondergem, C. Tanase, P. Blom, P. Smith, D. de Leeuw, *Nat. Mater.* 4 (2005) 601–606.
- [46] K.A. McGarry, W. Xie, C. Sutton, C. Risko, Y. Wu, V.G. Young, J.L. Brédas, C.D. Frisbie, C.J. Douglas, *Chem. Mater.* 25 (2013) 2254–2263.
- [47] S. Bergantin, M. Moret, *Cryst. Growth Des.* 12 (2012) 6035–6041.
- [48] Y. Diao, L. Shaw, Z. Bao, S.C.B. Mannsfeld, *Energy Environ. Sci.* 7 (2014) 2145–2159.
- [49] A. Stone, *The Theory of Intermolecular Forces*, Oxford Univ. Press, Oxford, 2013.
- [50] E.G. Hohenstein, J. Duan, C.D. Sherrill, *J. Am. Chem. Soc.* 133 (2011) 13244–13247.
- [51] S.M. Ryno, C. Risko, J.-L. Brédas, *Chem. Mater.* 28 (2016) 3990–4000.
- [52] W. Pauli, *Z. Phys.* 31 (1925) 765–783.
- [53] W. Pauli, *Phys. Rev.* 58 (1940) 716–722.
- [54] S.E. Wheeler, K.N. Houk, *Mol. Phys.* 107 (2009) 749–760.
- [55] V. Coropceanu, Y. Li, Y. Yi, L. Zhu, J.-L. Brédas, *Mater. Res. Soc. Bull.* 38 (2013) 57–64.
- [56] V. Coropceanu, J. Cornil, D.A. da Silva Filho, Y. Olivier, R. Silbey, J.-L. Brédas, *Chem. Rev.* 107 (2007) 926–952.
- [57] J.-L. Brédas, D. Beljonne, V. Coropceanu, J. Cornil, *Chem. Rev.* 104 (2004) 4971–5004.
- [58] B. Lee, Y. Chen, D. Fu, H.T. Yi, K. Czelen, H. Najafov, V. Podzorov, *Nat. Mater.* 12 (2013) 1125–1129.
- [59] Y. Liu, Y. Wang, W. Wu, Y. Liu, H. Xi, L. Wang, W. Qiu, K. Lu, C. Du, G. Yu, *Adv. Funct. Mater.* 19 (2009) 772–778.
- [60] K. Xiao, Y. Liu, T. Qi, W. Zhang, F. Wang, J. Gao, W. Qiu, Y. Ma, G. Cui, S. Chen, X. Zhan, G. Yu, J. Qin, W. Hu, D. Zhu, *J. Am. Chem. Soc.* 127 (2005) 13281–13286.
- [61] Y. Liu, X. Sun, C.-a. Di, Y. Liu, C. Du, K. Lu, S. Ye, G. Yu, *Chem. Asian J.* 5 (2010) 1550–1554.
- [62] T. Okamoto, K. Kudoh, A. Wakamiya, S. Yamaguchi, *Chem. Eur. J.* 13 (2007) 548–556.
- [63] M.L. Tang, T. Okamoto, Z. Bao, *J. Am. Chem. Soc.* 128 (2006) 16002–16003.
- [64] M.L. Tang, S.C.B. Mannsfeld, Y.-S. Sun, H.A. Becerril, Z. Bao, *J. Am. Chem. Soc.* 131 (2009) 882–883.
- [65] J.G. Laquindanum, H.E. Katz, A.J. Lovinger, *J. Am. Chem. Soc.* 120 (1998) 664–672.
- [66] K. Niimi, S. Shinamura, I. Osaka, E. Miyazaki, K. Takimiya, *J. Am. Chem. Soc.* 133 (2011) 8732–8739.
- [67] A.N. Sokolov, S. Atahan-Evrenk, R. Mondal, H.B. Akkerman, R.S. Sánchez-Carrera, S. Granados-Focil, J. Schrier, S.C.B. Mannsfeld, A.P. Zombelt, Z. Bao, A. Aspuru-Guzik, *Nat. Commun.* 2 (2011) 437.
- [68] J.-I. Park, J.W. Chung, J.-Y. Kim, J. Lee, J.Y. Jung, B. Koo, B.-L. Lee, S.W. Lee, Y.W. Jin, S.Y. Lee, *J. Am. Chem. Soc.* 137 (2015) 12175–12178.
- [69] T. Okamoto, K. Kudoh, A. Wakamiya, S. Yamaguchi, *Org. Lett.* 7 (2005) 5301–5304.
- [70] K. Yamada, T. Okamoto, K. Kudoh, A. Wakamiya, S. Yamaguchi, J. Takeya, *Appl. Phys. Lett.* 90 (2007) 072102.
- [71] T.V. Pho, J.D. Yuen, J.A. Kurzman, B.G. Smith, M. Miao, W.T. Walker, R. Seshadri, F. Wudl, *J. Am. Chem. Soc.* 134 (2012) 18185–18188.
- [72] A. Mukherjee, S. Tothadi, G.R. Desiraju, *Acc. Chem. Res.* 47 (2014) 2514–2524.
- [73] M.L. Tang, Z. Bao, *Chem. Mater.* 23 (2011) 446–455.
- [74] J. Mei, Y. Diao, A.L. Appleton, L. Fang, Z. Bao, *J. Am. Chem. Soc.* 135 (2013) 6724–6746.
- [75] S. Subramanian, S.K. Park, S.R. Parkin, V. Podzorov, T.N. Jackson, J.E. Anthony, *J. Am. Chem. Soc.* 130 (2008) 2706–2707.
- [76] M.R. Battaglia, A.D. Buckingham, J.H. Williams, *Chem. Phys. Lett.* 78 (1981) 421–423.
- [77] A.L. Ringer, M.O. Sinnokrot, R.P. Lively, C.D. Sherrill, *Chem. Eur. J.* 12 (2006) 3821–3828.

- [78] D. Holmes, S. Kumaraswamy, A.J. Matzger, K.P.C. Vollhardt, *Chem. Eur. J.* 5 (1999) 3399–3412.
- [79] Y. Sakamoto, T. Suzuki, M. Kobayashi, Y. Gao, Y. Fukai, Y. Inoue, F. Sato, S. Tokito, *J. Am. Chem. Soc.* 126 (2004) 8138–8140.
- [80] E. Yagodkin, Y. Xia, V. Kalihari, C.D. Frisbie, C.J. Douglas, *J. Phys. Chem. C* 113 (2009) 16544–16548.
- [81] H. Moon, R. Zeis, E.-J. Borkent, C. Besnard, A.J. Lovinger, T. Siegrist, C. Kloc, Z. Bao, *J. Am. Chem. Soc.* 126 (2004) 15322–15323.
- [82] C.R. Swartz, S.R. Parkin, J.E. Bullock, J.E. Anthony, A.C. Mayer, G.G. Malliaras, *Org. Lett.* 7 (2005) 3163–3166.
- [83] M. Chikamatsu, A. Itakura, Y. Yoshida, R. Azumi, K. Yase, *Chem. Mater.* 20 (2008) 7365–7367.
- [84] W. Li, S. Albrecht, L. Yang, S. Roland, J.R. Tumbleston, T. McAfee, L. Yan, M.A. Kelly, H. Ade, D. Neher, W. You, *J. Am. Chem. Soc.* 136 (2014) 15566–15576.
- [85] Z. Fei, P. Boufflet, S. Wood, J. Wade, J. Moriarty, E. Gann, E.L. Ratcliff, C.R. McNeill, H. Sirringhaus, J.-S. Kim, M. Heeney, *J. Am. Chem. Soc.* 137 (2015) 6866–6879.
- [86] X. Zhang, Z. Lu, L. Ye, C. Zhan, J. Hou, S. Zhang, B. Jiang, Y. Zhao, J. Huang, S. Zhang, Y. Liu, Q. Shi, Y. Liu, J. Yao, *Adv. Mater.* 25 (2013) 5791–5797.
- [87] J. Wolf, F. Cruciani, A. El Labban, P.M. Beaujuge, *Chem. Mater.* 27 (2015) 4184–4187.
- [88] J.W. Jo, J.W. Jung, H.-W. Wang, P. Kim, T.P. Russell, W.H. Jo, *Chem. Mater.* 26 (2014) 4214–4220.
- [89] B. Carsten, J.M. Szarko, H.J. Son, W. Wang, L. Lu, F. He, B.S. Rolczynski, S.J. Lou, L.X. Chen, L. Yu, *J. Am. Chem. Soc.* 133 (2011) 20468–20475.
- [90] H.-Y. Chen, J. Hou, S. Zhang, Y. Liang, G. Yang, Y. Yang, L. Yu, Y. Wu, G. Li, *Nat. Photonics* 3 (2009) 649–653.
- [91] A.C. Stuart, J.R. Tumbleston, H. Zhou, W. Li, S. Liu, H. Ade, W. You, *J. Am. Chem. Soc.* 135 (2013) 1806–1815.
- [92] L. Yang, J.R. Tumbleston, H. Zhou, H. Ade, W. You, *Energy Environ. Sci.* 6 (2013) 316–326.
- [93] A.L. Briseno, R.J. Tseng, M.M. Ling, E.H.L. Falcao, Y. Yang, F. Wudl, Z. Bao, *Adv. Mater.* 18 (2006) 2320–2324.
- [94] S.C. Price, A.C. Stuart, L. Yang, H. Zhou, W. You, *J. Am. Chem. Soc.* 133 (2011) 4625–4631.
- [95] B.C. Schroeder, Z. Huang, R.S. Ashraf, J. Smith, P. D’Angelo, S.E. Watkins, T.D. Anthopoulos, J.R. Durrant, I. McCulloch, *Adv. Funct. Mater.* 22 (2012) 1663–1670.
- [96] D.J. Gundlach, et al., *Nat. Mater.* 7 (2008) 216–221.
- [97] K. Do, Q. Saleem, M.K. Ravva, F. Cruciani, Z. Kan, J. Wolf, M.R. Hansen, P.M. Beaujuge, J.-L. Brédas, *Adv. Mater.* 28 (2016) 8197–8205.
- [98] J. Mei, Z. Bao, *Chem. Mater.* 26 (2014) 604–615.
- [99] F. Zhang, Y. Hu, T. Schuettfort, C.-a. Di, X. Gao, C.R. McNeill, L. Thomsen, S.C.B. Mannsfeld, W. Yuan, H. Sirringhaus, D. Zhu, *J. Am. Chem. Soc.* 135 (2013) 2338–2349.
- [100] T. Lei, J.-H. Dou, J. Pei, *Adv. Mater.* 24 (2012) 6457–6461.
- [101] J.E. Anthony, J.S. Brooks, D.L. Eaton, S.R. Parkin, *J. Am. Chem. Soc.* 123 (2001) 9482–9483.
- [102] J.E. Anthony, D.L. Eaton, S.R. Parkin, *Org. Lett.* 4 (2002) 15–18.
- [103] C.D. Sheraw, T.N. Jackson, D.L. Eaton, J.E. Anthony, *Adv. Mater.* 15 (2003) 2009–2011.
- [104] H. Ebata, T. Izawa, E. Miyazaki, K. Takimiya, M. Ikeda, H. Kuwabara, T. Yui, *J. Am. Chem. Soc.* 129 (2007) 15732–15733.
- [105] A. El Labban, J. Warnan, C. Cabanetos, O. Ratel, C. Tassone, M.F. Toney, P.M. Beaujuge, *ACS Appl. Mater. Interfaces* 6 (2014) 19477–19481.
- [106] K.R. Graham, C. Cabanetos, J.P. Jahnke, M.N. Idso, A. El Labban, G.O. Ngongang Ndjawa, T. Heumueller, K. Vandewal, A. Salleo, B.F. Chmelka, A. Amassian, P.M. Beaujuge, M.D. McGehee, *J. Am. Chem. Soc.* 136 (2014) 9608–9618.
- [107] C. Dyer-Smith, I.A. Howard, C. Cabanetos, A. El Labban, P.M. Beaujuge, F. Laquai, *Adv. Energy Mater.* 5 (2015) 1401778/1–1401778/11.
- [108] S.A. Arnstein, C.D. Sherrill, *Phys. Chem. Chem. Phys.* 10 (2008) 2646–2655.
- [109] M.O. Sinnokrot, C.D. Sherrill, *J. Am. Chem. Soc.* 126 (2004) 7690–7697.
- [110] M.O. Sinnokrot, C.D. Sherrill, *J. Phys. Chem. A* 110 (2006) 10656–10668.
- [111] M.O. Sinnokrot, C.D. Sherrill, *J. Phys. Chem. A* 108 (2004) 10200–10207.
- [112] A.L. Ringer, M.S. Figgs, M.O. Sinnokrot, C.D. Sherrill, *J. Phys. Chem. A* 110 (2006) 10822–10828.
- [113] M.S. Marshall, R.P. Steele, K.S. Thanthiriwatte, C.D. Sherrill, *J. Phys. Chem. A* 113 (2009) 13628–13632.
- [114] S.E. Wheeler, K.N. Houk, *J. Am. Chem. Soc.* 130 (2008) 10854–10855.
- [115] S.E. Wheeler, A.J. McNeil, P. Müller, T.M. Swager, K.N. Houk, *J. Am. Chem. Soc.* 132 (2010) 3304–3311.
- [116] S.E. Wheeler, *Acc. Chem. Res.* 46 (2013) 1029–1038.
- [117] S.E. Wheeler, J.W.G. Bloom, *Chem. Commun.* 50 (2014) 11118–11121.



- [118] S. Grimme, *Angew. Chem., Int. Ed.* 47 (2008) 3430–3434.
- [119] E.G. Hohenstein, C.D. Sherrill, *J. Chem. Phys.* 132 (2010) 184111.
- [120] R. Podeszwa, R. Bukowski, K. Szalewicz, *J. Phys. Chem. A* 110 (2006) 10345–10354.
- [121] B. Jeziorski, R. Moszynski, K. Szalewicz, *Chem. Rev.* 94 (1994) 1887–1930.
- [122] R. Podeszwa, K. Szalewicz, *Phys. Chem. Chem. Phys.* 10 (2008) 2735–2746.
- [123] J.M. Turney, et al., *WIREs Comput. Mol. Sci.* 2 (2012) 556–565.
- [124] The rate at which the interaction energy decreases will be dependent on the separation distance. At separation distances up to 4 Å, there will be exponential decrease as charge penetration will be a large contribution. At larger separations, there will be  $1/R^n$  dependence due to dispersion and various electrostatic multipole interactions.
- [125] The distance dependence of the electrostatics terms will be dependent on the rank of the interacting multipoles. The distance dependence takes the form  $1/R^{l+L+M}$ .
- [126] C. Sutton, M.S. Marshall, C.D. Sherrill, C. Risko, J.-L. Brédas, *J. Am. Chem. Soc.* 137 (2015) 8775–8782.
- [127] J.L. Brédas, J.P. Calbert, D.A. da Silva Filho, J. Cornil, *Proc. Natl. Acad. Sci. USA* 99 (2002) 5804–5809.
- [128] C. Sutton, J.S. Sears, V. Coropceanu, J.-L. Brédas, *J. Phys. Chem. Lett.* 4 (2013) 919–924.
- [129] M.R. Kennedy, A.R. McDonald, A.E. DePrince, M.S. Marshall, R. Podeszwa, C.D. Sherrill, *J. Chem. Phys.* 140 (2014) 121104.
- [130] O.A. von Lilienfeld, A. Tkatchenko, *J. Chem. Phys.* 132 (2010) 234109.
- [131] S. Wen, G.J.O. Beran, *J. Chem. Theory Comput.* 7 (2011) 3733–3742.
- [132] R. Podeszwa, B.M. Rice, K. Szalewicz, *Phys. Rev. Lett.* 101 (2008) 115503.
- [133] K. Szalewicz, *Acc. Chem. Res.* 47 (2014) 3266–3274.
- [134] L. Huang, Q. Liao, Q. Shi, H. Fu, J. Ma, J. Yao, *J. Mater. Chem.* 20 (2010) 159–166.
- [135] M. Takeshi, Y. Masashi, U. Masahito, Y. Masakazu, N. Akiko, T. Yoshinori, T. Junichi, K. Yasuo, M. Yusuke, S. Takatomo, *Jpn. J. Appl. Phys.* 49 (2010) 085502.
- [136] O. Shigeaki, M. Toshiaki, S. Yukihiro, *Jpn. J. Appl. Phys.* 53 (2014) 01AD02.
- [137] A previous computational study predicts three of the four crystal structures found experimentally for rubrene, with a triclinic crystal structure predicted to be the minimum configuration.
- [138] In addition to the orthorhombic crystal structure of rubrene, for which large mobilities have been measured, monoclinic and triclinic rubrene polymorphs have been identified. The monoclinic and triclinic polymorphs are not considered in this work for the sake of consistency.
- [139] D. Käfer, L. Ruppel, G. Witte, C. Wöll, *Phys. Rev. Lett.* 95 (2005) 166602.
- [140] T. Petrenko, O. Krylova, F. Neese, M. Sokolowski, *New J. Phys.* 11 (2009) 015001.
- [141] M. Kytka, L. Gisslen, A. Gerlach, U. Heinemeyer, J. Kovac, R. Scholz, F. Schreiber, *J. Chem. Phys.* 130 (2009) 214507.
- [142] D. Casanova, *J. Chem. Theory Comput.* 10 (2014) 324–334.
- [143] S. Duhm, Q. Xin, S. Hosoumi, H. Fukagawa, K. Sato, N. Ueno, S. Kera, *Adv. Mater.* 24 (2012) 901–905.
- [144] O.D. Jurchescu, A. Meetsma, T.T.M. Palstra, *Acta Crystallogr., Sect. B, Struct. Sci.* 62 (2006) 330–334.
- [145] J.E. Norton, J.-L. Brédas, *J. Am. Chem. Soc.* 130 (2008) 12377–12384.
- [146] R.K. Hallani, K.J. Thorley, Y. Mei, S.R. Parkin, O.D. Jurchescu, J.E. Anthony, *Adv. Funct. Mater.* 26 (2016) 2341–2348.
- [147] K.J. Thorley, C. Risko, *J. Mater. Chem. C* 4 (2016) 4040–4048.
- [148] D. Lehnher, A.R. Waterloo, K.P. Goetz, M.M. Payne, F. Hampel, J.E. Anthony, O.D. Jurchescu, R.R. Tykwinski, *Org. Lett.* 14 (2012) 3660–3663.
- [149] M. Mamada, H. Katagiri, M. Mizukami, K. Honda, T. Minamiki, R. Teraoka, T. Uemura, S. Tokito, *ACS Appl. Mater. Interfaces* 5 (2013) 9670–9677.
- [150] M. Mamada, T. Minamiki, H. Katagiri, S. Tokito, *Org. Lett.* 14 (2012) 4062–4065.
- [151] N.R. Tummala, C. Sutton, S.G. Aziz, M.F. Toney, C. Risko, J.-L. Brédas, *Chem. Mater.* 27 (2015) 8261–8272.
- [152] J.H. Hildebrand, R.L. Scott, *J. Chem. Phys.* 20 (1952) 1520–1521.
- [153] C.M. Hansen, *J. Paint Technol.* 39 (1967) 104.
- [154] N.R. Tummala, S. Mehraeen, Y.T. Fu, C. Risko, J.L. Brédas, *Adv. Funct. Mater.* 23 (2013) 5800–5813.
- [155] F. Machui, S. Abbott, D. Waller, M. Koppe, C.J. Brabec, *Macromol. Chem. Phys.* 212 (2011) 2159–2165.
- [156] F. Machui, S. Langner, X. Zhu, S. Abbott, C.J. Brabec, *Sol. Energy Mater. Sol. Cells* 100 (2012) 138–146.
- [157] D.T. Duong, B. Walker, J. Lin, C. Kim, J. Love, B. Purushothaman, J.E. Anthony, T.-Q. Nguyen, *J. Polym. Sci., Part B, Polym. Phys.* 50 (2012) 1405–1413.

- [158] D. Chen, A. Nakahara, D. Wei, D. Nordlund, T.P. Russell, *Nano Lett.* 11 (2010) 561–567.
- [159] Y.-H. Lin, Y.-T. Tsai, C.-C. Wu, C.-H. Tsai, C.-H. Chiang, H.-F. Hsu, J.-J. Lee, C.-Y. Cheng, *Org. Electron.* 13 (2012) 2333–2341.
- [160] N.R. Tummala, C. Bruner, C. Risko, J.-L. Brédas, R.H. Dauskardt, *ACS Appl. Mater. Interfaces* 7 (2015) 9957–9964.
- [161] Q. Zhao, J.R. Wood, H.D. Wagner, *Appl. Phys. Lett.* 78 (2001) 1748–1750.
- [162] C.B. Nielsen, R.S. Ashraf, N.D. Treat, B.C. Schroeder, J.E. Donaghey, A.J.P. White, N. Stingelin, I. McCulloch, *Adv. Mater.* 27 (2015) 948–953.
- [163] Y. Yi, V. Coropceanu, J.-L. Brédas, *J. Am. Chem. Soc.* 131 (2009) 15777–15783.
- [164] M. Linares, D. Beljonne, J. Cornil, K. Lancaster, J.-L. Brédas, S. Verlaak, A. Mityashin, P. Heremans, A. Fuchs, C. Lennartz, J. Idé, R. Méreau, P. Aurel, L. Ducasse, F. Castet, *J. Phys. Chem. C* 114 (2010) 3215–3224.
- [165] M.K. Ravva, T. Wang, J.-L. Brédas, *Chem. Mater.* 28 (2017) 8181–8189.
- [166] C.F.N. Marchiori, M. Koehler, *J. Phys. D, Appl. Phys.* 47 (2014) 215104.
- [167] G. D’Avino, Y. Olivier, L. Muccioli, D. Beljonne, *J. Mater. Chem. C* 4 (2016) 3747–3756.
- [168] T. Wang, M.K. Ravva, J.-L. Brédas, *Adv. Funct. Mater.* 26 (2016) 5913–5921.

# Noncovalent Interactions in Molecular Crystals

---

Gregory J.O. Beran, Yonatan N. Heit, Joshua D. Hartman

Department of Chemistry, University of California Riverside, Riverside, CA, USA

## 10.1 INTRODUCTION

---

At least half of all organic molecules exhibit polymorphism, or multiple distinct packing motifs, in the crystalline state [1]. For species such as flufenamic acid [2], the brightly colored red, orange, and yellow crystals of ROY (5-methyl-2-[(2-nitrophenyl)amino]-3-thiophenecarbonitrile) [3], and the explosive triacetone-triperoxide (TATP) [4], many different polymorphs are known. Crystal packing can have profound effects on crystal properties. It can alter the solubility and bioavailability of pharmaceutical crystals [5], impact the charge carrier mobility in organic semiconductor materials [6], or even change the taste of chocolate [7].

Crystal packing is governed by an often subtle competition between intramolecular conformation and intermolecular interactions. Experimentally observed polymorphs are typically separated by small energy differences. A 2015 computational survey of 508 organic crystal polymorph pairs found that over half the crystal pairs were separated by 2 kJ/mol or less, and 95% of them were separated by less than 7.2 kJ/mol [8]. In species that exhibit isotopic polymorphism, simply substituting hydrogen atoms with deuterium ones is sufficient to alter the preferred crystal packing motif [9–13].

Modeling the energetics in polymorphic molecular crystals requires careful, balanced treatment of the broad spectrum of noncovalent interactions, which includes exchange, electrostatics, polarization, and van der Waals dispersion interactions (see Chapter 1). This requirement can be demanding on the theoretical model chemistry. Dispersion-corrected density functional theory (DFT) models often perform well, though sometimes higher-accuracy wavefunction-based methods can be required. Advances in periodic Møller–Plesset perturbation theory and in fragment-based electronic structure methods have been particularly important in making correlated wave function models applicable to organic molecular crystals. Section 10.2 will discuss several of these techniques and their performance for organic molecular crystal modeling.

Section 10.3 will highlight several representative examples where electronic structure theory has proved useful in molecular crystal problems. First, we will examine the role of tem-

perature in molecular crystals. Molecular crystal unit cell volumes frequently expand 5–15% between the electronic energy minimized structure and room temperature, which can impact thermochemical, mechanical, and other properties. Next, we will discuss applications of electronic structure methods to the prediction of phase boundaries, including different phases in carbon dioxide and the proton ordering in ice XV. Finally, electronic structure techniques have proved helpful in modeling spectroscopic properties in molecular crystals. Examples from vibrational and nuclear magnetic resonance (NMR) spectroscopy will be highlighted. The important topic of crystal structure prediction is discussed separately in Chapter 11. For additional details and many more examples, the reader is referred to a 2016 review article [14].

## 10.2 TECHNIQUES FOR MODELING MOLECULAR CRYSTALS

Many different electronic structure techniques for modeling molecular crystals exist [14]. Here, we focus on the three main approaches: periodic density functional theory, periodic second-order Møller–Plesset perturbation theory (MP2), and fragment-based methods. Most applications found in the literature rely on DFT, but the other approaches can provide additional insights in cases where DFT predictions are inconclusive.

### 10.2.1 Periodic DFT

Van der Waals interactions play a crucial role in molecular crystals, and therefore dispersion must be included in the density functional treatment. As described in Chapters 5 and 6 and in review articles [15–18], many different approaches exist for handling dispersion, ranging from post-hoc semiclassical corrections to nonlocal density-based ones. Dispersion-corrected DFT is often the method of choice for modeling molecular crystals due to its combination of generally good performance and affordable computational cost (see Chapter 6).

Dispersion-corrected DFT has been particularly successful in the blind tests of crystal structure prediction. The empirical dispersion-corrected DFT model implemented in the GRACE software package was the first technique to achieve a 100% success rate in a single blind test [19], and it has correctly predicted the experimental structures as the most stable ones in 15 out of the 20 molecules included in the first five blind tests. Several of the five remaining crystals were “near-misses,” with the experimental structure being ranked among the top five [19–23]. GRACE performs crystal structure prediction by fitting force fields against DFT, using the force fields to generate candidate structures, and refining the most stable structures with full DFT. The GRACE methodology has been applied to many other problems as well. For example, it helped solve the long-unknown structure of form III acetaminophen (a.k.a. paracetamol) [24], identified a previously unknown polymorph of the drug dalcetrapib which was later confirmed experimentally [25], and even revealed numerous errors in structures reported in experimental powder X-ray diffraction studies [26].

Most of these aforementioned GRACE examples employed a relatively simple, empirical dispersion correction. However, there have been appreciable improvements in the treatment of dispersion in the past several years. As discussed in Chapters 5 and 6, modern dispersion corrections include the exchange-hole dipole moment (XDM) [27–30], the pair-

**TABLE 10.1** Mean absolute errors (MAD) in the lattice energies for dispersion-corrected DFT models on the X23 (or C21 in selected cases) benchmark set, in kJ/mol

Method	MAD	Source
DFTB-D3	10.4	Ref. [37]
PBE-MBD	5.9	Ref. [38]
PBE-XDM	4.6	Chapter 5
PBE-D3	4.6	Ref. [39]
PBE0-D3	5.0	Ref. [39]
PBE0-MBD	3.9	Ref. [38]

wise Tkatchenko–Scheffler (TS) correction [31], many-body dispersion (MBD) [32–34], and D3 corrections [35,36]. In all of these models, the atomic dispersion coefficients respond to the current molecular environment, making them much more physical and robust than earlier empirical corrections.

Many of these modern dispersion-corrections have been benchmarked on the C21 [40] or the slightly refined and expanded X23 [38] databases of molecular crystal structures and lattice energies, and representative lattice energy results are summarized in Table 10.1. Given that the lattice energies derived from experiment often have uncertainties of a few kJ/mol or more (see Chapter 11), we see similar performance from many of the models. Brandenburg and coworkers have also explored the use of HF-D3 [41] and inexpensive dispersion-corrected tight binding (DFTB-D3) [37] models in molecular crystals. Though not as accurate as many of the conventional DFT approaches (see Table 10.1), the DFTB-D3 model might allow for reasonable accuracy at substantially reduced computational cost. On the other hand, DFTB-D3 underestimates the molar volumes in ten ice polymorphs by 15% [42].

Several variants of dispersion-corrected DFT performed well in the 2016 sixth blind test of crystal structure prediction [43]. Other interesting examples of these modern dispersion-corrected DFT methods found in the literature include studies of the high-pressure phases of ice [42,44,45] and carbon dioxide [46]. Brandenburg and coworkers used PBE-D3 to investigate the solid-state packing of tribenzotriquinacenes, which form linear stacks of these bowl-shaped molecules [47]. Otero-de-la-Roza et al. [48] used DFT-XDM to predict the enantiomeric excess between enantiopure and racemic crystals for a series of amino acids in quite good agreement with experiment (mean error of only 10%), despite the difference between 0% and 95% enantiomeric excess corresponding to an energy range of only 4.5 kJ/mol.

Tkatchenko and coworkers have investigated the importance of many-body dispersion in various crystals. Glycine represents a particularly challenging case of crystal polymorphism, with sub-kJ/mol enthalpy differences separating the  $\alpha$ ,  $\beta$ , and  $\gamma$  polymorphs. Obtaining qualitatively reasonable relative stabilities required the use of the hybrid density functional PBE0 instead of PBE, many-body dispersion, and zero-point energy (see Fig. 10.1A) [49]. In acetaminophen, they found [32] that the inclusion of many-body dispersion significantly destabilized the putative form IV that had been proposed in a separate crystal structure prediction study [50], which would suggest that it is less likely to be observed experimentally. As discussed in Section 10.3.3, they have also used DFT-MBD to argue why form I aspirin is preferred experimentally, despite the apparent energetic degeneracy of forms I and II.

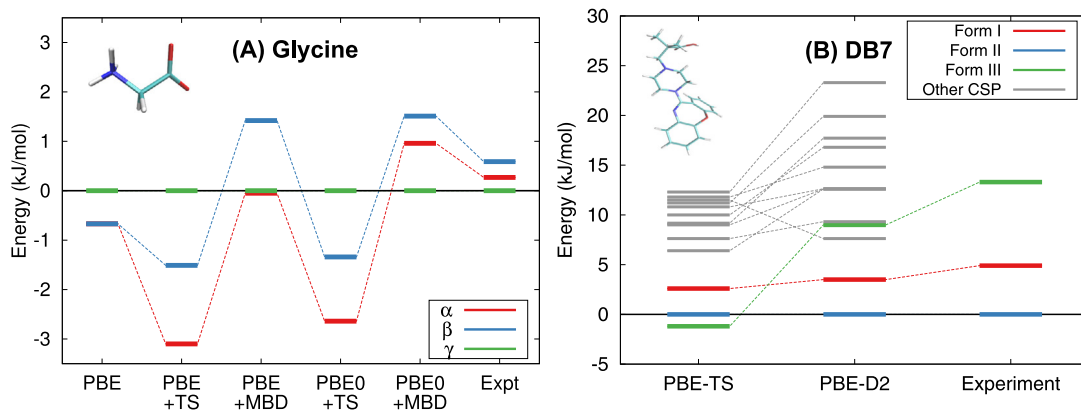


FIGURE 10.1 (A) Predicted energetics of different crystal structures of glycine [49] and (B) the drug DB7 [51] compared against relative enthalpies obtained from experiment [51]. “Other CSP” refers to other, experimentally unknown structures predicted during the crystal structure prediction study. Reprinted with permission from Ref. [14]. Copyright 2013 American Chemical Society.

As demonstrated by the examples discussed above, dispersion-corrected DFT models often make very successful predictions. However, polymorph energy differences can be very sensitive to subtle details in the electronic structure model. This sometimes leads to qualitatively different predictions from seemingly comparable DFT models. For example, periodic PBE calculations with either the D2 [52] or TS dispersion corrections predict substantially different relative polymorph energies in methylparaben [53] and two chemically related pharmaceutical candidates, DB7 and B5 [51]. In DB7, for example, PBE-D2 predicts an energetic ordering in qualitative agreement with differential scanning calorimetry (DSC) experiments,

$$\text{Form II} < \text{Form I} < \text{Form III},$$

while PBE-TS predicts that form III is actually the most stable,

$$\text{Form III} < \text{Form II} < \text{Form I}.$$

If one also considers other, experimentally unknown crystal structures generated during the DB7 crystal structure prediction study, many other differences in the energy rankings are observed (see Fig. 10.1B).

In applications where different density functional models make qualitatively different predictions and one does not have obvious reasons to prefer one density functional or dispersion correction over another, it can be challenging to decide which predictions to believe. In such cases, wavefunction-based methods provide an alternative set of predictions that can, at least in principle, be converged toward the exact result. The next sections describe periodic MP2 and fragment-based methods, which allow one to employ wavefunction model chemistries to molecular crystal problems.

### 10.2.2 Periodic MP2

MP2 algorithms for three-dimensional periodic systems have advanced considerably since 2000. Many of these algorithms use atom-centered basis functions (Gaussians or numerical orbitals) [54–62], while others use plane waves and the projector augmented approach [63,64] or a hybrid Gaussian and plane wave model [65–67]. The majority of periodic MP2 molecular crystal applications to date have been performed with the periodic local MP2 code developed by the CRYSCOR group [57,58] and include examinations of lattice energies [68,69], phase boundaries [70], and polymorph energies [71]. Basis set convergence can be difficult in Gaussian orbital periodic MP2 calculations due to problems with linear dependencies and other pragmatic issues [72], but use of explicitly correlated MP2 models helps considerably [73].

The massively parallel Gaussian and plane wave algorithm for periodic MP2 energies and nuclear gradients [65–67], has demonstrated 80% parallel efficiency on up to a hundred thousand processors, though it is limited to  $\Gamma$ -point calculations at present. Using a supercell approach to compensate for the lack of  $k$ -point sampling, its authors have shown favorable performance of the model in early crystal benchmarks and in its application to ice XV (see Section 10.3.2).

The major challenge associated with periodic MP2 is its poor performance for describing van der Waals dispersion interactions. Spin-component scaling [74,75] or local “incremental” corrections at a higher level of theory [76] are often needed to compensate for these deficiencies. See Section 10.2.3 for details.

### 10.2.3 Fragment Methods

Fragment-based electronic structure methods have become ubiquitous. The basic concept involves decomposing the total energy of the system into contributions from many smaller pieces, or fragments. In molecular crystals, fragments typically correspond to individual molecules, and the interactions between fragments are treated via a many-body expansion for the energy (see Chapters 1 and 4),

$$E_{\text{full}} = E_{1\text{-body}} + E_{2\text{-body}} + E_{3\text{-body}} + \cdots, \quad (10.1)$$

which can be expanded as

$$E_{\text{full}} = \sum_i E_i + \sum_{i>j} \Delta^2 E_{ij} + \sum_{i>j>k} \Delta^3 E_{ijk} + \cdots, \quad (10.2)$$

where  $E_i$  is the energy of each fragment,  $\Delta^2 E_{ij}$  is the interaction energy between pairs of fragments,

$$\Delta^2 E_{ij} = E_{ij} - E_i - E_j \quad (10.3)$$

and  $\Delta^3 E_{ijk}$  is a nonadditive three-body interaction contribution,

$$\Delta^3 E_{ijk} = E_{ijk} - \Delta^2 E_{ij} - \Delta^2 E_{ik} - \Delta^2 E_{jk} - E_i - E_j - E_k. \quad (10.4)$$

Note that the sums in Eq. (10.2) include interactions of molecules in the central unit cell with each other and with periodic image molecules.

The intramolecular (1-body) and short-range pairwise intermolecular (2-body) terms typically dominate in a molecular crystal, with long-range pairwise and many-body contributions typically accounting for only  $\sim 10\text{--}20\%$  of the lattice energy. Accordingly, most fragment approaches concentrate on capturing the 1- and 2-body terms accurately, while modeling the remaining many-body contributions more approximately. In general, the important 1- and 2-body terms can be treated with any electronic structure model chemistry capable of describing noncovalent interactions reliably (see Chapter 4). Different fragment models vary primarily in how they treat the many-body effects. Several examples of fragment methods which have been applied to molecular crystals are discussed below.

Note that many other fragment models exist beyond the handful described here, including some which do not rely on a many-body expansion. These models are described in several review articles [77–79]. Multiple authors have also presented generalized models [80,81] which encompass a variety of seemingly different fragment models found in the literature within a unified framework.

### **Incremental Methods**

First pioneered by Stoll in the 1990s, incremental methods [82–85] share conceptual features in common with multi-layer hybrid quantum mechanical/molecular mechanical (QM/MM) treatments like ONIOM [86]. Incremental methods treat the entire system at a low level of theory, with key contributions (“increments”) being refined at a higher level of theory. However, whereas the ONIOM model typically partitions the system spatially into regions treated using more exact and more approximate levels of theory, the incremental method partitioning is based on the type of interaction, and each molecule in the unit cell is treated equivalently. Incremental methods can be viewed as a multicenter ONIOM approach [87,88].

As an example of the incremental approach, one might model the crystal with periodic Hartree–Fock, and then correct the energies of the monomers and short-range (SR) pairwise interactions with CCSD(T) [89],

$$E_{\text{full}}^{\text{CCSD(T)}} \approx E_{\text{full}}^{\text{HF}} + \left( E_{1\text{-body}}^{\text{CCSD(T)}} - E_{1\text{-body}}^{\text{HF}} \right) + \left( E_{2\text{-body SR}}^{\text{CCSD(T)}} - E_{2\text{-body SR}}^{\text{HF}} \right). \quad (10.5)$$

Using Eq. (10.1), Eq. (10.5) can be rewritten as

$$E_{\text{full}}^{\text{CCSD(T)}} \approx E_{1\text{-body}}^{\text{CCSD(T)}} + E_{2\text{-body SR}}^{\text{CCSD(T)}} + E_{2\text{-body LR}}^{\text{HF}} + E_{\text{many-body}}^{\text{HF}} \quad (10.6)$$

where  $E_{2\text{-body LR}}^{\text{HF}}$  refers to the long-range pairwise interactions not included in the short-range CCSD(T) treatment  $E_{\text{many-body}}^{\text{HF}}$  refers to all three-body and higher terms. Other examples of the incremental method include rare gas crystals [90,91] and inorganic materials [85,92].

One is not constrained to using HF for the many-body terms. A number of authors have used the incremental approach to improve upon a DFT treatment of the entire system [93–96]. With current widely used density functionals, DFT may not be the most suitable model for correcting with the incremental approach, however. Problems in the descriptions of many-body polarization (due to delocalization error) and exchange can lead to erroneous descriptions of many-body interactions [97,98]. In periodic DFT, these many-body errors tend to



cancel somewhat with errors in the 1- and 2-body terms (see Chapter 5, particularly Section 5.3). In an incremental approach, however, treating these different terms at different levels of theory can disrupt the error cancellation.

Correlated wavefunction methods can also provide the low-level treatment. For instance, periodic local MP2 has been coupled with energy increments calculated at the coupled cluster level to obtain high accuracy lattice energies in several small-molecule crystals [76].

### Hybrid Many-Body Interaction

The hybrid many-body interaction (HMBI) model [99–103] is analogous to the incremental approach, except it treats the long-range pairwise interactions and many-body terms using a polarizable force field,

$$E_{\text{full}}^{\text{QM}} \approx E_{\text{full}}^{\text{MM}} + \left( E_{1\text{-body}}^{\text{QM}} - E_{1\text{-body}}^{\text{MM}} \right) + \left( E_{2\text{-body SR}}^{\text{QM}} - E_{2\text{-body SR}}^{\text{MM}} \right). \quad (10.7)$$

The polarizable force field can either be a standard one like Amoeba [104–106], or one can compute force field parameters on the fly as in the *ab initio* force field model [101,107,108]. Significant computational savings can be obtained via exploitation of space group symmetry [109]. This general model has been applied to a number of problems, including lattice energy prediction [100,101], polymorph energy ranking [110–112] and finite-temperature property prediction [113,114].

### Embedding Methods

The incremental and HMBI methods sum the many-body expansion to all orders, albeit with some terms treated at a higher accuracy than others. Alternatively, one can simply sum sufficient terms in the many-body expansion to approach convergence. In cases like benzene, which do not exhibit substantial many-body polarization effects, convergence is reached by including three-body and perhaps four-body terms [115]. Various groups have predicted the benzene lattice energy in this manner using coupled cluster theory [115,116] or symmetry adapted perturbation theory (SAPT) [117], for instance. Explicit summation of the many-body expansion can be challenging, however, due to the rapid increase in computational cost, numerical precision issues, and basis set superposition error associated with the higher-order terms [118–121].

Embedding methods effectively help capture many-body effects in the low-order terms of the many-body expansion. For instance, the binary interaction model determines a set of self-consistent embedding charges/dipoles for each unique species in the unit cell, and uses those to embed the 1-body and 2-body calculations [122,123]. By incorporating important polarization effects into the 1- and 2-body terms, this embedding diminishes the contribution from 3-body and higher terms. The periodic version of the generalized energy-based fragmentation (GEBF) model [124,125] combines energies from point-charge embedded small cluster calculations. Such fragment-based embedding methods have proved very useful, with molecular crystal applications including vibrational spectroscopy [125–132], phase transitions [128,129], NMR [133–135], and many other properties [132,136,137]. Embedding models that include exchange effects [138] or other more elaborate treatments of the embedding environment can also be constructed [139–144].

### ***Effective Electronic Structure Methods for Evaluating Fragment Contributions***

Regardless of the particular fragment model used, one must select an appropriate electronic structure method for evaluating the important fragment energy contributions (typically the 1- and 2-body terms). As noted previously, the key challenge is to treat the variety of inter- and intramolecular interactions with uniform reliability. As dimer noncovalent interaction energy benchmarks demonstrate [145], many electronic structure methods struggle to balance hydrogen bonding and dispersion interactions, for example.

Due to its relatively low  $\mathcal{O}(N^5)$  computational scaling with system size  $N$  and ability to describe a variety of noncovalent interactions, MP2 is probably the most widely used electronic structure method in fragment approaches. However, the performance of MP2 for van der Waals dispersion interactions is well-known to be problematic. MP2 substantially overestimates intermolecular dispersion interactions in  $\pi$  complexes [145], while it underestimates the dispersion in weakly polarizable systems like rare gas dimers [146]. Various approaches have been devised to correct this problematic behavior [74,75,147–149]. One of the most successful is the MP2C approach, which replaces the uncoupled HF treatment of dispersion in MP2 with coupled Kohn–Sham dispersion (see Chapter 3) [146,150]. MP2C provides near-CCSD(T) accuracy [151,152] at much lower cost [153] in many noncovalent dimer and crystal benchmarks. On the other hand, the MP2C dispersion correction is based on intermolecular perturbation theory and does not correct intramolecular dispersion interactions. This might lead to imbalances in systems where intramolecular dispersion interactions are important (e.g., peptide conformers).

If MP2-based methods do not provide sufficient accuracy, several alternatives exist, albeit with  $\mathcal{O}(N^6)$  scaling or higher. MP2.5, which averages MP2 and MP3, performs very well for noncovalent interactions [154]. CCSD(T) represents the “gold standard” of quantum chemistry, but its steep  $\mathcal{O}(N^7)$  cost limits its application. However, increasingly efficient coupled cluster algorithms which reduce the size of the virtual space through rank reduction techniques or local correlation approximations [155–159] have allowed it to be applied to a number of interesting crystals, including benchmark calculations on benzene that rival experimental accuracy [115,116]. Coupled cluster methods have also been used to correct periodic MP2 in an incremental scheme [76].

For all of these methods, the use of large basis sets, such as the Dunning correlation-consistent aug-cc-pVXZ sets with diffuse and high angular momentum functions, is important (see Chapter 4). Double-zeta basis sets like aug-cc-pVDZ are often too small to provide reliable molecular crystal energetics. Triple-zeta basis sets typically provide the first reasonable results, though extrapolating toward the complete basis set limit can often be a good idea [100,101]. Alternatively, one can use explicitly correlated F12 methods to accelerate the basis set convergence, especially at the MP2 level [160,161].

Employing counterpoise corrections for basis set superposition error (BSSE) is often beneficial (Chapter 4), especially in modest basis sets. Care sometimes needs to be taken, however. In the polymorphs of oxalyl dihydrazide, for instance, the five known polymorphs differ in the extent of intra- versus intermolecular hydrogen bonding [162,163]. Counterpoise correction can compensate for BSSE in the intermolecular interactions readily, but correcting the intramolecular BSSE is harder. This leads to an imbalance in the inter- and intramolecular interactions which results in an incorrect polymorph ordering in basis sets smaller than aug-cc-pVQZ basis. The polymorph ordering is predicted correctly only when

the basis sets are large enough to eliminate much of the BSSE without counterpoise correction [111].

## 10.3 REPRESENTATIVE APPLICATIONS

---

Having discussed some of the theoretical methods used commonly in molecular crystals, we next consider several examples of how these models can be applied to interesting molecular crystal problems. Specific examples include modeling molecular crystal structures, thermochemistry, and mechanical properties at finite temperatures, modeling features on molecular crystal phase diagrams, vibrational spectroscopy, and NMR spectroscopy.

### 10.3.1 Finite-Temperature Effects

Thermal expansion effects are potentially important in modeling molecular crystal properties at finite temperatures, but they are often ignored. As noted above, molecular crystals typically expand 5–15% upon heating to room temperature, and this expansion can impact crystal properties appreciably. It is often true, as argued by Gavezzotti and Filippini in 1995 [164], that the lattice vibrational entropy contributions are smaller than the enthalpy differences between polymorphs. Nevertheless, Nyman and Day found that room-temperature free energies reverse the stability ordering predicted by 0 K lattice energies in about 10% of 508 polymorphic pairs they surveyed [8]. This fraction would only increase if higher temperatures are considered. Indeed, the experimental literature contains many examples of enantiotropically related polymorphs, where the thermodynamically preferred crystal form changes with temperature. The phase diagrams of simple molecules like ice, dinitrogen, or carbon dioxide exhibit a rich variety of distinct structures which are stable only in certain temperature regimes (see Section 10.3.2).

Other crystal properties are affected by thermal expansion as well. In organic semiconductor materials, for instance, the transfer integral plays a central role in understanding transport properties in both the band and hopping regimes. The electron transfer (hopping) rate varies with the square of the transfer integral, and even modest changes in the spacing between anthracene molecules can alter the transfer integral by ~30% [165]. Thermal expansion has been identified as causing the narrowing of the valence and conduction bandwidths in materials like pentacene and rubrene [166]. Mechanically, thermal expansion can soften materials, making them more compressible. The bulk modulus of carbon dioxide decreases several fold between 0 K and 300 K, for instance [113].

One simple and widely used approach for modeling thermal expansion is to constrain the crystal structure at the experimentally observed lattice parameters measured at an appropriate temperature (Refs. [167] and [168], for example). However, experimental lattice parameters are not always available. One can also utilize molecular dynamics/free energy sampling techniques, but extensive configuration sampling can be cost-prohibitive using electronic structure methods. As a practical computational alternative, we have modeled the impact of thermal expansion on thermochemical and mechanical properties in several small-molecule crystals using a quasiharmonic approximation to the Gibbs free energy at a given

temperature  $T$  and pressure  $P$  [113,114],

$$G(T, P) = U_{\text{el}} + PV + F_{\text{vib}}(T) \quad (10.8)$$

where  $U_{\text{el}}$  is the electronic energy,  $PV$  is the pressure–volume term, and  $F_{\text{vib}}$  is the Helmholtz vibrational free energy,

$$F_{\text{vib}}(T) = N_a \sum_i \frac{\hbar\omega_i}{2} + k_B T \ln \left[ 1 - \exp\left(-\frac{\hbar\omega_i}{k_B T}\right) \right]. \quad (10.9)$$

In the expression above,  $N_a$  is Avogadro’s number,  $\hbar$  is Planck’s constant,  $k_B$  is the Boltzmann constant, and  $\omega_i$  are the phonon frequencies.

This quasiharmonic model approximates how each phonon frequency  $\omega_i$  varies with unit cell volume  $V$ ,

$$\omega_i = \omega_i^{\text{ref}} \left( \frac{V}{V^{\text{ref}}} \right)^{-\gamma_i} \quad (10.10)$$

in terms of mode-specific Grüneisen parameters  $\gamma_i$ , reference frequencies  $\omega_i^{\text{ref}}$ , and a reference cell volume  $V^{\text{ref}}$ . The Grüneisen parameters reflect how the phonon frequencies vary with unit cell volumes within the quasiharmonic approximation. The reference frequencies/volumes are typically obtained by minimizing the electronic energy of the structure, and the mode-specific Grüneisen parameters are defined as the derivative of the phonon frequencies with volume (computed via finite difference),

$$\gamma_i = - \left( \frac{\partial \ln \omega_i}{\partial \ln V} \right). \quad (10.11)$$

This quasiharmonic model enables one to estimate the Gibbs free energy at various temperatures and pressures, and thermal expansion is captured by minimizing the free energy at a given temperature and pressure. See Ref. [114] for details.

Note that similar models have been used previously in DFT and force field studies on ice, for example [169,170]. In 2016, Nyman and Day demonstrated good performance of the quasiharmonic approximation with force fields for the X23 crystal test set [171]. Other variants of the quasiharmonic approximation [172–174] or other approximations for estimating free energies also exist [173,175–177]. The quasiharmonic approximation has limitations, of course. Though it may behave well at lower temperatures, quasiharmonic crystals can expand too quickly at higher temperatures [178]. The temperature range of validity broadens at higher pressures, however. The behavior of quasiharmonic models for crystals containing flexible molecules with highly anharmonic vibrations remains an open question.

Quasiharmonic fragment-based HMBI calculations using large-basis MP2 or CCSD(T) accurately reproduce the temperature dependence of the volume for small-molecule crystals like carbon dioxide, ice, acetic acid, and imidazole [113,114]. In carbon dioxide, for instance, estimated complete-basis-set CCSD(T) calculations consistently underestimate the volume by less than 2% over a  $\sim 200$  K temperature range (Fig. 10.2). The neglect of three-body dispersion effects, which are typically repulsive in solids (Chapter 1), probably contributes to this volume underestimation.

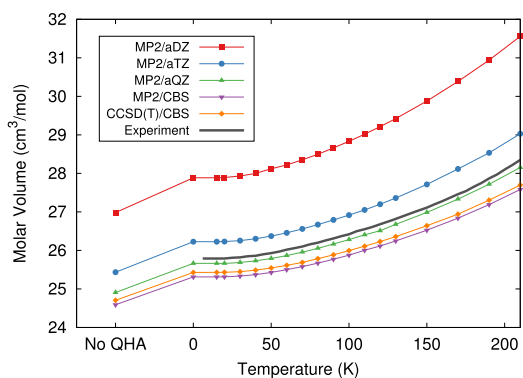


**FIGURE 10.2** Molar volume of phase I carbon dioxide as a function of temperature without consideration of quasiharmonic vibrational effects (“No QHA”) and at various temperatures within the quasiharmonic approximation [113]. Note: aXZ refers to aug-cc-pVXZ basis sets. Reprinted with permission from Ref. [114]. Copyright 2016 International Union of Crystallography.

Expansion of the crystal away from the electronic-energy minimum weakens the lattice energy, and it frequently reduces the magnitude of the low-frequency lattice phonon modes. Neglecting thermal expansion leads to overestimation of the sublimation enthalpy (due primarily to overestimation of the lattice energy) and overestimation of the sublimation entropy (due to the unphysically large lattice phonon frequencies in the crystal that cause  $S_{\text{crystal}}$  to be too small relative to  $S_{\text{gas}}$ ) at higher temperatures. These errors in  $\Delta H$  and  $T\Delta S$  can each amount to a couple kJ/mol at higher temperatures, which is on par with the lattice energy differences observed between polymorphs. Interestingly, however, the errors in the sublimation enthalpy and entropy often have the same signs, which causes the errors to cancel somewhat in the Gibbs free energy. In carbon dioxide, for instance, the predicted sublimation temperatures with and without thermal expansion are 198.0 K and 190.4 K, respectively. Both lie within a few degrees of experimental sublimation temperature, 194.7 K.

The quasiharmonic approximation can be applied to predict mechanical properties like the bulk modulus. To compute the bulk modulus, one computes the unit cell volume as a function of pressure at a given temperature. One then fits the  $P$ - $V$  curve to an equation of state, such as the Birch–Murnaghan [179] or Vinet equations [180]. As shown in Fig. 10.3A, thermal expansion significantly alters the predicted  $PV$  curves at the MP2/CBS limit, particularly at lower pressures [113]. This in turn leads to a nearly four-fold change in the predicted bulk modulus between a model which neglects thermal expansion (“no QHA”) and the thermally expanded crystal at room temperature [113]. Reported experimental bulk modulus values exhibit some variability, but the theoretical predictions are generally in good agreement with them (Fig. 10.3B).

Overall, the description of noncovalent forces is essential in accurately predicting crystalline Gibbs free energies. Neglecting the van der Waals dispersion, for instance, will have several significant implications. It leads to overly repulsive intermolecular interactions, which cause the crystal lattice energy to be underestimated (too weakly bound). This typically results in a crystal volume that is too large [181–183]. The erroneous treatment of noncovalent

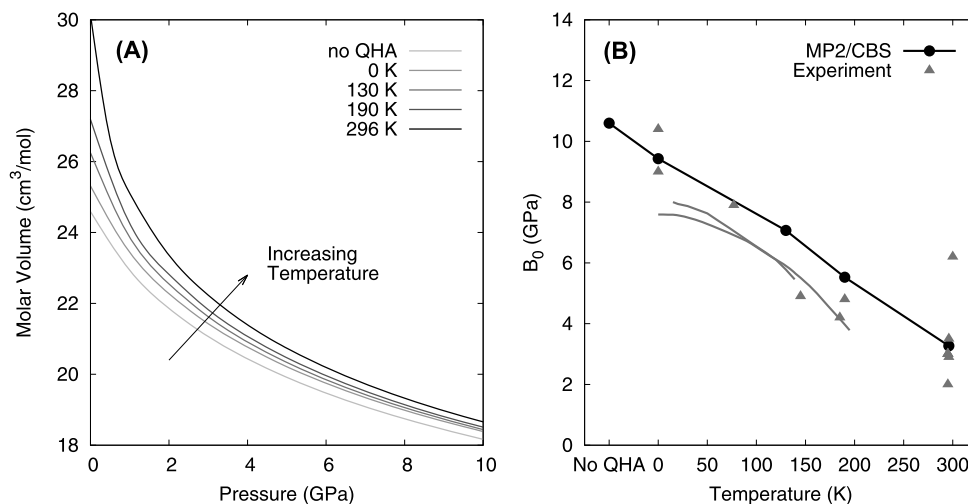


**FIGURE 10.3** (A) Pressure–volume curves for phase I carbon dioxide at various temperatures, and (B) bulk modulus values obtained by fitting the curves in (A) to the Vinet equation of state. Quasiharmonic predictions were made using the HMBI fragment approach at the complete-basis MP2/Amoeba level. The experimental data is taken from many different sources; see Ref. [113] for details.

interactions and exaggerated unit-cell volume translate into problematic property predictions. For example, dispersion has been shown to be important for predicting low-frequency phonon modes [184–186]. Without dispersion corrections, DFT also overestimates the bulk modulus of carbon dioxide [46].

### 10.3.2 Molecular Crystal Phase Diagrams

Mapping out molecular crystal phase diagrams represents a logical extension of molecular crystal free energy predictions. Traditional polymorph prediction has focused on identifying crystal structures which are observed at or near ambient conditions. However, a wide variety of phases are known to occur at more extreme temperatures and pressures. Even seemingly simple species can exhibit surprisingly rich diversity of phases. At least seventeen crystalline phases of ice [187,188], over a dozen crystalline phases of nitrogen [189], and nine solid phases of carbon dioxide are known [190]. At very high pressures, some of these phases become covalent/extended solids, but many others remain molecular in nature.

DFT has played an important role in elucidating structures for some of these high-pressure phases. For instance, the cubic gauche structure of polymeric nitrogen was predicted [191] a decade before it was produced and characterized experimentally [192]. Many of these studies have relied on evolutionary algorithms and other advanced search algorithms to discover unusual phases [193–195]. Here, we discuss examples from the phase diagrams of carbon dioxide and ice.

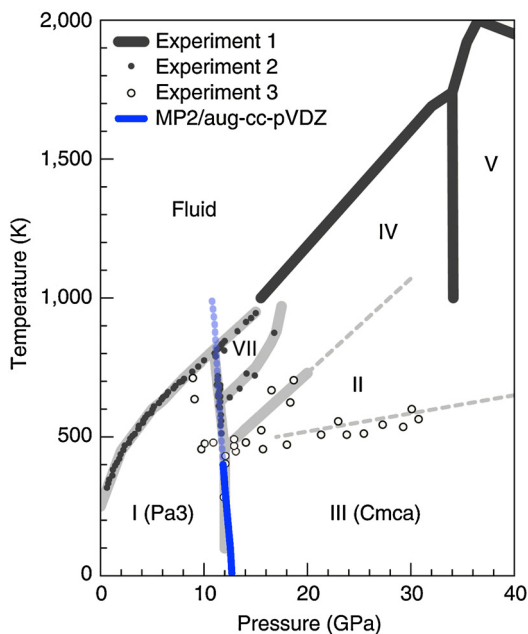


**FIGURE 10.4** Phase diagram of carbon dioxide and the fragment MP2 predictions of the phase I–III transition [129]. Reprinted with permission from Ref. [129]. Copyright 2013 Nature Publishing Group.

### Carbon Dioxide

The high-pressure phase diagram of carbon dioxide continues to elicit debate. Low-pressure phases like phase I (dry ice), III, and VII are molecular, while at very high pressures the phases become covalent solids with tetrahedral carbon geometries. However, there has been considerable debate about whether phases II and IV form intermediate phases, with bent molecules and elongated C–O bond lengths. Initial reports for phases II and IV argued for intermediate phases [196–198], but subsequent DFT calculations [46,199] and experimental studies [200,201] have argued in favor of more traditional molecular phases with linear carbon dioxide molecules. A number of other DFT studies [202–208] helped predict the structure of covalent phase V before it was subsequently confirmed via X-ray diffraction [209].

Another ambiguity surrounds the phase transition pressure between forms I and III. Experimentally, the transition is sluggish and occurs with significant hysteresis [210], which leads to a fairly broad range of reported phase transition pressures. However, fragment-based MP2 calculations by Li et al. predicted the transition around 12–13 GPa (Fig. 10.4), which is in fairly good agreement with various experimental studies placing it around 10–12 GPa [129].

### Ice XV

Ice also provides fertile ground for research, with new phases ice XV [211] and ice XVI [188] being discovered only in 2009 and 2014, respectively. Ice XV is the proton-ordered form

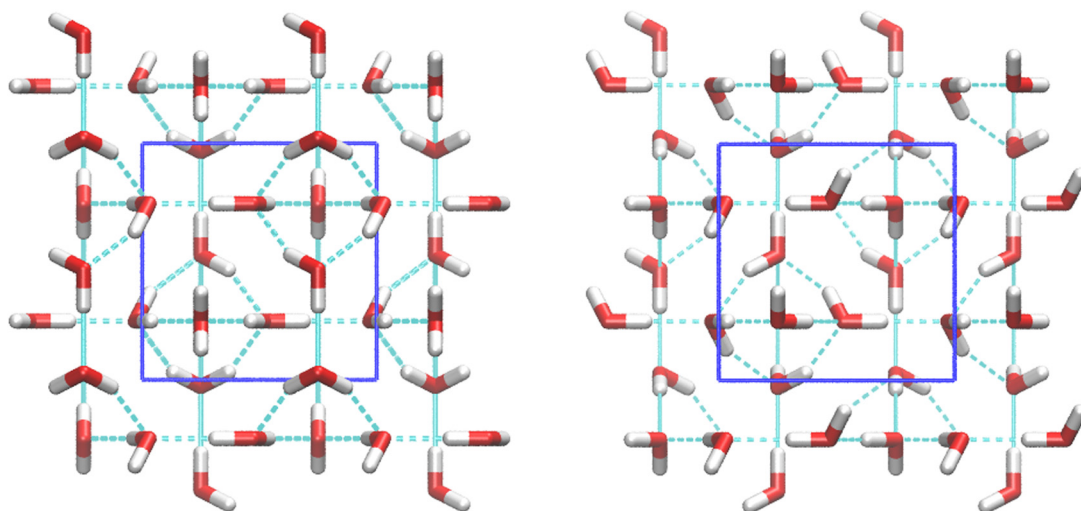


FIGURE 10.5 Low-energy antiferroelectric (left) and ferroelectric (right) proton orderings in the unit cell of ice XV. Solid lines reflect the unit cell boundaries, while dotted lines represent hydrogen bonds.

of ice VI, and it is stable around 1 GPa and below  $\sim 130$  K. The experimental structure was solved by powder X-ray diffraction, and the unit cell involves two interpenetrating networks of water molecules containing 5 molecules each. However, there has been controversy surrounding the arrangement of the protons. Prior to its experimental characterization, several DFT studies suggested a ferroelectric arrangement (i.e., having a nonzero net dipole in the unit cell) [212,213]. However, the subsequent interpretation of the powder X-ray diffraction results and Raman spectroscopy identified an antiferroelectric proton arrangement (zero net dipole in the unit cell) [211,214]. Fig. 10.5 shows both proton orderings. Fragment-based MP2 and CCSD(T) calculations appeared to confirm this antiferroelectric ordering as being the most stable [112], but fully periodic Gaussian and plane wave MP2 and RPA calculations (Chapter 3) once again favor the ferroelectric ordering [215]. If the ferroelectric proton ordering is indeed more stable, this raises the question of why the antiferroelectric ordering is observed experimentally. Del Ben and coworkers hypothesize that the antiferroelectric crystallization nuclei may be preferred in the electrostatic environment in which ice XV is formed [215]. Still, additional study may be needed to provide further clarity in this system.

### 10.3.3 Vibrational Spectroscopy

Vibrational spectroscopy provides a powerful experimental tool for probing crystal structures. Raman spectroscopy is often used to study high-pressure phases, while terahertz spectroscopy can provide “fingerprints” to characterize different crystal polymorphs. Accordingly, there has been considerable interest in predicting molecular crystal phonons for comparison with vibrational spectroscopy experiments [123,216–223]. Low-frequency tera-



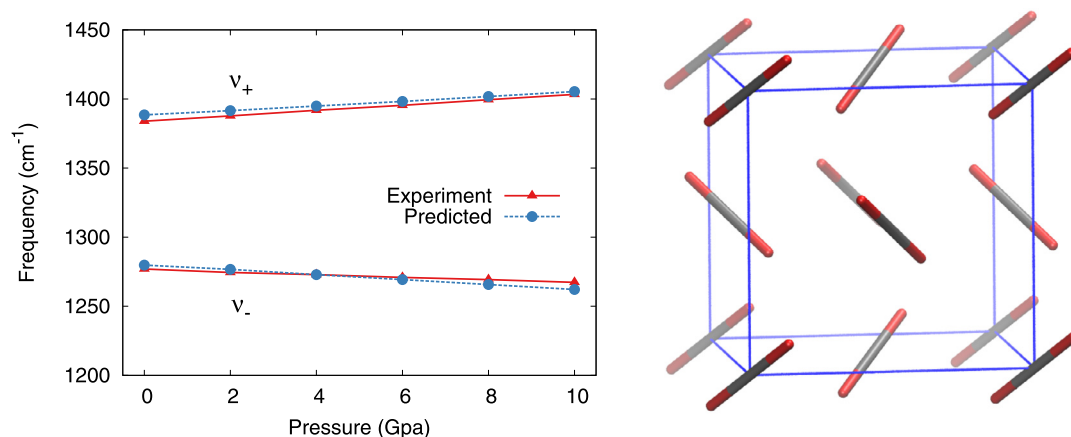


FIGURE 10.6 Comparison between experimental and predicted Raman frequencies for solid carbon dioxide at various pressures [130]. The carbon dioxide unit cell is shown at right.

hertz modes are particularly sensitive to the description of the intermolecular interactions and the unit cell volume, so it is important to treat intermolecular interactions (including van der Waals dispersion [184,185]) and finite-temperature effects carefully. A number of examples have been discussed elsewhere [14]. Here, we consider two examples.

### ***Fermi Resonance in Carbon Dioxide***

In carbon dioxide, the symmetric stretch ( $\nu_1$ ) and the first overtone of the bend ( $2\nu_2$ ) occur at nearly the same frequency and share the same symmetry. Anharmonic coupling between these two modes leads to a Fermi resonance, with two peaks  $\nu_+$  and  $\nu_-$  separated by  $\sim 100 \text{ cm}^{-1}$ . The specific splitting between these peaks varies with pressure, allowing geochemists to study the pressures under which carbon dioxide was entrapped in minerals during their formation and providing insights into mantle tectonics. Sode et al. [130] investigated this Fermi resonance in phase I carbon dioxide by coupling an accurate force field describing the intramolecular behavior of carbon dioxide with binary interaction MP2 to describe how the phonons in the crystal vary with pressure. The anharmonic coupling was then modeled using a full vibrational configuration interaction calculation, which expresses the anharmonic frequencies  $|\nu_{\pm}\rangle$  as a linear combination of the harmonic oscillator states,

$$|\nu_{\pm}\rangle = c_{\pm}|\nu_1\rangle + c'_{\pm}|2\nu_2\rangle + \dots; \quad (10.12)$$

see Ref. [130] for details. With this approach, the authors were able to semiquantitatively reproduce both the frequencies and intensities of the peaks arising from the Fermi resonance over the range 0–10 GPa (Fig. 10.6).

### ***Aspirin Polymorphism***

Another interesting application relevant to vibrational spectroscopy comes from aspirin. In this case, terahertz spectroscopy provides experimental support for a theoretical explanation

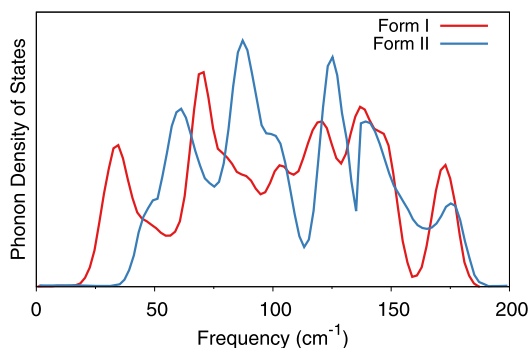


FIGURE 10.7 PBE-MBD phonon density of states for aspirin forms I and II. The overall shift toward lower frequency lattice modes, particularly the modes around  $30\text{ cm}^{-1}$ , help stabilize the room-temperature free energy of form I relative to form II [186].

of why form I aspirin is preferred over form II at room temperature. The structure of form II aspirin was first characterized only in 2005 [224–229], after it was predicted theoretically a year earlier [230]. The two crystals adopt very similar crystal packing that differs primarily in the weak interlayer hydrogen bonding involving the acetyl groups. In form I these groups form dimers, while in form II they adopt extended catemers (an extended zig-zag chain of hydrogen bonds). The form II structure can be generated from the form I one by simply “shifting” every second molecular plane. Crystallizing pure form II is difficult, and one often obtains mixed domains of forms I and II.

Fragment-based MP2 calculations indicate that these forms are nearly degenerate in lattice energy [110,153], but form I is clearly preferred experimentally. Reilly and Tkatchenko [186] confirmed the near degeneracy of the two forms at the electronic energy level with PBE-MBD, but they found that form I is preferred in terms of free energy at room temperature. In particular, they predict low-frequency phonon modes near  $\sim 30\text{ cm}^{-1}$  which occur only in the PBE-MBD model, not in the PBE-TS model (Fig. 10.7). The authors argue that these phonon modes arise from a coupling between many-body van der Waals interactions and the low-frequency phonon modes. Experimental support for this prediction comes from terahertz spectroscopy on form I, which reveals a peak at  $37\text{ cm}^{-1}$ . These low-frequency phonon modes, which are unique to form I, contribute substantially to the predicted 2.5 kJ/mol free energy preference for form I at room temperature. Both the vibrational entropy and the thermal contributions to the vibrational enthalpy are dominated by contributions from low-frequency modes [231].

### 10.3.4 NMR Spectroscopy

Solid-state NMR is an increasingly important tool for solving crystal structures in situations where one cannot perform single crystal X-ray diffraction experiments. The high sensitivity of NMR chemical shielding to local chemical environment makes it a particularly effective probe for crystal packing (including the positions of hydrogen atoms). Chemical shifts can be used to distinguish among crystal polymorphs, multicomponent crys-

tals, and even among symmetrically inequivalent molecules within a single unit cell [14,51,232–239].

The growing field of NMR crystallography combines powder X-ray diffraction (to obtain lattice and space group information), solid-state NMR, and computational modeling to refine [240–250] or solve crystal structures [251–254]. Electronic structure calculations are used to identify/refine potential crystal structures and to predict chemical shifts in those structures for comparison with experiment. Although chemical shifts provide a fingerprint for different crystal polymorphs, the changes in chemical shifts between polymorphs are often small (e.g., 1–3 ppm for  $^{13}\text{C}$  in sulfanilamide polymorphs [255]). Accordingly, high-quality chemical shift predictions are needed to correctly assign experimental spectra and discriminate among potential structures.

In NMR crystallography, noncovalent interactions are important in both determining the structure of the crystal and in the calculation of the chemical shifts. Chemical shifts can be very sensitive to both intramolecular conformation and intermolecular crystal packing. Proper treatment of both inter- and intramolecular interactions is essential for accurate chemical shift prediction in molecular crystals.

Van der Waals dispersion becomes critical when optimizing the crystal lattice parameters. Without dispersion, the intermolecular interactions are too repulsive and the optimized unit cells will be much too large [181–183], leading to poor-quality chemical shifts. If experimental X-ray crystal structures are available, optimizing the crystal while holding the experimental lattice parameters fixed reduces the negative impacts from neglecting dispersion [256], but dispersion forces should still be included to minimize the potential for unphysical interactions.

Electronic structure refinement of the experimental atomic positions in X-ray crystal structures can lead to substantial improvements in the quality of the predicted chemical shifts. Indeed, numerous cases exist where dispersion-corrected DFT was used to correct erroneous X-ray crystal structures [26,244,249,256]. Computational refinement of X-ray crystal structures is especially important for the hydrogen atom positions, but relaxing nonhydrogen atoms as well can lead to further improvements in the predicted chemical shifts [246,254]. The role of noncovalent interactions in computing chemical shifts will be discussed in the context of the fragment methods below.

### ***Gauge-Including Projector Augmented Wave Model***

First developed in 2001 [257] and subsequently adapted for ultrasoft pseudopotentials [258], the planewave gauge-including projector augmented wave (GIPAW) model paved the way for widespread prediction of NMR chemical shifts in the solid state. Chemical shielding is very sensitive to the electron density near the core. Use of the PAW approach provides a representation of those local atomic-like states from a planewave description. However, chemical shifts and other observable magnetic properties should be invariant to the magnetic field origin (the “gauge”). The localized functions introduced by the PAW transformation are not invariant to gauge transformation. Similar issues arise when using finite basis sets in atomic orbital approaches. GIPAW accounts for this via a field-dependent transformation operator which maintains translational invariance, which is similar to the explicit field-dependence built into the individual atomic orbital basis functions in the gauge-including atomic orbital approach (GIAO); see Refs. [232,257,258] for more details.

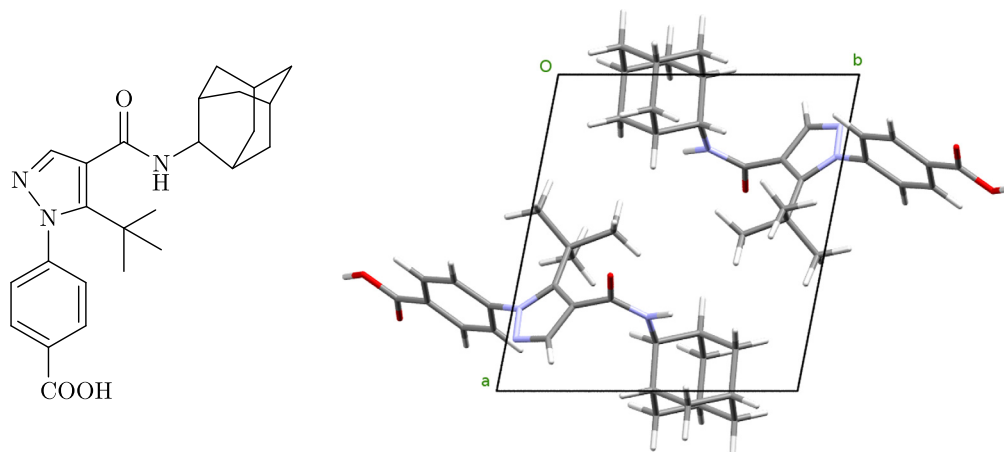


**FIGURE 10.8** Pharmaceutical compound AZD8329 (left) whose form 4 crystal structure (unit cell shown at right) was solved by combination of solid-state NMR, crystal structure prediction, and GIPAW chemical shift prediction [259].

GIPAW has been successfully applied to a host of organic and inorganic solids [232], often using the PBE density functional. For instance, testosterone ( $C_{19}H_{28}O_2$ ) represents a challenging case for solid-state NMR due to the crowded nature of its  $^{13}C$  spectrum. The  $\alpha$  polymorph of testosterone contains two symmetrically inequivalent molecules in the unit cell, resulting in two distinct isotropic shifts for each of the 19 carbons in a testosterone molecule. Of the 38 total  $^{13}C$  isotropic shifts, 30 occur in the 10–55 ppm range. Even with two-dimensional carbon–carbon correlation experiments [233], ten of the shifts could not unambiguously be assigned experimentally, nor could the correlation experiments identify which set of peaks belonged to which of the two molecules in the asymmetric unit. However, GIPAW PBE calculations enabled assignment of the two groups of peaks to the two molecules and suggested assignments for the ten remaining shifts [233].

The combination of crystal structure prediction and GIPAW is particularly promising [260,261], since chemical shift provides a criterion for assessing candidate structures that is “orthogonal” to thermodynamic stability. In a 2013 study, Baiaş and coworkers [259] used this combination to solve the previously unknown form 4 structure of the pharmaceutical AZD8329 (Fig. 10.8), which is a potential type 2 diabetes drug. Crystal structure prediction techniques were used to generate potential structures for this drug. AZD8329 contains six nontrivial torsional degrees of freedom, and crystal structure prediction was performed over an ensemble of 80 initial conformations in the 32 most common space groups. The *cis/trans* conformations about the amide bond proved important, and the crystal structure prediction generated 20 *trans* and 14 *cis* structures lying within 30 kJ/mol of the most stable ones.  $^1H$  and  $^{13}C$  chemical shifts for all 34 structures were then predicted using GIPAW. Interestingly, although the *cis* conformation structures were all predicted to be less stable than the *trans* ones, the lowest-energy *cis* structure (overall rank 21) proved the best match to the NMR data. This demonstrates that lattice energy rankings can be skewed by deficiencies in the energy model, and that having chemical shifts to compare against can help identify the correct structure. The

structure of AZD8329 determined from this study was subsequently confirmed via powder X-ray diffraction [259].

### Fragment-Based Methods

Fragment methods have begun to play a role in NMR chemical shift prediction for molecular crystals. The chemical shielding tensor is defined as the second derivative of the electronic energy with respect to the  $\alpha$ th component of the external magnetic field  $B_\alpha$  and the  $\beta$ th component of the nuclear magnetic moment on atom  $A$ ,  $\mu_\beta^A$ :

$$\sigma_{\alpha\beta}^A = \frac{\partial^2 E}{\partial B_\alpha \partial \mu_\beta^A}. \quad (10.13)$$

Accordingly, one can differentiate the many-body expansion of the energy in Eq. (10.2) to obtain an expansion for the shielding tensor  $\tilde{\sigma}_i^A$  of atom  $A$  on molecule  $i$  in the crystal,

$$\tilde{\sigma}_i^A = \sigma_i^A + \sum_{ij} \Delta^2 \sigma_{ij}^A + \sum_{ijk} \Delta^3 \sigma_{ijk}^A + \dots \quad (10.14)$$

where  $\sigma_i^A$  is the shielding tensor of the isolated monomer in its crystalline geometry, and  $\Delta^2 \sigma_{ij}^A$  and  $\Delta^3 \sigma_{ijk}^A$  are 2- and 3-body contributions to the shielding tensor arising from the interaction of that molecule with other molecules in the crystal.

The many-body expansion for the shielding tensor converges relatively rapidly [133], especially for nuclei like  $^{13}\text{C}$  and  $^1\text{H}$ . Many-body effects prove more important in nuclei like  $^{15}\text{N}$  and  $^{17}\text{O}$  [133,135]. These latter two nuclei exhibit broad chemical shift ranges and frequently exhibit lone pairs which actively participate in hydrogen bonding and other non-covalent interactions, making their chemical shifts more sensitive to the chemical environment.

For example, Fig. 10.9 plots the errors in absolute  $^{13}\text{C}$  and  $^{15}\text{N}$  chemical shieldings for a set of small molecular clusters containing 8–25 molecules at various truncations of the many-body expansion. For reference, chemical shift accuracies within  $\sim 1$ – $2$  ppm for  $^{13}\text{C}$  and  $\sim 4$ – $5$  ppm for  $^{15}\text{N}$  are typical for state-of-the-art models, as discussed below. A 1-body-only model neglects all intermolecular interactions and performs very poorly, with errors up to tens of ppm. Adding pairwise intermolecular interactions dramatically reduces the errors, and further improvements are seen as three-body interactions are added.

Electrostatic interactions are particularly important in the calculation of chemical shieldings. Including electrostatic point-charge embedding to mimic long-range interactions and many-body polarization effects accelerates the convergence of the many-body expansion of the chemical shieldings. In fact, the earliest fragment methods relied on electrostatically embedded monomer calculations [262,263]. Since 2014, embedded 1- and 2-body models have been shown to work very well for many nuclei [133–135]. In cases like oxygen, where explicit treatment of the local many-body effects can be important, one can also use clusters consisting of  $\sim 10$ – $15$  molecules [264,265], or a combination of a cluster plus longer-range pairwise fragment contributions [135].

The basis set requirements for NMR chemical shielding calculations are interesting. Describing the energetics of noncovalent interactions typically requires large basis sets. In con-

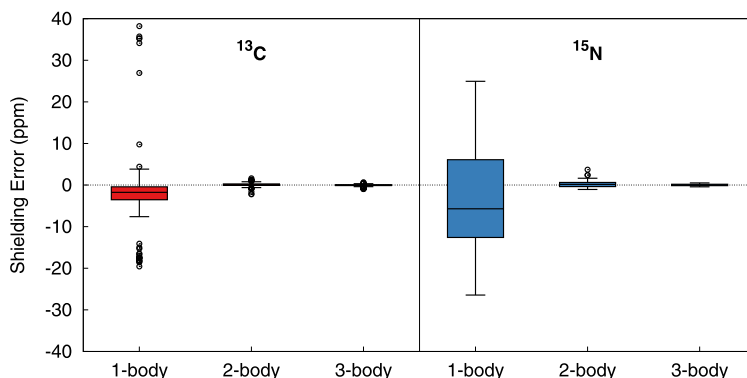


**FIGURE 10.9** Errors in absolute  $^{13}\text{C}$  and  $^{15}\text{N}$  isotropic chemical shieldings predicted for a set of small-molecule clusters for 1-body, 2-body, and 3-body fragment truncations of the many-body expansion relative to a full, conventional chemical shielding calculation [133].

trast, “locally dense” basis sets, which place many basis functions on the atoms of interest, and use many fewer basis functions further away, work very well for chemical shielding calculations [266–268]. In fragment approaches, for instance, one can employ a fairly large basis set on the atoms whose shifts are desired (e.g., 6-311+G(2d,p)), a modest basis set on nearest neighbor atoms (e.g., 6-311G(d,p) out to 4 Å), and a crude basis like 6-31G on the more distant atoms [269]. Even a small basis without polarization functions on these distant atoms is apparently sufficient for reproducing the electrostatic environment necessary to describe these shieldings. Remaining errors stemming from the finite basis set are often compensated for if one uses a linear regression model to map the chemical shieldings onto chemical shifts, as described below [134,135].

Fragment methods for chemical shielding offer several advantages compared to more conventional plane wave DFT. First, the computational scaling is independent of the number of symmetrically equivalent molecules in the unit cell, and it scales linearly with the number of symmetrically inequivalent molecules in the cell. Second, each individual monomer or dimer fragment job can be run on its own group of processors, allowing for very efficient parallel scaling on hundreds of processor cores. With enough processors available, one can often obtain chemical shifts for a pharmaceutical crystal within a few wall clock hours. Third, fragment methods allow the chemical shieldings to be computed with a variety of different electronic structure methods.

For example, we have demonstrated that the use of hybrid density functionals provides notable improvements in the chemical shifts compared to generalized gradient approximation (GGA) functionals. Hybrid functionals like B3LYP or PBE0 are computationally prohibitive in plane wave DFT, but they cost less than a factor of two more than GGAs in the Gaussian-basis sets used in fragment approaches. We constructed benchmark test sets of experimental isotropic shifts for four commonly studied NMR-active nuclei [134,135]:

- **Hydrogen**, 13 crystal structures & 80 shifts;
- **Carbon**, 25 crystal structures & 169 shifts;

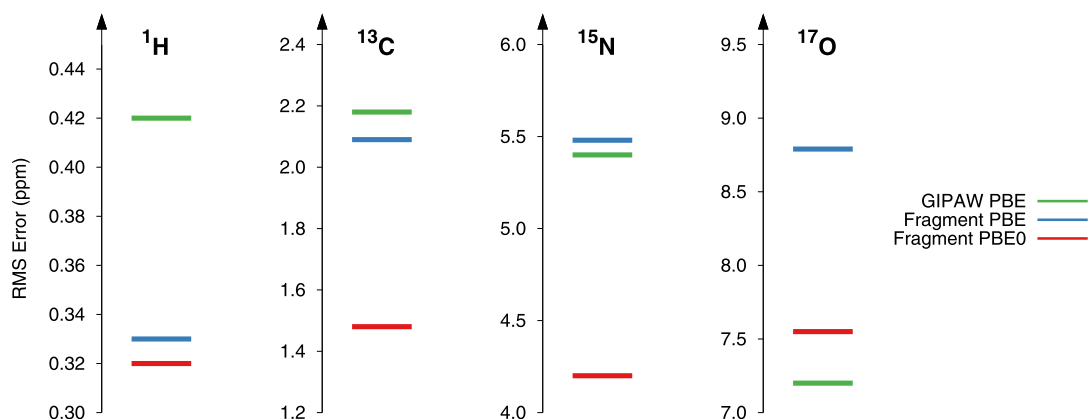


FIGURE 10.10 Root-mean-squared errors (in ppm) for the  $^1\text{H}$ ,  $^{13}\text{C}$ ,  $^{15}\text{N}$ , and  $^{17}\text{O}$  molecular crystal benchmark sets of chemical shifts. For oxygen, hybrid cluster/fragment results are shown.

- **Nitrogen**, 24 crystal structures & 51 shifts;
- **Oxygen**, 15 crystal structures & 28 shifts.

These sets include crystals composed of amino acids, sugars, DNA base pairs, pharmaceutically active compounds, etc. Fig. 10.10 compares the root-mean-squared (RMS) errors between GIPAW PBE, fragment PBE, and fragment PBE0. Here, the fragment models refer to an electrostatically embedded 1- and 2-body model for  $^1\text{H}$ ,  $^{13}\text{C}$ , and  $^{15}\text{N}$ , and a combined cluster/fragment approach for  $^{17}\text{O}$ . For hydrogen, the fragment approaches perform nominally better, though the differences are small compared to the typical  $\sim 0.1$  ppm uncertainties in the experimental chemical shifts. For carbon and nitrogen, fragment PBE and GIPAW PBE perform similarly, but switching to the hybrid PBE0 functional reduces the RMS errors appreciably.

For oxygen, the importance of many-body effects means that the best fragment model results are obtained with the combined cluster/fragment approach. In this case, GIPAW PBE does perform somewhat better than cluster/fragment PBE, but the improved performance of the hybrid PBE0 functional largely compensates for this difference. Notably, the experimental uncertainties for the  $^{17}\text{O}$  isotropic shifts in the benchmark range from 0.5–5 ppm, so the  $\sim 0.4$  ppm difference in RMS errors between GIPAW PBE and fragment PBE0 may not be statistically significant.

The improved accuracy provided by the fragment approach and hybrid density functionals allows for increased confidence in chemical shift assignment. In NMR crystallography, where one combines experimental chemical shifts and ones predicted on potential structures, the higher accuracy allows for increased discrimination between correct and incorrect structures. Finally, it could potentially assist in NMR-based crystal structure refinement, since the correct structures will exhibit closer agreement with the experimental values.

One of the challenges that arises in NMR chemical shift prediction is the mapping between the absolute chemical shieldings one predicts theoretically and the observable chemical shifts (which are the shieldings relative to that of a reference compound like tetramethylsilane,

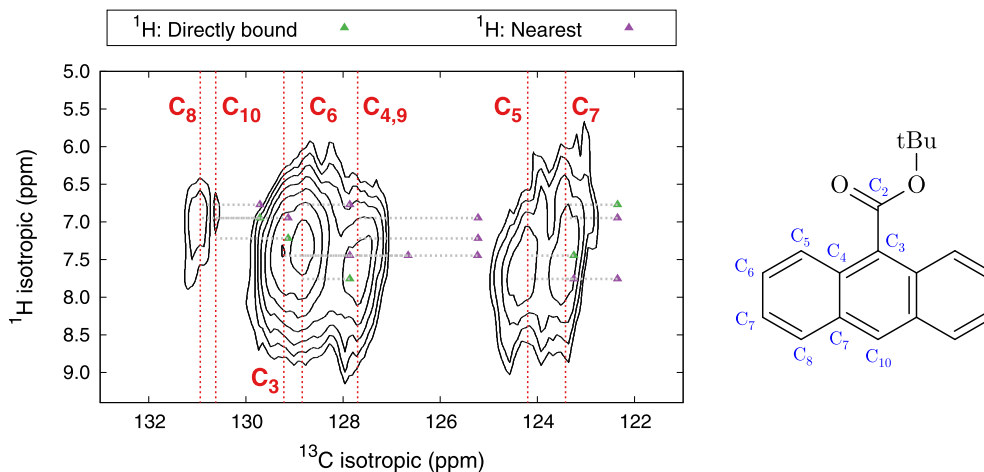


**FIGURE 10.11** Proposed  $^1\text{H}/^{13}\text{C}$  HETCOR assignments for the aromatic carbons and hydrogens in 9-TBAE. Contours indicate the experimental spectrum, vertical lines correspond to the experimental  $^{13}\text{C}$  shifts and their assignments. The symbols and horizontal lines indicate predicted cross-peak locations. Figure excerpted from Ref. [135] and licensed under the CC BY 3.0 (see <https://creativecommons.org/licenses/by/3.0/>, consulted August 2016).

TMS). One common approach converts shieldings  $\sigma$  to shifts  $\delta$  via a linear regression,

$$\delta = A\sigma + B, \quad (10.15)$$

where  $A$  and  $B$  are fitting parameters. Ideally,  $A$  would equal  $-1$  and  $B$  would be the chemical shielding of the reference compound. In practice, the slope deviates moderately from unity due to systematic errors in the electronic structure method and basis set. In addition to quantifying the accuracy of various chemical shift prediction models, the benchmark sets above also provide training data for fitting these regressions which can then be applied to other systems. Not only are these regression models transferable to other molecular crystals [135], but they have even been applied successfully to predicting the chemical shifts in large biomolecules [270].

The crystals of 9-*tert*-butyl anthracene ester (9-TBAE) provide a nice example of fragment-based chemical shift prediction. When exposed to light, molecules of 9-TBAE in nanorod crystals undergo a [4+4] photodimerization reaction, and the nanorods expand by up to 15% [271,272]. This property makes them potentially useful for performing photomechanical work, and the structures of these crystals and their photodimer product have been studied via X-ray diffraction and solid-state NMR. As part of these studies, fragment techniques were used to help assign the  $^1\text{H}/^{13}\text{C}$  heteronuclear correlation (HETCOR) spectrum. Cross-peaks in the aromatic region of the HETCOR spectrum proved particularly dense. However, the fragment PBE0 shift predictions allowed assignment of the carbon shifts. Combining the carbon peak assignments with the assumption that the HETCOR resonances are dominated by contributions from either directly bonded or nearest-neighbor hydrogen atoms, plausible assignments for all cross-peaks in the HETCOR spectrum could be made, as shown in Fig. 10.11.



## 10.4 SUMMARY

Molecular crystals provide sensitive tests for modeling noncovalent interactions using electronic structure methods. Thanks to advances in modeling noncovalent interactions using density functional theory, periodic MP2, and fragment methods, molecular crystal properties can now be routinely calculated with predictive accuracy. Many different representative applications have been discussed here, ranging from finite-temperature property prediction to NMR crystallography. In all cases, the theoretical predictions have contributed meaningfully to our experimental understanding of these problems.

### Acknowledgments

Support from the National Science Foundation (CHE-1362465) is gratefully acknowledged.

### References

- [1] A.J. Cruz-Cabeza, S.M. Reutzel-Edens, J. Bernstein, *Chem. Soc. Rev.* 44 (2015) 8619–8635.
- [2] V. López-Mejías, J.W. Kampf, A.J. Matzger, *J. Am. Chem. Soc.* 134 (2012) 9872–9875.
- [3] L. Yu, *Acc. Chem. Res.* 43 (2010) 1257–1266.
- [4] O. Reany, M. Kapon, M. Botoshansky, E. Keinan, *Cryst. Growth Des.* 9 (2009) 3661–3670.
- [5] R. Censi, P. Di Martino, *Molecules* 20 (2015) 18759–18776.
- [6] S. Haas, A.F. Stassen, G. Schuck, K.P. Pernstich, D.J. Gundlach, B. Batlogg, U. Berens, H.J. Kirner, *Phys. Rev. B* 76 (2007) 115203.
- [7] K. Roth, *Chem. Unserer Zeit* 39 (2005) 416–428.
- [8] J. Nyman, G.M. Day, *CrystEngComm* 17 (2015) 5154–5165.
- [9] J. Zhou, Y.-S. Kye, G.S. Harbison, *J. Am. Chem. Soc.* 126 (2004) 8392–8393.
- [10] S. Crawford, M.T. Kirchner, D. Bläser, R. Boese, W.I.F. David, A. Dawson, A. Gehrke, R.M. Ibberson, W.G. Marshall, S. Parsons, O. Yamamuro, *Angew. Chem. Int. Ed.* 48 (2009) 755–757.
- [11] V. Vasylyeva, T. Kedzioriski, N. Metzler-Nolte, C. Schauerer, K. Merz, *Cryst. Growth Des.* 10 (2010) 4224–4226.
- [12] N.P. Funnell, A. Dawson, D. Francis, A.R. Lennie, W.G. Marshall, S.A. Moggach, J.E. Warren, S. Parsons, *CrystEngComm* 12 (2010) 2573.
- [13] B.C.K. Ip, I.G. Shenderovich, P.M. Tolstoy, J. Frydel, G.S. Denisov, G. Buntkowsky, H.-H. Limbach, *J. Phys. Chem. A* 116 (2012) 11370–11387.
- [14] G.J.O. Beran, *Chem. Rev.* 116 (2016) 5567–5613, available online at <http://pubs.acs.org/doi/full/10.1021/acs.chemrev.5b00648>.
- [15] S. Grimme, A. Hansen, J.G. Brandenburg, C. Bannwarth, *Chem. Rev.* 116 (2016) 5105–5154.
- [16] K. Berland, V.R. Cooper, K. Lee, E. Schröder, T. Thonhauser, P. Hyldgaard, B.I. Lundqvist, *Rep. Prog. Phys.* 78 (2015) 066501.
- [17] L. Kronik, A. Tkatchenko, *Acc. Chem. Res.* 47 (2014) 3208–3216.
- [18] A.M. Reilly, A. Tkatchenko, *Chem. Sci.* 6 (2015) 3289–3301.
- [19] M.A. Neumann, F.J.J. Leusen, J. Kendrick, *Angew. Chem. Int. Ed.* 47 (2008) 2427–2430.
- [20] A. Asmadi, M.A. Neumann, J. Kendrick, P. Girard, M.A. Perrin, F.J.J. Leusen, *J. Phys. Chem. B* 113 (2009) 16303–16313.
- [21] H.C.S. Chan, J. Kendrick, F.J.J. Leusen, *Angew. Chem. Int. Ed.* 50 (2011) 2979–2981.
- [22] H.C.S. Chan, J. Kendrick, F.J.J. Leusen, *Phys. Chem. Chem. Phys.* 13 (2011) 20361–20370.
- [23] J. Kendrick, F.J.J. Leusen, M.A. Neumann, J. van de Streek, *Chem. Eur. J.* 17 (2011) 10736–10744.
- [24] M.-A. Perrin, M.A. Neumann, H. Elmaleh, L. Zaska, *Chem. Commun.* (2009) 3181–3183.
- [25] M.A. Neumann, J. van de Streek, F.P.A. Fabbiani, P. Hidber, O. Grassmann, *Nat. Commun.* 6 (2015) 7793.
- [26] J. van de Streek, M.A. Neumann, *Acta Crystallogr. B* 70 (2014) 1020–1032.
- [27] A.D. Becke, E.R. Johnson, *J. Chem. Phys.* 124 (2006) 014104.

- [28] A.D. Becke, E.R. Johnson, *J. Chem. Phys.* 127 (2007) 154108.
- [29] E.R. Johnson, *J. Chem. Phys.* 135 (2011) 234109.
- [30] A. Otero-de-la-Roza, E.R. Johnson, *J. Chem. Phys.* 136 (2012) 174109.
- [31] A. Tkatchenko, M. Scheffler, *Phys. Rev. Lett.* 102 (2009) 073005.
- [32] R.A. DiStasio, O.A. von Lilienfeld, A. Tkatchenko, *Proc. Natl. Acad. Sci. USA* 109 (2012) 14791–14795.
- [33] A. Tkatchenko, R.A. DiStasio, R. Car, M. Scheffler, *Phys. Rev. Lett.* 108 (2012) 236402.
- [34] A. Ambrosetti, A.M. Reilly, R.A. DiStasio, A. Tkatchenko, *J. Chem. Phys.* 140 (2014) 18A508.
- [35] S. Grimme, J. Antony, S. Ehrlich, H. Krieg, *J. Chem. Phys.* 132 (2010) 154104.
- [36] S. Grimme, S. Ehrlich, L. Goerigk, J. Comput. Chem. 32 (2011) 1456–1465.
- [37] J.G. Brandenburg, S. Grimme, *J. Phys. Chem. Lett.* 5 (2014) 1785–1789.
- [38] A.M. Reilly, A. Tkatchenko, *J. Chem. Phys.* 139 (2013) 024705.
- [39] J. Moellmann, S. Grimme, *J. Phys. Chem. C* 118 (2014) 7615–7621.
- [40] A. Otero-de-la-Roza, E.R. Johnson, *J. Chem. Phys.* 137 (2012) 054103.
- [41] J.G. Brandenburg, S. Grimme, *Top. Curr. Chem.* 345 (2014) 1–23.
- [42] J.G. Brandenburg, T. Maas, S. Grimme, *J. Chem. Phys.* 142 (2015) 124104.
- [43] A.M. Reilly, et al., *Acta Crystallogr. B* 72 (2016) 439–459.
- [44] B. Santra, J. Klimes, D. Alfe, A. Tkatchenko, B. Slater, A. Michaelides, R. Car, M. Scheffler, *Phys. Rev. Lett.* 107 (2011) 185701.
- [45] B. Santra, J. Klimeš, A. Tkatchenko, D. Alfè, B. Slater, A. Michaelides, R. Car, M. Scheffler, *J. Chem. Phys.* 139 (2013) 154702.
- [46] S. Gohr, S. Grimme, T. Söhnle, B. Paulus, P. Schwerdtfeger, *J. Chem. Phys.* 139 (2013) 174501.
- [47] J.G. Brandenburg, S. Grimme, P.G. Jones, G. Markopoulos, H. Hopf, M.K. Cyranski, D. Kuck, *Chem. Eur. J.* 19 (2013) 9930–9938.
- [48] A. Otero-de-la-Roza, B.H. Cao, I.K. Price, J.E. Hein, E.R. Johnson, *Angew. Chem. Int. Ed.* 53 (2014) 7879–7882.
- [49] N. Marom, R.A. DiStasio, V. Atalla, S. Levchenko, A.M. Reilly, J.R. Chelikowsky, L. Leiserowitz, A. Tkatchenko, *Angew. Chem. Int. Ed.* 52 (2013) 6629–6632.
- [50] M.A. Neumann, M.-A. Perrin, *CrystEngComm* 11 (2009) 2475.
- [51] D.E. Braun, J.A. McMahon, L.H. Koztecki, S.L. Price, S.M. Reutzel-Edens, *Cryst. Growth Des.* 14 (2014) 2056–2072.
- [52] J. Antony, S. Grimme, *Phys. Chem. Chem. Phys.* 8 (2006) 5287.
- [53] T. Gelbrich, D.E. Braun, A. Ellern, U.J. Griesser, *Cryst. Growth Des.* 13 (2013) 1206–1217.
- [54] P.Y. Ayala, K.N. Kudin, G.E. Scuseria, *J. Chem. Phys.* 115 (2001) 9698–9707.
- [55] A.F. Izmaylov, G.E. Scuseria, *Phys. Chem. Chem. Phys.* 10 (2008) 3421–3429.
- [56] A.F. Izmaylov, G.E. Scuseria, in: F. Manby (Ed.), *Accurate Quantum Chemistry in the Condensed Phase*, CRC Press, Boca Raton, FL, 2010, pp. 1–28.
- [57] L. Maschio, D. Usvyat, F.R. Manby, S. Casassa, C. Pisani, M. Schütz, *Phys. Rev. B* 76 (2007) 075101.
- [58] D. Usvyat, L. Maschio, F.R. Manby, S. Casassa, C. Pisani, M. Schütz, *Phys. Rev. B* 76 (2007) 075102.
- [59] D. Usvyat, L. Maschio, M. Schütz, *J. Chem. Phys.* 143 (2015) 102805.
- [60] M. Katouda, S. Nagase, *J. Chem. Phys.* 133 (2010) 184103.
- [61] X. Ren, P. Rinke, V. Blum, J. Wieferink, A. Tkatchenko, A. Sanfilippo, K. Reuter, M. Scheffler, *New J. Phys.* 14 (2012) 053020.
- [62] A.C. Ihrig, J. Weiferink, I.Y. Zhang, M. Ropo, X. Ren, P. Rinke, M. Scheffler, V. Blum, *New J. Phys.* (2014) 093020.
- [63] M. Marsman, A. Grüneis, J. Paier, G. Kresse, *J. Chem. Phys.* 130 (2009) 184103.
- [64] A. Grüneis, M. Marsman, G. Kresse, *J. Chem. Phys.* 133 (2010) 074107.
- [65] M. Ben Del, J. Hutter, J. VandeVondele, *J. Chem. Theory Comput.* 8 (2012) 4177–4188.
- [66] M. Ben Del, J. Hutter, J. VandeVondele, *J. Chem. Theory Comput.* 9 (2013) 2654–2671.
- [67] M. Ben Del, J. Hutter, J. VandeVondele, *J. Chem. Phys.* 143 (2015) 102803.
- [68] L. Maschio, D. Usvyat, M. Schütz, B. Civalleri, *J. Chem. Phys.* 132 (2010) 134706.
- [69] L. Maschio, D. Usvyat, B. Civalleri, *CrystEngComm* 12 (2010) 2429–2435.
- [70] D. Presti, A. Pedone, M.C. Menziani, B. Civalleri, L. Maschio, *CrystEngComm* 16 (2014) 102–109.
- [71] A. Erba, L. Maschio, S. Salustro, S. Casassa, *J. Chem. Phys.* 134 (2011) 074502.
- [72] D. Usvyat, B. Civalleri, L. Maschio, R. Dovesi, C. Pisani, M. Schutz, *J. Chem. Phys.* 134 (2011) 214105.
- [73] D. Usvyat, *J. Chem. Phys.* 139 (2013) 194101.
- [74] M. Gerenkamp, S. Grimme, *Chem. Phys. Lett.* 392 (2004) 229–235.

- [75] R.A. Distasio, M. Head-Gordon, *Mol. Phys.* 105 (2007) 1073–1083.
- [76] C. Müller, D. Usvyat, *J. Chem. Theory Comput.* 9 (2013) 5590–5598.
- [77] M.S. Gordon, D.G. Fedorov, S.R. Pruitt, L. Slipchenko, *Chem. Rev.* 112 (2012) 632–672.
- [78] M.A. Collins, R.P.A. Bettens, *Chem. Rev.* 115 (2015) 5067–5642.
- [79] K. Raghavachari, A. Saha, *Chem. Rev.* 115 (2015) 5643–5677.
- [80] R.M. Richard, J.M. Herbert, *J. Chem. Phys.* 137 (2012) 064113.
- [81] N.J. Mayhall, K. Raghavachari, *J. Chem. Theory Comput.* 8 (2012) 2669–2675.
- [82] H. Stoll, *Phys. Rev. B* 46 (1992) 6700–6704.
- [83] H. Stoll, *J. Chem. Phys.* 97 (1992) 8449.
- [84] H. Stoll, *Chem. Phys. Lett.* 191 (1992) 548–552.
- [85] B. Paulus, *Phys. Rep.* 428 (2006) 1–52.
- [86] L.W. Chung, W.M.C. Sameera, R. Ramozzi, A.J. Page, M. Hatanaka, G.P. Petrova, T.V. Harris, X. Li, Z. Ke, F. Liu, H.-B. Li, L. Ding, K. Morokuma, *Chem. Rev.* 115 (2015) 5678–5796.
- [87] B.W. Hopkins, G.S. Tschumper, *Mol. Phys.* 103 (2005) 309–315.
- [88] G.S. Tschumper, *Chem. Phys. Lett.* 427 (2006) 185–191.
- [89] A. Hermann, P. Schwerdtfeger, *Phys. Rev. Lett.* 101 (2008) 183005.
- [90] K. Rosciszewski, B. Paulus, P. Fulde, H. Stoll, *Phys. Rev. B* 60 (1999) 7905–7910.
- [91] P. Schwerdtfeger, B. Assadollahzadeh, A. Hermann, *Phys. Rev. B* 82 (2010) 205111.
- [92] C. Müller, B. Paulus, *Phys. Chem. Chem. Phys.* 14 (2012) 7605–7614.
- [93] O. Bludsky, M. Rubes, P. Soldan, *Phys. Rev. B* 77 (2008) 092103.
- [94] S. Tsuzuki, H. Orita, K. Honda, M. Mikami, *J. Phys. Chem. B* 114 (2010) 6799–6805.
- [95] C.R. Taylor, P.J. Bygrave, J.N. Hart, N.L. Allan, F.R. Manby, *Phys. Chem. Chem. Phys.* 14 (2012) 7739–7743.
- [96] A.P. Bartok, M.J. Gillan, F.R. Manby, G. Csanyi, *Phys. Rev. B* 88 (2013) 054104.
- [97] M.J. Gillan, *J. Chem. Phys.* 141 (2014) 224106.
- [98] J. Rezáč, Y. Huang, P. Hobza, G.J.O. Beran, *J. Chem. Theory Comput.* 11 (2015) 2065–3079.
- [99] G.J.O. Beran, *J. Chem. Phys.* 130 (2009) 164115.
- [100] G.J.O. Beran, K. Nanda, *J. Phys. Chem. Lett.* 1 (2010) 3480–3487.
- [101] S. Wen, G.J.O. Beran, *J. Chem. Theory Comput.* 7 (2011) 3733–3742.
- [102] K. Nanda, G.J.O. Beran, *J. Chem. Phys.* 137 (2012) 174106.
- [103] G.J.O. Beran, S. Wen, K. Nanda, Y. Huang, Y. Heit, *Top. Curr. Chem.* 345 (2014) 59–93.
- [104] P. Ren, J.W. Ponder, *J. Phys. Chem. B* 107 (2003) 5933–5947.
- [105] P. Ren, C. Wu, J.W. Ponder, *J. Chem. Theory Comput.* 7 (2011) 3143–3161.
- [106] J.C. Wu, G. Chattree, P. Ren, *Theor. Chem. Acc.* 131 (2012) 1138.
- [107] A. Sebetci, G.J.O. Beran, *J. Chem. Theory Comput.* 6 (2010) 155–167.
- [108] D.P.O. Neill, N.L. Allan, F.R. Manby, in: F. Manby (Ed.), *Accurate Quantum Chemistry in the Condensed Phase*, CRC Press, Boca Raton, FL, 2010, pp. 163–193.
- [109] Y. Heit, G.J.O. Beran, *J. Comput. Chem.* 35 (2014) 2205–2214.
- [110] S. Wen, G.J.O. Beran, *Cryst. Growth Des.* 12 (2012) 2169–2172.
- [111] S. Wen, G.J.O. Beran, *J. Chem. Theory Comput.* 8 (2012) 2698–2705.
- [112] K. Nanda, G.J.O. Beran, *J. Phys. Chem. Lett.* 4 (2013) 3165–3169.
- [113] Y.N. Heit, K.D. Nanda, G.J.O. Beran, *Chem. Sci.* 7 (2016) 246–255.
- [114] Y.N. Heit, G.J.O. Beran, *Acta Crystallogr. B* 72 (2016) 514–529.
- [115] J. Yang, W. Hu, D. Usvyat, D. Matthews, M. Schutz, G.K.-L. Chan, *Science* 345 (2014) 640–643.
- [116] M.R. Kennedy, A.R. McDonald, A.E. DePrince, M.S. Marshall, R. Podeszwa, C.D. Sherrill, *J. Chem. Phys.* 140 (2014) 121104.
- [117] R. Podeszwa, B.M. Rice, K. Szalewicz, *Phys. Rev. Lett.* 101 (2008) 115503.
- [118] R.M. Richard, K.U. Lao, J.M. Herbert, *J. Chem. Phys.* 141 (2014) 014108.
- [119] R.M. Richard, K.U. Lao, J.M. Herbert, *J. Phys. Chem. Lett.* 4 (2013) 2674–2680.
- [120] R.M. Richard, K.U. Lao, J.M. Herbert, *Acc. Chem. Res.* 47 (2014) 2828–2836.
- [121] J.F. Ouyang, M.W. Cvitkovic, R.P.A. Bettens, *J. Chem. Theory Comput.* 10 (2014) 3699–3707.
- [122] S. Hirata, *J. Chem. Phys.* 129 (2008) 204104.
- [123] S. Hirata, K. Gilliard, X. He, J. Li, O. Sode, *Acc. Chem. Res.* 47 (2014) 2721–2730.
- [124] T. Fang, W. Li, F. Gu, S. Li, *J. Chem. Theory Comput.* 11 (2015) 91–98.
- [125] T. Fang, J. Jia, S. Li, *J. Phys. Chem. A* (2016), <http://dx.doi.org/10.1021/acs.jpca.5b10927>.

- [126] X. He, O. Sode, S.S. Xantheas, S. Hirata, *J. Chem. Phys.* 137 (2012) 204505.
- [127] O. Sode, S. Hirata, *Phys. Chem. Chem. Phys.* 14 (2012) 7765–7779.
- [128] K. Gilliard, O. Sode, S. Hirata, *J. Chem. Phys.* 140 (2014) 174507.
- [129] J. Li, O. Sode, G.A. Voth, S. Hirata, *Nat. Commun.* 4 (2013) 2647.
- [130] O. Sode, M. Keceli, K. Yagi, S. Hirata, *J. Chem. Phys.* 138 (2013) 074501.
- [131] G. Cardini, V. Schettino, *J. Chem. Phys.* 140 (2014) 177101.
- [132] J. Li, O. Sode, S. Hirata, *J. Chem. Theory Comput.* 11 (2015) 224–229.
- [133] J.D. Hartman, G.J.O. Beran, *J. Chem. Theory Comput.* 10 (2014) 4862–4872.
- [134] J.D. Hartman, S. Monaco, B. Schatschneider, G.J.O. Beran, *J. Chem. Phys.* 143 (2015) 102809.
- [135] J.D. Hartman, R.A. Kudla, G.M. Day, L.J. Mueller, G.J.O. Beran, *Phys. Chem. Chem. Phys.* 18 (2016) 21686–21709.
- [136] S.Y. Willow, M.A. Salim, K.S. Kim, S. Hirata, *Nat. Sci. Rep.* 5 (2015) 14358.
- [137] M.A. Salim, S.Y. Willow, S. Hirata, *J. Chem. Phys.* 144 (2016) 204503.
- [138] P.J. Bygrave, N.L. Allan, F.R. Manby, *J. Chem. Phys.* 137 (2012) 164102.
- [139] F.R. Manby, M. Stella, J.D. Goodpaster, T.F. Miller, *J. Chem. Theory Comput.* 8 (2012) 2564–2568.
- [140] J.D. Goodpaster, T.A. Barnes, F.R. Manby, T.F. Miller, *J. Chem. Phys.* 140 (2014) 18A507.
- [141] G. Knizia, G.K.L. Chan, *J. Chem. Theory Comput.* 9 (2013) 1428–1432.
- [142] I.W. Bulik, W. Chen, G.E. Scuseria, *J. Chem. Phys.* 141 (2014) 054113.
- [143] M.E. Fornace, J. Lee, K. Miyamoto, F.R. Manby, T.F. Miller, *J. Chem. Theory Comput.* 11 (2015) 568–580.
- [144] T. Dresselhaus, J. Neugebauer, *Theor. Chem. Acc.* 134 (2015) 97.
- [145] K.E. Riley, M. Pitonak, P. Jurecka, P. Hobza, *Chem. Rev.* 110 (2010) 5023–5063.
- [146] A. Hesselmann, *J. Chem. Phys.* 128 (2008) 144112.
- [147] A. Tkatchenko, R.A. Distasio, M. Head-Gordon, M. Scheffler, *J. Chem. Phys.* 131 (2009) 094106.
- [148] S.M. Cybulski, M.L. Lytle, *J. Chem. Phys.* 127 (2007) 141102.
- [149] O. Marchetti, H.-J. Werner, *J. Phys. Chem. A* 113 (2009) 11580–11585.
- [150] M. Pitonak, A. Hesselmann, *J. Chem. Theory Comput.* 6 (2010) 168–178.
- [151] L.A. Burns, M.S. Marshall, C.D. Sherrill, *J. Chem. Phys.* 141 (2014) 234111.
- [152] Y. Huang, M. Goldey, M. Head-Gordon, G.J.O. Beran, *J. Chem. Theory Comput.* 10 (2014) 2054–2063.
- [153] Y. Huang, Y. Shao, G.J.O. Beran, *J. Chem. Phys.* 138 (2013) 224112.
- [154] R. Sedlak, K.E. Riley, J. Řezáč, M. Pitoňák, P. Hobza, *Chem. Phys. Chem.* 14 (2013) 698–707.
- [155] F. Neese, F. Wennmohs, A. Hansen, *J. Chem. Phys.* 130 (2009) 114108.
- [156] C. Riplinger, B. Sandhoefer, A. Hansen, F. Neese, *J. Chem. Phys.* 139 (2013) 134101.
- [157] A.G. Taube, R.J. Bartlett, *J. Chem. Phys.* 128 (2008) 164101.
- [158] A.E. DePrince, C.D. Sherrill, *J. Chem. Theory Comput.* 9 (2013) 2687–2696.
- [159] J. Yang, G.K.L. Chan, F.R. Manby, M. Schütz, H.J. Werner, *J. Chem. Phys.* 136 (2012) 144105.
- [160] J. Řezáč, P. Hobza, *Chem. Rev.* 116 (2016) 5038–5071.
- [161] O. Marchetti, H.-J. Werner, *Phys. Chem. Chem. Phys.* 10 (2008) 3400–3409.
- [162] S. Ahn, F. Guo, B.M. Kariuki, K.D.M. Harris, *J. Am. Chem. Soc.* 128 (2006) 8441–8452.
- [163] P.G. Karamertzanis, G.M. Day, G.W.A. Welch, J. Kendrick, F.J.J. Leusen, M.A. Neumann, S.L. Price, *J. Chem. Phys.* 128 (2008) 244708.
- [164] A. Gavezotti, G. Filippini, *J. Am. Chem. Soc.* 117 (1995) 12299–12305.
- [165] V. Coropceanu, J. Cornil, D.A. da Silva Filho, Y. Olivier, R. Silbey, J.-L. Brédas, *Chem. Rev.* 107 (2007) 926–952.
- [166] Y. Li, V. Coropceanu, J.-L. Brédas, *J. Phys. Chem. Lett.* 3 (2012) 3325–3329.
- [167] G.M. Day, S.L. Price, *J. Am. Chem. Soc.* 125 (2003) 16434–16443.
- [168] A.E. Gray, G.M. Day, M. Leslie, S.L. Price, *Mol. Phys.* 102 (2004) 1067–1083.
- [169] R. Ramírez, N. Neuerburg, C.P. Herrero, *J. Chem. Phys.* 137 (2012) 044502.
- [170] B. Pamuk, J.M. Soler, R. Ramírez, C.P. Herrero, P.W. Stephens, P.B. Allen, M.-V. Fernández-Serra, *Phys. Rev. Lett.* 108 (2012) 193003.
- [171] J. Nyman, O. Sheehan Pundyke, G.M. Day, *Phys. Chem. Chem. Phys.* 18 (2016) 15828–15837.
- [172] N.L. Allan, G.D. Barrera, T.H.K. Barron, M.B. Taylor, *Int. J. Thermophys.* 22 (2001) 535–546.
- [173] S. Baroni, S. de Gironcoli, A. Dal Corso, P. Giannozzi, *Rev. Mod. Phys.* 73 (2001) 516–562.
- [174] A. Otero-de-la-Roza, D. Abbasi-Pérez, V. Luaña, *Comput. Phys. Commun.* 182 (2011) 2232–2248.
- [175] G. Filippini, C.M. Gramaccioli, M. Simonetta, G.B. Suffritti, *Chem. Phys. Lett.* 35 (1975) 17–20.
- [176] G. Filippini, C.M. Gramaccioli, *Acta Crystallogr. A* 37 (1981) 335–342.

- [177] R. Ramírez, N. Neuerburg, C.P. Herrero, *J. Chem. Phys.* **137** (2012) 134503.
- [178] P. Carrier, R. Wentzcovitch, J. Tsuchiya, *Phys. Rev. B* **76** (2007) 064116.
- [179] F. Birch, *J. Geophys. Res.* **83** (1978) 1257–1268.
- [180] P. Vinet, J.R. Smith, J. Ferrante, J.H. Rose, *Phys. Rev. B* **35** (1987) 1945–1953.
- [181] B. Civalleri, C.M. Zicovich-Wilson, L. Valenzano, P. Ugliengo, *CrystEngComm* **10** (2008) 405–410.
- [182] E.F.C. Byrd, G.E. Scuseria, C.F. Chabalowski, *J. Phys. Chem. B* **108** (2004) 13100–13106.
- [183] D.C. Sorescu, E.F.C. Byrd, B.M. Rice, K.D. Jordan, *J. Chem. Theory Comput.* **10** (2014) 4982–4994.
- [184] M.D. King, T.M. Korter, *Cryst. Growth Des.* **11** (2011) 2006–2010.
- [185] F. Zhang, M. Hayashi, H.-W. Wang, K. Tominaga, O. Kambara, J.-i. Nishizawa, T. Sasaki, *J. Chem. Phys.* **140** (2014) 174509.
- [186] A.M. Reilly, A. Tkatchenko, *Phys. Rev. Lett.* **113** (2014) 055701.
- [187] C.G. Salzmann, P.G. Radaelli, B. Slater, J.L. Finney, *Phys. Chem. Chem. Phys.* **13** (2011) 18468–18480.
- [188] A. Falenty, T.C. Hansen, W.F. Kuhs, *Nature* **516** (2014) 231–233.
- [189] M. Frost, R.T. Howie, P. Dalladay-Simpson, A.F. Goncharov, E. Gregoryanz, *Phys. Rev. B* **93** (2016) 024113.
- [190] C.S. Yoo, *Phys. Chem. Chem. Phys.* **15** (2013) 7949–7966.
- [191] C. Mailhot, L.H. Yang, A.K. McMahan, *Phys. Rev. B* **46** (1992) 14419–14435.
- [192] M.I. Eremets, A.G. Gavriliuk, I.A. Trojan, D.A. Dzivenko, R. Boehler, *Nat. Mater.* **3** (2004) 558–563.
- [193] C.J. Pickard, R.J. Needs, *J. Phys. Condens. Matter* **23** (2011) 053201.
- [194] Q. Zhu, A.R. Oganov, C.W. Glass, H.T. Stokes, *Acta Crystallogr. B* **68** (2012) 215–226.
- [195] Y. Wang, Y. Ma, *J. Chem. Phys.* **140** (2014) 040901.
- [196] V. Iota, C.S. Yoo, *Phys. Rev. Lett.* **86** (2001) 5922–5925.
- [197] C. Yoo, H. Kohlmann, H. Cynn, M. Nicol, V. Iota, T. LeBihan, *Phys. Rev. B* **65** (2002) 1–6.
- [198] J.-H. Park, C.S. Yoo, V. Iota, H. Cynn, M.F. Nicol, T. LeBihan, *Phys. Rev. B* **68** (2003) 014107.
- [199] S.A. Boney, F. Gygi, T. Ogitsu, G. Galli, *Phys. Rev. Lett.* **91** (2003) 065501.
- [200] F. Datchi, V.M. Giordano, P. Munsch, A.M. Saitta, *Phys. Rev. Lett.* **103** (2009) 185701.
- [201] F. Datchi, B. Mallick, A. Salamat, G. Rousse, S. Ninet, G. Garbarino, P. Bouvier, M. Mezouar, *Phys. Rev. B* **89** (2014) 144101.
- [202] S. Serra, *Science* **284** (1999) 788–790.
- [203] J. Dong, J. Tomfohr, O. Sankey, *Phys. Rev. B* **61** (2000) 5967–5971.
- [204] J. Dong, J.K. Tomfohr, O.F. Sankey, K. Leinenweber, M. Somayazulu, P.F. McMillan, *Phys. Rev. B* **62** (2000) 14685–14689.
- [205] B. Holm, R. Ahuja, A. Belonoshko, B. Johansson, *Phys. Rev. Lett.* **85** (2000) 1258–1261.
- [206] A.R. Oganov, S. Ono, Y. Ma, C.W. Glass, A. Garcia, *Earth Planet. Sci. Lett.* **273** (2008) 38–47.
- [207] A. Togo, F. Oba, I. Tanaka, *Phys. Rev. B* **77** (2008) 184101.
- [208] J. Sun, D.D. Klug, R. Martonák, J.A. Montoya, M.-S. Lee, S. Scandolo, E. Tosatti, *Proc. Natl. Acad. Sci. USA* **106** (2009) 6077–6081.
- [209] F. Datchi, B. Mallick, A. Salamat, S. Ninet, *Phys. Rev. Lett.* **108** (2012) 125701.
- [210] M. Santoro, F.A. Gorelli, *Chem. Soc. Rev.* **35** (2006) 918–931.
- [211] C. Salzmann, P. Radaelli, E. Mayer, J. Finney, *Phys. Rev. Lett.* **103** (2009) 105701.
- [212] C. Knight, S.J. Singer, *J. Phys. Chem. B* **109** (2005) 21040–21046.
- [213] J.-L. Kuo, W.F. Kuhs, *J. Phys. Chem. B* **110** (2006) 3697–3703.
- [214] T.F. Whale, S.J. Clark, J.L. Finney, C.G. Salzmann, *J. Raman Spectrosc.* **44** (2013) 290–298.
- [215] M. Ben Del, J. VandeVondele, B. Slater, *J. Phys. Chem. Lett.* **5** (2014) 4122–4128.
- [216] A.M. Reilly, D.S. Middlemiss, M.M. Siddick, D.A. Wann, G.J. Ackland, C.C. Wilson, D.W.H. Rankin, C.A. Morrison, *J. Phys. Chem. A* **112** (2008) 1322–1329.
- [217] M. Dračinský, E. Procházková, J. Kessler, J. Šebestík, P. Matějka, P. Bouř, *J. Phys. Chem. B* **117** (2013) 7297–7307.
- [218] S.M. Peiris, C.P. Wong, F.J. Zerilli, *J. Chem. Phys.* **120** (2004) 8060–8066.
- [219] S. Hunter, T. Sutinen, S.F. Parker, C.A. Morrison, D.M. Williamson, S. Thompson, P.J. Gould, C.R. Pulham, *J. Phys. Chem. C* **117** (2013) 8062–8071.
- [220] M.D. King, T.N. Blanton, S.T. Mixture, T.M. Korter, *Cryst. Growth Des.* **11** (2011) 5733–5740.
- [221] M.D. King, E.A. Davis, T.M. Smith, T.M. Korter, *J. Phys. Chem. A* **115** (2011) 11039–11044.
- [222] M. Takahashi, Y. Ishikawa, H. Ito, *Chem. Phys. Lett.* **531** (2012) 98–104.
- [223] M.R.C. Williams, D.J. Aschaffenburg, B.K. Ofori-Okai, C.A. Schmuttenmaer, *J. Phys. Chem. B* **117** (2013) 10444–10461.

- [224] P. Vishweshwar, J.A. McMahon, M. Oliveira, M.L. Peterson, M.J. Zaworotko, *J. Am. Chem. Soc.* 127 (2005) 16802–16803.
- [225] A.D. Bond, R. Boese, G.R. Desiraju, *Angew. Chem. Int. Ed.* 46 (2007) 615–617.
- [226] A.D. Bond, R. Boese, G.R. Desiraju, *Angew. Chem. Int. Ed.* 46 (2007) 618–622.
- [227] E.J. Chan, T.R. Welberry, A.P. Heerdege, D.J. Goossens, *Acta Crystallogr. B* 66 (2010) 696–707.
- [228] J.D. Bauer, E. Haussuhl, B. Winkler, D. Arbeck, V. Milman, S. Robertson, *Cryst. Growth Des.* 10 (2010) 3132–3140.
- [229] A.D. Bond, K.A. Solanko, S. Parsons, S. Redder, R. Boese, *CrystEngComm* 13 (2011) 399.
- [230] C. Ouvrard, S.L. Price, *Cryst. Growth Des.* 4 (2004) 1119–1127.
- [231] D.C. Wallace, *Statistical Physics of Crystals and Liquids*, World Scientific, Singapore, 2002.
- [232] C. Bonhomme, C. Gervais, F. Babonneau, C. Coelho, F. Pourpoint, T. Azaïs, S.E. Ashbrook, J.M. Griffin, J.R. Yates, F. Mauri, C.J. Pickard, *Chem. Rev.* 112 (2012) 5733–5779.
- [233] R.K. Harris, S.A. Joyce, C.J. Pickard, S. Cadars, L. Emsley, *Phys. Chem. Chem. Phys.* 8 (2006) 137–143.
- [234] J.R. Smith, W. Xu, D. Raftery, *J. Phys. Chem. B* 110 (2006) 7766–7776.
- [235] A.L. Webber, L. Emsley, R.M. Claramunt, S.P. Brown, *J. Phys. Chem. A* 114 (2010) 10435–10442.
- [236] A. Abraham, D.C. Apperley, T. Gelbrich, R.K. Harris, U.J. Griesser, *Can. J. Chem.* 89 (2011) 770–778.
- [237] D.V. Dudenko, J.R. Yates, K.D.M. Harris, S.P. Brown, *CrystEngComm* 15 (2013) 8797.
- [238] E. Kucukbenli, K. Sonkar, N. Sinha, S.D. Gironcoli, *J. Phys. Chem. A* 116 (2012) 3765–3769.
- [239] D.E. Braun, L.H. Koztecki, J.A. McMahon, S.L. Price, S.M. Reutzel-Edens, *Mol. Pharm.* 12 (2015) 3069–3088.
- [240] R.A. Olsen, J. Struppe, D.W. Elliott, R.J. Thomas, L.J. Mueller, *J. Am. Chem. Soc.* 125 (2003) 11784–11785.
- [241] R. Witter, U. Sternberg, S. Hesse, T. Kondo, F.T. Koch, A.S. Ulrich, *Macromolecules* 39 (2006) 6125–6132.
- [242] J.C. Johnston, R.J. Iulicci, J.C. Facelli, G. Fitzgerald, K.T. Mueller, *J. Chem. Phys.* 131 (2009) 144503.
- [243] R.K. Harris, P. Hodgkinson, V. Zorin, J.-N. Dumez, B. Elena-Herrmann, L. Emsley, E. Salager, R.S. Stein, *Magn. Reson. Chem.* 48 (Suppl. 1) (2010) S103–S112.
- [244] D.C. Apperley, A.S. Batsanov, S.J. Clark, R.K. Harris, P. Hodgkinson, D.B. Jochym, *J. Mol. Struct.* 1015 (2012) 192–201.
- [245] E. Carignani, S. Borsacchi, J.P. Bradley, S.P. Brown, M. Geppi, *J. Phys. Chem. C* 117 (2013) 17731–17740.
- [246] J.K. Harper, R. Iulicci, M. Gruber, K. Kalakewich, *CrystEngComm* 15 (2013) 8693.
- [247] K. Kalakewich, R. Iulicci, K.T. Mueller, H. Eloranta, J.K. Harper, *J. Chem. Phys.* 143 (2015) 1–10.
- [248] P. Paluch, T. Pawlak, M. Oszajca, W. Lasocha, M.J. Potrzebowski, *Solid State Nucl. Magn. Reson.* 65 (2015) 2–11.
- [249] E. Pindelska, L. Szczeszczyk, D.M. Pisklak, Z. Majka, W. Kolodziejski, *J. Pharm. Sci.* 104 (2015) 2285–2292.
- [250] C.M. Widdifield, H. Robson, P. Hodgkinson, *Chem. Commun.* 52 (2016) 6685–6688.
- [251] J.C. Facelli, D.M. Grant, *Nature* 365 (1993) 325–327.
- [252] C. Martineau, J. Senker, F. Taulelle, *Ann. Rep. NMR Spectrosc.* 82 (2014) 1–57.
- [253] M. Dračinský, P. Hodgkinson, *RSC Adv.* 5 (2015) 12300–12310.
- [254] S.E. Ashbrook, D. McKay, *Chem. Commun.* 52 (2016) 7186–7204.
- [255] A. Portieri, R.K. Harris, R.A. Fletton, R.W. Lancaster, T.L. Threlfall, *Magn. Reson. Chem.* 42 (2004) 313–320.
- [256] J. van de Streek, M.A. Neumann, *Acta Crystallogr. B* 66 (2010) 544–558.
- [257] C. Pickard, F. Mauri, *Phys. Rev. B* 63 (2001) 245101.
- [258] J.R. Yates, C.J. Pickard, F. Mauri, *Phys. Rev. B* 76 (2007) 024401.
- [259] M. Baías, J.-N. Dumez, P.H. Svensson, S. Schantz, G.M. Day, L. Emsley, *J. Am. Chem. Soc.* 135 (2013) 17501–17507.
- [260] E. Salager, G.M. Day, R.S. Stein, C.J. Pickard, B. Elena, L. Emsley, *J. Am. Chem. Soc.* 132 (2010) 2564–2566.
- [261] M. Baías, C.M. Widdifield, J.-N. Dumez, H.P.G. Thompson, T.G. Cooper, E. Salager, S. Bassil, R.S. Stein, A. Lesage, G.M. Day, L. Emsley, *Phys. Chem. Chem. Phys.* 15 (2013) 8069–8080.
- [262] M.B. Ferraro, J.C. Facelli, *J. Mol. Struct.* 603 (2002) 159–164.
- [263] D. Stueber, *Concepts Magn. Reson. A* 28 (2006) 347–368.
- [264] S.T. Holmes, R.J. Iulicci, K.T. Mueller, C. Dybowski, *J. Chem. Phys.* 141 (2014) 164121.
- [265] S.T. Holmes, R.J. Iulicci, K.T. Mueller, C. Dybowski, *J. Chem. Theory Comput.* 11 (2015) 5229–5241.
- [266] D.B. Chesnut, K.D. Moore, *J. Comput. Chem.* 10 (1989) 648–659.
- [267] D. Chesnut, C. Phung, *Chem. Phys. Lett.* 183 (1991) 505–509.
- [268] D.B. Chesnut, B.E. Rusiloski, K.D. Moore, D.A. Egolfs, *J. Comput. Chem.* 14 (1993) 1364–1375.
- [269] J.D. Hartman, T.J. Neubauer, B.G. Caulkins, L.J. Mueller, G.J.O. Beran, *J. Biomol. NMR* 62 (2015) 327–340.

- [270] R.P. Young, B.G. Caulkins, D. Borchardt, D.N. Bulloch, C.K. Larive, M.F. Dunn, L.J. Mueller, *Angew. Chem. Int. Ed.* 55 (2016) 1350–1354.
- [271] R.O. Al-Kaysi, A.M. Müller, C.J. Bardeen, *J. Am. Chem. Soc.* 128 (2006) 15938–15939.
- [272] L. Zhu, A. Agarwal, J. Lai, R.O. Al-Kaysi, F.S. Tham, T. Ghaddar, L. Mueller, C.J. Bardeen, *J. Mater. Chem.* 21 (2011) 6258.

# Molecular Crystal Structure Prediction

---

*Sarah L. Price, Jan Gerit Brandenburg*

Department of Chemistry, University College London, London, UK

## 11.1 WHY PREDICT ORGANIC CRYSTAL STRUCTURES?

Noncovalent forces dictate how molecules come together to form crystals, and the physical properties of those crystals, such as the elastic tensor, morphology, phonon modes, hydroscopicity, solubility, and dissolution rates. Other molecular properties may be modified by the specific crystalline environment, such as color, spin state, and electronic conductivity. Hence, the intermolecular forces are central to the materials science tetrahedron [1], the close links between a crystal structure, its properties, and how its solid state can be processed, and the performance of the drug product. The application of modeling of noncovalent forces in molecular crystals, such as pharmaceuticals, starts from the crystal structure and then extends to predicting the properties of these crystals that are central to their industrial development [2,3].

Polymorphism is the ability of a molecule to crystallize in more than one structure [4]. As an every-day example, the mouth experience of chocolate depends on the polymorphic form of the cocoa butter. The most stable polymorph of cocoa butter (form VI) has a dull surface, soft texture and higher melting point, and chocolate containing it is “bloomed.” Thus the chocolatier has to prepare the chocolate to contain the metastable form V, which has the glossy surface sheen, crisp hardness and melts in the mouth at body temperature. Fortunately, there is a significant barrier for rearranging the lipid molecules from polymorph V to VI, so the transformation is very slow unless the chocolate is heated [5].

The ability to predict the crystal structures of a molecule can be seen as a test of our fundamental understanding of the factors that determine how a molecule crystallizes, including intermolecular forces and our ability to implement them in a computer code. The initial application envisaged for crystal structure prediction codes was for the design of new molecular materials with desired properties, to avoid the effort of synthesizing molecules that would not crystallize in an appropriate structure. For example, a molecule may have a large nonlinear optical coefficient and then crystallize in an inactive centro-symmetric crystal. A molecule such as octanitrocubane will not form a good energetic material unless it packs densely in the crystal. The conductivity of molecular electronic materials is very dependent on the molecular packing. Recently, considerable synthetic time has been saved in the devel-



opment of self-assembling porous organic cages by predicting whether the cage molecules will crystallize with their windows aligned to form pores [6–8]. Crystal structure prediction is intended to be applied to materials design without any experimental input for the specific molecule.

The other application of computational crystal structure prediction (CSP) is in developing organic products and crystallization processes. The molecule has been chosen for other properties, such as biological activity, and there is at least one crystallization in the manufacturing process, possibly producing the solid form incorporated in the final product, such as a pill. If the molecule readily and reliably crystallized to give just one crystalline material with reproducible properties, CSP would just be an academic exercise. However, polymorphism is a major issue for manufacturing molecular crystals. There are highly publicized cases where the supply of a drug treatment to patients has been disrupted by the unexpected crystallization of a new polymorph within the drug product. For example, rotigotine started to crystallize within Neupro transdermal patches which are used for treating Parkinson's disease [9].

In 1996, Abbott Laboratories lost the ability to produce the licensed formulation of the anti-HIV drug ritonavir as the production units started crystallizing a product that was significantly less soluble (see Fig. 11.1) [10]. A complete reformulation was required for ritonavir and new “cold chain” procedures for the storage of Neupro patches. These cases of late-appearing polymorphs cost the pharmaceutical companies a great deal financially and in reputation. Ritonavir is an example of a disappearing polymorph [11], when it becomes difficult to crystallize a polymorph reproducibly once the first sample of a more stable polymorph has been formed. This scientific anathema is becoming better understood as the role of inadvertent seeding and impurities in nucleating new polymorphs is becoming appreciated. The difficulty in experimentally being confident that all relevant solid forms are known for a given compound has led to the use of CSP as a complement to solid form development (see Section 11.4). The majority of organic molecules exhibit polymorphism when an industrial-style search for polymorphs has been conducted [4]. CSP has its greatest application as a route to predicting polymorphs and yet polymorphism considerably complicates the challenge of computationally predicting crystal structures.

## 11.2 BACKGROUND ON CRYSTAL STRUCTURE PREDICTION

Crystal structure prediction (CSP) is the challenge of predicting the crystal structure of an organic molecule from its molecular diagram. It has made considerable progress in the last two decades, when the inability to predict something as simple as how a molecule would crystallize was considered one of the continuing scandals in the physical sciences [12,13]. At that time, there was little awareness of polymorphism, and it was reasonable to assume that the observed crystal structure would be the most thermodynamically stable crystal structure.

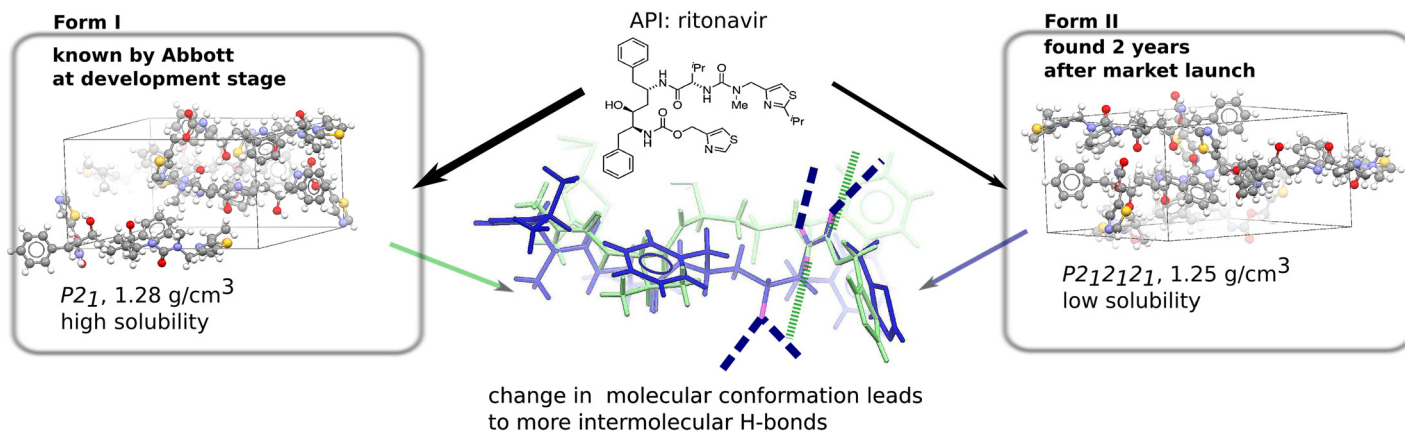


**FIGURE 11.1** Problems of late appearing polymorphs: The antiviral drug ritonavir was industrially produced in form I for 2 years. It suddenly started crystallizing into the more stable form II which has a much lower solubility and so required reformulation of a new drug product to provide an effective medicine that could be given to patients. Form II has two more intermolecular hydrogen bonds ( $\cdots$ ) than form I ( $---$ ) making it more stable and less soluble, but form I contains the molecule in the conformation that is dominant in solution.

### 11.2.1 General Algorithm

A typical work-flow of CSP is sketched in Fig. 11.2 and can be roughly broken down into four independent stages:

- a. The conformational space that the single molecule could adopt in the solid state has to be determined. In many methods, it is also necessary to decide which conformational degrees of freedom should be allowed to vary in each of the following steps.
- b. Plausible crystal structures have to be generated in all likely space groups (which differ in the number of molecules in the unit cell), by varying the cell parameters, relative orientations of the molecules within the unit cell, and for flexible molecules, varying the molecular conformation. Often the search is restricted to one independent molecule in the asymmetric unit cell ( $Z' = 1$ ), with all the other molecules in the unit cell being related by the symmetry elements of the space group.
- c. The generated crystal structures have to be optimized and ranked according to their lattice energy with high accuracy. The lattice energy is the energy of a hypothetical static, perfect crystal structure relative to the infinitely separated (noninteracting) molecules (or atoms) in their lowest energy conformation.
- d. Further refinement of the thermodynamics of the structures on the crystal energy landscape is usually desirable, along with the calculation of the properties of interest. The crystal energy landscape is defined as the set of crystal structures that are close enough to the most stable one to be thermodynamically plausible as polymorphs (within the likely errors associated with the computational lattice energy model).

This work-flow immediately brings up the two main challenges and requirements of the computational procedure. First, a huge search space of possible crystal packings has to be sampled efficiently. In practice, this means a very fast computation of relative crystal stabilities is combined with efficient methods to scan the search space. Second, the final stability ranking of the possible polymorphs has to be done with very high accuracy as most polymorphic energy differences are well below the “chemical accuracy” of 4.2 kJ/mol. Combining the two requirements results in a need for a hierarchy of lattice-energy evaluations, discarding the less stable structures that would not be among the most stable with a more accurate energy model. This requires a good sense for the likely errors in the intermolecular force models being employed for the specific molecule, as all subtle contributions to the energy could have a significant impact on the relative stability of the structures in the crystal energy landscape, depending on how they vary among those structures.

### 11.2.2 Discussion of the Common Assumptions Needed in CSP Algorithms

#### ***Thermodynamics Determines the Crystal Structures***

The basic assumption behind crystal structure prediction codes, that the observed crystal structure will be the most thermodynamically stable one, is complicated by polymorphism. At any given temperature and pressure, one polymorph is in principle more stable than the others, but this stability order can change under practically relevant conditions, let alone between ambient and the nominal 0 K of the lattice energy modeling. The energy differences between polymorphs are small, vary with temperature and are difficult to measure

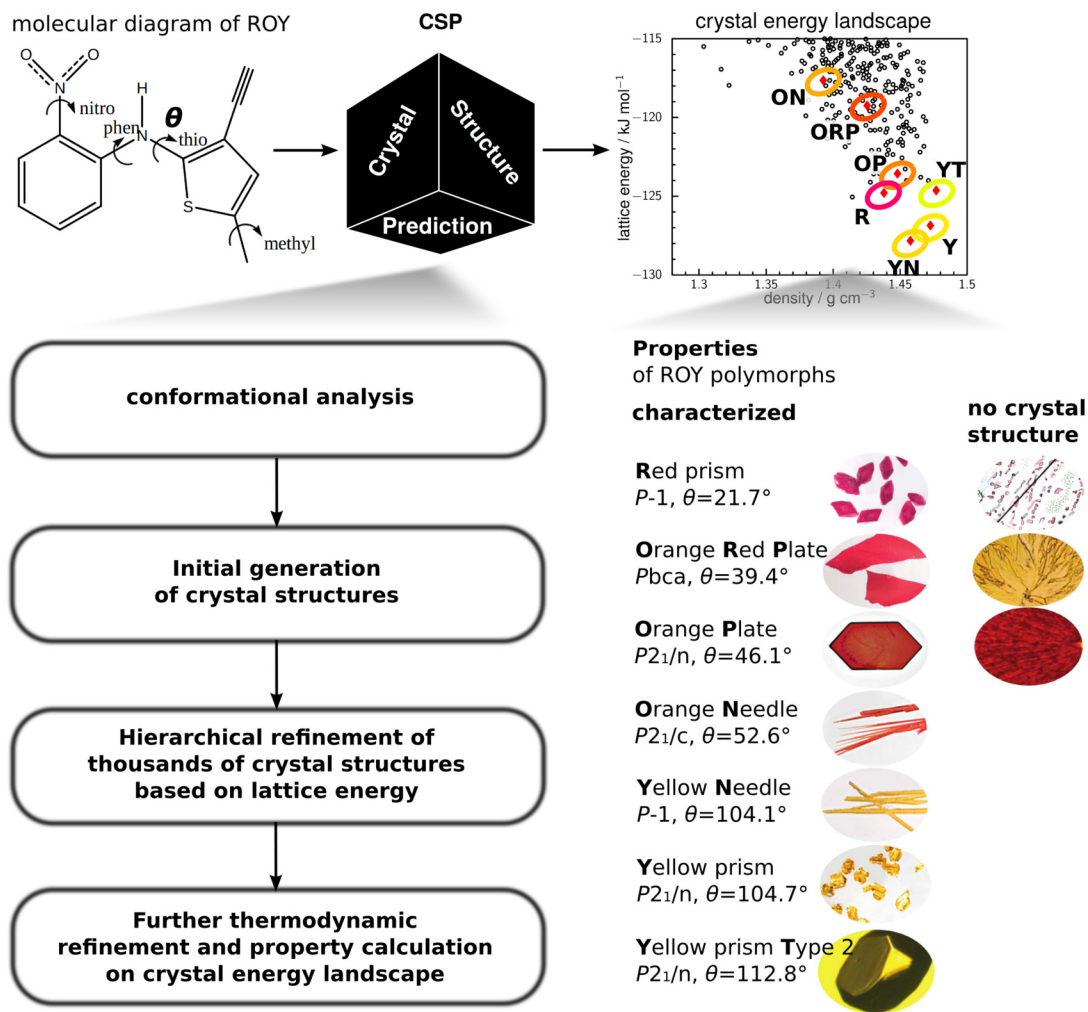


FIGURE 11.2 Typical crystal structure prediction work-flow: Starting from just the molecular diagram, a CSP method first generates and then filters millions of possible crystal packings through multiple stages of increasing accuracy of computational estimates of thermodynamic stability. The example given is for the molecule ROY (5-methyl-2-[(2-nitrophenyl)amino]-3-thiophenecarbonitrile) whose molecular flexibility leads to its polymorphs varying in color as well as morphology [14]. The computed crystal energy landscape, the set of structures which are thermodynamically plausible as polymorphs, is summarized by each point corresponding to a crystal structure [15]. Some correspond to the polymorphs whose crystal structures are known as labeled by the initials of the polymorphs. Some of the open black symbols may correspond to the samples where the crystals are not of quality or size to allow their structures to be derived from experimental data. *The crystal photographs are reproduced with permission from Ref. [14]. Copyright 2010 American Chemical Society.*

experimentally. A recent study [16] estimated the energy difference between all crystallographically well-determined pairs of polymorphs of small organic molecules using DFT-D lattice energy differences (a  $\Psi_{\text{cry}}$  model, see Section 11.2.2c). They found that the energy differences were less than 5.5 kJ/mol for 70% of cases [16]. A larger survey of 508 pairs of polymorphs, using distributed multipole models for the electrostatic component of the lattice energy (a  $\Psi_{\text{mol}}$  model, see Section 11.2.2c) found that over half had a lattice energy difference of less than 2 kJ/mol and only 5% had an energy difference greater than 7.2 kJ/mol. Including a rigid-molecule harmonic estimate of the free energy changed the relative stability by up to 2 kJ/mol, which changed which polymorph was the most stable at ambient conditions in 9% of cases [17]. These computational estimates seem realistic in light of the available experimental estimates [16]. The difficulty in comparing experimental and theoretical energy differences between polymorphs is explored further in Section 11.5.

It is not the thermodynamic energy difference that determines how readily a metastable polymorph transforms to the more stable, but the energy barrier for transformation. Single-crystal to single-crystal transformations between ordered polymorphs are rare even for structurally quite similar polymorphs [18]. Most polymorphic phases transform via the solution state. Indeed, long-term slurrying when two polymorphs are left in a saturated solution is a common method of determining their relative stability at that temperature. Hence, the assumption that the most stable structure can always be accessed in an experimental screening study is questionable [19]. This is particularly true for larger, flexible molecules that may have difficulty crystallizing at all, or where all the solvent-free polymorphs are found by desolvating solvates. Indeed, it is an important use of CSP to help experimentally target previously unobserved polymorphs, and CSP has inspired the finding of the most thermodynamically stable, but kinetically disfavored, form [20]. Thus, although the basic assumption that the thermodynamically stable form must be capable of existing can be questioned, it is a role for increasingly accurate methods of evaluating the relative thermodynamic stability to test this. Nonetheless, for smaller molecules, the ability to predict that the observed crystalline structures are at least very close in energy to the most stable computer-generated structures is a good test of whether evaluation of the noncovalent interactions is suitable for modeling the molecule in other phases. For instance, a model that can describe both the gas and the solid phase accurately can be expected to perform reasonably well in the liquid phase, where reliable reference data are less accessible.

### ***a) Molecular Bonding and Conformational Analysis***

A CSP search to generate putative crystal structures must make some assumptions about the range of possible crystal structures. All methods need to assume the covalent bonding and stoichiometry, e.g., the molecule defined by the chemical diagram, and for a solvate or cocrystal, the ratio of the two components. In an ideal CSP method, facile chemical transformations, such as proton rearrangements to a different tautomer or from a salt to a cocrystal, would be modeled. However, since many molecules of interest are not chemically stable, for example, explosive molecules are significantly less stable than nitrogen, carbon dioxide, and water, CSP is not a search for absolute thermodynamic stability.

Another molecule-dependent assumption is the extent to which the molecular flexibility has to be explicitly considered in the search space to ensure that a structure is generated near all local minima in the crystal energy. Conformational polymorphs are defined as the molecu-

lar conformations in the crystals minimizing to different low energy structures of the isolated molecule [16]. However, many conformations in crystals differ sufficiently from their corresponding isolated-molecule conformations, in shape though not in energy, that they could not be found by optimization of crystal structures generated with just conformational energy minima. Indeed, there is a tendency for larger molecules to adopt more extended conformations in their crystals than in isolation [21].

### **b) Crystallographic Space Covered by Initial Generation of Crystal Structures**

An assumption needs to be made about the crystallographic space covered. Most organic molecules crystallize in monoclinic space groups. The percentage of entries in the Cambridge Structural Database (CSD) with the most popular space group ( $P2_1/c$ ) varied little, from 36% to 34.6%, between 1983 and 2015. In the same time frame, the number of organic crystal structures reported in the CSD database increased from 50 000 [22] to 807 000 [23]. However, the range of space groups varies considerably with the type of molecule: an enantiopure chiral molecule can only crystallize in space groups without inversion symmetry, and are most commonly found to crystallize in  $P2_12_12_1$  (see Section 11.5). Although a racemic compound or nonchiral molecule could in principle crystallize in any of the 230 space groups, a search over the 60 most common space groups is likely to be adequate unless the molecule has high symmetry.

A second choice that needs to be made is the number of independent molecules in the asymmetric unit cell ( $Z'$ ) that the symmetry operations of the space group use to create the unit cell of  $Z$  molecules. Most CSP searches are restricted to  $Z' = 1$ , to avoid having to cover the variables defining the relative positions of the two molecules, something that cannot be avoided for multicomponent systems such as salts, cocrystals, or solvates. However, with time, the proportion of  $Z' > 1$  crystal structures has been increasing [24]. Whilst some high  $Z'$  structures approximate  $Z' = 1$  structures, there are cases where the independent molecules have very different conformations or use different hydrogen bonding donors and acceptors. Unfortunately, the incidence of  $Z' > 1$  structures is higher for industrially screened polymorphic systems (approximately 20%) than the bulk of the CSD [4]. In principle it is possible to not use crystallographic symmetry in the search but this would need at least 16 independent molecules in the unit cell, and still exclude space groups with three-fold or higher symmetry axis, which are not uncommon for some classes of molecules. The search space also increases drastically with the amount of molecular flexibility that needs to be considered explicitly at the search stage. Typically, we generate a million putative structures for a search in the 60 most popular space groups for a small achiral pharmaceutical molecule, and often find that this is insufficient to ensure with confidence that all  $Z' = 1$  structures within these space groups have been located.

### **c) Hierarchical Refinement of Lattice Energies**

The sheer number of crystal structures that need to be considered and the accuracy needed for the final relative energies leads to a range of lattice energy models being employed in CSP studies. We roughly categorize them in three classes.

1. Classical analytical atomistic force fields (FF) for both the intramolecular and intermolecular interactions.

2. *Atomistic* hybrid models that assume the identity of the organic molecule within the crystal structure. The theory of intermolecular forces is used to generate an analytical intermolecular potential (cf. Chapter 1), in an anisotropic atom–atom pairwise form. The intramolecular (conformational) energy and the parameters of the intermolecular potential are derived from the electronic structure of the molecule, and so this general approach will be denoted  $\Psi_{\text{mol}}$ .
3. *Periodic electronic* structure methods that directly describe the interactions of the electrons with the nuclei in evaluating the crystal lattice energy. They typically involve a wavefunction of the periodic crystal and so are denoted  $\Psi_{\text{cry}}$ .

Classical force fields are readily available for a large class of biologically relevant molecules. These classical potential functions which are based on interatomic distance and angle dependent terms have been used for decades to approximate molecular potential energy surfaces [25,26]. Conventional FFs assume transferability of the potential parameters between different molecules within a class of chemically similar compounds and are available in standard packages like GROMACS, AMBER, CHARMM, or TINKER. Much cruder force fields designed to find reasonably close packed crystal structures without steric clashes can also be used. However, molecule specific FFs, whose parameters have been fitted to a general functional form, are often more appropriate and effective for the initial crystal structure generation stage [27].

The atomistic hybrid models emerged as a response to the accuracy requirements in CSP at a time when method development concentrated on rigid molecules. It was clear that a molecule-specific parameterization of the intermolecular forces was required. The analytical intermolecular potential can be derived using theory of intermolecular forces by parameterizing the long-range forces from computed molecular properties and the short-range terms by, for instance, fitting to DFT-SAPT calculations as described in Chapters 1 and 2. In this approach, the lattice energy is calculated by summing the analytical intermolecular potential over all pairs of molecules in the crystal, to give the dominant intermolecular contribution  $U_{\text{inter}}$ . For flexible molecules, it is necessary to add the small energy penalty for any change in conformation from that of the isolated molecule ( $\Delta E_{\text{intra}}$ ), i.e., assuming

$$E_{\text{latt}} = U_{\text{inter}} + \Delta E_{\text{intra}} . \quad (11.1)$$

The ab initio calculation on the isolated molecule gives the molecular structure and also readily provides a molecule-specific electrostatic model. It has been found that using distributed multipole analysis (DMA, see Chapter 1) to parameterize an anisotropic atom–atom electrostatic model makes a significant difference to the success of CSP studies [28]. The atomic dipoles and quadrupoles represent the anisotropic electrostatic forces arising from the lone pairs and  $\pi$  electron density that are important in representing the hydrogen and halogen bonding and  $\pi$ – $\pi$  stacking interactions. These interactions compete with each other and the repulsion–dispersion interactions in defining the optimum, densely packed structure. The effect of the surrounding molecules in the crystal can be estimated by calculating the molecular charge density in a polarizable continuum of typical dielectric constant  $\epsilon = 3$  [29].

For many CSP applications, all the intermolecular forces apart from the distributed multipole electrostatic contribution are usually modeled by an isotropic atom–atom exp-6

repulsion–dispersion potential. These  $\text{exp-6}$  parameters have been explicitly fitted to crystal structures and heats of sublimation and so partially absorb some errors in the assumed functional form of the intermolecular potential and the neglect of thermal expansion and others [30]. This approach using the FIT potential [31] has recently been shown to be as accurate as many first-generation DFT-D methods for the X23 benchmark set of small molecular crystals [32].

The model for the intermolecular forces can be systematically improved, not only by improvements in the molecular charge distribution and in the method of deriving the electrostatic model, but also by using the molecule's atomic polarizabilities to model the induction contribution [31] and the atomic dispersion coefficients for the dispersion contribution (see Chapter 1). Anisotropic atom–atom models for the short-range interactions can be derived using the overlap model and fitting to dimer interaction energies such as those obtained using DFT-SAPT. Such nonempirical model potentials have been very successful in predicting the structures and properties of rigid-molecule crystals such as the chlorobenzenes [18,33]. Indeed, the ability to reproduce the known crystal structures as the more stable of those generated by CSP is a severe test of the quality of the intermolecular potential model. For flexible molecules, the molecular wavefunction has to be recalculated for sufficient conformations to cover the conformational variation of  $\Delta E_{\text{intra}}$  and the distributed multipoles within the crystal structures. The use of databases of the properties derived from the molecular wavefunction calculations [34] means that the optimization of the first crystal structure (Eq. (11.1)) requires many single molecule *ab initio* calculations on the different conformations, but the computational cost per crystal structure optimized rapidly decreases. This  $\Psi_{\text{mol}}$  approach with cruder grids for intramolecular energy can also be used in the crystal generation stage for highly flexible molecules, as in the versions designed for studying the pharmaceutical molecules of the CrystalPredictor code [35,36].

The most prominent method from the  $\Psi_{\text{cry}}$  class are periodic density functional approximations. As highlighted in several of the preceding chapters, most DFT methods do not describe the important London dispersion interaction, the universal attractive part of the van der Waals forces. Dispersion interactions are very important in most organic crystal structures. For instance, a molecule can crystallize in structures where dispersion determines the separation between layers of hydrogen bonded molecules. Even in crystals where strong hydrogen bonds span all three unit cell directions, the long-range nature of dispersion means that lattice summation over this contribution converges slowly to a significant energy. Thus, all semilocal DFT-based  $\Psi_{\text{cry}}$  methods have to be corrected for the missing dispersion and we refer to this group of methods as DFT-D (see Fig. 11.6).

#### ***d) Further Thermodynamic Refinement and Property Calculation***

At the lattice-energy refinement stage, each crystal is modeled as a static infinite perfect lattice. This ignores the energies associated with the surface, disorder or defects in real crystals. For example, the surface dipole correction term, which arguably should be applied to crystals in polar space groups and depends on the area of the polar surfaces, is ignored [37]. More importantly the calculation of the lattice energy ignores the effect of temperature on



the relative thermodynamic stability of the crystals. There are additional contributions to the enthalpy:

$$H(T) = \underbrace{E_{\text{latt}} + PV + E_{\text{ZPVE}}}_{\text{crystal at 0 K}} + \underbrace{\int_0^T dT' C_V(T')}_{H_{\text{vib}}}, \quad (11.2)$$

the Helmholtz free energy:

$$F(T) = \underbrace{E_{\text{latt}} + E_{\text{ZPVE}}}_{\text{crystal at 0 K}} + \underbrace{\int_0^T dT' C_V(T') - TS}_{F_{\text{vib}}}, \quad (11.3)$$

or the Gibbs free energy:

$$G(T) = \underbrace{E_{\text{latt}} + PV + E_{\text{ZPVE}}}_{\text{crystal at 0 K}} + \underbrace{\int_0^T dT' C_V(T') - TS}_{G_{\text{vib}}}. \quad (11.4)$$

The additional contributions, e.g.,  $F_{\text{vib}}$ , depend on the phonon spectrum of the crystal as introduced in Chapter 10. Here, we relate the vibrational contributions to the isochoric heat capacity  $C_V$  and entropy  $S$  of a crystal. At 0 K the zero-point vibrational energy  $E_{\text{ZPVE}}$  has to be considered and at finite temperatures additional thermal contributions are important. While the zero-point energy is dominated by the high-energy (mostly molecular covalent) frequency modes, the thermal contributions are most sensitive to the low energy modes which are predominantly intermolecular with some coupling to the low frequency modes of flexible molecules. The phonon mode frequencies are typically computed using the harmonic approximation. This is a reasonable simplification for all high frequency molecular modes, but is less reliable for the low energy modes that correspond to extremely flat intermolecular potential energy surfaces. All organic crystals show significant thermal expansion, which can be very anisotropic, showing the limitations of the harmonic approximation [38]. Even within the harmonic approximation, the accurate evaluation of such contributions to  $F_{\text{vib}}$  requires considerable care as well as a reliable potential energy surface (see Chapter 10) [32]. Many CSP applications therefore just use the relative lattice energies and neglect the differences in the zero-point and thermal energy.

Temperature has a significant effect on molecular crystals, as functional organic crystals are being used at temperatures that are far closer to their melting (or decomposition) temperatures than 0 K. For example, the polymorphs of ROY (Fig. 11.2) melt between 97 and 115°C. Because of molecular motions, many lattice energy minima may correspond to only one minimum in the free energy, significantly reducing the number of distinct crystal structures at practically relevant ambient temperatures. The proportion of structures that are artifacts of the neglect of temperature depends on the molecule and the crystal packing: there is a drastic reduction (approximately one order of magnitude) in the case of benzene whereas, for

5-fluorouracil, 25% of lattice energy minima were not free energy minima [39,40]. This reflects the degree of motion and ease of transformation between benzene polymorphs, in contrast to the 5-fluorouracil polymorphs, which have different hydrogen bonding patterns and do not interconvert without going through a liquid phase. Observed crystal structures can be dynamical averages over many static CSP idealized structures, ranging from rotationally disordered phases, to just having the methyl groups rotating freely. It is important to confirm that crystal structures optimized within space-group constraints are really mechanically stable minima. When the symmetry-constrained optimization has produced a transition state, removing the symmetry constraints can give such a small energy lowering that the observed structure is a dynamical average in the original space group.

Thus once the CSP computer algorithm has generated a set of lattice energy minima calculated with the most accurate model for the lattice energy that can be afforded or is justified, there needs to be an evaluation of how many structures fall within the crystal energy landscape, that is, the set of structures which are thermodynamically plausible as polymorphs [38]. This will include both the likely energy differences between polymorphs and a quantitative or qualitative estimate of the likely temperature effects and all other approximations in the estimates of the relative free energies of the crystal structures [38]. Once the crystal energy landscape is chosen, various properties can be calculated, whose accuracy will again depend on the quality of the model for the intermolecular forces and approximations made. For example, the powder X-ray diffraction pattern calculated from the lattice energy minima, even with the perfect model for the lattice energy, will be in error by the thermal and zero-point energy expansion. This stage of the CSP study will depend on the purpose of the study but also on the size of the energy gaps between the low energy crystal structure and the relationships between the crystal structures.

### ***Comparison of Crystal Structures***

During a CSP run it is essential to remove duplicate structures. This procedure needs to go beyond just removing the many mathematically equivalent sets of cell parameters. The definition of how much two crystal structures have to differ before they correspond to polymorphs (rather than sample, temperature or pressure dependent variations) is a practical issue with intellectual property and quality control implications. In practice, the ability to overlay the coordination sphere (usually a 15 molecule cluster, larger for multicomponent systems) with a reasonable root mean square difference is usually taken as a method of establishing that structures are effectively the same. The similarity between simulated powder X-ray diffraction patterns is often used, but this measure still has a gray area, and can be insensitive to hydrogen atoms or certain atomic exchanges [41]. In the CSP algorithms, there is the need to ensure that no minima that would correspond to distinct thermodynamically plausible polymorph structures in the most accurate energy model, are eliminated at an earlier stage.

A variety of tools are used to determine the relationships between the computer generated and known crystal structures. The hydrogen bonding pattern in each crystal can be described by graph sets to identify crystals with the same hydrogen-bonding motifs. Other forms of similarity in the packing, such as common dimers, stacks, or layers of molecules, can be found by pairwise comparison of the structures using XPac [42,43]. This type of analysis can be used to estimate whether structures are sufficiently distinct to be possible polymorphs. For exam-

ple, once structures with distinct hydrogen bonds are formed in the nucleation process there is likely to be a significant barrier to breaking the hydrogen bonds, thus the two structures may well be polymorphs. Structures which are similar could just crystallize in the same stable form or the observed crystal structure may incorporate the other structure in its dynamic or static disorder or as growth defects [44].

CSP methodology is still emerging as it is applied to an increasing range of molecular systems. The sheer number of different ways of packing organic molecules that need to be considered in a search means that all CSP methods with an extensive enough search involve a hierarchy of energy evaluation methods, with clustering to remove structures that are expected to correspond to the same eventual minimum. Of course, a limited search reduces the computational cost, but this runs the danger of concluding that no polymorphs are expected when a more extensive computational and experimental search finds them [45]. The final energy evaluations are likely to be the most expensive and accurate that can be afforded. However, the lattice energy of benzene has only recently been evaluated to a 1 kJ/mol accuracy, requiring the use of experimental data that is rarely available for less studied systems [46]. Hence, the success and impact of CSP methods comes from considerable cancellation of errors in the relative energies of the computer generated structures. Assessing the likely extent of this cancellation requires knowledge of the types of intermolecular forces operating for the given system as well as how much these interactions differ in the low energy crystal structures.

### 11.2.3 Example of CSP in Practice

As a practical example of the work-flow in Fig. 11.2, we describe a CSP study conducted on the nonsteroidal antiinflammatory drug naproxen [47]. The molecule is chiral (chiral center C11, see Fig. 11.3) and marketed in the homochiral form, which has to be separated from racemic mixtures that contain both hands of the molecule. The study was undertaken because there was no crystal structure for racemic naproxen in the CSD, and concurrent experimental studies could not grow a single crystal suitable for X-ray diffraction.

#### **Conformational Analysis**

The molecular diagram of naproxen (Fig. 11.3) shows three flexible torsion angles, with torsion  $\Phi_1$  being independent from the  $\Phi_2$  and  $\Phi_3$  torsion angles, which are coupled. A one dimensional potential energy surface scan for  $\Phi_1$  shows that one conformation is significantly lower in energy than all others, but that another more planar conformation is sufficiently low in energy that it might form crystal structures. This is confirmed by looking at structures in the CSD as there are two structures with the less favorable planar conformation (Fig. 11.3B). (This analysis also shows that if  $C_6$  or  $C_8$  had substituents other than hydrogen, a much larger conformational search space would have been needed.) The two local conformational minima (Fig. 11.3A) are sufficiently steep that the angle needs not be considered as a search variable in the crystal structure generation stage. A subsequent two-dimensional scan of  $\Phi_2$  and  $\Phi_3$  leads to the conclusion that 8 ab initio optimized conformations of the isolated molecule should provide a reasonable approximation to any crystalline conformers, and hence a rigid-molecule search method could be used. These calculations of the molecular wavefunctions

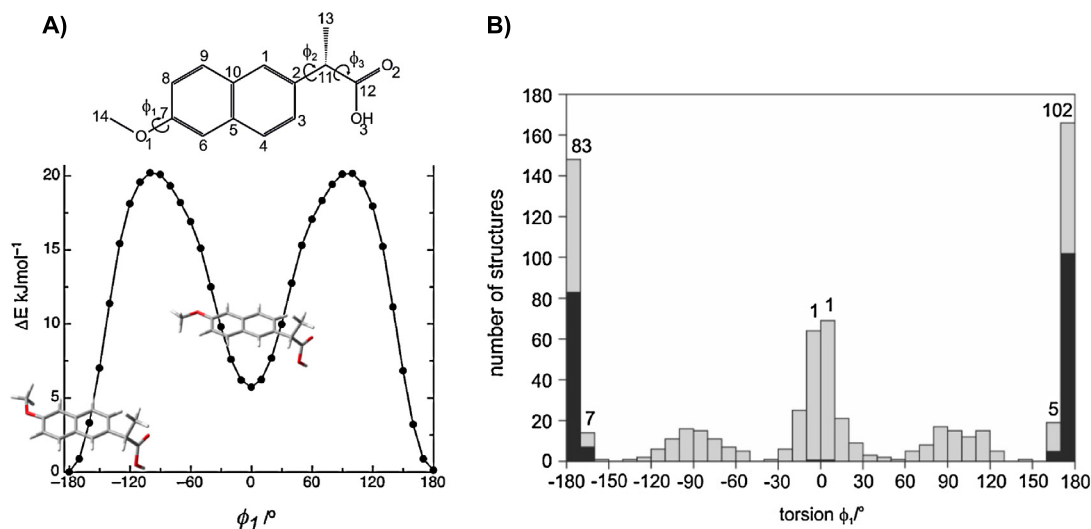


FIGURE 11.3 Molecular conformation of naproxen (see Ref. [47]). (A) The three flexible torsion angles are defined with an explicit one dimensional potential energy surface scan (PBE functional) with respect to  $\Phi_1$ . (B) Summary of the statistical evaluation of the torsion angle distribution of crystal structures containing  $\beta$ -methoxynaphthalene moieties (CSD database v5.32). Black (and numbers above bars) are structures where the ortho-substituent are hydrogen atoms ( $C_8H$ ,  $C_6H$ , as in naproxen) and gray are structures where  $C_6$  or  $C_8$  are substituted by larger functional groups.

also provided the relative conformational energies  $\Delta E_{\text{intra}}$ , and distributed multipoles for lattice energy calculations using each conformer.

### Initial Generation

The 8 rigid conformers were each used to generate crystal structures using MOLPAK [48] which performs a systematic grid search on the orientation for the rigid central molecule in 39 common coordination geometries of organic molecules (covering 19 common space groups), with one molecule in the asymmetric unit cell ( $Z' = 1$ ). Approximately 3000 of the most closely packed structures found with MOLPAK's pseudo-hard sphere potential were carried on to the refinement stage. When this initial CSP study and experimental evidence defined the space group of the racemic compound, a more extensive CrystalPredictor search was carried out in this space group.

### Refinement with $\Psi_{\text{mol}}$ Approach

An atomistic  $\Psi_{\text{mol}}$  hybrid model was used in both steps with distributed multipoles from the charge density of the isolated molecules partitioned into atomic contributions. First a rigid body minimization is conducted, which keeps the molecular structure fixed and relaxes all intermolecular degrees of freedom. The most stable of those structures are then reoptimized allowing for small changes in  $\Phi_1$ ,  $\Phi_2$  and  $\Phi_3$  and other bend and torsion angles, so that the bend in the naphthalene ring in the enantiopure crystal structure was reproduced.

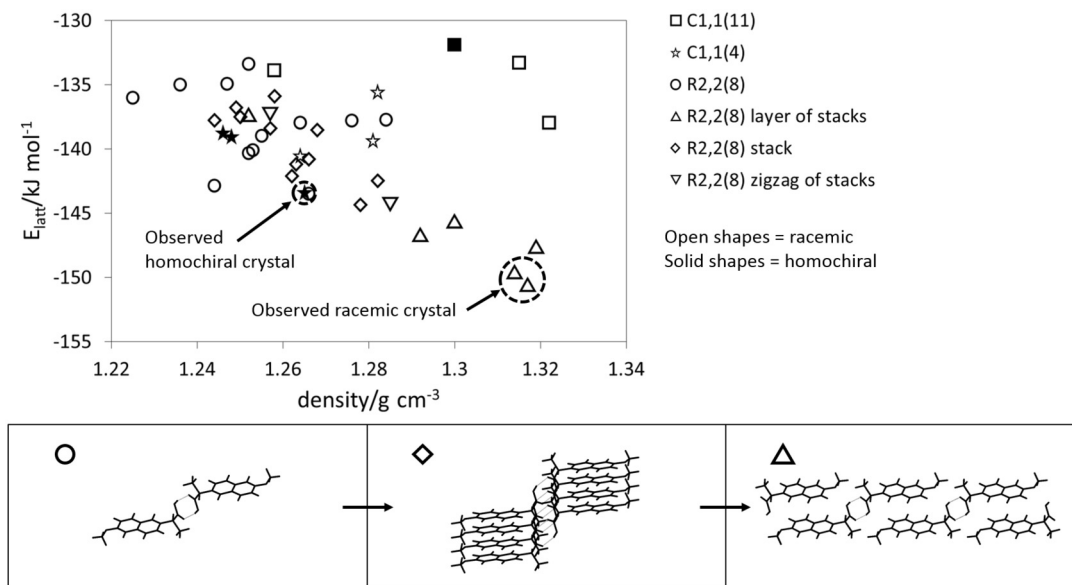


**FIGURE 11.4** Crystal energy landscape of naproxen [47]. Each symbol represents a stable crystal structure, classified by chirality, hydrogen-bonding graph set and common packing motifs. The XPac-derived packing motif hierarchy is illustrated below, with the layer observed in the racemic structure ( $\Delta$ ) being one of the ways of combining a stack of hydrogen bonded dimers ( $\diamond$ ) (another is a zigzag of stacks) with there being other unique structures containing this stack, and other structures that contain the dimer ( $\circ$ ), but not the stack. The two structures corresponding to the racemic crystal structure are the  $Z' = 1$  transition state found in the search and the very similar  $Z' = 2$  lattice energy minimum [47].

### Property Calculation

The lattice energies and densities of the structures on the crystal energy landscape are shown in Fig. 11.4 with each crystal structure labeled by its packing type. These labels were derived by considering whether the crystal was racemic or enantiopure (from the space group), its hydrogen bonding graph set and information from the XPac analysis. This showed (Fig. 11.4) that many low energy structures contained the same stack of hydrogen-bonded dimers, and some had the same layers in common.

The known enantiopure structure was the lowest energy structure in the chiral space groups. However, there were various lattice energy minima for racemic naproxen based on essentially the same layer containing the inversion-related carboxylic acids dimers. The lowest energy racemic structure in the  $Z' = 1$  search was actually mechanically unstable, and removing a symmetry constraint gave a  $Z' = 2$  lattice energy minimum. This was only 1 kJ/mol lower in energy, which is less than the estimated zero-point energy of the structure. Using these structures as a starting point allowed the solution of the experimental structure from powder X-ray diffraction data, but solid-state NMR had to be used to show that the structure was definitely a  $Z' = 1$  average over the lattice energy minima. From the lattice energies, or even rigid-body harmonic free energy calculations (see Eq. (11.3)), it is hard to conclude that the other layer structures would not correspond to free energy minima,

TABLE 11.1 Evolution of the CSP blind challenges

Year	Success <sup>a</sup>	Attempts <sup>b</sup>	Atoms	Flexible bonds	Elements	Z'' <sub>max</sub> <sup>c</sup>	Multicomponent
1999 [53]	3/4	6–11	11–28	0, 1, 2, 2	H, C, N, O	1	—
2001 [54]	2/3	11–15	18–28	0, 2, 2	H, B, C, N, O	1	—
2004 [55]	2/4	15–18	11–35	0, 0, 6, 0	H, B, C, N, O, S, Br	2	—
2007 [56]	4/4	12–14	8–32	1, 0, 4, 4	H, C, N, O, I	2	cocrystal
2010 [57]	6/6	10–14	13–55	0, 2, 4, 2, 10, 4	H, C, N, O, F, S, Cl, Br	2	hydrate, salt
2014 [58]	8/9 <sup>d</sup>	8–24	15–62	0, 7, 5, 6, 8	H, C, N, O, S, Cl	3	hydrated salt

<sup>a</sup>  $X/Y$  gives the number of targets structures ( $Y$ ) and the number of targets with at least one successful submission ( $X$ ). In the first five blind tests a success means that the experimental structure matches one out of three structures submitted by each group. In the sixth blind test, a success means the structure is found in any of the two lists of 100 structures that could be submitted.

<sup>b</sup> Minimum to maximum number of groups trying any of the  $Y$  targets.

<sup>c</sup> Largest number of independent molecules in the asymmetric unit cell.

<sup>d</sup> One target was polymorphic with 5 target structures.

capable of crystallizing separately as polymorphs. Kinetically, they are likely to appear as growth faults, possibly accounting for why it was not possible to grow single crystals of racemic naproxen. The determination of the racemic structure was the starting point to testing whether the energy differences between the racemic and enantiopure crystal structures could be evaluated sufficiently accurately for designing chiral separation by crystallization processes (Section 11.4)

### 11.3 BLIND TEST OF CRYSTAL STRUCTURE PREDICTION

Knowing the industrial interest in polymorph prediction (see Section 11.4), the Cambridge Crystallographic Data Centre (CCDC) hosts CSP blind test challenges every few years, to provide an unbiased assessment of the state-of-the-art ability to predict organic crystal structures. With the assumption that the target crystal structure is the most thermodynamically stable, this is an assessment of methods for modeling the thermodynamics of organic crystal structures (see Chapter 10 and Refs. [49,50]). The CSP blind tests assess the ability to calculate relative, rather than absolute, thermodynamic stabilities in contrast to the Assessment of Modeling Proteins and Ligands (SAMPL) [51,52]. In particular, it also tests the initial generation of crystal structures and all the other assumptions involved in a CSP protocol (see Section 11.2.2), stimulating advances in the field.

Table 11.1 summarizes the progress in CSP since 1999, both in terms of the size and flexibility of the molecules involved, and the number of groups with different codes and protocols participating and the success rate for the leading codes. Hence, the blind test papers provide a snapshot of the state of development of the field [53–58].

The difficulty of the CSP challenges has been increasing, and yet there is still a long way to go before CSP can be routinely used on most molecules of industrial interest. First, the sampling space that has to be covered has grown dramatically from small rigid molecules to a

molecule with eight flexible torsion angles, and an increase in the number of molecules in the asymmetric unit cell. Second, the challenge of describing the intra- and intermolecular forces grew with the introduction of heavier elements, hydrated crystals, and salts. The strong intermolecular forces involved in salt hydrates, for example, are challenging to the accuracy of many approximate density functionals (especially of the GGA level,  $\Psi_{\text{cry}}$ ) as well as methods based on the molecular charge density ( $\Psi_{\text{mol}}$ ). Thus, the CSP blind test challenges are testing many different aspects of computational modeling.

### 11.3.1 Evolution of CSP Methods

The first few blind tests showed that classical transferable intra- and intermolecular force fields (FFs), of the type used in many commercial modeling packages, including Polymorph-Predictor, are not accurate enough for reliable CSP. This can occur because the balance between the inter- and intramolecular forces is not sufficiently realistic to give the correct conformation in the crystal structure. An error in a torsional potential can have a major effect on the shape of the molecule and hence its packing. This, and problems in relative energy ranking may be attributed to using the same atomic charges for both the inter- and intramolecular forces [59]. Overall the first blind tests had limited successes, with most being from methods that use a hybrid atomistic  $\Psi_{\text{mol}}$  model with the electrostatic Coulomb interaction from distributed multipole analysis of the molecular wavefunction.

In the fourth blind test there was the first completely nonempirical model potential, using the  $\Psi_{\text{mol}}$  approach, with anisotropic repulsion as well as electrostatic terms derived using monomer long-range properties and SAPT calculations of dimer energies (see Chapter 2) [60]. This was achieved for  $\text{C}_6\text{Br}_2\text{ClFH}_2$ , where the polarization of the molecular charge distribution by the crystalline environment could be ignored and the molecule treated as rigid. This test also saw the company Avante-Garde Simulation introduce their CSP method using a periodic DFT (PBE functional) plus dispersion correction method that had been explicitly derived for modeling organic crystal structures [61]. This dispersion correction is similar in spirit to the D1 scheme [62]. The use of periodic electronic structure calculations in the final optimization and lattice energy evaluation has the advantage of automatically optimizing the molecular conformation and including the polarization energy. Their success was also based on fitting a molecule-specific tailored force-field to DFT-D data and using this to generate the structures using the code GRACE [63]. The use of the more accurate force field reduces the number of structures that need refinement by periodic DFT-D. This step-change in methodology enabled them to correctly predict all the target structures.

However, some of the limitations of this specific  $\Psi_{\text{cry}}$  approach became apparent in the fifth blind test with a salt and a hydrate system, whose intermolecular interactions are not well modeled by the PBE functional. The hydrate was particularly challenging, partly because many structures were essentially equivalent apart from the proton positions and very similar in energy. The calculations led to a reinterpretation of the diffraction data and a revised structure for form IV of gallic acid monohydrate, and to the discovery of a further polymorph and 22 solvates, many containing water [64]. The fifth blind test was the first to contain a molecule of the size and flexibility of the smaller pharmaceuticals in development, which was correctly predicted by two  $\Psi_{\text{mol}}$  methods [65]. This success inspired industrial

pharmaceutical scientists to collaborate on developing the application of CSP for use in the pharmaceutical industry (see Section 11.4).

The blind tests have also seen an evolution in the methods of generating plausible starting structures, as well as the number of variables that need to be considered explicitly in the generation stage. Multicomponent systems (or  $Z' = 2$  searches) need to consider the relative orientation of the molecules in the asymmetric unit cell, and each flexible torsion angle that can make a significant difference to the shape of the molecule adds another dimension to the search space. Different systematic methods of sampling are possible and can include (quasi)random searches, Monte-Carlo techniques, and evolutionary or particle swarm algorithms. For example, GRACE uses a modified simulated annealing search [66], and CrystalPredictor [36] is based on Sobol sequences. Both codes use fairly good lattice energy models for optimizing millions of crystal structures: either a tailor-made force field or an atomic charge plus  $\exp-6$  potential with a grid-based estimate of  $\Delta E_{\text{intra}}$ . Crucially, these codes have tests to determine the completeness of the search within the defined search space, in terms of the number of times the most promising structures are found. Aiming for a complete search (within the defined search space, see Section 11.2.2) can make the computational cost of the search vary considerably for similar molecules with the same flexibility. Though an essential step in the CSP task, we will not go into deeper discussion of these crystal structure generation techniques and concentrate on the modeling of noncovalent interactions.

### 11.3.2 State-of-the-Art CSP as a Test of Modeling Noncovalent Interactions

The sixth blind test had five target systems, shown in Fig. 11.5, and since target XXIII had uniquely been screened for polymorphs, allowed the submission of two lists of 100 structures. There was a considerable enlargement in the number of participating groups, with the 91 researchers from 14 countries introducing many new methods, described in the account of the test [58]. Only a few of the groups were able to attempt the  $Z' = 2$  polymorphs C and E of XXIII because of its size and flexibility (Fig. 11.5). The successes in finding the structures were dominated by the experienced groups: Avante-Garde Simulation was particularly successful, finding all but one structure (XXIII E,  $Z' = 2$ ) and academic groups using the  $\Psi_{\text{mol}}$  approach to CSP found all but the salt hydrate.

Considerably more was learned about the state of current periodic electronic structure ( $\Psi_{\text{cry}}$ ) methods in the post submission analysis. Many of the dispersion-corrected density-functional approximations discussed in this book were used, i.e., variants of the D2 scheme, D3, TS, MBD, XDM, and vdW-DF, mainly combined with the generalized gradient approximation PBE functional. This reflects the prohibitive computational cost of using a hybrid functional such as PBE0 on so many crystal structures. In the ranking of different structures of the same molecule, it could be hoped that many approximations in the treatment of intermolecular forces would cancel out, provided sufficient care had been taken to eliminate numerical errors in comparing very different sized and shaped unit cells (most CSP generated structures were  $Z' = 1$  with 2–8 molecules in the unit cell).

Four groups had entered reranking results, having been provided with large sets of structures by other groups with structure generation (search) capabilities. They were able to use these and the experimental structures to see the sensitivity to different models. This highlighted how much the differences in the types of intermolecular forces in the targets affected



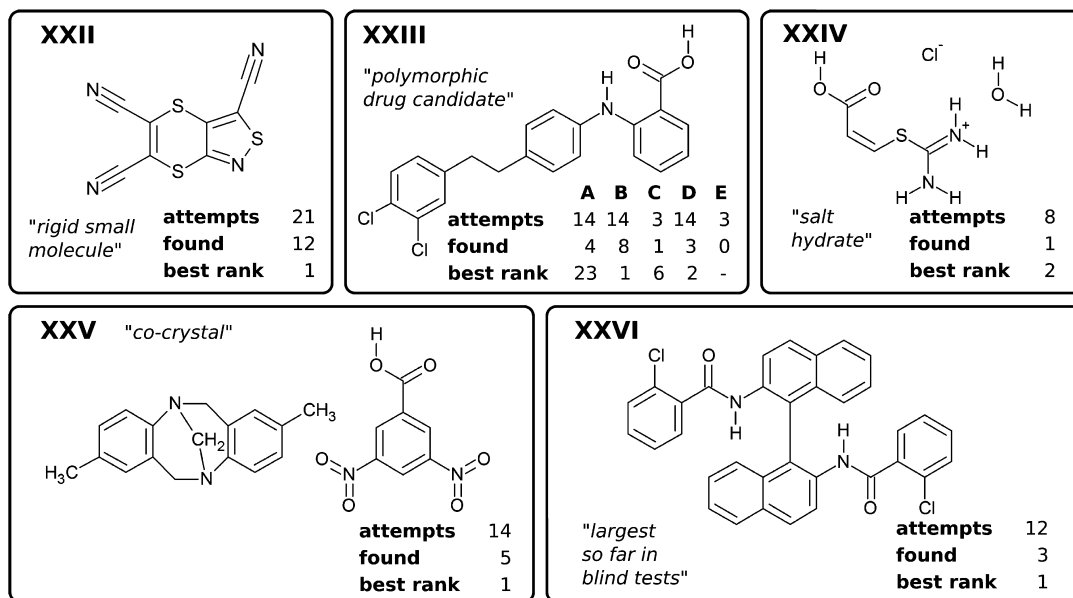
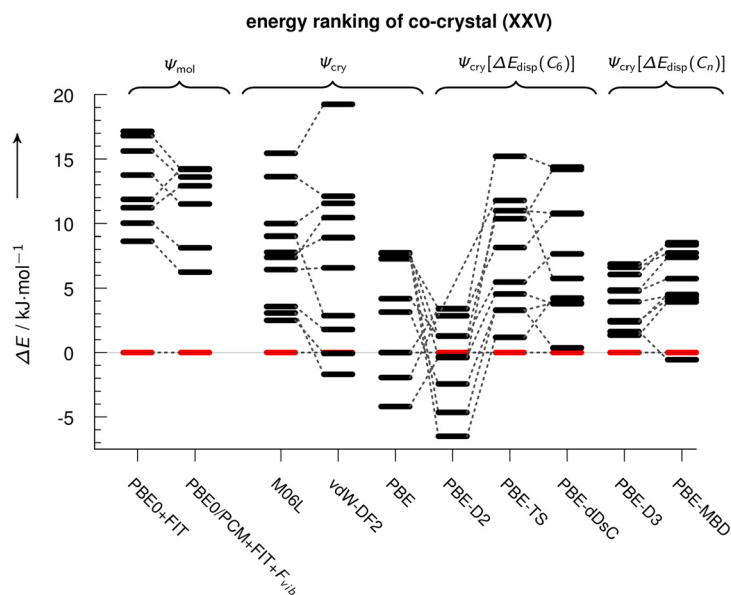


FIGURE 11.5 Target molecules and success rates in the sixth CSP blind test. For each target crystal structure, the number of attempts to predict the structure is given, along with the number of groups where the correct structure was found within their lists of 100 crystal structures. The best rank is the lowest rank in all submitted lists, e.g., a best rank of 1 means that it was found as the global energy minimum by at least one group.

which methods were necessary. The salt hydrate, with the relative positions of the three components in the asymmetric unit cell as additional search variables, was a major challenge to the search programs. The strength of the polarization around the ion means that  $\Psi_{\text{mol}}$  methods would not be expected to be able to evaluate relative lattice energies reliably. However, the  $\Psi_{\text{cry}}$  methods are able to cope with polarization and fine adjustments of the cation conformation. Moreover, the energy difference between the experimental and many other structures was sufficiently large that any reasonable  $\Psi_{\text{cry}}$  method could find the observed structure to be the most stable [67].

In contrast, the energy differences between plausible structures of the other molecules were much smaller, and the dispersion contribution was generally dominant. The relative energies of the polymorphs of XXIII were contrasted for several variants of both  $\Psi_{\text{mol}}$  and  $\Psi_{\text{cry}}$  methods, both as lattice energy differences and including various harmonic estimates of the free energy. The results show that most lattice energy models have all polymorphs within a plausible 10 kJ/mol in energy, but with major changes in the relative stability order [58]. In many cases, the free energy contribution changes the stability order of the polymorphs. Denser structures are generally stabilized by the dispersion contribution to the lattice energy and destabilized by the free energy contribution, and the density of structures of flexible molecules like XXIII is affected by how the intermolecular forces change the molecular conformation.



**FIGURE 11.6** Lattice energies of 10 hypothetical low energy structures for cocrystal XXV relative to the experimental structure, computed with various types of methods  $\Psi_{\text{mol}}$  or  $\Psi_{\text{cry}}$ .  $\Psi_{\text{mol}}$  shows the difference of the relative free energies using a rigid-body estimate for  $F_{\text{vib}}$  (see Eq. (11.3)) and molecular charge densities calculated in a polarizable continuum. For  $\Psi_{\text{cry}}$  we discriminate between dispersion corrections that describe only the leading order dispersion coefficient ( $C_6$ ) and schemes that include higher order contributions in both the many-body and the multipole sense ( $C_n$ ).

The effect of the dispersion correction for  $\Psi_{\text{cry}}$  methods is more clearly seen for XXV, a cocrystal of two fairly rigid molecules (Fig. 11.6). The  $\Psi_{\text{mol}}$  methods are able to predict the known structure as the most stable, independent of whether the molecular charge density is calculated in a polarizable continuum and a free energy difference is included. Many dispersion-corrected density functionals also find the known structure as the most stable, but only by a margin that raises the question as to whether free energy differences could change this.

Hence, more accurate methods for both energy and free energy contributions are needed to confidently identify the thermodynamically most stable crystal structure. Working with the assumption that the observed structure should be the most stable, the comparison of real and hypothetical structures is clearly still a challenge to whether the method is able to balance all the different contributions to the inter and intramolecular forces adequately (see Section 11.2.2). Most significantly, the performance of a periodic DFT-D method on the relative crystal stabilities in the sixth blind test correlates well with the accuracy for absolute sublimation enthalpies as tested with the X23 (or C21) set of crystal structures of small molecules [67].

The size of the crystallographic search space means that CSP has to involve a hierarchy of methods, so that the most expensive is only used on a computationally affordable number of structures. At each stage in a hierarchy, it is necessary to cover sufficient structures to be sure

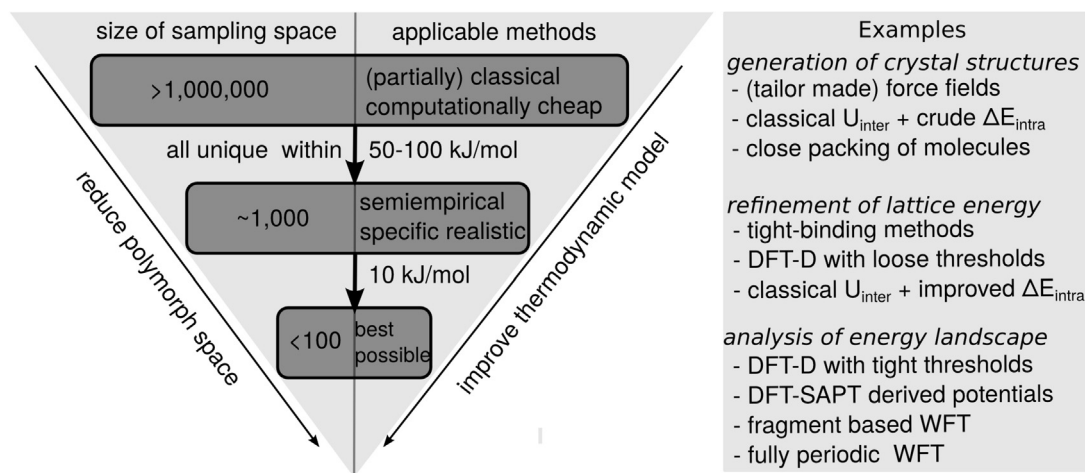


FIGURE 11.7 Sketch of possible hierarchies of methods to evaluate the crystal energies during a CSP study of a moderately sized flexible neutral molecule, with order of magnitude estimates of numbers of structures and energy differences that may be involved, which will depend on the specific molecule as well as method.

that the experimental structures are not eliminated. An illustration of possible hierarchical schemes for moderately sized molecules is shown in Fig. 11.7, looking forward to the wide application of the methods described within this book. The resources required for a thorough CSP study are determined by the specific molecule as the number of structures that are on the crystal energy landscape (i.e., within the energy range of be thermodynamically plausible polymorphs) varies enormously: monomorphic isocaffeine can be readily predicted with any reasonable CSP method, whereas there are about 500 low energy ordered crystal structures corresponding to the statically disordered low temperature crystal structure of caffeine, with energy differences that are so low that configurational entropy stabilizes this structure [68].

Before CSP can be routinely used in industry, the issue of computational cost and speed relative to the experimental timescales will have to be addressed. The reliability of different methods depends on the functional groups involved. The strong intermolecular forces involved in salt hydrates, for example, are challenging to the accuracy of many approximate density functionals (especially of the GGA level) as well as methods based on the molecular charge density. The  $\Psi_{\text{mol}}$  methods can use a far more accurate model for the charge density, and hence the electrostatic and other long-range forces, than  $\Psi_{\text{cry}}$  methods, provided that the atomistic intermolecular potential only has to be derived for a limited number of conformations.

Thus, the blind tests demonstrate whether CSP can predict the crystal structure of a molecule, prior to synthesis, and simultaneously provide a test bed for methods of predicting relative energies of known and competitive computer-generated structures. The target molecules are chosen from those where there is a well-determined crystal structure, within specified constraints or  $Z'$  and no disorder. The target structures are likely to be the polymorphs that crystallize most readily. Indeed, in some cases, further experiments have found polymorphs of target molecules after the blind tests. Whilst the blind tests are invaluable in

developing CSP methodology, the value of CSP is in what it can reveal about polymorphs and the control of crystallization processes in the manufacture of specialty organic chemicals.

## 11.4 CSP AS AN AID IN PHARMACEUTICAL DEVELOPMENT

The practical applications of CSP are not to predict easily crystallized structures, but to help find more polymorphs as a complement to experimental polymorph screening [3,77].

Such screening usually exposes the compounds to hundreds, even thousands, of crystallization conditions, often using automation to vary solvent, supersaturation, cooling rates, and other factors that would usually be controlled in a solvent crystallization process [78]. Crystallization from the melt is another standard means of looking for polymorphs and phase transitions for molecules that do not decompose. CSP is applied to determine the crystal energy landscape, the range of structures which are thermodynamically plausible as polymorphs, to see which unobserved types of crystal packing are thermodynamically competitive with the structures that are already known. Most pharmaceuticals that are in active development are rather larger, and more flexible, than the systems that have been extensively studied in the development of CSP methods such as the small generic drugs like aspirin and paracetamol. This brief survey of some of the recently published studies on the value of CSP in studying pharmaceutical materials (Fig. 11.8) aims to highlight how realistic modeling of noncovalent interactions could assist in predicting the properties of organic molecules that would be valuable in an industrial context [79,80]. Often this consists of giving a molecular overview of the crystallization behavior of a compound whose polymorphs do not all crystals of a size and quality suitable for experimental structure determination.

### 11.4.1 The Diversity of the Crystal Energy Landscape

The crystal energy landscape is very dependent on the individual molecule. For example, strychnine has one way of crystallizing with itself which is estimated to be 10 kJ/mol more stable than any other [79]. Hence, the fact that strychnine does not have polymorphs could have been confidently predicted by a far less computationally expensive method than the density functional calculations (PBE+TS) used in the CSP study. This is unusual, and the energy gaps, and hence the accuracy needed for ranking of very different types of crystal packings can differ considerably between closely related molecules.

Molecules that are similar enough to act at the same protein receptor can have dramatically different crystallization behavior. For example, two 5-HT<sub>2a</sub> agonists, LY2806920 (B5) and LY2624803 (DB7) (Fig. 11.8), which were under development for sleep disorders, posed very different challenges in developing appropriate solid forms for drug development. B5 readily and reliably crystallizes in just one solid form of the neutral molecule, whereas screening for DB7 found three neat polymorphs, two hydrates, three alcohol solvates, and an amorphous phase. Although the numbers of experiments in the solid-form screens were roughly equivalent, the ability to use an amorphous form of DB7 gave a greater ability to avoid the memory of the input material seeding the crystallizations [69]. The reason for the difference in the

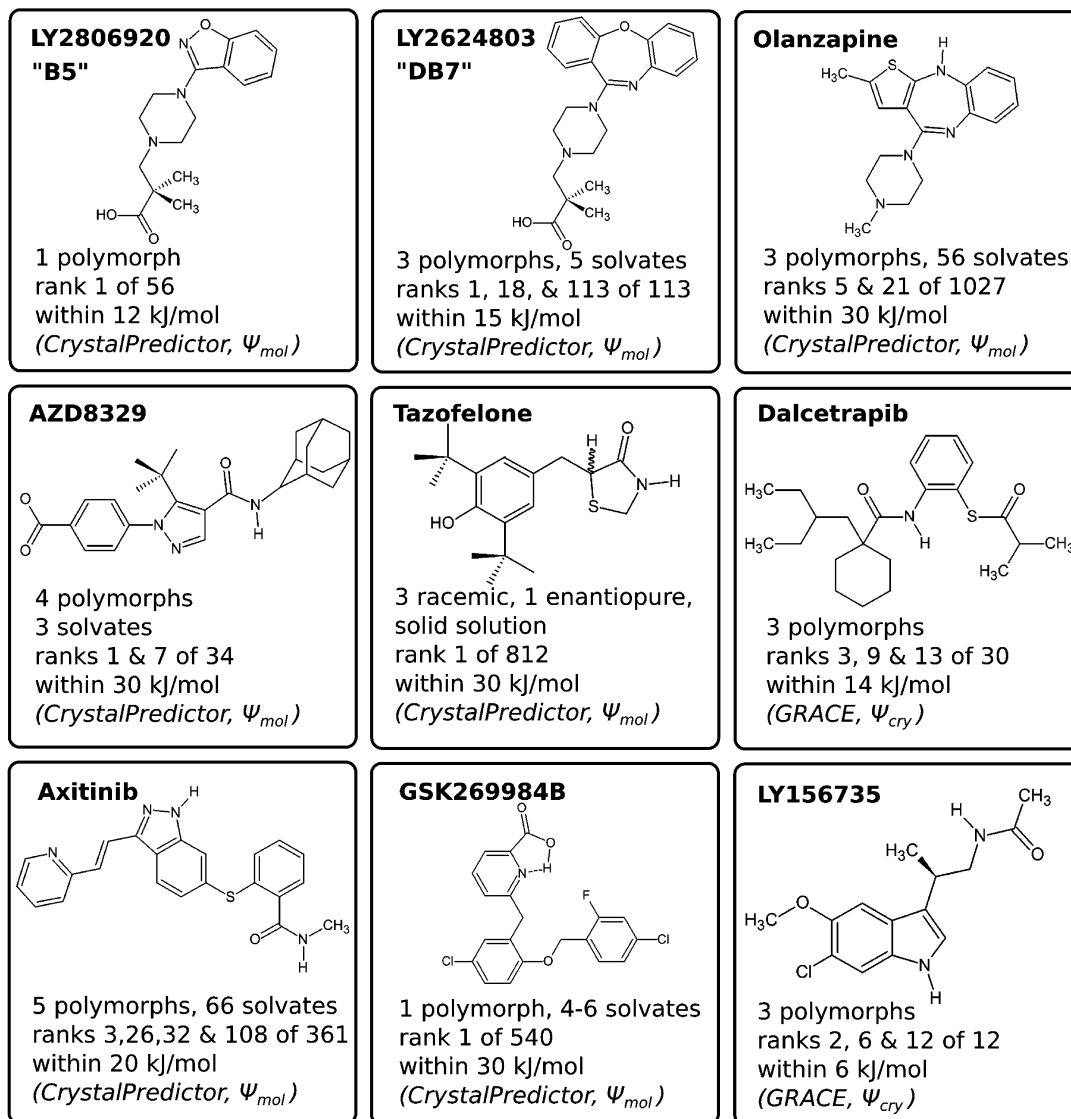


**FIGURE 11.8** Pharmaceuticals discussed in text where a CSP study has been performed to complement industrial solid-form screening, with the number of experimentally determined solid forms. The number of CSP generated structures which were carefully analyzed as being within the stated range of the most stable is given. The ranking of the polymorphs is given appropriate for the molecule and study (e.g., enantiopure structures only considered in chiral space groups;  $Z' = 2$  polymorphs are not found or ranked in a  $Z' = 1$  search). The references to the CSP and often experimental studies are LY2806920 "B5" [69], LY2624803 "DB7" [69], olanzapine [70], AZD8329 [71], tazofelone [72], dalcetrapib [73], axitinib [74], GSK269984B [75], and LY156735 [76].

solid forms of B5 and DB7 was not in the number or spacing of the lattice energy minima, but in their nature. B5 could pack densely with itself, with most low energy structures having an internal hydrogen bond. Hence trapping a long-lived, practically important metastable polymorph of B5 in competition with the readily crystallizing structure is unlikely. In contrast DB7 had no good way of packing densely with itself, and the low energy structures for DB7 mainly had intermolecular hydrogen bonds forming a range of motifs. This promotes solvate formation and long-lived metastable polymorphs, such as form III, which could only be obtained in polycrystalline form by desolvating the zwitterionic dihydrate [81].

The question of whether a molecule is prone to solvate formation is fundamental to both the experimental screening process and the relative energies of polymorphs [4]. The small amount of molecular and conformational rearrangement that is possible as solvent is removed from a crystal structure may mean that a higher energy polymorph is kinetically trapped, and so the energy differences between conformational polymorphs can be larger than for packing polymorphs. For promiscuous solvate formers such as axitinib [74], CSP will often generate structures with voids that can be stabilized by solvents, or even form inclusion compounds, however, in other cases such as olanzapine, the majority of solvates have the solvent separating olanzapine layers that do not stack readily [70].

#### 11.4.2 Finding the Most Stable Polymorph

It is usually preferred to use the most stable crystal form in a product to avoid the risk of transformation during storage in the range of temperatures and humidity operational throughout the world. The dangers of a late-appearing, more stable, polymorph mean that it is highly desirable to be able to confirm that the most stable crystal structure is known [45,82]. Manufacturing processes could subject the crystals to an even wider range of conditions, in particular shear pressure in a milling step which is often used to provide the required particle size distribution. Hence, the need to be able to reliably compute the relative stability of polymorphs over a wide range of conditions. There are cases of small molecules where CSP has led to the finding of the most stable form [20]. However, as already discussed (see Section 11.3), the challenge of performing a full search and accurate enough energy evaluations increases with the size of molecule or diminishing energy gaps between polymorphs. However, it may not be necessary to perform a full CSP study. For example, crizotinib, which was developed by Pfizer for the treatment of forms of lung cancer, was unusual in that extensive polymorph and hydrate screening found only one crystalline form. This structure not only had the lowest energy molecular conformation but also optimal intermolecular interactions, as confirmed by a CCDC solid form informatics “healthcheck” [83]. A simple CSP search, based on just four rigid, carefully selected conformers and the five most common chiral space groups, showed that the known structure was significantly more stable than any other generated, increasing the confidence that there was no danger of a late-appearing more stable form [84].

#### 11.4.3 Characterizing Polymorph Structure, Disorder, and Polymorphic Purity

The structure of a polymorph is the key to understanding, and eventually computationally predicting, all the relevant properties of the crystalline form for designing the drug product

and manufacturing process [1]. Hence, there is great interest in the ability to predict the morphologies, mechanical properties [85,86], etc., of polymorphs from the crystal structure [87]. Diffraction patterns can be readily simulated from CSP-generated structures and hence the output of a search can help with the structural characterization of samples when there is insufficient data for a confident assignment [88]. Many polymorphs do not readily grow crystals suitable for a single-crystal diffraction determination of the structure. Indeed, it has only recently become routine in academic labs to check that the single crystal selected is typical of the sample by comparing its simulated powder pattern to that of the experimental powder pattern of the batch of solid material. Concomitant crystallization, where more than one polymorph appears in the same sample, is relatively common [89]. Hence, a polycrystalline sample may be a mixture of polymorphs. Alternatively, the sample crystallization conditions can have a major influence on the degree of disorder within the crystallites. The use of CSP in combination with powder diffraction and solid-state NMR was able to solve the structure of form III of DB7 as an intrinsically disordered polymorph, obtained only by dehydration [81]. Whether a microcrystalline sample is a physical mixture of polymorphs or one form with variable disorder makes a huge difference to the problems that have to be circumvented in pharmaceutical development for quality control.

The Lilly blockbuster olanzapine, marketed for the treatment of schizophrenia, generated a lot of patent claims of “novel” polymorphs by generic companies. In many cases, the purported new forms were mixtures of the concomitantly crystallizing metastable polymorphs, forms II and III. The structure of form II was only determined in the year that olanzapine came off patent, when a single crystal suitable for X-ray could be picked out from a sample of olanzapine that had failed to cocrystallize with nicotinamide. It has not yet been possible to isolate a pure form III sample, but its powder diffraction pattern can be corrected for the presence of form II. The olanzapine crystal energy landscape included a structure that was a sufficient match to the form III powder pattern to give a structural model of form III as a different stacking of the same molecular layers as form II, rationalizing why forms II and III always crystallize concomitantly [70]. If the CSP study is being done only to help propose structural models from limited experimental data, then a more limited CSP search may be appropriate. For example, to find structures for the anhydrous forms of the antibiotic levofloxacin, an analysis was made of crystal structures of six carboxylic acid salt and hydrate forms to choose six likely  $\pi$  stacked dimer structures, which were optimized by electronic structure methods and held rigid during the CSP search [90]. Alternatively, if the space group can be established, a more complete search can be done on that specific space group as done for naproxen [47].

An increasing variety of methods are being used to characterize organic solid state samples, and so the range of spectral properties that are being calculated from the CSP-generated structures is increasing. An extreme example of the use of the calculated spectra of the structures on a crystal energy landscape was the characterization of a new polymorph of theophylline by electron diffraction, from a single crystallite polymorphic impurity. This polymorph could not be detected by powder X-ray diffraction on the sample [91]. The simulation of the solid state NMR spectrum from the crystal structure is more challenging, requiring special functionalized DFT or molecular methods (see Chapter 10) [92]. This is being combined with CSP for structural characterization, for example, for AZD8329, an 11-HSD1 inhibitor investigated for use in the treatment of type 2 diabetes. Form 4, one of two forms considered

to have superior properties for development, had a structure proposed by comparing the experimental proton solid state NMR spectrum with those calculated from CSP generated structures with both the *cis* and *trans* amide conformations [71].

A major strength of CSP is that it can generate closely related structures that are so similar in energy that the alternative packings are likely to appear in the crystals, either as growth errors or from configurational entropy stabilization of disorder [68]. For example, a study on tazofelone unexpectedly found a crystal of form III that had the same layer structure as known forms I and II, but was stacked in a different way [72]. The crystal energy landscape found alternative stackings of this layer close in energy to form II, the most stable form. This helped rationalize why the large single crystals of each polymorph varied in melting point, as there were sufficient stacking faults to be apparent in the raw diffraction data.

#### 11.4.4 Suggesting Experiments to Find Predicted Polymorphs

In the long-term, there should be sufficient understanding of the factors determining how a molecule crystallizes that the prediction of a polymorph would be associated with a suggestion of the experiment in which it could be found [44,93]. This is a distant goal, but there is some evidence of how solution behavior can modulate the polymorph form [94]. In the case of GSK269984B, the low energy structures on the crystal energy landscape had intermolecular hydrogen bonding compensating for adopting grossly different, higher energy conformations than in the observed most stable, internally hydrogen-bonded structure [75]. Further screening concentrated on solvents that would be likely to hydrogen bond to the active pharmaceutical ingredient (API). This produced some metastable solvates with the expected intermolecular hydrogen bonding, but the same gross conformation as in the neat form. Although solution NMR showed that a range of other conformations could exist in solution, it appeared that the fast crystallization of GSK269984B into its most stable form prevented the crystallization of metastable polymorphs with a different gross conformation as well as hydrogen bonding.

The use of pressure to favor higher density polymorphs has been successful in finding a polymorph that had been missed in extensive experimental screening of Roche's CETP inhibitor, dalcetrapib. The crystal energy landscape had two structures denser than the known stable form but very close in energy (based on the PBE-D3 level), which became more stable than the observed polymorph with a modest increase in pressure. Experiments recrystallizing dalcetrapib, either from solution or the melt, in a diamond anvil cell under modest pressure formed a new polymorph [73]. This matched the predicted polymorph, except for disorder in the hydrocarbon tail which could have been anticipated from other structures on the crystal energy landscape.

More specific targeting is becoming possible with the appreciation of the role of impurity crystals in templating the first nucleation of a crystal. The predicted cocrystallization of caffeine with benzoic acid needed an initial seeding with an isostructural cocrystal of caffeine with a fluorobenzoic acid [11]. New CSP-predicted polymorphs of carbamazepine (form V) and cyheptamide (form III) were found by sublimation onto an isostructural template of dihydrocarbamazepine form II. These polymorphs had not been found by extensive traditional polymorph screening [95]. Since synthetic impurities often have a marked effect on



the crystallization behavior, there is clearly considerable potential for templating different polymorphs, if we understood nucleation and growth better.

## 11.5 CHIRAL SEPARATION BY CRYSTALLIZATION

The separation of enantiomers by crystallization is an important industrial process, given their difference in biological activity [96]. Crystal structure prediction has always been recognized as a potentially important tool in designing such processes, as it should provide the lowest energy structure in the racemic and chiral space groups and their energy difference. However, it is clear that several complications can arise. The first problem may come with the assumption that the molecules will crystallize in the most stable crystal structure: a CSP study on 3-chloromandelic acid generated many structures that were simpler, denser, and thermodynamically competitive, if not more stable (using a range of different approaches), than the known structures [19]. Consideration of both experimental and computational evidence on the mandelic acids and other flexible chiral molecules raises questions of the role of the encounter statistics in crystallization kinetics in determining which structures can be nucleated and observed [97]. Indeed, experimental screening of LY1567365 could not find a crystal structure that was generated by CSP, but it was found in experiments using the inactive enantiomer [76].

Another problem may be the role of templating between crystal structures of large molecules where the chiral center has little influence on the packing preferences of the rest of the molecule. Tazofelone illustrates this, as seeding a melt of the two enantiomers with the enantiopure ( $Z' = 2$ ) crystal produces an isostructural solid solution [72]. The CSP study generated an isostructural racemic form more stable than the enantiopure crystal (but less stable than the racemic polymorphs). The two conformations in the enantiopure crystal could be readily replaced by molecules of the opposite chirality, meaning that the crystallization of enantiopure tazofelone could readily incorporate impurities of the other hand.

However, despite these counterexamples, CSP has been used to successfully predict the most stable crystal structures of the enantiopure and racemic compound for many molecules. The ability to separate out just one hand of the molecule from a racemic mixture depends on the relative solubility of the two enantiopure and racemic crystals. Predicting solubility is notoriously difficult but the solvation energy in an achiral solvent of the two enantiomers will be identical if the solution is ideal [98]. Similarly, the energy of a gas is the same regardless of the ratio of the two hands of the molecules. The melts of the racemic and enantiopure crystals may not be too different, depending on the molecule.

Hence, if we could assume that the heat capacities and zero-point energies ( $F_{\text{vib}}$ , see Eq. (11.3)) are the same for both crystals, the lattice energy difference corresponds to the free energy difference between the crystals. The enantiomeric excess (ee), the excess of one enantiomer over the other that results from crystallizing a racemic mixture (ee = 0), depends exponentially on the solubility difference. The enantiomeric excess has been predicted with reasonable success for 10 peptides by using lattice energy differences [99]. However, the difference in lattice energies will only dominate the difference in relative thermodynamic

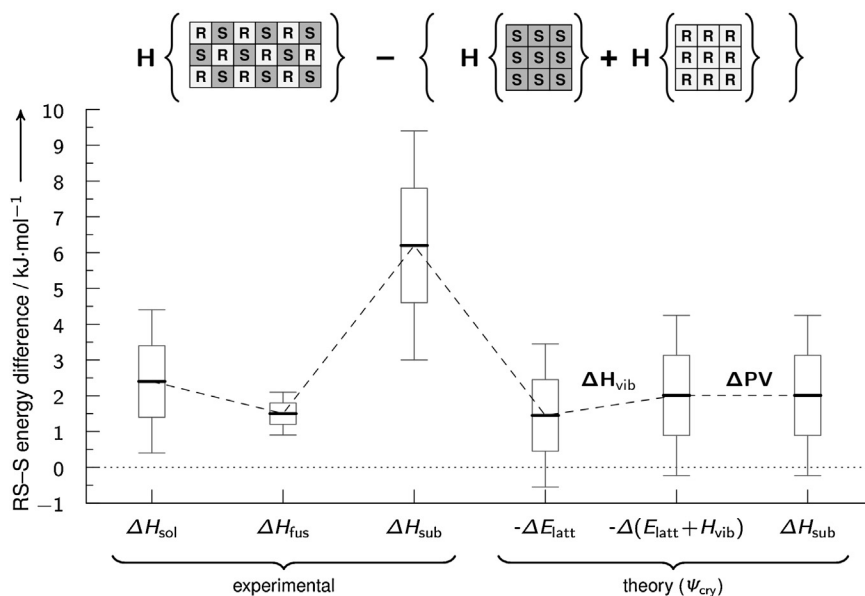


**FIGURE 11.9** Illustration of the different approximations to the difference in energies of the enantiopure and the more stable racemic crystal structures of naproxen. The experimental energies are contrasted with a TPSS-D3 estimate of the lattice energy, with the addition of harmonic phonon contributions, and the pressure–volume term to yield  $\Delta H_{\text{sub}}$ . The experimental energy difference derived from the solubility difference in ethanol/water [47] and the sublimation enthalpies are at normal conditions [100], while the enthalpy of fusion is measured at 427 K [47]. The boxplot gives the 68% and 95% confidence intervals either estimated from statistical experimental errors or, in the case of theory, estimated from typical errors derived from benchmark sets of organic crystals [99].

quantities for chiral systems, such as the sublimation energy or solubility difference, if this is larger than the errors in the assumptions being made [47].

This is illustrated by the antiinflammatory naproxen (Fig. 11.3), where the relative heats of solution,  $\Delta H_{\text{sol}}$  [47], differences in heats of fusion,  $\Delta H_{\text{fus}}$  [47], and sublimation enthalpy,  $\Delta H_{\text{sub}}$  [100], between the racemic and enantiopure crystals have been measured [100]. These data (Fig. 11.9) clearly show that the assumptions above, which lead to the approximate relationships between the crystal energies,

$$\Delta H_{\text{R+S-RS}}^{\text{cry}} \approx \Delta H_{\text{sol}} \approx \Delta H_{\text{fus}} \approx \Delta H_{\text{sub}} \approx -\Delta E_{\text{latt}}, \quad (11.5)$$

do not hold, even allowing for the experimental errors. For example, the experimental errors in measuring the two heats of fusion may be larger than the difference between the racemic and enantiopure liquid state.

Computationally, the  $\Psi_{\text{mol}}$  methods used in the original study (Fig. 11.4 [47]) can be improved by a recent  $\Psi_{\text{cry}}$  study (TPSS-D3, Fig. 11.9). The variations in the relative lattice energies  $E_{\text{latt}}$  with method will be qualitatively similar to those shown for the cocrystal XXV in Fig. 11.6, and hence could be larger the experimental differences. Fig. 11.9 also examines the approximations in the calculations of  $\Delta H_{\text{sub}}$ . The pressure–volume work ( $\Delta PV$ ) contri-

bution to  $\Delta H_{\text{sub}}$  is only 0.01 kJ/mol, though this will increase when there are larger density differences between the crystals. The thermal contribution,  $H_{\text{vib}}$ , is more problematic to calculate, with an error of 10 kJ/mol when using the very different unit cells rather than sampling the Brillouin zones sufficiently, a common problem in comparing polymorphs [17]. However, the converged difference from harmonic values is 0.5 kJ/mol, which, although small, could make a difference in the eutectic composition of up to 10%. Hence, as Fig. 11.9 indicates, the computational prediction of the parameters needed for designing chiral resolution processes is still an even greater challenge to theoretical methods than CSP.

## 11.6 CONCLUSIONS AND FUTURE CHALLENGES

The ability to predict organic crystal structures is both a stringent test of our ability to model intermolecular forces, and an industrially and scientifically relevant application of computer modeling. The vision of being able to design a pharmaceutical product aided by computer simulation is an exciting challenge to our fundamental scientific understanding of what determines the behavior of these molecules and how this can be encapsulated in computer codes. It requires not only the prediction of all potential solid forms, but also of all their properties relevant to processing, manufacture and use.

CSP has shown up the inadequacies of simple, transferable, isotropic atom–atom FFs, of the type in most commercial modeling packages, for molecule-specific modeling of the organic solid state. The success of GRACE in using a molecule-specific tailored force-field [66] derived by fitting to DFT-D data, of a functional form similar to the classical transferable force-fields, in the first step of crystal structure generation, shows the potential and limitations of optimizing the parameterization of this functional form.

The accurate evaluation of the relative energies (and solubilities) of polymorphs remains a challenge to computational chemistry, with the adequate evaluation of the interatomic forces as a major part of the challenge. Two approaches are currently being used, often successfully for practical purposes, in CSP on large molecules, namely those which rely on the theory of intermolecular forces and require calculations based on the molecular charge density ( $\Psi_{\text{mol}}$ ) and periodic electronic structure modeling ( $\Psi_{\text{cry}}$ ). Both methods have different strengths and weaknesses depending on different types and sizes of the target molecules.

The recent blind test shows that methods for evaluating the crystal energies, based on the various modern approaches to evaluating intermolecular forces are converging to being able to predict relative lattice energies well within 10 kJ/mol even for quite large molecules. Unfortunately, these errors are significant compared with polymorphic energy differences. It depends on the number and relationship of the low energy CSP generated structures whether this accuracy is sufficient to be able to predict the most thermodynamically stable structure at normal conditions.

Periodic electronic structure calculations ( $\Psi_{\text{cry}}$ ) require less assumptions and can be performed more automatically, but are still sensitive to the density functional and dispersion correction. Additionally, the computational costs can be high, and scale poorly with the number of crystal structures being used. The atomistic modeling of intermolecular forces, using anisotropic atom–atom models, with distributed multipoles and empirically fitted potentials,

has the advantage of absorbing at least some of the errors [101]. The model for the intermolecular interactions can be systematically improved using monomer properties and SAPT calculations of the various components such as anisotropic repulsion. Such intermolecular potentials, once derived, can be used very cheaply to model the crystal structures of rigid molecules. However, for flexible molecules, the conformation dependence of the intermolecular potential is an issue, and the need to allow the molecular conformation to adjust in response to the packing forces becomes computationally expensive. There is some hope that separating the intermolecular from intramolecular terms in the force-field may be a way to make anisotropic atom–atom force-fields more accurate, thereby by-passing the current need to do *ab initio* calculations on the molecule in each conformation relevant to its crystal packing [101].

Hence, molecular crystal structure prediction provides both a challenge in modeling accuracy, but also in modeling speed, so that a range of properties can be evaluated, and the calculations performed on a time and resource scale suitable for application in industry. Molecular dynamics studies will be needed for determining which CSP generated crystal structures are free energy minima, and which artifacts of the neglect of temperature, but this requires a force-field that is sufficiently realistic. Crystallization is a complex phenomenon, as shown by the phenomenon of polymorphism. However, separating out thermodynamics from kinetic aspects of nucleation and growth to allow predictive control of crystallization will remain both a fundamental and practically vital scientific question for some time to come.

## Acknowledgments

This work was supported by EPSRC (EP/K039229/1). J.G.B. acknowledges support by the Alexander von Humboldt foundation within the Feodor Lynen program.

## References

- [1] C.C. Sun, *J. Pharm. Sci.* 98 (2009) 1671–1687.
- [2] A. Gavezzotti, *Molecular Aggregation: Structure Analysis and Molecular Simulation of Crystals and Liquids*, Oxford University Press, 2006.
- [3] Y.A. Abramov, *Computational Pharmaceutical Solid State Chemistry*, John Wiley & Sons, 2016.
- [4] A.J. Cruz-Cabeza, S.M. Reutzel-Edens, J. Bernstein, *Chem. Soc. Rev.* 44 (2015) 8619–8635.
- [5] S.T. Beckett, *Science of Chocolate*, RSC Paperbacks, The Royal Society of Chemistry, 2000.
- [6] T. Hasell, J.L. Culshaw, S.Y. Chong, M. Schmidtman, M.A. Little, K.E. Jelfs, E.O. Pyzer-Knapp, H. Shepherd, D.J. Adams, G.M. Day, A.I. Cooper, *J. Am. Chem. Soc.* 136 (2014) 1438–1448.
- [7] J.T.A. Jones, T. Hasell, X. Wu, J. Bacsa, K.E. Jelfs, M. Schmidtman, S.Y. Chong, D.J. Adams, A. Trewin, F. Schiffman, F. Cora, B. Slater, A. Steiner, G.M. Day, A.I. Cooper, *Nature* 474 (2011) 367–371.
- [8] E.O. Pyzer-Knapp, H.P.G. Thompson, F. Schiffmann, K.E. Jelfs, S.Y. Chong, M.A. Little, A.I. Cooper, G.M. Day, *Chem. Sci.* 5 (2014) 2235–2245.
- [9] S. Perez-Lloret, M.V. Rey, P.L. Ratti, O. Rascol, *Fundam. Clin. Pharmacol.* 27 (2013) 81–95.
- [10] J. Bauer, S. Spanton, R. Henry, J. Quick, W. Dziki, W. Porter, *Pharm. Res.* 18 (2001) 859–866.
- [11] D.-K. Bučar, R.W. Lancaster, J. Bernstein, *Angew. Chem. Int. Ed.* 54 (2015) 6972–6993.
- [12] A. Gavezzotti, *Acc. Chem. Res.* 27 (1994) 309–314.
- [13] J. Maddox, *Nature* 335 (1988) 201.
- [14] L. Yu, *Acc. Chem. Res.* 43 (2010) 1257–1266.
- [15] M. Vasileiadis, A.V. Kazantsev, P.G. Karamertzanis, C.S. Adjiman, C.C. Pantelides, *Acta Crystallogr. B* 68 (2012) 677–685.
- [16] A.J. Cruz-Cabeza, J. Bernstein, *Chem. Rev.* 114 (2014) 2170–2191.

- [17] J. Nyman, G.M. Day, *CrystEngComm* 17 (2015) 5154–5165.
- [18] S.A. Barnett, C.K. Broder, K. Shankland, W.I.F. David, R.M. Ibberson, D.A. Tocher, *Acta Crystallogr. B* 62 (2006) 287–295.
- [19] R.K. Hylton, G.J. Tizzard, T.L. Threlfall, A.L. Ellis, S.J. Coles, C.C. Seaton, E. Schulze, H. Lorenz, A. Seidel-Morgenstern, M. Stein, S.L. Price, *J. Am. Chem. Soc.* 137 (2015) 11095–11104.
- [20] D.E. Braun, H. Oberacher, K. Arnhard, M. Orlova, U.J. Griesser, *CrystEngComm* 18 (2016) 4053–4067.
- [21] H.P.G. Thompson, G.M. Day, *Chem. Sci.* 5 (2014) 3173–3182.
- [22] A.D. Mighell, V.L. Himes, J.R. Rodgers, *Acta Crystallogr. A* 39 (1983) 737–740.
- [23] C.R. Groom, I.J. Bruno, M.P. Lightfoot, S.C. Ward, *Acta Crystallogr. B* 72 (2016) 171–179.
- [24] K.M. Steed, J.W. Steed, *Chem. Rev.* 115 (2015) 2895–2933.
- [25] H.C.J. Berendsen, *Simulating the Physical World: Hierarchical Modeling from Quantum Mechanics to Fluid Dynamics*, Cambridge University Press, 2007.
- [26] W.L. Jorgensen, J. Tirado-Rives, *Proc. Natl. Acad. Sci. USA* 102 (2005) 6665–6670.
- [27] M.A. Neumann, *J. Phys. Chem. B* 112 (2008) 9810–9829.
- [28] G.M. Day, W.D.S. Motherwell, W. Jones, *Cryst. Growth Des.* 5 (2005) 1023–1033.
- [29] T.G. Cooper, K.E. Hejczyk, W. Jones, G.M. Day, *J. Chem. Theory Comput.* 4 (2008) 1795–1805.
- [30] E.O. Pyzer-Knapp, H.P.G. Thompson, G.M. Day, *Acta Crystallogr. B* 72 (2016) 477–487.
- [31] S.L. Price, M. Leslie, G.W.A. Welch, M. Habgood, L.S. Price, P.G. Karamertzanis, G.M. Day, *Phys. Chem. Chem. Phys.* 12 (2010) 8478–8490.
- [32] J. Nyman, O.S. Pundyke, G.M. Day, *Phys. Chem. Chem. Phys.* 18 (2016) 15828–15837.
- [33] G.M. Day, S.L. Price, *J. Am. Chem. Soc.* 125 (2003) 16434–16443.
- [34] A.V. Kazantsev, P.G. Karamertzanis, C.S. Adjiman, C.C. Pantelides, *J. Chem. Theory Comput.* 7 (2011) 1998–2016.
- [35] C.C. Pantelides, C.S. Adjiman, A.V. Kazantsev, *Top. Curr. Chem.* 345 (2014) 25–58.
- [36] M. Habgood, I.J. Sugden, A.V. Kazantsev, C.S. Adjiman, C.C. Pantelides, *J. Chem. Theory Comput.* 11 (2015) 1957–1969.
- [37] B.P. van Eijck, J. Kroon, *J. Phys. Chem. B* 101 (1997) 1096–1100.
- [38] M. Rossi, P. Gasparotto, M. Ceriotti, *Phys. Rev. Lett.* 117 (2016) 115702.
- [39] P. Raiteri, R. Martoňák, M. Parrinello, *Angew. Chem. Int. Ed.* 44 (2005) 3769–3773.
- [40] P.G. Karamertzanis, P. Raiteri, M. Parrinello, M. Leslie, S.L. Price, *J. Phys. Chem.* 112 (2008) 4298–4308.
- [41] J. van de Streek, *Acta Crystallogr. B* 62 (2006) 567–579.
- [42] J. Bernstein, R.E. Davis, L. Shimoni, N.-L. Chang, *Angew. Chem. Int. Ed.* 34 (1995) 1555–1573.
- [43] T. Gelbrich, M.B. Hursthouse, *CrystEngComm* 7 (2005) 324–336.
- [44] S.L. Price, *Acta Crystallogr. B* 69 (2013) 313–328.
- [45] D.E. Braun, M. Orlova, U.J. Griesser, *Cryst. Growth Des.* 14 (2014) 4895–4900.
- [46] J. Yang, W. Hu, D. Usvyat, D. Matthews, M. Schütz, G.K.-L. Chan, *Science* 345 (2014) 640–643.
- [47] D.E. Braun, M. Ardid-Candel, E. D’Oria, P.G. Karamertzanis, J.-B. Arlin, A.J. Florence, A.G. Jones, S.L. Price, *Cryst. Growth Des.* 11 (2011) 5659–5669.
- [48] J.R. Holden, Z. Du, H.L. Ammon, *J. Comput. Chem.* 14 (1993) 422–437.
- [49] S. Grimme, A. Hansen, J.G. Brandenburg, C. Bannwarth, *Chem. Rev.* 116 (2016) 5105–5154.
- [50] G.J.O. Beran, *Chem. Rev.* 116 (2016) 5567–5613.
- [51] H.S. Muddana, C. Daniel Varnado, C.W. Bielawski, A.R. Urbach, L. Isaacs, M.T. Geballe, M.K. Gilson, *J. Comput.-Aided Mol. Des.* 26 (2012) 475–487.
- [52] H.S. Muddana, A.T. Fenley, D.L. Mobley, M.K. Gilson, *J. Comput.-Aided Mol. Des.* 28 (2014) 305–317.
- [53] J.P.M. Lommerse, W.D.S. Motherwell, H.L. Ammon, J.D. Dunitz, A. Gavezzotti, D.W.M. Hofmann, F.J.J. Leusen, W.T.M. Mooij, S.L. Price, B. Schweizer, M.U. Schmidt, B.P. van Eijck, P. Verwer, D.E. Williams, *Acta Crystallogr. B* 56 (2000) 697–714.
- [54] W.D.S. Motherwell, et al., *Acta Crystallogr. B* 58 (2002) 647–661.
- [55] G.M. Day, et al., *Acta Crystallogr. B* 61 (2005) 511–527.
- [56] G.M. Day, et al., *Acta Crystallogr. B* 65 (2009) 107–125.
- [57] D.A. Bardwell, et al., *Acta Crystallogr. B* 67 (2011) 535–551.
- [58] A.M. Reilly, et al., *Acta Crystallogr. B* 72 (2016) 439–459.
- [59] J. Kendrick, M.D. Gourlay, M.A. Neumann, F.J.J. Leusen, *CrystEngComm* 11 (2009) 2391–2399.
- [60] A.J. Misquitta, G.W. Welch, A.J. Stone, S.L. Price, *Chem. Phys. Lett.* 456 (2008) 105–109.

- [61] M.A. Neumann, M.-A. Perrin, *J. Phys. Chem. B* 109 (2005) 15531–15541.
- [62] S. Grimme, *J. Comput. Chem.* 25 (2004) 1463–1473.
- [63] J. Kendrick, F.J. Leusen, M.A. Neumann, *J. Comput. Chem.* 33 (2012) 1615–1622.
- [64] D.E. Braun, R.M. Bhardwaj, A.J. Florence, D.A. Tocher, S.L. Price, *Cryst. Growth Des.* 13 (2013) 19–23.
- [65] A.V. Kazantsev, P.G. Karamertzanis, C.S. Adjiman, C.C. Pantelides, S.L. Price, P.T. Galek, G.M. Day, A.J. Cruz-Cabeza, *Int. J. Pharm.* 418 (2011) 168–178.
- [66] M.A. Neumann, *J. Phys. Chem. B* 112 (2008) 9810–9829.
- [67] J.G. Brandenburg, S. Grimme, *Acta Crystallogr. B* 72 (2016) 502–513.
- [68] M. Habgood, *Cryst. Growth Des.* 11 (2011) 3600–3608.
- [69] D.E. Braun, J.A. McMahon, L.H. Koztecki, S.L. Price, S.M. Reutzel-Edens, *Cryst. Growth Des.* 14 (2014) 2056–2072.
- [70] R.M. Bhardwaj, L.S. Price, S.L. Price, S.M. Reutzel-Edens, G.J. Miller, I.D.H. Oswald, B.F. Johnston, A.J. Florence, *Cryst. Growth Des.* 13 (2013) 1602–1617.
- [71] M. Baías, J.-N. Dumez, P.H. Svensson, S. Schantz, G.M. Day, L. Emsley, *J. Am. Chem. Soc.* 135 (2013) 17501–17507.
- [72] L.S. Price, J.A. McMahon, S.R. Lingireddy, S.-F. Lau, B.A. Diserod, S.L. Price, S.M. Reutzel-Edens, *J. Mol. Struct.* 1078 (2014) 26–42.
- [73] M.A. Neumann, J. van de Streek, F.P.A. Fabbiani, P. Hidber, O. Grassmann, *Nat. Commun.* 6 (2015) 7793.
- [74] M. Vasileiadis, C.C. Pantelides, C.S. Adjiman, *Chem. Eng. Sci.* 121 (2015) 60–76.
- [75] S.Z. Ismail, C.L. Anderton, R.C.B. Copley, L.S. Price, S.L. Price, *Cryst. Growth Des.* 13 (2013) 2396–2406.
- [76] J. Kendrick, G.A. Stephenson, M.A. Neumann, F.J.J. Leusen, *Cryst. Growth Des.* 13 (2013) 581–589.
- [77] S.L. Price, L.S. Price, in: *Solid State Characterisation of Pharmaceuticals*, John Wiley & Sons, 2011, Chapter 12.
- [78] M.L. Peterson, et al., *J. Am. Chem. Soc.* 124 (2002) 10958–10959.
- [79] S.L. Price, D.E. Braun, S.M. Reutzel-Edens, *Chem. Commun.* 52 (2016) 7065–7077.
- [80] S.L. Price, S.M. Reutzel-Edens, *Drug Discov. Today* 21 (2016) 912–923.
- [81] D.E. Braun, L.H. Koztecki, J.A. McMahon, S.L. Price, S.M. Reutzel-Edens, *Mol. Pharm.* 12 (2015) 3069–3088.
- [82] D.E. Braun, H. Oberacher, K. Arnhard, M. Orlova, U.J. Griesser, *CrystEngComm* 18 (2016) 4053–4067.
- [83] N. Feeder, E. Pidcock, A.M. Reilly, G. Sadiq, C.L. Doherty, K.R. Back, P. Meenan, R. Docherty, *J. Pharm. Pharmacol.* 67 (2015) 857–868.
- [84] Y.A. Abramov, *Org. Process Res. Dev.* 17 (2013) 472–485.
- [85] M.H. Shariare, F.J.J. Leusen, M. de Matas, P. York, J. Anwar, *Pharm. Res.* 29 (2012) 319–331.
- [86] G.M. Day, S.L. Price, M. Leslie, *Cryst. Growth Des.* 1 (2001) 13–27.
- [87] P. Dandekar, Z.B. Kuvadia, M.F. Doherty, *Annu. Rev. Mater. Res.* 43 (2013) 359–386.
- [88] S. Habermehl, P. Mörschel, P. Eisenbrandt, S.M. Hammer, M.U. Schmidt, *Acta Crystallogr. B* 70 (2014) 347–359.
- [89] J. Bernstein, R.J. Davey, J.-O. Henck, *Angew. Chem. Int. Ed.* 38 (1999) 3440–3461.
- [90] S.S. Singh, T.S. Thakur, *CrystEngComm* 16 (2014) 4215–4230.
- [91] M.D. Eddleston, K.E. Hejczyk, E.G. Bithell, G.M. Day, W. Jones, *Chem. Eur. J.* 19 (2013) 7883–7888.
- [92] E. Salager, G.M. Day, R.S. Stein, C.J. Pickard, B. Elena, L. Emsley, *J. Am. Chem. Soc.* 132 (2010) 2564–2566.
- [93] J. Anwar, D. Zahn, *Angew. Chem. Int. Ed.* 50 (2011) 1996–2013.
- [94] R.J. Davey, S.L.M. Schroeder, J.H. ter Horst, *Angew. Chem. Int. Ed.* 52 (2013) 2166–2179.
- [95] V.K. Srirambhatla, R. Guo, S.L. Price, A.J. Florence, *Chem. Commun.* 52 (2016) 7384–7386.
- [96] H. Lorenz, A. Seidel-Morgenstern, *Angew. Chem. Int. Ed.* 53 (2014) 1218–1250.
- [97] A. Gavezzotti, L.L. Presti, *Cryst. Growth Des.* 15 (2015) 3792–3803.
- [98] R.E. Skyner, J.L. McDonagh, C.R. Groom, T. van Mourik, J.B.O. Mitchell, *Phys. Chem. Chem. Phys.* 17 (2015) 6174–6191.
- [99] A. Otero-de-la-Roza, B.H. Cao, I.K. Price, J.E. Hein, E.R. Johnson, *Angew. Chem. Int. Ed.* 53 (2014) 7879–7882.
- [100] H. Buchholz, V.N. Emelyanenko, H. Lorenz, S.P. Verevkin, *J. Pharm. Sci.* 105 (2016) 1676–1683.
- [101] O.G. Uzoh, P.T.A. Galek, S.L. Price, *Phys. Chem. Chem. Phys.* 17 (2015) 7936–7948.

# Noncovalent Interactions and Environment Effects

---

*Benedetta Mennucci*

Department of Chemistry, University of Pisa, Pisa, Italy

## 12.1 INTRODUCTION

---

In other chapters of this book, a detailed description of the physics underlying various types of noncovalent interactions has been given. Here, the focus will be on the theoretical models and computational strategies developed for including the effects of such interactions in the calculation of properties and processes in solvated or, more generally, embedded systems. We introduce here the term “embedded”, which extends the concept of environment effects to very different physical systems: a simple solvated molecule, a molecular system within a (bio)macromolecular matrix, composite systems such as molecules on surfaces in contact with a liquid solution, and more.

A large number of models have been developed over the years to account for environment effects. In particular, this chapter presents an overview of a specific subclass, namely models based on a partition of the real system in two (or more) subsystems, each being described at a different level of theory. The main advantage of this strategy (and the reason for its success) is that the same general framework can be used for all the different physical situations we have just mentioned, by simply adapting the boundaries between the subsystems and the theoretical description used for each. As a result, the size and the complexity of the systems that can be treated increase enormously with respect to the strategy of adopting the same accurate level of description for all the different components. In fact, the possibility of combining different methods for the different parts allows treating very different scales: from the molecular scale that characterizes the part of main interest, to the nanoscale of the embedding biological matrix, up to the macroscale of the bulk solvent. Due to this feature, the term “multiscale” is commonly used for this type of models.

In particular, the focus of this chapter will be on multiscale models in which only a small subset of the system, the region of interest, needs to be described with quantum mechanics (QM) while the other part(s) can be approximated with classical models. The resulting hybrid QM/classical approach is one of the most common computational strategies used to describe properties and processes in solvated or embedded systems. Two alternative formu-

lations of the classical part are possible: continuum models [1–3] and atomistic (or Molecular Mechanics, MM) models [4–7]. This is the most straightforward classification as it immediately identifies the two different approximations used. In the case of continuum models, the classical subsystem loses its atomistic nature and it is replaced by a dielectric continuum medium. The atomistic model, instead, maintains the concept of atoms but approximates them via classical particles by introducing an MM force field (FF). In the present chapter, however, a different classification will be used in terms of polarizable and nonpolarizable models. This classification is preferred because a unique description for both continuum and MM models can be introduced.

## 12.2 THE EFFECTIVE HAMILTONIAN

We consider the case of an embedded molecule in its ground state. Within a QM/classical framework, such a system is completely determined by solving an “effective” Schrödinger equation, where the Hamiltonian is the sum of three different terms, referring to the interactions (i) within the QM system, (ii) within the classical system, and (iii) between the QM and the classical systems, respectively:

$$\hat{H}^{\text{eff}} = \hat{H}^{\text{QM}} + \hat{H}^{\text{class}} + \hat{H}^{\text{QM/class}}. \quad (12.1)$$

The purely classical term,  $\hat{H}^{\text{class}}$ , merely causes a shift in the energy of the system but it cannot affect the wavefunction. In the above equation we have assumed a system for which the Hamiltonian does not depend on time.

The different formulations of QM/classical models are identified by the type of interactions included in the coupling term,  $\hat{H}^{\text{QM/class}}$ , and the way these interactions are represented. In principle,  $\hat{H}^{\text{QM/class}}$  should include all noncovalent interactions between the QM and the classical subsystems. In addition, if the boundary between the classical and the quantum subsystems crosses a chemical bond, it should contain covalent terms as well. The latter case is possible in biomolecular systems, for example, where the process of interest involves protein residues or cofactors chemically bonded to the embedding macromolecular matrix. In these cases, the severed bond at the QM boundary must be capped. In the literature, there are many different boundary strategies [8] but the most popular are those using “link-atom” schemes: an additional atomic center (the link atom, usually represented by a hydrogen atom) that is not part of the real system is introduced and covalently bound to the QM atom involved in the broken bond to saturate its free valence. The bonding interactions removed by the cut can be either neglected (if, for example, a QM/continuum approximation is used) or recovered within an MM/MM formulation according to the selected force field. To reduce the artifacts arising from these boundary schemes, the bond being cut should be far from the region where the process of interest is localized, and it should be nonpolar and not involved in any conjugation path. A typical good candidate is an aliphatic C–C bond.

Focusing now on noncovalent interactions, a common way of splitting the system is to partition  $\hat{H}^{\text{QM/class}}$  into the different contributions described in Chapter 1, namely electrostatic, induction (or polarization), dispersion, and repulsion:



$$\hat{H}^{\text{QM/class}} = \hat{H}^{\text{ele}} + \hat{H}^{\text{ind}} + \hat{H}^{\text{disp}} + \hat{H}^{\text{rep}}. \quad (12.2)$$

Because dispersion is a nonlocal electron correlation effect and repulsion arises from the Pauli exclusion principle, their reformulation within a hybrid QM/classical picture necessarily introduces much greater difficulties than electrostatics, which is an entirely classical interaction. To overcome such difficulties, dispersion and repulsion terms are commonly treated through empirical pair potentials. In most QM/MM formulations this is achieved using a Lennard-Jones (LJ) interaction between all pairs of atoms in the classical and the quantum subsystems. This means that the QM atoms are replaced by classical particles according to a selected force field:

$$\hat{H}^{\text{disp}} + \hat{H}^{\text{rep}} \approx \hat{H}^{\text{LJ}} = \sum_i^{N^{\text{QM}}} \sum_J^{N^{\text{MM}}} 4\epsilon_{iJ} \left[ \left( \frac{\sigma_{iJ}}{R_{iJ}} \right)^{12} - \left( \frac{\sigma_{iJ}}{R_{iJ}} \right)^6 \right], \quad (12.3)$$

where  $i$  and  $J$  run over the atoms in the QM and the MM subsystems, respectively, and  $\epsilon_{iJ}$  and  $\sigma_{iJ}$  are the LJ parameters for the  $iJ$  pair of atoms separated by an  $R_{iJ}$  distance.

In the case of QM/continuum models, where the classical subsystem does not preserve its atomistic nature, the repulsion and dispersion interactions are projected on the surface of the cavity containing the QM subsystem [9]. Alternatively, a linear relationship with the surface is used through proportionality factors that can be either obtained by fitting procedures or derived from specific models such as the surface tension model developed for solvents [2,10]. Within a continuum formulation, an additional repulsive term should be included related to the shape and the dimension of the QM subsystem considered as a rigid body. This contribution, often called “cavitation”, corresponds to the work involved in building the cavity of the appropriate shape and volume in which the QM subsystem is enclosed, with all the other QM/classical interactions (electrostatics and dispersion) switched off [3].

All these formulations of the nonelectrostatic contributions can only introduce a shift in the energy of the QM subsystem but have no effect on its wavefunction and the corresponding electron density. Attempts to define specific operators,  $\hat{H}^{\text{disp}}$  and  $\hat{H}^{\text{rep}}$ , which really act on the QM wavefunction, have been proposed within a QM/continuum framework [11–13]. An example is the self-consistent model developed by Amovilli and Mennucci [11]. In this model, the repulsion term is assumed to be proportional to the so-called “escaped charge”, i.e., the electron density of the QM subsystem that extends beyond the boundaries of the molecular cavity. The expression for the dispersion energy is obtained by generalizing the London formulation described in Chapter 1 to a continuum description, which is achieved via an apparent surface charge density induced on the cavity surface by the QM transition charge densities.

Contrary to dispersion and repulsion, electrostatic effects are easy to include in QM/classical models. In the case of QM/MM formulations, a QM operator  $\hat{H}^{\text{ele}}$  expressed in terms of point charges is generally used:

$$\hat{H}^{\text{ele}}(\mathbf{r}) = \sum_k^{N^{\text{MM}}} \frac{q_k^{\text{MM}}}{|\mathbf{r} - \mathbf{r}_k|}, \quad (12.4)$$

where the sum runs on all the MM sites bearing a charge  $q_k^{\text{MM}}$ . In some formulations the point charges are accompanied by higher-order multipolar contributions.

The resulting formulation is known as an “electrostatic embedding.” The parameters used (the charges and eventually dipoles, quadrupoles, etc.) have an atomistic nature and generally they are obtained through fits to calculated physical observables. A very well-known procedure to derive atomic charges is to perform a QM calculation of the molecule under investigation, evaluate its electrostatic potential on a grid around the molecule, and derive the charges with a fitting procedure so that they reproduce the QM potential [14].

Before moving to the continuum description, it is worth mentioning that alternative formulations of the QM/MM approach are possible. A well known example is the ONIOM method developed by Morokuma and coworkers [15]. In ONIOM, a “subtractive” (or “extrapolative”) scheme is introduced instead of the “additive” one presented here. Instead of writing the energy of the full system as the sum of the energy of the two subsystems plus their interaction, an extrapolated expression is used, namely:

$$E^{\text{ONIOM}} = E^{\text{MM}} + E_m^{\text{QM}} - E_m^{\text{MM}}, \quad (12.5)$$

where the index  $m$  stands for “model” subsystem, which is the part of the system which we want to describe at QM level and the subtractive operation removes the double-counted MM contributions. In its original formulation, the calculation on the model system did not account for the effects of the MM part, but more recently electrostatic-embedding (EE) ONIOM formulations have been proposed such that, the QM wave function (or charge density) of the model system can be polarized by the MM charge distribution of the environment represented in terms of atomic charges. Formally, ONIOM does not differ from the more common additive QM/MM formulation. However, its characteristic feature is that it can be easily generalized to more than two layers by combining different QM and/or classical descriptions.

In QM/continuum models, in which a dielectric medium is used instead of an atomistic classical subsystem, the electrostatic interactions are obtained by solving Poisson’s equation:

$$-\nabla \cdot [\varepsilon(\mathbf{r}) \nabla \Phi^{\text{tot}}(\mathbf{r})] = 4\pi\rho(\mathbf{r}), \quad (12.6)$$

where  $\rho$  is the density of the QM subsystem and  $\Phi^{\text{tot}}(\mathbf{r})$  is the total electrostatic potential. If a cavity is used and the dielectric medium surrounding it is assumed to be isotropic and homogeneous, the dielectric function  $\varepsilon(\mathbf{r})$  can be simplified into

$$\varepsilon(\mathbf{r}) = \begin{cases} 1 & \mathbf{r} \in \text{cavity}, \\ \epsilon & \mathbf{r} \notin \text{cavity}. \end{cases} \quad (12.7)$$

As a result the only parameters needed in this model are the bulk dielectric constant  $\epsilon$ , which represents the environment, and the molecular cavity in which the QM subsystem is embedded.

In the case of simple cavities (a sphere or an ellipse) and simplified representations of the density  $\rho$  in terms of a charge or a dipole, the solution of Poisson’s equation is analytical. This is the case in the Born [16] and Onsager [17] models of solvation. For realistic cavity shapes that follow the real geometrical structure of the QM subsystem and/or full descriptions of the

density in terms of the QM wavefunction, numerical methods are required to solve Poisson's equation.

A well-known approach is the generalized Born (GB) model, originally proposed in combination with a classical MM treatment of the subsystem of interest [18]. If we describe a solvated "molecule" as a set of charges  $q_1, \dots, q_N$ , the electrostatic solvation free energy, i.e., the difference in free energy between the isolated and the solvated molecule, is obtained as:

$$\Delta G^{\text{ele}} = \left(\frac{1}{\epsilon} - 1\right) \frac{1}{2} \sum_i^N \sum_{j \neq i} \frac{q_i q_j}{f_{\text{GB}}(r_{ij})}, \quad (12.8)$$

where  $f_{\text{GB}}(r_{ij})$  is a function that interpolates between an "effective Born radius" ( $R_i$ ) when the distance  $r_{ij}$  between atoms is short, and  $r_{ij}$  itself at large distances. The GB approach has been extended to QM descriptions by Cramer, Truhlar, and coworkers [2,19], by introducing an operator of the type:

$$\hat{H}^{\text{ele}}(\mathbf{r}_n) = \left(\frac{1}{\epsilon} - 1\right) \sum_{n'} \gamma_{nn'} q_{n'}, \quad (12.9)$$

where the indexes  $n$  and  $n'$  refer to atoms,  $\gamma_{nn'}$  is a Coulomb integral, and  $q_{n'}$  is a partial atomic charge. Note that Eq. (12.9) only defines  $\hat{H}^{\text{ele}}$  at the positions  $\mathbf{r}_n$  of the nuclei. However, those are the only locations where it is needed in the GB approximation. The resulting solvation model is known as SMx where the  $x$  indicates different versions of the prescriptions for atomic charges and radii [2,19].

The QM version of the GB approach, as well as the electrostatic formulation of QM/MM, can be used to describe the effect of the environment on the wavefunction of the QM subsystem and all the related electronic properties. In this way, the polarization of the QM charge distribution will be accounted for in addition to the electrostatic interaction. In both approaches, however, the polarization of the environment is only implicitly taken into account in the values of the point charges (QM/MM) and in the prefactor  $(1/\epsilon - 1)$  in the case of QM/GB. To go beyond this implicit formulation we need to introduce an explicitly polarizable description of the environment through a so-called "polarizable embedding" as described in the following section. For the sake of clarity, we shall assume that the QM subsystem is described through a self-consistent-field (SCF) approach either within the Hartree-Fock (HF) or the Kohn-Sham (KS) formulation of density functional theory (DFT). Extensions that go beyond this scheme will be presented and discussed in Section 12.4.

## 12.3 POLARIZABLE EMBEDDINGS

The coupling of a polarizable classical description of the environment with SCF-based methods, such as Hartree-Fock (HF) or Density Functional Theory (DFT), can be more effectively realized within a variational scheme. The global variational energy functional can be written as the sum of three terms: (i) a purely QM energy functional, i.e., the SCF energy functional of the QM subsystem, (ii) a purely classical term ( $\mathcal{E}^{\text{Class}}$ ), and (iii) a coupling term

( $\mathcal{E}^{\text{Coup}}$ ). If we introduce a representation of the molecular orbitals on a finite atomic basis set and we indicate with  $\mathbf{P}$  the electron density matrix of the QM subsystem on such a basis and with  $\mathbf{Q}$  the polarizable variables of the classical part, the variational energy functional becomes

$$\mathcal{E}(\mathbf{P}, \mathbf{Q}) = \mathcal{E}^{\text{QM}}(\mathbf{P}) + \mathcal{E}^{\text{Class}}(\mathbf{Q}) + \mathcal{E}^{\text{Coup}}(\mathbf{P}, \mathbf{Q}) = \mathcal{E}^{\text{QM}}(\mathbf{P}) + \mathcal{E}^{\text{Env}}(\mathbf{P}, \mathbf{Q}), \quad (12.10)$$

where in the right-hand side of the equation, coupling and classical energy functionals are merged in  $\mathcal{E}^{\text{Env}}$ .

Imposing the stationary conditions for the global functional in Eq. (12.10) gives the coupled QM/classical equations. In particular, a new (“effective”) Fock (or Kohn–Sham) matrix is obtained as the gradient of the global energy functional with respect to the density matrix, namely:

$$\mathbf{F}^{\text{eff}} = \frac{\partial \mathcal{E}(\mathbf{P}, \mathbf{Q})}{\partial \mathbf{P}} = \frac{\partial \mathcal{E}^{\text{QM}}(\mathbf{P})}{\partial \mathbf{P}} + \frac{\partial \mathcal{E}^{\text{Env}}(\mathbf{P}, \mathbf{Q})}{\partial \mathbf{P}} = \mathbf{F}^{(0)} + \mathbf{F}^{\text{Env}}, \quad (12.11)$$

where the term  $\mathbf{F}^{(0)}$  corresponds to the Fock matrix of the pure QM electronic problem, while  $\mathbf{F}^{\text{Env}}$  is the contribution to  $\mathbf{F}^{\text{eff}}$  from the classical environment.

By differentiating Eq. (12.10) with respect to  $\mathbf{Q}$  we obtain the equation that determines the response of the environment. The latter will be different for the different polarizable models. Below we focus on two specific cases: a continuum and a discrete description.

### 12.3.1 Continuum Embeddings: The Apparent Surface Charge Formulation

Within a continuum framework, the problem to solve is Poisson’s equation (Eq. (12.6)). One of the most effective ways to do that is to write the total potential  $\Phi^{\text{tot}}(\mathbf{r})$  as a sum of two terms: the electrostatic potential produced in vacuo by the QM charge density,  $\Phi^\rho$ , and a *reaction* potential  $W^\sigma$  due to the presence of the continuum. The latter can be then represented as the potential generated by an apparent surface charge (ASC) distribution,  $\sigma$ , on the boundary of the molecular cavity, the surface  $\Gamma$ . Namely, we have

$$\Phi^{\text{tot}}(\mathbf{r}) = \Phi^\rho(\mathbf{r}) + W^\sigma(\mathbf{r}) = \int_{\mathbb{R}^3} d\mathbf{r}' \frac{\rho(\mathbf{r}')}{|\mathbf{r} - \mathbf{r}'|} + \int_{\Gamma} ds \frac{\sigma(s)}{|\mathbf{r} - \mathbf{s}|}, \quad (12.12)$$

where the first integral is over the whole volume while the second is limited to the cavity surface. Different definitions are possible for  $\sigma(s)$  according to different formulations of the continuum model. It is worth mentioning that the most popular ones are the Conductor Solvation Model (COSMO) [20] and the Polarizable Continuum Model (PCM) [21]. In particular, PCM, originally developed by Miertus, Scrocco and Tomasi [22], has been reformulated many times. Nowadays, the two most popular versions are the IEF-PCM (Integral Equation Formalism PCM) [23], and the C-PCM (Conductor PCM) [24].

The alternative ASC formulations mainly differ in the way they define  $\sigma(s)$ . In all cases, however, the definition depends on the dielectric constant  $\epsilon$ , which describes the environment and some electrostatic properties of the QM subsystem (the electrostatic potential or the electric field) evaluated at the molecular surface. A general expression for the definition of  $\sigma(s)$  can be written as

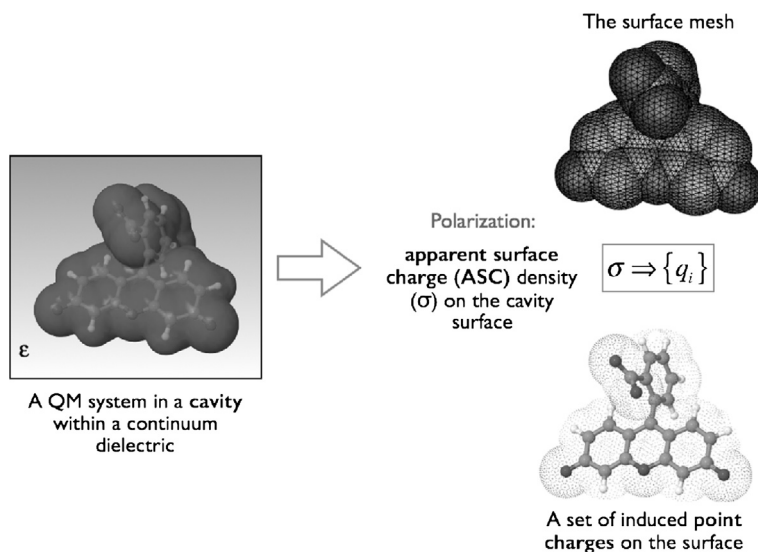


FIGURE 12.1 Graphical representation of the main steps involved in the numerical implementation of an ASC continuum model.

$$\mathcal{T}\sigma(s) = -\mathcal{R}\Phi^\rho(s), \quad (12.13)$$

where  $\mathcal{T}$  and  $\mathcal{R}$  are integral operators that depend on the shape of the cavity and  $\epsilon$ . Their exact definition depends on the specific ASC formulation. Due to its simpler form, we present here the COSMO expression

$$\begin{aligned} \mathcal{D}\sigma(s) = \mathcal{S}\sigma(s) &= \int_{\Gamma} \frac{\sigma(s')}{|s - s'|} ds', \\ \mathcal{R} &= f(\epsilon)\mathcal{I} = \frac{\epsilon - 1}{\epsilon + 0.5}\mathcal{I}, \end{aligned} \quad (12.14)$$

where  $\mathcal{I}$  is the identity operator.

All ASC continuum models, being based on the Poisson equation, assume that the solute's charge density is entirely supported inside the cavity. This is clearly not the case for a QM charge distribution. This limitation has been known since the very first QM formulations of continuum models and many numerical strategies have been proposed to correct the so-called “escaped charge” error. However, it is important to note that such an error is no longer an issue in modern formulations as their definition of  $\sigma$  also accounts for the electrostatic potential arising from the escaped charge [25,26].

In the numerical implementation of ASC models, a surface mesh is introduced such that the cavity surface is discretized into  $N$  elements of finite size (historically called “tesserae”) by introducing a surface mesh. As a result, the ASC distribution  $\sigma(s)$  is substituted by a set of point charges  $q(s_i)$  where  $s_i$  indicates the representative point of the surface element  $i$  (see Fig. 12.1).

Within this point-charge representation, the energy functional (Eq. (12.10)) becomes [27,28]

$$\mathcal{E}(\mathbf{P}, \mathbf{q}) = \mathcal{E}^{\text{QM}}(\mathbf{P}) + \frac{1}{2} \mathbf{q}^\dagger \mathbf{Y} \mathbf{q} + \mathbf{q}^\dagger \Phi^\rho, \quad (12.15)$$

where  $\mathbf{Y} = \mathbf{R}^{-1} \mathbf{T}$ , and  $\mathbf{T}$  and  $\mathbf{R}$  are the discretized form of the operators  $\mathcal{T}$  and  $\mathcal{R}$  defined in Eq. (12.13).  $\Phi^\rho$  is the vector that contains the electrostatic potential generated by the QM subsystem on the surface points  $s_i$ .

The minimum of this functional with respect to the charges ( $\mathbf{q}$ ) is obtained by setting its first derivative to zero, a condition that is equivalent to the solution of Eq. (12.13) after discretization. The effective Fock operator (Eq. (12.11)) becomes

$$\mathbf{F}^{\text{eff}} = \mathbf{F}^{(0)} + \mathbf{F}^{\text{Env}} = \mathbf{F}^{(0)} + \mathbf{q}^\dagger \mathbf{V}, \quad (12.16)$$

where  $\mathbf{V}$  is the matrix of the electrostatic potential integrals on the atomic basis set. Contrary to what we saw in the case of the GB formulation, the environment-induced term in this case ( $\mathbf{F}^{\text{Env}}$ ) depends on the electron density  $\mathbf{P}$  through the induced solvent charges  $\mathbf{q}$ . This is not a problem for SCF models, as an iterative procedure involving density dependent operators is employed by default, but it makes the coupling with post-SCF methods not straightforward, as will be shown in Section 12.4.

Eq. (12.16) is the main equation of the SCF implementation of continuum embeddings and it clearly shows that, by solving the resulting Fock (or Kohn–Sham) equations, new orbitals will be obtained that replace those of the isolated QM subsystem. These orbitals, when used to build the total wavefunction, will automatically include the effect of the polarization due to the environment. At the same time, the environment will be polarized by the QM subsystem and this polarization will be reflected in the final values of the induced surface charges  $\mathbf{q}$ .

### 12.3.2 Atomistic Embeddings: The Induced Dipole Formulation

To include mutual polarization within an atomistic formulation of hybrid QM/classical approaches, it is necessary to go beyond the electrostatic embedding presented above. Different alternative strategies have been proposed so far. Fixed point charges have been replaced by Drude oscillators [29], or by fluctuating charges [30,31], or have been supplemented with induced dipoles [32–41]. We shall focus on the induced dipole (ID) formulation. Within this framework, each polarizable MM site is characterized by a polarizability, which, in the most common formulations of the model, is approximated with the isotropic component,  $\alpha_i$ .

The QM subsystem and the static electrostatic component of the MM FF (in general represented by a multipolar charge distribution but more commonly by a set of point charges) generates an electric field at each polarizable MM site, which in turn induces an electric dipole moment at the same point. The set of all the  $N_{\text{Pol}}$  induced dipoles,  $\boldsymbol{\mu}$  is now the minimizer  $\mathcal{Q}$  of the functional in Eq. (12.10). If we focus on the polarizable part of  $\mathcal{E}^{\text{Env}}$  we have

$$\mathcal{E}^{\text{Pol}} = \frac{1}{2} \boldsymbol{\mu}^\dagger \mathbf{T}^{\text{dip}} \boldsymbol{\mu} - \boldsymbol{\mu}^\dagger \mathbf{F}, \quad (12.17)$$

where  $\mathbf{F}$  collects the electric field at each of the  $N_{\text{Pol}}$  polarizable sites. The symmetric matrix  $\mathbf{T}^{\text{dip}}$ , of  $3N_{\text{Pol}} \times 3N_{\text{Pol}}$  size, is defined as

$$\mathbf{T}^{\text{dip}} = \begin{pmatrix} \alpha_1^{-1} & \mathcal{T}_{12} & \dots & \mathcal{T}_{1N_{\text{Pol}}} \\ \mathcal{T}_{21} & \alpha_2^{-1} & \dots & \mathcal{T}_{2N_{\text{Pol}}} \\ \vdots & \vdots & \ddots & \vdots \\ \mathcal{T}_{N_{\text{Pol}}1} & \mathcal{T}_{N_{\text{Pol}}2} & \dots & \alpha_{N_{\text{Pol}}}^{-1} \end{pmatrix}, \quad (12.18)$$

where  $(\mathcal{T})_{ij}$  is a  $3 \times 3$  matrix defined as

$$\mathcal{T}_{ij}^{\beta\gamma} = -\frac{\delta_{\beta\gamma}}{r_{ij}^3} \lambda_3(r_{ij}) + 3 \frac{(\mathbf{r}_i - \mathbf{r}_j)_\beta (\mathbf{r}_i - \mathbf{r}_j)_\gamma}{r_{ij}^5} \lambda_5(r_{ij}), \quad (12.19)$$

with  $\beta$  and  $\gamma$  indicating Cartesian coordinates and  $\lambda_3$  and  $\lambda_5$  being distance-dependent damping functions. Under certain conditions, in fact, two induced dipoles at short distances can cause a ‘‘polarization catastrophe’’, due to the use of point polarizabilities instead of diffuse charge distributions (see Chapter 1 for more details). To avoid this problem, the 1–2 and 1–3 bonded polarization interactions are turned off and distance-dependent damping functions are introduced to screen the short-distance interactions [42,43].

As discussed above, it is possible to find the polarization energy as the minimum of  $\mathcal{E}^{\text{Pol}}$  with respect to the polarization variables  $\mathbf{Q}$ , which are now represented by the induced dipoles. This corresponds to the solution to the linear system

$$\frac{\partial \mathcal{E}^{\text{Pol}}}{\partial \boldsymbol{\mu}} = \mathbf{T}^{\text{dip}} \boldsymbol{\mu} - \mathbf{F} = 0. \quad (12.20)$$

Finally, to obtain the SCF equations, we have to define the proper effective Fock operator in the same way as we did in Eq. (12.16). For simplicity, let’s now limit the static multipolar distribution of the MM FF, to the monopole term (the atomic charges) as in the electrostatic embedding formulation reported in Eq. (12.4). Within this framework we get

$$\mathbf{F}^{\text{eff}} = \mathbf{F}^{(0)} + \mathbf{F}^{\text{env}} = \mathbf{F}^{(0)} + \mathbf{q}^\dagger \mathbf{V} - \boldsymbol{\mu}^\dagger \mathbf{F}_{\text{int}}, \quad (12.21)$$

where the matrices  $\mathbf{V}$ ,  $\mathbf{F}_{\text{int}}$  collect the electrostatic potential and the electric field integrals on the atomic basis calculated at each MM site. The introduction of induced dipoles requires the reparameterization of the static charges so to avoid double counting of the induction effects.

As for the continuum analog, the environment-induced term,  $\mathbf{F}^{\text{Env}}$  depends on the electron density matrix  $\mathbf{P}$ . However, in this case, the dependence is not through the charges  $\mathbf{q}$  which are fixed parameters but through the induced dipoles,  $\boldsymbol{\mu}$ . The simultaneous solution of Eqs. (12.20) and (12.21) completely determines mutual polarization effects between the QM and the classical subsystem.

---

## 12.4 BEYOND THE SCF ENERGY

---

Until now we have analyzed the problem of the simulation of an embedded system from a quite limited point of view, namely that of the system in its electronic ground state and

in equilibrium with its environment. In fact, the interest in simulating embedded systems is to predict their reactivity or their response to external perturbations such as applied electric and magnetic fields. In these cases, the models described so far have to be generalized to include nuclear motions within the QM subsystem and/or the coupling of the QM/classical interactions to external fields.

In a very general sense, environment effects on response properties of molecular systems can be described as “direct” or “indirect.” Direct effects are those due to the changes induced by the environment on the electronic charge distribution of the system. Indirect effects group all the modifications that affect the property under scrutiny indirectly, either by changing the geometry of the system or, when different conformational isomers are possible, by changing their relative energies thus affecting the Boltzmann populations.

The two polarizable embeddings we have described in the previous section are especially suited for investigating these environment effects. In fact, by acting directly on the wavefunction of the QM subsystem through the effective Hamiltonian, they can describe environment-induced changes in the electronic charge distribution and related properties. By being polarizable, they also allow the environment to respond. This is an important feature when simulating spectroscopic quantities and time-dependent processes. We present these generalizations in two parts, one focusing on processes that involve the ground electronic state only and the other on processes that involve electronic transitions.

### 12.4.1 Ground State Properties of Embedded Systems

The simulation of environment effects on ground state response properties, in particular those determining vibrational and magnetic spectroscopies, is a very important application of QM/classical approaches.

In particular, hybrid QM/continuum formulations have been largely used for simulating Infrared (IR) and Nuclear Magnetic Resonance (NMR) spectra of solvated (or embedded) molecular systems due to the fact that the computational strategy follows exactly the same path commonly used for isolated molecules. For example, the simulation of IR spectra is obtained by first optimizing the geometry of the solvated molecule and then calculating the vibrational frequencies and intensities at the equilibrium geometry in the harmonic approximation (HA). In the isolated molecule, frequencies are calculated as second derivatives of the energy with respect to the normal modes ( $\mathbf{Q}$ ) and intensities are given by the first derivative of the dipole moment, or equivalently as mixed second derivatives of the energy with respect to the nuclear displacements and the electric field  $\mathbf{F}$ :

$$A_p \propto \left( \frac{\partial \boldsymbol{\mu}}{\partial \mathbf{Q}_p} \right)^2 \propto \left( \frac{\partial^2 E}{\partial \mathbf{Q}_p \partial \mathbf{F}} \right)^2, \quad (12.22)$$

where the index  $p$  identifies a specific normal mode. The only difference between the solvated and the isolated molecule is that the energy includes the solute–solvent interactions.

While the theoretical formalism of calculating the energy derivatives in QM/continuum approaches is well defined [3], numerical difficulties are present. For example, the implementation of the ASC formulation of continuum models we described in Section 12.3.1 uses



a discretization of the cavity surface into elements. Discontinuities in the energy may appear when, due to a change in the solute geometry, the number of surface elements changes, or when two elements get unphysically close. As a consequence, geometry optimizations can become cumbersome or, in some cases, fail to converge. For the same reason, the coupling of these models with molecular dynamics simulations is not feasible as the energy is not always conserved. Numerical techniques that circumvent these problems are available [44–46], which provide a smooth energy as a function of the nuclear coordinates.

As an alternative to QM/continuum models, QM/MM models can be used to simulate IR spectra as well, although the analysis is more intricate. For example, in order to apply the HA, we have to be in a minimum of the potential energy surface but, generally, the environment configurations used in a QM/MM description do not correspond to a minimum. Instead, they are commonly obtained from molecular dynamics simulations. A possible strategy to recover the validity of the HA is to perform a partial optimization of the QM subsystem in a frozen configuration of the environment. Unfortunately, this optimization has to be repeated for each different configuration. As a result, the computational cost becomes very high. A much more suitable strategy to get vibrational spectra from a QM/MM description is by Fourier transform (FT) of proper time-dependent correlation functions. For example, the FT of the autocorrelation function of electric dipoles gives the IR spectrum

$$A(\omega) \propto \int_{-\infty}^{+\infty} \langle \mu(0) \cdot \mu(t) \rangle e^{-i\omega t} dt. \quad (12.23)$$

The correlation functions can be directly obtained performing a QM/MM dynamics or using a classical MD and extracting configurations from the resulting trajectory on which QM/MM calculations of the electric dipole are performed. In the first case, the computational cost is very high and generally only short time windows for small molecular systems are possible if the QM method used is accurate; longer trajectories and larger systems are feasible if using semiempirical QM methods. The use of a classical MD highly increments both the time window that can be explored and the size of the system that can be treated. However, the quality of the results strongly depends on the MM force field used in the classical MD. Moreover, thousands of QM/MM calculations have to be completed at the configurations obtained from the MD.

The application of QM/classical methods to magnetic spectroscopies presents additional challenges. For example, by definition, the nuclear magnetic shielding is a property which is significantly affected even by small changes in the local chemical environment of the selected nucleus. Therefore, it is also extremely sensitive to possible specific interactions between the nucleus of interest and the atoms in the environment. For example, significant effects occur when hydrogen bondings are present.

Not all nuclei are equally sensitive to the effects of the environment. In particular, carbon does not present a large sensitivity to the solvent while other nuclei, such as H, N or O, show important solvent-induced effects, especially when the selected nucleus is exposed to the solvent and it interacts with it through hydrogen bonds. In all these cases a purely QM/continuum approach is not sufficient and a QM/MM description has to be used. Sometimes, even this description is not sufficient, as the interactions can include some charge-transfer to the environment that, even if small, can affect magnetic properties. In this case, the “solvated

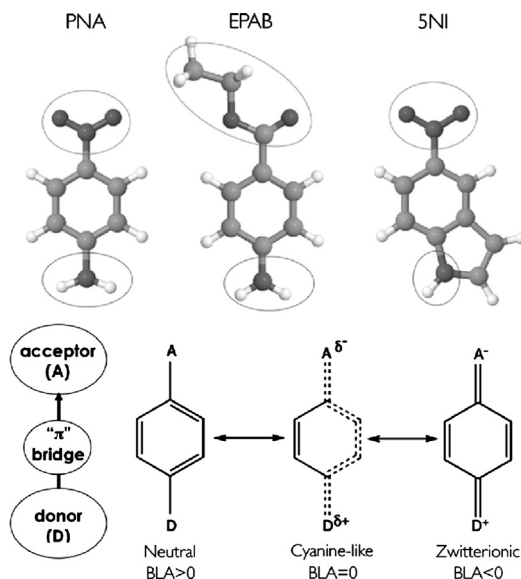


FIGURE 12.2 (Top) The three investigated push-pull systems. (Bottom) Limit structures of a typical push pull molecule, and dependence of BLA on the neutral/zwitterionic character.

supermolecule” approach is very effective. In this method, the definition of the QM subsystem is extended to a cluster including also some solvent molecules (those more strongly interacting with the nucleus of interest) and the longer-range effects are added either using a continuum or an averaged MM description.

To exemplify this analysis, we report a summary of a study [47] carried out on the NMR properties of three push-pull molecules characterized by a central conjugated system capped with donor and acceptor groups. The investigated probes are paranitroaniline (PNA), ethyl para-aminobenzoate (EPAB), and 5-nitroindole (5NI). These molecules present an aromatic ring para-substituted with a donor group ( $\text{NH}_2$  for PNA and EPAB,  $\text{NH}$  for 5NI) and an acceptor group ( $\text{NO}_2$  for PNA and 5NI,  $\text{COO}$  for EPAB), as shown in Fig. 12.2. DFT has been used for the description of both geometries and NMR properties, and solvent effects have been included in all calculations via the IEFPCM version of continuum models.

Push-pull molecules are generally represented in terms of resonance limit forms with a neutral and a zwitterionic character, respectively. By changing the relative strengths of the donor (D) and acceptor (A) groups and/or changing the polarity of the solvent, a significant change of the  $\pi$  electron structure is obtained with consequences on the geometry, as well. An effective way to quantify such changes is through the analysis of the structural index known as “bond length alternation” (BLA). The BLA is commonly defined as the difference in the average length of single and double bonds along the conjugated system. As shown in Fig. 12.2, if the system can be described mostly in terms of a neutral form, its BLA will be positive, while a form which charge separation will be characterized by a negative BLA (since the double and single bond pattern is now reversed relative to the neutral form). A BLA value equal to zero means that the system is completely delocalized (the term “cyanine-like” is also used).

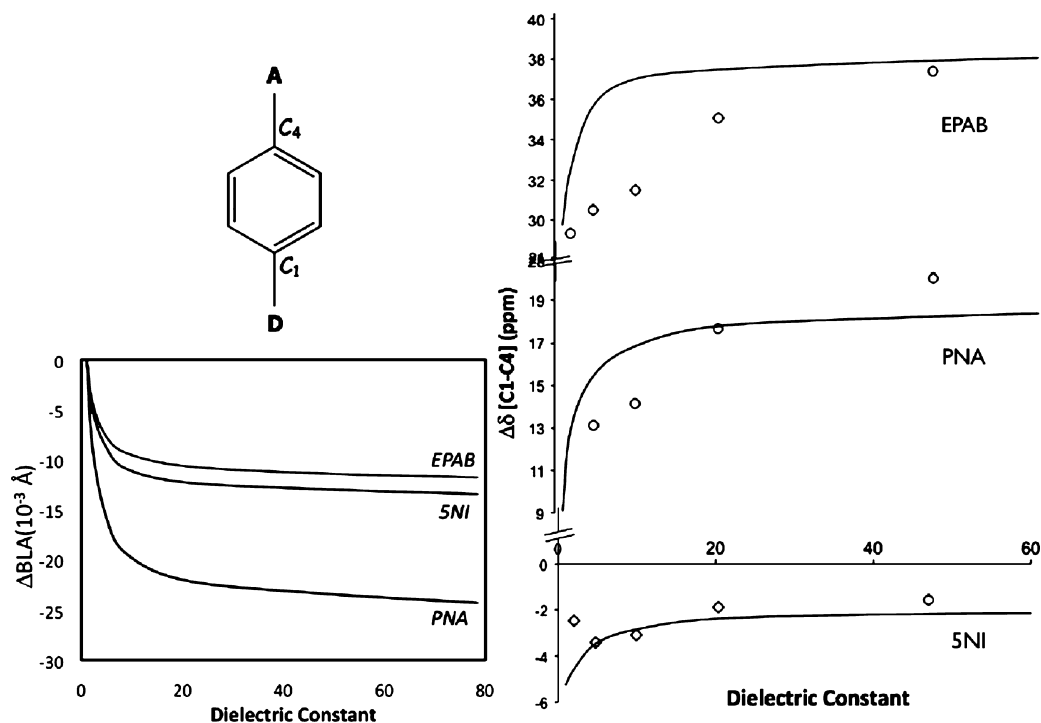


FIGURE 12.3 (Left)  $\Delta\text{BLA} = \text{BLA}(\text{sol}) - \text{BLA}(\text{vac}) (10^{-3} \text{ \AA})$  as a function of the solvent dielectric constant for PNA, EPAB, and 5NI systems. (Right) Comparison between trends of experimental and computed  $\Delta\delta[\text{C}_1\text{-C}_4]$  (in ppm) for the three probes as a function of the solvent dielectric constant. Empty circles refer to experimental data, whereas lines refer to MPW3PBE/IEFPCM calculations.

To quantify the effect of the solvent on the electronic charge distribution of the three push-pull systems, an NMR measurement of the chemical shift of the carbon atoms ( $\text{C}_1$  and  $\text{C}_4$ ) directly bonded to the donor and acceptor groups has been performed in solvents of increasing polarity. A parallel computational investigation has been performed at DFT/PCM level. Fig. 12.3 reports the comparison of measured and calculated  $\Delta\delta = \delta(\text{C}_1) - \delta(\text{C}_4)$  as a function of the dielectric constant of the solvent.

The  $\Delta\delta$  values are positive for EPAB and PNA, where  $\text{C}_1$  is more deshielded than  $\text{C}_4$ , and they increase with increasing polarity of the solvent, as  $\text{C}_1$  ( $\text{C}_4$ ) becomes more deshielded (shielded). The higher  $\Delta\delta$  values measured in EPAB can be related to the weaker acceptor character of the COOR group with respect to the nitro group present in PNA. Such a weaker electron attracting capacity makes the  $\text{C}_4$  more shielded than in PNA with a consequently larger  $\Delta\delta$  value. For 5NI, very small (and negative)  $\Delta\delta$  values are found in all solvents due to a very effective dispersion of the electronic charge on the entire indole group with consequent shielding of the  $\text{C}_1$  atom.

The measured trends of  $\Delta\delta$  are well reproduced by the calculations, both regarding solvent effects and the differences among the three compounds. The solvent effects on the electronic charge distribution causing the change in the chemical shifts can be quantified in terms of

changes in the BLA values. In Fig. 12.3 we report the calculated changes in BLA going from the isolated to the solvated molecule. For all three compounds in all solvents we found negative  $\Delta$ BLA values indicating that the presence of a solvent (even one of low polarity) enhances the charge flux from the donor to the acceptor group. As expected by the nature of the donor/acceptor groups, the overall variation of BLA is largest for PNA, and slightly larger in 5NI than in EPAB. This result supports the interpretation of the growing importance of the zwitterionic form (with respect to the neutral one) for representing the three probes in solvents with increasing dielectric constant.

The discrepancies between calculated and measured NMR properties may have different sources. For example, the model used to simulate the solvent is based on a continuum description where the solvent response is determined by its macroscopic dielectric constant, which is a bulk property: this picture cannot account for possible specific effects present in the first solvation shells. This is particularly true for water that can hydrogen-bond with both donor and acceptor groups. In addition, the same model includes only electrostatic effects, so any other solute–solvent interactions, such as possible dispersion effects, are completely neglected. Both effects are reflected in the shape of the calculated curves for which the increase is steeper and the saturation is reached faster than in experiment.

### 12.4.2 Electronic Transitions in Embedded Systems

QM/classical approaches allow the inclusion of environment effects not only on the ground state properties, but also on the electronic transitions. However, a new aspect has to be considered. During an electronic transition, we commonly assume that the geometry of the system does not change due to the ultrafast nature of the process, which happens on a femtosecond timescale. In the same way, we assume that the “slower” nuclear degrees of freedom of the environment will remain “frozen” in the configuration corresponding to the ground state of the system. Only the “fast” electronic degrees of freedom of the environment will respond. This generates a “nonequilibrium” regime, where only part of the environment is equilibrated with the excited QM subsystem. If the lifetime of the excited state is longer than the environment relaxation, the nonequilibrium regime will relax to a new state in which the environment is fully equilibrated.

The QM/classical models introduced above are able to describe the nonequilibrium regime, by differentiating between the “fast” and “slow” (also called “dynamical” and “inertial”) environment degrees of freedom [48,49]. In particular, in continuum descriptions of the environment, the different degrees of freedom can be accounted for by introducing a frequency-dependent dielectric function,  $\epsilon(\omega)$ . In most applications, however, a simplification can be introduced by assuming that all the degrees of freedom which are faster than the process of interest, are described by the optical dielectric constant  $\epsilon_\infty$  (which coincides with the square of the refractive index). Within this framework, we do not need to know  $\epsilon(\omega)$  at all frequencies, but only its extremes:  $\epsilon_\infty$  and its zero-frequency (static) counterpart,  $\epsilon_0$ . Applied to the ASC formulation of continuum models, the induced charges that represent the polarization of the environment will be split into a dynamic and an inertial component, each of them being characterized by a very different response time. In particular, only the dynamic induced charges will change during an electronic excitation and they will relax self-

consistently with the excited state charge distribution. On the contrary, the inertial charges will remain frozen at the values calculated for the initial (ground state) QM subsystem.

A similar description within a QM/MM polarizable embedding using induced dipoles can be obtained by minimizing the polarization energy (Eq. (12.20)) twice: once for the QM subsystem in the ground state and once for the excited state. In this framework, the inertial component of the environment is implicitly accounted for by the electrostatic embedding contribution due to the fixed MM charges which do not move nor change their magnitude during the excitation process.

The same nonequilibrium scheme can be also applied to the reverse process, namely the emission from an excited state to the ground state. The only difference is that the inertial component of the response has to be calculated for the excited state (which is assumed to have relaxed and reached equilibrium with the environment before emitting), while the dynamic component refers to the vertical ground state. This is rather easy to do within a continuum formulation. The geometry of the relaxed excited state is calculated exactly as one should do for an isolated molecule, and the inertial and dynamic induced charges are obtained self-consistently with the wavefunction from the effective Hamiltonian of the excited and ground state, respectively.

The same extension within MM polarizable embeddings is not as straightforward. In addition to knowing the excited state geometry, the corresponding relaxed configuration of the environment is also required. Because in most QM/MM approaches the configuration of the environment is obtained from classical MD, and force fields are commonly available for ground-state molecules only, this method is not practicable. A possible way to proceed is to perform a classical MD where the “solute” is kept frozen (in its internal degrees of freedom) at the excited state geometry obtained with a QM/continuum formulation, and its electrostatic parameters (i.e., the atomic charges) are determined at the excited state charge distribution. The Lennard-Jones parameters are instead assumed not to change significantly in the excited state. From such an MD, new configurations of the environment will be obtained and they will be used for the subsequent QM/MM calculations of the emission energy.

Up to this point, we have focused on the electrostatic plus induction (or polarization) effects. However, it is known that other noncovalent interactions can affect transition processes as well. For example, dispersion interactions can be different for the ground and the excited states of the QM subsystem. As a result, an additional shift in the excitation energy can be induced. In 1950, Bayliss proposed the first continuum model to explain the dispersion shift in nonpolar solvents, which was related to the oscillator strength of the transition and to the square of the refractive index [50]. Another approach within a QM description involves calculating dispersion effects on the excitation energies as the difference in the dispersion stabilization energy from ground to excited state obtained using a semiempirical configuration interaction treatment of both solute and solvent molecules [51]. In more recent years, the interest in the modeling of dispersion effects on solvatochromic shifts has grown further, and progress has been made [52–54].

To investigate this aspect, we introduce a simplified continuum model which is reminiscent of the Onsager model for solute–solvent interactions, namely a dipolar solute in a spherical cavity. Within such a model the response of the solvent is described by a reaction

field that is proportional to the solute dipole moment where the proportionality factor is

$$f = \frac{1}{a^3} \frac{2(\epsilon - 1)}{2\epsilon + 1}, \quad (12.24)$$

where  $a$  is the radius of the spherical cavity. If now we apply the nonequilibrium model described before and we assume that during the electronic transition only the dynamic component of this reaction field will change, the excitation energy can be written as

$$\begin{aligned} \Delta E &= \Delta E_0 - \frac{1}{2} f_d |\boldsymbol{\mu}_{\text{GS}} - \boldsymbol{\mu}_{\text{exc}}|^2 - f_d |\boldsymbol{\mu}^T|^2 - \frac{1}{2\pi} \int_0^\infty d\omega f(i\omega) (\alpha_{\text{exc}}(i\omega) - \alpha_{\text{GS}}(i\omega)) \\ &= \Delta E_0 + \Delta E_{\text{Pol}} + \Delta E_{\text{Res}} + \Delta E_{\text{dis}}, \end{aligned} \quad (12.25)$$

where  $f_d$  is nonequilibrium form of Eq. (12.24) obtained by substituting  $\epsilon$  with its optical counterpart,  $\epsilon_\infty$ .  $\alpha_{\text{GS}}(i\omega)$  and  $\alpha_{\text{exc}}(i\omega)$  represent the polarizabilities of the solute in its ground and excited states, respectively, calculated at the imaginary frequency  $i\omega$ . In the same equation,  $\boldsymbol{\mu}_{\text{GS}}$  are the ground and excited-state electric dipoles of the solute, and  $\boldsymbol{\mu}^T$  is the transition dipole moment.

The term  $\Delta E_0$  represents the excitation energy in a solvent (both its dynamic and inertial responses) frozen in the ground-state configuration whereas  $\Delta E_{\text{Pol}}$ , which is proportional to the square of the dipole difference, accounts for the dynamic response of the solvent to the change of the electron density of the QM system upon excitation, which is the term discussed above. The  $\Delta E_{\text{Res}}$  term depends on the transition density between ground and excited state (in a dipolar approximation, the transition dipole) and it can be seen as an inductive resonance between the solute excitation and the solvent dynamic response [51,55,56]. The last term,  $\Delta E_{\text{dis}}$ , is the difference in dispersion energies of ground and excited states.

In polar solvents,  $\Delta E_0$  dominates because it is the only term that is determined by the full response of the solvent (including the inertial response). Among the other terms, the  $\Delta E_{\text{Pol}}$  term is expected to be rather small if not negligible when the excitation does not lead to a significant change in the electron density. A similar behavior is expected for the dispersion term. On the contrary, the “resonance” term is expected to be important for allowed excitations where the transition dipole is large.

Finally, we note that the analysis reported in Eq. (12.25) for the absorption process can be repeated for emission with the only difference that the initial state is now the excited state fully equilibrated with the solvent.

To give an example of the accuracy of QM/classical models in describing absorption and emission processes, we report a summary of a study performed by Jacquemin and coworkers [57], on the prediction of the 0–0 energy ( $E^{0-0}$ ) for a set of 40 solvated molecules (see Fig. 12.4).

The 0–0 energy is the difference between the ground (GS) and excited state (ES) energies obtained at their respective equilibrium geometries ( $E^{\text{adia}}$ ) and corrected for the difference in zero-point vibrational energy (ZPVE):

$$\begin{aligned} E^{0-0} &= E^{\text{adia}} - \Delta E^{\text{ZPVE}}, \\ E^{\text{adia}} &= E^{\text{vert-f}} + E^{\text{vert-a}} - E^{\text{adia}} + E^{\text{reorg-GS}} - E^{\text{reorg-ES}}, \\ \Delta E^{\text{ZPVE}} &= E^{\text{ZPVE}}(R^{\text{GS}}) - E^{\text{ZPVE}}(R^{\text{ES}}), \end{aligned} \quad (12.26)$$

where all the energetic terms used are shown in Fig. 12.5.

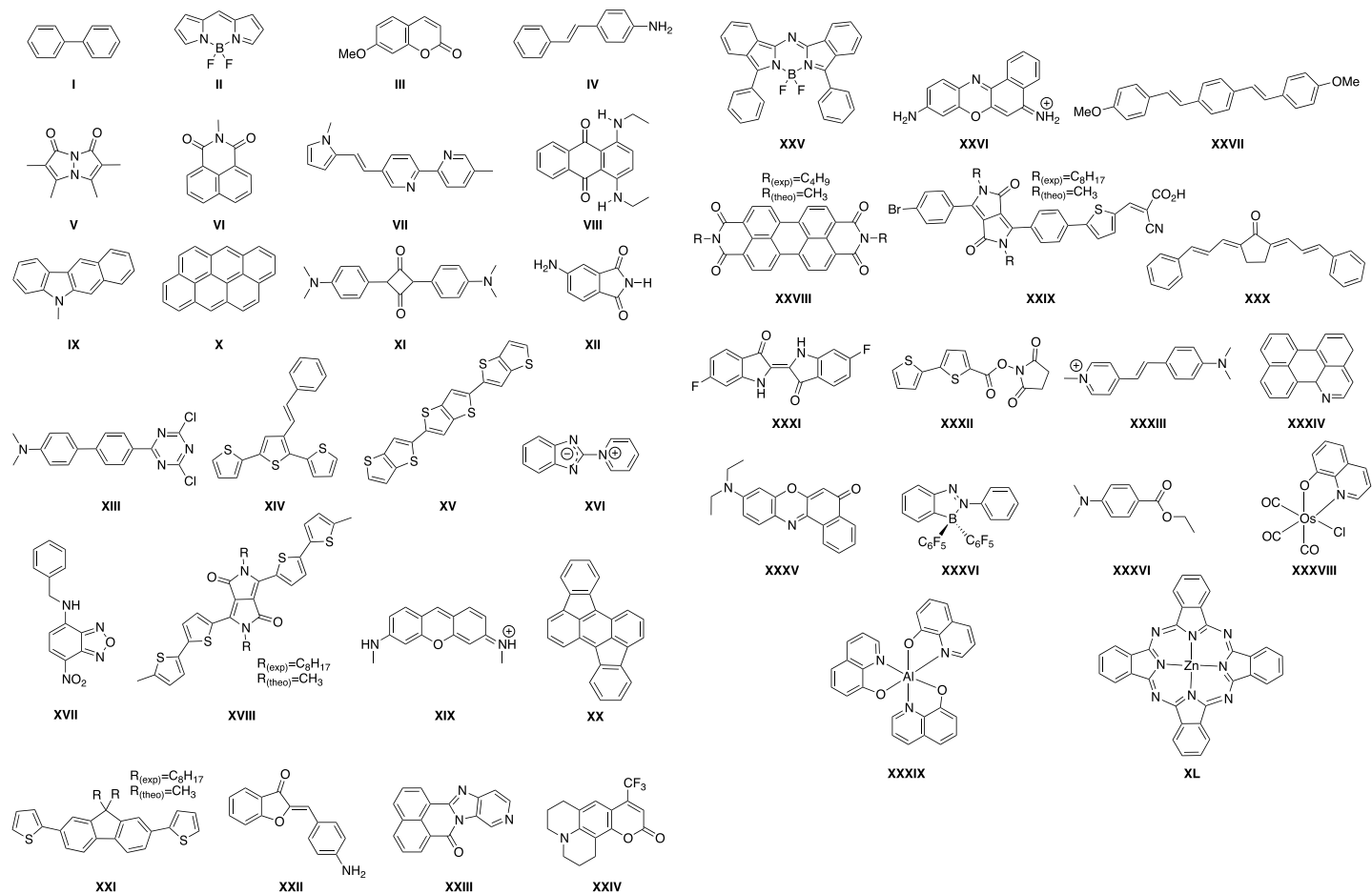
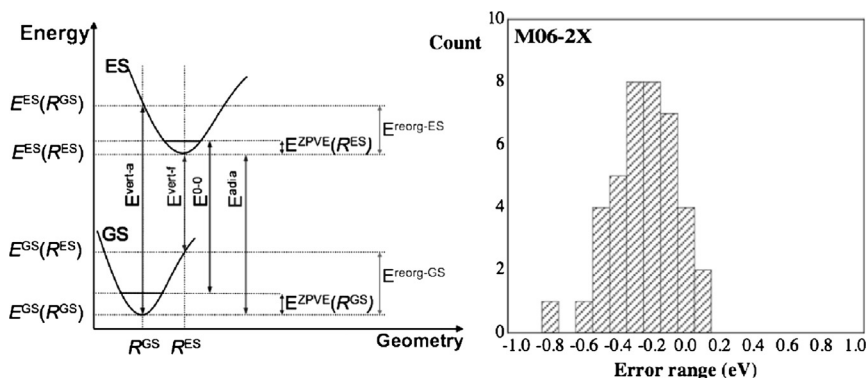


FIGURE 12.4 The set of 40 molecules for which the 0-0 energy has been investigated at TDDFT/IEFPCM level.



**FIGURE 12.5** (Left) Graphical representation of the different energy components defining the 0–0 energy,  $E^{0-0}$ . (Right) Histograms of the errors (in eV) computed between the calculated and the experimental  $E^{0-0}$  for the 40 investigated molecules.

As shown by Eq. (12.26), the evaluation of  $E^{0-0}$  requires the equilibrium geometry of both the ground and the excited state together with the corresponding Hessian to get the ZPVE corrections of each state. The geometry optimizations of both the ground and excited state of a set of forty molecules (Fig. 12.4) was performed within the DFT framework and its extension to excited state (Time-Dependent DFT) using the M06-2X functional [58] and the 6-31+G(d) basis set.

The GS and ES vibrational frequencies were computed using analytical and numerical derivatives, respectively. Besides obtaining the ZPVE, these vibrational calculations were used to ascertain that both the GS and ES geometries are true minima of their respective potential energy surfaces. In all calculations, solvent effects were included via the continuum (IEFPCM) model and considering, when needed, the nonequilibrium regime discussed before. Dispersion interactions with the solvent were neglected.

Fig. 12.5 shows the main results of the study in terms of a statistical analysis of the error with respect to experiments. The TDDFT/continuum description shows a good agreement with experiments, except for a few outliers presenting large errors. Errors below 0.3 eV in  $E^{0-0}$  are well within the standard error of TDDFT calculations for isolated systems.

This example shows that hybrid QM/continuum approaches are well suited to describe absorption and emission process of solvated molecules. Clearly, it is expected that such a type of model will be less accurate when the environment becomes less homogeneous. In particular, it is known that the changes induced by the environment on both the absorption and emission frequencies of pigments embedded in a protein matrix are poorly described by a continuum-only approach. The specific interactions that different residues (some of them charged) have with the embedded chromophore cannot be accounted for with the homogeneous description given by a continuum dielectric. In those cases, different strategies can be used. The most complete approach is to use a fully atomistic description of the protein (and eventually the external solvent) using an MM FF. However, a polarizable embedding is also necessary in order to correctly reproduce the response of the residues to the excitation. Alternatively, one could opt for a simpler description by including within the QM subsystem those



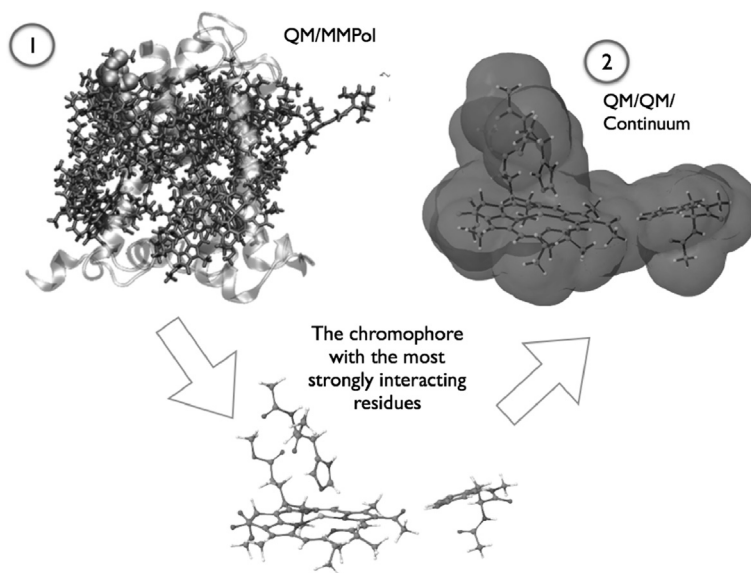


**FIGURE 12.6** Example of an embedded pigment: a chlorophyll molecule within the protein matrix. (Top) Two possible models to account for the environment effect. (1) An atomistic approach where the pigment is treated at QM level and the whole protein is treated at MMPol level and (2) a mixed atomistic–continuum approach, in which the QM subsystem is enlarged to include the strongly interacting residues and the longer-range effects are included using a continuum. (Bottom) The protein residues that interact more strongly with the pigments.

residues that interact with the system more strongly and accounting for the longer-range effects of the rest of the protein via a continuum description [59]. An example of these possible strategies is shown in Fig. 12.6 for the most common pigment found in the light-harvesting pigment–protein complexes of photosynthetic organisms.

## 12.5 OUTLOOK

---

Solvated or embedded molecular systems are a perfect example of the fundamental role that noncovalent interactions have in determining the world as we know it. The way through which the environment influences the behavior of a molecule is at the heart of many of the processes of interest in chemistry, physics, and biology. In this chapter we have presented an overview of the most popular models used for describing such changes. In particular, we have focused on hybrid QM/classical models, although other promising strategies are now emerging. In particular, it is worth mentioning the fragment or subsystem approaches that introduce QM/QM embedding schemes [60–63]. These approaches aim to go beyond hybrid QM/classical formulations by introducing embedding effects calculated at QM level thus allowing a more correct inclusion of exchange and Pauli repulsion. Unfortunately, the formal difficulties involved in their theoretical formulation and the computational cost still

prevent their use at a large scale. QM/classical approaches instead are characterized by a reduced computational cost and a large versatility and ease of implementation. Thus, we are confident that they will last for a long time as one of the most powerful strategies to account for environment effects.

## References

- [1] J. Tomasi, M. Persico, *Chem. Rev.* 94 (1994) 2027–2094.
- [2] C. Cramer, D. Truhlar, *Chem. Rev.* 99 (1999) 2161–2200.
- [3] J. Tomasi, B. Mennucci, R. Cammi, *Chem. Rev.* 105 (2005) 2999–3093.
- [4] M.J. Field, P.A. Bash, M. Karplus, *J. Comput. Chem.* 11 (1990) 700–733.
- [5] J. Gao, *Acc. Chem. Res.* 29 (1996) 298–305.
- [6] H. Lin, D.G. Truhlar, *Theor. Chem. Acc.* 117 (2006) 185–199.
- [7] H.M. Senn, W. Thiel, *Angew. Chem. Int. Ed.* 48 (2009) 1198–1229.
- [8] A. Monari, J.-L. Rivail, X. Assfeld, *Acc. Chem. Res.* 46 (2013) 596–603.
- [9] F.M. Floris, J. Tomasi, J.L.P. Auhir, *J. Comput. Chem.* 12 (1991) 784–791.
- [10] I. Soteras, C. Curutchet, A. Bidon-Chanal, M. Orozco, F.J. Luque, *J. Mol. Struct. THEOCHEM* 727 (2005) 29–40.
- [11] C. Amovilli, B. Mennucci, *J. Phys. Chem. B* 101 (1997) 1051–1057.
- [12] D.A. Scherlis, J.-L. Fattebert, F. Gygi, M. Cococcioni, N. Marzari, *J. Chem. Phys.* 124 (2006) 074103.
- [13] A. Pomogaeva, D.M. Chipman, *J. Phys. Chem. A* 117 (2013) 5812–5820.
- [14] B.H. Besler, K.M. Merz, P.A. Kollman, *J. Comput. Chem.* 11 (1990) 431–439.
- [15] L.W. Chung, W.M.C. Sameera, R. Ramezani, A.J. Page, M. Hatanaka, G.P. Petrova, T.V. Harris, X. Li, Z. Ke, F. Liu, H.-B. Li, L. Ding, K. Morokuma, *Chem. Rev.* 115 (2015) 5678–5796.
- [16] M. Born, *Z. Phys.* 1 (1920) 45–48.
- [17] L. Onsager, *J. Am. Chem. Soc.* 58 (1936) 1486–1493.
- [18] D. Bashford, D.A. Case, *Annu. Rev. Phys. Chem.* 51 (2000) 129–152.
- [19] C.J. Cramer, D.G. Truhlar, *Science* 256 (1992) 213–217.
- [20] A. Klamt, *WIREs Comput. Mol. Sci.* 1 (2011) 699–709.
- [21] B. Mennucci, *WIREs Comput. Mol. Sci.* 2 (2012) 386–404.
- [22] S. Miertus, E. Scrocco, J. Tomasi, *Chem. Phys.* 55 (1981) 117–129.
- [23] E. Cancès, B. Mennucci, J. Tomasi, *J. Chem. Phys.* 107 (1997) 3032–3041.
- [24] V. Barone, M. Cossi, *J. Phys. Chem. A* 102 (1998) 1995–2001.
- [25] D.M. Chipman, *J. Chem. Phys.* 112 (2000) 5558.
- [26] E. Cancès, B. Mennucci, *J. Chem. Phys.* 115 (2001) 6130–6135.
- [27] F. Lipparini, G. Scalmani, B. Mennucci, E. Cancès, M. Caricato, M.J. Frisch, *J. Chem. Phys.* 133 (2010) 014106.
- [28] F. Lipparini, G. Scalmani, B. Mennucci, M.J. Frisch, *J. Chem. Theory Comput.* 7 (2011) 610–617.
- [29] E. Boulanger, W. Thiel, *J. Chem. Theory Comput.* 8 (2012) 4527–4538.
- [30] R.A. Bryce, R. Buesnel, I.H. Hillier, N.A. Burton, *Chem. Phys. Lett.* 279 (1997) 367–371.
- [31] F. Lipparini, V. Barone, *J. Chem. Theory Comput.* 7 (2011) 3711–3724.
- [32] M.A. Thompson, G.K. Schenter, *J. Phys. Chem.* 99 (1995) 6374–6386.
- [33] M.S. Gordon, M.A. Freitag, P. Bandyopadhyay, J.H. Jensen, V. Kairys, W.J. Stevens, *J. Phys. Chem. A* 105 (2001) 293–307.
- [34] L. Jensen, P.T. van Duijnen, J.G. Snijders, *J. Chem. Phys.* 119 (2003) 3800–3809.
- [35] C.B. Nielsen, O. Christiansen, K.V. Mikkelsen, J. Kongsted, *J. Chem. Phys.* 126 (2007) 154112.
- [36] C.J.R. Illingworth, K.E.B. Parkes, C.R. Snell, G.G. Ferenczy, C.A. Reynolds, *J. Phys. Chem. A* 112 (2008) 12151–12156.
- [37] C. Curutchet, A. Muñoz-Losa, S. Monti, J. Kongsted, G.D. Scholes, B. Mennucci, *J. Chem. Theory Comput.* 5 (2009) 1838–1848.
- [38] D. Si, H. Li, *J. Chem. Phys.* 133 (2010) 144112.
- [39] A.H. Steindal, K. Ruud, L. Frediani, K. Aidas, J. Kongsted, *J. Phys. Chem. B* 115 (2011) 3027–3037.
- [40] Q. Zeng, W. Liang, *J. Chem. Phys.* 143 (2015) 134104.

- [41] J.W. Ponder, C. Wu, P. Ren, V.S. Pande, J.D. Chodera, M.J. Schnieders, I. Haque, D.L. Mobley, D.S. Lambrecht, R.A. DiStasio Jr., M. Head-Gordon, G.N.I. Clark, M.E. Johnson, T. Head-Gordon, *J. Phys. Chem. B* 114 (2010) 2549–2564.
- [42] B.T. Thole, *Chem. Phys.* 59 (1981) 341–350.
- [43] P.T. van Duijnen, M. Swart, *J. Phys. Chem. A* 102 (1998) 2399–2407.
- [44] D. York, M. Karplus, *J. Phys. Chem. A* 103 (1999) 11060–11079.
- [45] G. Scalmani, M.J. Frisch, *J. Chem. Phys.* 132 (2010) 114110.
- [46] A.W. Lange, J.M. Herbert, *J. Phys. Chem. Lett.* 1 (2010) 556–561.
- [47] A. Marini, S. Macchi, S. Jurinovich, D. Catalano, B. Mennucci, *J. Phys. Chem. A* 115 (2011) 10035–10044.
- [48] H.J. Kim, J.T. Hynes, *J. Chem. Phys.* 93 (1990) 5194–5210.
- [49] M.M. Karelson, M.C. Zerner, *J. Phys. Chem.* 96 (1992) 6949–6957.
- [50] N. Bayliss, *J. Chem. Phys.* 18 (1950) 292–296.
- [51] N. Roesch, M. Zerner, *J. Phys. Chem.* (1994) 5817–5823.
- [52] T. Renger, B. Grundkötter, M.E.-A. Madjet, F. Müh, *Proc. Natl. Acad. Sci. USA* 105 (2008) 13235–13240.
- [53] A.V. Marenich, C.J. Cramer, D.G. Truhlar, *J. Chem. Theory Comput.* (2013) 3649–3659.
- [54] L. Cupellini, C. Amovilli, B. Mennucci, *J. Phys. Chem. B* 119 (2015) 8984–8991.
- [55] S. Corni, R. Cammi, B. Mennucci, J. Tomasi, *J. Chem. Phys.* 123 (2005) 134512.
- [56] C. Zhu, A. Dalgarno, S. Porsev, A. Derevianko, *Phys. Rev. A* 70 (2004) 032722.
- [57] D. Jacquemin, A. Planchat, C. Adamo, B. Mennucci, *J. Chem. Theory Comput.* 8 (2012) 2359–2372.
- [58] Y. Zhao, D.G. Truhlar, *Acc. Chem. Res.* 41 (2008) 157–167.
- [59] S. Jurinovich, L. Viani, I.G. Prandi, T. Renger, B. Mennucci, *Phys. Chem. Chem. Phys.* 17 (2015) 14405–14416.
- [60] M.S. Gordon, D.G. Fedorov, S.R. Pruitt, L.V. Slipchenko, *Chem. Rev.* 112 (2012) 632–672.
- [61] C.R. Jacob, J. Neugebauer, *WIREs Comput. Mol. Sci.* 4 (2014) 325–362.
- [62] F. Libisch, C. Huang, E.A. Carter, *Acc. Chem. Res.* 47 (2014) 2768–2775.
- [63] T.A. Wesolowski, S. Shedje, X. Zhou, *Chem. Rev.* 115 (2015) 5891–5928.

# Surface Adsorption

---

Jeffrey R. Reimers<sup>\*,†</sup>, Musen Li<sup>\*</sup>, Dongya Wan<sup>\*</sup>, Tim Gould<sup>‡</sup>,  
Michael J. Ford<sup>†</sup>

<sup>\*</sup>International Centre for Quantum and Molecular Structure, College of Sciences,  
Shanghai University, Shanghai, China <sup>†</sup>School of Mathematical and Physical Sciences,  
University of Technology Sydney, Sydney, Australia <sup>‡</sup>Queensland Micro- and  
Nanotechnology Centre, Griffith University, Nathan, Australia

## 13.1 INTRODUCTION

---

The adsorption of molecules onto surfaces is critical to many fields including catalysis, surface corrosion, surface protection, nanoparticle formation and use, semiconductor device manufacture, 2D material structural support and property modification, medical diagnostic, treatment, and prosthetic technologies, etc. It also provides relatively simple ways to address complex 3D issues such as protein folding and polymer structure. In April 2016, SCOPUS<sup>®</sup> indicates over 2000 publications concerning van der Waals forces and surface adsorption. Many of these involve experimental studies supported by model calculations exposing the importance of attractive van der Waals dispersion forces, e.g., in regard to the properties of soils [1], the removal of pesticides from water supplies [2], the protection of wood surfaces [3], the removal of chemical waste products from soils [4], and in the design of drug delivery systems [5], to list just a few. The time is coming when all sorts of applications of this type will yield to atomistic *a priori* electronic structure calculations, and this chapter provides insight into some *ab initio* and density-functional theory (DFT) computational methods now available, as well as those still needed.

Using empirical molecular mechanics force fields, atomistic calculations involving van der Waals forces have been performed for over 40 years now for simulations in chemistry, biochemistry, and materials science. Modern applications often cross these disciplines, e.g., the recent study of cytochrome c on Au(111) [6], a field of great interest in the biosensor community. Force-field methods almost always represent the dispersion contributions to the van der Waals force using pairwise additive London terms obtained by summing interatomic interactions, though more apt variants for surface adsorption phenomena are also well established [7]. They involve parameters which are usually either fitted to experimental data and/or fitted to data coming from high-level calculations on model systems. As force fields

are very computationally inexpensive, they can be applied to study dynamical properties of systems on very long time scales, allowing kinetic control mechanisms to be directly studied. However, their accuracy will always be limited by the appropriateness of the force field parameters to the current circumstance, something that is not always easy to determine. Simulation methods based on solving the electronic structure problem in order to determine intermolecular interactions offer the benefit of increased accuracy and more general applicability but at the cost of vastly increased computer requirements and simulation times. In recent years, the critical role of dispersion interactions in relation to carbon nanotubes interfaces [8], graphene interfaces [9,10], silicon interfaces [11], intermaterial junctions [12], gas-metal scattering [13], and catalysis [14,15] has been demonstrated. Development of computational methods capable of treating systems containing tens of thousands of atoms [16, 17] that can model current-generation silicon transistors more accurately than they can be empirically modeled [18], as well as linear scaling approximations that have been applied to 150,000 atom proteins [19], indicate a promising future for this field.

The most common *a priori* method used to model chemical, materials, and biochemical systems has been DFT using either the generalized-gradient approximation (GGA) or else some hybrid functional containing also a component of the exact exchange operator. While these treatments usually ignore dispersion interactions, in almost all cases, there is no doubt that these do contribute significantly to the process. In the future, the routine inclusion of dispersion will be essential in any calculation attempting to get the right answer for the right reason.

To understand the nature and impact of dispersion in a holistic way, a classification of the general types of expected effects is required. Section 13.2 overviews the classification scheme of Dobson [20] and its impact on understanding the limitations of the London approach to calculating dispersion energies between molecules or materials separated by very large distances. Section 13.3 then overviews modern computational methods in this context, demonstrating that most practical methods unfortunately depict incorrect asymptotic forms of the dispersion interaction. However, typical applications do not involve large-distance interactions but rather the interactions at van der Waals contact distances for which these methods can apparently perform well [21–38]. As the various contributions to the dispersion force are universal rather than being applicable on only certain length scales, these facts present a conundrum. The remaining sections investigate this by examining some iconic example systems. In addition, a central focus for these systems is consideration of how neglect of dispersion interactions in standard DFT leads to not just inaccurate predictions of physisorption binding energies but also to fundamentally incorrect understanding of key chemical processes. In addition, it is also shown how inclusion of dispersion can lead to quantitative predictions of free energies of formation and polymorphism of self-assembled monolayer (SAM) formation, which provides a basic understanding of the controlling chemical and thermodynamic features. These issues discussed in the context of surface adsorption parallel exciting new fields in small-molecule chemistry and catalysis research, with dispersion forces being demonstrated to facilitate unexpectedly strong bonds [39–47] and unexpected chemical processes [45,48–52].

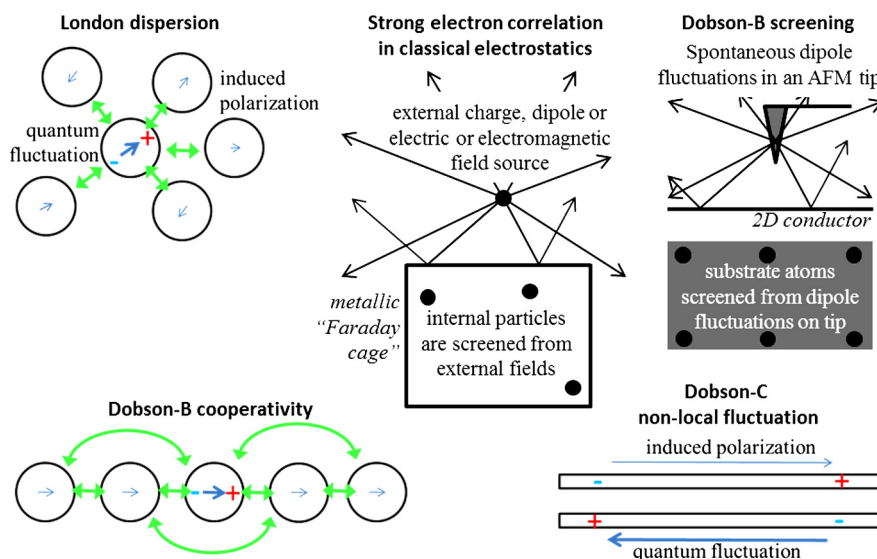


FIGURE 13.1 The London dispersion term (possibly including Dobson-A corrections) is contrasted to Dobson-B and Dobson-C contributions. The Dobson-B corrections parallel profound strong electron correlation effects in classical electrostatics like Gauss' law and Faraday cages, with, e.g., experimentally demonstrated screening effects between AFM tip and substrate that reduce the dispersion force by two orders of magnitude [53].

## 13.2 DOBSON'S CLASSIFICATION SCHEME FOR DISPERSION ENERGY COMPONENTS AND THEIR APPLICATION TO ASYMPTOTIC SCALING LAWS FOR SOME PARADIGMATIC SITUATIONS

The London dispersion expression assumes that local quantum dipole fluctuations on each atom occur as demanded by Heisenberg's uncertainty principle, and that these generate attractive polarization responses from all surrounding atoms. This process is illustrated in Fig. 13.1. Key contributions to the dispersion energy have been classified by Dobson [20]. Initially, all quantum fluctuations and polarization responses are taken to occur locally on atoms and to occur independently of each other. These assumptions lead to the London dispersion force in which all interatomic interactions scale as  $R^{-6}$  for large enough  $R$  that dipolar fluctuations dominate, where  $R$  is the interatomic separation, with the total London energy arising from pairwise sums over all atoms in each molecule (see Chapter 1). At the simplest level, Dobson includes the additional assumption that all atoms of an element are regarded as being the same independent of chemical environment. He then defines three corrections to this reference treatment:

**Dobson-A:** this correction allows atoms to be chemically distinguishable and so different London parameters are required for each atom depending on environment. The form or type

of included interaction does not change so no new sketch is given in Fig. 13.1. Almost all approaches to modeling dispersion include these effects.

**Dobson-B:** these allow for many-body effects in which all responding polarizability centers interact with *each other* as well as with the original quantum dipole fluctuation. The requirement of quantum fluctuations makes dispersion an intrinsically quantum effect, but, once the fluctuations are generated, the response is in essence one of *classical electrostatics*. While there is no quantum equivalent of Gauss' law, the basic principle still applies [54] and indicates that the electrostatic interactions will be *screened* by electrical conductors and other electrically polarizable bodies present in the system. How this happens is depicted in Fig. 13.1. Gauss' law depicts the effects of very strong electron correlation and indicates that many-body effects in a conductor prevent the penetration of external electric fields. This occurs *independent* of the nature of the source of the electric field, the field from a quantum fluctuation dipole suffering the same fate as the field from, e.g., permanent charges or applied radiation. Consequentially, dispersion forces can be orders of magnitude less than naively expected. Indeed, this has been demonstrated experimentally by measuring the dispersion force between an STM tip and its substrate through intermediary insulating (fluorographene) or conducting (graphene) 2D materials (see Fig. 13.1) [53]. On the other hand, as Fig. 13.1 also shows, many-body effects can bring about significant enhancement of polarization (and hence the dispersive interaction) when induced dipoles act to induce parallel dipoles on neighboring molecules, an example of a Dobson-B many-body effect known as *cooperativity*. Many instances are now being found where Dobson-B effects have profound influence on surface adsorption and on surface attraction. Silicon dioxide nanoparticles have been shown to attract each other in a complex way not describable by either  $R^{-6}$  descriptions or these plus just three-body terms [55]. This type of interaction is of great relevance in nanotechnology and in colloid science and is the type of problem that modern computational methods need to be addressing. It is not confined to large nanoparticles but has also been found for interacting fullerenes [56] as well as nanotubes, graphene and its fragments, and certain kinds of molecular crystals [23–26,30,57]. It is even important for understanding properties of ice clusters [58,59]. It is typically most pronounced in systems which have at least one “small” and one “large” spatial dimension.

**Dobson-C:** these many-body effects allow the quantum fluctuation in metals to become long-ranged rather than to reside locally on atoms. They occur in systems with zero energy gap in each well-separated component. The range allowed is of the order of the femtosecond-timescale quantum fluctuation duration multiplied by the Fermi velocity of the metal and can possibly extend to hundreds of nanometers. Hence the charge fluctuation can extend over distances larger than inter-object distances and, as Fig. 13.1 shows, this converts the dispersion interaction into an effective form resembling a spontaneous quantum *charge* fluctuation interacting with an induced *charge*. Dobson-C effects can also occur in finite systems with degeneracies, and lead to dynamic dipole interactions (dispersion) between model triangular  $H_3$  molecules that obey the same power law as static dipole interactions [60]. The finite speed of light (quantum electrodynamics) is not usually taken into account in quantum chemical electronic structure codes but would act to reduce perceived Dobson-C contributions; when relativistic effects are included one speaks of the *Casimir effect* [61].

The simplest way to understand the nature of the London force and its three corrections is via the distance ( $d$ ) dependence of inter-surface interaction energy  $E$  between objects of

**TABLE 13.1** Asymptotic form of the dispersion interaction energy  $E$  between two parallel materials separated by distance  $d$  as determined from sums of atomic London  $R^{-6}$  terms and from (nonrelativistic) RPA calculations [20,62–68]. The RPA prefactor  $A'$  can differ significantly from its summed counterpart  $A$

System	Summed $R^{-6}$ terms	RPA result
Parallel semiconducting/insulating sheets	$-Ad^{-4}$	$-A'd^{-4}$
Parallel graphene sheets	$-Ad^{-4}$	$-A'd^{-3}$
Parallel 2D metallic sheets	$-Ad^{-4}$	$-A'd^{-5/2}$
Parallel semiconducting/insulating nanorods	$-Ad^{-5}$	$-A'd^{-5}$
Parallel metallic nanorods	$-Ad^{-5}$	$-A'd^{-2}\log(d/d_0)^{-3/2}$
3D materials (metals, insulators)	$-Ad^{-2}$	$-A'd^{-2}$

different conductivity and dimensionality. This can be expressed as

$$E = -Ad^{-p} \quad (13.1)$$

for long-distance interactions, where  $p$  expresses a power-law scaling and  $A$  is a scaling factor. Particular interest is on the surface adhesion properties of 1D and 2D metallic systems [20,62–68]. Results are summarized [20] in Table 13.1 where the asymptotic distance dependences evaluated using the random phase approximation (RPA) [63,69–72], typically applied in the TDDFT framework (see Chapter 3), are compared to those obtained by summing pairwise-additive London terms. As discussed in the next section, the RPA method is believed to contain enough of the essential physics to predict correct power laws for these applications. Summed London terms predict the correct asymptotic behavior when nonconducting materials of any dimension interact with each other and when 3D metals interact. This means that summed London terms give the correct power law  $p$  but does not imply that they will also give the correct scaling factor  $A$  required for accurate numerical results. Significant deviations in  $p$  occur for interactions involving 1D or 2D conducting materials such as nanotubes, metal sheets, and graphene. For parallel 2D metallic sheets, the power law from pairwise sums is  $d^{-4}$  compared to the RPA result of  $d^{-5/2}$ , whilst for two parallel nanorods it changes from  $d^{-5}$  to  $d^{-2}\log(d/d_0)^{-3/2}$  where  $d_0$  is the fluctuation length scale. These RPA results quoted do not include quantum electrodynamic effects [61] but they can be included [73] and are believed to only influence the relatively minor  $\log(d/d_0)^{-3/2}$  term [62]. There remains much fundamental science still to be discovered, however [64]. For graphene, Dobson-C effects are generally small owing to the low electron velocity at the Dirac point, but post-RPA many-body interactions are susceptible to quantum electrodynamic effects [64].

### 13.3 CONTRIBUTIONS TO THE DISPERSION INTERACTION INCLUDED IN MODERN COMPUTATIONAL METHODS

While different computational methods treat the London dispersion term and its three corrections in different ways, much of the story of dispersive forces on surfaces parallels that in other areas [74]. Other asymptotic features that also depict the applicability of different computational methods in different scenarios include what happens in the unified-atom



TABLE 13.2 List of correct asymptotic properties for some commonly used computational methods

Method	Low band gap	Unified atom	Dobson-A <sup>a</sup>	Dobson-B	Dobson-C
HF, CIS	no	yes	no	no	no
CASSCF	yes	yes	part <sup>b</sup>	part <sup>b</sup>	part <sup>b</sup>
LDA, GGA, hybrids	yes	yes	no	no	no <sup>f</sup>
Double hybrids	yes	yes	scaled <sup>g</sup>	no	no <sup>f</sup>
MP2	no	yes	yes	no	no
CASPT2	yes	yes	yes	part <sup>b</sup>	part <sup>b</sup>
MRCI, MRCC	yes	yes	yes	yes	yes
RPA, TDDFT	yes	yes	yes	yes	yes
QMC	yes	yes	yes	yes	yes
GW	yes	yes	yes	yes	yes
D2, D3(0), D3(BJ)	yes	no	yes	indirect <sup>c</sup>	no <sup>f</sup>
D3(ABC)	yes	no	yes	part <sup>c,d</sup>	no <sup>f</sup>
MBD	yes	no	yes	yes	no <sup>f</sup>
vdW-DF	yes	yes	yes	no	no <sup>f</sup>
XDM	yes	no	yes	indirect <sup>e</sup>	no <sup>f</sup>

<sup>a</sup> Plus any London term.

<sup>b</sup> Only that within the active space.

<sup>c</sup> London contributions changed based on included range of common chemical environments.

<sup>d</sup> Axilrod–Teller term included explicitly.

<sup>e</sup> London contributions modified by the way the exchange hole perceives the chemical environment.

<sup>f</sup> Included implicitly in LDA and related density functionals in a way that typically works well at covalent and ionic bond-length separations.

<sup>g</sup> MP2 contributions usually scaled down so treatment is incomplete.

limit (e.g., what happens as the atoms in H<sub>2</sub> are squashed together to make He), and what happens when the band gap goes to zero. Table 13.2 expands the work of Dobson [20] to categorize some significant computational methods in terms of how they perform in regard to these limits. Note, however, that not all computational packages may implement all possible described features of these computational methods.

The simplest *ab initio* electronic-structure computational method, pure Hartree–Fock (HF) theory for ground states, does not allow for dispersion at all, nor does the simplest method based on it for treating excited states, configuration interaction (CI) singles [75–77] (CIS). Second-order Møller–Plesset theory [78] (MP2) is the simplest level of ground-state theory that does allow for dispersion, seamlessly including Dobson-A contributions (see Chapter 4). This method has been very widely applied to treat dispersion in chemical and biological systems, but it become inappropriate when metals are involved as it ignores Dobson-C contributions [20] and is based on an inappropriate single-determinant expansion of the wavefunction. It also excludes Dobson-B corrections.

Higher-level and related *ab initio* methods (see Chapter 4) like CI singles and doubles (CISD), the RPA method (Chapter 3) already utilized in Table 13.1 [63,69–72], and coupled-cluster-based methods like coupled-cluster singles and doubles (CCSD), as well with additional perturbative triples, CCSD(T) [35], do include both Dobson-B and Dobson-C [20], but these methods are still based on single-reference configurations and so remain inappropriate for conducting surfaces. Hence their multireference analogue, complete-active-space

self-consistent field [79] (CASSCF) theory, is often used to provide the starting point for second-order perturbation-theory calculations (CASPT2) [80] or multireference coupled cluster methods (MRCC) [81,82]. These methods can be applied to periodic systems [81–90], often using some form of embedding technique [58,85–87,90–96]. CASPT2 includes partial Dobson-B and Dobson-C corrections, becoming sufficient for large enough active spaces, whilst MRCC methods naturally include both terms and only require depiction of sufficient multireference character so as to adequately describe orbitals near the Fermi energy. Choice of the subspace presents an undesired arbitrary parameter involved in both of these methods but nevertheless they are *ab initio* as the exact answer is obtained when all orbitals are included. The required computer time formally scales as the factorial of the size of the active space times either  $n^5$  scaling for CASPT2 or  $n^6$  scaling for MRCC. However, modern computational approaches can reduce this scaling considerably [83,84,97–99], even perhaps to linear scaling even for CCSD(T) [82].

An alternative approach to *ab initio* evaluation of surface interactions that includes all Dobson corrections and beyond is through use of the quantum Monte Carlo (QMC) scheme [94, 100–102]. All terms are also included in the “GW” method [103] when used as an energy functional.

In search of procedures that have the generality and accuracy of *ab initio* Hartree–Fock or QMC based approaches combined with the speed and versatility of DFT, a range of modern methods have also been developed that merge post-HF and DFT methods [73,90,93,104–109]. These approaches combine the good description of in-close electron correlation afforded by DFT with the ability of *ab initio* approaches to seamlessly include long-range effects.

However, as methods combining post-HF and DFT based approaches remain impractical for many problems of interest, in modern times DFT with added empirical corrections for dispersion has become widely used (see Chapters 5 and 6). A 40-year-old alternative [110, 111] is the addition of empirical dispersion corrections to Hartree–Fock theory, an approach currently undergoing renaissance [112–115]. In particular for protein and DNA systems, this offers significant advantages of both stability and accuracy compared to DFT-based approaches [116]. Dispersion corrections to DFT can be made in various ways, and we consider some commonly applied options.

The simplest approach involves expansion in pairwise-additive atom–atom terms, akin to the way dispersion is included in molecular-mechanics force fields but without the large disadvantage of requiring new parameters for every molecule and its environment. For approaches of this type, modern research is dominated by the D3 method of Grimme et al. In its original form [117] it is now often called “D3(0)” (see Chapter 6) but it also has modern variants like D3(ABC), which also contains Axilrod–Teller three-body interactions [117], and its mostly-used improvement D3(BJ) [114] embodying Becke–Johnson [118] damping; an older variant known as D2 is also in common use [30]. All method variations include Dobson-A corrections whilst only D3(ABC) contains partial Dobson-B corrections; Dobson-C is not currently included in any D3 scheme.

An alternative approach that has been widely employed has been the development of density functionals that themselves embody dispersion, most noticeably the Rutgers–Chalmers method of Dion, Rydberg, Schröder, Langreth, and Lundqvist [119] (vdW-DF, see Chapter 8), and its latest variant known as “vdW-DF2” [120]. These schemes again include neither

Dobson-B nor Dobson-C terms [20] but are based on a first-principles approach to determining the Dobson-A effects.

Other related methods are also available for surfaces [121–123], including in particular the exchange-hole dipole moment dispersion model (XDM), described in Chapter 5 [121,124]. This method is reasonably new and is not discussed in detail in this chapter, but discussion is included elsewhere.

An alternative semiempirical correction scheme is the Tkatchenko–Scheffler method [125] (TS) and its significant improvement the many-body dispersion (MBD) [22–27] approach; these methods have been further improved and made available [21] in VASP [126] and many other packages [26]. By using local harmonic oscillator models they generate semiempirical descriptions of the electron correlation arising from local fluctuations [22–27] that, unlike the D3 scheme, are solved nonperturbatively [20,127] and so include Dobson-B contributions. Under the MBD scheme, these local dipolar fluctuations can cooperate to produce very long-wavelength polarization waves, but the electrons themselves are each tied to an oscillator and cannot move through space to produce the large charge displacements that embody Dobson-C effects. Hence these methods do not reproduce many known asymptotic limits [20,68]. Indeed, reported MBD distance dependences for two parallel nanowires are of order  $d^{-4.3}$  or higher [27], close to the pairwise-additive limit of  $d^{-5}$  and far from the correct value of  $d^{-2} \log(d/d_0)^{-3/2}$ . Computational methods that include Dobson-C effects do not suffer from this limitation [65,128,129]. At short range, corrections to London-dispersion descriptions of up to a factor of 3 have been reported coming from MBD theory, and the computational method is designed to deal efficiently with problems of this type.

Indeed, central to *all* above-mentioned DFT approaches is the approximation that dispersion is dominated by *local* atomic fluctuations in the electron density that can be treated by *locality-based* perturbation theory [20] (see Chapters 5 and 6), as described in Fig. 13.1, thus not including Dobson-C. However, if computational methods are able to detect environments subject to Dobson-B terms, then these effects can be mimicked as Dobson-A type by varying atomic London-dispersion coefficients [121]. Such approaches still give incorrect asymptotic behavior but are optimized for short-range performance. In D3 and MBD, recognition of chemical environment is programmed explicitly whereas the XDM method evaluates it directly. vdW-DF instead focuses on evaluation of accurate Dobson-A parameters, preventing the empirical inclusion of Dobson-B terms by this process.

At short and intermediate separations, calculated dispersion energies deviate from the discussed asymptotic power laws. MBD differs from methods like D3 and XDM in that its dispersion energy is sensitive to the entire system structure rather than just to local representations of it. If the structure is highly anisotropic, then this sensitivity is advantageous as long-range anisotropy can significantly affect details of local optimized atomic geometries [27,68]. A curious feature of this is that, at intermediate distances, apparent MBD power-law expansions can appear similar to those expected asymptotically owing to Dobson-C effects [27]. However, at larger separations, MBD calculations reveal their true, deviant, asymptotic power laws [27,68].

The importance of Dobson-C effects in the subasymptotic regime remains an important open question. On the one hand, it is clear that they can contribute to energy differences. On the other hand, local approximations are usually based on a metallic homogeneous electron gas, and thus include short-range Dobson-C effects in their model exchange-correlation

holes. Hence Dobson-C terms are implicitly included in all DFT approaches in a way known empirically to work well at the scale of chemical bond lengths, but the significant changes to these contributions that occur at longer distances are not included in double hybrid, D3, MBD, vdW-DF, or XDM approaches. The short-range accuracy of local approximations may also explain the general success of all listed approaches for short-range binding physics. The fact that these methods are basically just GGA in the short-range is often missed in discussions. However, the recent demonstrations that HF-D3 for organic molecules and crystals, protein structures, and silica structures leads to descriptions of basic properties that are better than those afforded at the GGA level [112–116], indicates the intimate connection between the long-range correlation effects that manifest as dispersion and the short-range ones affecting chemical processes.

A very different approach widely used in small-molecule chemistry research is the use of double-hybrid density functionals that include both nonlocal exchange and nonlocal correlation through an MP2-like ansatz [130,131]. The MP2 contribution is often scaled down, however, so that these methods usually still need some additional dispersion correction such as D3. They can achieve similar accuracy to coupled-cluster theory and represent the state-of-the-art in DFT calculations applied in the fields of chemistry and biochemistry [132,133]. They are, however, not readily applicable to metallic systems and low band-gap semiconductors owing to the use of the Møller–Plesset approach to electron correlation which is based on the assumption of a wide band gap. While extension of these methods to CASPT2-type approaches could overcome this limitation, a more profound problem is that they do not include Dobson-B and Dobson-C corrections [20]. Alternatively, a (more expensive) general first-principles based approach that provides a nonperturbative treatments of the dispersion energy and includes all Dobson contributions is TDDFT which also formally scales as  $n^6$  [134, 135]. However, accurate and efficient TDDFT methods are being developed [72,136], offering significant prospects for this fundamental approach.

## 13.4 BENZENE ON CU, AG, AND AU SURFACES

The adsorption of benzene on Cu, Ag, and Au surfaces has long been a benchmark system for understanding the effects of dispersive interactions on self-assembly and catalysis [23, 26,28,29,117,121–123,137,145,146,148–151,153–159]. In Table 13.3, a summary is given of some key results obtained using basic density functions with and without dispersion correction, as well as the Meta-GGA M06-L [160] functional and *ab initio* MP2 and CASPT2 calculations on model cluster systems.

Without dispersion corrections, the local-density approximation (LDA) typically performs erratically and often significantly overestimates van der Waals attractions [137], as Table 13.3 depicts. The table shows that GGA functionals underestimate the weak binding of benzene to (111) surfaces by an order of magnitude [29,121,123,137,146,148–151] and by a factor of 4 for the reactive Cu(110) surface [146,151]. This change is particularly significant in terms of understanding surface chemistry and will be addressed in detail later. MP2 and CASPT2 results using cluster models are qualitatively indicative of critical chemical features, but these are difficult to apply quantitatively owing to the typical use of small atomic basis sets em-

**TABLE 13.3** Observed and calculated binding energies  $-\Delta E$ , in eV, for benzene adsorbed on Cu, Ag, and Au surfaces, as well as the mean average deviation (MAD) for the (111) surfaces compared to the latest two sets of experimental data. A constant correction for zero-point energy of  $0.06 \pm 0.01$  eV is used for estimating the MAD [137]

Method	Cu(111)	Ag(111)	Au(111)	MAD(111)	Cu(110)
Obs.	0.71 <sup>a</sup> 0.69 <sup>p</sup>	0.69 <sup>a</sup> 0.68 <sup>p</sup>	0.76 <sup>a</sup> 0.65 <sup>p</sup>		1.0 <sup>b</sup>
MP2	0.35 <sup>c</sup>	0.33 <sup>c</sup>	0.31 <sup>c</sup>	0.40–0.45	1.12 <sup>d</sup> 1.43 <sup>d</sup>
CASPT2					
M06-L <sup>e</sup>	0.51	0.56	0.55	0.19–0.24	
LDA <sup>f</sup>	0.73	0.72	0.96	0.07–0.10	
PW91 <sup>g</sup>	0.03	0.05–0.08	0.08–0.09	0.67–0.72	0.25
PBE <sup>h</sup>	0.06–0.08	0.06–0.09	0.06–0.08 <sup>n</sup>	0.66–0.71	
PBE-D3(0) <sup>i</sup>	1.01	0.74	0.86	0.10–0.14	1.15
PBE-D3(BJ) <sup>i</sup>	0.96	0.79	0.87 <sup>n</sup>	0.09–0.14	1.17
PBE-D3(ABC) <sup>i</sup>	0.79	0.62	0.73	0.06–0.08	0.96
PBE-vdW-DF <sup>j</sup>	0.17	0.87	0.84	0.22–0.28	
revPBE-vdW-DF <sup>q</sup>	0.53	0.55	0.56	0.19–0.23	
opt-PBE-vdW-DF <sup>q</sup>	0.68	0.71	0.71	0.03–0.08	
GGA-vdW-DF <sup>k</sup>	0.49–0.82	0.52–0.76	0.42–0.82		
PBE-XDM <sup>l</sup>	0.74	0.56	0.72	0.07–0.11	
PBE-XDM16 <sup>o</sup>	0.54	0.58	0.61	0.20–0.16	
B86bPBE-XDM <sup>o</sup>	0.59	0.68	0.64	0.10–0.14	
PW91-XDM <sup>l</sup>	0.74	0.58	0.72	0.06–0.10	
PBE-vdWsurf <sup>m</sup>	0.86–0.91	0.75–0.81	0.74		
PBE-TS			0.41 <sup>n</sup>		
PBE-MBD			0.70 <sup>n</sup>		

<sup>a</sup> From Ref. [29] based on new analyses [138] of original reports of 0.58 eV [139,140] for Cu(111), 0.53 eV [140–142] for Ag(111), and 0.64 eV [140,143] for Au(111).

<sup>b</sup> From data in Ref. [144].

<sup>c</sup> Ref. [145].

<sup>d</sup> Ref. [146].

<sup>e</sup> Meta-GGA, from Ref. [147].

<sup>f</sup> Ref. [137].

<sup>g</sup> Refs. [121,146].

<sup>h</sup> Refs. [29,121,123,137,148].

<sup>i</sup> Refs. [28,29].

<sup>j</sup> Ref. [123].

<sup>k</sup> Many GGA functionals other than PBE and PW91, from Refs. [29,149–151].

<sup>l</sup> Ref. [121].

<sup>m</sup> Refs. [122,123].

<sup>n</sup> This work, using VASP [126] (with parameters VDW\_SR = 0.83, LVDWEXPANSION = true, and PREC = ACCURATE).

<sup>o</sup> Ref. [124].

<sup>p</sup> Ref. [152].

<sup>q</sup> Ref. [153].

bodying large basis-set superposition errors [145,146]. Also, because of the small-band-gap natures of metallic clusters, only CASPT2 or MRCC and not MP2 are actually appropriate methods to use.

Results obtained using the vdW-DF correction [119] appear quite good when used with the opt-PBE density functional but vary by a factor of two depending on the GGA used [29, 149–151, 153]. This is a particularly disappointing result that echoes early studies indicating that the robust correction methods were difficult to find [137]. This approach defines a dispersion correction and then goes in search of some density functional to which it could be paired in order to give realistic results. If such a functional can be found, then the combined pair could only be used for chemical problems to which that functional happens to give a realistic description.

Alternatively, the D3 scheme and its variants can be applied to any of the multitude of currently available density functionals with sensible results expected for basic chemical reactions in solution or the gas phase [113] (see Chapter 6). From the results in Table 13.3, the now widely used strategy of combining the PBE functional [161] with D3 variants appears more stable, with D3(0) and its replacement B3(BJ) predicting similar binding energies and the enhanced three-body method D3(ABC) predicting binding energies within 10% (0.07 eV) of experiment [28, 29].

The alternative XDM dispersion correction method [121] (Chapter 5) gives results that are comparable. This method has been recently revised [124] and we label the new results PBE-XDM16. While these results are not quite as good, the new approach of combining XDM with the B86bPBE functional recovers some of the lost ground. Results from the vdWsurf method [122, 123, 159], which does not assume the local fluctuations dominate the dispersion energy, are also similar to the D3(ABC) ones. An early result presented for the first time in Table 13.3 suggest that the MBD method [22–27], the latest and most advanced method of this type, may prove generally reliable; MBD appears to give significantly improved results compared to its older TS counterpart.

Hence we see that inclusion of dispersion corrections is essential to achieve realistic calculations of binding energies. However, early calculations performed using pure GGA functionals actually often provided realistic descriptions of the band profiles and spectroscopic properties [146, 154, 162]. How to interpret these results was the major question, focusing on possible commercial applications in designing new catalysts for reactions with benzene. That dispersion forces contributed to the binding in terms of energy and geometry changes was always appreciated but the effect was naively thought not to vary greatly with geometry or environment. Hence the significant increase in binding [139, 163] of benzene on Cu(110) (Table 13.3) was interpreted in terms of a significant increase in *chemical* bonding in this system [164].

Considering spectroscopy, the induced surface dipoles for benzene on Cu(111), Ag(111), Au(111), and Cu(110) caused by the binding, as deduced from changes in the surface work-function, are of the correct magnitude and sign, indicating that some important surface properties are being adequately modeled by calculations [146] using the PW91 GGA density functional [165] (but less so [149] using PBE). If the bonding is purely dispersive then the benzene HOMO energy with respect to the metal Fermi energy would not be expected to be calculated correctly owing to the asymptotic potential error obtained using GGA density functionals, whereas if chemical bonds form then realistic band alignment is implied. On Cu(111) for PW91 this error is 2.5 eV, reducing to 0.4 eV on Cu(110) [146]. This effect therefore indicates a significant increase in the chemical character of the bonding on Cu(110). The calculated LUMO orbital energies would also be expected to be quite poor in absolute terms

owing to the band-gap error in GGA DFT [166], but relative changes should be better reproduced. In going from Cu(111) to Cu(110), the LUMO level is observed [167,168] to change by  $-1.4$  eV, in good agreement with the PW91 calculations [146]. This result also suggests that the change in the chemical nature of the binding is being correctly represented by the GGA calculations.

Demonstration of the critical role of dispersion was established not using density functional theory but instead [146] through the use of CASPT2 calculations. This *ab initio* technique does not require the choice of approximate density functionals or dispersion corrections, but it has the disadvantages of not fully including Dobson-B corrections and not being able to treat periodic systems. The method therefore had to be applied to copper clusters [169] representing the metal surface, an approach often taken to facilitate the application of advanced methods beyond GGA DFT. Its application in this context was successful as the cluster used was large enough to contain key interactions yet small enough for perturbation theory to remain appropriate. Also of significance was that it was applied to calculate only the *difference* between the representation of the intermolecular energy apparent in PW91 and that of CASPT2, this difference being added onto the calculated binding energies coming from periodic-surface PW91 calculations [146]. The method was later applied to understand polymorphism of aromatic monolayers on graphite surfaces, providing the first method capable of realistically modeling binding energies, their geometry dependence, and physisorption-induced surface restructuring [170], processes now easily modeled by dispersion-corrected DFT.

The above example depicts the general problems that can be expected when cluster models are used to investigate surface processes. The reactivity of surface atoms can often be much less than the reactivity of cluster atoms owing to the increased coordination. When DFT calculations are applied to the copper cluster models [169,171], the calculated energies of binding  $\Delta E$  are  $0.4$ – $0.6$  eV larger than those calculated using periodic slab calculations, the same magnitude as the actual ignored dispersion correction to GGA calculations [146]. It was thus intuitive to assume that the GGA calculations could be used to deduce the binding mechanism whereas in fact they gave qualitative agreement with experiment only through the cancellation of sizable errors associated with the use of GGA density functionals and the neglect of dispersion. Copper, silver, and gold metals are particularly susceptible to this effect as participation of the valence *s* orbitals in internal chemical interactions makes surfaces noble rather than show the expected reactivity [172]. Application of this principle to the monolayers formed by sulfur compounds on gold is the topic of Section 13.6.

The most important consequence of the neglect of dispersion in the old calculations of benzene on Cu, Ag, and Au surfaces is that it led to the wrong description of the critical chemical effect: the explanation of why Cu(110) surfaces show strong binding with catalytic activity whilst the (111) surfaces do not. While the calculations correctly identified that chemical bonding effects were much more significant on Cu(110), the neglect of dispersion led to the extrapolation that the bonding on Cu(110) was purely covalent in nature [169]. It was concluded that benzene became promoted from its ground state to its lowest-energy triplet state, and that this state then formed Cu–C covalent bonds that were strong enough to overcome the large triplet promotion energy. The observation [173] that benzene can be pushed by a scanning tunneling microscope (STM) tip across a Cu(110) surface shows that

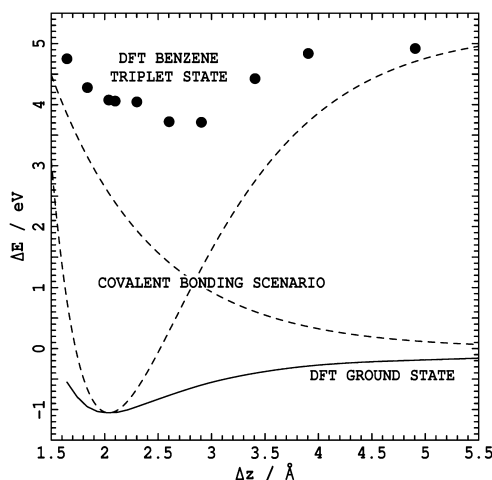


**FIGURE 13.2** The DFT calculated ground-state potential-energy surface for benzene approaching a Cu cluster at minimum carbon to copper surface–plane separation  $\Delta z$ , along with the calculated surface for the lowest triplet state of benzene, compared to the generic form [169] of these surfaces expected in the scenario that a covalent bond is formed between the two species. Reproduced from A. Bilic, J.R. Reimers, N.S. Hush, R.C. Hoft, M.J. Ford, *J. Chem. Theory Comput.* 2 (2006) 1093, with permission of The American Chemical Society.

this interpretation is not correct as it would involve high-energy transition states associated with breaking and remaking the Cu–C bonds. Also, it is possible from GGA calculations alone to deduce that this mechanism is incorrect because the ground-state of the adsorbate species would need to correlate with the benzene triplet state and, to conserve spin, some local surface triplet state would need to be present as the molecule is withdrawn from the surface. Calculated surfaces [146] for this ground state as well as the corresponding excited-state surfaces are reproduced in Fig. 13.2 using a cluster model for the interaction. The ground state of the adsorbed species clearly correlates with separated ground-state benzene and Cu cluster, while the excited states also directly correlate with each other. Alternatively, the correlation diagrams expected if the adsorption involved four Cu–C bonds demands that extraction of the molecule must pass over a high-energy conical intersection.

What these results show is that the dispersion correction to GGA density functionals cannot be considered as simply providing an additive term needed only to predict absolute binding energies. Its effects are profound and need to be included in calculations of surface properties. While use of GGA density functionals in surface science has a long and successful history, it is not possible to know in advance when dispersive effects are critical. For benzene on Cu(110) it results in *amplification* of the chemical bonding effects that make this surface different from the (111) surface. The amplification happens because the chemical bonding effects reduce exchange repulsion to allow the adsorbate molecule to penetrate closer to the surface, and the great sensitivity of the  $R^{-6}$  London attraction comes into play to make the net increase in bonding twice that expected from the covalent terms alone [146]. Ignoring dispersion allows for the possibility that cancellation of this with other



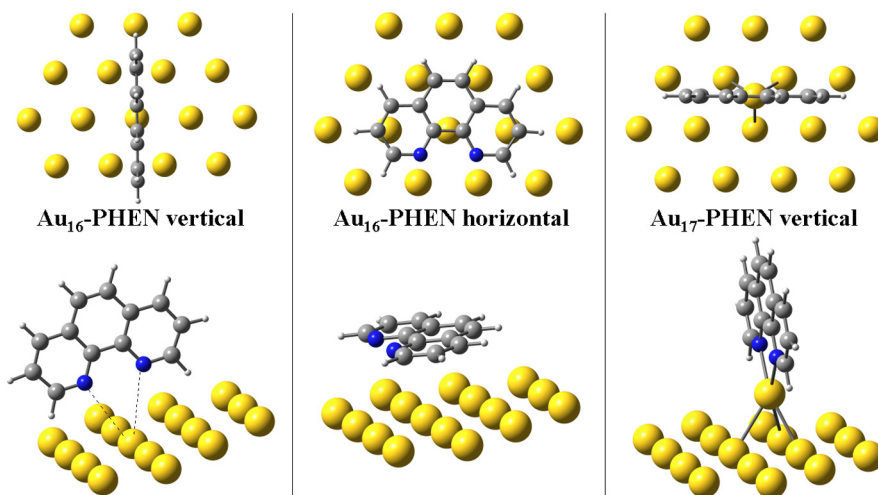


FIGURE 13.3 The cluster models used to provide CASPT2 corrections to SAM formation energies. *Reproduced from P.F. Cafe, A.G. Larsen, W. Yang, A. Bilic, I.M. Blake, M.J. Crossley, J. Zhang, H. Wackerbarth, J. Ulstrup, J.R. Reimers, J. Phys. Chem. C 111 (2007) 17285, with permission of The American Chemical Society.*

significant errors in GGA calculations leads to the incorrect description of observed phenomena.

### 13.5 STRONG VAN DER WAALS FORCES: 1,10-PHENANTHROLINE MONOLAYERS ON AU(111)

A major advance made 10 years ago concerning the stabilization of gold surfaces and nanoparticles by sulfur [174–177] and nitrogen [170] compounds was the observation of species bound not to flat surfaces but instead to gold adatoms located above the surface. In both cases, dispersive interactions dominate the surface adhesion, but understanding of the binding in the important sulfur compounds took a long time as covalent forces are also involved, as discussed in detail in Section 13.6. Here we consider the simpler situation of the binding of 1,10-phenanthroline to Au(111), a situation for which the strong interactions between the doubly occupied lone pair orbitals of the nitrogen base and the doubly occupied Au *d* orbitals occur, a process that can lead to strong attractive Dobson-A effects.

Under usual conditions, 1,10-phenanthroline (PHEN in Fig. 13.3) self-assembles on Au(111) edge-on in chains, the molecule erecting perpendicular to the surface in a  $(4 \times 4)$ -3 supercell [178]. Such monolayers are in constant motion owing to the similar binding experienced by molecules lying flat on the surface, making the ends of the chains intrinsically unstable. However, it can also be observed to form in a  $(4 \times \sqrt{13})R46^\circ$ -3 cell on a highly pitted surface in a very stable self-assembled monolayer (SAM), identified as an adatom-bond

**TABLE 13.4** Calculated binding energies  $\Delta E$  for 1,10-phenanthroline adsorbed on Au(111), in eV

Structure	PW91-CASPT2 <sup>a</sup>	PBE-D3(BJ)	PBE-MBD	revPBE-vdW-DF	PBE-vdW-DF
Flat	-0.65	-1.02	-1.07	-0.95	-0.71
Vertical	-0.95	-0.93	-0.98	-0.86	-0.82
Adatom-bound	-0.87	-0.94	-0.98	-0.86	-0.87

<sup>a</sup> From Ref. [170], including large BSSE corrections.

species [170]. Understanding the chemistry of this process requires understanding the factors controlling the free energy of SAM formation from solution of adsorbate molecules lying flat on the surface, erected vertically, and bound to adatoms, structures depicted in Fig. 13.3. Such free-energy calculations have not been performed but a key component of the process is understanding the energies of binding  $\Delta E$  of the three species involved.

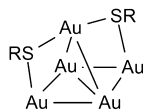
Calculations performed using various methods are shown in Table 13.4. Originally, an *ad hoc* scheme was used in which periodic SAM calculations at the PW91 level were augmented by correction factors obtained from cluster models by comparison of PW91 and CASPT2 results [170]. This approach proved qualitatively indicative of the chemical processes controlling SAM polymorphism: vertical binding either directly to the surface or via adatoms occurred with about the same binding energy (the calculations include the energy to extract the gold adatoms from pits in the surface), and also that the binding of flat molecules was strong enough to destabilize the ends of the molecular chains, explaining the kinetic instability of directly bound motifs. Table 13.4 also shows results from the PBE-D3(BJ), PBE-vdW-DF, revPBE-vdW-DF, and PBE-MBD approaches. The PBE-D3(BJ) and PBE-MBD methods give very similar results, with PBE-MBD giving 5% stronger binding. Compared to these results, PW91-CASPT2 predicts similar binding for both vertically bound structures but much weaker binding for the flat structure. This difference could originate from the very large BSSE of the flat structure (the LANL2DZ/6-31G\* basis set was used), making that calculation unreliable. revPBE-vdW-DF predicts binding for all structures that is systematically 10% less than that predicted by PBE-D3(BJ) and PBE-MBD, with PBE-vdW-DF predicting similar results for the vertical structures but again much less for the flat one. Note that the prediction by PBE-D3(BJ), PBE-MBD, and revPBE-vdW-DF methods that the flat structure binds more strongly does not mean that this structure is predicted to be a competitive polymorph as polymorphism is actually controlled by relative free energies per unit surface area. However, the results do serve to highlight the instability of the chain ends to toppling over, a critical feature of the observed STM images.

## 13.6 THE DISPERSIVE NATURE OF THE AU-S BOND TO SURFACES AND NANOPARTICLES

Much of nanotechnology concerns the properties of gold surfaces and nanoparticles stabilized by sulfur ligands SR, where R is some alkyl or aryl group, for biosensing, drug delivery, and other applications [179–183]. Various synthetic strategies for these nanoparticles are known; the most commonly used method is the Brust–Schiffrin synthesis which has

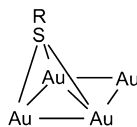
been applied over 4000 times in the literature to make gold nanoparticles from Au(III) and thiols in the presence of a strong reducing agent [184,185]. Much is known about the reaction mechanism [186,187], but a major advance was made recently [172] with the discovery of a new reaction intermediate. Its involvement was predicted [172] through consideration of the known reaction features [188], the properties of related [189–194] reactions, the properties of gold–sulfur molecular compounds [195,196], and the properties of related adsorbate species bound by C, N, O, Se, and Te [195,197–199], including the PHEN linked systems [170] discussed in the preceding section. The unifying understanding is that Au–S bonds can be dominantly covalent in character, as has been always assumed, but that dispersion forces are always present and of comparable magnitude: the covalent contribution dominates for small compounds but is inhibited by the strong Au–Au bonds present in nanoparticles and on surfaces owing to the noble character of the metal. Lack of appreciation of the role of dispersion forces therefore led historically to lack of understanding of the covalent forces and hence it was not possible to qualitatively rationalize chemical reaction mechanisms and products [52].

Of particular significance to understanding Au–S surface bonding is the considerable structural diversity [200,201] found in SR bonding to gold surfaces, with bonds forming either to adatoms on bridge sites above regular gold surfaces [174–177]:



SCHEME 13.1

and related chain structures [174,176,202–204], or else directly to surfaces, e.g., a distorted bridge-FCC site [205–214] above the (111) surface:



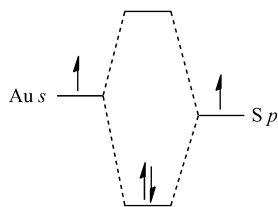
SCHEME 13.2

On nanoparticles, the surface curvature preferentially stabilizes the adatom form [215], but the directly bound motif is produced whenever R is too bulky [216–218], charged tail groups are nearby [219], or attractive packing forces and lattice constraints dictate [220]. Mixed adatom and directly bound motifs can even be made in the same SAM [220]. This diversity is useful if one is concerned with, say, surface chirality and its control [200] but atom-bound motifs, like in the case of PHEN monolayers, are always associated with surface pitting (the source of the gold adatoms) and hence are irregular; this property may hinder device applications [201].

GGA density-functional theory has been extremely successful in understanding most of the structural and spectroscopic properties of SR-covered gold surfaces and nanoparticles [172,175–177,200,201,205–215,217,219–221]. Calculated geometries and binding energies are accurate enough, and the interpretation of spectroscopic properties has been critical to the

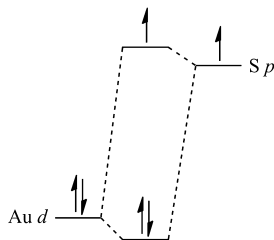
advancement of the field and the characterization of the adatom-bound motifs [222]. Their success reinforced the assumption that dispersion was, as usual, only of minor importance to the bonding. They got the right answer for the wrong reason.

In small compounds and molecular films, Au bonds to RS through an interaction of its valence  $s$  orbital with a  $p$ -dominated sulfur orbital:



SCHEME 13.3

leading to essentially covalent compounds. As sulfur is slightly more electronegative than gold, the Au-S bond is polarized toward sulfur and hence the standard chemical nomenclature for such an inorganic compound is an *Au(I)-thiolate* species. When sulfur is replaced by the electropositive metal tellurium, the bonding is similar but the polarization swings to favor gold, resulting in these compounds being named *Te(II)-aurides*. However, the strong Au-Au  $s$ - $s$  interactions present in nanoparticles and metal surfaces takes most of the  $s$  electron density far from the Fermi energy, making the interaction between the gold  $d$  electrons and the sulfur dominant:



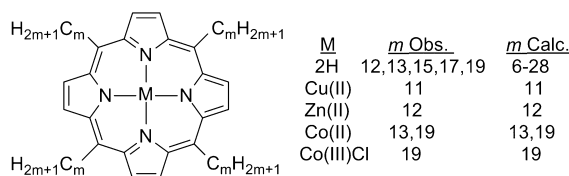
SCHEME 13.4

Hence the interface structure in these systems takes on *Au(0)-thiyl* form, and understanding the difference between this and the chemically or spectroscopically accessible alternate Au(I)-thiolate form provides the basis for understanding the synthetic chemistry and spectroscopy of nanoparticles and protected surfaces. When circumstances allow for Au(I)-thiolate production, nanoparticles are not formed directly and surfaces are etched rather than protected.

Hence we see that understanding the strength of dispersion interactions at surfaces is key to understanding synthetic mechanisms. Interestingly, the same effect has recently been reported for sulfur-iron bonds in cytochrome P450, with again the dispersion contributions to the bonds being essential for qualitative chemical understanding of the observed valence tautomerization [96].

### 13.7 DISPERSION AND FREE ENERGY CALCULATIONS OF SAM FORMATION AND POLYMORPHISM FROM SOLUTION

Most reactions are done in solution, and often subtle changes in free energy control products. Dispersion interactions form a major part of solvation energies as well as their effects on the substrate–SAM interaction. Involved solvation energies include those between the molecules and the solvent in solution, those between the solvent and the substrate, and those between the assembled SAM and the solvent. Not just the direct binding energy but also zero-point energies, enthalpies, and entropies all depend on how the various dispersion energies interplay. A current research topic that brings these issues into focus is the understanding of polymorphism of SAMs, particularly those formed through van der Waals processes. One significant system is the adsorption of tetraalkylporphyrins  $M-C_mP$ :



SCHEME 13.5

on highly ordered pyrolytic graphite (HOPG) surfaces from organic solution, with many structures having been observed [223–227]. Deduced polymorph free energies have then been compared to calculated values [223,224,228]. As an illustration, atomic structures fitted to observed STM images for some low-density “L” and medium density “M” polymorphs are shown in Fig. 13.4. The general question as to what controls polymorphism of SAMs remains open, and accurate methods for the experimental or computational characterization are scarce [223,229–237]. Recently, it was concluded [238] that “The Achilles’ heel of [the current] approach is the semitheoretical evaluation of the dewetting enthalpy which at this point necessarily relies on plausible assumptions.” Discussion often concerns whether kinetic or thermodynamic effects control polymorphism [223,229–232,235,236,239–248]. Slow-moving SAMs in thermodynamic equilibrium can have free energies determined directly from dynamics observed in the STM [237]. The development of computational methods to take on these challenges of surface adsorption is therefore critical.

An issue that this brings into focus is that the role of dispersion forces in surface adsorption may not necessarily be too different to their role in solvating organic molecules. What is certainly clear is that computational methods looking at surface adsorption from solution must balance these forces delicately in order to achieve sensible results. If the solvent is represented atomistically and the same dispersion method applied to all interactions, then this balance would be achieved. However, solvents are typically represented implicitly in calculations using dielectric continuum models in order to greatly enhance computational speed and facilitate application of accurate methods for the atomistic interactions included (see Chapter 12). Hence balancing the resulting disparate treatments of dispersive forces becomes a nontrivial matter. The only way to establish a robust method is by calibrating each part against relevant experimental data.

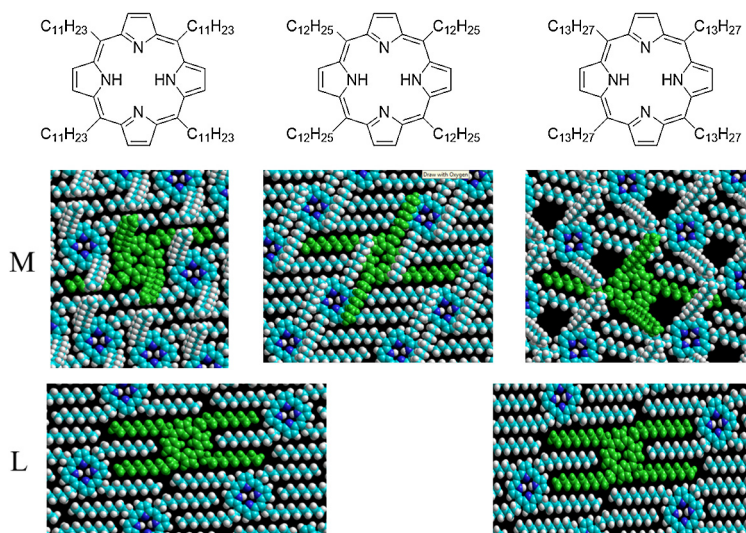


FIGURE 13.4 Atomic SAM structures fitted to observed STM images for “L” and “M” polymorphs of 2H- $C_m$ P on HOPG formed from organic solution [223–227].

The M- $C_m$ P system provides a means of making this possible. By varying the chain length  $m$ , effects attributed to the central porphyrin and the chains can be separated, both experimentally and computationally [224]. Primary experimental data is taken from observed free energies of SAM formation [224], combined with thermodynamic data for alkane–HOPG interactions [7]. The alkane–HOPG results are incorporated into a fitted molecular-mechanics (MM) force field. To make a reference computational method for the evaluation of dispersion-corrected density functionals, this data is combined with the very widely used AMBER force field [249] to describe intermolecular interactions and the B3LYP [250]/6-31G\* post-GGA density-functional method for estimating intramolecular distortion energies. We label this reference scheme as “QM/MM.” The most significant contribution ( $\sim 75\%$ ) to the electronic interaction energy is that coming directly from the experimental force field, with the AMBER intermolecular contribution accounting for most of the rest [224]. By considering the asymptotic chain length ( $m$ ) dependence of the binding energy contribution  $d\Delta E/dm$  to the free energy, the influence of the B3LYP and porphyrin parts of the interaction energy can be subtracted away, further increasing the reliability of the reference method.

Table 13.5 shows the asymptotic chain length dependence  $d\Delta G/dm$  evaluated using the QM/MM reference method as well as PBE-D3(BJ), PBE-vdW-DF, and revPBE-vdW-DF. The alkane–HOPG force field contributes  $-0.28$  eV to  $d\Delta G/dm$  whilst the AMBER force field contributes  $-0.12$  eV, making  $-0.40$  eV total. This agrees well with the PBE-D3(BJ) value of  $-0.41$  eV but revPBE-vdW-DF is too attractive at  $-0.50$  eV and PBE-vdW-DF is extremely attractive at  $-1.08$  eV.

Also shown in Table 13.5 are the interaction energy contributions to the free energy, evaluated for 2H- $C_{11}$ P using a variety of methods. Again, the QM/MM results dominated by the experimentally derived and AMBER force fields are in excellent agreement with PBE-D3(BJ).

**TABLE 13.5** Asymptotic chain-length dependence  $d\Delta E/dm$  of the binding energy for tetraalkylporphyrins  $2\text{H-C}_m\text{P}$  on HOPG, as well as the binding energy  $\Delta E$  for  $2\text{H-C}_{11}\text{P}$ , in eV, calculated using various methods

System	$d\Delta E/dm$	$2\text{H-C}_{11}\text{P } \Delta E$
QM/MM <sup>a</sup>	-0.40 <sup>d</sup>	-5.7 <sup>c</sup>
PBE-D3(BJ)	-0.41 <sup>d</sup>	-5.6 <sup>c</sup>
revPBE-vdW-DF	-0.50	-6.8 <sup>b</sup>
PBE-vdW-DF	-1.08	-9.4
PBE-TS		-6.2
PBE-MBD		-5.7

<sup>a</sup> Deriving large from an empirical force field fitted to experimental data [7] for alkane-HOPG interactions, with ca. 25% contribution also from the AMBER force field.

<sup>b</sup> -6.2 eV at PBE-D3(BJ) optimized geometry calculated by SIESTA using atomic basis sets after 2 eV BSSE correction [223] reevaluated as -6.5 eV by VASP using plane waves, relaxation energy to geometry minimum 0.3 eV.

<sup>c</sup> From Ref. [223].

<sup>d</sup> From Ref. [224].

They are also in excellent agreement with the PBE-MBD value, whilst PBE-TS differs by 10% and revPBE-vdW-DF by 20%; PBE-vdW-DF is unrealistic and overbinds by 60%. For  $2\text{H-C}_{19}\text{P}$ , QM/MM portrays a binding of -8.5 eV close to the PBE-D3(BJ) value of -8.8 eV and are both consistent with qualitative experimental observations, while revPBE-vdW-DF predicts an unrealistic value of -10.7 eV (the porphyrin concentration required for SAM formation would be reduced by 24 orders of magnitude compared to that required for  $2\text{H-C}_{11}\text{P}$ ).

A possible indication of the likely errors in the QM/MM results can be made by comparing observed and calculated free energies of formation  $\Delta G$  for various polymorphs of  $2\text{H-C}_{11}\text{P}$ - $2\text{H-C}_{13}\text{P}$  which differ by just 0.25 eV [223]. However, the free energy of formation (from -0.48 to -0.61 eV) arises from a near complete cancellation of the large binding energies  $\Delta E$  (for PBE-D3(BJ), 0.6-1.1 eV from PBE and -4.8-6.9 eV from D3) with large desolvation (3.0-4.8 eV) and entropy (1.1-1.7 eV) costs. Hence the good agreement between observed and calculated free energies could have resulted from cancellation of errors associated with these various terms. However, both PBE-D3(BJ) and QM/MM have been shown to predict relative free energies of different polymorphs to an accuracy of just 0.1 eV [228]. Also, the domination of the QM/MM result by the experimentally derived alkane-HOPG force field suggests that the errors in  $\Delta E$  are actually likely to be small.

Fig. 13.5 shows the relative magnitudes of the contributions to the free energy of formation of the "L" and "M" polymorphs (see Fig. 13.4) of  $2\text{H-C}_{11}\text{P}$  obtained using the QM/MM and PBE-D3(BJ) methods. This emphasizes the cancellation between surface binding, desolvation, and entropy contributions mentioned earlier [223]. Each contribution has its own asymptotic scaling with chain length  $m$ , and this balance must be maintained so as to explain the observed formation of SAMs of this polymorph from  $m = 11$  to at least  $m = 19$ . Calculated PBE-D3(BJ) and PBE-MBD energies reflect the experimental scenario and hence there must be a good balance between these methods and the empirical dispersion description [251] of

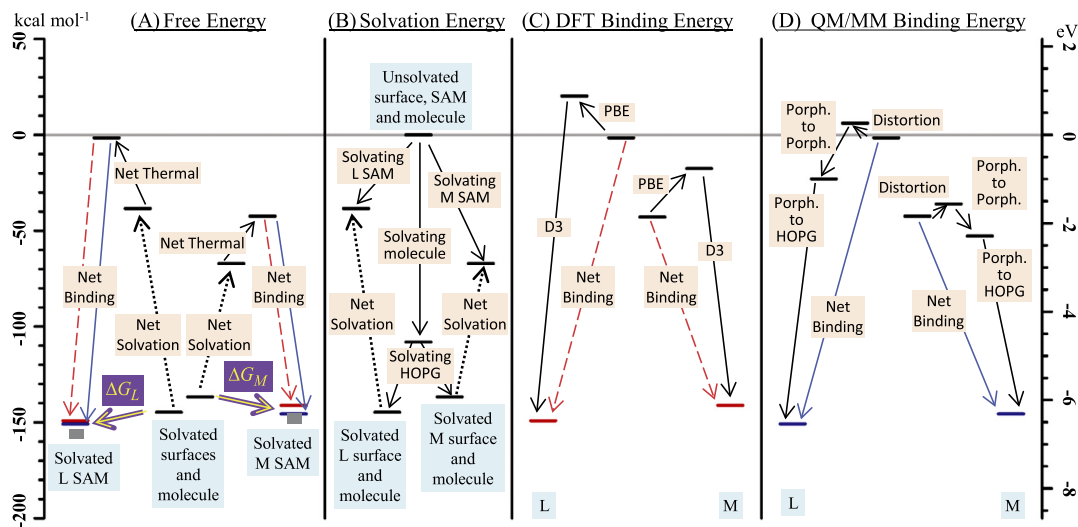


**FIGURE 13.5** Contributions to the free energy of SAM formation from solution for the “L” and “M” polymorphs of 2H-C<sub>11</sub>P on HOPG, obtained using (color online only): red (PBE-D3(BJ)), blue (QM/MM), and gray box (observed) [223]. The total free energies are decomposed into net binding ( $\Delta E$ ), desolvation, and thermal (essentially entropic) effects in (A), how different terms contribute to the desolvation process are shown in (B), the PBE and D3(BJ) contributions to the PBE-D3(BJ) binding are shown in (C), while the molecular distortion energy, porphyrin to graphite energy, and intermolecular energies from the QM/MM approach are shown in (D). Reproduced from J.R. Reimers, D. Panduwinata, J. Visser, Y. Chin, C. Tang, L. Goerigk, M.J. Ford, M. Sintic, T.-J. Sum, M.J.J. Coenen, B.L.M. Hendriksen, J.A.A.W. Elemans, N.S. Hush, M.J. Crossley, *Proc. Natl. Acad. Sci. USA* 112 (2015) E610, with permission of the USA National Academy of Sciences.

Floris, Tomasi and Pascual Ahuir from 1991 that was used in these calculations to model desolvation. Alternatively, the revPBE-vdW-DF method is out of balance with this dispersion solvation description, predicting far stronger interactions.

## 13.8 COMPUTATIONAL EFFICIENCY

The simplest *ab initio* method that includes Dobson-A terms is MP2 which formally scales as  $n^5$  with system size, while the simplest methods that include Dobson-B and Dobson-C terms like RPA, TDDFT, and CCSD scale formally as  $n^6$ . However, by using resolution-of-the-identity and frequency quadrature techniques, RPA can be implemented with  $n^4 \log n$  scaling [72], allowing efficient first-principles DFT-based approaches that are currently receiving much attention [136]. Efficient approaches are also being generated for other methods [83,84, 97–99], including also linear CCSD(T) [82]. In the past, however, ground-state DFT schemes offer in principle much better service, enabling larger systems to be treated. Compared to the cost of a GGA calculation like PBE, dispersion corrections such as D3(BJ) require very little computer time, although D3(ABC), which scales as  $n^3$ , could consume a significant amount. The TS method is also very efficient, whilst vdW-DF does cost significant time but only of



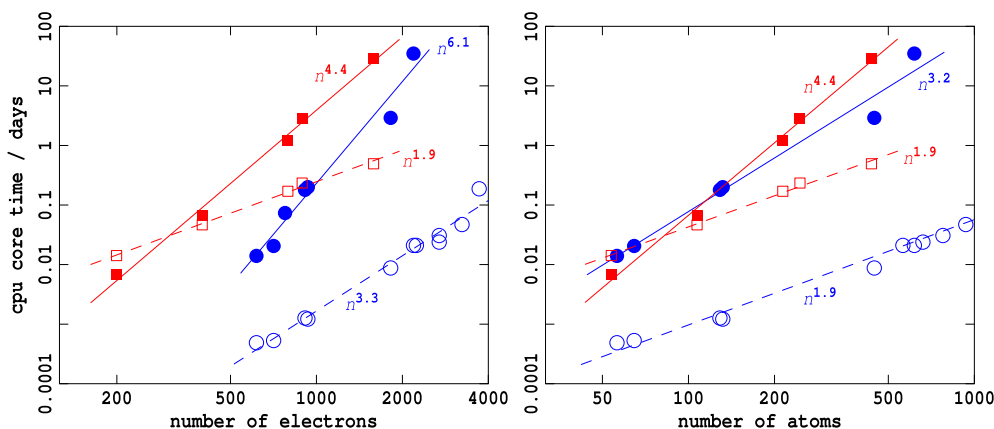


FIGURE 13.6 Scaling of the computer time per force calculation (using VASP) with the number of electrons or the number of atoms ( $n$ ) for PBE (dashed lines, open circles and squares) and for the MBD part of a PBE-MBD calculation (solid lines, filled circles and squares), fitted to yield scaling laws, for hBN solid (red squares) and for SAMs (blue circles).

the order of the original GGA calculation and hence is an efficient method. The MBD method offers inclusion of *all* Dobson-B many-body effects at only a cost scaling roughly as  $n^3$ , where  $n$  is specifically the number of atoms in the system [21].

The MBD method is, however, worth of special note as the prefactor multiplying its scaling is substantial, at least when evaluated using the current implementation in VASP [21], meaning that it could not be applied to many of the systems of interest described in this article. Methods like PBE in VASP have complicated scaling relating to the volume of the unit cell and the number of electrons. To capture the basic ideas, we plot in Fig. 13.6 the computer time required (in CPU core days) to complete one force calculation against either the number of atoms or the number of electrons. A log–log scale is used so that the slope of the resulting curves tells the power scaling law. Two series of data are plotted in the figure. One (in blue circles) is from calculations described in this paper on analogous series of SAMs, while the other (in red squares) is for some sample calculations on a much simpler system, hexagonal boron nitride (hBN) solid.

The PBE calculations (open circles and squares, dashed lines in Fig. 13.6) scaled as  $n^{1.9}$  versus the number of atoms for both sets of data, and again at  $n^{1.9}$  versus the number of electrons for the simple case of hBN solid. However, for the SAMs the way the vacuum region is treated influences the results, in this case leading to  $n^{3.3}$  scaling. However, the MBD calculations (filled circles and squares, solid lines) scale as  $n^{4.4}$  versus either number of electrons or atoms for hBN and at  $n^{3.2}$  versus atoms or  $n^{6.1}$  versus electrons for the SAMs. For significantly sized solids, MBD took 80 times more computer time than PBE, increasing to 3000 times more for SAMs. This result is significant as many-body effects become more important as system size grows. Larger systems allow more bodies to participate, perhaps demanding approaches like MBD to be used, but in these circumstances the MBD method unfortunately becomes impractical.

## 13.9 CONCLUSIONS

*Ab initio* computational methods that provide qualitatively correct descriptions of dispersion interactions associated with surface adsorption on arbitrary surfaces over a wide range of interaction distances [35,81–90] are very expensive, scaling formally at least by order  $n^6$  in system size, though embedding [58,85–87,90–95] and mixed DFT–*ab initio* [73,90,93,104–109] approaches can be effective in making calculations practical. Such methods are usually applied to situations involving very weak binding like noble gas or H<sub>2</sub> adsorption [83,90] or for extended conducting systems like graphene on metals [35,36], as well as when dissociation curves are required [87] and also for accurate lattice energies or phase transition energies [82, 84–87,89] of all types of solids. Using DFT-based approaches, a first-principles method is TDDFT [134,135] but this also scales formally as  $n^6$  and so again has been rarely applied. Methods including full or part  $n^6$ -scaling include Dobson-A, Dobson-B, and Dobson-C contributions to the simplest London description of the dispersion energy [20]. They also give the correct form of the results in the unified-atom limit. Much effort is now being spent in developing implementations of these methods that are fast enough for general practical use [72, 82–84,136]. Alternatively, the QMC *ab initio* method includes all these effects plus any other possible contribution but is expensive and scales (*only*) with the square of the desired absolute accuracy. Nevertheless, real QMC applications on interesting systems are currently possible [94,100–102], and, as it is a wavefunction-based method, any property of interest is readily calculable from the computational results.

However, in search of still more computationally tractable methods, a variety of combined *ab initio*/DFT approaches have been developed, as well as a range of more empirical DFT schemes, and we focus on the later in this review. All of the existing more empirical schemes currently omit Dobson-C corrections beyond those implicit in the base density functional, implying that they are not necessarily accurate for conducting systems. Despite this, they have been shown to be very useful for many properties of current interest when applied to many surfaces, including conducting ones. This is because these methods have been optimized, either directly through setting values of parameters or by choosing specific functional forms for involved terms, and/or indirectly by selecting specific density functionals with which the dispersion methods perform well for the desired applications. All computational methods need to be applied with caution, considering suitability to the intended application.

When considering suitability, the critical issues are how well the method treats the band gap (or lack thereof) of the system, and how well each Dobson term is treated. All modern approaches include Dobson-A corrections, either explicitly or implicitly. The Dobson-B many-body terms can also be treated explicitly, as in say MBD or, to a lesser extent, in D3(ABC), or else included through effective Dobson-A terms if the method is capable of recognizing the chemical environment and adapting. Such approaches may work well for short-range interactions but fail at long range. Likewise, approaches that recognize the chemical environment could include Dobson-C terms as effective Dobson-A terms. How profound the influence of the Dobson-B and Dobson-C terms can be must always be remembered, however, with screening, cooperatively, and nonlocal fluctuation effects being capable of increasing or decreasing the London dispersion energy by orders of magnitude. Hence how computational methods that adopt effective Dobson-A strategies recognize chemical environment becomes

critical. Perhaps the most advanced method of this type is XDM as the exchange-hole dipole moment upon which it is based is sensitive to the full chemical environment (see Chapter 5) [121,124]. On the other hand, the vdW-DF method is intended to evaluate the Dobson-A terms nonempirically and hence makes no allowance for Dobson-B or Dobson-C contributions (see Chapter 8) [20]. Detection of chemical environment is explicitly programmed into the D3-type methods for various common scenarios. Its applications therefore need always to be within the scope of this parameterization (see Chapter 6). In particular, it should be noted that the quality of the parameterization across the periodic table is not likely to be uniform, and that uncommon chemical environments may not be properly represented.

Of the three methods (vdW-DF, D3, and MBD) considered in detail in this review, the vdW-DF approach appears to be the least suitable as a robust method for evaluating surface adsorption. When used with the PBE density functional it gives poor results in general (Tables 13.3, 13.4, 13.5). It has been proposed for use with a variety of modified forms of PBE, in search of a functional that empirically could be found to give good results. In this vein, vdW-DF is used in its latest version [120] in conjunction with the old, quite poor, BP86 density functional. While improved descriptions of dispersion have been noted [105,150,151,252], the limitations of the underlying functional will necessarily be introduced. The method fails to include both Dobson-B and Dobson-C contributions to the dispersion energy and does not include enough explicit empiricism so as to be able to produce robust results for typical systems of interest. From a practical perspective, this method is also quite difficult to apply as in many existing implementations it required extensive parameter files to be generated and used as input to calculations, requiring much technical expertise. Its continued use is not recommended.

Always the PBE-MBD and PBE-D3(BJ) methods are found to give results in good agreement with experimental data, experimentally derived data, or CASPT2 calculations (Tables 13.3, 13.4, 13.5). Other studies have reported similar results, with perhaps MBD appearing to be slightly better [21], and as systems get larger, D3(BJ) will deteriorate. The striking feature is that these methods work at all when low-dimensional conducting systems are involved as they both ignore critical Dobson-C effects. The enhanced results for MBD come as it treats many-body dispersion effects better, which is especially important in systems with anisotropic geometries. To capture at least some of these effects it would seem good practice to routinely use D3(ABC) instead of D3(0) or D3(BJ), but this is not the current norm. D3(ABC) can even implicitly correct for intrinsic weaknesses in the description of short-range correlation within density functionals (see Chapter 5) [124]. However, that these methods typically work for low dimensional systems in close contact is now well established [21–38]. An empirical guide, originating in basic ideas of classical electrostatics, is that Dobson-B effects are important over length ranges in the order of the interobject separation  $d$ , perhaps explaining the success of D3(BJ) and D3(ABC). What is clear is that these empirical schemes have been parameterized to data involving close molecular interactions and successfully predict (usually via GGAs) this type of data in many systems within and without of the parameterization set. However, they will not correctly describe long-range interactions involving low-dimensional conductors, and so their application needs to be made with due caution, especially where attractive long-range forces may be enhanced by the geometry.

Since its inception, DFT has been applied to surface chemistry problems without regard for dispersive forces. Including them is not just about getting binding energies more accurate, or

even about the often more serious issue of getting binding geometries more accurate. The critical feature is that without proper treatment of dispersion, DFT is typically not capable of providing a qualitative description of surface binding. While in many cases the difference between a van der Waals bond and a covalent bond is obvious, this is not always the case. Here we focused on situations in which the distinction becomes blurred, with dispersive forces either adding to or else competing against traditional covalent-bonding scenarios. Dispersive forces have long been misinterpreted as covalent bonds concerning the stabilization of gold nanoparticles and surfaces by sulfur-bound ligands [172], with analogous recent results demonstrating the generation of valence tautomerization in cytochrome P450 [96]. Dispersive forces are strong enough to reconstruct the gold surface when bound to PHEN, and play a critical role in catalysis of benzene on Cu(100). In all these situations, understanding the strength, poor directionality (related more to atom–atom distances  $R$  rather than to coordination bond angles), and significance of van der Waals dispersion interactions is critical to basic chemical understanding of reactivity and structure.

## Symbols

$\Delta G$	Free energy of surface adsorption
$\Delta E$	Surface–adsorbate interaction energy
$R$	Interatomic distance
$d$	Inter-surface separation
$p$	Power-law scaling
$A$	Scaling coefficient in asymptotic scaling laws

## Acknowledgments

We thank Prof. John Dobson from Griffith University for his help in preparing this manuscript and the Chinese National Science Foundation for support through grant 1167040630.

## References

- [1] B. Dolinar, *Bull. Eng. Geol. Environ.* 74 (2015) 697–703.
- [2] C. Ding, D. Gong, P. Yu, J. Shao, M.E. Zhong, *Desalin. Water Treat.* (2016) 1–12.
- [3] N.A. Mamleeva, V.V. Lunin, *Russ. J. Phys. Chem. A* 90 (2016) 658–663.
- [4] B. Mu, A. Wang, *J. Environ. Chem. Eng.* 4 (2016) 1274–1294.
- [5] L. Li, L. Chen, H. Zhang, Y. Yang, X. Liu, Y. Chen, *Mater. Sci. Eng. C* 61 (2016) 158–168.
- [6] C. Peng, J. Liu, J. Zhou, *J. Phys. Chem. C* 119 (2015) 20773–20781.
- [7] L. Battezzati, C. Pisani, F. Ricca, *J. Chem. Soc. Faraday Trans. II* 71 (1975) 1629–1639.
- [8] J. Moreno, S. Aspera, M. David, H. Kasai, *Carbon* 94 (2015) 936–941.
- [9] M. Muruganathan, J. Sun, T. Imamura, H. Mizuta, *Nano Lett.* 15 (2015) 8176–8180.
- [10] C. Yelgel, *J. Appl. Phys.* 119 (2016) 065307.
- [11] R.G.A. Veiga, R.H. Miwa, A.B. McLean, *Phys. Rev. B* 93 (2016) 115301.
- [12] M. Farmanbar, G. Brocks, *Phys. Rev. B* 93 (2016) 085304.
- [13] M. Del Cueto, A.S. Muzas, G. Fuchsels, F. Gatti, F. Martín, C. Díaz, *Phys. Rev. B* 93 (2016) 060301.
- [14] L. Álvarez-Falcón, F. Viñes, A. Notario-Estévez, F. Illas, *Surf. Sci.* 646 (2016) 221–229.
- [15] S. Gautier, S.N. Steinmann, C. Michel, P. Fleurat-Lessard, P. Sautet, *Phys. Chem. Chem. Phys.* 17 (2015) 28921–28930.
- [16] V. Michaud-Rioux, L. Zhang, H. Guo, *J. Comput. Phys.* 307 (2016) 593–613.
- [17] H.J. Kulik, N. Luehr, I.S. Ufimtsev, T.J. Martinez, *J. Phys. Chem. B* 116 (2012) 12501–12509.

- [18] L.N. Zhang, F. Zahid, Y. Zhu, L. Liu, J. Wang, H. Guo, P.C.H. Chan, M.S. Chan, *IEEE Trans. Electron Devices* 60 (2013) 3527–3533.
- [19] P. Canfield, M. Dahlbom, J. Reimers, N. Hush, *J. Chem. Phys.* 124 (2006) 024301.
- [20] J.F. Dobson, *Int. J. Quant. Chem.* 114 (2014) 1157–1161.
- [21] T. Bucko, S. Lebegue, T. Gould, J.G. Angyan, *J. Phys. Condens. Matter* 28 (2016) 045201.
- [22] A. Tkatchenko, R.A. DiStasio, R. Car, M. Scheffler, *Phys. Rev. Lett.* 108 (2012) 236402.
- [23] V.G. Ruiz, W. Liu, A. Tkatchenko, *Phys. Rev. B* 93 (2016) 035118.
- [24] A. Tkatchenko, *Adv. Funct. Mater.* 25 (2015) 2054–2061.
- [25] A.M. Reilly, A. Tkatchenko, *Chem. Sci.* 6 (2015) 3289–3301.
- [26] R.J. Maurer, V.G. Ruiz, A. Tkatchenko, *J. Chem. Phys.* 143 (2015) 102808.
- [27] A. Ambrosetti, N. Ferri, R.A. DiStasio, A. Tkatchenko, *Science* 351 (2016) 1171–1176.
- [28] W. Reckien, F. Janetzko, M.F. Peintinger, T. Bredow, *J. Comput. Chem.* 33 (2012) 2023–2031.
- [29] W. Reckien, M. Eggers, T. Bredow, *Beilstein J. Org. Chem.* 10 (2014) 1775–1784.
- [30] D. Mollenhauer, C. Brieger, E. Voloshina, B. Paulus, *J. Phys. Chem. C* 119 (2015) 1898–1904.
- [31] R. Ovcharenko, Y.S. Dedkov, E. Voloshina, *J. Phys. Condens. Matter* 28 (2016) 364003.
- [32] J. Tesch, P. Leicht, F. Blumenschein, L. Gragnaniello, M. Fonin, L.E.M. Steinkasserer, B. Paulus, E. Voloshina, Y. Dedkov, *Sci. Rep.* 6 (2016) 23439.
- [33] A.A. Tonkikh, E.N. Voloshina, P. Werner, H. Blumtritt, B. Senkovskiy, G. Güntherodt, S.S.P. Parkin, Y.S. Dedkov, *Sci. Rep.* 6 (2016) 23547.
- [34] E. Voloshina, R. Ovcharenko, A. Shulakov, Y.S. Dedkov, *J. Chem. Phys.* 138 (2013) 154706.
- [35] E. Voloshina, *Phys. Rev. B* 85 (2012) 045444.
- [36] E. Voloshina, Y.S. Dedkov, *Phys. Chem. Chem. Phys.* 14 (2012) 13502.
- [37] Y.S. Dedkov, E.N. Voloshina, *J. Phys. Condens. Matter* 27 (2015) 303002.
- [38] Y.S. Dedkov, E.N. Voloshina, M. Fonin, *Phys. Status Solidi B* 252 (2015) 451.
- [39] H. Schmidbauer, A. Schier, *Chem. Soc. Rev.* 37 (2008) 1931–1951.
- [40] D.J. Liptrot, P.P. Power, *Nat. Rev. Chem.* 1 (2017) 0004.
- [41] J.D. Guo, D.J. Liptrot, S. Nagase, P.P. Power, *Chem. Sci.* 6 (2015) 6235–6244.
- [42] P.R. Schreiner, L.V. Chernish, P.A. Gunchenko, E.Y. Tikhonchuk, H. Hausmann, M. Serafin, S. Schlecht, J.E.P. Dahl, R.M.K. Carlson, A.A. Fokin, *Nature* 477 (2011) 308–311.
- [43] A.A. Fokin, L.V. Chernish, P.A. Gunchenko, E.Y. Tikhonchuk, H. Hausmann, M. Serafin, J.E.P. Dahl, R.M.K. Carlson, P.R. Schreiner, *J. Am. Chem. Soc.* 134 (2012) 13641–13650.
- [44] S. Grimme, P.R. Schreiner, *Angew. Chem. Int. Ed.* 50 (2011) 12639–12642.
- [45] E. Lyngvi, I.A. Sanhueza, F. Schoenebeck, *Organometallics* 34 (2015) 805–812.
- [46] J.P. Wagner, P.R. Schreiner, *J. Chem. Theory Comput.* 12 (2016) 231–237.
- [47] M.M. Hänninen, K. Pal, B.M. Day, T. Pugh, R.A. Layfield, *Dalton Trans.* 45 (2016) 11301–11305.
- [48] M. Kumar, R.V. Chaudhari, B. Subramaniam, T.A. Jackson, *Organometallics* 33 (2014) 4183–4191.
- [49] L.P. Wolters, R. Koekkoek, F.M. Bickelhaupt, *ACS Catal.* 5 (2015) 5766–5775.
- [50] L. Schweighauser, M.A. Strauss, S. Bellotto, H.A. Wegner, *Angew. Chem. Int. Ed.* 54 (2015) 13436–13439.
- [51] C.L. Wagner, L. Tao, E.J. Thompson, T.A. Stich, J. Guo, J.C. Fettinger, L.A. Berben, R.D. Britt, S. Nagase, P.P. Power, *Angew. Chem. Int. Ed.* 55 (2016) 10444–10447.
- [52] J.R. Reimers, M.J. Ford, S.M. Marcuccio, J. Ulstrup, N.S. Hush, *Nat. Rev. Chem.* 1 (2017) 0017.
- [53] S. Isoi, P. Dev, A.L. Friedman, R. Stine, J.T. Robinson, T.L. Reinecke, P.E. Sheehan, *ACS Nano* 8 (2014) 12410–12417.
- [54] J. Reimers, N. Hush, *J. Phys. Chem. B* 105 (2001) 8979–8988.
- [55] H.-Y. Kim, J.O. Sofo, D. Velegol, M.W. Cole, A.A. Lucas, *J. Chem. Phys.* 124 (2006) 074504.
- [56] A. Ruzsinszky, J.P. Perdew, J. Tao, G.I. Csonka, J.M. Pitarke, *Phys. Rev. Lett.* 109 (2012) 233203.
- [57] A.M. Reilly, A. Tkatchenko, *Phys. Rev. Lett.* 113 (2014) 055701.
- [58] M.J. Gillan, D. Alfè, P.J. Bygrave, C.R. Taylor, F.R. Manby, *J. Chem. Phys.* 139 (2013) 114101.
- [59] J. Reimers, R. Watts, M. Klein, *Chem. Phys.* 64 (1982) 95.
- [60] J.F. Dobson, A. Savin, J.G. Angyan, R.-F. Liu, *arXiv:1608.02660v2*, 2016.
- [61] R. Jaffe, *Phys. Rev. D* 72 (2005) 021301.
- [62] J.F. Dobson, A. White, A. Rubio, *Phys. Rev. Lett.* 96 (2006) 073201.
- [63] S. Lebègue, J. Harl, T. Gould, J.G. Ángyán, G. Kresse, J.F. Dobson, *Phys. Rev. Lett.* 105 (2010) 196401.
- [64] J.F. Dobson, T. Gould, G. Vignale, *Phys. Rev. X* 4 (2014) 021040.

- [65] R.F. Liu, J.G. Angyan, J.F. Dobson, *J. Chem. Phys.* 134 (2011) 114106.
- [66] M. Boström, B.E. Sernelius, *Phys. Rev. B* 61 (2000) 2204–2210.
- [67] D.B. Chang, R.L. Cooper, J.E. Drummond, A.C. Young, *Phys. Lett. A* 37 (1971) 311–312.
- [68] V.V. Gobre, A. Tkatchenko, *Nat. Commun.* 5 (2013) 2341.
- [69] F. Furche, *Phys. Rev. B* 64 (2001) 195120.
- [70] J. Jung, P. García-González, J.F. Dobson, R.W. Godby, *Phys. Rev. B* 70 (2004) 205107.
- [71] J.F. Dobson, T. Gould, *J. Phys. Condens. Matter* 24 (2012) 073201.
- [72] H. Eshuis, J. Bates, F. Furche, *Theor. Chem. Acc.* 131 (2012) 1084.
- [73] A.J. Misquitta, B. Jeziorski, K. Szalewicz, *Phys. Rev. Lett.* 91 (2003) 033201.
- [74] K.E. Riley, M. Pitoňák, P. Jurečka, P. Hobza, *Chem. Rev.* 110 (2010) 5023–5063.
- [75] R.G. Parr, D.P. Craig, I.G. Ross, *J. Chem. Phys.* 18 (1950) 1561–1563.
- [76] R.J. Buenker, J.L. Whitten, *J. Chem. Phys.* (1968) 5241–5244.
- [77] J.B. Foresman, M. Head-Gordon, J.A. Pople, M.J. Frisch, *J. Phys. Chem.* 96 (1992) 135.
- [78] C. Møller, M.S. Plesset, *Phys. Rev. A* 46 (1934) 618.
- [79] D. Hegarty, M.A. Robb, *Mol. Phys.* 38 (1979) 1795.
- [80] K. Andersson, P.Å. Malmqvist, B.O. Roos, *J. Chem. Phys.* 96 (1992) 1218–1226.
- [81] A. Grüneis, *J. Chem. Phys.* 143 (2015) 102817.
- [82] Z. Rolik, L. Szegedy, I. Ladjánszki, B. Ladóczki, M. Kállay, *J. Chem. Phys.* 139 (2013) 094105.
- [83] D. Usvyat, L. Maschio, M. Schütz, *J. Chem. Phys.* 143 (2015) 102805.
- [84] M. Del Ben, J. Hutter, J. VandeVondele, *J. Chem. Phys.* 143 (2015) 102803.
- [85] H. Stoll, B. Paulus, P. Fulde, *Chem. Phys. Lett.* 469 (2009) 90–93.
- [86] B. Paulus, *Phys. Rep.* 428 (2006) 1–52.
- [87] C. Müller, B. Paulus, *Phys. Chem. Chem. Phys.* 14 (2012) 7605–7614.
- [88] M. Marsman, A. Grüneis, J. Paier, G. Kresse, *J. Chem. Phys.* 130 (2009) 184103.
- [89] E. Voloshina, B. Paulus, *J. Chem. Theory Comput.* 10 (2014) 1698–1706.
- [90] M.P. de Lara-Castells, R. Fernandez-Perea, F. Madzharova, E. Voloshina, *J. Chem. Phys.* 144 (2016) 244707.
- [91] H. Stoll, *Phys. Rev. B* 46 (1992) 6700–6704.
- [92] H. Stoll, *J. Chem. Phys.* 97 (1992) 8449–8454.
- [93] M.P. de Lara-Castells, A.O. Mitrushchenkov, H. Stoll, *J. Chem. Phys.* 143 (2015) 102804.
- [94] G.H. Booth, A. Grüneis, G. Kresse, A. Alavi, *Nature* 493 (2013) 365–370.
- [95] L. Schimka, J. Harl, A. Stroppa, A. Grüneis, M. Marsman, F. Mittendorfer, G. Kresse, *Nat. Mater.* 9 (2010) 741–744.
- [96] P.K. Das, S. Samanta, A.B. McQuarters, N. Lehnert, A. Dey, *Proc. Natl. Acad. Sci. USA* (2016) 6611.
- [97] K. Eichkorn, O. Treutler, H. Öhm, M. Häser, R. Ahlrichs, *Chem. Phys. Lett.* 242 (1995) 652.
- [98] F. Weigend, M. Häser, *Theor. Chim. Acta* 97 (1997) 331.
- [99] C. Hättig, F. Weigend, *J. Chem. Phys.* 113 (2000) 5154–5161.
- [100] Y.S. Al-Hamdani, M. Ma, D. Alfè, O.A. von Lilienfeld, A. Michaelides, *J. Chem. Phys.* 142 (2015) 181101.
- [101] G.H. Booth, A.J.W. Thom, A. Alavi, *J. Chem. Phys.* 131 (2009) 054106.
- [102] M. Dubecký, L. Mitas, P. Jurečka, *Chem. Rev.* 116 (2016) 5188–5215.
- [103] F. Aryasetiawan, O. Gunnarsson, *Rep. Prog. Phys.* 61 (1998) 237.
- [104] M.P. de Lara-Castells, H. Stoll, B. Civalieri, M. Causa, E. Voloshina, A.O. Mitrushchenkov, M. Pi, *J. Chem. Phys.* 141 (2014) 151102.
- [105] M.P. de Lara-Castells, M. Bartolomei, A.O. Mitrushchenkov, H. Stoll, *J. Chem. Phys.* 143 (2015) 194701.
- [106] A. Heßelmann, G. Jansen, M. Schütz, *J. Chem. Phys.* 122 (2005) 014103.
- [107] A. Heßelmann, *J. Chem. Phys.* 128 (2008) 144112.
- [108] M. Pitoňák, A. Heßelmann, *J. Chem. Theory Comput.* 6 (2010) 168–178.
- [109] C. Tuma, J. Sauer, *J. Chem. Phys.* 143 (2015) 102810.
- [110] J. Hepburn, G. Scoles, R. Penco, *Chem. Phys. Lett.* 36 (1975) 451–456.
- [111] R. Ahlrichs, *Chem. Phys.* 19 (1977) 119–130.
- [112] L. Roskop, D.G. Fedorov, M.S. Gordon, *Mol. Phys.* 111 (2013) 1622–1629.
- [113] L. Goerigk, S. Grimme, *Phys. Chem. Chem. Phys.* 13 (2011) 6670–6688.
- [114] S. Grimme, S. Ehrlich, L. Goerigk, *J. Comput. Chem.* 32 (2011) 1456–1465.
- [115] J. Brandenburg, S. Grimme, *Top. Curr. Chem.* 345 (2014) 1–23.
- [116] L. Goerigk, C.A. Collyer, J.R. Reimers, *J. Phys. Chem. B* 118 (2014) 14612–14626.

- [117] S. Grimme, J. Antony, S. Ehrlich, H. Krieg, *J. Chem. Phys.* 132 (2010).
- [118] A.D. Becke, E.R. Johnson, *J. Chem. Phys.* 127 (2007) 154108.
- [119] M. Dion, H. Rydberg, E. Schröder, D.C. Langreth, B.I. Lundqvist, *Phys. Rev. Lett.* 92 (2004) 246401.
- [120] K. Lee, É.D. Murray, L. Kong, B.I. Lundqvist, D.C. Langreth, *Phys. Rev. B* 82 (2010) 081101.
- [121] T.S. Chwee, M.B. Sullivan, *J. Chem. Phys.* 137 (2012) 134703.
- [122] V.G. Ruiz, W. Liu, E. Zojer, M. Scheffler, A. Tkatchenko, *Phys. Rev. Lett.* 108 (2012) 146103.
- [123] W. Liu, V.G. Ruiz, G.X. Zhang, B. Santra, X. Ren, M. Scheffler, A. Tkatchenko, *New J. Phys.* 15 (2013) 053046.
- [124] M.S. Christian, A. Otero-de-la-Roza, E.R. Johnson, *J. Chem. Theory Comput.* 12 (2016) 3305–3315.
- [125] A. Tkatchenko, M. Scheffler, *Phys. Rev. Lett.* 102 (2009) 073005.
- [126] G. Kresse, J. Hafner, *Phys. Rev. B* 47 (1993) 558–561.
- [127] J.F. Dobson, J. Wang, B.P. Dinte, K. McLennan, M.L.E. Hung, *Int. J. Quant. Chem.* 101 (2005) 579–598.
- [128] A.J. Misquitta, R. Maezono, N.D. Drummond, A.J. Stone, R.J. Needs, *Phys. Rev. B* 89 (2014) 045140.
- [129] A.J. Misquitta, J. Spencer, A.J. Stone, A. Alavi, *Phys. Rev. B* 82 (2010) 075312.
- [130] M. Ernzerhof, *Chem. Phys. Lett.* 263 (1996) 499–506.
- [131] J.C. Sancho-García, C. Adamo, *Phys. Chem. Chem. Phys.* 15 (2013) 14581–14594.
- [132] L. Goerigk, S. Grimme, *WIREs Comput. Mol. Sci.* 4 (2014) 576–600.
- [133] L. Goerigk, S. Grimme, *J. Chem. Theory Comput.* 7 (2011) 3272–3277.
- [134] T. Olsen, K. Thygesen, *Phys. Rev. B* 88 (2013) 115131.
- [135] T. Gould, *J. Chem. Phys.* 137 (2012) 111101.
- [136] J. Erhard, P. Bleiziffer, A. Görling, *Phys. Rev. Lett.* 117 (2016) 143002.
- [137] E.R. McNellis, J. Meyer, K. Reuter, *Phys. Rev. B* 80 (2009) 205414.
- [138] C.T. Campbell, J.R.V. Sellers, *J. Am. Chem. Soc.* 134 (2012) 18109–18115.
- [139] M. Xi, M. Yang, S. Jo, B. Bent, P. Stevens, *J. Chem. Phys.* 101 (1994) 9122.
- [140] P.S. Bagus, K. Hermann, C. Wöll, *J. Chem. Phys.* 123 (2005) 184109.
- [141] X.-L. Zhou, M. Castro, J. White, *Surf. Sci.* 238 (1990) 215.
- [142] T.J. Rockey, M. Yang, H.-L. Dai, *J. Phys. Chem. B* 110 (2006) 19973–19978.
- [143] D. Syomin, J. Kim, B.E. Koel, G.B. Ellison, *J. Phys. Chem. B* 105 (2001) 8387–8394.
- [144] J. Lomas, C. Baddeley, M. Tikhov, R. Lambert, *Langmuir* 11 (1995) 3048.
- [145] R. Caputo, B.P. Prascher, V. Staemmler, P.S. Bagus, C. Wöll, *J. Phys. Chem. A* 111 (2007) 12778–12784.
- [146] A. Bilic, J. Reimers, N. Hush, R. Hoft, M. Ford, *J. Chem. Theory Comput.* 2 (2006) 1093–1105.
- [147] L. Ferrighi, G.K.H. Madsen, B. Hammer, *J. Chem. Phys.* 135 (2011) 084704.
- [148] K. Tonigold, A. Groß, *J. Chem. Phys.* 132 (2010) 224701.
- [149] K. Toyoda, Y. Nakano, I. Hamada, K. Lee, S. Yanagisawa, Y. Morikawa, *Surf. Sci.* 603 (2009) 2912–2922.
- [150] D.J. Carter, A.L. Rohl, *J. Comput. Chem.* 35 (2014) 2263–2271.
- [151] J. Matos, H. Yildirim, A. Kara, *J. Phys. Chem. C* 119 (2014) 1886–1897.
- [152] W. Liu, F. Maaß, M. Willenbockel, C. Bronner, M. Schulze, S. Soubatch, F.S. Tautz, P. Tegeder, A. Tkatchenko, *Phys. Rev. Lett.* 115 (2015) 036104.
- [153] H. Yildirim, T. Greber, A. Kara, *J. Phys. Chem. C* 117 (2013) 20572–20583.
- [154] F.A. Asmuruf, N.A. Besley, *J. Chem. Phys.* 129 (2008) 064705.
- [155] M. Mura, A. Gulans, T. Thonhauser, L. Kantorovich, *Phys. Chem. Chem. Phys.* 12 (2010) 4759–4767.
- [156] J. Wellendorff, A. Kelkkanen, J.J. Mortensen, B.I. Lundqvist, T. Bligaard, *Top. Catal.* 53 (2010) 378–383.
- [157] K. Toyoda, I. Hamada, S. Yanagisawa, Y. Morikawa, *J. Nanosci. Nanotechnol.* 11 (2011) 2836–2843.
- [158] L. Buimaga-Iarinca, C. Morari, *Theor. Chem. Acc.* 133 (2014) 1–11.
- [159] B. Liu, L. Cheng, L. Curtiss, J. Greeley, *Surf. Sci.* 622 (2014) 51–59.
- [160] Y. Zhao, D.G. Truhlar, *J. Chem. Phys.* 125 (2006) 194101.
- [161] J.P. Perdew, W. Burke, M. Ernzerhof, *Phys. Rev. Lett.* 77 (1996) 3865–3868.
- [162] B. Rogers, J. Shapter, M. Ford, *Surf. Sci.* 548 (2004) 29.
- [163] S. Lukes, S. Vollmex, G. Witte, C. Wöll, *J. Chem. Phys.* 114 (2001) 10123.
- [164] R. Chatterjee, Z. Postawa, N. Winograd, B. Garrison, *J. Phys. Chem. B* 103 (1999) 151.
- [165] J.P. Perdew, Y. Wang, *Phys. Rev. B* 45 (1992) 13244–13249.
- [166] J.P. Perdew, *Int. J. Quant. Chem.* 28 (1985) 497–523.
- [167] T. Komeda, Y. Kim, Y. Fujita, Y. Sainoo, M. Kawai, *J. Chem. Phys.* 120 (2004) 5347.
- [168] K.H. Frank, R. Dudde, E.E. Koch, *Chem. Phys. Lett.* 132 (1986) 83–87.
- [169] L. Triguero, L. Pettersson, B. Minaev, H. Gren, *J. Chem. Phys.* 108 (1998) 1193–1205.

- [170] P.F. Cafe, A.G. Larsen, W. Yang, A. Bilic, I.M. Blake, M.J. Crossley, J. Zhang, H. Wackerbarth, J. Ulstrup, J.R. Reimers, *J. Phys. Chem. C* 111 (2007) 17285–17296.
- [171] L. Pettersson, H. Gren, Y. Luo, L. Triguero, *Surf. Sci.* 408 (1998) 1.
- [172] J.R. Reimers, M.J. Ford, A. Halder, J. Ulstrup, N.S. Hush, *Proc. Natl. Acad. Sci. USA* 113 (2016) E1424–E1433.
- [173] M. Doering, H.-P. Rust, B. Briner, A. Bradshaw, *Surf. Sci.* 410 (1988) L736.
- [174] P. Maksymovych, D.C. Sorescu, J.T. Yates, *Phys. Rev. Lett.* 97 (2006) 146103.
- [175] R. Mazzarello, A. Cossaro, A. Verdini, R. Rousseau, L. Casalis, M.F. Danisman, L. Floreano, S. Scandolo, A. Morgante, G. Scoles, *Phys. Rev. Lett.* 98 (2007) 16102.
- [176] A. Cossaro, R. Mazzarello, R. Rousseau, L. Casalis, A. Verdini, A. Kohlmeyer, L. Floreano, S. Scandolo, A. Morgante, M.L. Klein, G. Scoles, *Science* 321 (2008) 943–946.
- [177] H. Häkkinen, *Nat. Chem.* 4 (2012) 443–455.
- [178] F. Cunha, Q. Jin, N.J. Tao, C.Z. Li, *Surf. Sci.* 389 (1997) 19.
- [179] R. Sardar, A.M. Funston, P. Mulvaney, R.W. Murray, *Langmuir* 25 (2009) 13840–13851.
- [180] G.J. Hutchings, M. Brust, H. Schmidbaur, *Chem. Soc. Rev.* 37 (2008) 1759–1765.
- [181] J.C. Love, L.A. Estroff, J.K. Kriebel, R.G. Nuzzo, G.M. Whitesides, *Chem. Rev.* 105 (2005) 1103–1169.
- [182] H. Schmidbaur, *Chem. Soc. Rev.* 24 (1995) 391–400.
- [183] G.M. Whitesides, P.E. Laibinis, *Langmuir* 6 (1990) 87–96.
- [184] M. Brust, J. Fink, D. Bethell, D.J. Schiffrin, C. Kiely, *J. Chem. Soc., Chem. Commun.* (1995) 1655–1656.
- [185] M. Brust, M. Walker, D. Bethell, D.J. Schiffrin, R. Whyman, *J. Chem. Soc., Chem. Commun.* (1994) 801–802.
- [186] P.J.G. Goulet, R.B. Lennox, *J. Am. Chem. Soc.* 132 (2010) 9582–9584.
- [187] L. Zhu, C. Zhang, C. Guo, X. Wang, P. Sun, D. Zhou, W. Chen, G. Xue, *J. Phys. Chem. C* 117 (2013) 11399–11404.
- [188] M.K. Corbierre, R.B. Lennox, *Chem. Mater.* 17 (2005) 5691–5696.
- [189] X. Ji, X. Song, J. Li, Y. Bai, W. Yang, X. Peng, *J. Am. Chem. Soc.* 129 (2007) 13939–13948.
- [190] J. Kimling, M. Maier, B. Okenve, V. Kotaidis, H. Ballot, A. Plech, *J. Phys. Chem. B* 110 (2006) 15700–15707.
- [191] J. Turkevich, P. Stevenson, J. Hillier, *Discuss. Faraday Soc.* 11 (1951) 55–75.
- [192] Y. Negishi, T. Tsukuda, *J. Am. Chem. Soc.* 125 (2003) 4046–4047.
- [193] D. Armstrong, Q. Sun, R. Schuler, *J. Phys. Chem.* 100 (1996) 9892–9899.
- [194] R.K. Chadha, R. Kumar, D.G. Tuck, *Can. J. Chem.* 65 (1987) 1336–1342.
- [195] P. Pyykkö, *Angew. Chem. Int. Ed.* 43 (2004) 4412–4456.
- [196] M. Jansen, *Chem. Soc. Rev.* 37 (2008) 1826–1835.
- [197] Q. Tang, D.-E. Jiang, *J. Phys. Chem. C* (2014) 10804.
- [198] T. Zaba, A. Noworolska, C.M. Bowers, B. Breiten, G.M. Whitesides, P. Cyganik, *J. Am. Chem. Soc.* 136 (2014) 11918–11921.
- [199] W. Kurashige, S. Yamazoe, M. Yamaguchi, K. Nishido, K. Nobusada, T. Tsukuda, Y. Negishi, *J. Phys. Chem. Lett.* 5 (2014) 2072–2076.
- [200] J. Yan, R. Ouyang, P.S. Jensen, E. Ascić, D.A. Tanner, B. Mao, J. Zhang, C. Tang, N.S. Hush, J. Ulstrup, J.R. Reimers, *J. Am. Chem. Soc.* 136 (2014) 17087–17094.
- [201] Y. Wang, Q.-J. Chi, J.-D. Zhang, N.S. Hush, J.R. Reimers, J. Ulstrup, *J. Am. Chem. Soc.* 133 (2011) 14856–14859.
- [202] P.D. Jadzinsky, G. Calero, C.J. Ackerson, D.A. Bushnell, R.D. Kornberg, *Science* 318 (2007) 430–433.
- [203] D.C. Sheppard, G.S. Parkinson, A. Hentz, A.J. Window, P.D. Quinn, D.P. Woodruff, P. Bailey, T.C.Q. Noakes, *Surf. Sci.* 605 (2011) 138–145.
- [204] P. Maksymovych, D.C. Sorescu, O. Voznyy, J.T. Yates, *J. Am. Chem. Soc.* 135 (2013) 4922–4925.
- [205] D. Fischer, A. Curioni, W. Andreoni, *Langmuir* 19 (2003) 3567–3571.
- [206] H. Grönbeck, A. Curioni, W. Andreoni, *J. Am. Chem. Soc.* 122 (2000) 3839–3842.
- [207] W. Andreoni, A. Curioni, H. Grönbeck, *Int. J. Quant. Chem.* 80 (2000) 598.
- [208] K. Hamaguchi, S. Machida, K. Mukai, Y. Yamashita, J. Yoshinobu, *Phys. Rev. B* 62 (2000) 7576.
- [209] M. Vargas, P. Giannozzi, A. Selloni, G. Scoles, *J. Phys. Chem. B* 105 (2001) 9509–9513.
- [210] Y. Yourdshahyan, H.K. Zhang, A.M. Rappe, *Phys. Rev. B* 63 (2001) 081405.
- [211] Y. Yourdshahyan, M. Rappe, *J. Chem. Phys.* 117 (2002) 825–833.
- [212] J. Gottschalck, B. Hammer, *J. Chem. Phys.* 116 (2002) 784–790.
- [213] R. Di Felice, A. Selloni, E. Molinari, *J. Phys. Chem. B* 107 (2002) 1151–1156.
- [214] A. Bilic, J. Reimers, N. Hush, *J. Chem. Phys.* 122 (2005) 094708.
- [215] J.R. Reimers, Y. Wang, B.O. Cankurtaran, M.J. Ford, *J. Am. Chem. Soc.* 132 (2010) 8378–8384.



- [216] J.-i. Nishigaki, R. Tsunoyama, H. Tsunoyama, N. Ichikuni, S. Yamazoe, Y. Negishi, M. Ito, T. Matsuo, K. Tamao, T. Tsukuda, *J. Am. Chem. Soc.* 134 (2012) 14295–14297.
- [217] Y. Wang, N.S. Hush, J.R. Reimers, *J. Phys. Chem. C* 111 (2007) 10878–10885.
- [218] Q. Chi, J. Zhang, J. Ulstrup, *J. Phys. Chem. B* 110 (2006) 1102–1106.
- [219] J. Zhang, A. Bilic, J.R. Reimers, N.S. Hush, J. Ulstrup, *J. Phys. Chem. B* 109 (2005) 15355–15367.
- [220] R. Ouyang, J. Yan, P.S. Jensen, E. Ascic, S. Gan, D.A. Tanner, B. Mao, L. Ni, J. Zhang, C. Tang, N.S. Hush, J.R. Reimers, J. Ulstrup, *ChemPhysChem* 16 (2015) 928–932.
- [221] Y. Wang, Q. Chi, N.S. Hush, J.R. Reimers, J. Zhang, J. Ulstrup, *J. Phys. Chem. C* 115 (2011) 10630–10639.
- [222] A. Chaudhuri, M. Odelius, R.G. Jones, T.L. Lee, B. Detlefs, D.P. Woodruff, *J. Chem. Phys.* 130 (2009) 124708.
- [223] J.R. Reimers, D. Panduwinata, J. Visser, Y. Chin, C. Tang, L. Goerigk, M.J. Ford, M. Sintic, T.-J. Sum, M.J.J. Coenen, B.L.M. Hendriksen, J.A.A.W. Elemans, N.S. Hush, M.J. Crossley, *Proc. Natl. Acad. Sci. USA* 112 (2015) E6101–E6110.
- [224] J.R. Reimers, D. Panduwinata, J. Visser, Y. Chin, C. Tang, L. Goerigk, M.J. Ford, M. Sintic, T. Sum, M.J.J. Coenen, B.L.M. Hendriksen, J.A.A.W. Elemans, N.S. Hush, M.J. Crossley, *J. Phys. Chem. C* 120 (2016) 1739–1748.
- [225] M.J.J. Coenen, D. den Boer, F.J. van den Bruele, T. Habets, K.A.A.M. Timmers, M. van der Maas, T. Khoury, D. Panduwinata, M.J. Crossley, J.R. Reimers, W.J.P. van Enckevort, B.L.M. Hendriksen, J.A.A.W. Elemans, S. Speller, *Phys. Chem. Chem. Phys.* 15 (2013) 12451–12458.
- [226] Y. Chin, D. Panduwinata, M. Sintic, T.J. Sum, N.S. Hush, M.J. Crossley, J.R. Reimers, *J. Phys. Chem. Lett.* 2 (2011) 62–66.
- [227] N. Katsonis, J. Vicario, T. Kudernac, J. Visser, M.M. Pollard, B.L. Feringa, *J. Am. Chem. Soc.* 128 (2006) 15537–15541.
- [228] J.R. Reimers, M.J. Ford, L. Goerigk, *Mol. Simul.* 42 (2015) 494–510.
- [229] U. Mazur, K.W. Hipps, *Chem. Commun.* 51 (2015) 4737–4749.
- [230] A. Bhattarai, U. Mazur, K.W. Hipps, *J. Am. Chem. Soc.* 136 (2014) 2142–2148.
- [231] F. Hu, Y. Gong, X. Zhang, J. Xue, B. Liu, T. Lu, K. Deng, W. Duan, Q. Zeng, C. Wang, *Nanoscale* 6 (2014) 4243–4249.
- [232] M.O. Blunt, J. Adisojojoso, K. Tahara, K. Katayama, M. Van der Auweraer, Y. Tobe, S. De Feyter, *J. Am. Chem. Soc.* 135 (2013) 12068–12075.
- [233] W. Song, N. Martsinovich, W.M. Heckl, M. Lackinger, *J. Am. Chem. Soc.* 135 (2013) 14854–14862.
- [234] B.J. Killian, J.Y. Kravitz, M.K. Gilson, *J. Chem. Phys.* 127 (2007) 024107.
- [235] D. Künzel, A. Groß, *Beilstein J. Nanotechnol.* 4 (2013) 269–277.
- [236] C. Meier, M. Roos, D. Künzel, A. Breitruck, H.E. Hoster, K. Landfester, A. Gross, R.J. Behm, U. Ziener, *J. Phys. Chem. C* 114 (2010) 1268–1277.
- [237] P.N. Nirmalraj, D. Thompson, H.E. Riel, *Sci. Rep.* 5 (2015) 10116.
- [238] W. Song, N. Martsinovich, W.M. Heckl, M. Lackinger, *Phys. Chem. Chem. Phys.* 16 (2014) 13239–13247.
- [239] A. Jahanbekam, S. Vorpahl, U. Mazur, K.W. Hipps, *J. Phys. Chem. C* 117 (2013) 2914–2919.
- [240] B.A. Friesen, A. Bhattarai, U. Mazur, K.W. Hipps, *J. Am. Chem. Soc.* 134 (2012) 14897–14904.
- [241] W.A. English, K.W. Hipps, *J. Phys. Chem. C* 112 (2008) 2026–2031.
- [242] Y. Miyake, T. Nagata, H. Tanaka, M. Yamazaki, M. Ohta, R. Kokawa, T. Ogawa, *ACS Nano* 6 (2012) 3876–3887.
- [243] T. Ikeda, M. Asakawa, K. Miyake, M. Goto, T. Shimizu, *Langmuir* 24 (2008) 12877–12882.
- [244] J. Otsuki, S. Kawaguchi, T. Yamakawa, M. Asakawa, K. Miyake, *Langmuir* 22 (2006) 5708–5715.
- [245] T. Ikeda, M. Asakawa, M. Goto, K. Miyake, T. Ishida, T. Shimizu, *Langmuir* 20 (2004) 5454.
- [246] R. Gutzler, T. Sirtl, J.F. Dienstmaier, K. Mahata, W.M. Heckl, M. Schmittel, M. Lackinger, *J. Am. Chem. Soc.* 132 (2010) 5084–5090.
- [247] T. Sirtl, W. Song, G. Eder, S. Neogi, M. Schmittel, W.M. Heckl, M. Lackinger, *ACS Nano* 7 (2013) 6711–6718.
- [248] W. Song, N. Martsinovich, W.M. Heckl, M. Lackinger, *Chem. Commun.* 50 (2014) 13465–13468.
- [249] W.D. Cornell, P. Cieplak, C.I. Bayly, I.R. Gould, K.M. Merz Jr., D.M. Ferguson, D.C. Spellmeyer, T. Fox, J.W. Caldwell, P.A. Kollman, *J. Am. Chem. Soc.* 117 (1995) 5179–5197.
- [250] A.D. Becke, *J. Chem. Phys.* 98 (1993) 5648–5652.
- [251] F. Floris, J. Tomasi, J.L. Pascual Ahuir, *J. Comput. Chem.* 12 (1991) 784–791.
- [252] K. Lee, K. Berland, M. Yoon, S. Andersson, E. Schröder, P. Hyldgaard, B.I. Lundqvist, *J. Phys. Condens. Matter* 24 (2012) 424213.

# Noncovalent Interactions in Nanotechnology

Valentino R. Cooper<sup>\*</sup>, Christopher N. Lam<sup>†</sup>,  
Yangyang Wang<sup>†</sup>, Bobby G. Sumpter<sup>†</sup>

<sup>\*</sup>Materials Science and Technology Division, Oak Ridge National Laboratory, Oak Ridge, TN, USA <sup>†</sup>Center for Nanophase Materials Science, Oak Ridge National Laboratory, Oak Ridge, TN, USA

## 14.1 INTRODUCTION

In his now famous lecture titled “*There is plenty of room at the bottom*” [1] Richard Feynman speculated that in the year 2000 scientists would look back and wonder why it was not until the 1960s that anybody began to seriously think about the role that controlling matter at the levels of atoms could play in shaping future technology. Indeed, it was not until the early 21st century that we saw an explosion in the study of nanomaterials (Fig. 14.1A). A nanomaterial is any material in which at least one of the dimensions is between 1 and 100 nm. Materials with only 1 dimension of nanoscale size encompass two-dimensional (2D) materials (i.e., extended in the other 2 dimensions) like graphene and its layered analogue graphite. Two-dimensional confinement gives rise to extended materials in 1 dimension such as nanowires and polymers. While confinement in 3 dimensions results in what are typically referred to as nanoparticles. But how small is a nanometer? The width of a typical human hair ( $\sim 100\ \mu\text{m}$ ) is roughly 100,000 times the size of a nanometer [2]! Manipulating and controlling matter at this level requires more advanced techniques than were available in the 1960s. Thus, it is no coincidence that the explosion in the field of nanoscience coincided with the advent of the electron microscope which made it possible to examine materials down to the level of atoms [3–6].

Nanoscience and the subsequent technologies that stem from it, e.g., nanotechnology, build from the fact that new properties and processes emerge when materials are confined at the nanoscale ( $<100\ \text{nm}$ ) [8]. At this length scale the quantum nature of a material is most evident. For example, gold—a noble metal—is typically inert to surface interactions, yet at the nanoscale, gold particles and supported thin films become highly reactive catalysts (Fig. 14.2) [9–12]. This reactivity has been attributed to a combination of factors such as the presence

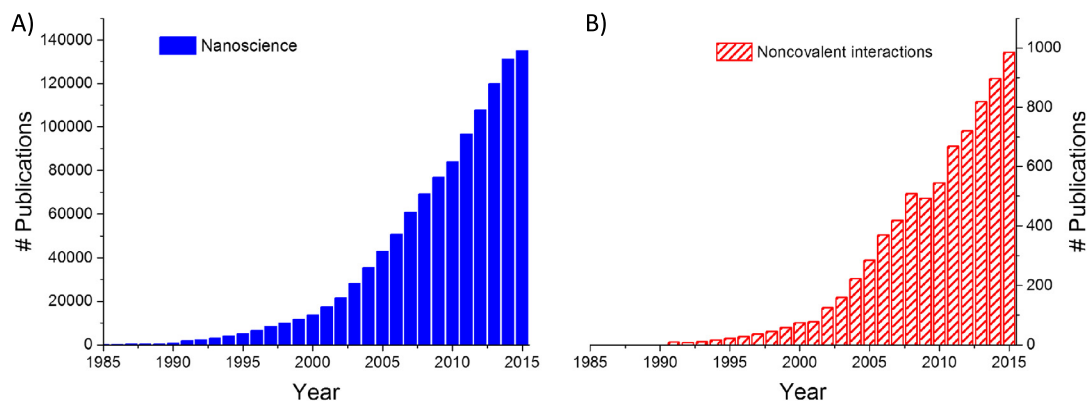


**FIGURE 14.1** (A) Total yearly publications in the field of nanoscience. (B) Publications in the field of nanoscience that reference any type of noncovalent interactions. Data for the years 1945–2015 from Web of Science [7]. Copyright 2016 Thomson Reuters.

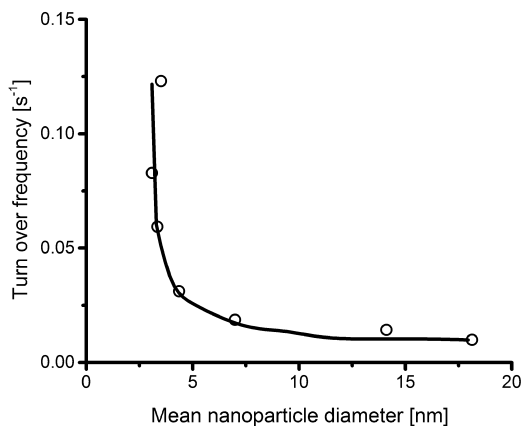


**FIGURE 14.2** Turnover frequency for CO oxidation (i.e., the rate of conversion of CO to CO<sub>2</sub>) on TiO<sub>2</sub>-supported Au nanoparticles as a function of nanoparticle mean diameter size. A strong enhancement in turnover frequency can be observed for nanoparticles with smaller mean diameters. Open circles represent data extracted and replotted with permission from Ref. [10]. Copyright 1993 Academic Press.

of coordinatively unsaturated surface atoms (i.e., fewer nearest neighbors than in the bulk), quantum size effects which change the electronic band structure (resulting in an emptying of the ordinarily filled gold *d*-orbitals) and/or charge transfer between the gold atoms and the underlying support material. Strikingly, gold is no longer its familiar yellow color at the nanoscale, rather it can be red or purple [8,13,14]. One interesting application of gold nanoparticles comes from the fact that they selectively accumulate in tumors [15–17], thereby making them ideal for imaging [18–21] and assisting in precise drug delivery to unwanted cells [22–27].

A hallmark of nanomaterial systems is the fact that the distance between particle, 2D layers and/or 1D polymer chains is typically larger than, or comparable in size to, the nanomaterial itself. Even in solution, it is no longer true that solvent molecules or solvated ions are negligibly small compared to the nanoparticle or spacing between 2D layers or polymer strands. Under such conditions, noncovalent interactions can play a critical role in defining the structure of a material and what it can be used for. Noncovalent interactions binding layers of two-dimensional materials, like graphite, are responsible for the adsorption and uptake of small molecules in nanoporous materials, and are the driving force behind the self-assembly of organic molecules on surfaces. In this context, nanomaterials offer exciting potential for technological advances that could have positive impacts on our daily lives such as health and medicine (e.g., drug delivery), batteries, catalysts, hydrogen storage for alternative energy sources, carbon capture for the remediation of greenhouse gases, molecular sieves for processes such as water desalination, and molecular electronics [28–34].

Advances in theory (such as those discussed in Chapters 1–8) coupled with new capabilities, like the electron microscope which allow scientists to observe and control materials down to the nanometer [35], have brought new understanding to the role that noncovalent interactions play at the nanoscale and how these interactions can be manipulated to tune the functionality or response of a material [31,32]. Indeed, the study of noncovalent interactions in the context of nanomaterials has become exceedingly popular in the last decade (Fig. 14.1). This popularity mirrors developments in both theory (such as those for accounting for noncovalent interactions from a first principles perspective) and material growth techniques (as will be discussed in later sections of this chapter).

In this chapter, we discuss the importance of noncovalent interactions in the design of functional nanostructures (Fig. 14.3). We focus on providing an overview of application areas where noncovalent interactions are particularly important but spend less time on the theoretical specifics and computational aspects, since those are treated in great detail in other chapters. We start with a brief discussion of the various types of noncovalent interactions and their relevance for nanostructured systems. Section 14.3 then discusses advances in material growth techniques, while Sections 14.4 to 14.6 examine a subset of nanomaterials, highlighting the role of noncovalent interactions. Of particular interest when considering noncovalent interactions are layered, two-dimensional (2D) materials, nanoporous materials, soft matter and molecular crystal structures. Since molecular crystal structures are discussed extensively in previous chapters (see Chapters 10 and 11), this chapter will only explore the remaining classes of materials. Finally, we will conclude with a discussion on the outlook and challenges in nanomaterials as seen from the perspective of understanding and controlling noncovalent interactions.

## 14.2 RELEVANT NONCOVALENT INTERACTIONS

In general, small changes in the chemical structure of molecules or materials can result in large changes in the overall interaction energy between and within them and, consequently, can induce large changes in macroscopic structure, properties, and orientation. The intrinsic importance of weak, noncovalent interactions is evident even in polymer studies where

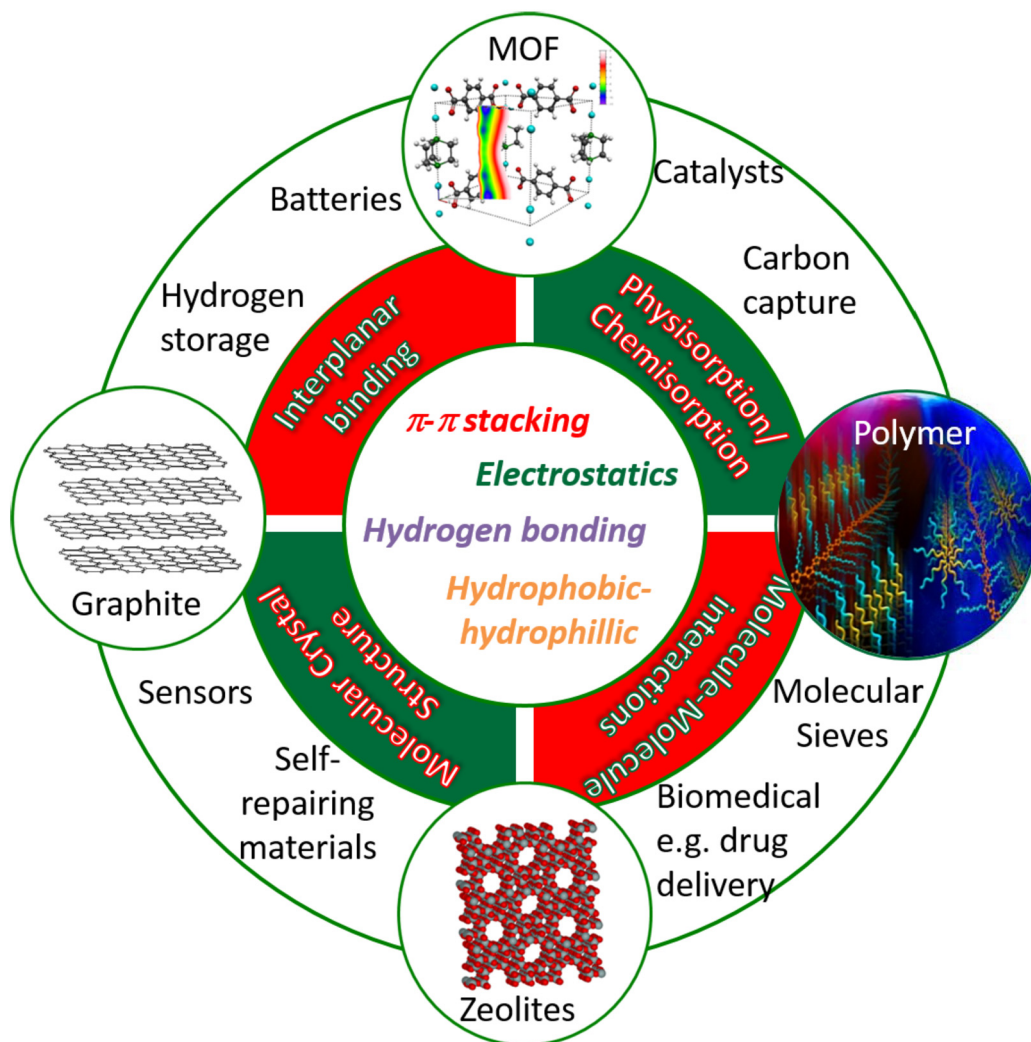


**FIGURE 14.3** Nanomaterials that enable nanotechnology through noncovalent interactions. The inner circle lists some of the relevant noncovalent interactions in nanotechnology. The middle circle lists the processes that these interactions facilitate. While the outer circle contains examples of applications. The bubbles depict some of the nanomaterials or nanostructures where noncovalent interactions play an important role.

the physical properties change as a function of the number  $n$  of a small repetitive unit such as  $-(\text{CH}_2)_n-$ ; here materials with even  $n$  can have very different properties from those with odd  $n$ . These so-called odd–even effects determine the properties of both bulk and nanoscale materials—for example, the stability and packing densities of self-assembled monolayers (SAMs) as well as the melting points of  $n$ -alkanes [36,37].

Important parameters governing the structural, thermodynamic and dynamic (diffusion or atomic reorganization due to bond disassociation and formation) properties of nanoscale materials include the strength and directionality of their noncovalent interactions. Compared to typical chemical bonds, which have bond strengths varying from 24 to 96 kcal/mol, noncovalent interactions are generally significantly weaker, having typical bond strengths of 2.4–15, 60, and 0–12 kcal/mol for hydrogen bonding, electrostatic, and  $\pi$ – $\pi$  interactions, respectively [38]. The range of hydrophobic interaction strengths is more difficult to quantify [38]. Bonds that are too weak will have extremely short lifetimes ( $\tau < 1 \mu\text{s}$ ), i.e., they will dissociate quickly and give rise to materials that lack any definite structure. Conversely, bonds that are too strong have appreciably long lifetimes ( $\tau > 1 \text{ min}$ ), thereby producing more rigid structures that do not exhibit interesting dynamical properties [28]. Intermediate bond lifetimes (those with energies on the order of a few  $k_B T$ , where  $k_B$  is Boltzmann's constant and  $T$  is temperature), however, manifest in many different ways. For instance, they allow for associating polymers to form large interconnected (supramolecular) networks with strong, yet reversible bonds [28,38].

The different types and strengths of noncovalent interactions lead to a myriad of applications found in nature and in synthetic materials, ranging from proteins to graphene and synthetic polymers. *Hydrogen bonding* is a unique case of dipole–dipole interaction in which a hydrogen atom covalently bonded to an electronegative atom is attracted to another nearby electronegative atom. Although relatively weak in comparison to covalent bonds, the importance of the hydrogen bond can be readily appreciated by its effect on the phase behavior of water, affording water with physical properties capable of sustaining life. Hydrogen bonding is also extremely important in biological systems, providing the attractions necessary to stabilize higher order structures in biomolecules such as DNA and proteins. *Hydrophobic interactions* result from attractions between nonpolar species in an aqueous environment. The intricately folded structures of enzymes are stabilized in part due to hydrophobic interactions, and the hydrophobic character of graphene also favors interactions with amphiphilic molecules that help stabilize the dispersion of individual graphene layers in aqueous or organic media.  $\pi$ – $\pi$  interactions have bond energies similar to those of hydrogen bonding, allowing interesting reversibly assembling dynamical systems. Although individual  $\pi$ – $\pi$  interactions are relatively weak, in an extended  $\pi$  system such as graphene, the overall strength of the many  $\pi$ – $\pi$  interactions can be strong [39–41]. These types of interactions generally require that molecules have  $\pi$ -conjugated systems and geometries/configurations amenable to overlapping  $\pi$  orbitals, which often include planar aromatic groups like benzene. The weak, reversible nature of  $\pi$ – $\pi$  interactions is important for numerous applications involving graphene-based nanostructures and molecular crystals, as stacking and packing due to these interactions can have significant effects on properties such as electrical conductivity and mechanical strength (see Chapter 9). *Electrostatic interactions* are able to provide stabilizing repulsive or attractive forces between point charges, and such interactions are often useful in systems involving charged molecules such as DNA, proteins, and polyelectrolytes.

### 14.2.1 Hydrogen Bonding

Hydrogen bonds are reversible (i.e., can form, break, and reform easily), directional, and have a range of strengths, thus making them suitable for the controlled design of nanoscale

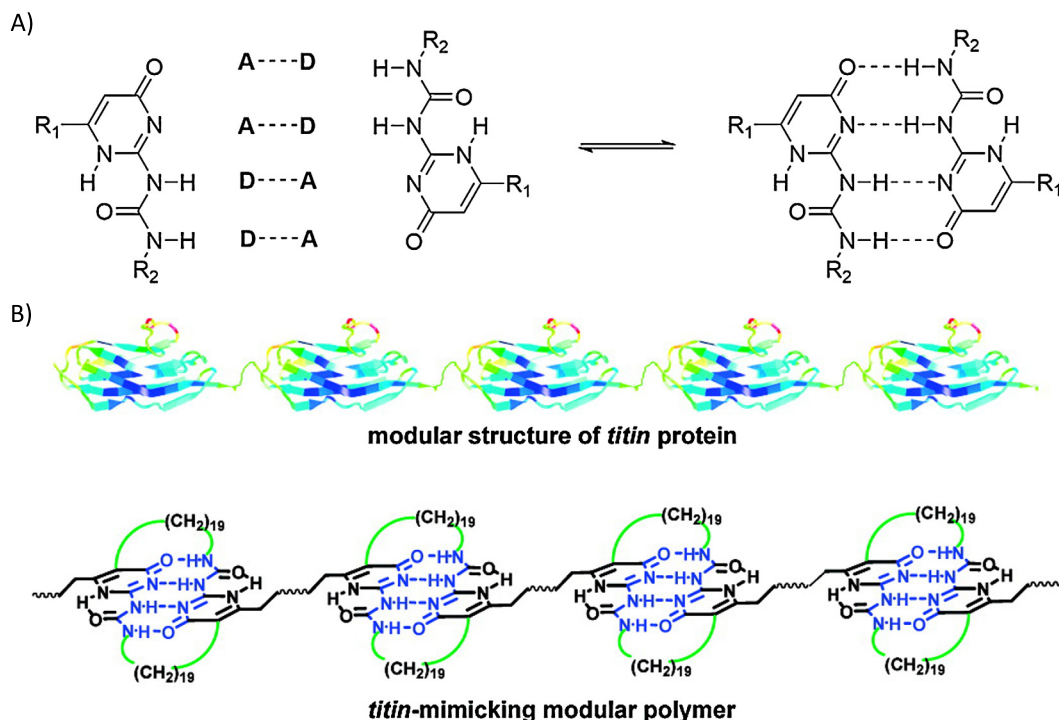


**FIGURE 14.4** (A) Schematic of dimerization equilibrium of 2-ureido-4-pyrimidone (UPy). “A” represents hydrogen acceptor and “D” represents hydrogen bond donor. (B) Schematic showing the design of a biomimetic linear polymer containing cyclic UPy groups to mimic the structure of the skeletal muscle protein titin. Reprinted with permission from Ref. [46]. Copyright 2009 American Chemical Society.

materials [42–44]. For example, the design of self-healing materials—materials capable of dynamical reorganization at the molecular level for self-repair in response to a defect or damage at the macroscopic scale—requires a judicious balance between material stiffness and dynamical bond reversibility. The relatively wide range of bond strengths accessible through different hydrogen bonding groups or moieties makes these interactions ideal for incorporation in self-healing materials. A good example of self-healing polymers based on extensive H-bonding are those developed by Leibler and coworkers using three motifs of urea-derived functional groups [45]. In addition to having similar mechanical properties to those of a soft rubber, this material demonstrated the ability to self-heal under ambient conditions [45]. The observation that the healing efficiency—the ability for broken network bonds to reform across the broken interface—was inversely proportional to the waiting time before two cut surfaces were brought together indicated that the self-healing was achieved through freely available H-bonding sites.

One well-known H-bonding motif is the 2-ureido-4-pyrimidone (UPy) that can form an array of quadruple hydrogen bonds in a self-complementary fashion (i.e., it can hydrogen-bond with itself; see Fig. 14.4A). Numerous supramolecular polymers have been developed

using the UPy association [47–52], and temperature can be used as a stimulus to disrupt the H-bonding interactions, thereby decreasing the viscosity and allowing for facile material processing or self-healing. One material based upon the UPy group has been commercialized under the product name SupraB. This material exhibits strong elastic behavior at room temperature and low viscous melt behavior at elevated temperatures. One specific application of SupraB involves dissolving the material in a suitable solvent, allowing it to be spray cast into flexible films of different thicknesses with excellent mechanical performance. Multiple cycles of spontaneous self-healing can be readily achieved by elevating the temperature to 140°C [53]. UPy hydrogen bonding interactions have also been incorporated into linear polymers to mimic the design of the skeletal muscle protein titin. Here, cyclic UPy dimers (Fig. 14.4B), without strong interactions that may interfere with the UPy hydrogen bonding interactions, were incorporated into the polymer structure, allowing the system to mimic the breaking and reforming of intramolecular interactions in titin. Such reversible intramolecular interactions allow the polymer to absorb energy as it breaks and reforms its bonds. As such, similar to titin, this biomimetic polymer possesses a combination of desirable properties including high modulus, toughness, and self-healing [46].

Additionally, hydrogen bonding systems using UPy associations have demonstrated material properties suitable for biomedical applications in protein and drug delivery as well as tissue engineering [54–56]. For such applications, the ability to control the release profile of the drug or protein is important for maintaining the appropriate concentration needed for treatment. Multiple hydrogen-bonded polymer networks have exhibited nonlinear behavior in their erosion and release profiles that can be tailored, making them potential systems for medical applications [57]. Through incorporation of the UPy associating moieties either along the polymer backbone or at the chain end, the stability of polymer network hydrogels can be controlled such that they remain stable for longer than two weeks or can be dissolved within days in a physiological salt solution, respectively, demonstrating that hydrogen bonding interactions in these associating polymer networks can be used to develop materials for either long-term or short-term delivery [58].

Hydrogen bonding interactions have also found utility in materials for applications in energy and electronics. Many rechargeable batteries become susceptible to mechanical fractures over multiple cycles and thus would benefit from self-repairing materials that incorporate noncovalent interactions such as hydrogen bonding networks. Bao, Cui, and coworkers [59], for example, developed an H-bonding polymer network to make a self-healing electrode for energy storage that retains a high capacity and that has a cycle life that exceeds those of state-of-the-art anodes made from silicon microparticles by ten-fold. Many self-healing materials are designed to repair mechanical properties, and fewer studies have focused on restoring high bulk electrical conductivity in materials for applications in electronics. Recently, Bao and coworkers combined a hydrogen-bonding polymer network with nickel microparticles to develop an electronic skin system [60] that, in addition to mechanical self-repair, also enabled the initial material conductivity to be repeatedly and rapidly restored with approximately 90% efficiency after a healing time of 15 seconds. Such electronic skin materials have potential as a human skin mimetic material that can be used in soft robotics and bioprosthetics [61,62].



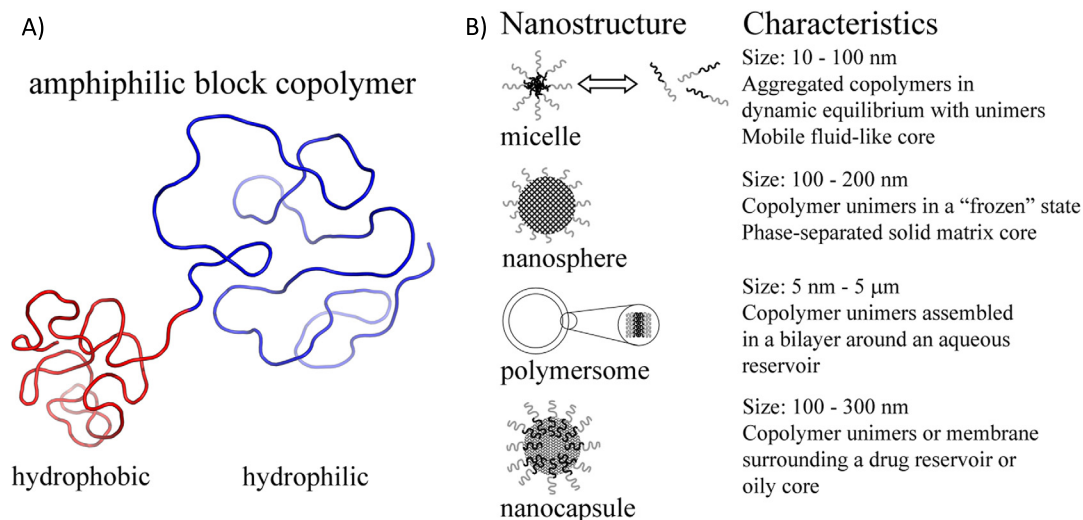


**FIGURE 14.5** (A) Schematic of an amphiphilic block copolymer. In aqueous solution, the hydrophilic block is well hydrated and swollen with solvent, while the hydrophobic block is in a collapsed configuration. (B) Nanostructures formed by amphiphilic block copolymers and their characteristics. Reprinted with permission from Ref. [63]. Copyright 2006 Elsevier B.V. All rights reserved.

## 14.2.2 Hydrophobic Interactions

Hydrophobes are nonpolar molecules that associate in aqueous solution to minimize the surface area in contact with water. The incorporation of hydrophobic blocks in block copolymer systems can lead to various nanostructuring. An amphiphilic diblock copolymer, for example, adopts a tadpole-like structure in aqueous solution where the hydrophilic block is in contact with the solvent and swells, while the hydrophobic block collapses to minimize contact with the solvent (Fig. 14.5). A critical micelle concentration (CMC) [63] exists at which these diblock copolymers will aggregate into micelles with a hydrophobic core and a hydrophilic corona, occurring at a concentration where the favorable energy of aggregation balances the concomitant loss in entropy [64]. In addition to forming micelles, numerous other nanostructures have been formed by amphiphilic block copolymers, including nanospheres, nanocapsules, and polymersomes, depending upon the block copolymer length, composition, molecular geometry, and on the methods of preparation (Fig. 14.5B) [63]. The micellization of amphiphilic block copolymers has been studied for the application of these self-assembled nanostructures as drug delivery vehicles [65–72]. In biomedical applications, amphiphilic block copolymers are often designed with biocompatible and biodegradable hydrophobic polymers such as polyesters or poly(amino acids) and hydrophilic polymers such as poly(ethylene glycol) (PEG), poly(*N*-vinyl-2-pyrrolidone), poly(2-ethyl-2-oxazoline), and poly(acrylic acid) [73–78].

Aside from using block copolymers with hydrophobic polymers, the introduction of a small fraction of hydrophobic groups along a polymer chain can have a significant impact on rheological behavior for application in oil recovery. In aqueous solutions, the hydrophobic

groups will associate, increasing the hydrodynamic size (apparent size of the dynamic hydrated/solvated “particle”) of the polymer, which leads to a subsequent increase in solution viscosity. This property allows water-soluble associating polymers to have great potential as mobility control agents in an oil reservoir containing brine of high salinity and high divalent ion concentration [79]. Additionally, the rheological properties of these associating polymers may also find useful application in drilling fluids and in conformance control applications [79]. Above the overlap concentration or critical aggregation concentration, intermolecular association through hydrophobic interactions results in a viscosity enhancement. Below the overlap concentration, however, intramolecular association is favored, which leads to a slight decrease in the viscosity. Bock et al. prepared copolymers of *N*-octylacrylamide and acrylamide [80] with varying hydrophobe content from 0 to 1 mol%. The intrinsic viscosity of these materials was observed to decrease with increasing hydrophobe content due to intramolecular association in dilute solution. In contrast, in the semidilute regime, a low amount of hydrophobe content increased the viscosity by orders of magnitude due to intermolecular association. The effect of hydrophobe content and type revealed the general trend that increasing the quantity of hydrophobic interactions enhances viscosity. The introduction of a small fraction of hydrophobic moieties in conventional water-soluble polymers used in oil recovery can significantly change their rheological properties and enhance their performance.

### 14.2.3 $\pi$ - $\pi$ Interactions

$\pi$ - $\pi$  stacking interactions arise between aromatic groups due to the intermolecular overlapping of *p*-orbitals in  $\pi$ -conjugated systems (Fig. 14.6). The relative weak bonding strength of  $\pi$ - $\pi$  interactions can be easily and reversibly disrupted by temperature, enabling supramolecular  $\pi$ - $\pi$  systems to have self-healing properties (thermoreversibility). Burattini et al. [83] reported the first synthesis of a self-healing polymer network based on the electronically complementary aromatic  $\pi$ - $\pi$  stacking interactions, using  $\pi$ -electron-rich pyrenyl endgroups of a polyamide to intercalate into folds of a polyimide with  $\pi$ -electron-deficient bis(diimide) motifs (Fig. 14.6). Similar to the temperature-induced self-healing properties of hydrogen-bonded supramolecular polymer networks, increasing temperature reversibly dissociates the  $\pi$ - $\pi$  interactions, facilitating chain mobility and spontaneous self-healing.

In a separate study, Burattini et al. [81] synthesized a pyrenemethylurea end-capped polymer that forms a thermoreversible self-healing material using similar  $\pi$ - $\pi$  stacking interactions with a polyimide. The novelty here is that the additional pair of hydrogen bonds from the urea NH groups to a single diimide carbonyl group reinforces the  $\pi$ - $\pi$  interactions (Fig. 14.6A, B), resulting in a significantly higher tensile modulus than the analogous purely hydrogen-bonded system [45]. Molecular mechanics simulations corroborated the synergistic effects of both  $\pi$ - $\pi$  stacking and H-bonding interactions in this system. An additional modification made to this supramolecular motif was to synthesize tweezer-type [84–88] bis-pyrenyl end groups (Fig. 14.6C, D) [82]. Increasing the number of associations with the polydiimide through this molecular design alteration enhanced the material’s tensile strength and increased the modulus of toughness and elongation to break compared to the polyamide with only pyrenyl endgroups.

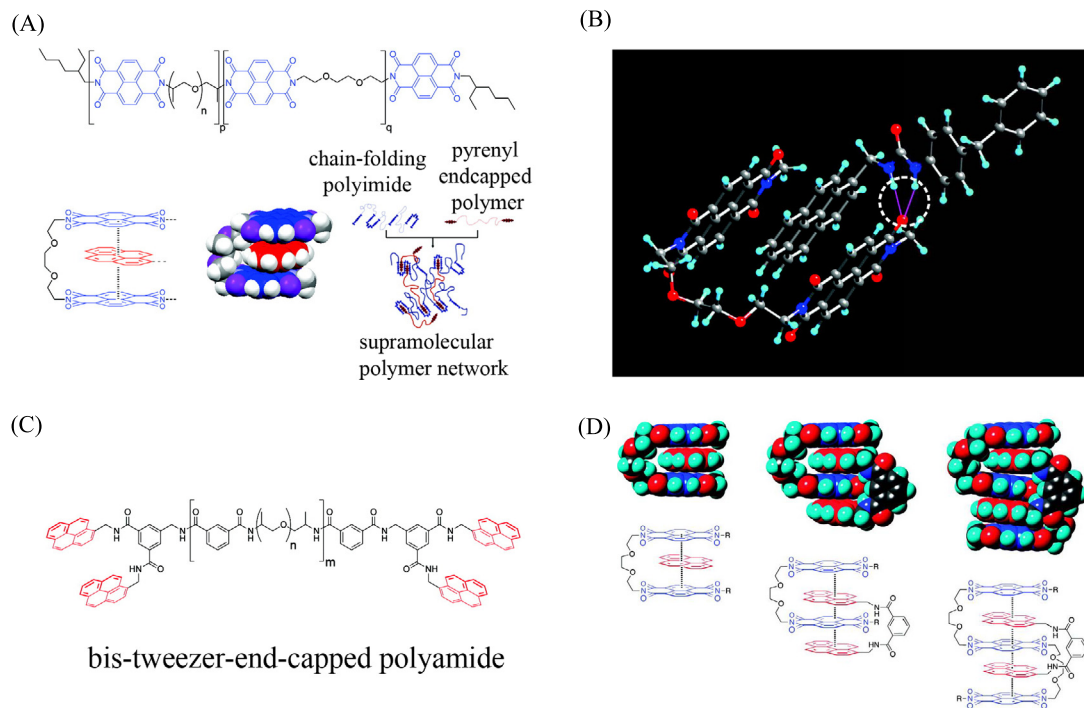


**FIGURE 14.6** (A) Chemical structure of a chain-folding polyimide shown at the top. Bottom shows the proposed structure and energy-minimized model of the electronically complementary  $\pi$ - $\pi$  stacking interaction between a bis(diimide) chain fold (represented by segment  $\eta$ ) and a pyrenyl residue; also shown is a schematic of a supramolecular network formed between the polyimide and a bis(pyrenyl) end-capped polymer. (B) Energy-minimized computational model of the interaction between a pyrenemethylurea end group of a polyurethane and a chain fold of the polyimide in (A). The lines shown in magenta represent a pair of strong, convergent hydrogen bonds between the urea and diimide carbonyl group. (C) Schematic of a bis-tweezer-end-capped polyamide. (D) Energy-minimized models for complexes formed between pyrene or a tweezer-type derivative (red) and naphthalene diimide oligomers (blue) containing two, three, or four face-to-face  $\pi$ - $\pi$  stacking interactions (color online only). (A) and (B) reprinted with permission from Ref. [81]. Copyright 2010 American Chemical Society. (C) and (D) reprinted with permission from Ref. [82]. Copyright 2011 American Chemical Society.

While associating polymer networks based upon  $\pi$ - $\pi$  interactions can form durable materials that can self-heal, most of the technological interest in  $\pi$ - $\pi$  stacking supramolecular networks is due to their potential use in supramolecular electronic applications at the nanometer scale, including field-effect transistors, photovoltaics, and light-emitting diodes. It has been well documented that material electrical behavior such as charge transport and conductivity can be improved significantly through the highly ordered alignment of functional molecules (see Chapter 9) [89–92]. A diverse set of  $\pi$ -conjugated polymers—polyaniline, polyacetylene, polypyrrole, polyphenylenevinylene, to name a few—have been used to fabricate self-assembled nanowires and nanofibers [93] to prototype nanosized field-effect transistors. However, it is difficult to achieve fine control of the supramolecular nanostructured dimen-

sions using polydisperse  $\pi$ -conjugated polymers. In this regard, monodisperse oligomers are more amenable to forming well-defined supramolecular architectures [94,95].

One system designed for nanoelectronics uses the self-complementary UPy associating groups to guide the self-assembly of  $\pi$ -conjugated oligo(*p*-phenylene vinylene) [96]. Molecules with specific architectures such as dendron rod-coils have also been demonstrated to form one-dimensional, well-defined nanoribbons with uniform width and thickness that can reach a length on the order of a micrometer via a cooperative effect from  $\pi$ - $\pi$  and H-bonding interactions for electronic applications. One-dimensional columnar stacking of molecules based upon the disc-like polycyclic aromatic hydrocarbon hexabenzocoronene (HBC) has been used to assemble fibers [97,98]. Xiao et al. [97], for example, synthesized contorted hexabenzocoronenes that organized into molecular stacks that further self-assembled into cables or fibers, and by using an elastomeric stamp, individual fibers were isolated for device alignment, enabling the development of field-effect transistors. While the development of functioning photovoltaic devices based upon supramolecular polymers is still nascent,  $\pi$ -conjugated polymers are promising for photovoltaic device applications. Supramolecular structures of perylene bisimide (electron-accepting) and oligo(*p*-phenylene vinylene) (electron-donating) have been self-assembled into fibers [99,100], incorporating both acceptor and donating components that demonstrated electron transfer upon photoillumination. Additional details on noncovalent interactions in molecular electronics may be found in Chapter 9.

#### 14.2.4 Electrostatic Interactions

Coulombic interactions are long-range noncovalent interactions that can lead to the self-organization of charged species reliably and easily at relatively low cost and with demonstrated utility in a broad range of applications. Electrostatic interactions between oppositely charged polyelectrolytes lead to the formation of polyion complex (PIC) micelles, also known as complex coacervate core micelles. PIC micelles are highly water soluble and can be formed between a pair of oppositely charged block copolymers [101,102] or by mixing an oppositely charged pair of block copolymers with a variety of polyelectrolytes, including vinyl polymers, poly(amino acid)s, oligonucleotides, and enzymes [103–107]. Enzymes are the quintessential catalysts, and their complexation in coacervate core micelles can lead to numerous pharmaceutical and biomedical applications. Harada and Kataoka, for example, demonstrated that electrostatic interactions between chicken egg white lysozyme and poly(ethylene glycol)-*b*-poly( $\alpha$ ,  $\beta$ -aspartic acid) can regulate the lytic activity of lysozyme as a molecular bioreactor through the formation and disassociation of complex core micelles by controlling the solution ionic strength [108]. Amphiphiles that are synthesized through noncovalent interactions, known as superamphiphiles, have recently garnered interest as stimuli-responsive self-assembling materials. An enzyme-responsive polymeric system has been developed using the negatively charged molecule adenosine 5'-triphosphate (ATP) and the double hydrophilic block copolymer methoxy-poly(ethylene glycol)-*b*-poly(L-lysine hydrochloride) (PEG-*b*-PLKC) to form a polymeric superamphiphile in aqueous solution; the addition of phosphatase hydrolyzes ATP, leading to the disassociation of the self-assembled supra-amphiphile [109]. The electrostatic complexation between positively charged lipids and DNA form highly organized packing motifs that are promising gene delivery vehicles

[110–112]. Other complexation systems involving biological or naturally occurring polyelectrolytes are promising candidates for the fabrication of drug delivery systems [113,114].

Electrostatic interactions can also lead to novel self-assemblies with interesting material properties. For example, an alginate-polyacrylamide hybrid gel combines both ionic and covalent crosslinks, leading to enhanced stretchability: Gels containing 90% water can be stretched beyond 20 times their initial length and have high fracture energies. Here, toughness of the hydrogel can be attributed to both noncovalent and covalent networks [115]. Electrostatic complexation between soybean lipids and cationic polyelectrolytes has led to the assembly of a phase with high extensibility and a high storage modulus  $G'$ , which is related to the elasticity of a material.  $G'$  was measured to be  $10^6$  Pa between  $10^\circ\text{C}$  and  $100^\circ\text{C}$  [116]. In this case, the particular self-assembled phase and material properties have been observed to be highly sensitive to lipid composition [117]. Materials with ultra-low surface tension have also been fabricated from the complexation of polyelectrolytes with fluorinated surfactants [118]. Guan et al. showed that oppositely charged dyes consisting of a cationic perylene diimide and a negatively charged copper-phthalocyanine tetrasulfonate formed one-dimensional chains [119], with discotic stacking stabilized by electrostatic interactions, demonstrating that using ionic interactions to assemble appropriately designed polymer chemistries can be used for electro-optic and solar cell devices.

## 14.3 GROWTH

---

Directing and controlling matter at the atomic scale is one of the grand challenges for science and technology in the 21st century [120]. Such unprecedented control can only be facilitated by a clear understanding of the interactions that define the properties of a material. In this regard, it is the advances in our grasp of noncovalent interactions which have led to the most successful new paths for the growth or fabrication of nanomaterials. Currently, there are two broad approaches used for the design of nanoscale systems, a top-down and a bottom-up approach [121].

### 14.3.1 Top-Down Approaches

Top-down approaches, as the name implies, involve the reduction of large structures “down to the nanoscale”. This is conceptually similar to the way that a sculptor forms a work of art that bears no resemblance to the stone slab it was carved from. As in the case of sculpting, top-down processes can be wasteful, i.e., they often require more starting matter than which ultimately ends up in the nanomaterial. Furthermore, top-down routes can be challenging as they often yield structures with difficult-to-predict physical, chemical, or electric properties. Two types of top-down approaches used to produce two-dimensional materials include the mechanical exfoliation technique popularized by Novoselov, Geim and collaborators for graphene [122–126] and a liquid exfoliation technique in which chemical solutions are used to etch off layers of the bulk material [127–130]. Both techniques depend on overcoming the noncovalent interactions that bind layers together and have been successful in isolating single layer flakes. However, as typical of top-down approaches for material growth, they

suffer from a lack of control; often resulting in multilayers in cases where only a single sheet is desired [35,131,132]. Nevertheless, these techniques have been extensively used to study materials properties and have led to a number of scientific breakthroughs, some of which will be discussed in the following sections.

### 14.3.2 Bottom-Up Approaches

Alternatively, the bottom-up approach involves the creation or “build-up” of nanomaterials and nanostructures from smaller units (i.e., atoms and molecules). Think LEGO® building blocks. These approaches utilize elements of molecular self-assembly which involve noncovalent intermolecular and substrate–molecule interactions. Such approaches also pose numerous difficulties rooted in the controlled self-assembly which often lead to unknown and often size-dependent macroscopic properties [133]. At the nanoscale, intramolecular interactions as well as molecule–substrate interactions remain poorly understood due to the presence of many-body interactions, particularly the weak, noncovalent interactions which are strongly influenced by the substrate’s atomic and electronic structure. Nevertheless, methods such as powder vaporization, molecular beam epitaxy (MBE), pulsed laser deposition (PLD), or chemical vapor deposition (CVD) have been successful in the design of a wide range of materials [134–142]. These methods have the advantage of being highly scalable, i.e., useful for growth both under experimental lab conditions and amenable to industrial manufacturing processes, but are susceptible to defects and imperfections due to extreme growth conditions [35].

Functional nanomaterials can also be fabricated from the bottom-up self-assembly of block copolymers [143], i.e., molecules that consist of two or more chemically distinct polymers. In a solution which is solvent selective for one of the constituent blocks (i.e., preferably dissolves one polymer over the other), different micellar nanostructures may form. Amphiphilic block copolymers, for example, are often designed to form core-shell micelles in aqueous environments for drug delivery with the drug loaded into the hydrophobic core. The ability to self-assemble into myriads of morphologies and nanostructures makes block copolymers fruitful building blocks for diverse applications—further details can be found in the literature [144,145]. Recently, studies incorporating proteins into protein-containing block copolymers have demonstrated hybrid protein–polymer conjugate molecules that retain the active functionality of the protein or enzyme and that can also self-assemble into useful nanostructures for addressing challenges in catalysis, energy, medicine, and defense, among others [146–148].

### 14.3.3 Alternative Approaches

A third approach for the design of nanostructures combines aspects of top-down with bottom-up technologies [121]. Here, complementary methods that use focused electron and ion-beams to grow and sculpt nanomaterials have demonstrated compelling alternative pathways to achieving atomically precise manufacturing of 3D structures in solids, liquids, and at interfaces (see Fig. 14.7). What sets these techniques apart is that electron and ion microscopies offer a platform that can often simultaneously observe structures at the nano and

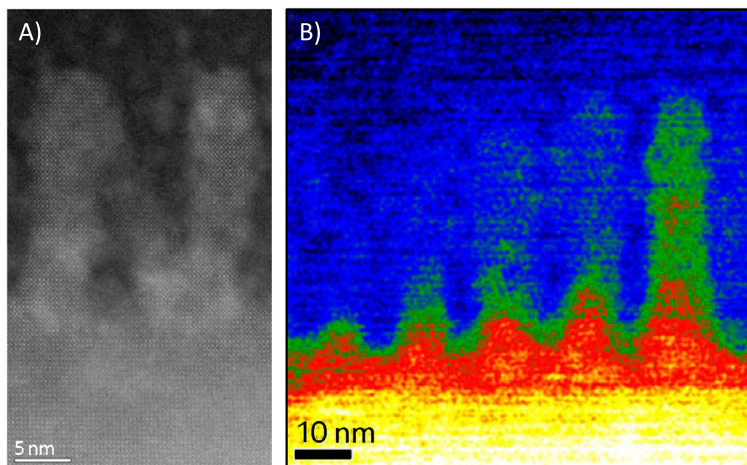


**FIGURE 14.7** (A) Patterned letter “N”, ~20 nm wide and 25 nm long, in clear epitaxial registry with the SrTiO<sub>3</sub> substrate. (B) High angle annular dark field-scanning transmission electron microscopy (HAADF-STEM) of the electron-beam-fabricated epitaxial SrTiO<sub>3</sub> rods highlighting the electron dose rate dependence of the growth. Reprinted with permission from Ref. [121]. Copyright 2016 American Chemical Society.

atomic scales as they are being produced thus allowing more control of structural rearrangements and chemical transformation *in situ* [149–151].

## 14.4 LAYERED MATERIALS

In 2004, Geim and Novoselov were able to, for the first time, separate graphite into individual layers of graphene [122,153]. Graphite, the prototypical layered material, is comprised of stacks of hexagonal sheets of covalently bonded carbon atoms (graphene, see Fig. 14.8A). Noncovalent interactions between the layers of graphene are important for many of graphite’s uses, such as lubricants and as the tips of pencils. Arguably, their experiment—in its simple beauty of using only adhesive tape and pencil leads—jump-started a new field of research into the properties of two-dimensional (2D) materials. The success of this Nobel prize-winning exfoliation technique [154] hinged on the fact that interactions between graphene sheets are primarily through London dispersion (or  $\pi$ - $\pi$  stacking) forces.

### 14.4.1 Graphene: A Prototype

Two-dimensional graphene is perfectly flat due to the  $sp^2$  bonding between C atoms arranged in a honeycomb (hexagonal) lattice (Fig. 14.8A). The strong  $\sigma$  bonding between the C  $s$ ,  $p_x$  and  $p_y$  orbitals are responsible for graphene’s superior mechanical properties. Graphene has a tensile strength (force required to pull it apart) of 130 GPa [155]; making it 100 times stronger than any comparably sized steel [154]. Remarkably, as pointed out in the Nobel prize

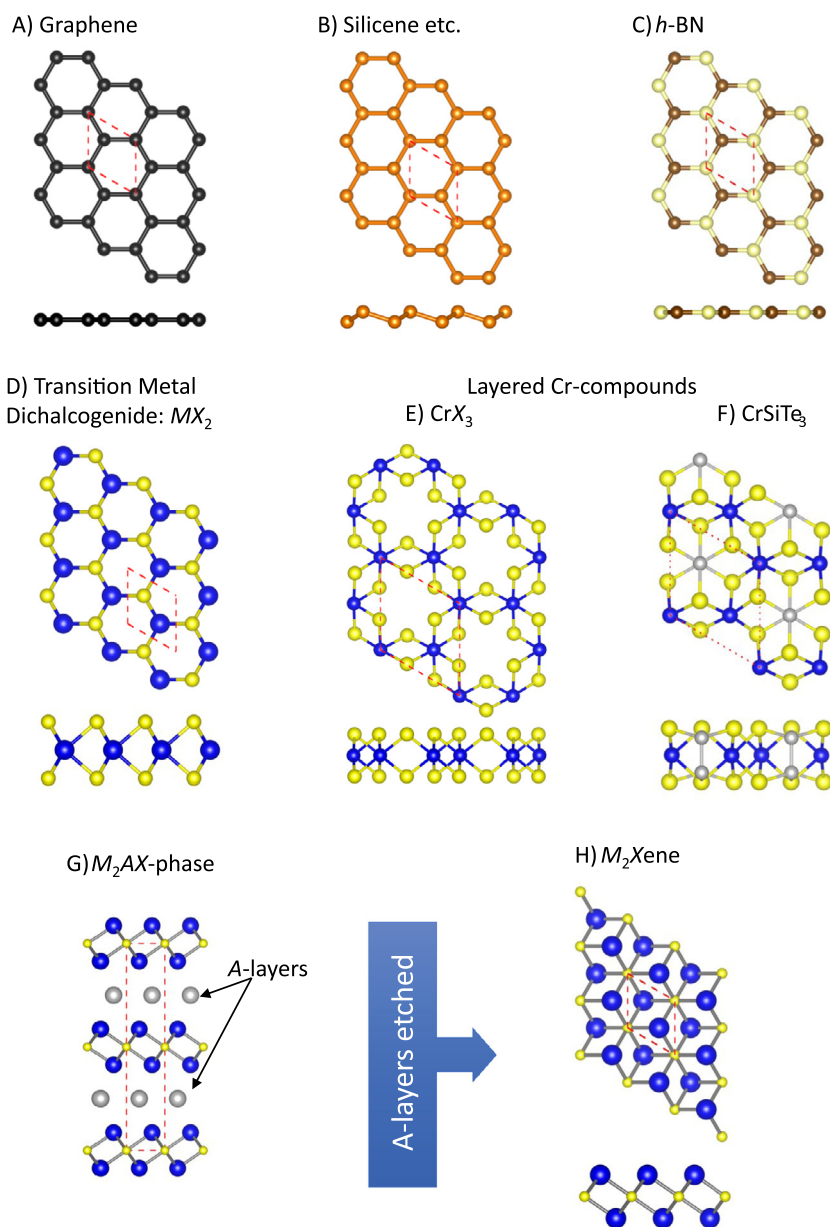


**FIGURE 14.8** Top and side views of the atomic structure of representative 2D materials. (A) Graphene, (B) silicene displaying the buckling found in many mono-elemental compounds such as germanene, stanene, and phosphorene, (C) hexagonal boron nitride (*h*BN), (D) a transition metal dichalcogenide with the formula  $MX_2$ . Structures (E)  $CrX_3$  and (F)  $CrSiTe_3$  are representative Cr-layered compounds. The bottom panel depicts a bulk (G)  $M_2AX$ -phase from which the *A*-layer is etched to form the 2D (H)  $M_2X$ -ene compound. In figures (D) to (H) *M* represents a transition metal depicted in blue, *X* are for the other nonmetal constituent depicted in yellow and gray atoms are for the *A* atom in the  $M_2AX$  and Si in  $CrSiTe_3$  (color online only). A similar figure can be found in Ref. [152].



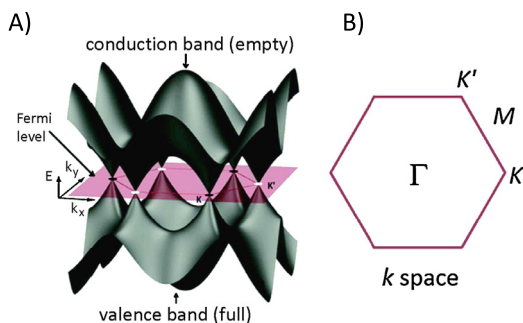


**FIGURE 14.9** (A) Schematic of the graphene band structure emphasizing the Dirac points at K and K'.  $E$  is energy of the bands, positive  $E$  signify empty bands while negative  $E$  are filled bands.  $k_x$  and  $k_y$  denote direction in  $k$  space. (B) Brillouin zone of graphene specifying the special  $k$ -points at M, K, and K'. Adapted with permission from Ref. [152]. Copyright 2012 IOP Publishing. All rights reserved.

announcement, a 1 m<sup>2</sup> hammock could support the weight of a 4 kg cat yet “would weigh less than [...] one of the cat’s whiskers” [154]!

The  $sp^2$  bonding and hexagonal arrangement of atoms also results in many unique optical and electronic features due to the  $\pi$  bonding between the remaining  $p_z$  orbitals. For instance, graphene absorbs very little light (only  $\sim 2.3\%$  of the total light intensity), which means that hammock would be invisible (or transparent) [156]. Of particular interest is the presence of the linear dispersion in the electronic band structure at K and K' in the graphene Brillouin zone (see Fig. 14.9) [157–159]. These so-called Dirac cones are of both fundamental and technological importance. From a basic scientific perspective, this unique electronic structure means that the electrons in graphene are massless charged fermions residing in 2D space [158]. Consequently, they are subject to unique relativistic behavior, which has a myriad of effects on the electronic transport and optical properties of these materials [158,160–164].

Another recent technological application of graphene involves the realization of nanopores in the sheet, thereby creating the thinnest possible sieve/membrane [165]. Such a membrane has been proposed for and used in applications ranging from the separation [166] of He<sup>3</sup> from He<sup>4</sup> to the removal of salt from sea water [167].

## 14.4.2 Beyond Graphene

The advent of graphene has sparked the discovery and predictions of many new “classes” of 2D materials. The ability to create many of these materials hinges upon the strength of the interlayer interactions in their bulk counterparts. One measure of the strength of this interaction is the exfoliation energy (i.e., the energy required to remove a sheet of graphene from the surface of graphite). Experiments based on the exfoliation of polycyclic aromatic hydrocarbons (PAHs also called polyaromatic hydrocarbons) from the graphite surface estimate the graphene exfoliation energy to be 5.02 kJ/mol per atom [39]. Interestingly, the quantum Monte Carlo value of 5.40 kJ/mol per atom for the graphite interplanar binding energy agrees remarkably well with experiment [40]. Another method of quantifying the magnitude of this interaction is to consider the cleavage energy for graphite. Recent experiments indicate that

**TABLE 14.1** Cleavage energies (in  $\text{J}/\text{m}^2$ ) obtained from theory and experiment for a number of two-dimensional materials

System	Method	$E_{\text{cleavage}}$	Ref.
Graphene	Experiment	0.37	[41]
Graphene	DFT:VV10 [170]	0.43	[168]
MoS <sub>2</sub>	DFT:VV10 [170]	0.27	[168]
CrI <sub>3</sub>	DFT:vdW-DF-optB86b [171]	0.30	[169]
CrSiTe <sub>3</sub>	DFT-D2 [172]	0.35	[173]
CrGeTe <sub>3</sub>	DFT-D2 [172]	0.38	[173]

the cleavage energy (i.e., the energy needed to cut bulk graphite in half) is close to  $0.37 \text{ J}/\text{m}^2$  [41]. Again, theoretical electronic structure calculations using density functional theory, for example, with the van der Waals density functional (vdW-DF; see Chapter 8) [168], are in excellent agreement with experimental values for cleavage energies (see Table 14.1). A survey of theoretical calculations on a range of known 2D materials shows that the cleavage energies are typically of the same magnitude [169]. These relatively weak interlayer nonbonding interactions facilitate the isolation of single or few layers of graphene and of many other 2D materials.

The first subset of beyond-graphene 2D materials falls into the general category of mono-elemental [174], single-atom-thick materials like graphene [122,153] and include silicene [175, 176], germanene [177], stanene [178], phosphorene [179], and borophene [180], where confinement to 2D introduces rather interesting and useful physical and mechanical properties. Unlike graphene and hexagonal boron nitride (*h*-BN, see Fig. 14.8C), these materials are not strictly 2D due to buckling in the layers (Fig. 14.8B). In many cases, alternative approaches to exfoliation are used to fabricate these materials. These mostly involve a bottom-up approach (Section 14.3.2) like the epitaxial growth of a single layer on a substrate and often mean that the substrate can have significant effects on the electronic, physical and chemical properties of the 2D material.

The above-mentioned substrate effect is perhaps best exemplified through the consideration of silicene on an Ag(111) substrate, where angle resolved photoemission spectroscopy (ARPES) [175] (an optical approach for experimentally probing the band structure of a material) results for silicene on Ag(111) suggested that the Dirac cone predicted for free standing (perfectly flat) [181,182] silicene would remain despite the buckling of Si atoms. Subsequent density functional theory calculations, however, showed that the observed linear dispersion was a consequence of states arising from hybridization between Ag and silicene, and thus not fundamental to the physical properties of the silicene sheet [176,183].

Given the desire to remove substrate effects, numerous approaches to the growth of single layer materials have been developed. These include the suspension of parts of the 2D sheet in order to create a “free standing” film as well as growth on other 2D materials [177,184,185]. Interestingly, theoretical predictions of the growth of 2D materials on other van der Waals structures have spawned a new field of van der Waals heterostructures [35,186,187]. This type of van der Waals heterostructures are comprised of alternating stacks of one or a few layers of two or more 2D materials. Not only do such heterostructures allow for decoupling of layers from the substrate but they also result in interesting electronic structure features. For ex-

ample, it was predicted that the growth of graphene on hexagonal boron nitride (*h*BN) could result in an opening of the band gap (effectively making graphene semiconducting) [132,188], a necessary step in using graphene as a replacement for silicon in electronic devices. Further predictions suggested that such an *h*BN substrate could also be used to decouple the electronic structure of 2D silicene from its underlying substrate, thereby allowing for more precise measurements of the physical properties of silicene [176]. These approaches emphasize the role of noncovalent interactions in the growth and characterization of layered materials.

Indeed, this vibrant field of study continues to evolve and other classes of layered materials with improved physicochemical and/or mechanical properties continue to be discovered. New types of layered materials include single and few layered transition metal dichalcogenides (TMDs) and their various lateral and vertical heterostructures [35,186,187]. TMD monolayers have the general formula  $MX_2$ , with one layer of *M* transition metal atoms (Mo, W, etc.) sandwiched between two layers of *X* chalcogen atoms (S, Se, or Te), see Fig. 14.8D. The fact that TMDs are semiconducting, i.e., have an electronic band gap, provides an intrinsic advantage for the use of these materials over graphene. These materials offer a large degree of flexibility in tuning their electro-optic properties. Similar to the monovalent materials, the creation of van der Waals heterostructures has been successfully used to tune their optical properties. Recent efforts have demonstrated that solid solutions of, for example, MoSe<sub>2</sub> and WSe<sub>2</sub>, can be used to tune the photoluminescence of these materials [189,190]. Even more relevant here, is the fact that the physisorption of molecules such as H<sub>2</sub>O and O<sub>2</sub> can also have profound effects on their electronic structure properties [191,192].

Another class of material are those derived from the group of layered compounds referred to as *MAX* phases:  $M_{n+1}AX_n$  (where  $n = 1-3$ , *M* is an early transition metal, *A* is typically a group 13 or 14 element, and *X* is C and/or N; Fig. 14.8G) [129-131,193]. The resulting class of 2D carbides or carbonitrides, *MX*-enes (Fig. 14.8H), can comprise 3, 5 or 7 atomic layers with various surface functionalization groups (e.g., -O, -OH, -F). This chemical diversity offers a great degree of tunability. *MX*-enes have been proposed for use in a vast number of applications such as energy storage, supercapacitors, fuel cells, and metal ion-batteries [131]. The layered Cr ternary (e.g., CrSiTe<sub>3</sub> and CrGeTe<sub>3</sub>; Fig. 14.8F) and binary (like CrX<sub>3</sub>, where *X* = halide; Fig. 14.8E) compounds have also generated recent interest [169,173,194-197]. These materials are magnetic, which is important for spin- and magneto-electronic applications [198]. Further interest arises from the possibility of discovering 2D ferromagnets in this class of materials [169,173,194-197].

## 14.5 NONCOVALENT INTERACTIONS IN NANOPOROUS MATERIALS

---

Porous media, i.e., materials characterized by voids encompassed by a network of solid material, have tremendous importance in the world around us. Sponges, bone, cement and ceramics are examples of macroporous materials that touch our daily lives. Similarly, porous materials with nanometer size pores are being used in a wide range of applications, including sensors, molecular sieves and catalysts. Recently, climate change concerns and alternative energy research has pushed the development of nanoporous materials for use as carbon cap-

ture and hydrogen storage media. Nanoporous media come in all shapes and sizes from bulk materials to single-atom thin molecular sieves.

In macroporous materials, the effect of the host material on properties such as catalytic activity and absorption can be correlated with the effective surface area of the pores [199,200]. However, as pore size becomes comparable to that of the adsorbed molecules, noncovalent interactions between the host material and adsorbates become important [201–204]. Fundamentally, the efficiency (i.e., selectivity, permeability, and rate of gas uptake) of nanoporous media depends on the interactions (in many cases noncovalent interactions) of small to moderate sized molecules with the host material as well as nanopore size and porosity [205–207].

### 14.5.1 Porosity

Porosity is a measure of the open spaces within a material. The density, size and connectivity of these voids or pores ultimately define uptake of small molecules, reactive surface area for catalytic reactions and selectivity (the preference to adsorb or filter one molecular species over another) of nanoporous materials. Modern characterization techniques have allowed for a wealth of understanding of how pores are arranged and connected. These methods run the gamut from scanning transmission electron microscopy (STEM) which probe local atomic arrangements to X-ray and neutron scattering techniques (in particular small angle neutron scattering, SANS) which provide information on the size, distribution and connectivity of pores [208,209].

A poignant example are nanoporous carbon materials which, although comprising the same material, can result in extremely different absorption behavior. STEM images and computational modeling techniques indicate that nanoporous materials are a mixture of  $sp^2$  (graphene like) and  $sp^3$  (diamond like) bonding [211–216]. At the atomic scale, STEM images highlight the presence of 5–7-membered rings (dislocations) which form grain boundaries (Fig. 14.10A, B) [210,217–220]. At larger length scales, it is evident that  $sp^2$  bonding tends to dominate the pore regions, while diamond-like bonding comprises the backbone of the host material. These observations have led to the practice of using expanded graphene as a model for computational exploration of absorption in these materials, where the pores are simply viewed as voids or slits between sheets of graphene or PAHs [221–224].

While the local structure features are common among many nanoporous carbons, different processing conditions and starting materials typically result in vastly different absorptive behavior [209,225]. For example, SANS studies have revealed that both ultra-microporous carbons (UMC) [226–228], created from wood-based, chemically activated material, and polyfurfuryl alcohol-derived activated carbon (PFAC), produced through activation with  $\text{CO}_2$  of a polymer precursor material, have pore-sizes on the order of  $\sim 1$  nm (see Fig. 14.10C). However, UMCs have nearly 4 times the  $\text{H}_2$  excess uptake than PFACs (Fig. 14.10D) [229,230]. (In this context, excess uptake refers to adsorption above the ideal gas absorption expected for a specific volume, temperature and pressure in the absence of interactions with the surrounding absorbing medium.)

Conversely, UMCs exhibit much slower (roughly tenfold) adsorption kinetics than PFACs. The difference in materials has been attributed to a combination of factors. These include the available (or effective Brunauer–Emmett–Teller, BET [200]) surface area, porosity and percentage of voids (i.e., pore volume density) [209,225]. UMC has both a larger BET surface area

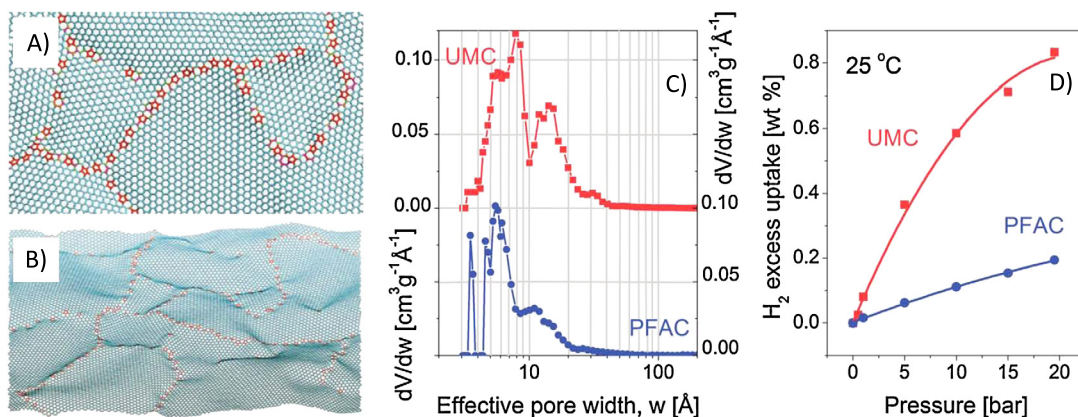


**FIGURE 14.10** Simulated defective graphene sheet (A) top view, (B) side-on view, illustrating the five to seven-membered ring dislocation structures (in red) observed in microscopy images. (C) Differential pore volume for ultra-microporous carbon (UMC) and for polyfurfuryl alcohol-derived activated carbon (PFAC). (D) Hydrogen adsorption isotherms for UMC and PFAC. In both (C) and (D) UMC are represented by red squares while PFAC data points are plotted with blue circles (color online only). Figures (A) and (B) reproduced with permission from Ref. [210]. Figures (C) and (D) reproduced with permission from Ref. [209]. Copyright 2013 Royal Society of Chemistry.

(2630 m<sup>2</sup>/g) and pore volume density (1.4 cm<sup>3</sup>/g) than PFAC (BET surface area, 1530 m<sup>2</sup>/g; pore volume density, 0.99 cm<sup>3</sup>/g) [229,230]. This is in-line with long standing findings which indicate that, for H<sub>2</sub> storage materials, there is an almost linear relationship between the BET surface area of a pore and the adsorption or H<sub>2</sub> uptake within that pore [199,200]. However, kinetics in these materials are more likely driven by the specific interactions of H<sub>2</sub> molecules and the pore surface which, in this case, arise due to noncovalent interactions.

### 14.5.2 Adsorption in Nanopores

In general, adsorption and diffusion of molecules within a pore are defined by a range of interactions. In some instances, like catalysts, adsorbates may chemisorb to a surface whereas gas uptake is often mediated by noncovalent interactions leading to physisorption. Understanding the role that noncovalent interactions play in adsorption processes requires building links between theory/computation and experiment. Yet, as discussed in earlier chapters, computational modeling of systems that have a combination of covalent/ionic bonding (host materials) and noncovalent interactions (such as those between neutral nonpolar molecules and the pore-structure) present unique challenges.

Initial strategies for modeling physisorption in porous media sought to use accurate quantum chemical methods (like those discussed in Chapters 3 and 4) to explore the interactions between molecules and fragments of the porous material. For example, quantum chemical calculations were employed to investigate the adsorption of hydrogen in metal–organic framework (MOFs) materials [232]. MOFs are comprised of metal clusters connected by organic linkers, which create networks of cavities or channel pores. However, due to computational limitations, these methods were only able to examine the interactions between

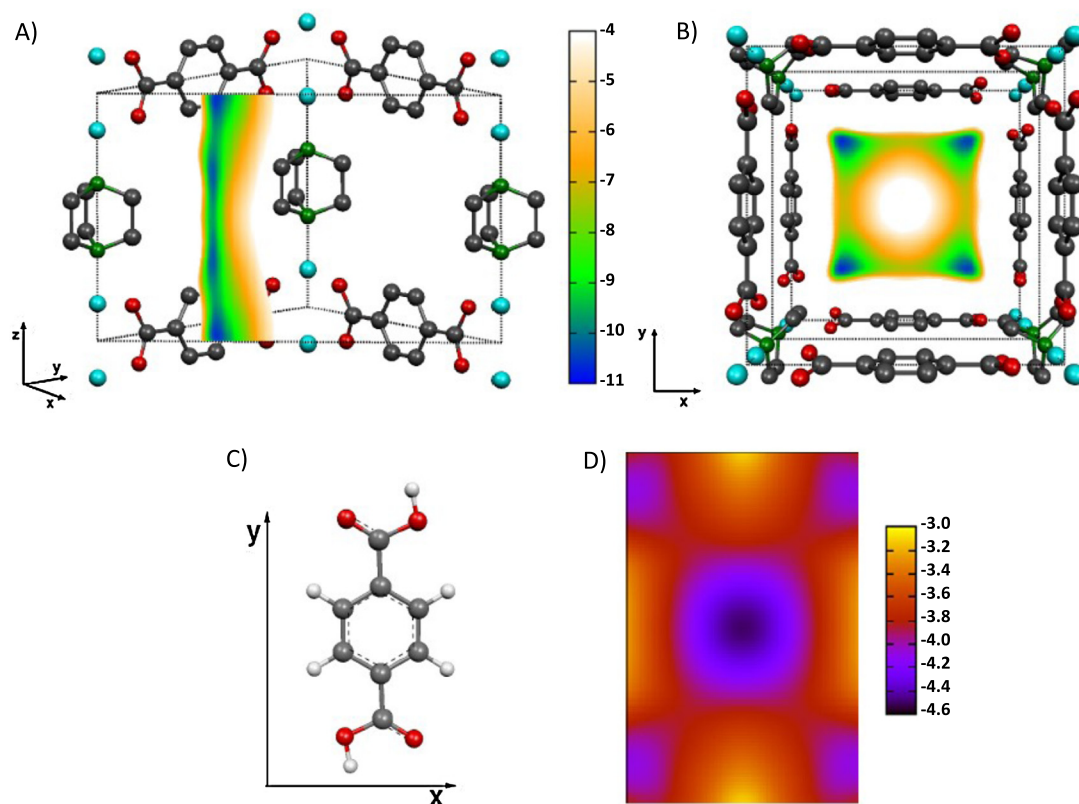


**FIGURE 14.11** (A) Diagonal side and (B) top views of the Zn(benzene dicarboxylate)(triethyl-diamine) MOF, showing a contour energy map of the strongest H<sub>2</sub> binding channel. (C) Structure of the benzene dicarboxylate (bdc) linker molecule. (D) Contour energy map of the bdc-H<sub>2</sub> binding energy showing the strongest binding sites are in the center of the isolated linker. All calculations were performed with the van der Waals density functional and all energies are in kJ/mol. Figures (A) and (B) reproduced with permission from Ref. [231]. Copyright 2010 Published by Elsevier B.V.

hydrogen molecules and linker fragments. Predictions examining the interactions between H<sub>2</sub> and the benzene dicarboxylate (bdc; C<sub>8</sub>H<sub>4</sub>O<sub>4</sub>, see Fig. 14.11C) linker found a bdc-H<sub>2</sub> interaction energy on the order of 4.5 kJ/mol (Fig. 14.11D). Based on this, it was estimated that isoreticular (IR) MOFs comprising solely the bdc linker would have a gravimetric storage density of 6.5 wt% or a volumetric storage density of up to 40 kg H<sub>2</sub>/m<sup>3</sup> [232]. Conversely, experiments on bdc containing MOFs showed only modest uptake. For example, only 2.1 wt% in Zn(bdc)(ted)<sub>0.5</sub> (where ted = triethyl diamine; C<sub>6</sub>H<sub>12</sub>N<sub>2</sub>) [233].

One source of the difference is the fact that the computational study did not take into account the presence of the ted-pillar molecule. Subsequent calculations employing the van der Waals density functional (discussed in Chapter 8) to study the full Zn(bdc)ted<sub>0.5</sub> MOF, further demonstrated that neglecting the full framework material not only resulted in an underesti-

mate of the magnitude of the interactions ( $\sim 11$  kJ/mol in the pore which is in agreement with the experimental heat of adsorption [234]), but could also result in the incorrect identification of the strongest binding sites (i.e., they form channels in the pore as seen in Fig. 14.11A, B) [231,234,235]. A common misconception has been that London dispersion interactions felt by a molecule in a pore could be constructed from the superposition of interactions derived from just the molecule and a single wall of that pore (e.g., the molecule and a single linker)—the so-called additive assumption. However, more recent studies now challenge the notion that dispersion interactions are additive [201–204] (i.e., do not scale as a superposition of interactions), thus advocating for full scale studies of the true porous material.

Accurate theoretical descriptions of noncovalent interactions have been fundamental in the ability to model and understand experimental characterization techniques such as infrared (IR) spectroscopy, X-ray scattering and nuclear-magnetic resonance (NMR) as well as the prediction of heats of adsorption [236–238]. Such collaborations between theory and experiment can be fundamental in providing insights into how noncovalent interactions assist in the mechanisms that result in the degradation of a material as well as those behind uptake, i.e., the interactions that control adsorption dynamics due to binding and diffusivity of molecules in pores. This knowledge can then be used in the design of new, more robust materials. For example, using IR spectroscopy and theory it was observed that noncovalent interactions, i.e., hydrogen bonding between water molecules and the MOF host material, were the leading cause of air sensitivity inducing the degradation of the MOFs. Using this information, first principles calculations were then able to predict that this effect could be avoided through the incorporation of hydrophobic fluoride ligands in the framework of the MOF. Remarkably, subsequent synthesis of the so-called fluorinated MOFs (F-MOFs) confirmed this prediction, demonstrating unprecedented air stability [239].

The chemisorption of molecules at surfaces and in nanopores presents yet another challenge for understanding and controlling molecular processes such as self-assembly and catalytic reactions. Take, for example, the adsorption of styrene molecules on the surface of the defective H-terminated Si surface. Despite the fact that the magnitude of the intermolecular noncovalent  $\pi$ - $\pi$  interaction is only  $\sim 15\%$  of the total molecule-substrate binding energy, it is the defining feature which determines styrene nanowire growth, turning a repulsive intermolecular interaction into and attractive one [240].

Numerous studies aimed at creating molecular devices and enhancing organic catalytic reactions and self-assembly have lead to the examination of noncovalent interactions between molecules and surfaces in cases where the molecule forms a chemical (typically covalent) bond with the surface. Many of these studies show that noncovalent interactions not only alter the arrangement of molecules relative to the surface, but this change can have profound effects on energy level alignment, which ultimately control the usefulness of a molecule in an integrated circuit or the binding strength of a molecule to a surface which may affect the rate of a chemical reaction [241–244].

Using a hybrid second order Møller-Plesset theory plus density functional theory (MP2:DFT or “periodic” MP2) approach, Tuma and Sauer examined the role of noncovalent interactions on the protonation of isobutane within a zeolite pore. Astonishingly, they found that the inclusion of noncovalent interactions through the periodic MP2 calculations resulted in substantial differences in the binding energies of reactants, products and transition states as compared to standard DFT (which notably at the time was unable to account for

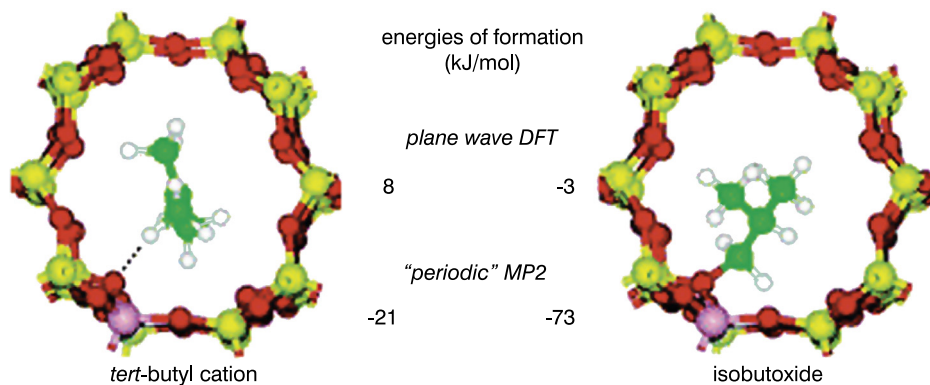


FIGURE 14.12 Formation energies for two different molecules in a zeolite pore using the hybrid MP2:DFT method (which accurately includes noncovalent interactions) and a standard DFT calculation (known to exclude noncovalent interactions). Reprinted with permission from Ref. [245]. Copyright 2006.

London dispersion interactions within the zeolite pore). For instance, using DFT the reactant *tert*-butyl molecules were predicted not to bind to the surface of the pore, while the periodic MP2 approach found a physisorbed state with a binding energy of 21 kJ/mol. Even more surprising was the fact that the adjustment was not the same for different reaction steps (see Fig. 14.12) [245]. The periodic MP2 method predicted a chemisorbed state for the final product with a binding energy of 73 kJ/mol, 70 kJ/mol larger than the DFT simulations which predicted a very weakly bound physisorbed state. The failure of some DFT methods in the initial studies of noncovalent molecule–surface interactions [243] has driven the redevelopment of approaches that account for noncovalent interactions within DFT. In particular, highlighting the need to treat the many-body nature of the nonlocal, noncovalent interactions [246] and giving insights into the nonadditivity of these interactions [203,204].

## 14.6 NONCOVALENT INTERACTIONS IN SOFT MATTER

Soft materials such as polymers, biomolecules, colloids, and gels are integral to a range of scientific and technological applications (Fig. 14.13) such as organic electronics, energy-harvesting organic photovoltaic devices (OPVs), new display and lighting technologies (OTFTs, OLEDs), new solid-state electrolytes and separation membranes, and advanced medical devices and therapies (implants, tissue engineering, drug delivery, personalized medicine, etc.); see Chapter 9. Soft materials are distinguished from traditional hard materials by the time and length scales involved in processes governing their behavior, and by their degree of disorder (e.g., mostly defects with a few crystals as opposed to mostly crystalline with a few defects).



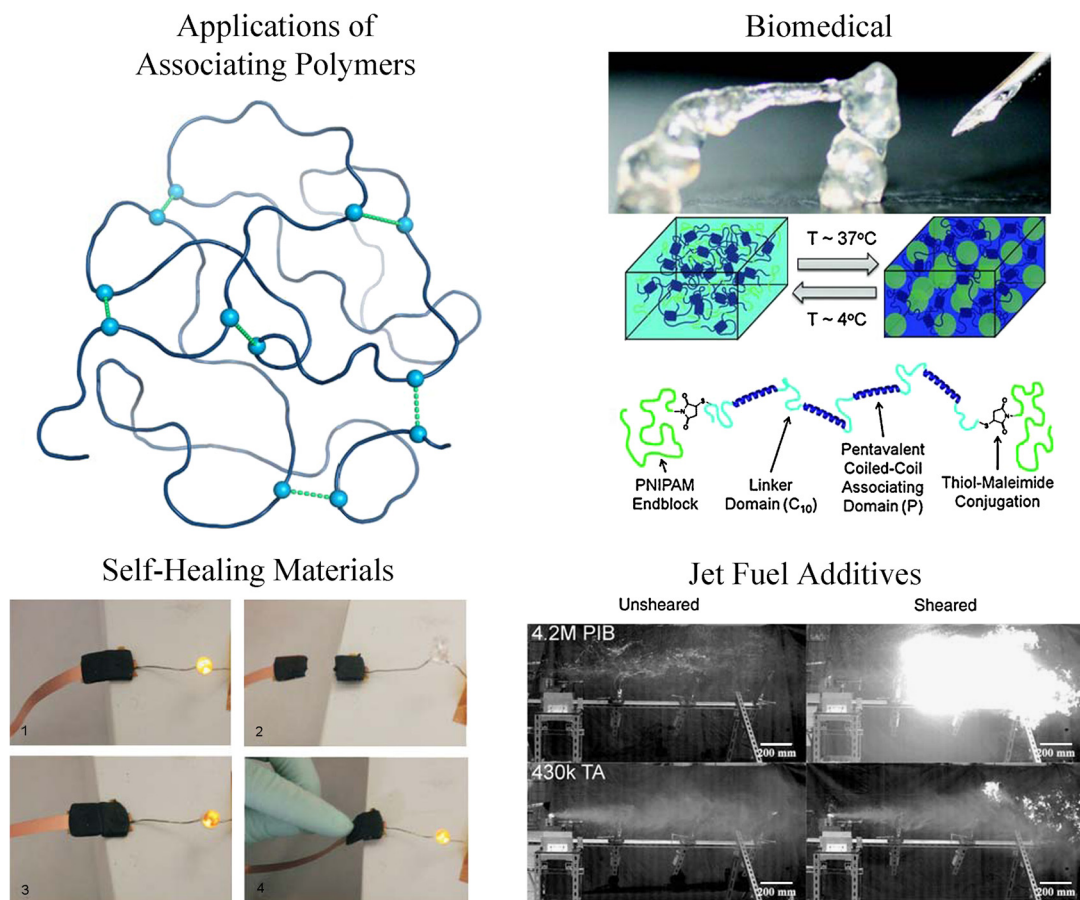


**FIGURE 14.13** Applications of associating polymer systems. (Top left) Schematic of a polymer with associating groups represented by spheres. (Bottom left) Electrical and mechanical self-healing capabilities of a self-healing polymer composite electrode for battery applications [59]. (Top right) Photograph of a shear-thinning injectable protein hydrogel developed from coiled-coil associations with rapid recovery [247]. Schematic of a protein-polymer block copolymer with poly(*N*-isopropylacrylamide) (PNIPAM) domains that hydrophobically collapse at physiological conditions designed to reinforce an injectable shear-thinning hydrogel network for biomedical applications [248]. (Bottom right) Ultralong polyisobutylene (PIB) (4200 kg/mol, 0.35 wt%) confers mist control that prevents flame propagation, but PIB loses efficacy after shearing. Long telechelic polymers with pairwise end-associations, however, provide mist control both before and after severe shearing [249]. *Bottom left reprinted with permission from Ref. [59]. Copyright 2013 Rights Managed by Nature Publishing Group. Top right reprinted with permission from Ref. [247]. Copyright 2010 American Chemical Society. Top right also reprinted with permission from Ref. [248]. Bottom right reprinted with permission from Ref. [249].*

### 14.6.1 Challenges in Polymer Physics Underpinned by Noncovalent Interactions

Polymers and their high processability, mechanical properties, and affordable price have found utility in and transformed numerous materials used in everyday applications. In-

spired by biological systems such as the cell cytoskeleton, which performs vital cell functions through reversible polymerization of its protein subunits, novel polymers that incorporate noncovalent interactions are garnering interest as synthetic analogs to these “smart” and responsive materials found in nature. An important aspect that helps advance the design and application of new bioinspired polymeric materials is a fundamental understanding of the physics governing their structure, dynamics, and behavior under different conditions.

An example that highlights the impact of polymer physics toward application can be seen in the fundamental studies and applications of stimuli-responsive polymers such as poly(*N*-isopropylacrylamide) (PNIPAM). PNIPAM exhibits solubility below a certain temperature, called the lower critical solution temperature (LCST). This behavior depends on parameters such as molecular weight and concentration. The polymer chain remains dissolved and solvated in water at low temperature, but at temperatures above the LCST (32°C), hydrogen bonds between water and PNIPAM are disrupted, leading to a hydrophobic collapse of the polymer. Through conjugation of stimuli-responsive polymers to proteins and enzymes, this coil-to-globule thermal transition is utilized for applications in affinity separations [250–252], enzymatic reactions [253–255], and biosensors [256]. For such applications, it is critical to understand the physics of the polymers under different environments, and many studies have focused on the molecular details of the coil-to-globule transition of PNIPAM, using scattering experiments and simulations, to guide experimental design [257–264].

Having a fundamental understanding of the general polymer physics governing the behavior of novel associating polymers, regardless of the diversity of noncovalent interaction types and strengths, will help guide and provide a rational framework for developing new functional materials. Understanding associating polymers, however, is more difficult than understanding polymers without any noncovalent interacting groups. For instance, depending upon the strength and quantity of the noncovalent interaction present per polymer chain and the concentration, a solution of associating polymers can macrophase-separate (like oil and water, the two phases separate completely).

Fig. 14.14A represents the qualitative temperature–concentration phase diagram of associating polymers. A coexistence curve separates a single-phase region and a two-phase, macrophase-separated region that contains a concentrated and a dilute phase. A transition exists within the single-phase window (dashed curve in Fig. 14.14A) between a liquid-like sol phase (dispersed clusters) and a physical gel phase (continuous three-dimensional network). The nature of the reversible transition from a solid to a gel, known as the reversible gelation transition—whether it is thermodynamic or not—has been a controversial topic for many decades. Many experimental and theoretical investigations have directed their efforts toward understanding gelation in associating polymers [266–280]. It is worth noting that the original Flory theory [266] does not predict the transition to be thermodynamic, and more recently, Semenov and Rubinstein developed a mean-field theory for associating polymers [280] and predicted that the gelation transition is not thermodynamic. Monte Carlo simulations corroborate the notion that reversible gelation is not a higher-order thermodynamic transition [281] and explains the similarity between gelation and the vitrification of typical liquids [282]. The gelation of associating polymers is more accurately viewed as a dynamic and connective transition that leads to a system with a percolating network that is constantly changing in size, shape, and connectivity over time.

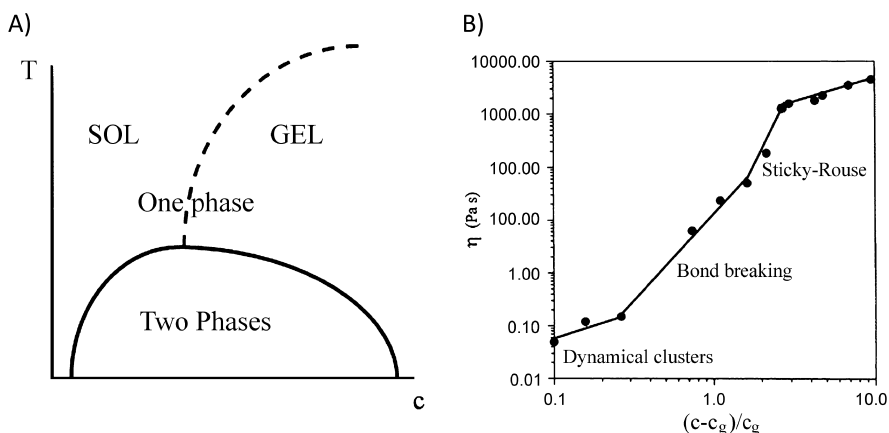


**FIGURE 14.14** (A) Schematic phase diagram of a solution of associating polymers. The coexistence curve separates the one-phase and two-phase regions. The gelation transition is shown as the dashed curve. (B) Measured viscosity of thermoreversible hydrogels of poly(ethylene oxide)-*b*-poly(propylene oxide)-*b*-poly(ethylene oxide)-*g*-poly(acrylic acid) as a function of concentration relative to the gelation concentration showing different rheological regimes. (A) and (B) reprinted with permission from Ref. [265]. Copyright 1999 Elsevier Science Ltd. All rights reserved.

The dynamical clustering and gelation of associating polymer networks with increasing concentration has a profound effect on their rheological and mechanical properties, leading to distinct rheological regimes. In dilute solutions of associating polymers well below their gel transition point, the system consists of small clusters that exist with a relaxation time that is shorter than the cluster lifetime—the time it takes for the noncovalent physical bonds holding the cluster together to break. Therefore, these clusters are similar to polymer clusters formed by irreversible chemical bonds, and the rheology in this regime is similar to that for chemical gelation [283–285]. As concentration and cluster size continue to grow, the cluster relaxation time and lifetime will increase and decrease, respectively, and the system will be composed of a polydisperse set of clusters that actively break and reform—the dynamical cluster regime [283,286]. In the vicinity of the gelation concentration, the rheology is governed by dynamical clusters that have grown to reach a crossover size, in which the lifetime and relaxation time are comparable. The clusters continue to grow until the point where elastic strands of the physical network become smaller than the crossover dynamical clusters but still remain larger than the individual chains, when the system relaxes by breaking critical bonds along the elastic strands; this is referred to as the bond breaking regime. At sufficiently high concentrations where a physical gel network is well developed, the sticky motion regime is delineated by strong intermolecular interactions, and the chains will experience multiple associations with the network. These bonds dominate the energy dissipation and relaxation time of the gel. These different regimes have been experimentally observed in viscosity measurements of hydrogels of poly(ethylene oxide)-*b*-poly(propylene oxide)-*b*-poly(ethylene oxide)-*g*-poly(acrylic acid) (Fig. 14.14B) [287].

In contrast to conventional covalently bonded polymers, the presence of molecular associations complicates the theoretical treatment of the dynamics of associating polymers. During

the past half century, the developments of the Rouse model [288] and the reptation model [289,290] have provided profound insight into the dynamics of unentangled and entangled polymer chains. It still remains unclear if and how much of our understanding of covalently bonded polymer dynamics may be generalizable to associating polymer systems. The goal is ultimately to have a unified theoretical framework that can relate the strength of noncovalent interactions, polymer chain rigidity, molecular weight, and other molecular parameters to the molecular level dynamics and macroscopic rheological behavior of associating polymers. Various models have been developed to explain and understand the mechanical behavior and chain dynamics of associating polymers, including the “living” reptation model by Cates [291,292], the “sticky” Rouse model [293], the “sticky” reptation model by Leibler, Rubinstein, Colby, and Semenov [294–296], and the phenomenological theories of transient networks [297–300]. These models provide a predictive relationship between molecular details and macroscopic mechanical properties. The “sticky” Rouse/reptation model, for example, can describe the rheological behavior of an associating polymer based upon the average number of associating groups per chain, the average fraction of bonded associations, and the average bonded association lifetime.

These models, however, only provide descriptions of parameters such as the viscosity and the chain relaxation time and still are unable to satisfactorily describe additional details of the mechanical spectra. Many computer experiments using molecular dynamics, Brownian dynamics, Monte Carlo, and hybrid MD/Monte Carlo algorithms have focused on associating polymer dynamics [301–307]. Improved synthetic techniques and computational capabilities continue to provide more powerful tools to approach the challenges in understanding the structure and dynamics of associating polymers.

---

## 14.7 CONCLUSION AND OUTLOOK

---

Our ability to guide materials formation through synthesis as well as directed assembly and fabrication continues to rapidly improve. These developments have opened the door to the possibility of not only improving upon materials properties but to begin making materials by design that can be used to address global challenges ranging from clean energy to health and human welfare. In this regard, nanostructured materials and nanotechnology are fundamental to the advancement of many fields. The fact that noncovalent interactions are ubiquitous in these materials underscores the importance of fully understanding the role that these interactions play in materials formation and function.

To date, various noncovalent interaction types have been utilized through different chemistries to design a myriad of reversible, supramolecular associating polymer materials, 2D materials, and nanoporous structures which have the potential to advance a new generation of materials that are highly interactive and that possess novel functionalities due to their reversible dynamical properties. Here, we have discussed different noncovalent bonding types, highlighting how such interactions play a key role in growth methods as well as defining structure and function. Indeed, we see that a vast array of application potential has already been demonstrated in the field of nanomaterials.

Fundamental to the design, discovery and understanding of new nanomaterials is the communication between theory and experiment. For example, we have discussed how a joint theory and experimental study led to the creation of a novel metal–organic framework material which exhibited enhanced resistance to degradation in air. Concomitant with our understanding of thermodynamic equilibrium properties as can be obtained from electronic structure methods is the need for better understanding of dynamics in nanomaterials systems. Here we discussed the thermodynamics and dynamics of associating polymers, including the current development and understanding of models that relate molecular information of associating polymers to their material properties. However, there are innumerable ways of incorporating different chemistries with varying numbers of noncovalent bond types, strengths, and the number of association groups in a polymer chain. As such, it is important to develop a predictive theory of associating polymers that encompasses all these different parameters.

Nevertheless, as theoretical methods that account for noncovalent interactions continue to mature, there is no doubt that even more novel materials will be discovered and understood, thus leading to their potential application in countless areas such as alternative energy technology, drug delivery, filtration and catalysis, which will have significant impacts on our daily lives.

## Acknowledgments

VRC was supported by the US Department of Energy, Office of Science, Basic Energy Sciences, Materials Sciences and Engineering Division. BGS, YW, and CNL acknowledge support at the Center for Nanophase Materials Sciences, a US Department of Energy Office of Science User Facility.

## References

- [1] R.P. Feynman, *Caltech Eng. Sci.* 23 (1960) 22.
- [2] Size of the nanoscale, <http://www.nano.gov/nanotech-101/what/nano-size>.
- [3] S.J. Pennycook, P.D. Nellist (Eds.), *Scanning Transmission Electron Microscopy—Imaging and Analysis*, Springer, 2011.
- [4] E. Ruska, *Rev. Mod. Phys.* 59 (1987) 627–638.
- [5] A.V. Crewe, J. Wall, J. Langmore, *Science* 168 (1970) 1338–1340.
- [6] A.V. Crewe, *Science* 154 (1966) 729–738.
- [7] Thomson Reuters, Web of Science, [www.webofknowledge.com](http://www.webofknowledge.com).
- [8] E. Roduner, *Chem. Soc. Rev.* 35 (2006) 583–592.
- [9] M. Haruta, *Chem. Rec.* 3 (2003) 75–87.
- [10] M. Haruta, S. Tsubota, T. Kobayashi, H. Kageyama, M. Genet, B. Delmon, *J. Catal.* 144 (1993) 175–192.
- [11] M.S. Chen, D.W. Goodman, *Science* 306 (2004) 252–255.
- [12] C.T. Campbell, J.C. Sharp, Y.X. Yao, E.M. Karp, T.L. Silbaugh, *Faraday Discuss.* 152 (2011) 227–239.
- [13] M. Faraday, *Philos. Trans. R. Soc. Lond.* 147 (1857) 145–181.
- [14] U. Kreibig, M. Vollmer, *Optical Properties of Metal Clusters*, Springer, 1995.
- [15] X. Qian, X.-H. Peng, D.O. Ansari, Q. Yin-Goen, G.Z. Chen, D.M. Shin, L. Yang, A.N. Young, M.D. Wang, S. Nie, *Nat. Biotechnol.* 26 (2008) 83.
- [16] A.Y. Sajjadi, A.A. Suratkar, K.K. Mitra, M.S. Grace, *J. Nanotechnol. Eng. Med.* 3 (2012) 021002.
- [17] J. Conde, F. Tian, Y. Hernández, C. Bao, D. Cui, K.-P. Janssen, M.R. Ibarra, P.V. Baptista, T. Stoeger, J.M. de la Fuente, *Biomaterials* 34 (2013) 7744–7753.
- [18] M. Horisberger, J. Rosset, *J. Histochem. Cytochem.* 25 (1977) 295–305.
- [19] E.L. Romano, M. Romano, *Immunochemistry* 14 (1977) 711–715.
- [20] R. Fetni, R. Drouin, N. Lemieux, P.E. Messier, C.L. Richer, *Proc. Natl. Acad. Sci.* 88 (1991) 10916–10920.

- [21] H. Kasamatsu, W. Lin, J. Edens, J.P. Revel, *Proc. Natl. Acad. Sci.* 80 (1983) 4339–4343.
- [22] A.C. Eifler, C.S. Thaxton, in: J.S. Hurst (Ed.), *Biomedical Nanotechnology: Methods and Protocols*, Humana Press, Totowa, NJ, 2011, pp. 325–338.
- [23] G. Han, P. Ghosh, V.M. Rotello, *Nanomedicine* 2 (2007) 113.
- [24] G. Han, P. Ghosh, V.M. Rotello, *Adv. Exp. Med. Biol.* 620 (2007) 48.
- [25] R. Langer, *Acc. Chem. Res.* 33 (2000) 94–101.
- [26] J.D. Gibson, B.P. Khanal, E.R. Zubarev, *J. Am. Chem. Soc.* 129 (2007) 11653–11661.
- [27] J. Conde, J. de la Fuente, P. Baptista, *Front. Pharmacol.* 4 (2013) 134.
- [28] T. Aida, E.W. Meijer, S.I. Stupp, *Science* 335 (2012) 813–817.
- [29] R. Dong, Y. Zhou, X. Huang, X. Zhu, Y. Lu, J. Shen, *Adv. Mater.* 27 (2015) 498–526.
- [30] C.R. Kagan, L.E. Fernandez, Y. Gogotsi, P.T. Hammond, M.C. Hersam, A. Nel, R.M. Penner, C.G. Willson, P.S. Weiss, *ACS Nano* 10 (2016) 9093–9103.
- [31] K. Liu, Y. Kang, Z. Wang, X. Zhang, *Adv. Mater.* 25 (2013) 5530–5548.
- [32] V. Georgakilas, J.N. Tiwari, K.C. Kemp, J.A. Perman, A.B. Bourlinos, K.S. Kim, R. Zboril, *Chem. Rev.* 116 (2016) 5464–5519.
- [33] K. Park, *ACS Nano* 7 (2013) 7442–7447.
- [34] P. Rogers (Ed.), *Nanoscience and Technology: A Collection of Reviews from Nature Journals*, 1st ed., World Scientific and Nature Publishing Group, Singapore, London, 2009.
- [35] G.R. Bhimanapati, et al., *ACS Nano* 9 (2015) 11509–11539.
- [36] L. Jiang, C.S. Sangeeth, C.A. Nijhuls, *J. Am. Chem. Soc.* 137 (2015) 10659.
- [37] N. Nerngchamnong, L. Yuan, D.-C. Qi, J. Li, D. Thompson, C.A. Nijhuis, *Nat. Nanotechnol.* 8 (2013) 113.
- [38] J.W. Steed, J.L. Atwood, *Supramolecular Chemistry*, John Wiley & Sons, 2013.
- [39] R. Zacharia, H. Ulbricht, T. Hertel, *Phys. Rev. B* 69 (2004) 155406.
- [40] L. Spanu, S. Sorella, G. Galli, *Phys. Rev. Lett.* 103 (2009) 196401.
- [41] W. Wang, S. Dai, X. Li, J. Yang, D.J. Srolovitz, Q. Zheng, *Nat. Commun.* 6 (2015) 7853.
- [42] T. Park, E.M. Todd, S. Nakashima, S.C. Zimmerman, *J. Am. Chem. Soc.* 127 (2005) 18133.
- [43] B.A. Blight, A. Camara-Campos, S. Djurdjevic, M. Kaller, D.A. Leigh, F.M. McMillan, H. McNab, A.M.Z. Slawin, *J. Am. Chem. Soc.* 131 (2009) 14116.
- [44] B.A. Blight, C.A. Hunter, D.A. Leigh, H. McNab, P.I.T. Thomson, *Nat. Chem.* 3 (2011) 244.
- [45] P. Cordier, F. Tournilhac, C. Soulié-Ziakovic, L. Leibler, *Nature* 451 (2008) 977–980.
- [46] A.M. Kushner, J.D. Vossler, G.A. Williams, Z. Guan, *J. Am. Chem. Soc.* 131 (2009) 8766.
- [47] R.P. Sijbesma, F.H. Beijer, L. Brunsveld, B.J.B. Folmer, J.H.K.K. Hirschberg, R.F.M. Lange, J.K.L. Lowe, E.W. Meijer, *Science* 278 (1997) 1601.
- [48] O.A. Scherman, G.B.W.L. Ligthart, R.P. Sijbesma, E.W. Meijer, *Angew. Chem. Int. Ed.* 45 (2006) 2072.
- [49] M.M.L. Nieuwenhuizen, T.F.A. de Greef, R.L.J. van der Bruggen, J.M.J. Paulusse, W.P.J. Appel, M.M.J. Smulders, R.P. Sijbesma, E.W. Meijer, *Chem. Eur. J.* 16 (2010) 1601.
- [50] T.F.A. de Greef, G. Ercolani, G.B.W.L. Ligthart, E.W. Meijer, R.P. Sijbesma, *J. Am. Chem. Soc.* 130 (2008) 13755.
- [51] K.E. Feldman, M.J. Kade, E.W. Meijer, C.J. Hawker, E.J. Kramer, *Macromolecules* 42 (2009) 9072.
- [52] K.E. Feldman, M.J. Kade, E.W. Meijer, C.J. Hawker, E.J. Kramer, *Macromolecules* 43 (2010) 5121.
- [53] G.M.L. van Gemert, J.W. Peeters, S.H.M. Söntjens, H.M. Janssen, A.W. Bosman, *Macromol. Chem. Phys.* 213 (2012) 234.
- [54] P.Y.W. Dankers, M.C. Harmsen, L.A. Brouwer, M.J.A.V. Luyn, E.W. Meijer, *Nat. Mater.* 4 (2005) 568.
- [55] P.Y. Dankers, E.N. van Leeuwen, G.M. van Gemert, A. Spiering, M.C. Harmsen, L.A. Brouwer, H.M. Janssen, A.W. Bosman, M.J. van Luyn, E. Meijer, *Biomaterials* 27 (2006) 5490.
- [56] P.Y. Dankers, J.M. Boomker, A.H. van der Vlag, E. Wisse, W.P. Appel, F.M. Smedts, M.C. Harmsen, A.W. Bosman, W. Meijer, M.J. van Luyn, *Biomaterials* 32 (2011) 723.
- [57] P.Y. Dankers, T.M. Hermans, T.W. Baughman, Y. Kamikawa, R.E. Kieltyka, M. Bastings, H.M. Janssen, N.A. Sommerdijk, A. Larsen, M.J. van Luyn, A.W. Bosman, *Adv. Mater.* 24 (2012) 2703.
- [58] P.Y.W. Dankers, M.J.A. van Luyn, A.H. van der Vlag, G.M.L. van Gemert, A.H. Petersen, E.W. Meijer, H.M. Janssen, A.W. Bosman, E.R. Popa, *Biomaterials* 33 (2012) 5144.
- [59] C. Wang, H. Wu, Z. Chen, M.T. McDowell, Y. Cui, Z. Bao, *Nat. Chem.* 5 (2013) 1042.
- [60] B.C.K. Tee, C. Wang, R. Allen, Z. Bao, *Nat. Nanotechnol.* 7 (2012) 825.
- [61] F. Iliovski, A.D. Mazzeo, R.F. Shepherd, X. Chen, G.M. Whitesides, *Angew. Chem.* 123 (2011) 1930–1935.

- [62] R.F. Shepherd, F. Ilievski, W. Choi, S.A. Morin, A.A. Stokes, A.D. Mazzeo, X. Chen, M. Wang, G.M. Whitesides, *Proc. Natl. Acad. Sci. USA* 108 (2011) 20400–20403.
- [63] K. Letchford, H. Burt, *Eur. J. Pharm. Biopharm.* 65 (2007) 259.
- [64] M. Rubinstein, A.V. Dobrynin, *Trends Polym. Sci.* 5 (1997) 181.
- [65] R.T. Liggins, H.M. Burt, *Adv. Drug Deliv. Rev.* 54 (2002) 191.
- [66] M.C. Jones, J.C. Leroux, *Eur. J. Pharm. Biopharm.* 48 (1999) 101.
- [67] G.S. Kwon, *Crit. Rev. Ther. Drug* 15 (1998) 32.
- [68] G.S. Kwon, K. Kataoka, *Adv. Drug Deliv. Rev.* 16 (1995) 295.
- [69] A. Lavanifar, J. Samuel, G.S. Kwon, *Adv. Drug Deliv. Rev.* 54 (2002) 169.
- [70] C. Allen, D. Maysinger, A. Eisenberg, *Colloids Surf. B* 16 (1999) 3.
- [71] K. Kataoka, A. Harada, Y. Nagasaki, *Adv. Drug Deliv. Rev.* 47 (2001) 113.
- [72] G. Gaucher, M. h. Dufresne, V.P. Sant, N. Kang, D. Maysinger, J.C. Leroux, *J. Control. Release* 109 (2005) 169.
- [73] H.M. Burt, X. Zhang, P. Toleikis, L. Embree, W.L. Hunter, *Colloids Surf. B* 16 (1999) 161.
- [74] H.S. Yoo, T.G. Park, *J. Control. Release* 70 (2001) 63.
- [75] B.S. Lele, J.C. Leroux, *Macromolecules* 35 (2002) 6714.
- [76] C. Kim, S.C. Lee, J.H. Shin, J.S. Yoon, I.C. Kwon, S.Y. Jeong, *Macromolecules* 33 (2000) 7448.
- [77] G. Kwon, M. Naito, M. Yokoyama, T. Okano, Y. Sakurai, K. Kataoka, *Langmuir* 9 (1993) 945.
- [78] K. Letchford, J. Zastre, R. Liggins, H. Burt, *Colloids Surf. B* 35 (2004) 81.
- [79] K.C. Taylor, H.A. Nasr-El-Din, *J. Pet. Sci. Eng.* 19 (1998) 265.
- [80] J. Bock, P.L. Valint, S.J. Pace, D.B. Siano, D.N. Schulz, S.R. Turner, in: G.A. Stahl, D.N. Schulz (Eds.), *Water-Soluble Polymers for Petroleum Recovery*, Springer US, Boston, MA, 1988, p. 147.
- [81] S. Burattini, B.W. Greenland, D.H. Merino, W. Weng, J. Seppala, H.M. Colquhoun, W. Hayes, M.E. Mackay, I.W. Hamley, S.J. Rowan, *J. Am. Chem. Soc.* 132 (2010) 12051.
- [82] S. Burattini, B.W. Greenland, W. Hayes, M.E. Mackay, S.J. Rowan, H.M. Colquhoun, *Chem. Mater.* 23 (2011) 6.
- [83] S. Burattini, H.M. Colquhoun, J.D. Fox, D. Friedmann, B.W. Greenland, P.J.F. Harris, W. Hayes, M.E. Mackay, S.J. Rowan, *Chem. Commun.* 44 (2009) 6717.
- [84] H.M. Colquhoun, Z. Zhu, *Angew. Chem.* 116 (2004) 5150.
- [85] H.M. Colquhoun, Z. Zhu, C.J. Cardin, M.G.B. Drew, Y. Gan, *Faraday Discuss.* 143 (2009) 205.
- [86] H.M. Colquhoun, Z. Zhu, C.J. Cardin, Y. Gan, *Chem. Commun.* 23 (2004) 2650.
- [87] H.M. Colquhoun, Z. Zhu, C.J. Cardin, Y. Gan, M.G.B. Drew, *J. Am. Chem. Soc.* 129 (2007) 16163.
- [88] H.M. Colquhoun, Z. Zhu, D.J. Williams, *Org. Lett.* 5 (2003) 4353.
- [89] S. Patwardhan, S. Sengupta, L.D.A. Siebbeles, F. Würthner, F.C. Grozema, *J. Am. Chem. Soc.* 134 (2012) 16147.
- [90] D.M. Eisele, C.W. Cone, E.A. Bloemsma, S.M. Vlaming, C.G.F. van der Kwaak, R.J. Silbey, M.G. Bawendi, J. Knoester, J.P. Rabe, D.V. Bout, *Nat. Chem.* 4 (2012) 655.
- [91] S.S. Babu, S. Prasanthkumar, A. Ajayaghosh, *Angew. Chem. Int. Ed.* 51 (2012) 1766.
- [92] Y. Sagara, T. Kato, *Angew. Chem.* 123 (2011) 9294.
- [93] A.P.H.J. Schenning, E.W. Meijer, *Chem. Commun.* 26 (2005) 3245.
- [94] R.E. Martin, F. Diederich, *Angew. Chem. Int. Ed.* 38 (1999) 1350.
- [95] J.M. Tour, *Chem. Rev.* 96 (1996) 537.
- [96] A. El-Ghayoury, E. Peeters, A.P.H.J. Schenning, E.W. Meijer, *Chem. Commun.* 19 (2000) 1969.
- [97] S. Xiao, J. Tang, T. Beetz, X. Guo, N. Tremblay, T. Siegrist, Y. Zhu, M. Steigerwald, C. Nuckolls, *J. Am. Chem. Soc.* 128 (2006) 10700.
- [98] B. El Hamaoui, L. Zhi, W. Pisula, U. Kolb, J. Wu, K. Mullen, *Chem. Commun.* 23 (2007) 2384.
- [99] A.P.H.J. Schenning, J. van Herrikhuyzen, P. Jonkheijm, Z. Chen, F. Würthner, E.W. Meijer, *J. Am. Chem. Soc.* 124 (2002) 10252.
- [100] E.H.A. Beckers, S.C.J. Meskers, A.P.H.J. Schenning, Z. Chen, F. Würthner, P. Marsal, D. Beljonne, J. Cornil, R.A.J. Janssen, *J. Am. Chem. Soc.* 128 (2006) 649.
- [101] A. Harada, K. Kataoka, *Macromolecules* 28 (1995) 5294.
- [102] A. Harada, K. Kataoka, *Science* 283 (1999) 65.
- [103] K. Kataoka, H. Togawa, A. Harada, K. Yasugi, T. Matsumoto, S. Katayose, *Macromolecules* 29 (1996) 8556.
- [104] A. Harada, K. Kataoka, *J. Macromol. Sci. A* 34 (1997) 2119.
- [105] A. Harada, K. Kataoka, *Macromolecules* 31 (1998) 288.
- [106] A.V. Kabanov, S.V. Vinogradov, Y.G. Suzdaltseva, V.Y. Alakhov, *Bioconj. Chem.* 6 (1995) 639.
- [107] A.V. Kabanov, T.K. Bronich, V.A. Kabanov, K. Yu, A. Eisenberg, *Macromolecules* 29 (1996) 6797.

- [108] A. Harada, K. Kataoka, *J. Am. Chem. Soc.* 121 (1999) 9241.
- [109] C. Wang, Q. Chen, Z. Wang, X. Zhang, *Angew. Chem.* 122 (2010) 8794–8797.
- [110] I. Koltover, T. Salditt, J.O. Rädler, C.R. Safinya, *Science* 281 (1998) 78.
- [111] J.O. Rädler, I. Koltover, T. Salditt, C.R. Safinya, *Science* 275 (1997) 810.
- [112] C.R. Safinya, *Curr. Opin. Struct. Biol.* 11 (2001) 440.
- [113] A.F. Thünemann, J. Beyeremann, C. von Ferber, H. Löwen, *Langmuir* 16 (2000) 850.
- [114] V.P. Torchilin, *J. Control. Release* 73 (2001) 137.
- [115] J.-Y. Sun, X. Zhao, W.R.K. Illeperuma, O. Chaudhuri, K.H. Oh, D.J. Mooney, J.J. Vlassak, Z. Suo, *Nature* 489 (2012) 133.
- [116] C. Faul, M. Antonietti, *Adv. Mater.* 15 (2003) 673–683.
- [117] M. Antonietti, A. Wenzel, A. Thünemann, *Langmuir* 12 (1996) 2111.
- [118] M. Antonietti, S. Henke, A. Thünemann, *Adv. Mater.* 8 (1996) 41.
- [119] Y. Guan, S.H. Yu, M. Antonietti, C. Böttcher, C.F.J. Faul, *Chem. Eur. J.* 11 (2005) 1305.
- [120] Department of Energy, Directing matter and energy: five challenges for science and the imagination, [http://science.energy.gov/~media/bes/pdf/reports/files/gc\\_rpt.pdf](http://science.energy.gov/~media/bes/pdf/reports/files/gc_rpt.pdf), 2007.
- [121] S. Jesse, A.Y. Borisevich, J.D. Fowlkes, A.R. Lupini, P.D. Rack, R.R. Unocic, B.G. Sumpter, S.V. Kalinin, A. Belyaninov, O.S. Ovchinnikova, *ACS Nano* 10 (2016) 5600.
- [122] K.S. Novoselov, D. Jiang, F. Schedin, T.J. Booth, V.V. Khotkevich, S.V. Morozov, A.K. Geim, *Proc. Natl. Acad. Sci.* 102 (2005) 10451–10453.
- [123] S. Bertolazzi, D. Krasnozhan, A. Kis, *ACS Nano* 7 (2013) 3246–3252.
- [124] W.J. Yu, Z. Li, H. Zhou, Y. Chen, Y. Wang, Y. Huang, X. Duan, *Nat. Mater.* 12 (2013) 246.
- [125] T. Georgiou, R. Jalil, B.D. Belle, L. Britnell, R.V. Gorbachev, S.V. Morozov, Y.-J. Kim, A. Gholinia, S.J. Haigh, O. Makarovsky, L. Eaves, L.A. Ponomarenko, A.K. Geim, K.S. Novoselov, A. Mishchenko, *Nat. Nanotechnol.* 8 (2013) 100.
- [126] C.R. Dean, A.F. Young, I. Meric, C. Lee, L. Wang, S. Sorgenfrei, K. Watanabe, T. Taniguchi, P. Kim, K.L. Shepard, J. Hone, *Nat. Nanotechnol.* 5 (2010) 722.
- [127] E.N. Hoffman, G. Yushin, M.W. Barsoum, Y. Gogotsi, *Chem. Mater.* 17 (2005) 2317–2322.
- [128] E.N. Hoffman, G. Yushin, T. El-Raghy, Y. Gogotsi, M.W. Barsoum, *Microporous Mesoporous Mater.* 112 (2008) 526–532.
- [129] M. Naguib, V. Presser, N. Lane, D. Tallman, Y. Gogotsi, J. Lu, L. Hultman, M.W. Barsoum, *RSC Adv.* 1 (2011) 1493–1499.
- [130] M. Naguib, M. Kurtoglu, V. Presser, J. Lu, J. Niu, M. Heon, L. Hultman, Y. Gogotsi, M.W. Barsoum, *Adv. Mater.* 23 (2011) 4248–4253.
- [131] M. Naguib, V.N. Mochalin, M.W. Barsoum, Y. Gogotsi, *Adv. Mater.* 26 (2014) 982.
- [132] S.J. Haigh, A. Gholinia, R. Jalil, S. Romani, L. Britnell, D.C. Elias, K.S. Novoselov, L.A. Ponomarenko, A.K. Geim, R. Gorbachev, *Nat. Mater.* 11 (2012) 764.
- [133] B.G. Sumpter, L. Liang, A. Nicolai, V. Meunier, *Acc. Chem. Res.* 47 (2014) 3395.
- [134] S. Wang, X. Wang, J.H. Warner, *ACS Nano* 9 (2015) 5246–5254.
- [135] Y. Jung, J. Shen, Y. Sun, J.J. Cha, *ACS Nano* 8 (2014) 9550–9557.
- [136] C. Huang, S. Wu, A.M. Sanchez, J.J.P. Peters, R. Beanland, J.S. Ross, W.Y. Pasqual Rivera, D.H. Cobden, X. Xu, *Nat. Mater.* 13 (2014) 1096.
- [137] Y. Gong, et al., *Nat. Mater.* 13 (2014) 1135.
- [138] X. Duan, C. Wang, J.C. Shaw, R. Cheng, Y. Chen, H. Li, X. Wu, Y. Tang, Q. Zhang, A. Pan, J. Jiang, R. Yu, Y. Huang, X. Duan, *Nat. Nanotechnol.* 9 (2014) 1024.
- [139] M.-Y. Li, Y. Shi, C.-C. Cheng, L.-S. Lu, Y.-C. Lin, H.-L. Tang, M.-L. Tsai, C.-W. Chu, K.-H. Wei, J.-H. He, W.-H. Chang, K. Suenaga, L.-J. Li, *Science* 349 (2015) 524–528.
- [140] J.H. Yu, H.R. Lee, S.S. Hong, D. Kong, H.-W. Lee, H. Wang, F. Xiong, S. Wang, Y. Cui, *Nano Lett.* 15 (2015) 1031–1035.
- [141] Y. Yu, S. Hu, L. Su, L. Huang, Y. Liu, Z. Jin, A.A. Purezky, D.B. Geohegan, K.W. Kim, Y. Zhang, L. Cao, *Nano Lett.* 15 (2015) 486–491.
- [142] H. Heo, J.H. Sung, G. Jin, J.-H. Ahn, K. Kim, M.-J. Lee, S. Cha, H. Choi, M.-H. Jo, *Adv. Mater.* 27 (2015) 3803–3810.
- [143] F.S. Bates, G.H. Fredrickson, *Phys. Today* 52 (1999) 32.
- [144] Y. Mai, A. Eisenberg, *Chem. Soc. Rev.* 41 (2012) 5969.



- [145] J.K. Kim, S.Y. Yang, Y. Lee, Y. Kim, *Prog. Polym. Sci.* 35 (2010) 1325.
- [146] B.D. Olsen, *Macromol. Chem. Phys.* 214 (2013) 1659.
- [147] A.C. Obermeyer, B.D. Olsen, *ACS Macro Lett.* 4 (2015) 101.
- [148] B.D. Olsen, *AIChE J.* 59 (2013) 3558.
- [149] S. Jesse, Q. He, A.R. Lupini, D.N. Leonard, M.P. Oxley, O. Ovchinnikov, R.R. Unocic, A. Tselev, M. Fuentes-Cabrera, B.G. Sumpter, S.J. Pennycook, S.V. Kalinin, A.Y. Borisevich, *Small* 11 (2015) 5895–5900.
- [150] R.R. Unocic, A.R. Lupini, A.Y. Borisevich, D.A. Cullen, S.V. Kalinin, S. Jesse, *Nanoscale* 8 (2016) 15581–15588.
- [151] J.D. Fowlkes, R. Winkler, B.B. Lewis, M.G. Stanford, H. Plank, P.D. Rack, *ACS Nano* 10 (2016) 6163–6172.
- [152] E.Y. Andrei, G. Li, X. Du, *Rep. Prog. Phys.* 75 (2012) 056501.
- [153] K.S. Novoselov, A.K. Geim, S.V. Morozov, D. Jiang, Y. Zhang, S.V. Dubonos, I.V. Grigorieva, A.A. Firsov, *Science* 306 (2004) 666–669.
- [154] The 2010 Nobel Prize in Physics – press release, [http://www.nobelprize.org/nobel\\_prizes/physics/laureates/2010/press.html](http://www.nobelprize.org/nobel_prizes/physics/laureates/2010/press.html).
- [155] C. Lee, X. Wei, J.W. Kysar, J. Hone, *Science* 321 (2008) 385–388.
- [156] R.R. Nair, P. Blake, A.N. Grigorenko, K.S. Novoselov, T.J. Booth, T. Stauber, N.M.R. Peres, A.K. Geim, *Science* 320 (2008) 1308.
- [157] D. Song, S. Liu, V. Paltoglou, D. Gallardo, L. Tang, J. Zhao, J. Xu, N.K. Efremidis, Z. Chen, *2D Mater.* 2 (2015) 034007.
- [158] A.H. Castro Neto, F. Guinea, N.M.R. Peres, K.S. Novoselov, A.K. Geim, *Rev. Mod. Phys.* 81 (2009) 109–162.
- [159] J.C. Charlier, P.C. Eklund, J. Zhu, A.C. Ferrari, in: A. Jorio, G. Dresselhaus, M.S. Dresselhaus (Eds.), *Carbon Nanotubes: Advanced Topics in the Synthesis, Structure, Properties and Applications*, Springer-Verlag, Berlin, Heidelberg, 2008, p. 673.
- [160] K. Novoselov, A.K. Geim, S. Morozov, D. Jiang, M. Katsnelson, I. Grigorieva, S. Dubonos, A. Firsov, *Nature* 438 (2005) 197–200.
- [161] H.L. Stormer, P. Kim, *Nature* 438 (2005) 201.
- [162] M. Katsnelson, K. Novoselov, A. Geim, *Nat. Phys.* 2 (2006) 620.
- [163] E. Hendry, P.J. Hale, J. Moger, A.K. Savchenko, S.A. Mikhailov, *Phys. Rev. Lett.* 105 (2010) 097401.
- [164] F. Bonaccorso, Z. Sun, T. Hasan, A.C. Ferrari, *Nat. Photonics* 4 (2010) 611.
- [165] D.-E. Jiang, V.R. Cooper, S. Dai, *Nano Lett.* 9 (2009) 4019–4024.
- [166] J. Schrier, *J. Phys. Chem. Lett.* 1 (2010) 2284–2287.
- [167] S.P. Surwade, S.N. Smirnov, I.V. Vlassiouk, R.R. Unocic, G.M. Veith, S. Dai, S.M. Mahurin, *Nat. Nanotechnol.* 10 (2015) 459.
- [168] T. Björkman, A. Gulans, A.V. Krasheninnikov, R.M. Nieminen, *Phys. Rev. Lett.* 108 (2012) 235502.
- [169] M.A. McGuire, H. Dixit, V.R. Cooper, B.C. Sales, *Chem. Mater.* 27 (2015) 612–620.
- [170] O.A. Vydrov, T. Van Voorhis, *J. Chem. Phys.* 133 (2010) 244103.
- [171] J. Klimeš, D.R. Bowler, A. Michaelides, *Phys. Rev. B* 83 (2011) 195131.
- [172] S. Grimme, *J. Comput. Chem.* 27 (2006) 1787–1799.
- [173] X. Li, J. Yang, *J. Mater. Chem. C* 2 (2014) 7071–7076.
- [174] S. Balendhran, S. Walia, H. Nili, S. Sriram, M. Bhaskaran, *Small* 11 (2015) 640.
- [175] P. Vogt, P. De Padova, C. Quaresima, J. Avila, E. Frantzeskakis, M.C. Asensio, A. Resta, B. Ealet, G. Le Lay, *Phys. Rev. Lett.* 108 (2012) 155501.
- [176] S. Cahangirov, M. Audiffred, P. Tang, A. Iacomino, W. Duan, G. Merino, A. Rubio, *Phys. Rev. B* 88 (2013) 035432.
- [177] L. Li, M. Zhao, *Phys. Chem. Chem. Phys.* 15 (2013) 16853–16863.
- [178] F. Zhu, W. Chen, Y. Xu, C. Gao, D. Guan, C. Liu, D. Qian, S. Zhang, J. Jia, *Nat. Mater.* 14 (2015) 1020.
- [179] H. Liu, A.T. Neal, Z. Zhu, Z. Luo, X. Xu, D. Tománek, P.D. Ye, *ACS Nano* 8 (2014) 4033–4041.
- [180] Z.A. Piazza, H.-S. Hu, W.-L. Li, Y.-F. Zhao, J. Li, L.-S. Wang, *Nat. Commun.* 5 (2014) 3113.
- [181] K. Takeda, K. Shiraishi, *Phys. Rev. B* 50 (1994) 14916–14922.
- [182] G.G. Guzmán-Verri, L.C. Lew Yan Voon, *Phys. Rev. B* 76 (2007) 075131.
- [183] Y.-P. Wang, H.-P. Cheng, *Phys. Rev. B* 87 (2013) 245430.
- [184] H. Liu, J. Gao, J. Zhao, *J. Phys. Chem. C* 117 (2013) 10353–10359.
- [185] A. Ramirez-Torres, D. Le, T.S. Rahman, *IOP Conf. Ser., Mater. Sci. Eng.* 76 (2015) 012011.
- [186] S.Z. Butler, et al., *ACS Nano* 7 (2013) 2898–2926.
- [187] P. Miro, M. Audiffred, T. Heine, *Chem. Soc. Rev.* 43 (2014) 6537–6554.
- [188] S. Dai, et al., *Nat. Nanotechnol.* 10 (2015) 682.

- [189] X. Li, A.A. Puzetzy, X. Sang, S. KC, M. Tian, F. Ceballos, M. Mahjouri-Samani, K. Wang, R.R. Unocic, H. Zhao, G. Duscher, V.R. Cooper, C. Rouleau, D.B. Geohegan, K. Xiao, *Adv. Funct. Mater.* (2016), <http://dx.doi.org/10.1002/adfm.201603850>.
- [190] X. Li, M.-W. Lin, L. Basile, S.M. Hus, A.A. Puzetzy, J. Lee, Y.-C. Kuo, L.-Y. Chang, K. Wang, J.C. Idrobo, A.-P. Li, C.-H. Chen, C.M. Rouleau, D.B. Geohegan, K. Xiao, *Adv. Mater.* 28 (2016) 8240–8247.
- [191] Y. Cai, Q. Ke, G. Zhang, Y.-W. Zhang, *J. Phys. Chem. C* 119 (2015) 3102–3110.
- [192] X. Li, J. Feng, E. Wang, S. Meng, J. Klimeš, A. Michaelides, *Phys. Rev. B* 85 (2012) 085425.
- [193] B. Anasori, Y. Xie, M. Beidaghi, J. Lu, B.C. Hosler, L. Hultman, P.R.C. Kent, Y. Gogotsi, M.W. Barsoum, *ACS Nano* 9 (2015) 9507.
- [194] L.L. Handy, N.W. Gregory, *J. Am. Chem. Soc.* 74 (1952) 891–893.
- [195] B. Morosin, A. Narath, *J. Chem. Phys.* 40 (1964) 1958–1967.
- [196] I. Pollini, *Solid State Commun.* 106 (1998) 549–554.
- [197] H. Wang, V. Eyert, U. Schwingenschlöggl, *J. Phys. Condens. Matter* 23 (2011) 116003.
- [198] C. Felsler, G. Fecher, B. Balke, *Angew. Chem. Int. Ed.* 46 (2007) 668–699.
- [199] M. Hirscher, B. Panella, in: *Proceedings of the 9th International Symposium on Metal–Hydrogen Systems, Fundamentals and Applications (MH2004)*, *J. Alloys Compd.* 404–406 (2005) 399–401.
- [200] S. Brunauer, P.H. Emmett, E. Teller, *J. Am. Chem. Soc.* 60 (1938) 309–319.
- [201] C.A. Silvera Batista, R.G. Larson, N.A. Kotov, *Science* 350 (2015) 6257.
- [202] A.M. Reilly, A. Tkatchenko, *Chem. Sci.* 6 (2015) 3289–3301.
- [203] R.A. DiStasio, O.A. von Lilienfeld, A. Tkatchenko, *Proc. Natl. Acad. Sci.* 109 (2012) 14791–14795.
- [204] C. Wagner, N. Fournier, V.G. Ruiz, C. Li, K. Müllen, M. Rohlfing, A. Tkatchenko, R. Temirov, F.S. Tautz, *Nat. Commun.* 5 (2014) 5568.
- [205] N. Planas, A.L. Dzubak, R. Poloni, L.-C. Lin, A. McManus, T.M. McDonald, J.B. Neaton, J.R. Long, B. Smit, L. Gagliardi, *J. Am. Chem. Soc.* 135 (2013) 7402–7405.
- [206] G. Román-Pérez, M. Moaied, J.M. Soler, F. Yndurain, *Phys. Rev. Lett.* 105 (2010) 145901.
- [207] R. Poloni, B. Smit, J.B. Neaton, *J. Am. Chem. Soc.* 134 (2012) 6714–6719.
- [208] K.S. Sing, in: *Proceedings of the Third International TRI/Princeton Workshop Characterization of Porous Materials: From Angstroms to Millimeters*, *Colloids Surf. A* 241 (2004) 3–7.
- [209] J.R. Morris, C.I. Contescu, M.F. Chisholm, V.R. Cooper, J. Guo, L. He, Y. Ihm, E. Mamontov, Y.B. Melnichenko, R.J. Olsen, S.J. Pennycook, M.B. Stone, H. Zhang, N.C. Gallego, *J. Mater. Chem. A* 1 (2013) 9341.
- [210] J. Guo, J.R. Morris, Y. Ihm, C.I. Contescu, N.C. Gallego, G. Duscher, S.J. Pennycook, M.F. Chisholm, *Small* 8 (2012) 3283–3288.
- [211] P.J.F. Harris, *Crit. Rev. Solid State Mater. Sci.* 30 (2005) 235–253.
- [212] T.X. Nguyen, N. Cohaut, J.-S. Bae, S.K. Bhatia, *Langmuir* 24 (2008) 7912–7922.
- [213] Y. Shi, *J. Chem. Phys.* 128 (2008) 234707.
- [214] J. Pikunic, C. Clinard, N. Cohaut, K.E. Gubbins, J.-M. Guet, R.J.-M. Pellenq, I. Rannou, J.-N. Rouzaud, *Langmuir* 19 (2003) 8565–8582.
- [215] W. Dmowski, C.I. Contescu, A. Llobet, N.C. Gallego, T. Egami, *J. Phys. Chem. C* 116 (2012) 2946–2951.
- [216] L.J. Peng, J.R. Morris, *Carbon* 50 (2012) 1394–1406.
- [217] M.A. Smith, H.C. Foley, R.F. Lobo, *Carbon* 42 (2004) 2041–2048.
- [218] Y. Liu, B.I. Yakobson, *Nano Lett.* 10 (2010) 2178–2183.
- [219] T. Lenosky, X. Gonze, M. Teter, V. Elser, *Nature* 355 (1992) 333.
- [220] F. Banhart, J. Kotakoski, A.V. Krasheninnikov, *ACS Nano* 5 (2011) 26–41.
- [221] S. Patchkovskii, J.S. Tse, S.N. Yurchenko, L. Zhechkov, T. Heine, G. Seifert, *Proc. Natl. Acad. Sci. USA* 102 (2005) 10439–10444.
- [222] Y. Ihm, V.R. Cooper, L. Peng, J.R. Morris, *J. Phys. Condens. Matter* 24 (2012) 424205.
- [223] Y. Ihm, V.R. Cooper, N.C. Gallego, C.I. Contescu, J.R. Morris, *J. Chem. Theory Comput.* 10 (2014) 1–4.
- [224] I. Cabria, M.J. López, J.A. Alonso, *Phys. Rev. B* 78 (2008) 075415.
- [225] S. Beyaz, F.D. Lamari, B. Weinberger, P. Langlois, *Int. J. Hydrogen Energy* 35 (2010) 217–224.
- [226] F.S. Baker, R.K. Beckler, J.R. Miller, Z.Q. Yan, Highly microporous carbons and process of manufacturing, US patent 5965483, 1999.
- [227] F.S. Baker, Production of highly microporous activated carbon products, US patent 5416056, 1995.
- [228] F.S. Baker, Highly microporous carbon, US patent 5710092, 1998.
- [229] V.V. Bhat, C.I. Contescu, N.C. Gallego, F.S. Baker, *Carbon* 48 (2010) 1331–1340.

- [230] M. Jordá-Beneyto, F. Suárez-García, D. Lozano-Castelló, D. Cazorla-Amorós, A. Linares-Solano, *Carbon* 45 (2007) 293.
- [231] V. Cooper, L. Kong, D. Langreth, *Phys. Proc.* 3 (2010) 1417–1430.
- [232] T. Sagara, J. Ortony, E. Ganz, *J. Chem. Phys.* 123 (2005) 214707.
- [233] J. Lee, D. Olson, L. Pan, T. Emge, J. Li, *Adv. Funct. Mater.* 17 (2007) 1255–1262.
- [234] A. Lan, K. Li, H. Wu, L. Kong, N. Nijem, D.H. Olson, T.J. Emge, Y.J. Chabal, D.C. Langreth, M. Hong, J. Li, *Inorg. Chem.* 48 (2009) 7165–7173.
- [235] L. Kong, V.R. Cooper, N. Nijem, K. Li, J. Li, Y.J. Chabal, D.C. Langreth, *Phys. Rev. B* 79 (2009) 081407.
- [236] S. Zuluaga, P. Canepa, K. Tan, Y.J. Chabal, T. Thonhauser, *J. Phys. Condens. Matter* 26 (2014) 133002.
- [237] N. Nijem, H. Wu, P. Canepa, A. Marti, K.J. Balkus, T. Thonhauser, J. Li, Y.J. Chabal, *J. Am. Chem. Soc.* 134 (2012) 15201–15204.
- [238] W.S. Drisdell, R. Poloni, T.M. McDonald, J.R. Long, B. Smit, J.B. Neaton, D. Prendergast, J.B. Kortright, *J. Am. Chem. Soc.* 135 (2013) 18183–18190.
- [239] N. Nijem, P. Canepa, U. Kaipa, K. Tan, K. Roodenko, S. Tekarli, J. Halbert, I.W.H. Oswald, R.K. Arvapally, C. Yang, T. Thonhauser, M.A. Omary, Y.J. Chabal, *J. Am. Chem. Soc.* 135 (2013) 12615–12626.
- [240] G. Li, V.R. Cooper, J.-H. Cho, S. Du, H.-J. Gao, Z. Zhang, *Phys. Rev. B* 84 (2011) 241406.
- [241] G. Li, I. Tamblyn, V.R. Cooper, H.-J. Gao, J.B. Neaton, *Phys. Rev. B* 85 (2012) 121409.
- [242] G. Li, T. Rangel, Z.-F. Liu, V.R. Cooper, J.B. Neaton, *Phys. Rev. B* 93 (2016) 125429.
- [243] G. Mercurio, E.R. McNellis, I. Martin, S. Hagen, F. Leyssner, S. Soubatch, J. Meyer, M. Wolf, P. Tegeder, F.S. Tautz, K. Reuter, *Phys. Rev. Lett.* 104 (2010) 036102.
- [244] M. Dell'Angela, G. Kladnik, A. Cossaro, A. Verdini, M. Kamenetska, I. Tamblyn, S.Y. Quek, J.B. Neaton, D. Cvetko, A. Morgante, L. Venkataraman, *Nano Lett.* 10 (2010) 2470–2474.
- [245] C. Tuma, J. Sauer, *Phys. Chem. Chem. Phys.* 8 (2006) 3955–3965.
- [246] A. Tkatchenko, R.A. DiStasio, R. Car, M. Scheffler, *Phys. Rev. Lett.* 108 (2012) 236402.
- [247] B.D. Olsen, J.A. Kornfield, D.A. Tirrell, *Macromolecules* 43 (2010) 9094.
- [248] M.J. Glassman, J. Chan, B.D. Olsen, *Adv. Funct. Mater.* 23 (2013) 1182.
- [249] M. Wei, B. Li, R.L.A. David, S.C. Jones, V. Sarohia, J.A. Schmitgal, J.A. Kornfield, *Science* 350 (2015) 72.
- [250] J.P. Chen, A.S. Huffman, *Biomaterials* 11 (1990) 631–634.
- [251] Y.G. Takei, T. Aoki, K. Sanui, N. Ogata, Y. Sakurai, T. Okano, M. Matsukata, A. Kikuchi, *Bioconjug. Chem.* 5 (1994) 577–582.
- [252] R.B. Fong, Z. Ding, A.S. Hoffman, P.S. Stayton, *Biotechnol. Bioeng.* 79 (2002) 271–276.
- [253] M. Taniguchi, M. Kobayashi, M. Fujii, *Biotechnol. Bioeng.* 34 (1989) 1092–1097.
- [254] T. Shimoboji, E. Larenas, T. Fowler, S. Kulkarni, A.S. Hoffman, P.S. Stayton, *Proc. Natl. Acad. Sci. USA* 99 (2002) 16592–16596.
- [255] K.J. Mackenzie, M.B. Francis, *J. Am. Chem. Soc.* 135 (2013) 293–300.
- [256] M. Gupta, B. Mattiasson, *Methods of Biochemical Analysis: Bioanalytical Applications of Enzymes*, Wiley Online Library, vol. 36, 2006, pp. 1–34.
- [257] E. Krasovitski, Y. Cohen, H. Bianco-Peled, *J. Polym. Sci., Part B, Polym. Phys.* 42 (2004) 3713–3720.
- [258] A. Meier-Koll, V. Pipich, P. Busch, C.M. Papadakis, P. Müller-Buschbaum, *Langmuir* 28 (2012) 8791–8798.
- [259] K. Nishi, T. Hiroi, K. Hashimoto, K. Fujii, Y.-S. Han, T.-H. Kim, Y. Katsumoto, M. Shibayama, *Macromolecules* 46 (2013) 6225–6232.
- [260] T. Koga, F. Tanaka, R. Motokawa, S. Koizumi, F.M. Winnik, *Macromol. Symp.* 291–292 (2010) 177–185.
- [261] M. Alaghemandi, E. Spohr, *Macromol. Theory Simul.* 21 (2012) 106–112.
- [262] E. Autieri, E. Chiessi, A. Lonardi, G. Paradossi, M. Sega, *J. Phys. Chem. B* 115 (2011) 5827–5839.
- [263] S.A. Deshmukh, S.K.R.S. Sankaranarayanan, K. Suthar, D.C. Mancini, *J. Phys. Chem. B* 116 (2012) 2651–2663.
- [264] S.A. Deshmukh, Z. Li, G. Kamath, K.J. Suthar, S.K. Sankaranarayanan, D.C. Mancini, *Polymer* 54 (2013) 210–222.
- [265] M. Rubinstein, A.V. Dobrynin, *Curr. Opin. Colloid Interface Sci.* 4 (1999) 83–87.
- [266] P.J. Flory, *J. Am. Chem. Soc.* 63 (1941) 3083.
- [267] W.H. Stockmayer, *J. Chem. Phys.* 11 (1943) 45.
- [268] A. Coniglio, H.E. Stanley, W. Klein, *Phys. Rev. Lett.* 42 (1979) 518.
- [269] A. Coniglio, H.E. Stanley, W. Klein, *Phys. Rev. B* 25 (1982) 6805.
- [270] M. Daoud, A. Coniglio, *J. Phys. A* 14 (1981) L301.
- [271] F. Tanaka, A. Matsuyama, *Phys. Rev. Lett.* 62 (1989) 2759.

- [272] F. Tanaka, *Macromolecules* 22 (1989) 1988.
- [273] F. Tanaka, *Macromolecules* 23 (1990) 3784.
- [274] W.H. Stockmayer, *Macromolecules* 24 (1991) 6367.
- [275] F. Tanaka, M. Ishida, *Physica A* 204 (1994) 660.
- [276] F. Tanaka, W.H. Stockmayer, *Macromolecules* 27 (1994) 3943.
- [277] F. Tanaka, *Adv. Colloid Interface Sci.* 63 (1996) 23.
- [278] M. Ishida, F. Tanaka, *Macromolecules* 30 (1997) 3900.
- [279] A.N. Semenov, I.A. Nyrkova, M.E. Cates, *Macromolecules* 28 (1995) 7879.
- [280] A.N. Semenov, M. Rubinstein, *Macromolecules* 31 (1998) 1373.
- [281] S.K. Kumar, A.Z. Panagiotopoulos, *Phys. Rev. Lett.* 82 (1999) 5060.
- [282] S.K. Kumar, J.F. Douglas, *Phys. Rev. Lett.* 87 (2001) 188301.
- [283] M. Rubinstein, A.N. Semenov, *Macromolecules* 31 (1998) 1386.
- [284] M.E. Cates, *J. Phys. (Paris)* 46 (1985) 1059.
- [285] M. Muthukumar, *J. Chem. Phys.* 83 (1985) 3161.
- [286] M.E. Cates, T.C.B. McLeish, M. Rubinstein, *J. Phys. Condens. Matter* 2 (1990) 749.
- [287] L. Bromberg, *Macromolecules* 31 (1998) 6148–6156.
- [288] P.E. Rouse, *J. Chem. Phys.* 21 (1953) 1272.
- [289] P.G. de Gennes, *J. Chem. Phys.* 55 (1971) 572.
- [290] M. Doi, S.F. Edwards, *The Theory of Polymer Dynamics*, Oxford University Press, Oxford, 1986.
- [291] M.E. Cates, *Europhys. Lett.* 4 (1987) 497.
- [292] M.E. Cates, *Macromolecules* 20 (1987) 2289.
- [293] Q. Chen, G.J. Tudryn, R.H. Colby, *J. Rheol.* 57 (2013) 1441.
- [294] L. Leibler, M. Rubinstein, R.H. Colby, *Macromolecules* 24 (1991) 4701.
- [295] M. Rubinstein, A.N. Semenov, *Macromolecules* 34 (2001) 1058.
- [296] A.N. Semenov, M. Rubinstein, *Macromolecules* 35 (2002) 4821.
- [297] M.S. Green, A.V. Tobolsky, *J. Chem. Phys.* 14 (1946) 80.
- [298] A.S. Lodge, *Trans. Faraday Soc.* 52 (1956) 120.
- [299] F. Tanaka, S.F. Edwards, *Macromolecules* 25 (1992) 1516.
- [300] M. Yamamoto, *J. Phys. Soc. Jpn.* 11 (1956) 413.
- [301] Y. Masubuchi, *Annu. Rev. Chem. Biomol. Eng.* 5 (2014) 11.
- [302] C.E. Sing, A. Alexander-Katz, *Phys. Rev. Lett.* 107 (2011) 198302.
- [303] Z. Li, H. Djohari, E.E. Dormidontova, *J. Chem. Phys.* 133 (2010) 184904.
- [304] Y. Li, B. Abberton, M. Kröger, W. Liu, *Polymers* 5 (2013) 751.
- [305] R.S. Hoy, G.H. Fredrickson, *J. Chem. Phys.* 131 (2009) 224902.
- [306] P.G. Khalatur, A.R. Khokhlov, D.A. Mologin, *J. Chem. Phys.* 109 (1998) 9602.
- [307] P.G. Khalatur, A.R. Khokhlov, D.A. Mologin, *J. Chem. Phys.* 109 (1998) 9614.

# Subject Index

---

## Symbols

- $\delta^{\text{HF}}$  correction, 15
- $\pi$ - $\pi$  interactions, 421, 425–427
- $\pi$ -interactions, 105, 119–122
- $\sigma$ -hole, 23
- $\sigma$ -interactions, 119–122

## A

- Ab initio methods, 137–157, 392, 393
- ACP, *see* Atom-centered potentials
- Active pharmaceutical ingredient, 357
- Adatom-bound ligands, 400, 402
- Additivity, 3
- Adiabatic connection, 74, 75, 78, 79, 87–90
- Adiabatic connection fluctuation-dissipation theorem (ACFDT), 74, 75, 87–90
- Adiabatic connection formula, 244
- ALL, *see* Andersson–Langreth–Lundqvist functional
- AMBER force field, 405
- Andersson–Langreth–Lundqvist functional (ALL), 248
- Antisymmetry, 5
- Argon dimer, 22
- Asymmetric unit cell, 339
- Asymptotic correction, 8
- Asymptotic limit, 246
- ATM, *see* Dispersion, Axilrod–Teller–Muto term
- Atom-centered potentials (ACP), 222, 224–237
- Atomistic model, 339
- Avante-Garde Simulation, 348

## B

- Band transport, 280
- Base functional, 186–189
- Basis set convergence, 307, 310
- Basis set extrapolation, 84, 85, 92, 93, 124–126, 144, 145
- Basis set incompleteness, 230, 237
- Basis set superposition error (BSSE), 7, 142, 143, 309–311
- BDE, *see* Bond dissociation enthalpy
- Becke–Roussel exchange-hole model (BR), 174–176
- BEEF-vdW, 268
- Binding energy, 138, *see also* Interaction energy
- Block copolymers, 424, 427, 429
- Bond dissociation enthalpy (BDE), 235–237
- Born–Mayer repulsion, 13

- Born–Mayer repulsion (modified), 13
- BR, *see* Becke–Roussel exchange-hole model (BR)
- Brueckner equation, 83, 84
- BSSE, *see* Basis set superposition error

## C

- C21 set, 191, 305
- Cambridge Crystallographic Data Centre, 347
- Carbon dioxide (crystalline)
  - bulk modulus, 311, 313
  - Fermi resonance, 317
  - molar volume, 312
  - phase diagram, 315
  - sublimation temperature, 313
  - thermochemistry, 312, 313
- Carbon nanotubes, 388
- Casimir effect, 390
- Casimir–Polder Equation, 203
- CASPT2 method, 393, 398, 399, 401
- CASSCF, *see* Complete active space SCF method
- Cavitation energy, 367
- CCSD, *see* Coupled-cluster theory with singles and doubles
- CCSD(T), *see* Coupled-cluster theory with singles, doubles, and perturbative triples
- Charge penetration, 278
- Charge transfer, 58–60
- Charge-carrier transport, 280
  - hopping process, 280
  - in anthradithiophenes, 290, 291
- Charge-transfer energy, 17, 22
- Chiral separation, 358
- Cholesky decomposition, 149–151
- CIS, *see* Configuration interaction singles
- CISD, *see* Configuration interaction singles and doubles
- Cleavage energy, 432, 433
- Closure approximation, 170
- Clustering, 343
- Complete active space SCF method (CASSCF), 393
- Configuration interaction singles and doubles (CISD), 392
- Configuration interaction singles (CIS), 392
- Conformational minima, 344
- Copper (110) surface
  - benzene adsorption, 395–400

- Copper (111) surface  
  benzene adsorption, 395–400
- Correlation potential (Kohn–Sham), 91, 109  
  influence of van der Waals interactions, 110
- Coulomb/exchange potentials, 223
- Counterpoise correction, 142, 143, 310, *see also* Basis set  
  superposition error
- Coupled MP2 (MP2C), 161, 310
- Coupled-cluster theory  
  dispersion weighted, 153, 163  
  explicitly correlated, 152, 153  
  multireference (MRCC), 393  
  singles, doubles, and perturbative triples (CCSD(T)),  
    67, 92, 138, 143, 144, 162, 163, 392  
  singles and doubles (CCSD), 67, 161, 392  
  spin-component-scaled singles and doubles  
    (SCS-CCSD), 161, 162  
  use in fragment methods, 308, 310, 312, 316
- Coupling constant, 244
- Coupling constant integration, 250
- Crystal structure prediction (CSP), 333–358  
  blind tests, 304  
  method hierarchy, 351  
  multicomponent systems, 349  
  NMR crystallography, 320, 321  
  stoichiometry, 338  
  work-flow, 336
- Crystallographic space, 339
- CrystalPredictor, 345
- CSP, *see* Crystal structure prediction
- Cytochrome c, 387
- D**
- Damping function, 183–186  
  Becke–Johnson, 183–186  
  Tang–Toennies, 20
- DCACP, *see* Dispersion-correcting atom centered  
  potentials
- DCP, *see* Dispersion-correcting potentials
- DDsC, *see* Density-dependent correction model (dDsC)
- Deformation energy, 126
- Deformation simulations, 294
- Delocalization error, 189
- Delta-HF correction, 15
- Density fitting, 147–151
- Density-dependent correction model (dDsC), 176, 177
- Density-functional theory (DFT), 163, 164, 241
- Density-functional tight binding (DFTB), 305
- DFT, *see* Density-functional theory
- DFT-D2 method, 196–198, 393
- DFT-D3 method, 198, 305, 393, 397, 401, 405, 409, 410  
  C-six-only variant, 202, 203  
  effects on non-covalent interaction energies, 212  
  HF-D3, 395  
  three-body dispersion, 209, 210  
  with Becke–Johnson damping, 201, 202, 393, 397, 409,  
    410  
  with zero damping, 201, 393, 397  
  with zero damping (DFT-D3(0)), 198  
  DFT-D3(0), *see* DFT-D3 method with zero damping  
  DFT-D3(BJ), *see* DFT-D3 method with Becke–Johnson  
    damping, *see also* Damping function,  
    Becke–Johnson  
  DFT-D3(CSO), *see* DFT-D3 method, C-six-only variant  
  DFT-SAPT, 6, *see also* SAPT(DFT)
- DFTB, *see* Density-functional tight binding
- Dielectric tensor, 251
- Diffusion quantum Monte-Carlo (DMC), 105
- Dipole moment, 8, 111, 112
- Dipole oscillator strength distribution (DOSD), 114, 115
- Dipole–dipole polarizabilities, 112–114
- Disordermer, 291  
  benzodithiophene, 291
- Dispersion, 7, 18–21, 32, 60, 61, 67, 70, 93, 102, 103, 109,  
  139, 279, 389  
  Axilrod–Teller–Muto (ATM) term, 209  
  balancing intermolecular and solvent dispersion, 404,  
    406  
  competitive dispersive and covalent forces, 399  
  damping function, 20  
  dispersion coefficients, 19, 21, 114, 115, 169–186,  
    195–210, 247–249  
  dispersion coefficients environment dependence, 182,  
    183  
  Drude model, 18  
  effects on molecular geometries, 213, 214  
  effects on thermochemistry, 213  
  implicit solvent dispersion, 404  
  intramolecular interactions, 105–108  
  London formula, 247, 389  
  London model, 169–171  
  many-body, 21, 73  
  multipole expansion, 19  
  Salem model, 171
- Dispersion energy, 5, 7, 18–21
- Dispersion-correcting atom centered potentials  
  (DCACP), 228
- Dispersion-correcting potentials (DCP), 228–237  
  B3LYP-DCP, 233, 234
- Distributed multipoles, 11
- Distributed multipoles analysis (DMA), 340
- Distributed polarizabilities, 16
- DMA, *see* Distributed multipoles analysis
- DMC, *see* Diffusion quantum Monte-Carlo

- Dobson's classification of dispersion contributions,  
389–395, 409, 410  
cooperativity (Dobson-B), 390  
long-range fluctuations (Dobson-C), 390, 391, 395, 409  
many-body effects (Dobson-B), 390  
screening (Dobson-B), 390
- Double-hybrid density functionals, 395
- Drude model, 17
- ## E
- ECP, *see* Effective core potentials
- EDA | *see* energy decomposition analysis, 28
- Effective core potentials (ECP), 222–224
- Electronic coupling, 280  
in azapentacenes, 289, 290
- Electronic structure method, 339
- Electrostatic energy, 7
- Electrostatic interactions, 7–11, 32, 51–56, 278, 421, 427, 428  
base functional effects, 188, 189
- Embedding, 365, 366  
apparent surface charge (ASC) formulation, 370–372  
atomistic models, 366  
continuum models, 366  
electronic transitions, 378–383  
electrostatic, 309, 321, 368  
induced dipole formulation, 372, 373  
polarizable models, 369–373
- Enantiomeric excess, 358
- Energy barrier, 338
- Energy decomposition analysis (EDA), 28, 29  
absolutely localized molecular orbital (ALMO), 44, 45  
block-localized-wavefunction (BLW), 44, 45  
comparison, 48–61  
Hayes and Stone conditions, 28  
in H<sub>2</sub> triplet, 48–61  
in simple molecules, 51–61  
interacting quantum atoms (IQA), 45–48  
Kitaura–Morokuma, 42, 43  
localized molecular orbital (LMOEDA), 43, 44  
natural EDA (NEDA), 44  
orbital-based methods, 41–45  
pair interaction EDA (PIEDA), 44, 45  
real-space methods, 41, 42, 45–48  
supermolecular approaches, 40–48  
Ziegler–Rauk (ZREDA), 43
- Energy landscape, 23  
benzene dimer, 23  
helium dimer, 66, 110
- Enhancement factor, 253
- Entropy, 406
- Environment effects, 365, 366  
direct and indirect effects, 374
- Escaped charge, 367
- Exchange, 5
- Exchange enhancement factor, 186–188
- Exchange hole, 171, 172
- Exchange-correlation energy, 243
- Exchange-correlation hole, 245
- Exchange-correlation potential, 243
- Exchange-dispersion, 6, 7, 37, 38
- Exchange-hole dipole moment model (XDM), 171–173, 304, 305, 394, 397, 410  
dispersion coefficients environment dependence, 182, 183  
for periodic systems, 189–192  
pairwise dispersion coefficients, 177–180  
three-body dispersion coefficients, 179, 180
- Exchange-induction, 6, 7, 37, 38
- Exchange-repulsion, 12–14, 33–35, 37, 56–58, 279  
base functional effects, 186–188  
density overlap model, 13
- Exchange-repulsion energy, 7
- Exfoliation energy, 432
- ## F
- FCI, *see* Full configuration interaction
- Feynman conjecture, 109
- Fluctuation-dissipation theorem, 87–90
- Fluorination of polymers, 281, 282
- Fluorination of small aromatic molecules, 281
- Focal-point analysis, 145–147
- Fock equation, 223
- Force field, 339
- Fragment methods, 156, 157, 307–309, *see also* Hybrid  
many-body interaction  
binary interaction, 309, 315, 317  
chemical shielding, 321–324  
generalized energy-based fragmentation, 309  
incremental methods, 308, 309
- Free energy  
in crystals, 311–314, 316  
in polymorphism, 404  
of self assembly, 404
- Frozen natural orbitals, 150, 151
- Full configuration interaction (FCI), 67
- ## G
- Gas–metal scattering, 388
- Gauge-including projector augmented wave model (GIPAW), 319–321
- Gaussian expansion, 224
- Gelation, 441, 442
- Generalized Born model, 369
- Generalized gradient approximation (GGA), 241  
GGA, *see* Generalized gradient approximation

- GIPAW, *see* Gauge-including projector augmented wave model
- Gold (111) surface  
1,10-phenanthroline adsorption, 400, 401  
benzene adsorption, 395–400
- Gold nanoparticles, 417, 418
- Gold–sulfur bonding, 401–403  
Au(0)-thiyl, 403  
Au(I)-thiolate, 403
- Graphene, 388, 430–432
- Growth of nanomaterials, 428–430  
alternative growth techniques, 429, 430  
bottom-up growth, 429  
top-down growth, 428, 429
- GW method, 393
- ## H
- Halogen bond, 23
- Hansen solubility parameters, 293
- Hartree–Fock method (HF), 66, 392, 393, 395
- Helium dimer, 66, 110
- HF, *see* Hartree–Fock method
- HF dimer, 22
- HF...CIF dimer, 23
- Hildebrand parameters, 293
- Hirshfeld atomic partition, 181
- Homogeneous electron gas, 72
- Host–guest complex, 123
- Hybrid many-body interaction  
applications, 316, 318  
quasiharmonic approximation, 312, 313  
theory, 309
- Hydrocarbon conformers, 105
- Hydrogen bond, 22, 93, 102, 421–423
- Hydrophobic interactions, 421, 424, 425
- ## I
- Ice phase XV, 315, 316
- IDISP set, 105–108
- Implicit solvent dispersion, 404
- Induction, 7, 14–18, 32, 58–60, 279  
base functional effects, 188, 189  
co-operativity, 15  
Drude model, 17  
multipole expansion, 16  
non-additivity, 14
- Induction energy, 5, 7, 14–16
- Interacting quantum atoms (IQA), 45–48
- Interaction energy, 137  
argon dimer, 22  
benzene dimer, 23  
helium dimer, 66, 110  
HF dimer, 22
- HF...CIF dimer, 23
- Interaction energy benchmark systems  
IDISP benchmark systems, 105–108  
S12L benchmark systems, 123, 124  
S22 benchmark systems, 92–100  
S66 benchmark systems, 100–105
- Interaction tensors, 10
- Intermediate normalization, 29
- Intermolecular interactions  
in conventional DFT, 227, 228
- Intramolecular interactions, 105–108
- ISA, *see* Iterated stockholder analysis
- Iterated stockholder analysis (ISA), 11
- ## K
- Kannemann–Becke set, 179, 184
- Kernel, 253
- ## L
- Lattice energy, 156, 157, 304–311, 336–343  
benchmarks, 305  
benzene crystal, 151, 156  
C21 set, 305  
static infinite lattice, 341  
X23 set, 305
- LDA, *see* Local density approximation
- Lennard–Jones repulsion, 13
- Link atom, 224, 366
- Local correlation methods, 154–156
- Local density approximation (LDA), 241, 395
- Local potential, 223
- Locally dense basis set, 321, 322
- London formula, 247
- London model, 169–171
- ## M
- Many-body dispersion method (MBD), 305, 316, 394, 397, 401, 405, 406, 408–410
- Many-body expansion, 156, 157  
chemical shielding, 321  
energy, 307, 308
- Many-body theory, 246
- Material junctions, 388
- MAX phase materials, 434
- MBD, *see* Many-body dispersion method
- Metal nobility, 402
- Metal–organic framework materials (MOFs), 436–438
- Mixed ab initio/DFT methods, 393, 409
- MOF, *see* Metal–organic framework materials
- Molecular properties, 109–115  
dipole moments, 111, 112  
dipole–dipole polarizabilities, 112–114  
dispersion (van der Waals) coefficients, 114, 115



- Møller–Plesset perturbation theory (MP2), 67, 106, 159, 392  
coupled MP2 (MP2C), 161, 310  
dispersion-weighted, 160  
MP2.5, 161, 310  
periodic, 307  
spin-component scaled, 159, 160  
use in fragment methods, 310
- MOLPAK, 345
- MP2, *see* Møller–Plesset perturbation theory
- MP2.5, 161, 310
- MP2C, *see* Coupled MP2
- MRCC, *see* Multireference coupled cluster theory
- Multipole expansion, 10
- Multipole moments, 8–10  
distributed, 11  
general, 9  
hexadecapole, 9  
octopole, 9  
quadrupole, 8
- Multireference coupled cluster theory (MRCC), 393
- Multiscale methods, 365
- N**
- Nanomaterials, 417–419
- Nanoporous carbon, 435, 436
- Natural bond orbitals, 18
- NBO method, 18
- NMR, *see* Nuclear magnetic resonance
- Noncovalent interactions in conventional DFT, 227, 228
- Nonlocal exchange-correlation, 241
- Nonlocal potential, 223
- Nuclear magnetic resonance (NMR), 318–324  
9-*tert*-butyl anthracene ester (9-TBAE) chemical shifts, 324  
applications, 319–321, 324  
benchmarks, 322, 323  
chemical shielding, 318–324  
chemical shift referencing, 323, 324  
crystallography, 318, 319  
fragment-based methods, 321–324  
GIPAW approach, 319–321
- O**
- OEP, *see* Optimized effective potential method
- ONIOM method, 368
- Optimized effective potential method (OEP), 91, 92
- Organic semiconductors, 277, 311
- P**
- Pair correlation function, 73
- Pairwise additivity, 3, 156
- Pauli principle, 5
- Pauli repulsion, 223
- Penetration effects, 7, 8
- Penetration energy, 11
- Penetration error, 11
- Perturbation theory, 29–33, 105–107  
Brillouin–Wigner, 30, 31  
interaction energy expansion, 108  
Murrell–Shaw / Musher–Amos (MS-MA), 35  
polarization approximation, 31–33  
Rayleigh–Schrödinger, 29–31  
Stone–Hayes intermolecular perturbation theory, 36, 37  
symmetry-adapted, 6
- Phase diagrams, 313–316
- Phonons, 314, *see also* Quasiharmonic approximation  
quasiharmonic approximation, 312  
thermochemistry, 312, 318
- Plane wave simulations, 227
- Plasmon dispersion, 252
- Plasmon frequency, 248
- Plasmon oscillation, 72
- Plasmon-pole approximation, 252
- Polarizability  
atom-in-molecule, 181, 182  
dipole–dipole, 14  
dipole–quadrupole, 16  
distributed polarizabilities, 16  
frequency-dependent, 19  
imaginary-frequency, 19  
quadrupole–quadrupole, 16
- Polarization, 14
- Polarization catastrophe, 16
- Polymers, 440–443
- Polymorph screening, 353
- Polymorphic impurity, 356
- Polymorphism, 303, 333, 404  
acetaminophen (paracetamol), 304, 305  
aspirin, 305, 317, 318  
chiral crystals, 305  
conformational, 303, 319–321, 338  
disappearing polymorphs, 334  
disordered polymorph, 356  
free energy, 404  
glycine, 305  
isotopic, 303  
manufacturing process, 355  
polymorph screening, 353  
polymorphic impurity, 356
- Promolecular density, 181
- Pseudo-orbitals, 222, 223
- Pseudohalogen, 225
- Q**
- QCP, *see* Quantum capping potentials

- QM/continuum models, 368  
 simulation of IR and NMR spectra, 374–378  
 QM/MM methods, 224–227, 366–369  
 QMC, *see* Quantum Monte-Carlo  
 Quadrupole moment, 8  
 Quantum capping potentials (QCP), 225–227  
 Quantum electrodynamics, 390, 391  
 Quantum fluctuations, 389–391  
 Quantum Monte-Carlo (QMC), 393  
 Diffusion quantum Monte-Carlo (DMC), 105, 128  
 Quasiharmonic approximation  
 applications, 312, 313  
 theory, 311, 312
- R**
- Random-phase approximation (RPA), 72, 391, 392  
 based on Kohn–Sham reference determinants, 74–76  
 derivation, 77–80  
 equations, 77, 78  
 excitation energies, 77  
 EXX-RPA method, 82  
 in beryllium dimer, 85, 86  
 including additional many-body terms, 82–84  
 including exchange interactions, 80–82  
 including third-order corrections, 84  
 normal RPA, 77  
 orbital-optimized RPA, 91, 92  
 ORPA method, 92  
 particle–particle RPA, 90, 91  
 range-separated, 84–87  
 RPA+rSE method, 83  
 RPAX method, 85, 86  
 RPAX-SO1 method, 86, 87  
 RPAX-SO2 method, 86, 87  
 RPAX2 method, 81, 82  
 sccRPA method, 112  
 SOSEX method, 81  
 Range separation (of the Coulomb operator), 85  
 Rare gas dimers, 22, 67, 110  
 Reduced gradient, 253  
 Reduced solvent, 30  
 Repulsion, 12–14  
 anisotropic, 13  
 Response function, 244  
 Riccati equation, 80  
 RPA, *see* Random-phase approximation  
 Rubrene, 278, 288, 289, 311
- S**
- S12L set, 123, 124  
 S22 set, 92–100  
 S66 set, 100–105  
 Salem model, 171
- SAPT, *see* Symmetry-adapted perturbation theory  
 SAPT(DFT), 6, 39, 40, *see also* DFT-SAPT  
 Scaling of computational cost, 388, 393, 395, 407, 408  
 linear scaling, 388  
 Self-assembly, 426, 427, 429, 438  
 free energy, 404  
 porphyrin on graphite, 404–407  
 self-assembled monolayers, 404–407  
 Shielding potential, *see* Local potential  
 Short-range repulsion, 12–14  
 Sigma-hole, 23  
 Silicon dioxide nanoparticles, 390  
 Silicon interfaces, 388  
 Silicon transistors, 388  
 Silver (111) surface  
 benzene adsorption, 395–400  
 Size consistency, 67, 68  
 Size extensivity, 67, 68  
 Stockholder analysis  
 in pyridine, 11  
 iterated, 11  
 Stockholder procedure, 11  
 Supermolecular method, 66, 108  
 Symmetry-adapted perturbation theory (SAPT), 6,  
 33–40, 108, 109, 115–119, 163, 164  
 in crystals, 309
- T**
- Tamm–Dancoff approximation (TDA), 78, *see also*  
 Configuration interaction singles (CIS)  
 TDA, *see* Tamm–Dancoff approximation  
 TDDFT, *see* Time-dependent density-functional theory  
 TDHF, *see* Time-dependent Hartree–Fock  
 Templating, 357, 358  
 Thermal expansion, 312, 313  
 Thermodynamic energy, 338  
 Time-dependent density-functional theory (TDDFT),  
 391, 395  
 Time-dependent Hartree–Fock (TDHF), 73  
 Tkatchenko–Scheffler method (TS), 305, 394  
 Transition metal dichalcogenides, 434  
 Triplet instability, 74  
 Truncation error, 11  
 TS, *see* Tkatchenko–Scheffler method  
 Two-dimensional materials, 430–434
- U**
- Unsöld approximation, *see* Closure approximation
- V**
- Valence tautomerization, 403  
 Van der Waals heterostructures, 433, 434  
 Van der Waals interactions, 304–307, 310, 313, 314,  
 317–319, *see also* Dispersion

- VdW-DF functionals, 241
    - self-consistency, 256
    - spin, 256
    - vdW-DF1, 264, 393, 394, 396, 397, 401, 405, 409, 410
    - vdW-DF1-C09, 267
    - vdW-DF1-cx, 267
    - vdW-DF1-optB88, 267
    - vdW-DF1-optPBE, 267
    - vdW-DF2, 265, 393, 394, 396, 397, 401, 405, 409, 410
  - Vibrational spectroscopy, 316–318, *see also* Phonons
    - Fermi resonance, 317
    - terahertz, 316, 317
  - VV09 method, 258
  - VV10 method, 258, 269
- X**
- X23 set, 191, 305
  - XDM, *see* Exchange-hole dipole moment model
- Z**
- Zeolite catalysts, 438, 439